Ewa Piętka
Jacek Kawa (Eds.)

Information Technologies in Biomedicine

Volume 2

Springer

Advances in Intelligent and Soft Computing   69

Editor-in-Chief: J. Kacprzyk

Advances in Intelligent and Soft Computing

Editor-in-Chief

Prof. Janusz Kacprzyk
Systems Research Institute
Polish Academy of Sciences
ul. Newelska 6
01-447 Warsaw
Poland
E-mail: kacprzyk@ibspan.waw.pl

Further volumes of this series can be found on our homepage: springer.com

Ewa Piętka and Jacek Kawa (Eds.)

Information Technologies in Biomedicine

Volume 2

Springer

Editors

Prof. Ewa Piętka
Silesian University of Technology
Faculty of Automatic Control
Electronics and Computer Science
ul. Akademicka 16
44-100 Gliwice
Poland
E-mail: epietka@polsl.pl

Prof. Jacek Kawa
Silesian University of Technology
Faculty of Automatic Control
Electronics and Computer Science
ul. Akademicka 16
44-100 Gliwice
Poland
E-mail: jkawa@polsl.pl

Foreword

Significant development in medical diagnosis and therapy, observed in recent years, is undoubtedly connected with the development of computer systems of information processing on the basis of the improvement of technology and construction of electronic devices, application of theory and appropriate algorithms as well as development of tools used in the software development process. Possible benefits obtained in all branches of medicine are unquestionable.

The progress of civilization results in an increase of the disease rate in muscoskeletal and cardiovascular systems, tumours being predominant in medical statistics. Furthermore, factors concerning aging of population, traffic accidents, sports activity, in particular extreme sports, demand modern medical techniques and technologies. The solution of complex problems concerning diagnostics and medical therapy is possible thanks to the development of interdisciplinary cooperation of experts from diverse branches of medical and engineering fields. The engineering knowledge defined as biomedical engineering is covering biosystems, biomaterials, biomechanics and rehabilitation engineering, biomedical imaging as well as computer and telemedicine systems, neural networks and medical physics.

The development of biomedical engineering undoubtedly reflects the present state of the art and knowledge of biological reality. Mainly, it depends on the application of new cognitive and diagnostic methods that use the latest achievements from the field of natural sciences and technology.

Issues concerning biomedical engineering are actively developed in many scientific and clinical centres all over the world, which is manifested by a stream of reports, publications and papers. Thus, their periodic analysis and synthesis is required. In consequence, comprehensive studies enriching the present state of the art are published. The studies will be useful in the

arrangement of knowledge and its application, in the production of medical devices and the elaboration of innovative diagnostic and therapeutic procedures in clinical practice. The papers presented in this book are pursuing the above denoted aims.

Gliwice, June 2010   Jan Marciniak

Preface

Information Technology in Biomedicine is an interdisciplinary research area, that bridges the gap between methodological achievements in engineering and clinical requirements in medical diagnosis and therapy. It is an emerging field focusing on collaboration between physicians, scientists, and technicians in order to define and meet patients needs. Many of these areas are recognized as research and development frontiers in employing new technology in clinical environment. These include image-guided diagnosis and treatment, biotechnology, biomaterials, biometrics, telemedicine and home care. New approaches to information technologies increase the efficiency of medical diagnostic and treatment and permit more information to be extracted from the acquired data. In this book, members of the academic society of technical and medical background present their research results and clinical implementation in order to satisfy the functional requirements of authorized physicians for the benefit of the patients.

An extended area is covered by the articles. It includes biomedical signals, medical image processing, computer-aided diagnosis and surgery, biometrics, healthcare and telemedicine, biomechanics, biomaterials, bioinformatics. Section on bronchoscopy presents the basis as well as new research studies performed in this field. Papers present various theoretical approaches and new methodologies based on fuzzy sets, mathematical statistics, mathematical morphology, fractals, wavelets, syntactic methods, artificial neural networks, graphs and many others.

We would like to express our gratitude to all paper reviewers as well as the authors who have contributed their original research papers.

Gliwice,   Ewa Piętka
June 2010   Jacek Kawa

Contents

Part II: Computer Aided Surgery

Computer-Assisted Navigation in Brain Tumor Surgery 203
Zbigniew Kotwica, Agnieszka Saracen

**Computer Aided Alternative Methods of Dental Implants
Placement** 211
Jarosław Żmudzki

Part III: Biometrics

**An Idea of Human Voice Reaction Measurement System
under the Aspect of Behavioral Biometric** 219
Andrzej W. Mitas, Marcin D. Bugdol

Biomedically Aided Car Driver Safety System 229
Andrzej W. Mitas, Artur Ryguła

Part IV: Signal Processing

Part VI: Telemedicine

**Data Integration in Multimodal Home Care Surveillance
and Communication System**   391
Piotr Augustyniak, Magdalena Smoleń, Anna Broniec, Jacek Chodak

**Open Standards as a Basis of the Information Services
Platform in Health Care Area**   403
Kazimierz Frączkowski, Michał Szczepaniak

Part VII: Biomechanics

**Application of Motion Analysis Systems in the Designing
of a Rehabilitation Device**   417
*Robert Michnik, Jacek Jurkojć, Zbigniew Paszenda,
Andrzej Michnik, Michał Bachorz, Wiesław Rycerski, Jan Janota*

Part IX: Magnetic Field

On a Hybrid Fuzzy Clustering Method

Tomasz Przybyła, Janusz Jeżewski, and Dawid Roj

Abstract. This paper presents a new hybrid fuzzy clustering method. In the proposed method, cluster prototypes are values that minimize the introduced generalized cost function. The proposed method can be considered as a generalization of fuzzy c–means (FCM) method as well as the fuzzy c–median (FCMed) clustering method. The generalization of the cluster cost function is made by applying the L_p norm. The values that minimize the proposed cost function have been chosen as the cluster prototypes. The weighted myriad is a special case of the cluster prototype when the L_p norm is the L_2 norm. The cluster prototypes are the weighted meridians for the L_1 norm. Artificial data set is used to demonstrate the performance of proposed method, and the obtained results are compared to the results from the FCM method.

1 Introduction

Let us consider a set of objects $\mathbf{O} = \{o_1, \ldots, o_N\}$. The object set consists of unlabeled data, i.e. labels are not assigned to objects. The goal of clustering is to find existing subsets in the $\mathbf{O}$ set. Objects from one group have a high degree of similarity, while they have a high degree of dissimilarity with objects from other groups. Subsets that are found among the objects of the $\mathbf{O}$ set are called *clusters* [1, 2].

In most cases, each o_i object from the $\mathbf{O}$ object set is represented by an $\mathbf{x}$ vector in the s-dimensional space i.e. $\mathbf{x} \in \mathbb{R}^s$. The set $\mathbf{X} = \{\mathbf{x}_1, \ldots, \mathbf{x}_N\}$ is called the object

Tomasz Przybyła
Silesian University of Technology, Institute of Electronics,
Akademicka Str 16, 44-101 Gliwice, Poland
e-mail: Tomasz.Przybyla@polsl.pl

Janusz Jeżewski · Dawid Roj
Institute of Medical Technology and Equipment ITAM, Departament of Biomedical
Informatics, Roosvelta Str 118, 41-800 Zabrze, Poland

data representation of **O**. In such a case, the l-th component of the k-th feature vector $\mathbf{x}_k$ gives a measure of l-th feature (e.g. length of flower petal, age of car, weight) of the k-th object o_k.

One of the most popular clustering method is the fuzzy c–means (FCM) method. In this method, cluster prototypes are computed as the fuzzy means [2]. However, one of the most important inconvenience of the FCM method is its sensitivity to outliers i.e. there are feature vectors which component (or components) have quite different value compared to other feature vectors. There are many modifications for the limitation of the outliers influence. In the first modification, the L_2 norm is replaced by the L_1 norm and by the generalized L_p norm [3]. Another approach has been proposed by Krishnapuram and Keller [4, 5]. This clustering approach is based on possibilistic theory instead on fuzzy theory. One of the most interesting modification has been proposed by Kersten. In this method the L_2 norm is replaced by the L_1 norm, and the cluster prototypes are computed as fuzzy medians [6].

The use of heavy tailed distribution to model the impulsive noise gives better results than the use of Gaussian distribution [7, 8, 9, 10]. One of the havy tailed distribution is the Cauchy distribution, where the location parameter is called (sample) myriad [11]. The fuzzy myriads have been used as the cluster prototypes in the fuzzy c–myriads (FCMyr) clustering method [12]. Another example of the heavy tailed distribution is the Meridian distribution proposed by Aysal and Berner [13]. The location parameter for the Meridian distribution is called (sample) meridian. In the adaptative fuzzy c–meridians (AFCMer) clustering method, the cluster prototypes were computed as fuzzy meridians [14]. The myriad is the maximum likelihood estimator of the location parameter for the Cauchy distribution, so is the meridian for the Meridian distribution. The form of cost function for sample meridian is very similar to the sample meridian cost function. The L_2 norm is used for the myriad cost function, where for the meridian cost function, the L_1 norm is used. In this paper, the generalized cost function is presented. In the proposed cost function, the L_p norm is used. Assuming $p = 2$ the generalized cost function becomes the myriad cost function, while for $p = 1$ the proposed cost function becomes the meridian cost function. Such a generalized cost function is used to determine the cluster prototypes in proposed clustering algorithm. The paper is organized as follows. Section II gives the genaralized cost function. The proposed clustering algorithm is introduced in Section III. Section IV contains numerical examples. The last section contains some conclusions and ideas for future research.

2   Generalized Cost Function

2.1   *Weighted Myriad*

The probability density function (PDF) of the Cauchy distribution is described in the following way

$$f(x;\Theta) = \left(\frac{K}{\pi}\right)\frac{1}{K^2+(x-\Theta)^2} \quad , \tag{1}$$

where Θ is the location parameter, and K is the scaling factor ($K > 0$). The Figure 1 shows the PDF of the Cauchy distribution for scale parameter $K = 1$ and location $\Theta = 0$ (solid line) and the PDF of the normal distribution $N(0,1)$ (dashed line). It can be noticed that the Cauchy distribution has heavier tails.

(a)   (b)
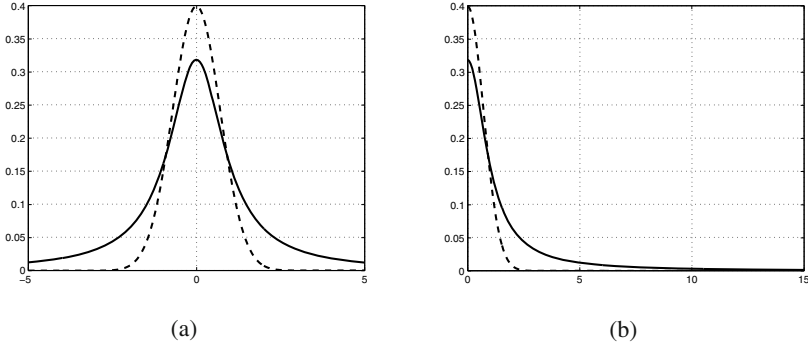
Fig. 1 Cauchy (solid line) and Normal (dashed line) probability density functions

For the given set of N independent and identically distributed (i.i.d.) samples each obeying the Cauchy distribution with the common scale parameter K, the sample myriad $\hat{\Theta}_K$ is a value that minimizes the cost function Ψ_K defined as follows [15]

$$\begin{aligned}
\hat{\Theta}_K &= \arg\min_{\Theta \in \mathbb{R}} \sum_{k=1}^{N} \log\left[K^2 + (x_k - \Theta)^2\right] \\
&= \arg\min_{\Theta \in \mathbb{R}} \Psi_K(\mathbf{x};\Theta) \\
&= myriad\left\{x_k|_{k=1}^{N};K\right\}
\end{aligned} \tag{2}$$

By assigning non–negative weights to the input samples, the weighted myriad $\hat{\Theta}_K$ is derived as a generalization of the sample myriad. For the N i.i.d. observations $\{x_k\}_{k=1}^{N}$ and the $\{u_k\}_{k=1}^{N}$, the weighted myriad can be computed from the following expression

$$\begin{aligned}
\hat{\Theta}_K &= \arg\min_{\Theta \in \mathbb{R}} \sum_{k=1}^{N} \log\left[K^2 + u_k(x_k - \Theta)^2\right] \\
&= \arg\min_{\Theta \in \mathbb{R}} \Psi_K(\mathbf{x},\mathbf{u};\Theta) \\
&= myriad\left\{u_k * x_k|_{k=1}^{N};K\right\}
\end{aligned} \tag{3}$$

The value of weighted myriad depends on the data set **x**, the assigned weights **u** and the parameter K, called a linearity parameter. Two interesting cases may occur. First, when the K value tends to infinity (i.e. $K \to \infty$), then the value of weighted myriad converges with the weighted mean, that is

$$\lim_{K \to \infty} \hat{\Theta}_K = \frac{\sum_{k=1}^{N} u_k x_k}{\sum_{k=1}^{N} u_k} \quad , \tag{4}$$

where $\hat{\Theta}_K = myriad \left\{ u_k * x_k |_{k=1}^{N}; K \right\}_{k=1}^{N}$. This property is called myriad linear property [11, 15].

Second case, called modal property, occurs when the value of K parameter tends to zero (i.e. $K \to 0$). In this case the value of the weighted myriad is always equal to one of most frequent values in the input data set, i.e.:

$$\hat{\Theta}_0 = \arg \min_{x_j \in \Xi} \prod_{k=1, x_k \neq x_j}^{N} \left| x_k - x_j \right| \quad , \tag{5}$$

where

$$\hat{\Theta}_0 = \lim_{K \to 0} \hat{\Theta}_K \quad ,$$

and Ξ is a set that contains the most frequent data in the input data set **x**. The value $\hat{\Theta}_K$ is defined in the same way as in the linear property.

For the data set $\mathbf{x} = \{0.13, 0.16, 0.27, 0.39, 0.86, 0.90, 0.95, 0.97, 0.99\}$ and the assigned weights $\mathbf{u} = \{0.70, 0.60, 0.39, 0.94, 0.26, 0.02, 0.04, 0.08, 0.05\}$, the example of possible shapes of the weighted myriad cost function (3) are presented in Figure 2.

2.2 Weighted Meridian

The random variable formed as the ratio of two independent zero–mean Laplacian distributed random variables is refered to as the Meridian distribution. The Meridian distribution has been proposed by Aysal and Berner [13]. The form of the proposed distribution is given by

$$f(x; \delta) = \left(\frac{\delta}{2} \right) \frac{1}{(\delta + |x|)^2} \quad . \tag{6}$$

The standard Cauchy and Meridian PDFs are plotted in Figure 3 , where $K = \delta = 1$. It can be seen that the Meridian distribution has heavier tails than the Cauchy distribution. For the given set of N i.i.d. samples $\{x_k\}_{k=1}^{N}$ each obeying the Meridian distribution with the common scale parameter δ, the sample meridian $\hat{\beta}_\delta$ is given by [13]
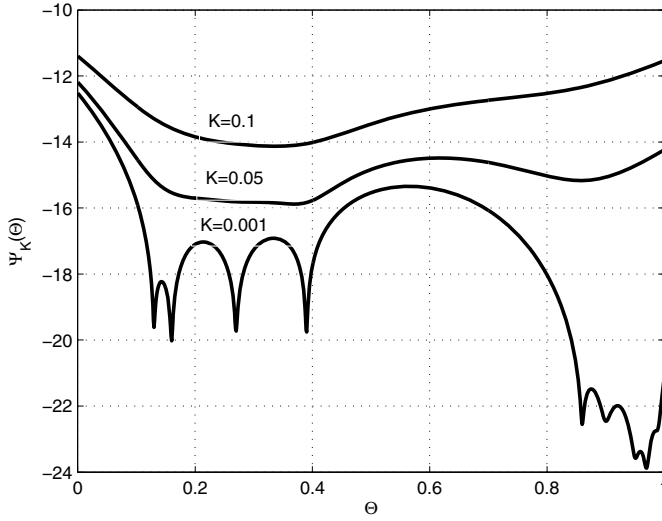
Fig. 2 An illustration of the shape of weighted myriad cost function
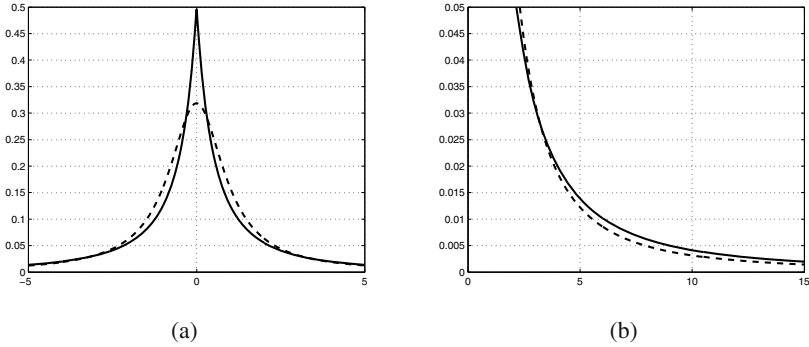
Fig. 3 The Meridian distribution (solid line) and the Cauchy (dashed line) distribution

$$\hat{\beta}_\delta = \arg \min_{\beta \in \mathbb{R}} \sum_{k=1}^{N} \log \left[\delta + |x_k - \beta| \right]$$
$$= \arg \min_{\beta \in \mathbb{R}} \phi_\delta \left(\mathbf{x}; \beta \right) \quad , \tag{7}$$
$$= meridian \left\{ x_k |_{k=1}^{N}; \delta \right\}$$

where Φ_δ is the sample meridian cost function. Parameter δ is called the medianity parameter.

The sample meridian $\hat{\beta}_\delta$ is the ML estimator of the location parameter for the Meridian distribution. The sample meridian can be generalized to the weighted

meridian by assigning non–negative weights to the input samples. So, the weighted meridian is given by

$$
\begin{aligned}
\hat{\beta}_\delta &= \arg \min_{\beta \in \mathbb{R}} \sum_{k=1}^{N} \log \left[\delta + u_k |x_k - \beta| \right] \\
&= \arg \min_{\beta \in \mathbb{R}} \phi_\delta \left(\mathbf{x}, \mathbf{u}; \beta \right) \\
&= meridian \left\{ u_k * x_k |_{k=1}^{N}; \delta \right\}
\end{aligned} \tag{8}
$$

The behavior of the weighted meridian significantly depends on the value of its medianity parameter δ. Two interesting cases may occur. The first case occurs when the value of the medianity parameter tends to infinity (i.e. $\delta \to \infty$), the the weighted meridian is equivalent to the weighted median [13]. For the given data set of N i.i.d. samples $x_1, \cdots, x_N$ and assigned weights $u_1, \cdots, u_N$, the following equation holds true

$$
\lim_{\delta \to \infty} \hat{\beta}_\delta = \lim_{\delta \to \infty} meridian \left\{ u_k * x_k |_{k=1}^{N}; \delta \right\} = median \left\{ u_k * x_k |_{k=1}^{N} \right\} . \tag{9}
$$

This property is called the median property. The second interesting case, called the modal property, occurs when the medianity parameter δ tends to zero. In this case, the weighted meridian $\hat{\beta}_\delta$ is equal to one of the most repeated values in the input data set. Furthermore

$$
\lim_{\delta \to 0} \hat{\beta}_\delta = \arg \min_{x_j \in X_i} \left[\frac{1}{u_j^r} \prod_{k=1, x_k \neq x_j}^{N} u_k |x_k - x_j| \right] , \tag{10}
$$

where X_i is the set of the frequently repeated values, and r is the number of occurrences of a member of X_i in the sample set.

Like for the weighted myriad cost function example, the Figure 4 shows shapes of the weighted meridian cost function for different values of δ parameter.

2.3   Generalized Cost Function

Comparing the properties of the weighted myriad cost function and weighted meridian cost function common features can be found. One of them is the behavior of the both cost function when the K parameter and the δ parameter tend to zero. Then, for the same data set $\mathbf{X}$, the value of weighted myriad is equal to the value of the weighed meridian. Another common feature of both functions is their similar form, but the weighted myriad cost function uses the L_2 norm while the weighted meridian cost function uses the L_1 norm.

Let the L_p norm be defined as follows
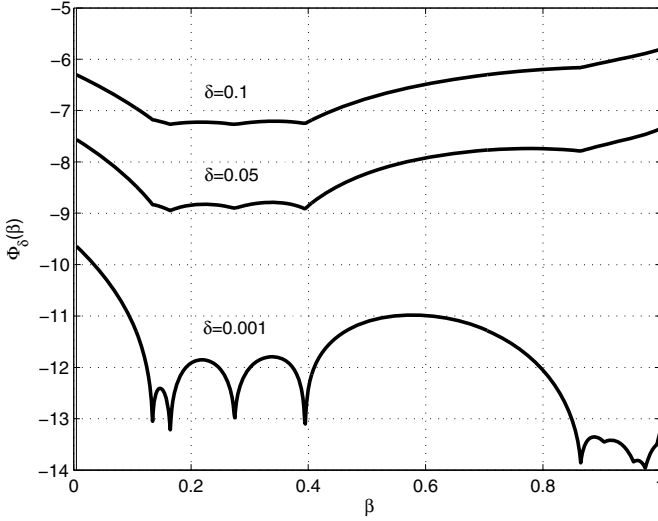
Fig. 4 An illustration of the shapes of weighted meridian cost function for the sample data and different values of the medianity parameter δ

$$||\mathbf{z}||_p = \left(\sum_{l=1}^{s} |z_l|^p \right)^{\frac{1}{p}} \quad , \tag{11}$$

where $\mathbf{z}$ is an s–dimensional real vector (i.e. $\mathbf{z} \in \mathbb{R}^s$). Applying the L_p norm to the weighted myriad cost function (3) or weighted meridian cost function (8), the generalized cost function can be expressed in the following form

$$\chi_\gamma^{(p)}(v) = \sum_{k=1}^{N} \log \left[\gamma + u_k ||x_k - v||_p \right] \quad , \tag{12}$$

where $|| \cdot ||_p$ is the L_p norm to the p power, and parameter γ corresponds to medianity parameter δ for $p = 1$ and corresponds to linearity parameter K for $p = 2$. It should be mentioned, that for $p = 1$ the γ parameter is equal to medianity parameter δ, but for $p = 2$ parameter γ is equal to the square root of the linearity parameter K (i.e. $\gamma = \sqrt{K}$).

For the given data set $\{x_k\}_{k=1}^{N}$ and the assigned weights $\{u_k\}_{k=1}^{N}$, let the $\hat{v}_\gamma$ be the value minimizing the cost function (12), i.e.

$$
\begin{aligned}
\hat{v}_\gamma &= \arg \min_{v \in \mathbb{R}} \chi_\gamma^{(p)}(v) \\
&= \arg \min_{v \in \mathbb{R}} \sum_{k=1}^{N} \log \left[\gamma + u_k ||x_k - v||_p \right]
\end{aligned} \tag{13}
$$

Properties of the $\hat{v}_\gamma$ value are presented in Table 1.

Table 1 Properties of the $\hat{v}_\gamma$ estimator

γ	$p = 1$	$p = 2$
$\gamma \to 0$	most repeated values in the input data set	
$0 < \gamma < \infty$	$\hat{v}_\gamma = meridian(u_k * x_k\|_{k=1}^N; \gamma)$	$\hat{v}_\gamma = myriad(u_k * x_k\|_{k=1}^N; \sqrt{\gamma})$
$\gamma \to \infty$	$\hat{v}_\gamma = median(u_k * x_k\|_{k=1}^N)$	$\hat{v}_\gamma = mean(u_k * x_k\|_{k=1}^N) = \frac{\sum_{k=1}^N u_k x_k}{\sum_{k=1}^N u_k}$

The function $\chi_\gamma^{(p)}(v)$ can be regarded as a generalized cost function. For $p = 1$ a weighted meridian is a special case of $\hat{v}_\gamma$, and for $p = 2$ the weighted myriad is a special case of $\hat{v}_\gamma$.

Assuming without loss of generality that the weights are in the unit interval (i.e. $u_k \in [0,1]$ where $1 \leq k \leq N$), the weights can be interpreted as membership degrees. Then, a weighted myriad $\hat{\Theta}_K$ or a weighted meridian $\hat{\beta}_\delta$ can be interpreted as a fuzzy myriad or fuzzy meridian, respectively. In the rest of this paper, the weights will be treated as a membership degrees and the weighted myriad and weighted meridian will be interpreted as fuzzy myriad and fuzzy meridian. Also, the $\hat{v}_\gamma$ value will be interpreted as a fuzzy value.

3 Hybrid Clustering Method

Let us consider a clustering category in which partitions of data set are built on the basis of some performance index, known also as an objective function [2, 16]. The minimization of a certain objective function can be considered as an optimization approach leading to suboptimal configuration of the clusters. The main design challenge is formulating an objective function that is capable of reflecting the nature of the problem so that its minimization reveals a meaningful structure in the data set.

The partition of an input data set can be described by $c \times N$ matrix (where c is the number of clusters, and N is the number of data samples), called the partition matrix. For the fuzzy clustering methods, the fuzzy partition matrix is defined as follows

$$M_{fCN} = \left\{ \begin{array}{c} \mathbf{U} \in [0,1]^{c \times N}| \\ \sum_{i=1}^c u_{ik} = 1, \ 1 \leq k \leq N; \ \sum_{k=1}^N u_{ik} > 0, \ 1 \leq i \leq c \end{array} \right\} . \quad (14)$$

The proposed method is an objective functional based on fuzzy c–partitions of the finite data set [2, 16]. The suggested objective function can be an extension of the classical functional of within–group sum of an absolute error.

The objective function of the chosen method can be described in the following way

$$J_m^{(p)}(\mathbf{U},\mathbf{V}) = \sum_{i=1}^{c}\sum_{k=1}^{N}\sum_{l=1}^{s}\log\left[\gamma + u_{ik}^m||x_k(l) - v_i(l)||_p\right] \quad, \tag{15}$$

where c is the number of clusters, N is the number of the data samples, s is the number of features describing the clustered objects. The γ parameter controls the behavior of cluster prototypes, $u_{ik} \in \mathbf{U}$ is the membership degree of the k–sample to the i–th cluster, the $\mathbf{U}$ is the fuzzy partition matrix, $x_k(l)$ represents the l–th feature of the k–th input data from the data set, and m is the fuzzfing exponent called the fuzzyfier.

The optimization objective function $J_m^{(p)}$ is completed with respect to the partition matrix $\mathbf{U}$ and the prototypes of the clusters $\mathbf{V}$. By minimizing (15) using Lagrangian multipliers, the following new membership u_{ik} update equation

$$u_{ik} = \left(\sum_{j=1}^{c}\left(\frac{||\mathbf{x}_k - \mathbf{v}_i||_p}{||\mathbf{x}_k - \mathbf{v}_j||_p}\right)^{1/(m-1)}\right) \quad, \tag{16}$$

can be derived. For the case, where $||\mathbf{x}_k - \mathbf{v}_i||_p = 0$, then $u_{ik} = 1$ and $u_{jk} = 0$ for $j \in \{1\cdots c\} - \{i\}$.

For the fixed number of clusters c and the partition matrix $\mathbf{U}$ as well as for the exponent m, the prototype values minimizing (15) are the values described as follows

$$v_i(l) = \arg\min_{v \in \mathbb{R}}\sum_{k=1}^{N}\log\left[\gamma + u_{ik}^m||x_k(l) - v||_p\right] \quad, \tag{17}$$

where i is the cluster number $1 \le i \le c$ and l is the component (feature) number $1 \le l \le s$.

3.1 Data Clustering with the Hybrid Clustering Method

The proposed hybrid clustering method can be described as follows:

1. For the given data set $\mathscr{X} = \{\mathbf{x}_1,\cdots,\mathbf{x}_N\}$ where $\mathbf{x}_i \in \mathbb{R}^s$, fix the number of clusters $c \in \{2,\cdots,N\}$, the fuzzyfing exponent $m \in [1,\infty)$ and assume the tolerance limit ε. Initialize randomly the partition matrix $\mathbf{U}$ and fix the value of parameter γ, fix $l = 0$,
2. calculate the prototype values $\mathbf{V}$ for each feature of $\mathbf{v}_i$ based on (17),
3. update the partition matrix $\mathbf{U}$ using (16),
4. if $\left\|\mathbf{U}^{(l+1)} - \mathbf{U}^{(l)}\right\| < \varepsilon$ then STOP the clustering algorithm, otherwise $l = l+1$ and go to (2).

4 Numerical Experiments

In the numerical experiments the fuzzfing exponent has been fixed to $m = 2$, and the tolerance limit $\varepsilon = 10^{-5}$. For a computed set of prototype vectors $\mathbf{V}$ the clustering accuracy has been measured as the Frobenius norm distance between the true centers μ and the prototype vectors. The matrix $\mathbf{A}$ is created as $||\mu - \mathbf{V}||_F$, where $||\mathbf{A}||_F$:

$$||\mathbf{A}||_F = \left(\sum_{i,k} A_{i,k}^2 \right)^{1/2} .$$

The familiar fuzzy c–means method (FCM) has been used as the reference clustering method.

The purpose of this experiment is to investigate sensitivity to outliers of the proposed method. The left column of the table 2 gives the number of outliers included in the data set.

The Figure 5 shows the data of 42 samples, used in the numerical experiment. The data set consists of well–separated two radial clusters centered at $\mu_1 = [0.3 \, 0.3]^\top$ and $\mu_2 = [0.8 \, 0.3]^\top$. Moreover, in the data set at $o = [10.0 \, 10.0]^\top$ the various number of outliers have been placed. The purpose of this experiment is to investigate sensitivity to outliers. The obtained results are presented in the Table 2.
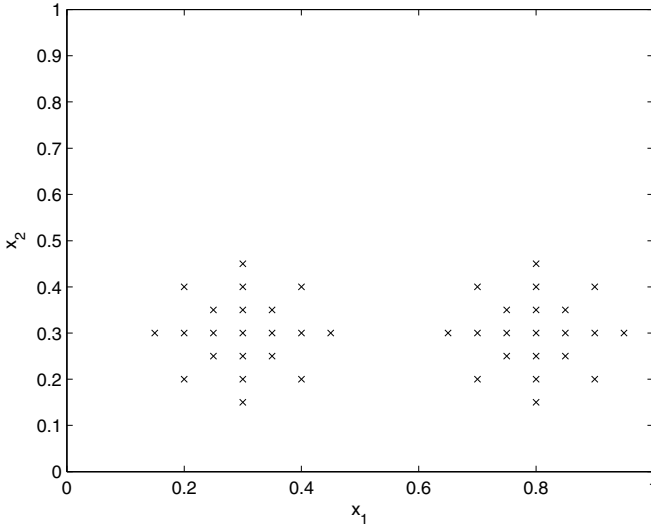
Fig. 5 "Two cluster data" scatterplot

For the number of 20 outliers, there was no deterioration in the quality of clustering for small values of parameter γ (i.e. $\gamma \leq 0.1$). The small value of parameter

Table 2 The difference among computed cluster centers $\mathbf{V}$ and the true centers μ

outliers	$p = 2$ γ					$p = 1$ γ					FCM
	100	10	1	0.1	0.01	100	10	1	0.1	0.01	
0	0.0321	0.0321	0.0321	0.0297	0.0008	0	0	0	0	0	0.0018
1	13.1382	13.1382	0.0338	0.0297	0.0008	0	0	0	0	0	13.3712
2	13.2558	13.2558	0.0384	0.0297	0.0008	0	0	0	0	0	13.3713
3	13.2945	13.2945	0.0453	0.0297	0.0008	0	0	0	0	0	13.3713
4	13.3139	13.3139	0.0534	0.0297	0.0008	0	0	0	0	0	13.3713
5	13.3253	13.3253	0.0625	0.0297	0.0008	0	0	0	0	0	13.3713
6	13.3331	13.3331	0.0722	0.0297	0.0008	0	0	0	0	0	13.3713
7	13.3385	13.3385	0.0823	0.0297	0.0008	0	0	0	0	0	13.3713
8	13.3426	13.3426	0.0926	0.0298	0.0008	0	0	0	0	0	13.3713
9	13.3458	13.3458	0.1033	0.0297	0.0008	0	0	0	0	0	13.3713
10	13.3484	13.3484	0.1140	0.0298	0.0008	0	0	0	0	0	13.3713
12	13.3522	13.3522	0.1363	0.0298	0.0008	0	0	0	0	0	13.3713
14	13.3550	13.3550	0.1595	0.0298	0.0008	0	0	0	0	0	13.3713
16	13.3570	13.3570	0.1834	0.0298	0.0008	0.4031	0.4031	0	0	0	13.3713
18	13.3586	13.3586	0.2091	0.0299	0.0008	0.4031	0.4528	0	0	0	13.3713
20	13.3599	13.3599	0.2351	0.0300	0.0008	0.1658	0.4528	0	0	0	13.3713

γ affects the selectivity of the determination of the cluster prototypes. For the value of parameter $\gamma = 0.01$, the assumed norm does not influence on the quality of clustering. For the L_2 norm and the values of parameter $\gamma \geq 10$, the obtained clustering results are almost identical with those obtained by the FCM method. It shows that the proposed method can be regarded as a generalization of the FCM method. For the L_1 norm, the obtained results are generally better than the results obtained for the L_2 norm for the same values of parameter γ. This feature arises from the fact, that the proposed method can also be regarded as the generalization of the fuzzy c–median method, which is more robust than the fuzzy c–means method.

The fuzzy c–means method dramatically breaks down for one outlier.

5   Conclusions

In many cases, the real data are corrupted by noise and outliers. Hence, the clustering methods should be robust for noise and outliers. In this paper the hybrid clustering method has been presented. The word *hybrid* stands for different cluster estimation which is dependent on two parameters. The proposed method can be treated as a generalization of two clustering methods: the fuzzy c–means method and the fuzzy c–medians method.

The presented generalization of the cost function allows the application of the L_p norm, where $1 < p < 2$ or $p < 1$. In such cases, it is difficult to interpret and identify the value $\hat{v}$.

The current work solves the local minima problem and the performance of the cluster centers estimation for large data sets.

References

1. Kaufman, L., Rousseeuw, P.: Finding Groups in Data. Wiley–Interscience, Chichester (1990)
2. Bezdek, J.C.: Pattern Recognition with Fuzzy Objective Function Algorithms. Plenum, New York (1981)
3. Hathaway, R.J., Bezdek, J.C., Hu, Y.: Genalized Fuzzy c-Means Clustering Strategies Using L_p Norm Distances. IEEE Trans. on Fuzzy Sys. 8, 576–582 (2000)
4. Krishnapuram, R., Keller, J.M.: A Possibilistic Approach to Clustering. IEEE Trans. on Fuzzy Sys. 1, 98–110 (1993)
5. Krishnapuram, R., Keller, J.M.: The Possibilistic C–Means Algorithm: Insights and Recomendations. IEEE Trans. on Fuzzy Sys. 4, 385–396 (1996)
6. Kersten, P.R.: Fuzzy Order Statistics and Their Application to Fuzzy Clustering. IEEE Trans. on Fuzzy Sys. 7, 708–712 (1999)
7. Huber, P.: Robust statistics. Wiley, New York (1981)
8. Dave, R.N., Krishnapuram, R.: Robust Clustering Methods: A Unified View. IEEE Trans. on Fuzzy System 5, 270–293 (1997)
9. Chatzis, S., Varvarigou, T.: Robust Fuzzy Clustering Using Mixtures of Student's–t Distributions. Pattern Recognition Letters 29, 1901–1905 (2008)
10. Frigui, H., Krishnapuram, R.: A Robust Competitive Clustering Algorithm With Applications in Computer Vision. IEEE Trans. Pattern Analysis and Machine Intelligence 21, 450–465 (1999)
11. Arce, G.R., Kalluri, S.: Fast Algorithm For Weighted Myriad Computation by Fixed Point Search. IEEE Trans. on Signal Proc. 48, 159–171 (2000)
12. Przybyła, T.: Fuzzy c–Myriad Clustering Method, System Modeling Control, pp. 249–254 (2005)
13. Aysal, T.C., Barner, K.E.: Meridian Filtering for Robust Signal Processing. IEEE Trans. on Signal Proc. 55, 3949–3962 (2007)
14. Przybyła, T., Jeżewski, J., Horoba, K.: The Adaptive Fuzzy Meridian and Its Application to Fuzzy Clustering. In: Advances in Intelligent and Soft Computing, vol. 57, pp. 247–256. Springer, Heidelberg (2009)
15. Arce, G.R., Kalluri, S.: Robust Frequency–Selective Filtering Using Weighted Myriad Filters admitting Real–Valued Weights. IEEE Trans. on Signal Proc. 49, 2721–2733 (2001)
16. Pedrycz, W.: Konwledge–Based Clustering. Wiley Interscience, Chichester (2005)

Complete Gradient Clustering Algorithm for Features Analysis of X-Ray Images

Małgorzata Charytanowicz, Jerzy Niewczas, Piotr Kulczycki, Piotr A. Kowalski, Szymon Łukasik, and Sławomir Żak

Abstract. Methods based on kernel density estimation have been successfully applied for various data mining tasks. Their natural interpretation together with suitable properties make them an attractive tool among others in clustering problems. In this paper, the Complete Gradient Clustering Algorithm has been used to investigate a real data set of grains. The wheat varieties, Kama, Rosa and Canadian, characterized by measurements of main grain geometric features obtained by X-ray technique, have been analyzed. The proposed algorithm is expected to be an effective tool for recognizing wheat varieties. A comparison between the clustering results obtained from this method and the classical *k*-means clustering algorithm shows positive practical features of the Complete Gradient Clustering Algorithm.

1 Introduction

Clustering is a major technique for data mining, used mostly as an unsupervised learning method. The main aim of cluster analysis is to partition a given population into groups or clusters with common characteristics, since similar objects are

Małgorzata Charytanowicz · Jerzy Niewczas
Institute of Mathematics and Computer Science,
The John Paul II Catholic University of Lublin, Konstantynów 1 H,
PL 20-708 Lublin, Poland
e-mail: {mchmat,jniewczas}@kul.lublin.pl

Piotr Kulczycki
Department of Automatic Control and Information Technology,
Cracow University of Technology, Warszawska 24, PL 31-155 Cracow, Poland
e-mail: kulczycki@pk.edu.pl

Piotr A. Kowalski · Szymon Łukasik · Sławomir Żak
Systems Research Institute, Polish Academy of Sciences, Newelska 6,
PL 01-447 Warsaw, Poland
e-mail: {pakowal,slukasik,slzak}@ibspan.waw.pl

grouped together, while dissimilar objects belong to different clusters [9, 12]. As a result, a new set of categories of interest, characterizing the population, is discovered. The clustering methods are generally divided into six groups: hierarchical, partitioning, density-based, grid-based, and soft-computing methods. These numerous concepts of clustering are implied by different techniques of determination of the similarity and dissimilarity between objects. A classical partitioning k-means algorithm is concentrated on measuring and comparing the distances among them. It is computationally attractive and easy to interpret and implement in comparison to other methods. On the other hand, the number of clusters is assumed here by user in advance and therefore the nature of the obtained groups may be unreliable for the nature of the data, usually unknown before processing.

The rigidity of arbitrary assumptions concerning the number or shape of clusters among data can be overcome by density-based methods that let the data detect inherent data structures. In the paper [8], the Complete Gradient Clustering Algorithm was introduced. The main idea of this algorithm assumes that each cluster is identified by local maxima of the kernel density estimator of the data distribution. The procedure does not need any assumptions concerning the data and may be applied to a wide range of topics and areas of cluster analysis [3, 8].

The main purpose of this work is to propose an effective technique for forming proper categories of wheat. In the earliest attempts to classify wheat grains a geometry and set of parameters were defined. The size, shape and colour of grain because of their heritable characters, can be used for wheat variety recognition. Accomplished studies showed that digital image processing techniques commonly used in multivariate analysis give reliable results in classification process [11, 14, 16]. In this paper, the algorithm proposed in [8] will be used to identify wheat varieties, using their main geometric features.

2   Complete Gradient Clustering Algorithm (CGCA)

In this section, the Complete Gradient Clustering Algorithm, for short the CGCA, is shortly described. The principle of the proposed algorithm is based on the distribution of the data; the implementation of the CGCA needs to estimate its density. Each cluster is characterized by a local maximum of the kernel density estimator. As a result, regions of high densities of objects are recognized as clusters, while areas with sparse distributions of objects divide one group from another. Data points are assigned to clusters by using an ascending gradient method, i.e. points moving to the same local maximum are put into the same cluster. The algorithm works in an iterative manner until a termination criterion has been satisfied.

2.1   Kernel Density Estimation

Suppose that $x_1, x_2, \ldots, x_m$ is a random sample of m points in n-dimensional space from an unknown distribution with density f. Its kernel estimator can be defined as

$$\hat{f}(x) = \frac{1}{mh^n} \sum_{i=1}^{m} K\left(\frac{x - x_i}{h}\right), \tag{1}$$

where the positive coefficient h is called the smoothing parameter or bandwidth, while the measurable function $K : R^n \to [0, \infty)$ of unit integral $\int_{R^n} K(x)\mathrm{d}x = 1$, unimodal and symmetrical with respect to zero, takes the name of a kernel [4, 13].

It is generally accepted, that the choice of the kernel K is not as important as the choice of the coefficient h and thank to this, it is possible to take into account the primarily properties of the estimator obtained. Most often the standard normal kernel given by

$$K(x) = \frac{1}{2\pi^{n/2}} e^{-\frac{x^T x}{2}} \tag{2}$$

is used. It is differentiable up to any order and assumes positive values in the whole domain.

The practical implementation of the kernel density estimators requires a proper choice of the bandwidth h. The best value of h is mostly taken as the value that minimizes the mean integrated square error. A frequently used bandwidth selection method is based on the approach of least-squares cross validation [4, 13]. The value of h is chosen to minimize the function $M : (0, \infty) \to R$ given by the rule:

$$M(h) = \frac{1}{m^2 h^n} \sum_{i=1}^{m} \sum_{j=1}^{m} \widetilde{K}\left(\frac{x_j - x_i}{h}\right) + \frac{2}{mh^n} K(0), \tag{3}$$

where $\widetilde{K}(x) = K^{*2}(x) - 2K(x)$ and K^{*2} is the convolution square of the function K; for the standard normal kernel (2):

$$K^{*2}(x) = \frac{1}{(4\pi)^{n/2}} e^{-\frac{x^T x}{4}}. \tag{4}$$

In this case the influence of the smoothing parameter on particular kernels is the same. The individualization of this effect may be achieved through the modification of the smoothing parameter. This relies on introducing the positive modifying parameters $s_1, s_2, \ldots, s_m$ mapped on particular kernels, described by the formula

$$s_i = \left(\frac{\hat{f}_*(x_i)}{\widetilde{s}}\right)^{-c}, \tag{5}$$

where $c \in [0, \infty)$, $\hat{f}_*$ is the kernel estimator in its basic form (1) and $\widetilde{s}$ denotes the geometrical mean of the numbers $\hat{f}_*(x_1)$, $\hat{f}_*(x_2)$, ..., $\hat{f}_*(x_m)$. The value of the parameter c implies the intensity of modification of the smoothing parameter. Based on indications for the criterion of the mean integrated square error the value 0.5 as c is proposed. Finally, the kernel estimator with modification of the smoothing parameter is defined as

$$\hat{f}(x) = \frac{1}{mh^n} \sum_{i=1}^{m} \frac{1}{s_i^n} K\left(\frac{x - x_i}{hs_i}\right). \tag{6}$$

Additional procedures improving the quality of the estimator obtained, such as a linear transformation and support boundary, as well as the general aspects of the theory of statistical kernel estimators are found in [4, 5, 13]. Exemplary practical applications are presented in the publications [1, 3, 6, 7].

2.2 Procedures of the CGCA

Consider the data set containing m elements $x_1, x_2, \ldots, x_m$ in n-dimensional space. Using the methodology introduced in Subsect. 2.1, the kernel density estimator $\hat{f}$ may be constructed. The idea of the CGCA is based on the approach proposed by Fukunaga and Hostetler [2]. Thus given the start points:

$$x_j^0 = x_j \text{ for } j = 1, 2, \ldots, m, \tag{7}$$

each point is moved in an uphill gradient direction using the following iterative formula:

$$x_j^{k+1} = x_j^k + b \frac{\nabla \hat{f}(x_j^k)}{\hat{f}(x_j^k)} \text{ for } j = 1, 2, \ldots, m \text{ and } k = 0, 1, \ldots, \tag{8}$$

where $\nabla \hat{f}$ denotes the gradient of kernel estimator $\hat{f}$, the value of the parameter b is proposed as $h^2/(n+2)$ and the coefficient h is the bandwidth of $\hat{f}$.

The algorithm will be stopped when the following condition is fulfilled:

$$|D_k - D_{k-1}| \leq \alpha D_0, \tag{9}$$

where D_0 and D_{k-1}, D_k denote sums of Euclidean distances between particular elements of the set $x_1, x_2, \ldots, x_m$ before starting the algorithm as well as after the $(k-1)$-th and k-th step, respectively. The positive parameter α is taken arbitrary and the value 0.001 is primarily recommended. This k-th step is the last one and will be denoted hereinafter by k^*.

Finally, after the k^*-th step of the algorithm (7)-(8) the set

$$x_1^{k^*}, x_2^{k^*}, \ldots, x_m^{k^*}, \tag{10}$$

considered as the new representation of all points $x_1, x_2, \ldots, x_m$, is obtained. Following this, the set of mutual Euclidean distances of the above elements:

$$\left\{ d(x_i^{k^*}, x_j^{k^*}) \right\}_{\substack{i=1,2,\ldots,m-1 \\ j=i+1,i+2,\ldots,m}} \tag{11}$$

is defined. Using the methodology presented in Subsect. 2.1, the auxiliary kernel estimator $\hat{f}_d$ of the elements of the set (11), treated as a sample of a one-dimensional random variable, is created under the assumption of nonnegative support. Next, the first (i.e. obtained for the smallest value of an argument) local minimum of the function $\hat{f}_d$ belonging to the interval $(0, D)$, where D means the maximum value of the set (11) is found. This local minimum will be denoted as x_d, and it can be interpreted as the half-distance between potential closest clusters. Finally, the clusters are created. First, the element of the set (11) is taken; it initially creates a one-element cluster containing it. An element of the set (11) is added to the cluster if the distance between it and any element belonging to the cluster is less than x_d. Every added element is removed from the set (11). If there are no more elements belonging to the cluster, the new cluster is created. The procedure of assigning elements to clusters is repeated as long as the set (11) is not empty.

Procedures described above constitute the Complete Gradient Algorithm in its basic form. The values of the parameters used are calculated automatically, using optimization criteria. However, by an appropriate change in values of these parameters it is possible to influence the size of number of clusters, and also the proportion of their appearnce in dense areas in relation to sparse regions of elements in this set. Namely, lowering (raising) the value of smoothing parameter h results in raising (lowering) the number of local maxima. A change in the value of that parameter of between -25% and +50% is recommended. Next, raising the intensity c of the smoothing parameter modification results in decreasing the number of clusters in sparse areas of data and increasing their number in dense regions. Inverse effects can be seen in the case of lowering this parameter value. The value of the parameter c to be between 0 and 1.5 is recommended. Finally, an increase of both parameters c and h can be proposed. Then the additional formula

$$h^* = \left(\frac{3}{2}\right)^{c-0.5} h \tag{12}$$

is used for calculating the smoothing parameter h^*, where the value of the parameter h is calculated on the criterion of the mean integrated square error. The joint action of both these factors results in a twofold smoothing of the function $\hat{f}$ in the regions where the elements of the set $x_1, x_2, \ldots, x_m$ are sparse. Meanwhile these factors more or less compensate for each other in dense areas, thereby having small influence on the detection of clusters located there. Detailed information on the CGCA procedures and their influences on the clustering results is described in [8].

3   Materials and Methods

The proposed algorithm has been applied for wheat variety recognition. Studies were conducted using combine harvested wheat grain originating from experimental fields, explored at the Institute of Agrophysics of the Polish Academy of Sciences

in Lublin. The examined group comprised kernels belonging to three different varieties of wheat: Kama, Rosa and Canadian, 70 elements each, randomly selected for the experiment. High quality visualization of the internal kernel structure was detected using a soft X-ray technique. It is non-destructive and considerably cheaper than other more sophisticated imaging techniques like scanning microscopy or laser technology. The images were recorded on 13×18 cm X-ray KODAK plates. Figure 1 presents the X-ray images of these kernels.
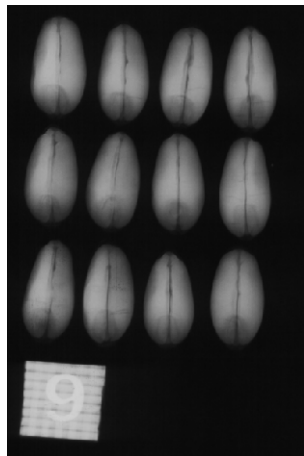
Fig. 1 X-ray photogram (13×18 cm) of kernels

The X-ray photograms were scanned using the Epson Perfection V700 table photo-scanner with a built-in transparency adapter, 600 dpi resolution and 8 bit gray scale levels. Analysis procedures of obtained bitmap graphics files were based on the computer software package GRAINS, specially developed for X-ray diagnostic of wheat kernels [10, 15]. To construct the data, seven geometric parameters of wheat kernels: area A, perimeter P, compactness $C = 4\pi A/P^2$, length of kernel, width of kernel, asymmetry coefficient and length of kernel groove, were measured from a total of 210 samples (see Fig. 2). All of these parameters were real-valued continuous.

In our investigations, the data was reduced to be two-dimensional after applying the Principal Component Analysis [12] to validate the results visually.

4 Results and Discussion

The data's projection on the axes of the two greatest principal components, with wheat varieties being distinguished symbolically, is presented in Fig. 3. Samples were labeled by numbers: 1-70 for the Kama wheat variety, 71-140 for the Rosa wheat variety, and 141-210 for the Canadian wheat variety. To discuss the clustering
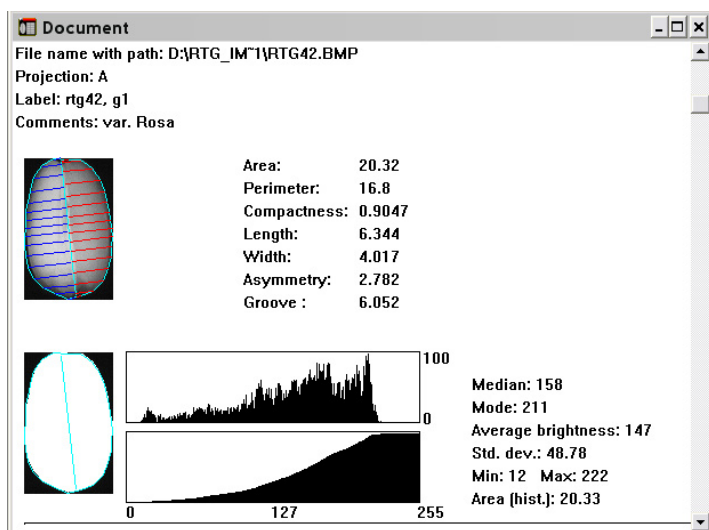
Fig. 2 Document window with geometric parameters of a kernel and statistical parameters of its image (as a unit of measure millimeters were used)

results obtained by the CGCA, mistakenly classified samples are displayed with their labels (see Fig. 3).

Using procedures described in Subsect. 2.2 allowing elimination of clusters in sparse areas, the CGCA created three clusters corresponding to Rosa, Kama, and Canadian varieties, containing 69, 65, and 76 elements respectively. Thus, the samples 9 and 38, which belong to the Kama wheat variety are incorrectly grouped into the cluster associated with the Rosa wheat variety. What is more, the samples 125, 136, 139, which belong to the Rosa wheat variety, and the samples 166, 200, 202, which belong to the Canadian wheat variety are mistakenly classified into the cluster associated with the Kama wheat variety. In addition, the samples 20, 27, 28, 30, 40, 60, 61, 64, 70, which belong to the Kama wheat variety are mistakenly classified into the cluster associated with the Canadian wheat variety. It is worth noticing however, that in the case of samples 9 and 38, misclassification can be justifiable – both samples lie close to the area of a high density of the Rosa wheat variety samples. The same problem is discerned with samples 125, 136, 139 and 166, 200, 202, which are placed close to samples of the Kama wheat variety. Similarly, mistakenly classified samples 20, 27, 28, 30, 40, 60, 61, 64, 70 lie very close to samples of the Canadian wheat variety. Thus, taking into consideration characteristics of wheat varieties, the CGCA seems to be an effective technique for wheat variety recognition.

Clustering results, containing numbers of samples classified properly and mistakenly into clusters associated with Rosa, Kama and Canadian varieties, are shown in Table 1.

According to the results of the CGCA, out of 70 kernels of the Rosa wheat variety, 67 were classified properly. Only 2 of the Kama variety were classified mistakenly as
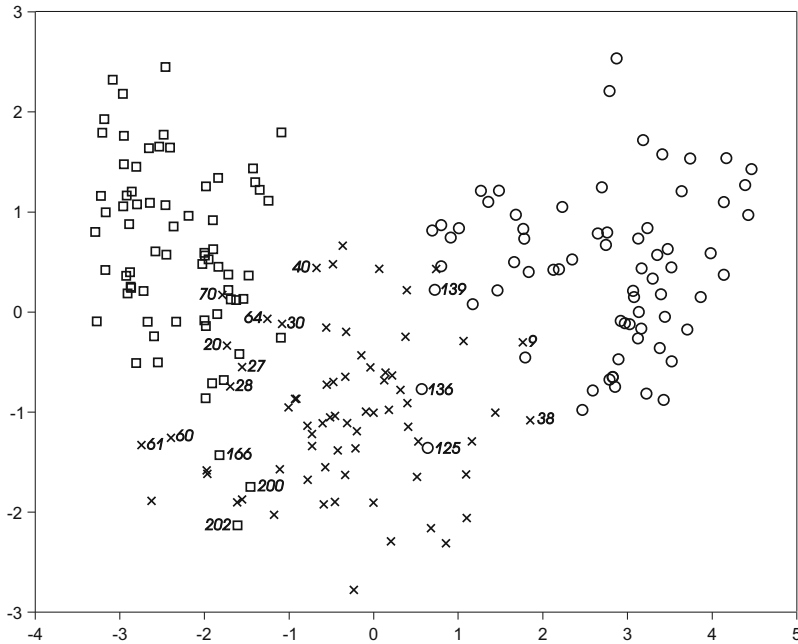
Fig. 3 Wheat varieties data set on the axes of the two greatest principal components: (○) the Rosa wheat variety, (×) the Kama wheat variety, (□) the Canadian wheat variety

Table 1 Clustering results for the wheat varieties data set

	Number of elements in clusters		
Clusters	Correctly classified	Incorrectly classified	Total
Rosa	67	2	69
Kama	59	6	65
Canadian	67	9	76

the Rosa variety. For the other two varieties, the CGCA created clusters containing 65 elements (the Kama variety) and 76 elements (the Canadian variety). In regard to the Kama variety, 59 kernels were classified correctly, while 6 of the other varieties were incorrectly identified as the Kama variety. For the Canadian variety, 67 kernels were correctly identified and 9 kernels of the Kama variety were mistakenly identified as the Canadian variety. The results of Kama and Canadian varieties are not so satisfactory as for Rosa, and this implies that these two varieties could not be so clearly distinguished as the Rosa variety, when using main geometric parameters.

It is worth underlining that the proper number of clusters has also been obtained when only two varieties are chosen to examine the CGCA. Thus, for Kama and Canadian varieties two clusters were created, containing 64 (Kama - 61, Canadian - 3) and 76 (Canadian - 67, Kama - 9) elements respectively.

Table 2 Correctness percentages for the wheat varieties data set

Wheat Varieties	Correctness %
Rosa	96
Kama	84
Canadian	96

The percentages of correctness of classification for a total of 210 samples are presented in Table 2. The proposed algorithm achieved an accuracy of about 96% for the Rosa wheat variety, 84% for the Kama wheat variety, and 96% for the Canadian wheat variety.

The comparable percentages of correctness of classification has been obtained when the *k*-means algorithm with arbitrary taken cluster number of 3 was used. It is worth stressing however, that this algorithm availed of the a priori assumed correct number of clusters, which in many applications may not be known, or even such a "correct" – from a theoretical point of view – number might not exist at all. The CGCA instead does not require strict assumptions regarding the desired number of cluster, which allows the number obtained to be better suited to a real data structure. Moreover, in its basic form, values of parameters may be calculated automatically. However, there exists the possibility of their optional change. A feature specific to it is the possibility to influence the proportion between the number of clusters in areas where data elements are dense as opposed to their sparse regions. In addition, by the detection of one-element clusters the algorithm allows the identification of outliers, which enables their elimination or designation to more numerous clusters, thus increasing the homogeneity of the data set.

5 Conclusions

The proposed clustering algorithm, based on kernel estimator methodology, is expected to be an effective technique for wheat variety recognition. It performs comparably with respect to the classical *k*-means algorithm, however it requires no a priori information about the data. The data reduced after applying the Principal Component Analysis, contained apparent clustering structures according to their classes. The amount of 193 kernels, giving almost 92% of the total, was classified properly. The wheat varieties used in the study showed differences in their main geometric parameters. The Rosa variety is better recognized, whilst Kama variety and Canadian variety are less successfully differentiated. Further research is needed on grain geometric parameters and their ability to identify wheat kernels.

References

1. Charytanowicz, M., Kulczycki, P.: Nonparametric Regression for Analyzing Correlation between Medical Parameters. In: Pietka, E., Kawa, J. (eds.) Advances in Soft Computing - Information Technologies in Biomedicine. Springer, Heidelberg (2008)
2. Fukunaga, K., Hostetler, L.D.: The estimation of the gradient of a density function, with applications in Pattern Recognition. IEEE Transactions on Information Theory 21, 32–40 (1975)
3. Kowalski, P., Łukasik, S., Charytanowicz, M., Kulczycki, P.: Data-Driven Fuzzy Modeling and Control with Kernel Density Based Clustering Technique. Polish Journal of Environmental Studies 17, 83–87 (2008)
4. Kulczycki, P.: Kernel Estimators for Systems Analysis. WNT, Warsaw (2005) (in Polish)
5. Kulczycki, P.: Kernel Estimators for Systems Research. In: Kulczycki, P., Hryniewicz, O., Kacprzyk, J. (eds.) Information Technologies in Systems Research. WNT, Warsaw (2007) (in Polish)
6. Kulczycki, P.: Kernel estimators in industrial applications. In: Prasad, B. (ed.) Soft Computing Applications in Industry. Springer, Berlin (2008)
7. Kulczycki, P., Charytanowicz, M.: Bayes Sharpening of Imprecise Information. International Journal of Applied Mathematics and Computer Science 15, 393–404 (2005)
8. Kulczycki, P., Charytanowicz, M.: A Complete Gradient Clustering Algorithm Formed with Kernel Estimators. International Journal of Applied Mathematics and Computer Science 20 (2010) (in press)
9. Mirkin, B.: Clustering for Data Mining: A Data Recovery Approach. Chapman and Hall/CRC, London (2005)
10. Niewczas, J., Woźniak, W.: Application of "GRAINS" program for characterisation of X-ray images of wheat grains at different moisture content. In: Xth Seminar, Properties of Water in Foods, Department of Food Engineering. Warsaw Agricultural University (1999)
11. Niewczas, J., Woźniak, W., Guc, A.: Attempt to application of image processing to evaluation of changes in internal structure of wheat grain. International Agrophysics 9, 343–347 (1995)
12. Rencher, M.: Methods of Multivariate Analysis. Wiley, New York (2004)
13. Silverman, B.W.: Density Estimation for Statistics and Data Analysis. Chapman and Hall, London (1986)
14. Shouche, S.P., Rastogi, R., Bhagwat, S.G., Sainis, J.K.: Shape analysis of grain of Indian wheat varieties. Computers and Electronics in Agriculture 33, 55–76 (2001)
15. Strumiłło, A., Niewczas, J., Szczypiński, P., Makowski, P., Woźniak, W.: Computer system for analysis of X-ray images of wheat grains. International Agrophysics 13, 133–140 (1999)
16. Utku, H., Koksel, H., Kayhan, S.: Classification of wheat grains by digital image analysis using statistical filters. Euphytica 100, 171–178 (1998)

Dynamics of the Clusterization Process in an Adaptative Method of Image Segmentation

Aleksander Lamża and Zygmunt Wróbel

Abstract. In this paper a new method of automatic image segmentation is presented. In proposed approach a region merging method is applied, where pixels or pixel groups are merged to bigger areas. In the proposed method of the region merging seed settings, segmentation parameter definition, and number of outcoming areas determining can be ommited. Homogeneous clusters (consisting of continuous groups of pixels) are the part of the growth process. The clusters are merged when the homogeneousness condition is fulfilled. The threshold value changes during segmentation process, appropriate to the changeable conditions.

1 Introduction

Image segmentation is a long standing problem in computer vision. The image segmentation process can be considered as method where specific parameter areas of a given image are distinguished [1, 2, 4, 8, 10]. A region merging method is frequently used and still modified by many researchers [2, 5, 6, 7, 8]. In the merging process some image pixels are grouped to larger areas. In the first stage of such process, so called initial pixels (seeds) are determined. After that step, the image is divided into areas which are equal to the number of initial pixels. This solution allows to decide, how many areas should be determined in the given image , and which pixels are the most typical in a given image area [1, 3]. In this paper the new automatic, adaptive method of the growth areas generating was described. Taking into account proposed algorithms, many parameter determining can be ignored, for example necessity of setting the number of outcome areas, defining the seeds and segmentation

Aleksander Lamża · Zygmunt Wróbel
Department of Biomedical Computer Systems, Institute of Computer Science,
Faculty of Computer and Materials Science, University of Silesia in Katowice,
ul. Bedzinska 39, 41–200 Sosnowiec
e-mail: `aleksander.lamza@us.edu.pl, zygmunt.wrobel@us.edu.pl`

parameters. Proposed algorithm allows to decrease of the homogeneous clusters during neighbours merging procedure. Algorithm is automatically stopped, when merging procedure can not be further applied.

2 Definitions and Fundamentals

In the first sequence generating, clusters merging and conception of a homogeneous cluster should be explained and defined.

A *homogeneous cluster* is a continuous group of pixels, which fulfill the similarity condition. A group of pixels building a homogeneous cluster is labeled as H_m, where: m – the number of the following cluster. Each cluster is a set of pixels $H_m = \{\mu_1, \mu_2, ..., \mu_i\}$, where μ_i – the gray level of a given pixel in the cluster m, i – the number of pixels in that cluster.

According to that notation, we shall denote the gray level of a pixel i in a cluster m by $\mu_i(H_m)$.

As it was above mentioned, pixels form the cluster, and clusters should be continuous. In other words it means that each element of the cluster should have at least one neighbour of the same cluster. These are the conditions for clusters:

- No cluster can be an empty set: $H_m \neq \emptyset$, where m is the cluster number, M – the number of clusters.
- The sum of all clusters must cover the whole image: $\bigcup_{m=1}^{M} H_m = X$, where m is the area number, M – the number of clusters, X – the set of all elements (pixels) of an image.
- The clusters can not have common elements: $H_m \cap H_n = \emptyset$, where m and n are area numbers, M – the number of areas.

3 Segmentation Algorithm

There are two phases in a proposed segmentation algorithm: *initial processing* – generating the initial set of clusters and *merging of the clusters* – checking the homogeneousness condition and merging the clusters, which fulfilled that condition. In the first phase, the initial number of homogeneous clusters is generated automatically. It's usually much bigger than expected, because some homogeneous clusters have the same parameters in different parts of a given image. In the second step the adaptive growth of the individual clusters is performed, what results from merging of the clusters that fulfil the homogeneousness condition. The number of clusters decreases when appropriate areas successive merge with their neighbours. The algorithm stops when remained clusters can not be merged.

3.1 Generating the Initial Set of Clusters

In the first step the initial set of clusters must be determined. For this reason, in the analysed image continuous areas of pixels with similar gray levels are searched. The image is successively scanned row by row, starting at the pixel (0, 0). The algorithm for clusters building is based on recurrence. Such algorithm checking of the pixels' neighbours and merging them to the appropriate clusters.

3.2 Merging the Clusters

The main part of the proposed algorithm is the adaptive merging of the clusters that fulfil the homogeneousness condition. As the merging minimal number of the clusters for the given image is produced. The algorithm has iterative form. Each iteration consists of the following steps:

- random choosing of the cluster H_m from the clusters set H,
- checking the similarity condition between the cluster H_m and all its neighbours H_n,
- if clusters H_m and H_n fulfil the homogeneousness condition, all elements of the neighbouring cluster are merged with the cluster H_m.

In the first step the algorithm randomly chooses the cluster, which will be later checked for similarity condition. Each element of a cluster stores information about its neighbourhood.

If the cluster H_m was randomly indicated, the neighborhood table for that cluster is created. To check the homogeneousness condition for every cluster H_n neighboring the H_m, the variance of the sum of elements for both clusters is computed. Based on the gray levels variance of all merged clusters elements, the homogeneousness condition is estimated. The variance estimation of a single cluster by means of equation (1) can be calculated:

$$\sigma^2(H_m) = \frac{1}{|H_m|} \sum_{i=1}^{|H_m|} \left[\mu_i(H_m) - \overline{\mu(H_m)} \right]^2, \tag{1}$$

where:
  $\sigma^2(H_m)$ – the variance of the elements in the cluster H_m,
  $|H_m|$ – the number of the elements in the cluster H_m,
  $\mu_i(H_m)$ – the gray level of the element i from the cluster H_m,
  $\overline{\mu(H_m)}$ – the average gray level of the elements in the cluster H_m.
  In the proposed algorithm the variance of the two clusters' sum (the first cluster randomly indicated, and the second one as its neighbour) is always determined.

$$\sigma^2(H_m, H_n) = \sigma^2(H_m \cup H_n) \tag{2}$$

The variance is calculated from the equations (3, 4):

$$\sigma^2(H_m, H_n) = \frac{1}{|H_m| + |H_n|} \left[\sum_{i=1}^{|H_m|} \left[\mu_i(H_m) - \overline{\mu(H_m, H_n)} \right]^2 + \right.$$

$$\left. + \sum_{j=1}^{|H_n|} \left[\mu_j(H_n) - \overline{\mu(H_m, H_n)} \right]^2 \right], \tag{3}$$

$$\overline{\mu(H_m, H_n)} = \frac{1}{|H_m| + |H_n|} \left[\sum_{i=1}^{|H_m|} \mu_i(H_m) + \sum_{j=1}^{|H_n|} \mu_j(H_n) \right], \tag{4}$$

where:

$\sigma^2(H_m, H_n)$ – the variance of the sum of the elements in H_m and H_n,

$|H_m|, |H_n|$ – the number of the elements in the cluster H_m and H_n,

$\mu_i(H_m), \mu_i(H_n)$ – the gray level of the element i (j) from the H_m (H_n),

$\overline{\mu(H_m, H_n)}$ – the average gray level of all elements in the clusters H_m and H_n.

When the variance of the cluster H_m and all its neighbors H_n is calculated, the algorithm chooses a neighboring cluster for which the lowest value of the variance was estimated, according to the equation (3). Then, it checks the global condition, determining if the estimated variance is smaller than the threshold value σ^2_{max}:

$$\sigma^2(H_m, H_n) < \sigma^2_{max}. \tag{5}$$

If the condition is filled, the merging process begins. All elements of the cluster $H_n - \mu(H_n)$ are transferred to the cluster H_m. Then the cluster H_n is removed from the cluster set H. If the condition isn't filled, the clusters aren't merged and the algorithms jumps to the first step – the random choosing of another cluster.

3.3 Adaptation of the Threshold Variance

In the presented algorithm the parameter responsible for determining if the clusters will merge or not is the threshold variance σ^2_{max}. Up to this point it's been treated as constant. In that case for every image, regardless of objects size and texture, the segmentation would proceed in a fixed way and the results wouldn't be satisfactory. A possible solution would be to estimate the threshold variance based on the image content, but the main purpose was to avoid any external parameters. To automatize the process a model of the threshold variance adaptation based on the segmentation process dynamics was developed.

As mentioned before, the value of the variance σ^2_{max} has to change during the segmentation process. In a case when, in a given iteration, a cluster can't merge with any of its neighbors, the threshold value should be adequately increased to allow the merging. On the other hand, immediate increasing this value to the needed level would result in merging all the clusters in a one cluster covering the whole image. This can't happen.

Therefore, a model of variance adaptation should change the value σ_{max}^2 smoothly, not allowing it to increase excessively. Thus – when the merging doesn't occur (the homogeneousness condition isn't fulfilled), the threshold variance increases according to equation (6):

$$\sigma_{max}^2(i) = \sigma_{max}^2(i-1) \cdot \left[1 - \exp\left(-\frac{i}{\tau_1}\right)\right],\qquad(6)$$

where:
i – the number of the current iteration,
τ_1 – the time constant of the variance increase (expressed in iterations).

If the clusters merge in the current iteration, the value of threshold variance decreases until the next unsuccessful merging occurs.

$$\sigma_{max}^2(i) = \sigma_{max}^2(i') \cdot \left[1 - \exp\left(-\frac{i-i'}{\tau_2}\right)\right],\qquad(7)$$

where:
i – the number of the current iteration,
i' – the iteration, for which the last successful merging occurred,
τ_2 – the time constant of the variance decrease (expressed in iterations).

The value of the variance σ_{max}^2 is calculated in every step of the algorithm. The time constants τ_1 (increase) and τ_2 (decrease) have their values determined experimentally. The variance σ_{max}^2 oscillates during the clusters' merging. At the end of the segmentation process a rapid fluctuation is visible. This sudden increase of the threshold value results in merging the clusters which shouldn't be merged. Therefore, the large area of an image is „flooded" by a single cluster. This increase was triggered by small number of clusters and a high value of variance. The unsuccessful mergings occur often, resulting in a constant increase of the threshold variance value. To avoid such situations, a parameter correcting the time constant of the variance increase (τ_1) was introduced. During the segmentation process the number of clusters decreases successively. Along with that decrease, the time constant τ_1 should increase to induce a slower rate of the threshold variance growth.

$$\tau_1 = \tau_0 \cdot M_0 \cdot \frac{1}{M_i}\qquad(8)$$

where:
τ_1 – the time constant of the variance increase,
τ_0 – a parameter determined experimentally,
M_i – the number of the areas in the iteration i,
M_0 – the initial number of the areas.

After introducing the correcting parameter much better results were achieved.

3.4   Dynamics of the Merging Process

Regardless of the input image characteristics, three phases can be distinguished in the course of the variance during successive iterations. Figures 1 – 3 ilustrates this fact. Three values of the variance are marked on the graphs: σ_p^2 – the variance for the merged areas, σ_n^2 – the variance for the unsuccessful merging and σ_{max}^2 – the threshold variance.

The phase I – *merging* (Fig. 1) is characterized by a considerable frequency of changes in the merged clusters variance σ_p^2 with rare fluctuations of the unmerged clusters variance σ_n^2. It should be mentioned, that when the growth of the variance occurs, the value of σ_{max}^2 equals the variance of unmerged clusters after a few iterations.
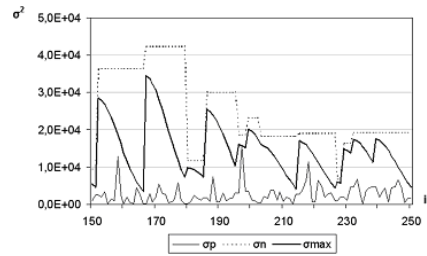
Fig. 1 The values of variance in successive iterations for phase I (*merging*)

In the phase II – *stabilization* (Fig. 2) – clusters merge sporadically. The variance σ_n^2 fluctuations occur much more often, yet they are rather homogeneous. The value of the variance σ_{max}^2 doesn't reach the maximum because of the increase of the time constant τ_1.
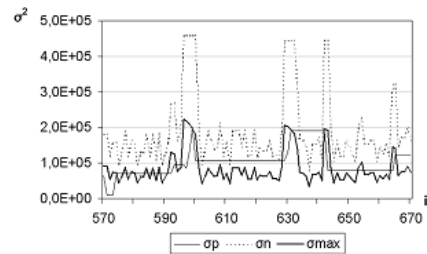
Fig. 2 The values of variance in successive iterations for phase II (*stabilization*)

The phase III – *separation* (Fig. 3) – is characterized by a visible distinction between the variances σ_n^2 and σ_{max}^2. The value of the variance σ_p^2 is at its lowest level and at some point it disappears, which means the process of the clusters merging is done.

By the end of the second phase, the results of the segmentation are usually satisfactory. The number of clusters varies from ten to several dozen (depending on the

Fig. 3 The values of variance in successive iterations for phase III (*separation*)

(a)

(b)

(c)
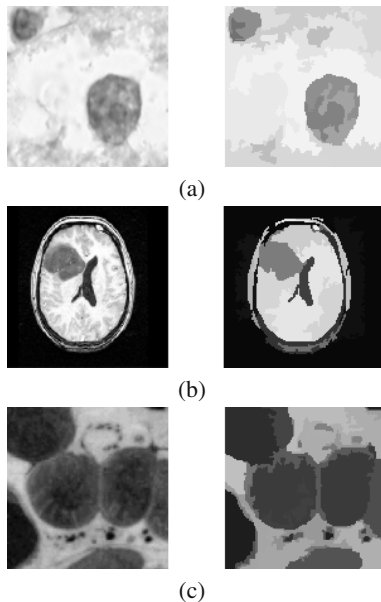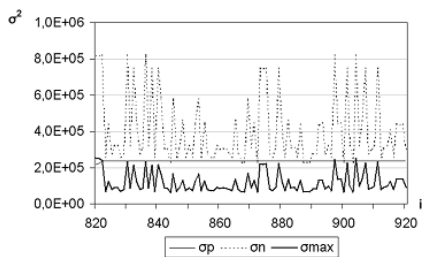
Fig. 4 The original image (left) and the image by the end of segmentation (right)

image complexity). The size of the merged clusters was also analysed. The Fig. 4a shows the size of merged clusters in successive iterations, and their average value. The factor k expresses the proportion between the smaller cluster and the bigger one:

$$k = \frac{min\left(|H_n|, |H_m|\right)}{max\left(|H_n|, |H_m|\right)} \tag{9}$$

As we can see, the average value of k is more or less constant and oscillates around 0.4.

The merging of big clusters is inadvisable, because in such cases inaccuracies in defining segments may occur. It does not happen in the first and the second phase, because the threshold variance value is then relatively low. Yet, in the third phase the merging of big clusters may at some point happen, despite of the growth of the variance increase time constant. Therefore, a modification of the clusters

choosing algorithm in the third stage was proposed. The clusters are no more chosen by chance: only the biggest ones are checked for their possibility to merge with the smaller, neighbouring ones. This stopped big clusters from merging and precipitated the end of the segmentation process.

4   Conclusions

Below some examples of segmentation for different classes of images are shown. These include real images – obtained from a microscope, computer tomography and magnetic resonance (Fig. 4).

An important problem when analyzing real images is the detail level of segmentation. In the proposed algorithm segmentation details level depends on the size of the image. The presented segmentation method was tested by means of various classes of images and obtained results were very satisfactory. The details level of the image segmentation depends on the image size, hence, global segmentation can be completed with a detailed one, proceeded on chosen, earlier isolated parts of an image. In the future the proposed algorithm for colour images using HSL will be adapted.

References

1. Cour, T., Benezit, F., Shi, J.: Spectral segmentation with multiscale graph decomposition. Computer Vision and Pattern Recognition 2, 1124–1131 (2005)
2. Dhawan, A.: Medical Image Analysis. Wiley-IEEE Press (2003)
3. Gonzalez, R.C., Woods, R.E.: Digital Image Processing. Prentice Hall, New Jersey (2002)
4. Hoover, A., Jean-Baptiste, G., Jiang, X.: An Experimental Comparison of Range Image Segmentation Algorithms. IEEE Trans. Pat. Anal. and Mach. Intell. 18(7), 673–689 (1996)
5. Lamecker, H., Lange, T., Seebß, M.: Automatic Segmentation of the Liver for Preoperative Planning of Resections. In: Proceedings MMVR. Studies in Health Technologies and Informatics, vol. 94, pp. 171–174 (2003)
6. Lamza, A., Trela, M., Bialy, S., Wrobel, Z.: Agent-based method of automatic image segmentation with dynamic threshold. IEEE Signal Processing, 71–74 (2004)
7. Pantofaru, C., Hebert, M.: A Comparison of Image Segmentation Algorithms. Technical Report CMU-RI-TR-05-40, Robotics Institute, Carnegie Mellon University (2005)
8. Porikli, F.: Automatic Image Segmentation by Wave Propagation. In: SPIE Conference on Image Processing: Algorithms and Systems III, vol. 5298, pp. 536–543 (2004)
9. Soille, P.: Morphological Image Analysis: Principles and Applications. Springer, Heidelberg (2004)
10. Veenman, C.J., Reinders, M.J.T., Backer, E.: A Cellular Coevolutionary Algorithm for Image Segmentation. IEEE Transactions on Image Processing 12(3), 304–316 (2003)
11. Wang, H., Suter, D.: A Model-Based Range Image Segmentation Algorithm Using a Novel Robust Estimator. In: 3rd International Workshop on Statistical and Computational Theories of Vision, Nice, France (2003)
12. Wrobel, Z., Koprowski, R.: Praktyka przetwarzania obrazu w programie MATLAB. Wydawnictwo Exit, Warszawa (2004)
13. Zielinski, K.W., Strzelecki, M.: Komputerowa analiza obrazu biomedycznego. Wstep do morfometrii i patologii ilosciowej. Wydawnictwo Naukowe PWN, Warszawa – Lodz (2002)

Application of Adaptive Weighed Averaging to Digital Filtering of 2D Images

Alina Momot

Abstract. In many biomedical fields there is a need of digital image analysis. The images often contain some disturbances in addition to the useful data. These disturbances should be reduces (or even eliminated, if it is possible) in order to improve the quality of the analysis. One of the possible methods of noise attenuation is low-pass filtering such as arithmetic mean and its generalization, namely weighted mean filtering where the weights are tuned by some adaptive algorithm.

This paper presents application of Bayesian weighted averaging to digital filtering 2D images which is some modification of the existing empirical Bayesian weighted averaging method created originally for noise reduction in electrocardiographic signal. The description of the new filtering method and a few results of its application are also presented with comparison to traditional arithmetic average filtering and median filtering.

1 Introduction

Image enhancement approaches fall into two broad categories: spatial domain methods and frequency domain methods. The term spatial domain refers to the aggregate of pixels composing an image. Spatial domain methods directly operate on these pixels. Spatial domain processes could be denoted by $g(x,y) = T[f(x,y)]$ where $f(x,y)$ is the input image, $g(x,y)$ is the output image and T is an operator on f, defined over some neighborhood of (x,y) [4]. The process of spatial filtering consists of moving the filter mask form point to point in an image.

For linear spatial filtering the response of the filter is given by a sum of products of the filter coefficients and the corresponding image pixels in the area spanned by

Alina Momot
Silesian University of Technology, Institute of Computer Science, 16 Akademicka St.,
44-100 Gliwice, Poland
e-mail: `alina.momot@polsl.pl`

the filter mask. If all the coefficients are the same and sum up to one, this is called arithmetic mean filtering.

Mean filtering is a simple, intuitive and easy to implement method of smoothing images, i.e. reducing the amount of intensity variation between one pixel and the next. It is often used to reduce noise in images. The idea of mean filtering is simply to replace each pixel value in an image with the mean ('average') value of its neighbors, including itself. This procedure reduces the influence of pixel values which are unrepresentative of their surroundings.

Mean filtering is usually thought of as a convolution filter. Like other convolutions it is based around a kernel, which represents the shape and size of the neighborhood to be sampled when calculating the mean. Often a 3×3 square kernel is used, although larger kernels (e.g. 5×5 squares) can be used for more severe smoothing [6].

Sometimes the pixel at the center of the mask is multiplied by a higher value than any other, thus giving this pixel more importance in the calculation of the average. This is some way to reduce blurring in the smoothing process. Mask coefficients could be a discrete approximation of the 2-dimensional Gaussian distribution function [1], such Gaussian filter is an example of the weighted average filter.

Like the mean filter, the median filter considers each pixel in the image in turn and looks at its nearby neighbors to decide whether or not it is representative of its surroundings. Instead of simply replacing the pixel value with the mean of neighboring pixel values, it replaces it with the median of those values. The median is calculated by first sorting all the pixel values from the surrounding neighborhood into numerical order and then replacing the pixel being considered with the middle pixel value. Median filtering could be also thought of as a convolution filter however in this case the mask coefficients are not always constant. There is only one non-zero coefficient (equal one) and which coefficient is non-zero depends on result of the sorting operation.

One of the major problems with the median filter is that it is relatively expensive and complex to compute. To find the median it is necessary to sort all the values in the neighborhood into numerical order and this is relatively slow, even with fast sorting algorithms such as *quicksort*. The basic algorithm can, however, be enhanced somewhat for speed. A common technique is to notice that when the neighborhood window is slid across the image, many of the pixels in the window are the same from one step to the next, and the relative ordering of these with each other will obviously not have changed [2].

In the case of convolution filters where the mask coefficients are not always constant there is a need of procedure how to compute the coefficients. In 2005 Xu et al. [7] proposed adaptive fuzzy weighted average filter (AFWA) which regards the pixels in the filter window as a fuzzy set and every pixel in the filter window can be depicted by membership function, which is actually the weight of this pixel. Here author proposes a new algorithm for computing values of the mask coefficient based on the existing empirical Bayesian weighted averaging method created originally for noise reduction in electrocardiographic signal [5]. The performance of the

new algorithm is experimentally compared with the traditional average filtering and median filtering for both synthetic and real images.

2 Weighted Averaging Methods

Below there is presented the original empirical Bayesian weighted averaging method (EBWA) created for noise reduction in electrocardiographic (ECG) signal and next there is presented its modification to computing the mask coefficients for adaptive linear spatial filtering. ECG signal is characterized by quasi-cyclical, repetitive pattern that is why the needed noise attenuation may be obtained by means of averaging signals cycle-wise.

2.1 EBWA Method

Let us assume that in each signal cycle $f_i(j)$ is the sum of a deterministic (useful) signal $s(j)$, which is the same in all cycles, and a random noise $n_i(j)$ with zero mean and variance in the ith cycle equal to σ_i^2 . Thus,

$$f_i(j) = s(j) + n_i(j),\qquad(1)$$

where i is the cycle index $i \in \{1,2,\ldots,M\}$, and j is the sample index in the single cycle $j \in \{1,2,\ldots,N\}$ (all cycles have the same length N). The weighted average is given by

$$v(j) = \sum_{i=1}^{M} w_i f_i(j),\qquad(2)$$

where w_i is a weight for ith signal cycle and $v = [v(1),v(2),\ldots,v(N)]$ is the averaged signal.

The iterative weighted averaging algorithm for electrocardiographic signal can be described as follows, where ε is a preset parameter [5]:

1. Initialize $v^{(0)}$. Set the iteration index $k = 1$.
2. Calculate the hyperparameter $\alpha_i^{(k)}$ for $i = 1,2,\ldots,M$ and $\beta^{(k)}$

$$\alpha_i^{(k)} = \frac{N}{\sum_{j=1}^{N} \left(f_i(j) - v^{(k-1)}(j)\right)^2},\qquad(3)$$

$$\beta^{(k)} = \frac{N}{\sum_{j=1}^{N} \left(v^{(k-1)}(j)\right)^2}.\qquad(4)$$

3. Update the averaged signal $v^{(k)}$ for kth iteration.

$$v^{(k)}(j) = \frac{\sum_{i=1}^{M} \alpha_i^{(k)} f_i(j)}{\beta^{(k)} + \sum_{i=1}^{M} \alpha_i^{(k)}} \tag{5}$$

4. If $||v^{(k)} - v^{(k-1)}|| > \varepsilon$ then $k \leftarrow k+1$ and go to 2, else stop.

2.2 Adaptive Linear Spatial Filtering

Described above algorithm could be modified for application to adaptive linear spatial filtering. In the case of 2-dimensional grayscale image the parameter N is set to one and as result it is obtained gray level of one pixel. It is worth noting that for color images the parameter N could be set to the dimension of the color space.

Let us assume that r is the radius of the square mask, i.e. $r = (m-1)/2$ where m is the size of mask, X and Y are dimensions of the input $X \times Y$ image f. The output image g size is $(X - 2r) \times (Y - 2r)$. For each pixel $f(x,y)$, i.e. $x \in \{r+1, r+2, \ldots, X-r\}$ and $y \in \{r+1, r+2, \ldots, Y-r\}$, there is created $D = (2r+1)^2$-dimensional vector $t = [f(x-r, y-r), \ldots, f(x+r, y+r)]$ based on the neighborhood of the pixel. Each pixel $g(x,y)$ of the output image is the sum

$$g(x,y) = \sum_{i=1}^{D} w_i t_i, \tag{6}$$

although the weights w_i are not explicitly computed and the value $g(x,y)$ is calculated by following iterative algorithm:

1. Initialize $g(x,y)^{(0)}$ as the arithmetic average of t. If the sample variance of t is greater than zero set the iteration index $k = 1$ else stop.
2. Calculate the hyperparameter $\alpha_i^{(k)}$ for $i = 1, 2, \ldots, D$ and $\beta^{(k)}$

$$\alpha_i^{(k)} = \left(t_i - g(x,y)^{(k-1)} \right)^{-2}, \tag{7}$$

$$\beta^{(k)} = \left(g(x,y)^{(k-1)} \right)^{-2}. \tag{8}$$

3. Update the average $g(x,y)^{(k)}$ for kth iteration.

$$g(x,y)^{(k)} = \frac{\sum_{i=1}^{D} \alpha_i^{(k)} t_i}{\beta^{(k)} + \sum_{i=1}^{D} \alpha_i^{(k)}} \tag{9}$$

4. If $\left(g(x,y)^{(k)} - g(x,y)^{(k-1)} \right)^2 > \varepsilon$ then $k \leftarrow k+1$ and go to 2, else stop.

Algorithm described above assumes that the values $f(x,y) \in [0,1]$. Thus parameter $\beta^{(k)}$ is always positive, although for some i the parameter $\alpha_i^{(k)}$ could be undefined because $t_i - g(x,y)^{(k-1)}$ could be equal zero. For such index i the parameter $\alpha_i^{(k)}$

should be set to a value significantly greater than other parameters $\alpha_i^{(k)}$ because the pixel represented by i is equal the average $g(x,y)^{(k-1)}$ in kth iteration.

3 Numerical Experiments

In this section there is presented performance of the described method for synthetic and real images in presence of salt-and-pepper and Gaussian noise. The noise attenuation results are compared with mean filtering and median filtering. In all experiments, using proposed averaging, the parameter ε is equal to 10^{-6} and for such value the number of iterations required to obtain weights for single pixel did not exceed 10 (typically equal 3 or 4). For computed output images the performance of tested methods is evaluated by the root mean-square error (RMSE) between the original image (without noise) and the output image. All experiments were run in the R environment (www.r-project.org).

3.1 Experiments with Salt-and-Pepper Noise

First there are presented the noise attenuation results of the considered methods, i.e. proposed adaptive weighted averaging and traditional filtering using mean and median, for salt-and-pepper noise (appearing as white and black dots superimposed on an image). Figure 1(a) presents the synthetic grayscale image of size 256×256 with only 3 gray levels appearing in the image. This image was disturbed by salt-and-pepper noise where the probability of the black pixel is equal 0.05 and the probability of the white pixel is also equal 0.05. The result of this procedure is presented in figure 1(b).

(a)   (b)
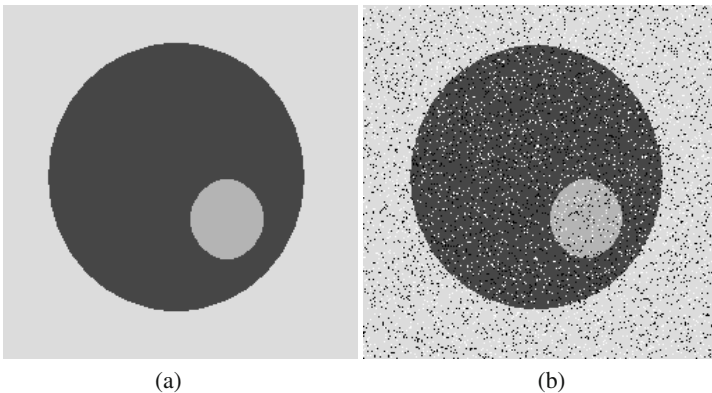
Fig. 1 (a) Original synthetic 3-gray level image of size 256×256, (b) the same image with salt-and-pepper noise

For the image from figure 1(b) there was performed filtration using all described above methods. The radius of mask was equal 2, i.e. filter mask of size 5×5. The output images are presented in figure 2. On the left there is the result of application square averaging filter mask, in the middle there is the result of application proposed adaptive weighted averaging method and on the right there is the result of application median filter mask.

(a) (b) (c)
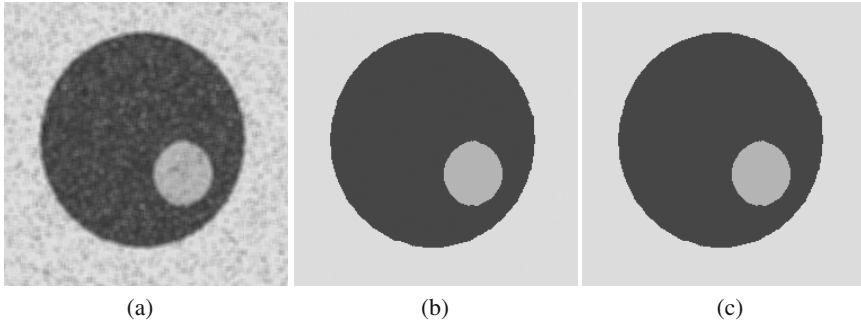
Fig. 2 Results of noise reduction for image from figure 1(b) using:(a) mean filter, (b) adaptive weighted averaging, (c) median filter

The table 1 presents the root mean-square error between the original image, i.e. figure 1(a), and the output images 2(a), (b) or (c). It can be seen that the best result was obtained for the median filter and the worst for the mean filter. Using the proposed method results in a much better RMSE than the mean filter and slightly worse than the median filter.

Table 1 Root mean-square error for noise reduction in image from figure 1(b)

method	RMSE
mean filter	0.06085189
adaptive weighted averaging	0.02402858
median filter	0.02374963

Next there were performed experiments with another synthetic image with 256-gray level and salt-and-pepper noise. The original and disturbed images are presented in figure 3. As in the previous noisy image, the probability of black or white pixels was equal 0.05.

For the image from figure 3(b) there was also performed filtration with filter mask of size 5×5. The output images are presented in figure 4 and the table 2 presents the root mean-square error between the original image, i.e. figure 3(a), and the output images 4(a), (b) or (c).

Next there were performed experiments with real biomedical image and salt-and-pepper noise. The original and disturbed images are presented in figure 5. Like

(a)   (b)
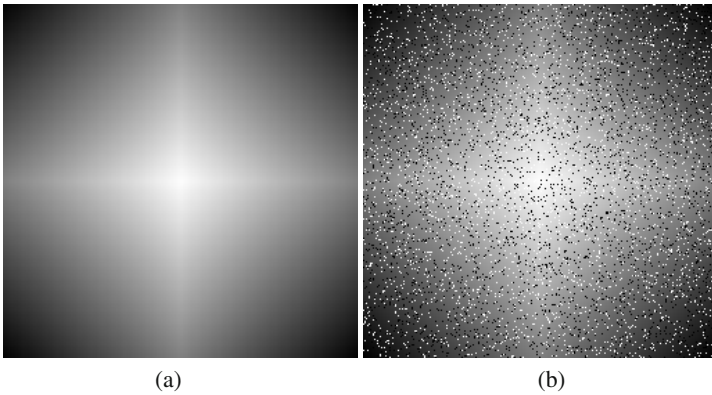
Fig. 3 (a) Original synthetic 256-gray level image of size 256×256, (b) the same image with salt-and-pepper noise

(a)   (b)   (c)
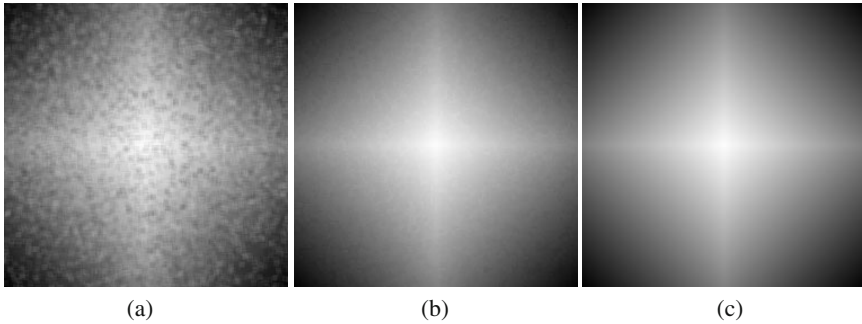
Fig. 4 Results of noise reduction for image from figure 3(b) using:(a) mean filter, (b) adaptive weighted averaging, (c) median filter

Table 2 Root mean-square error for noise reduction in image from figure 3(b)

method	RMSE
mean filter	0.039152
adaptive weighted averaging	0.007201034
median filter	0.0009701716

earlier, the probability of black or white pixels was equal 0.05. Square mask of size 5×5 filtration applied to the image from figure 5(b) gives the output images presented in figure 6 and the table 3 presents the root mean-square error between the original image, i.e. figure 3(a), and the output images 4(a), (b) or (c).

In all described above experiments the best result was obtained for the median filter and the worst for the mean filter. Such results can be expected because in presence of impulse noise, such as salt-and-pepper noise, median filters are particularly

(a)   (b)
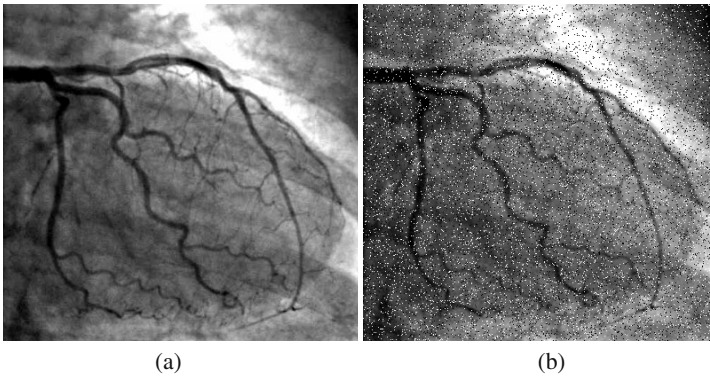
Fig. 5 (a) Original real biomedical image of size 400×380, (b) the same image with salt-and-pepper noise

(a)   (b)   (c)
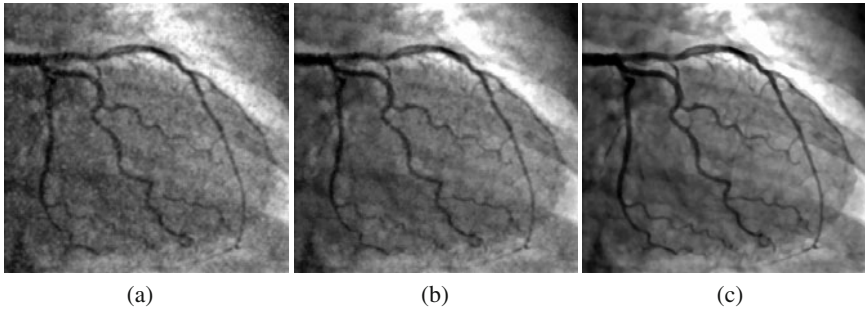
Fig. 6 Results of noise reduction for image from figure 5(b) using:(a) mean filter, (b) adaptive weighted averaging, (c) median filter

Table 3 Root mean-square error for noise reduction in image from figure 5(b)

method	RMSE
mean filter	0.04771754
adaptive weighted averaging	0.03733040
median filter	0.02283560

effective [4]. Using the proposed method usually results in a much better RMSE than the mean filter and slightly worse than the median filter.

3.2 Experiments with Gaussian Noise

Below there are presented the noise attenuation results of the considered methods, i.e. proposed adaptive weighted averaging and traditional filtering using mean and

median, for Gaussian noise. Figure 7 presents the 3-gray level synthetic grayscale image of size 256×256 and the same image disturbed by zero-mean white Gaussian noise with standard deviation equal 0.15.

(a)   (b)
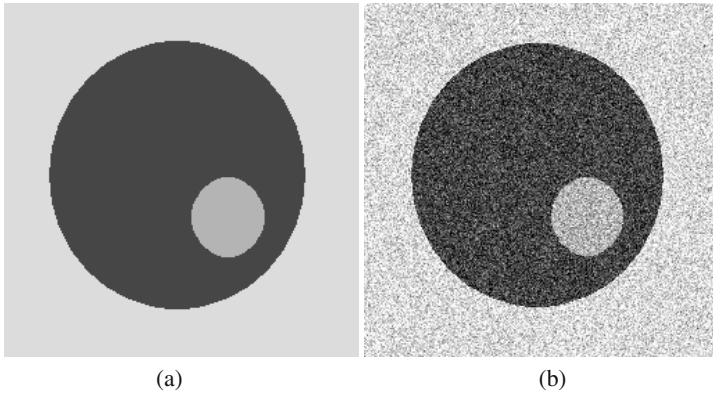
Fig. 7 (a) 3-gray level synthetic image, (b) the same image with Gaussian noise

For the image from figure 7(b) there was performed filtration with filter mask of size 5×5. The output images are presented in figure 8 and the table 4 presents the root mean-square error between the original image, i.e. figure 7(a), and the output images 8(a), (b) or (c).

(a)   (b)   (c)
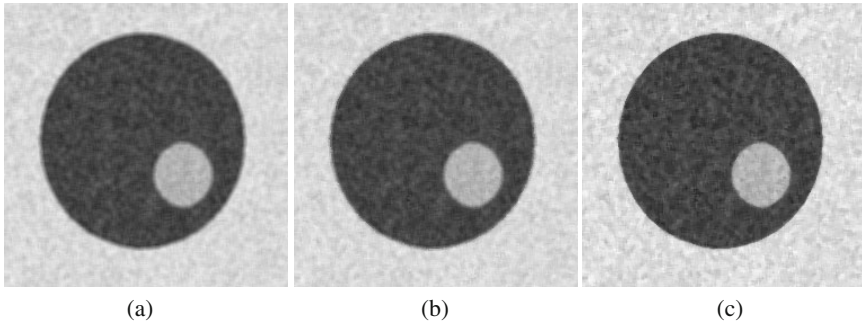
Fig. 8 Results of noise reduction for image from figure 7(b) using:(a) mean filter, (b) adaptive weighted averaging, (c) median filter

In the case of Gaussian noise it can be expected that the best result should be obtained by application the mean filter and however the results presented in table 4 shows that using the median filter has given the smallest root mean-square error, all results are similar. Possible explanation of this fact is small number of different gray levels in the original image which are concentrated in only three areas.

Table 4 Root mean-square error for noise reduction in image from figure 7(b)

method	RMSE
mean filter	0.04715002
adaptive weighted averaging	0.04546692
median filter	0.04463237

Next there were performed experiments with another synthetic image with 256-gray level of size 256×256 and the same as previously described Gaussian noise. The original and disturbed images are presented in figure 9.

(a)   (b)
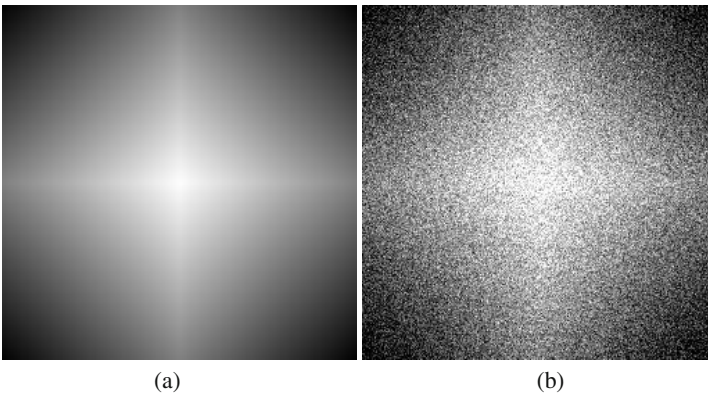
Fig. 9 (a) 256-gray level synthetic image, (b) the same image with Gaussian noise

For the image from figure 9(b) there was performed filtration and the output images are presented in figure 10. The table 5 presents the root mean-square error between the original image, i.e. figure 9(a), and the output images 10(a), (b) or (c).

(a)   (b)   (c)
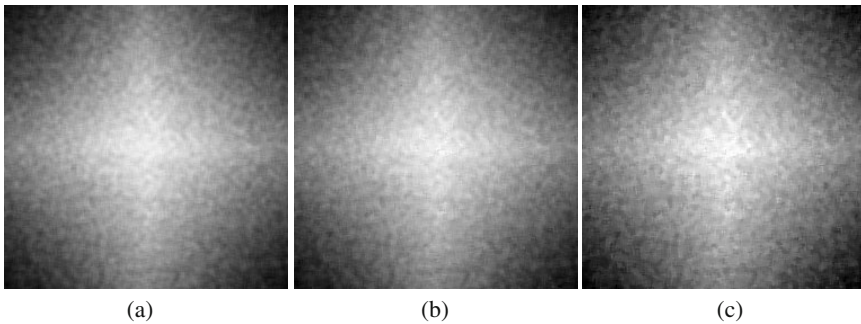
Fig. 10 Results of noise reduction for image from figure 9(b) using:(a) mean filter, (b) adaptive weighted averaging, (c) median filter

Table 5 Root mean-square error for noise reduction in image from figure 9(b)

method	RMSE
mean filter	0.02996932
adaptive weighted averaging	0.03124959
median filter	0.03728408

In this case it can be seen that the best result was obtained for the mean filter and the worst for the median filter. Using the proposed method results in a much better RMSE than the median filter and slightly worse than the mean filter. Such results confirm the expectation for reducing of Gaussian noise.

Last there were performed experiments with a real biomedical image of size 400×380 and the same as previously described Gaussian noise. The original and disturbed images are presented in figure 11. For the image from figure 11(b) there was performed filtration and the output images are presented in figure 12. The table 6 presents the root mean-square error between the original image, i.e. figure 11(a), and the output images 12(a), (b) or (c). In this case again, as expected, the best result was obtained for the mean filter, the worst for the median filter and using the proposed method results in a much better RMSE than the median filter and slightly worse than the mean filter.

(a)   (b)
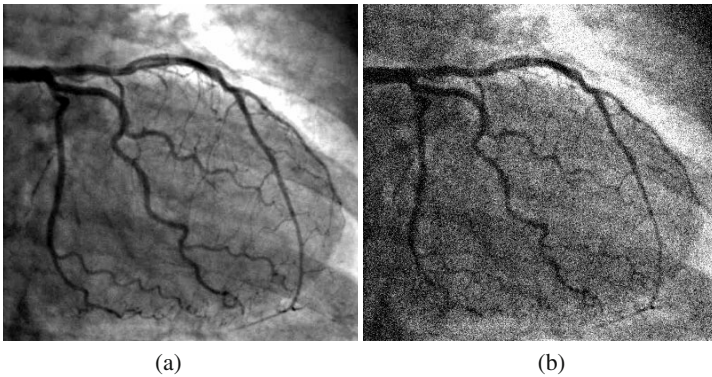
Fig. 11 (a) Original real biomedical image, (b) the same image with Gaussian noise

Table 6 Root mean-square error for noise reduction in image from figure 11(b)

method	RMSE
mean filter	0.04090487
adaptive weighted averaging	0.0416553
median filter	0.04503859
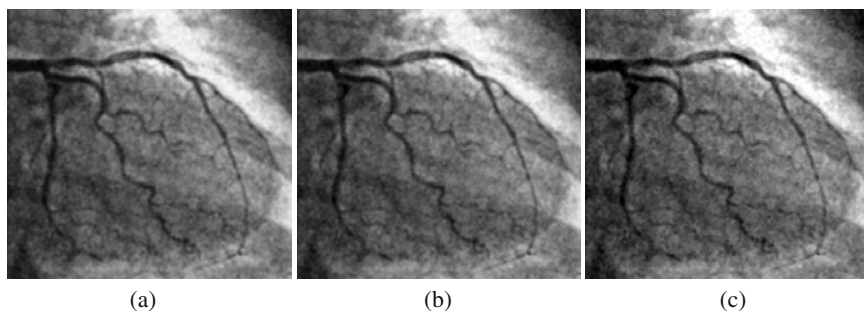
Fig. 12 Results of noise reduction for image from figure 11(b) using:(a) mean filter, (b) adaptive weighted averaging, (c) median filter

4 Conclusions

Results of performed experiments show that proposed adaptive weighted averaging filtering method is close to optimal for both salt-and-pepper and Gaussian noise. In reality noise is usually characterized by mixture of these two types and author expects that the new method could be useful in application to real images.

The main disadvantage of the proposed method is its computational complexity significantly greater than the mean filtering and similar to the median filtering. However it is worth noting that the iterative procedures to obtain weights for each pixel in image could be performed parallel. Lately NVIDIA has developed the CUDA programming model and software environment to let programmers write scalable parallel programs using a straightforward extension of the C language [3]. Thus author intends to implement the proposed method in the CUDA environment.

References

1. Brandt, S.: Statistical and Computational Methods in Data Analysis. Springer, New York (1997)
2. Davies, E.R.: Machine Vision: Theory, Algorithms and Practicalities. Academic Press, San Diego (1990)
3. Garland, M., et al.: Parallel Computing Experiences with CUDA. IEEE Micro. 28(4), 13–27 (2008)
4. Gonzalez, R.C., Woods, R.E.: Digital Image Processing. Prentice Hall, Upper Saddle River (2002)
5. Momot, A.: Fuzzy Weighted Averaging of Biomedical Signal Using Bayesian Inference. In: Man-Machine Interactions. Advances in Intelligent and Soft Computing, vol. 59, pp. 133–140 (2009)
6. Vernon, D.: Machine Vision: Automated Visual Inspection and Robot Vision. Prentice-Hall, New York (1991)
7. Xu, Q., et al.: Adaptive Fuzzy Weighted Average Filter for Synthesized Image. In: Gervasi, O., Gavrilova, M.L., Kumar, V., Laganá, A., Lee, H.P., Mun, Y., Taniar, D., Tan, C.J.K. (eds.) ICCSA 2005. LNCS, vol. 3482, pp. 292–298. Springer, Heidelberg (2005)

Photodynamic Image e-Atlas in Diagnostic and Treatment Procedures

Ewa Pietka, Aleksander Sieron, Dominik Spinczyk, Przemyslaw Szabelak, Sebastian Kwiatek, and Jakub Murawski

Abstract. There is a rapidly growing interest in electronic atlases including images with medical reports and quantitative description of pathological regions of interest. The e-atlases are mostly used by students and residents for teaching and training. However, an atlas my also be employed in everyday clinical practice. An imaging system that integrates an e-atlas of photodynamic studies with computer assisted diagnostic and therapeutic procedures is presented. Image processing results are stored in the database and may also be applied in the teaching and training process. The e-atlas includes photodynamic studies with clinical reports, location of the biopsy enter, selected points of the highest autofluorescence intensity to be subjected to the therapeutic light exposure.

1 Introduction

Photodynamic diagnosis and therapy is a non-invasive procedure employed in an early stage of neoplastic diseases. It improves the detection of neoplastic tissues that may not be visible in traditional procedure with white endoscopy light. Photodynamic diagnostics is based on natural phenomenon of light emission from tissues after excitation with laser light of endogenous and exogenous substances selectively absorbed in neoplastic tissues. Autofluorescence images show pathological tissues as pseudo-color in red color scale and healthy tissue as green color scale. Clinical

Ewa Pietka · Dominik Spinczyk · Przemyslaw Szabelak · Jakub Murawski
Silesian University of Technology, Gliwice, Poland
e-mail: ewa.pietka@polsl.pl, dominik.spinczyk@polsl.pl,
przemyslaw.szabelak@polsl.pl, jakub.murawski@polsl.pl

Aleksander Sieron · Sebastian Kwiatek
Department of Internal Diseases, Angiology and Physical Medicine,
Center for Laser Diagnostics and Therapy, Bytom, Poland
e-mail: sieron1@tlen.pl, sebastiankwiatek@tlen.pl

experiences indicate [1, 2, 3, 4] that red color intensity is highly correlated with histological stage of neoplastic tissue.

The demand of an imaging system that manages a data repository and assists the medical diagnosis and therapy has become stronger and stronger. Since human observation is influenced by internal (coming form the observer) as well as external (often independent from the observer) impacts, the system is required to increase the objectivity and speed up the decision process. An access to clinical image data with medical reports and image analysis findings is also descried for student education and training attended by residents.

An imaging system requires two components which influence its effectiveness [5]. The first one is associated with an image processing methodology, the other deals with the data visualization or, in general, with a user friendly graphical interface. An overall "intelligent" workstation design becomes an important chain in modern medical diagnosis and therapy.

The photodynamic imaging e-atlas developed in this study supports the patient and image data acquisition, storage and communication as well as assists the physicians in selecting the point of the highest autofluorescence intensity for the biopsy and directs the light to the area of the skin where the photosensitize drug has been admitted. The system contains three modules, namely image acquisition, image archive and presentation, computer aided diagnosis and therapy. The following sections present the structure and integration of the these modules.

2　Acquisition Module

The acquisition module has been developed in order integrate the archive and presentation module with the existing acquisition station (Fig. 1). The local acquisition station registers the endoscopic images and stores them in a file system of a local workstation. The system is lacking the access policy, hierarchy, concurrent access, and data structure.

In this study a data structure has been built. The hierarchy reflects the dataflow. Patient data is introduced and assigned to the patient visit. Then, the interface scans the local directory (Fig. 2), indicates new data and (if required) transfers it to the patient record in the database. Thus, the visit record is updated by adding a single image or an image series. The management of the patient data, image data and medical reports is supported by the image archive and presentation module.

3　Image Archive and Presentation Module

The image archive and presentation module is based on a three-layer structure. It contains a data layer, an application layer, and a presentation layer.
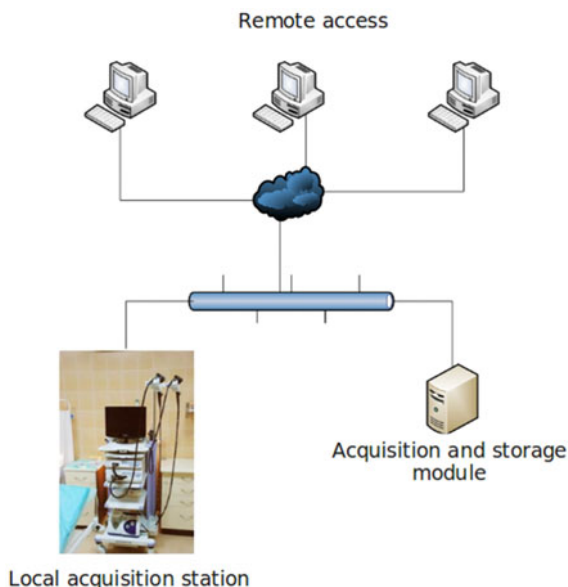
Fig. 1 System architecture

At the first layer a database management system (DBMS) is selected. It is responsible for the data archive and distribution. There are certain features that the database engine has to provide. They do not differ significantly from a general database system, yet some of them are of particular importance.

Authorized access to the data, shared among various users and processes, has to be granted remotely. Security constrains define rules to be checked whenever an access is attempted to sensitive data. Different constrains need to be established for each type of access (retrieve, insert, delete, etc.) to each piece of information in the database.

Inconsistency need to be avoided particularly when a standard set of data is built. All data updates have to be propagated. Integrity (i.e. ensuring that the data in the database is correct) should be maintained. Centralized control of the database can help in avoiding such problems by permitting the data administrator to define (and the DBMS to implement) integrity constraints [6].

Discussing the database structure one has to keep in mind, that a medical database contains various types of information. Since the data layer stores the images and the corresponding data, a patient record contains alphanumerical data (patient data, medical reports), images (a single image or an image series), regions of interest selected from a diagnostic image, extracted features, user data etc.

The data repository can be entered for clinical as well as education purpose (Fig. 3). The aim of the clinical unit is (1) to update the medical record and (2) present the data during medical procedures. First, the database is searched by the patient name or patient ID. Medical fields including reports, the histopathological
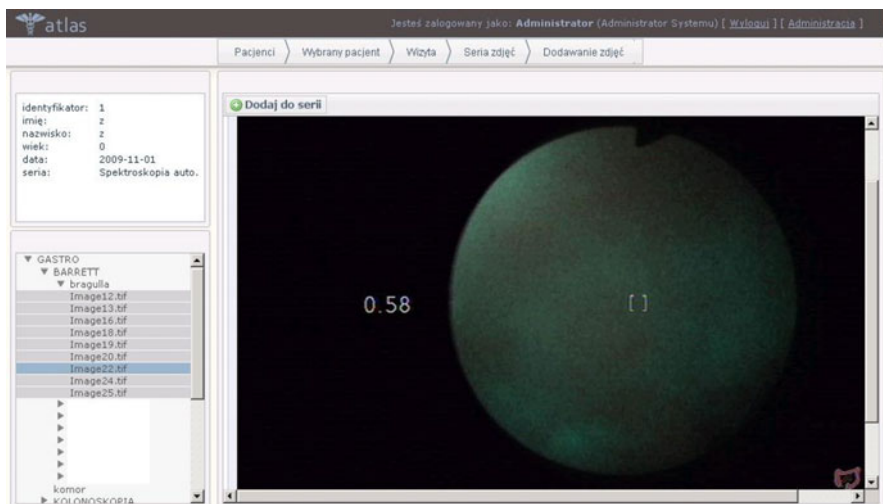
Fig. 2 Image acqusition management window

record, image processing findings are updated. Image processing tools, required for the quantitative image description are incorporated into the computer aided diagnosis and therapy module and described in Sec. 4.

Patient data already stored in the data repository is then available for clinical performance. A monitoring of the patient therapy by comparing follow-ups is also granted.

For education, a Teaching and Training Unit has been developed. The database is searched by diseases. All studies collected in the database are accessible from the Teaching and Training Unit level. Two access modes are available. One refers to the teaching activity, the other one (the training mode) permits also a user to train the preparation of complete medical report.

For teaching purpose the entire anonymous patient record is displayed. Thus, image data with the corresponding medical record describing the case is presented to the user. A student can enter all available cases of a particular disease.

In the Training Unit only the image data is shown and the user may try to report it. Thus, the user selects a particular disease. Then, a randomly selected image data of one patient is displayed without a report. The student/resident reports the case and then compares it with the medical record of this patient that has been prepared by an expert.

The system allows also the computerized image analysis to be trained. A delineation of the region of interest has been implemented as an interactive process of locating elements using vector graphics elements in an application working on the client side (in a web browser). Circles, polygons consisting of segments or Bezier curves may be applied to outline a region (Fig. 4). A region delineated by a student working in the training mode is then compared with an region selected by an expert.
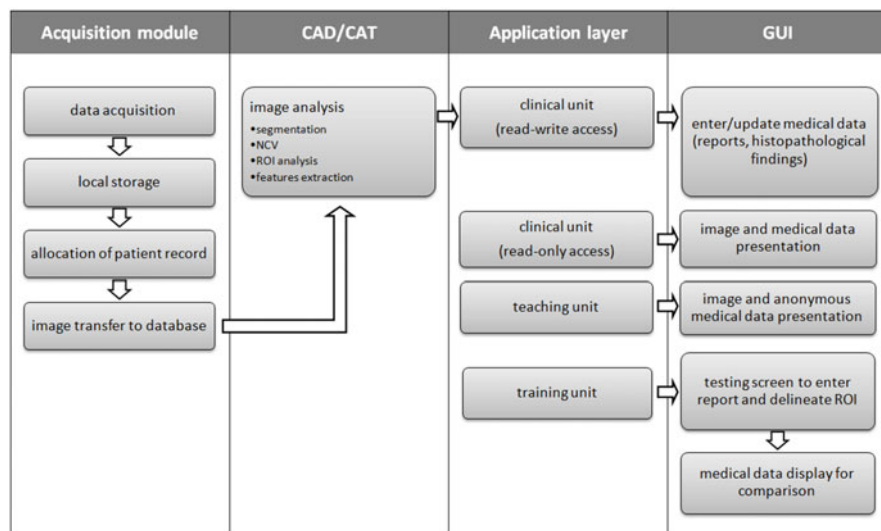
Fig. 3 Flow chart of the e-atlas integrated with CAD and CAT procedures

The ROI selection and analysis procedures are included in the computer assisted diagnosis and treatment module (as described in the following section).

The content of database is available to the authorized user through the graphical user interface (GUI) referred to as the presentation layer. The GUI offers an access to the data through navigation panels in a web browser window. A main bar on the top of the GUI window contains links to the Teaching and Training Units, help and the data acquisition module. In order to provide an access at various levels, four types of a user account have been created: read and write all, read and write new examination, read only, read only anonymous data. The read and write as well as read only modes are assigned to clinicians, whereas the later is given to students and residences for teaching and training.

4 Computer Aided Diagnosis and Therapy

The e-atlas incorporates image analysis procedures able to assist the diagnosis and treatment procedure. The analysis includes the quantification analysis, region of interest segmentation, location of the biopsy enter, location of the target tissue subjected to the therapeutic light exposure.

The analysis starts with a background removal that features a high red to green colour components ratio that serves as a feature in further image processing. The analysis is performed on a grayscale representation of the image, which allows the threshold used for the background removal to be adjusted. The gray scale representation image is generated with a commonly used formula
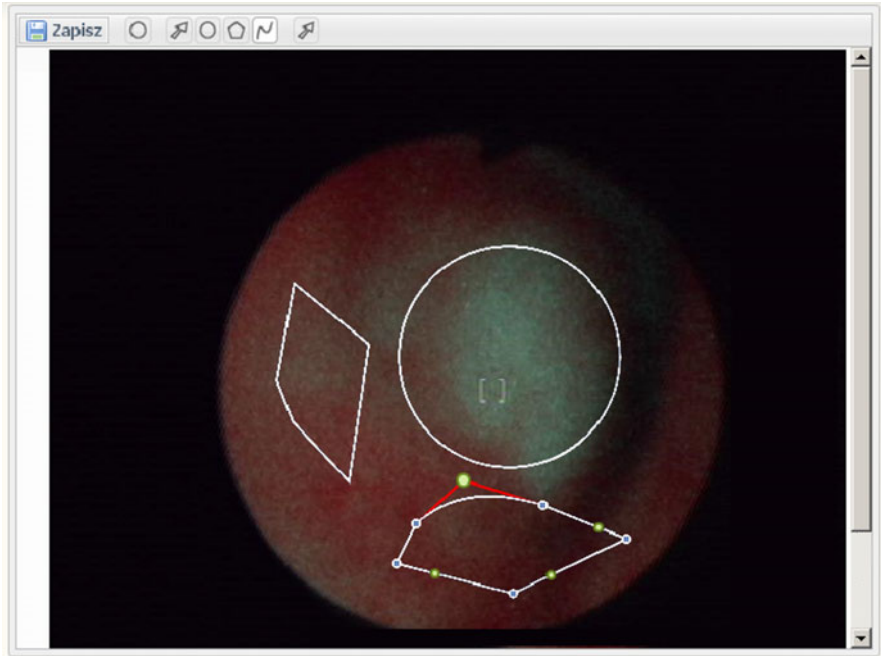
Fig. 4 Selecting regions of interest

$$Y = 0.3 \cdot R + 0.59 \cdot G + 0.11 \cdot B \tag{1}$$

where: R, G, B are red, green and blue colour components of the saturated image.

The threshold value is selected at the very periphery of the image close to the image edge. The segmentation result is presented on the separate tab in the application window. The background pixels are removed form the colour image as well.

The next step of the image analysis is the quantification of the colour values. A Numerical Colour Value (NCV) is defined as the ratio of a red colour components to green colour components in each pixel [1]. A histogram of the NCV matrix is found and employed for the ROI selection (Fig. 5). Displayed to the clinician it permits the threshold value to be adjusted. Since the threshold value is case-dependant (depends on the type of tissue and type of disease), it is selected by the clinician. Then, a region of interest is selected. In a separate image a set of points corresponding to the selected regions is superimposed over the original image. Within the ROI the greatest value of the NCV is found and marked in the image. It shows the point to be confirmed by the histological procedure.

When using the programme a user can observe all four stages on the tab control placed in the main window of the application. The original photodynamic image with the NCV value and the pixel position can be tracked when moving the camera.
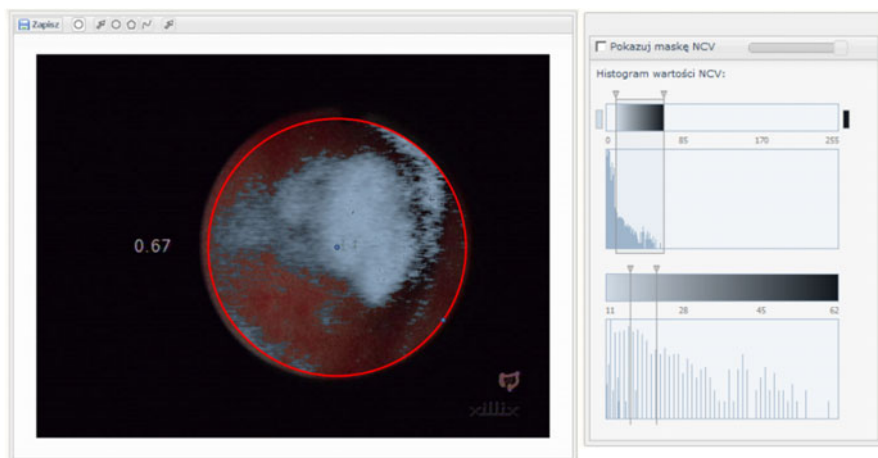
Fig. 5 Sample NCV mask

The procedure permits also follow-ups to be compared. The entire analysis is performed after a treatment therapy has been applied to the patient. The images are subjected to the thresholding procedure, following by the NCV analysis.

During the therapy, the light activates oxygen molecules that destroy certain types of cancer cells. The light source needs to be directly applied to the target tissue for a specific period of time [7].

A navigation system for the surface skin therapy has been built. It navigates the light source in order to direct the light to the area of the skin where the photosensitize drug has been admitted. The system contains a smart robotic arm used to fix the light source and direct the light to the target. The position of the arm is controlled by a navigation system which sets the required angle and distance above the tumor tissue and changes it during the procedure.

The navigation is also supported by the image analysis. Once the red to green colour component map is also found, the region of interest is selected as described above. It shows the cancer and precancer area to be subjected to the light exposure.

5 Results

The e-altas includes a set of 150 clinical cases, including images of Barrett's esophagus, esophageal cancer, gastric ulcers, gastric cancer, colitis ulcerosa, many types of polyps in colon, solitary rectal ulcers, colonic cancer, rectal cancer and also skin lesions like Morbus Bowen, Basal Cell Carcinoma, Squamous Cell Carcinoma, and actinic keratosis, oral lesions like oral leukoplakia and oral cancer, images captured during AFL bronchoscopy with many types of epithelial lesions to be displayed by GUI. A user can interactively indicate abnormalities. The NCV (red to green colour components ratio of pixel) analysis has been implemented. The comparison of

normal and pathological cases is also available. All studies with medical reports have been collected at the Clinical Department of Internal Diseases, Angiology and Physical Medicine in Bytom. Before being archived in the database, all cases have been histopathologically confirmed.

6   Summary

Autofluorescence and photodynamic diagnostics allows the detection of small focal neoplastic tissues even not visible in traditional white light endoscopy. An imaging system that acquires the image data from a local workstation and archives it in a data repository has been built. Then, using the computer aided diagnosis module, processing functions are applied and assist physicians during the region of interest analysis. The data repository is used for both clinical and educational purpose. An access to photodynamic studies increases the knowledge in the area of photodynamic diagnosis and treatment and shows its importance in the early stage of neoplastic diseases.

References

1. Sieron, A., Gibinski, P., Pustelny, T., Kwiatek, S., Opilski, Z., Krawczyk-Krupka, A., Woznica, W., Maciak, E., Kubica, W., Urbanczyk, U., Latos, W.: Optical biopsy using spectral camera in BCC nad oral leukoplakia. Photodiagnosis and Photodynamic Therapy 5, 271–275 (2008)
2. Svanberg, K., Klintenberg, C., Nilsson, A., Wang, I., Andersson-Engels, S., Svanberg, S.: Laser-based spectroscopic methods in tissue characterization. Ann. NY Acad. Sci. 838, 123–129 (1998)
3. Won, Y., Hong, S.H., Yu, H.Y., Kwon, Y.H., Yun, S.J., Lee, S.C., Lee, J.B.: Photodetection of basal cell carcinoma using methyl 5-aminolaevulinate-induced protoporphyrin IX based on fluorescence image analysis. Clin. Exp. Dermatol. 32(4), 423–429 (2007)
4. Sieron, A., Kwiatek, S.: Twenty years of experience with PDD and PDT in Poland - Review. Photodiagnosis and Photodynamic Therapy 6, 73–78 (2009)
5. Pietka, E., Gertych, A., Witko, K.: Informatics Infrastructure of CAD system. Comp. Med. Img. Graph. 29, 157–169 (2005)
6. Date, C.J.: An Introduction to Database Systems. Addison-Wesley, Reading (2000)
7. Panjehpour, M., Julius, C.E., Phan, M.N., Vo-Dinh, T., Overholt, S.: Laser induced fluorescence spectroscopy for in vivo diagnosis of nonmelanoma skin cancers. Lasers Surg. Med. 31(5), 367–373 (2002)

Multiseries MR Data in Brain Tumours Segmentation

Jacek Kawa, Paweł Szwarc, Barbara Bobek-Billewicz, and Ewa Piętka

Abstract. The paper deals with the segmentation of brain tumours in magnetic resonance (MR) images. The segmentation method developed is based on the analysis of two MR series, and namely contrast enhanced T1W images and perfusion maps. The contrast enhanced T1W images are segmented with the use of the Kernelised Weighted C-Means (KWCM) method, yielding a binary mask of the suspected tumour. Next, the mask is superimposed over the perfusion maps. The perfusion intensities of corresponding areas in both brain hemispheres are compared. The results obtained for three subjects with glioblastoma multiforme (GBM) and anaplastic astrocytoma (AA) are discussed.

1 Introduction

Brain tumours remain one of the most difficult tumours to be treated as they often affect areas where the treatment of choice, namely the total tumour resection, is virtually impossible. Correct decisions concerning surgery, radiotherapy and

Jacek Kawa · Paweł Szwarc · Ewa Piętka
Silesian University of Technology, Gliwice, Poland
e-mail: jkawa@polsl.pl,
pszwarc@polsl.pl, epietka@polsl.pl

Barbara Bobek-Billewicz
Radiodiagnostics Department of the Maria Skłodowska-Curie Memorial Cancer Centre and Institute of Oncology, Gliwice Branch, Gliwice, Poland
e-mail: rtgsekretariat@io.gliwice.pl

chemotherapy planning strictly depend on the accurateness of tumour segmentation performed by a radiologist. This work done manually by a radiologist is a tedious and time-consuming task.

The aim of this research is to create an automatic algorithm that may be a most valuable tool for radiologists, assisting them in brain tumours segmentation in MR images.

1.1 Brain Tumours

Intracranial brain tumours are divided into two groups depending on the origin of cells building them: intraaxial and extraaxial tumours. Most of the intraaxial tumours consist of glial cells. These tumours called gliomas constitute some 50% of all brain tumours. Mostly, gliomas are built of astrocytal cells. These tumours comprising about 35% of all brain tumours are called astrocytomas. The glioblastoma multiforme (GBM) is an astrocytoma tumour, classified by the World Health Organisation as having the highest IVth grade of malignancy (WHO IV) and thus being one of the most aggressive tumours. The GBM's constitute one fifth of all brain tumours [1]. The anaplastic astrocytoma is a WHO III astrocytoma, accounting for about 4% of all brain tumours [1].

These tumours are histologically very weakly delimited from healthy tissue. Necrosis, haemorrhage into the lesion and tumour angiogenesis are often to be encountered. Extended oedema is also frequently diagnosed. These characteristics make the proper delineation of high-grade astrocytomas boundaries a laborious and difficult task [1].

The relapse tendency of GBM's, even after radical resection and intensive radio- and chemotherapy treatment, results in very poor survival rates, with median survival rate with and without treatment of ca. 3 and 8 months respectively, the 3-year survival rate after GBM diagnosis being as small as 2% [1, 2]. The median survival rate for subjects with anaplastic astrocytomas ranges from 2 to 5 years [3].

Nevertheless, new treatment methods are tested and introduced, their efficiency being dependent on the correct tumour segmentation and quantification of its volume. Thus, the assistance to radiologists in the process of the GBM segmentation in MR images proves to be extremely vital.

1.2 Nature of MR Imaging Data

The segmentation method developed is based on the analysis of two MR series of subjects with diagnosed GBM or anaplastic astrocytoma, namely T1W images after the injection of Gadovist contrast agent and perfusion maps obtained on the basis of Perfusion-Weighted Imaging (PWI) series by means of manufacturer's software. The images were acquired with a 3.0T Phillips MR and a 1.5T Siemens MR. Both imaging series are transverse-type and made with the same angle positioning in coronal and sagittal planes. The use of a contrast agent allows the regions of broken brain blood barrier to be separated. The enhancement of signal intensity, resulting

from the shortening of the T1 time and caused by the accumulation of gadolinium compounds, is best to be noticed in T1W images. The irregular, ring-shaped signal intensity enhancement, specific for GBM's [4], is well to be seen in most of the images.

PWI plays an important role in treating primary brain tumours, as it makes it possible to find the most malignant part of the tumour. It seems that the enhancement of the relative cerebral blood volume (RCBV), whose amount is represented by the image intensity level of the perfusion maps in the lesion area, is caused by tumour angiogenesis, which may indicate the grade of malignancy of the tumour [1]. The RCBV coefficient is also helpful in telling the actual tumour areas from the radionecrosis areas and postoperative granulation tissue, all of them being hyperintensive in T1W images after contrast agent administration.

The midline structures are often displaced due to an expansive lesion, which makes it difficult to correctly establish the brain symmetry line in MR images. The brain symmetry itself may also often be disturbed by the tumour due to the mass effect [1].

1.3   Brain Tumour Segmentation Approaches

Most of the approaches to brain tumour segmentation are studies on automatic segmentation algorithms, although semi-automatic methods are also common. However, none of them has yet succeeded in creating universal software able to facilitate the segmentation of all kinds of brain tumours. The difficulty of the problem lies mainly in the variety of shapes and locations of lesions.

As far as semi-automatic brain tumours segmentation methods are concerned, the most widespread algorithms are defined respectively as seeded region growing and active contours and are dealt with for T1W contrast images [5]. In the active contours algorithm the geodesic deformable model provided by [6] and the geometric active contours method based on the theory of curve evolution were implemented [5].

Various approaches to the automatic brain tumour segmentation have been applied. One-class Support Vector Machine (SVM) was developed to separate tumour and non-tumour regions in [7]. Structural analysis-based tumour segmentation scheme was presented in [8]. The authors of [9] presented Gaussian Mixture Model (GMM) and SVM-based methods for brain segmentation.

2   Segmentation Algorithm

The segmentation algorithm developed in this study consists of two phases. The segmentation of contrast enhanced T1W series is followed by the analysis of perfusion maps.

2.1 Segmentation of Contrast Enhanced T1W Series

The basic algorithm, permitting the segmentation of brain matter, cerebrospinal fluid and contrast enhanced areas in the contrast enhanced T1W series, is the Kernelised Weighted C-Means (KWCM). This method emerged directly from the standard Fuzzy C-Means (FCM) method [10, 11].

FCM is a clustering method based on the minimisation of an objective function. It divides a finite set of elements into c clusters with respect to some given criterion [11, 12]. The data clustering methods using kernel functions allow a nonlinear transposal of the data into a high-dimensional space. The KWCM method fully transposes the clustering process into that high-dimensional space [13, 14]. The Radial Basic Function (RBF) is used as kernel function for the KWCM algorithm in the software. The feature incorporated in the clustering process is the signal intensity.

The FCM objective function for partitioning a dataset

$$\mathbf{X} = \{x_1, x_2, \ldots, x_i, \ldots, x_N\} \tag{1}$$

into c clusters can be defined as [11]

$$J(\mathbf{U}) = \sum_{k=1}^{c} \sum_{i=1}^{N} u_{ki}^{\beta} d_{ki}, \tag{2}$$

β being the fuzzyfication parameter, d_{ki} the distance measure selected between the ith object and the kth cluster centre and u_{ki} the elements of $\mathbf{U}$ - the fuzzy partition matrix.

In each tth iteration of the FCM algorithm, for each cluster k, the fuzzy cluster centre [12]

$$v_k^{(t)} = \frac{\sum_{i=1}^{N} u_{ki}^{\beta} x_i}{\sum_{i=1}^{N} u_{ki}^{\beta}} \tag{3}$$

is calculated using fuzzy membership values in the partition matrix $\mathbf{U}^{(t)}$. In the first iteration $\mathbf{U}^{(1)}$ as well as the cluster centres are set to random values. In the next steps $\mathbf{U}^{(t+1)}$ values are recomputed following the equation [12]

$$u_{ki}^{(t+1)} = \frac{1}{\sum_{j=1}^{c} \left(\frac{d_{ki}}{d_{ji}} \right)^{\frac{1}{\beta-1}}}, \tag{4}$$

where d denotes the distance metric selected. When the selected norm $\|\mathbf{U}^{(t+1)} - \mathbf{U}^{(t)}\| \leq \varepsilon$, the computations stop and the defuzzyfication makes the analysed data x_i belong to the class k, if the u_{ki} fuzzy membership value is the highest of all u_{ji} $(j = 1, \ldots, c)$ values.

The Kernelised Fuzzy C-Means (KFCM) algorithm adopts a kernel-induced distance metric, the objective function being [15]

$$J(\mathbf{U}, \phi) = \sum_{k=1}^{c} \sum_{i=1}^{N} u_{ki}^{\beta} \|\phi(x_i) - \phi(v_k)\|^2, \tag{5}$$

with ϕ denoting a nonlinear mapping function into a higher dimensional feature space.

Substituting the Gaussian RBF

$$\phi_G(x, y) = \exp\left(\frac{-\|x - y\|^2}{\sigma^2}\right) \tag{6}$$

as the kernel function and bearing in mind that $\phi_G(x, x) = 1$, equation (5) can be simplified to

$$J(\mathbf{U}, \phi) = 2 \sum_{k=1}^{c} \sum_{i=1}^{N} u_{ki}^{\beta} (1 - \phi_G(x_i, v_k)). \tag{7}$$

Taking the first derivative of $J(\mathbf{U}, \phi)$ with respect to u_{ki} and comparing it to zero yields the following equation for the fuzzy partition matrix values [15]

$$u_{ki}^{(t+1)} = \frac{(1 - \phi_G(x_i, v_k))^{\frac{-1}{\beta - 1}}}{\sum_{j=1}^{c} (1 - \phi_G(x_i, v_j))^{\frac{-1}{\beta - 1}}}. \tag{8}$$

The KWCM algorithm is a generalised version of the KFCM method, if the condition

$$v_k^{(t)} = \frac{\sum_{i=1}^{N} u_{ki}^{\beta} \phi(x_i)}{\sum_{i=1}^{N} u_{ki}^{\beta}} \tag{9}$$

is imposed [16].

On the basis of the analysis of clusters and the fuzzy membership values brain matter, background, cerebrospinal fluid and suspected tumour or fat areas are segmented. The masks achieved in that way are processed with mathematical morphology operations, yielding the white and grey matter areas and thus narrowing down the region of interest. At this stage the location of lateral ventricles and eyeballs is also detected. After further automatic corrections, including the Quickhull [17] algorithm, the final suspected tumour areas mask is computed [16] (Fig. 1 and 2).

In the case of high-grade astrocytomas the discontinuousness of tumour areas caused by the necrotic tissue inside the tumour is often to be encountered (Fig. 2). The necrotic tissue seems to be correctly qualified by the KWCM algorithm as non-tumourous.

2.2 Perfusion Maps Analysis

As already mentioned, both imaging series have the same length, angle positioning in coronal and sagittal planes and identical location of the brain in the field of view
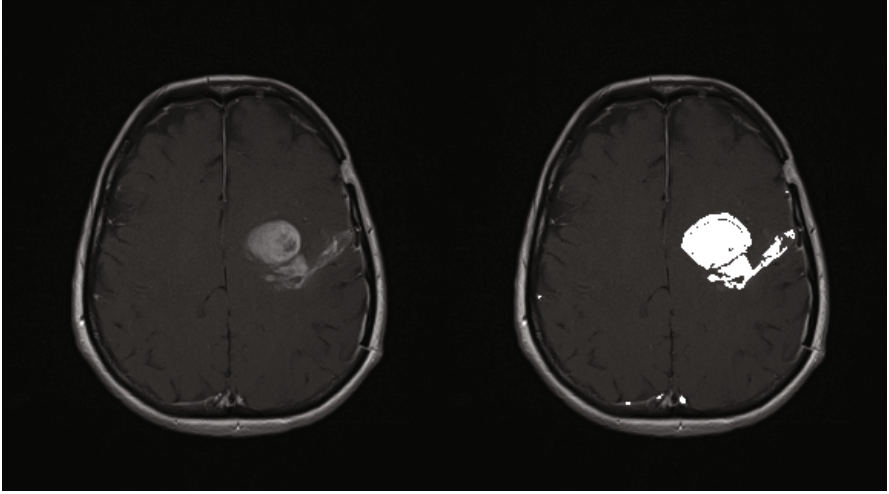
Fig. 1 Original contrast enhanced T1W image selected from study no. 1 of subject no. 1. (left) and the same image with the suspected tumour areas mask superimposed (right)
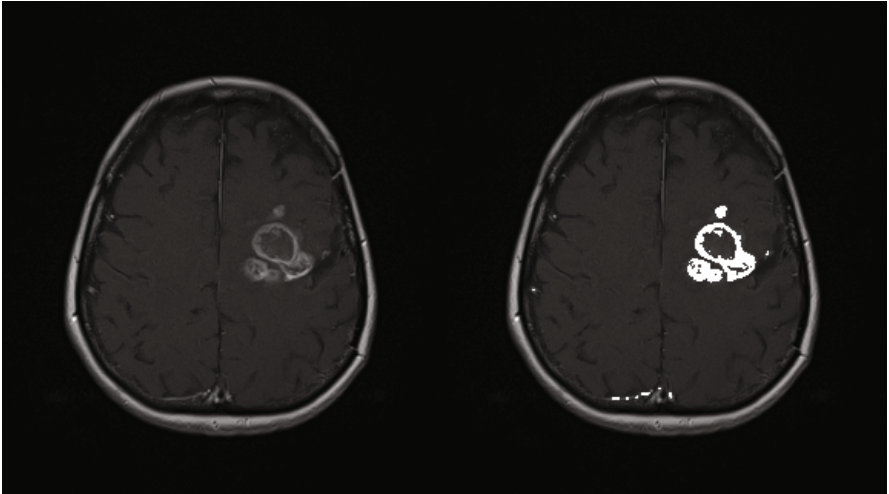
Fig. 2 Original contrast enhanced T1W image selected from a follow-up study of subject no. 1 (left) and the same image with the suspected tumour areas mask superimposed (right)

of the images. The perfusion maps, originally having a 128×128 pixel resolution, are first pre-processed with the bicubic interpolation algorithm [18] to achieve the same pixel dimensions as the contrast enhanced T1W images, thus making it possible to match corresponding slices coming from two analysed series.

The brain mask on the perfusion maps is found after interpolation by means of simple image thresholding and hole filling. The number of pixels common with the brain mask from the contrast enhanced T1W series, obtained during its segmentation process, is calculated. Then, the brain mask from the perfusion maps is shifted a given number of pixels in different directions. The number of pixels common with the brain mask from the contrast enhanced T1W series is calculated for each shifting. The shifting, for which the number of common pixels is the highest, is considered as the best alignment matching the two series.

Next the perfusion maps are examined on the basis of their signal intensity. For each lth lesion, belonging to the final suspected tumour areas mask, the mean pixel intensity value m_l is computed. The mean pixel intensity s_l is also computed for the area lying symmetrically to the lth lesion in the opposite hemisphere.

This requires the brain symmetry line to be located, since the head during an examination may not be centred within the field of view of an image. The symmetry line is searched in a set of candidate lines created by shifting to the left and to the right and rotating the image symmetry line. The line which has the least common pixels with the mask of brain hemispheres is considered to match best the real brain midline and is thus defined as the symmetry line. In most cases the defined symmetry line is slightly shifted and rotated in respect to the image symmetry line.

If the mean pixel intensities ratio $\frac{m_l}{s_l} < T_1$, where T_1 denotes the user-selected threshold for the whole analysis of perfusion maps, the analysed lesion is classified as non-tumourous and discarded from further analysis. The user may additionally discard lesions that are less than a given number of pixels in size.

For pixels belonging to the yet not discarded lesions a similar analysis is applied, i.e. pixels whose symmetry-based signal intensity ratio is less than the user-defined T_2 threshold value, are rejected. This is performed in order to eliminate artefacts. The tumour areas mask is thus finally obtained (Fig. 3, 4, 5 and 6).

In the tumour areas the number of pixels is calculated and multiplied by the unit voxel volume based on the DICOM data (slice thickness plus the interslice gap, which are 5mm and 1.5mm respectively for the imaging data acquired with the 1.5T MR and 4.0mm and 0.0mm respectively for the imaging data acquired with the 3.0T MR), yielding the final tumour volume.

3 Results

The tests have been performed on MR data of three subjects with diagnosed high-grade astrocytomas, namely one subject with GBM (subject no. 1) and two subjects with anaplastic astrocytoma (subjects no. 2 and no. 3). For one subject three consecutive MR studies were available. For each of the other subjects there was one MR study available. Four studies performed on the 1.5T MR consisted of 19 slices and
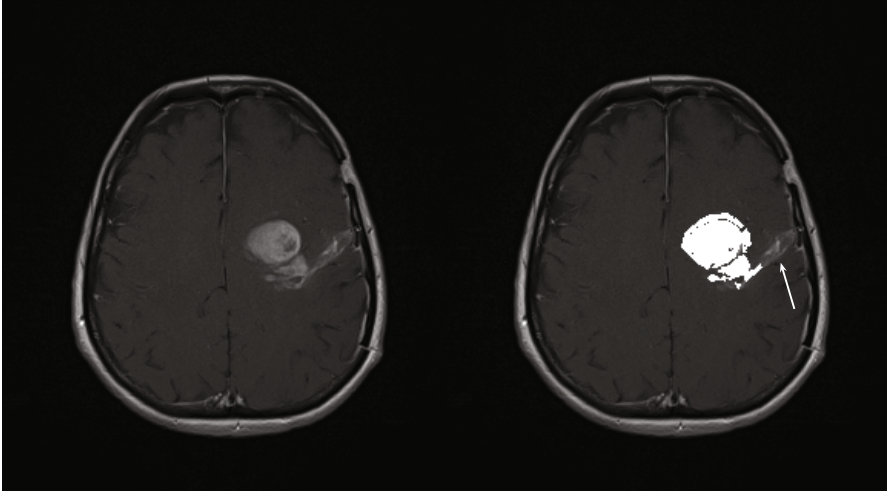
Fig. 3 Original contrast enhanced T1W image selected from study no. 1 of subject no. 1. (left) and the same image with the final tumour areas mask superimposed (right). An arrow indicates the postoperative granulation tissue area.
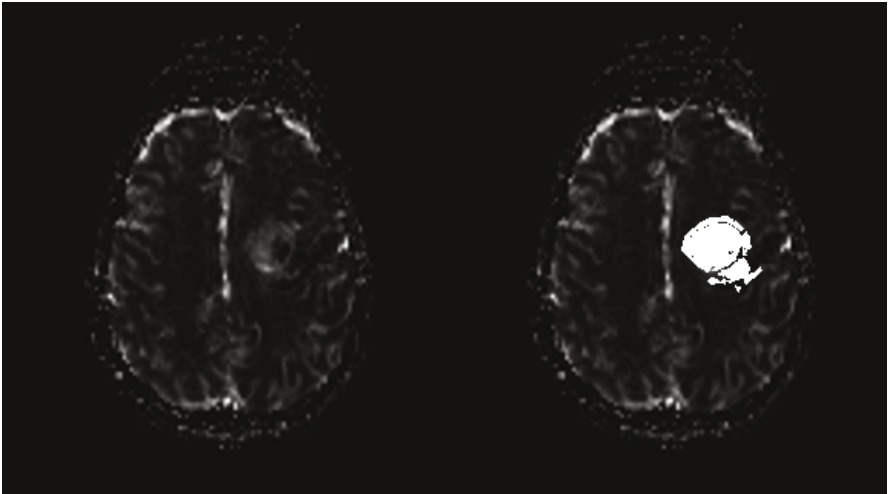
Fig. 4 Original perfusion map corresponding to the T1W contrast image in Fig. 1 (left) and the same map with the final tumour areas mask superimposed (right)
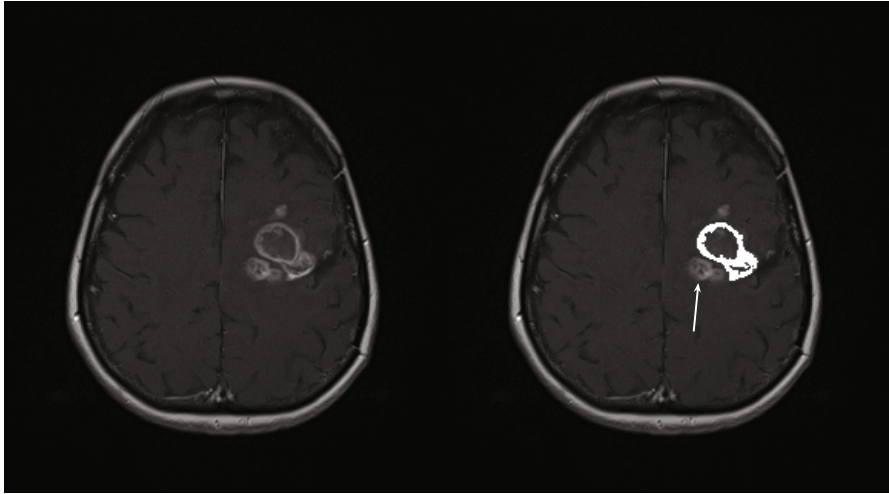
Fig. 5 Original contrast enhanced T1W image selected from a follow-up study of subject no. 1 (left) and the same image with the final tumour areas mask superimposed (right). An arrow indicates the radionecrotic tissue area.
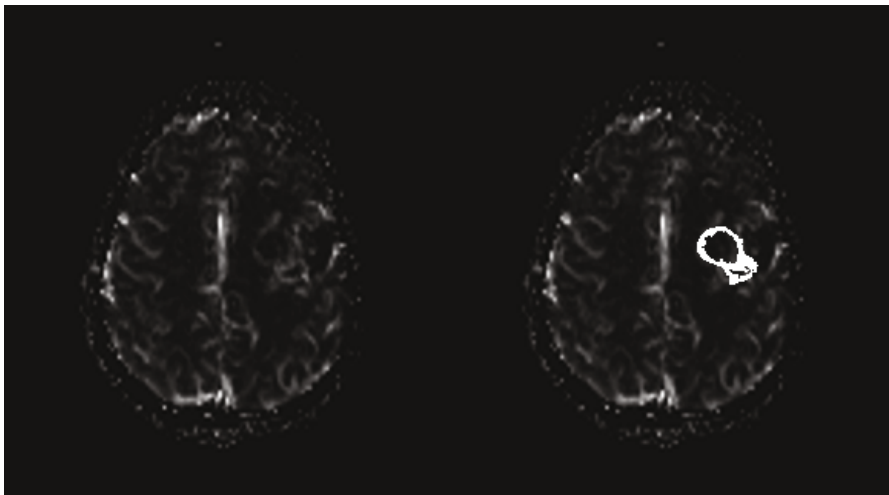
Fig. 6 Original perfusion map corresponding to the T1W contrast image in Fig. 2 (left) and the same image with the final tumour areas mask superimposed (right)

one study performed on the 3.0T MR consisted of 36 slices, yielding the total of 112 slices analysed.

The detailed results obtained at the subsequent steps of the segmentation algorithm are presented in Fig. 1-6. The selected images, shown in Fig. 1, 3 and 4, come from the study performed after partial resection of the tumour, before radiotherapy treatment. The exclusion of the postoperative granulation tissue, indicated by an arrow in Fig. 3 from the final tumour areas mask due to the analysis of the perfusion map is well to be noted.

Radiotherapy resulted in a decrease in the tumour volume, although a hyperintensive area of radionecrotic tissue appears instead in the T1W contrast image (Fig. 2) coming from a follow-up study of the same subject. The analysis of the corresponding perfusion map resulted in the exclusion of the radionecrotic tissue area (arrow in Fig. 5), from the final tumour areas mask. All the obtained segmentation results were compared with manual segmentation verified by a radiologist. Three similarity measures were used, namely sensitivity

$$S = \frac{TP}{TP+FN} \cdot 100\%, \tag{10}$$

specificity

$$P = \frac{TN}{TN+FP} \cdot 100\% \tag{11}$$

and the Dice Similarity Coefficient

$$DSC = \frac{2 \cdot TP}{2 \cdot TP+FP+FN} \cdot 100\%, \tag{12}$$

where TP denotes the number of true positives, TN the number of true negatives, FP the number of false positives and FN the number of false negatives. The similarity coefficients for all the analysed studies are gathered in Tab. 1. In case of subjects no. 2 and no. 3 all the hyperintensive lesions in the contrast enhanced T1W series are radionecrotic tissue areas, so only specificity is calculated for these studies.

Table 1 Automatic Segmentation Results

Subject no.	Study no.	S(%)	P(%)	DSC(%)
1	1	80.965	99.924	74.381
1	2	78.892	99.944	75.630
1	3	67.736	99.963	67.218
2	4	-	99.928	-
3	5	-	99.971	-

4 Conclusions

The brain tumours segmentation results achieved by using the segmentation algorithm described above seem to be very promising. Future work will include further improving the segmentation method and performing tests on a larger amount of imaging data of subjects with diagnosed high-grade gliomas as well as on MR images of subjects with other types of brain tumours.

References

1. Brant, W.E., Helms, C.A.: Fundamentals of Diagnostic Radiology, vol. I. MediPage, Warszawa (2007) (Polish translation)
2. Krex, D., Klink, B., Hartmann, C., et al.: Long-Term Survival with Glioblastoma Multiforme, http://brain.oxfordjournals.org/cgi/content/full/130/10/259
3. Kennedy, B., Bruce, J.N.: Astrocytoma (2009), http://emedicine.medscape.com/article/283453-overview
4. Runge, V.M.: Clinical MRI. Elsevier Urban and Partner, Wrocław (2007) (Polish translation)
5. Salman, Y.M., et al.: Validation Techniques for Quantitative Brain Tumours Measurement. In: IEEE Engineering in Medicine and Biology 27th Annual Conference, Shanghai, China (2005)
6. Kimmel, R., Caselles, V., Sapiro, G.: Geodesic Active Contours. International Journal on Computer Vision 1, 61–97 (1997)
7. Zhou, J., et al.: Extraction of Brain Tumour from MR Images Using One-Class Support Vector Machine. In: IEEE Engineering in Medicine and Biology 27th Annual Conference, Shanghai, China (2005)
8. Xuan, X., Qingmin, L.: Statistical Structure Analysis in MRI Brain Tumour Segmentation. In: Fourth International Conference on Image and Graphics, Chengdu (2007)
9. Hongmin, C.: Probabilistic Segmentation of Brain Tumours Based on Multimodality Magnetic Resonance Images. In: Fourth IEEE International Symposium on Biomedical Imaging From Nano to Macro, Washington, DC (2007)
10. Bezdek, J.C.: Pattern Recognition with Fuzzy Objective Function Algorithms. Plenum Press, New York (1981)
11. Xu, R., Wunsch, D.: Survey of Clustering Algorithms. IEEE Transactions Neural Networks 16, 645–678 (2005)
12. Mekhalfa, F., Goumeïdane, A.B., Nacereddine, N.: Unsupervised Algorithm for Radiographic Image Segmentation Based on the Gaussian Mixture Model. In: EUROCON 2007 The International Conference on Computer as a Tool, Warsaw (2007)
13. Girolami, M.: Mercer Kernel-Based Clustering in Feature Space. IEEE Transactions Neural Networks 13, 780–784 (2002)
14. Wu, Z., et al.: Fuzzy C-Means Clustering Algorithm Based on Kernel Method. In: 5th International Conference on Computational Intelligence and Multimedia Applications (ICCIMA 2003), Xi'an, China, pp. 49–54 (2003)

15. Zhang, D., et al.: Kernel-Based Fuzzy Clustering Incorporating Spatial Constraints for Image Segmentation. In: Proceedings of the Second International Conference on Machine Learning and Cybernetics, Xi'an, China (2003)

16. Kawa, J.: Fuzzy Methods in Segmentation of Demyelination Plaques in Brain MR Images, PhD Thesis, Silesian University of Technology, Department of Automatic Control, Electronics and Computer Science, Institute of Electronics, Gliwice (2007) (in Polish)

17. Barber, C.B., et al.: The Quickhull Algorithm for Convex Hulls. ACM Transactions on Mathematical Software 22, 469–483 (1996)

18. Keys, R.G.: Cubic Convolution Interpolation for Digital Image Processing. IEEE Transactions on Acoustics, Speech and Signal Processing ASSP 29, 1153–1160 (1981)

Symmetry Plane of the Brain on Perfusion MR Images

Rafał Henryk Kartaszyński and Paweł Mikołajczak

Abstract. In this paper we present algorithm which purpose is to estimate real symmetry plane of the brain on the MRI perfusion studies. Because perfusion slices are acquired in low resolution and larger distances, than standard MR studies, symmetry plane of the brain must be evaluated on the slice-by-slice basis. Presented algorithm therefore searches for symmetry line taking into consideration only anatomical information on each slice, ignoring adjacent slices. After presenting the method and sample results, we present results of tests.

1 Introduction

Perfusion MRI study [1, 2] is based on the use of injected contrast agent that changes the magnetic susceptibility of blood and thereby the MR signal which is repeatedly measured during bolus passage. Because images must be acquired very quickly and often, quality must be reduced and distance between slices increased. As the result of one study we get about 400 - 500 images (about 10 images per 40 passes). Fig. 1 shows example set of images acquired by a single pass.

As is known brain consists of two symmetrical cerebral hemispheres. Often to check for abnormalities, differences, two adjacent hemispheres on the same image are compared. To automatize this process, there is a need to find the symmetry plane of the brain. In this article we are using the term *symmetry line/plane* to describe a symmetry plane of the brain itself, not symmetry line of the data on image. Because image acquisition plane is not perpendicular to the brain symmetry plane, acquired slices rarely show symmetrical image (Fig. 1). Therefore only chance to find a symmetry plane is to find anatomical structures that appoint it.

Rafał Henryk Kartaszyński · Paweł Mikołajczak
Maria Curie Skłodowska University, Maria Curie-Skłodowska 1 square, 20 - 031 Lublin, Poland
e-mail: `hatamoto@op.pl, mikfiz@goblin.umcs.lublin.pl`
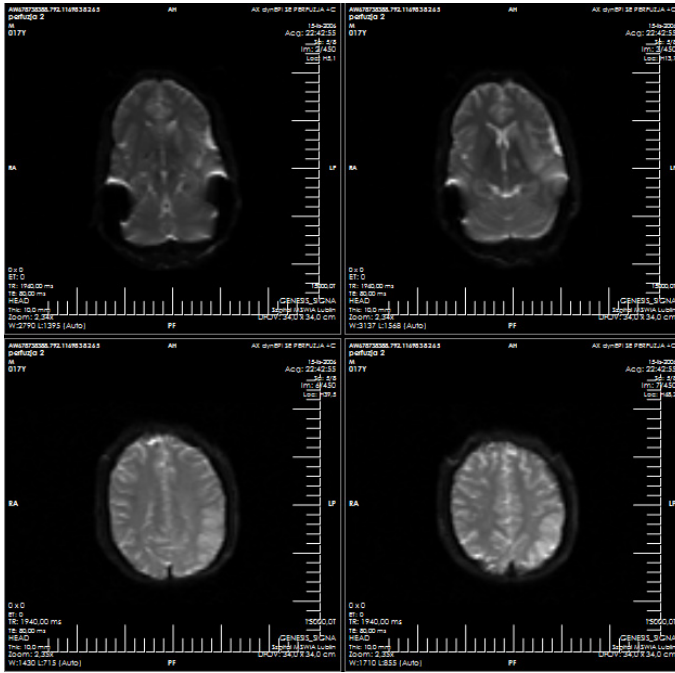
Fig. 1 Example MRI perfusion study (first pass) - part 1

Because this algorithm is to be used as a part of semi-automatic methods for comparing images of both cerebral hemispheres, we do not require it to be very correct. 1-2 degree deviation is acceptable.

2 Method

Due to the distance between slices, we are evaluating symmetry lines for each slice separately - we are not treating set of slices as a complete volume. Method itself can be divided into following steps:

1. Data preprocessing
2. Finding of the Characteristic Points (CP)
3. Linear regression

One of the main assumption of this algorithm is that brain symmetry line is not deviated more than about 10-15 degrees from the AP axis.
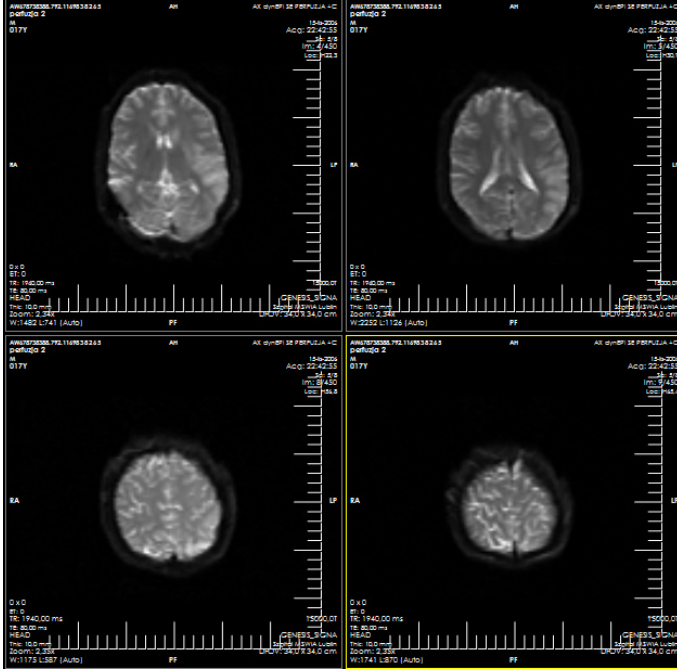
Fig. 2 Example MRI perfusion study (first pass) - part 2

3 Data Preprocessing

First step of presented algorithm is to remove background noise and other tissues surrounding brain. This can be achieved by simple thresholding to the certain value. By analyzing looks of the general histogram of the MRI perfusion slice (Fig. 3) we can find two main peaks on in. First on the left, represents numerous low frequency background pixels. With increasing intensity of pixels (to the right of the diagram) this peak / number of pixels decreases reaching local minimum (I0) and increasing again to reach another local maximum (IB). In general case of MRI study segmentation at the level I0 would be sufficient, but in the case of the perfusion images and for needs of this algorithm (see another step of the algorithm) we need a *deeper* segmentation. Therefore we have set the threshold value at

$$I_P = I_0 + \frac{(I_B - I_0)}{4} \tag{1}$$

Fig. 3 General histogram for the MRI perfusion slice

4   Finding Characteristic Points

To have some starting point for estimation of symmetry line algorithm is finding notches between hemispheres in the front and the back of the brain (Fig. 4). To find them image is scanned from beginning and from end line-by-line. According to assumption of brain not being too much rotated, we are narrowing the search to the 25% middle of the image (vertical *trench*). In the case of an average slice having 120x120 pixels, this *trench* would be 30px wide. Generally we are looking for the deepest (closest to the middle of the brain) notch in the front and back tissue of the brain. If there are several notches found, on the similar *deepness* and the difference (in deepness) is not greater than 2% (of the whole image size) then problem is not resolved and no CP is found. The same situation is when the *notch* is to wide (more than 4%) - de facto there is no notch (Fig.4.).
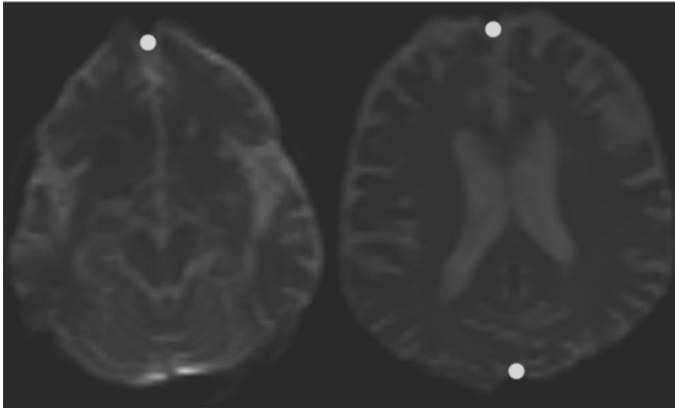
Fig. 4 First two CP (on the right). Case when one of the CP cannot be found (on the left).

From obvious reasons finding of these points is not always possible - on some slices there are no notches detectable. Also sometimes these points can be badly found, so they cannot be the only CP used to fit symmetry line into. Therefore

we have also incorporated method for finding other anatomical structures that can describe symmetry plane of the brain.

To do this we are continuing to scan-line the *trench* between first two CP or places where previous step have ended. The algorithm is searching for local minima or maxima on these scan lines that have local maxima or minima, respectively, on both its sides (see Fig. 5). On this figure one can see ideal cases that do not leave place for misinterpretation. And only such cases are used later. We do not need a lot of points in later step of the algorithm - linear regression. Most important is quality and accuracy of these points.

Of course in many cases good points will be found on adjacent scan lines. For each set of six points that are adjacent (occupy six neighbouring horizontal lines) middle one is selected as CP to represent all six points. Thanks to this step, only reasonable number of CP will be used in regression.
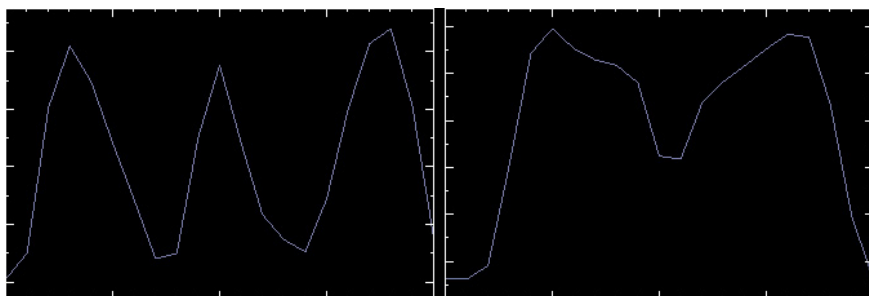
Fig. 5 Horizontal scan lines of the trench for two different slices

5   Perpendicular Regression

Given a set of Characteristic Points it is possible to fit a straight line into this set by using linear regression [3, 4, 5]. When we perform a regression fit of a straight line to a set of (x, y) data points we typically minimize the sum of squares of the *vertical* distance between the data points and the line. However in this case we have to optimize the perpendicular distances to the line.

One way of approaching this is to find the *principle directions* of the data points. Let's say we have the (x, y) coordinates of n data points. To make it simple, let's first compute the average of the x values, and the average of the y values, calling them X and Y respectively. The point (X,Y) is the centroid of the set of points. Then we can subtract X from each of the x values, and Y from each of the y values, so now we have a list of n data points whose centroid is (0, 0). To find the principle directions, imagine rotating the entire set of points about the origin through an angle q. This sends the point (x, y) to the point (x', y') where

$$x' = x * cos(q) + y * sin(q) \tag{2}$$

$$y' = -x * sin(q) + y * cos(q) \tag{3}$$

Now, for any fixed angle q, the sum of the squares of the vertical heights of the n transformed data points is $S = \sum [y']^2$, and we want to find the angle q that minimizes this. (We can look at this as rotating the regression line so the perpendicular corresponds to the vertical). To do this, we take the derivative with respect to q and set it equal to zero. The derivative of $[y']^2$ is $2y'(\frac{dy'}{dq})$, so we have

$$\frac{dS}{dq} = 2 \sum [-x * sin(q) + y * cos(q)][-x * cos(q) - y * sin(q)] \tag{4}$$

We set this to zero, so we can immediately divide out the factor of 2. Then, expanding out the product and collecting terms into separate summations gives

$$[\sum x * y] * sin^2(q) + [\sum (x^2 - y^2)] * sin(q) * cos(q) - [\sum x * y] * cos^2(q) = 0 \tag{5}$$

Dividing through by $cos^2(q)$, we get a quadratic equation in tan(q):

$$x * y * tan^2(q) + x^2 - y^2 * tan(q) - x * y = 0 \tag{6}$$

where the *curly braces* indicate that we take the sum of the contents over all n data points (x, y). Dividing through by the sum $x * y$ gives

$$tan^2(q) + A * tan(q) - 1 = 0 \tag{7}$$

where $A = \frac{x^2 - y^2}{x * y}$. Solving this quadratic for $tan(q)$ gives two solutions, which correspond to the *principle directions*, i.e., the directions in which the *scatter* is maximum and minimum. We want the minimum. Having the angle q we can find symmetry line, which is passing through the centroid of the data.

6   Results and Tests

Following are the sample results, obtained by presented method.

We have tested this method on ten data sets from two sources - Clinical Hospitals. In 92% cases (failed on 8 images out of 100 - 10 first pass images from 10 studies) method have managed to find more than four CP and perform regression. We must note that images, on which the method has failed were difficult cases located in the lower parts of the brain. Generally all abnormalities that must be located by the perfusion study are located in higher parts of the brain. Therefore, for tested data sets, method proved to find CP in all diagnostic meaningful cases.

To evaluate quality of symmetry lines, found by the algorithm, we have compared it's results with ones provided by the experts. We have asked three physicians
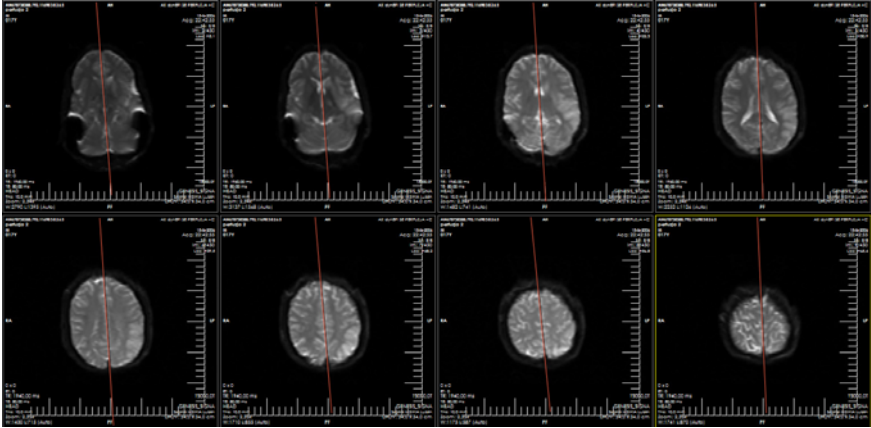
Fig. 6 Example results of symmetry line finding for the whole set
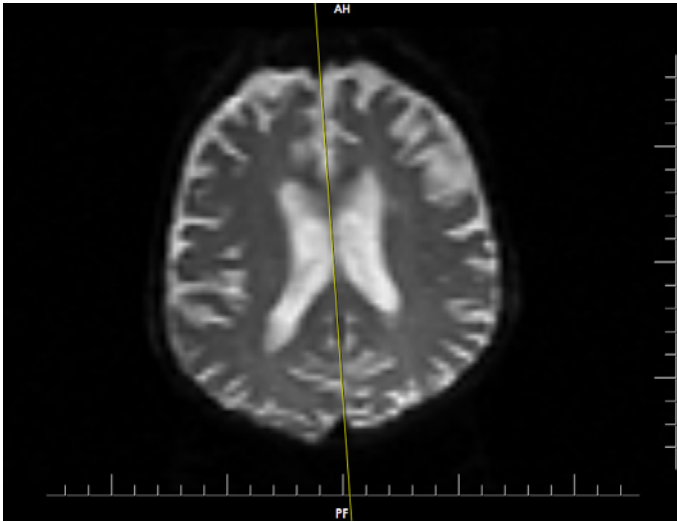
Fig. 7 Example result for the one slice (different data set)

to mark symmetry lines on first pass images from each study. Each expert received six data sets. Studies were divided in the manner that three data sets were common for each expert. This was our control set to estimate average error between expert. Because expert skills are subjective - each one will mark symmetry line little differently - we wanted to check what difference is not significant for them.

As indicators for comparing two symmetry line we have compared angles (from vertical axis in means of percents of 45 degrees) and distance between these lines [6].

First of all we have compared results for control sets. Maximal difference in distance, between experts, was about 5% (of image width in pixels). Difference in case of the angles was about 2,5% (2% of 45 degrees = 0,9 degree). Mean difference for the distance was 4% and angle about 2%.

Next we have compared expert results with that acquired by presented method. Comparison showed mean difference in distance of 5,5% and 3,5% in angle. On image this differences mean about 6-7 pixels, and 1,50.

We had also asked our experts to rate results obtained with our method. In their opinion algorithm produces satisfying result (only in few cases they noted that it could done better).

As mentioned on the beginning of this article, algorithm will be used as a part of other methods that will statistically compare images of both cerebral hemispheres, therefore quality of found symmetry lines, even in *worst* cases, is very satisfying.

7   Conclusions

Algorithm presented in this article may be used for finding symmetry lines on low resolution, sparse images of MRI brain perfusion studies. Because these images are acquired in specific manner, only way to locate line between cerebral hemispheres is to analyze brain anatomy. Therefore method is trying to find characteristic anatomical places that describe middle point of the brain. Using linear regression, line is then fitted into found set of characteristic points. Of course some presumptions are made for these method. First of all deviation of symmetry line from the vertical axis cannot be greater than 10-15% (which may occur only in special cases). We also do not require found symmetry lines to be perfect, small deviation from ideal are possible.

After comparing acquired results with results given by experts, we have came to the conclusion that method produces satisfying results for diagnostic meaningful cases.

References

1. Thacker, N.A.: Tutorial: Functional MRI Analysis, Tina Memo No. 2001-001 (2002)
2. Phillips, M.D.: Brain Perfusion Imaging. Seminars in Cerebrovascular Diseases and Stroke 1(4) (2001)
3. Acton, F.S.: Analysis of Straight-Line Data. Dover, New York (1966)
4. Chatterjee, S., Hadi, A., Price, B.: Simple Linear Regression. In: Regression Analysis by Example, 3rd edn., ch. 2, pp. 21–50. Wiley, New York (2000)
5. Edwards, A.L.: The Regression Line on. In: An Introduction to Linear Regression and Correlation, ch. 3, pp. 20–32. W.H. Freeman, San Francisco (1976)
6. Eberly, D.: 3D Game Engine Design, Section 2.6. Distance Methods (2001)

A Two-Step Method for Detection of Architectural Distortions in Mammograms

Magdalena Jasionowska, Artur Przelaskowski,
Aleksandra Rutczynska, and Anna Wroblewska

Abstract. Early detection of breast cancer is very important. It increases breast cancer treatment and reduces mortality rates by 30 - 70%. Architectural distortion (AD) is one of the commonly missed signs of breast cancer. It is estimated that 12 - 45% of missed breast cancer in mammography are ADs. Our ultimate goal is to develop a CAD module through creating of ADs detection method (`ArDist method`). We rely on fact that AD is a group of line structures of different orientation. The `ArDist method` consists of two stages: detection of ROI with potential ADs based on analysis with Gabor filters (`GF method`) and recognition of ADs using 2D Fourier transform in polar coordinates (`DD method`). The method was tested with 33 mammograms containing ADs, from the database `DDSM`. Experimental results are promising in comparison with the results of the model method and the efficiency of commercial CAD systems. The sensitivity of `ArDist method` amounts to 68% with 0.86 false positives per image.

1 Introduction

Screening mammography is the most effective tool for early detection of breast cancer. There are three typical types of abnormal findings: microcalcifications, masses and architectural distortions [7]. Early detection of them increases breast cancer treatment and the survival rate. However, the sensitivity of screening mammography which is affected by many elements (e.g. image quality, the radiologist's level of expertise) is not perfect. In screening mammography only 3% of detected by

Magdalena Jasionowska · Artur Przelaskowski · Aleksandra Rutczynska
Institute of Radioelectronics, Warsaw University of Technology, Nowowiejska 15/19,
Warsaw, Poland
e-mail: mjasiono@ire.pw.edu.pl, arturp@ire.pw.edu.pl,
arachock@ire.pw.edu.pl

Anna Wroblewska
Wyzsza Szkola Przedsiebiorczosci i Nauk Spolecznych, Armii Krajowej 13, Otwock, Poland

radiologists lesion are architectural distortions, whereas 61% of detected findings are mass, microcalcifications - 90% [4]. Therefore, we develop one of CAD modules in order to aid radiologists in ADs detection.

1.1 *Architectural Distortion*

Architectural distortion (AD) is a subtle sign of abnormality in mammography (Fig.1a). This finding is a breast lesion in which the normal structure of the breast parenchyma is distorted as if being pulled into a central point, without a visible central density [2]. AD is a single sign or an early sign of breast cancer [7]. During
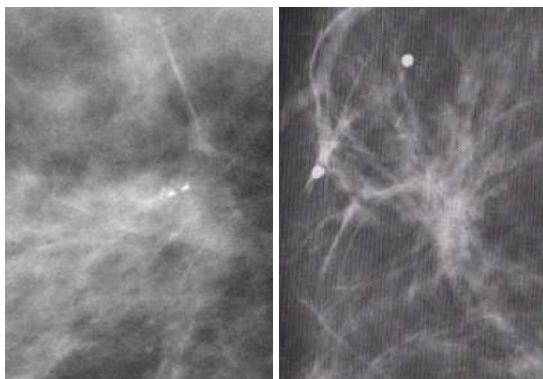
Fig. 1 (a) ROI containing architectural distortion with spiculations radiating and (b) ROI with radial scar - a benign lesion of the breast [6, 7]

description of mammograms radiologists can make mistakes - the views of scarring from previous surgery, radial scar[1] (Fig.1b) and crossing breast structures can be diagnosed as architectural distortions. Architectural distortions have indefinite characteristic features, e.g. number of spicules, width and length of spicules, density. It makes difficulties in detection process.

2 Materials

Several automated methods for ADs detection have been reported. All of them rely on fact that AD is a group of line structures of different orientation. The particulars about detecting process are described in [8, 9, 15, 17]. The six following stages can be distinguished:

---

[1] Radial scar - a complex sclerosing lesion; it has a black star appearance with long, thin spicules radiating from a radiolucent central area.

1. breast segmentation - mammogram segmentation into breast region and background, usually using region growing methods;
2. preprocessing of mammogram - preliminary filtering in order to sharpen the spicules of ADs and reduce the noise;
3. enhancement of spicules - extracting of texture orientation (line structures of different orientation):

   - filtering in the Radon domain; basic idea is to design matched filters for the ADs features [17];
   - extraction of the surface direction by the sign of the mean curvature and calculation of the concentration index (ADs correspond to the high concentration regions) [9];
   - filtering with a bank of Gabor filters of different texture orientation angles [1, 14, 15];

4. selection of ROI containing potential ADs - analysis of extracted texture orientation:

   - phase portrait modelling - the oriented texture is analyzed to produce three maps, whereas only one of them (a node map) is further analyzed to detect the sites of ADs [1, 14, 15];

5. estimation of characteristic features for ADs in order to reduce the false positives:

   - the fractal dimension (e.g. using Hausdorff dimension or by 2D Fourier power spectrum) [8, 15];
   - the following features: the size of the suspected region, the mean pixel value of the suspected region, the mean concentration index of the suspected region, the isotropic index, the contrast between the suspected region and surrounding region, two features of power spectra which are obtained from 2D Fourier transform [9];
   - the Haralick's texture measures (using the joint occurrence or co-occurrence of gray levels, known as the gray-level co-occurrence matrix) [15, 19];

6. features classification:

   - using support vector machine (SVM); the SVM bases on maximization of the separating margin between the two classes: normal breast tissue and ADs [8, 10];
   - using radial basis function neutral networks (RBF) [8].

The efficiencies of quoted solutions are unsatisfactorily. There is either the low sensitivity or the high number of false positives per image (FPI). Ichikawa et al. [9] received the sensitivity for detection of ADs - only 56% at FPI = 0.96. The sensitivity of ADs detection method created by Sampat et al. [17] was 80% at the unacceptable number of FPI = 14. The results of Guo et al. [8] showed that the best classification of ADs is SVM (72% correct answers). The sensitivity of 84% at a high false-positive rate of 7.4 per image was received by Rangayyan et al. [14].

Generally, the sensitivity of interpreting radiologists and CAD systems for ADs detection is low in comparison with the other findings. The commercial CAD systems [5, 13] correctly marked 90% cases of masses and microcalcifications (it is average sensitivity of masses and microcalcifications), whereas the sensitivity of ADs detection has been reported to be only ca. 40% [16]. The R2 Image Checker system [13] successfully identified 49% cases containing ADs with 0.7 false positives per image. The CADx Second Look system [5] successfully detected 33% cases of ADs with 1.27 false positives per image [16]. Additionally, only 48 - 60% of ADs that are biopsied are found to be cancer [11, 16].

3   ArDist Method

In image processing, ADs are modeled as the group of line structures of different orientation. Therefore, orientation transformations (that enhance texture orientation of image) are used in order to detect the ADs. We propose `ArDist method` (Fig.2) which consists of two steps: detection of ROIs with potential ADs, based on Gabor filtering (`GF method`) and ADs recognition in selected ROIs, using 2D Fourier transform in polar coordinates (`DD method`).
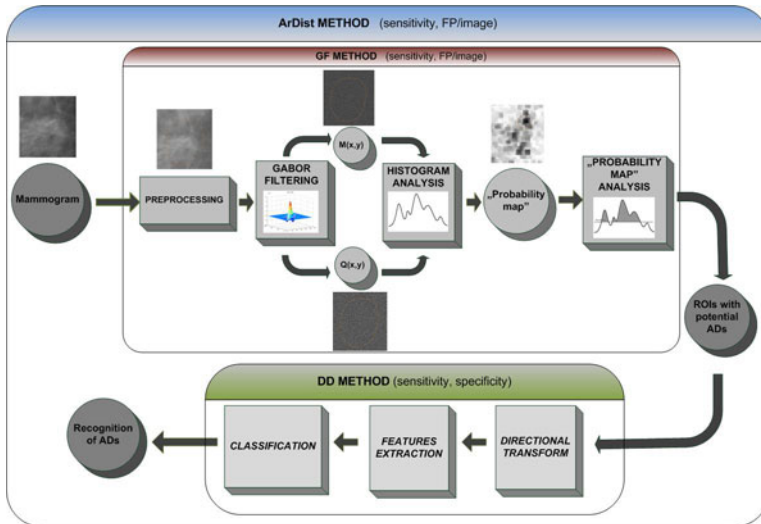
Fig. 2 Schema of ArDist method. The first stage - detection of ROIs with potential ADs, using Gabor filtering (GF method) and the second stage - ADs recognition in selected ROIs (DD method).

3.1 GF Method

We propose GF method based on analysis of ADs spicules (line structures of different orientation) using Gabor filters with selected impulse response. GF method consists of four steps: i) preprocessing, ii) Gabor filtering, iii) Gabor maps histogram analysis and iv) "probability map"analysis (Fig.2). It is necessary to reduce the noise and the influence of the low-frequency components of the mammogram in estimating the texture orientation. Therefore, the mammogram is low-pass and then high-pass filtered. Next, we filter the mammogram with the bank of 180 Gabor filters of different orientation. The Gabor filter is a sinusoidally modulated Gaussian functions, defined as follows:

$$g_k(x,y) = \exp([-\frac{1}{2}[(\frac{x'}{S_x'})^2 + (\frac{y'}{S_y'})^2]]) * \cos(2\pi f x') \qquad (1)$$

where $x' = x\cos\theta_k + y\sin\theta_k$, $y' = y\cos\theta_k - x\sin\theta_k$, the angle of texture orientation $\theta_k \in [-\pi/2, \pi/2]$, the frequency of sinusoidal function $f = 0.075$, parameters that determine width of Gabor filter and elongation in the y direction: $S_x = 4$, $S_y = 4$ (Fig.3). All parameters were chosen experimentally.
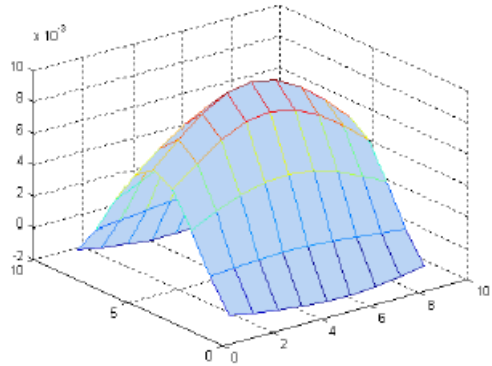
Fig. 3 Gabor filter mask of size 9x9 with applied parameters: $S_x = 4$, $S_y = 4$, $f = 0.075$, $\theta_k = \pi/2$

The texture orientation at a pixel is estimated as the highest magnitude of amplitude at the pixel among 180 values (for 180 corresponding filter responses). As the result of Gabor filtering we receive two Gabor maps. The map with the maximum values of amplitude $M(x,y)$ (Fig.4b) is estimated as the highest magnitude of amplitude among 180 values of different orientation (for 180 corresponding filter responses). The second map $Q(x,y)$ contains the dominant texture orientation angles (Fig.4c), i.e. angles for which the magnitude of amplitudes is maximum.

In order to select ROIs with potential ADs, histogram analysis of Gabor maps is employed by blocks $K \times K$ pixels and as the result a "probability map"is created. ADs spicules are characterized by high magnitude of amplitudes. Therefore,

(a)   (b)   (c)
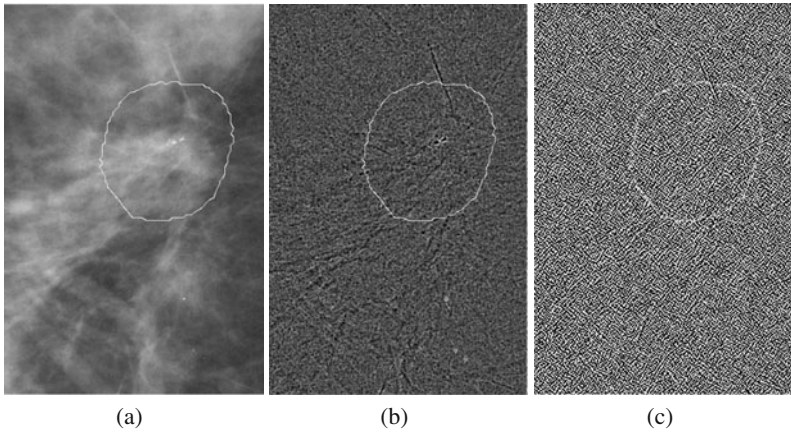
Fig. 4 The result of Gabor filtering: (a) ROI from original mammogram, (b) the map with the maximum values of amplitude $M(x,y)$ and (c) the map with the dominant angles of texture orientation $Q(x,y)$

the map $M(x,y)$ is thresholded with $T_1 = 0.75 * A_{MAX}$, where A_{MAX} - the maximum value of amplitude in mammogram. We expect that in the blocks $(K \times K)$ the calculated histogram of map $Q(x,y)$ (Fig. 5) for ADs should show several dominant peaks (correlating with the dominant texture orientation angles). For normal tissue
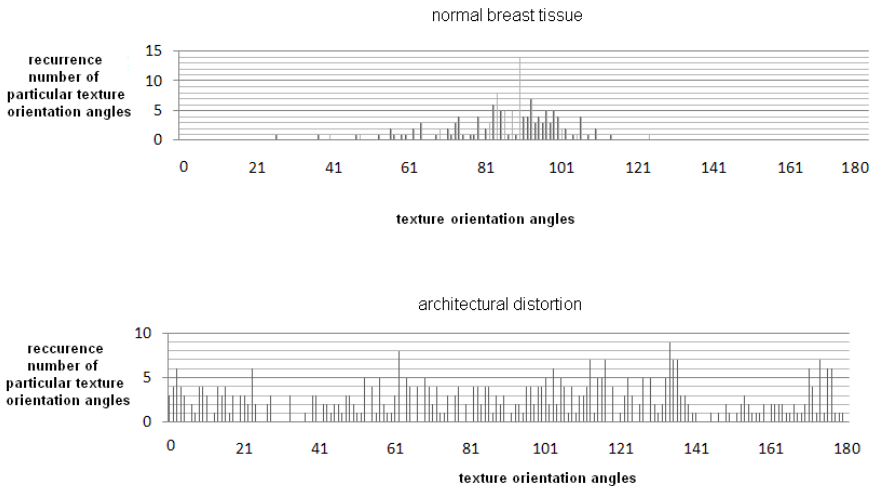
Fig. 5 The exemplary histograms of map $Q(x,y)$ for blocks 100×100 pixels with normal breast tissue and with architectural distortion

one dominant peak is expected. Performing histogram analysis of $Q(x,y)$ we utilize threshold T_2 to eliminate texture orientation angles with low recurrence number. Additionally, any dominant direction in mammogram texture can be visible on histogram of blocks $(K \times K)$ as several near-lying peaks which values are averaged when form sequence is longer than threshold value T_3. Finally, the "probability map "(Fig.6b) is created by assignment the highest probability of ADs appearance (reflected as a maximum gray scale value MAX) to blocks, in which after the histogram analysis the number n peaks (n dominant angles) is equal or higher than the characteristic number N (established experimentally). For the other blocks the scale is extended as follows: $(n * MAX)/N$. Next, the blocks with the highest probability of ADs appearance are marked with stars (Fig.7).
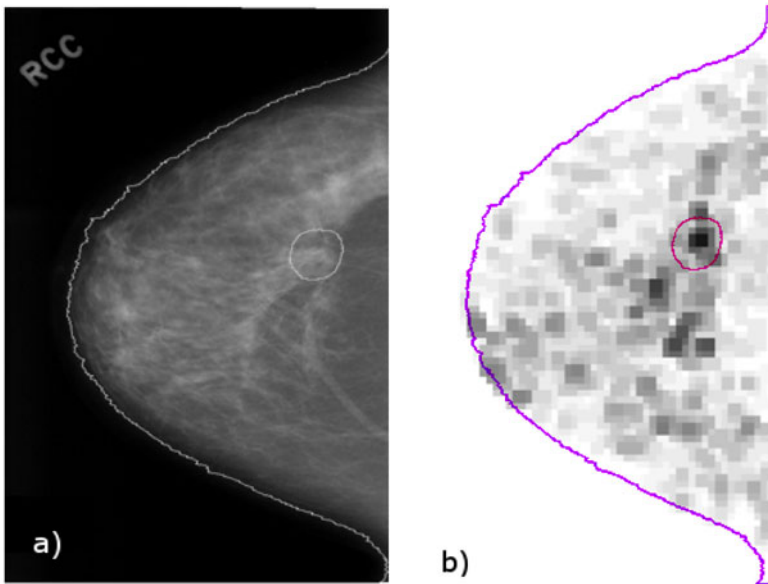
Fig. 6 The result of Gabor maps histogram analysis: (a) original mammogram with AD and (b) the "probability map". The marked circle indicates the sites of AD, detected by radiologist

3.2 DD Method

Our DD method (differential directions method) of ADs recognition in selected ROIs consists of three steps: i) directional transform, using 2D Fourier transform in polar coordinates, ii) extraction (with reduction) of features and iii) features classification (Fig. 2). Gabor filtering assigns the local texture orientation. We apply the other texture orientation extractor (including whole region of interest) to acquire the
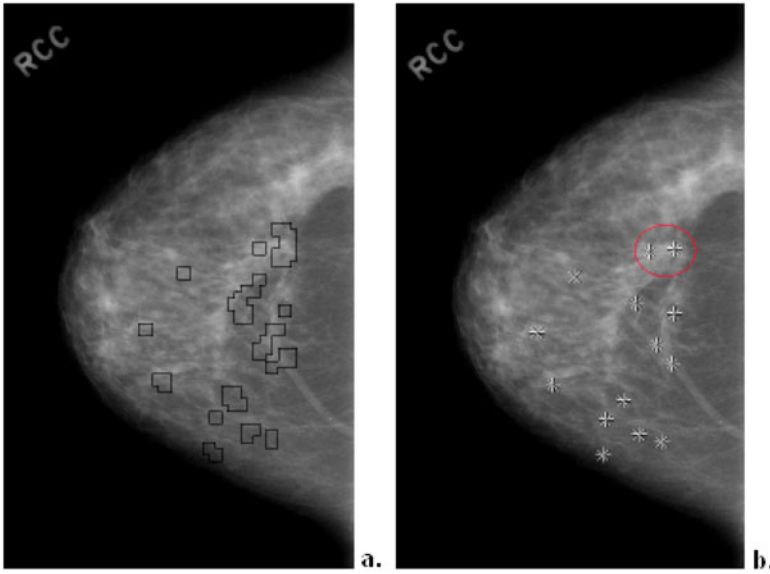
Fig. 7 The finally results of GF method: (a) thresholded "probability map"and (b) the output image with marked by stars sites of potential ADs. AD is correctly detected (in the marked circle). The high number of false positives is re reduced in the second stage - DD method.

high directional resolution. We use the directional transform in order to enhance only strong ADs spicules (Fig. 8). To this effect, the 2D Fourier transform in polar
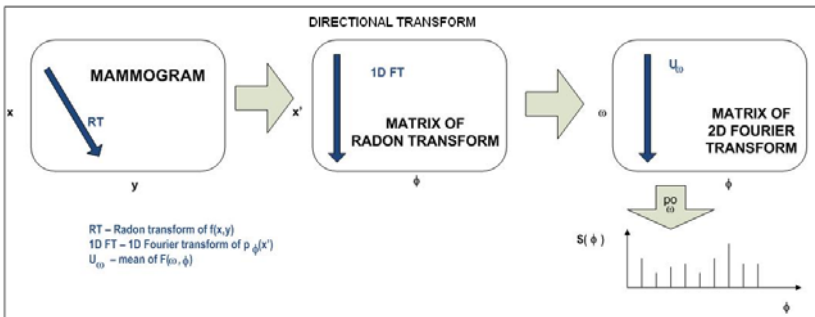
Fig. 8 Schema of directional transform, using 2D Fourier transform in polar coordinates

coordinates is computed using first Radon transform of selected by `GF method` ROI $f(x,y)$:

$$p_\phi(x') = \sum_{(x,y)\in\phi} f(x,y) = \sum_{y'} f(x'\cos\phi - y'\sin\phi, x'\sin\phi + y'\cos\phi) \qquad (2)$$

where $x' = x\cos\phi + y\sin\phi$ and $y' = -x\sin\phi + y\cos\phi$. We receive the projections $p_\phi(x')$ as the sum of $f(x,y)$ values along definite direction (the line at the angle ϕ). However, in order to define frequency characteristic of analyzed object (potential AD) along definite direction, 1D Fourier transform $p_\phi(x')$ has to be computed for each projection:

$$F\{p_\phi(x')\} \equiv P_\phi(\omega) = \sum_{x'} p_\phi(x')\exp(-i\omega x') \tag{3}$$

substituting equation (2):

$$P_\phi(\omega) = \sum_{x'}\sum_{y'} f(x'\cos\phi - y'\sin\phi, x'\sin\phi + y'\cos\phi)\exp(-i\omega x') \tag{4}$$

1D Fourier transform of projection $p_\phi(x')$ is equivalent to transformation of $f(x,y)$ in angular and frequency domain:

$$P_\phi(\omega) = \sum_{x}\sum_{y} f(x,y)\exp(-i\omega(x\cos\phi + y\sin\phi)) \tag{5}$$

Therefore,

$$P_\phi(\omega) = F\{f(x,y)|\phi\} = F(\omega_x, \omega_y)|\phi = F(\omega, \phi) \tag{6}$$

where $F(\omega, \phi)$ - the expected 2D Fourier transform in polar co-ordinates. To receive complete directional characteristic of analyzed ROI (for all 180 angles ϕ), the mean of $|F(\omega, \phi)|$ by $\omega = 1, ..., M$ has to be calculated in two manners:

- the mean of $|F(\omega, \phi)|$ (Fig. 9):

$$|S_1(\phi)| = \frac{1}{M}\sum_{\omega}|F(\omega, \phi)| \tag{7}$$

- the mean of $|F_r(\omega, \phi)|$ with soft thresholding of $|F(\omega, \phi)|$, defined as follows:

$$|F_r(\omega, \phi)| = 0 < r(\phi) \tag{8}$$

$$|F_r(\omega, \phi)| = |F(\omega, \phi)| - r(\phi) > r(\phi) \tag{9}$$

where $r(\phi) = \frac{1}{M}\sum_{\omega}|F_t(\omega, \phi)|$ is calculated for each projection. The angular spectrum $|S_2(\phi)|$ seems to be more effective for mammograms:

$$|S_2(\phi)| = \frac{1}{M}\sum_{\omega}|F_t(\omega, \phi)| \tag{10}$$

For assigned angular spectrum $|S(\phi)|$ 13 directional features are extracted, including:

- the features based on gray-level co-occurrence matrix (GCM) for $\alpha = 0°$ [19]: contrast, correlation, energy, entropy, homogeneity;
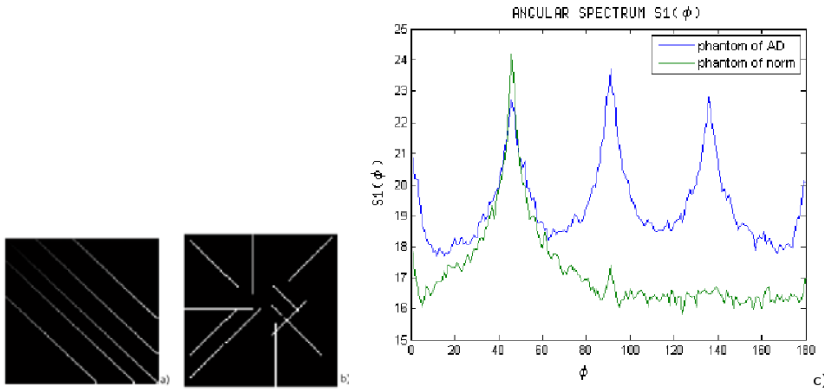
Fig. 9 Two created phantoms: (a) phantom of normal breast tissue - with one lines direction and (b) phantom of AD - with chosen four lines directions. (c) The angular spectrum $|S_1(\phi)|$ of two phantoms.

- the statistic features: variance, standard deviation, kurtosis, skewness, energy, entropy
- two features computed using approximation of angular spectrum (slope and point of intersection with *y*-axis).

Additionally, to better ADs recognition image features of selected ROI are extracted: i)the features based on GCM for $\alpha = 0°, 45°, 90°, 135°$ and ii) the statistic features including also central moments. As the criterion of image features reduction (to assess the significance of every feature for separating two labeled groups: AD or normal tissue) we set area between the empirical receiver operating characteristic curve and the random classifier slope. We normalize the features values and utilize the correlation between features values. The support vector classifier with linear kernel and regularization (from MATLAB toolbox - PRTools4 [12]) is used to classification.

3.3 Results of ArDist Method

Our database of mammograms containing ADs consists of 33 images from digital database DDSM (image resolution 43.5 - 50um) [6]. We achieved the sensitivity of GF method equal 79% (26 cases of ADs are detected) at the number of false positives per image FPI = 7.8 (Table 1). The sensitivity of GF method is worse than the model method [14] at the same number of FPI, but it is worth underling fact that the computational complexity of GF method is much lower than the model method. However, the number of false positives was unacceptable. We achieved 292 ROIs (including 34 ROIs with ADs - in one case AD has been marked by two stars). In order to recognize ROIs with ADs DD method is used. To reduce an influence of training and classifying data on classification results was necessary a

cross validation. The acceptable result of classification was gained for selected 10 image features of low-pass and then high-pass filtered ROIs and all 13 direction features of angular spectrum. As the finally result, we achieved the sensitivity of 86% and the specificity of 89% (Table 1).

Table 1 Efficiency of GF, DD and ArDist method

Method	Sensitivity	FP/image or Specificity [*]
GF Method	79%	0.78
DD Method	86%	89%
ArDist Method	68%	0.86

[*] FP/image (the number of false positives per image) - in GF and ArDist method; specificity - DD method.

Table 2 Comparison between ArDist method and commercial CAD systems

Detection Method	Number of images	Sensitivity	FP/image[*]
ArDist	33	68%	0.86
Image Chacker R2	45	49%	0.7
CADx Second Look	45	33%	1.27

[*] FP/image (the number of false positives per image)

Final result of our ArDist method is promising. The sensitivity of ArDist method amounts to 68% at FPI = 0.86. In comparison with the commercial CAD systems we achieved the higher sensitivity at the comparable number of FPI (Table 2). However, it is necessary to underline databases variety.

4   Conclusion

Our ArDist method gives promising results and seems to have high capability to aid radiologists in their work, but method parameters were fitted experimentally to optimize algorithm for concrete data set. More general, adaptive procedures are necessary to conclude the results more reliably. Moreover, in the future research we should improve our ArDist method by adjusting the parameters of Gabor filter to expected features of ADs. Next, the better directional features for improved differentiating ADs from normal tissue of breast are searched. Scalable, two dimensional transforms with nonseparable, flexible kernels are planned to be considered. Families of countourlets, curvelets, beamlets etc. are potentially useful for further ADs detection enhancement.

References

1. Ayres, F.J., Rangayyan, R.M.: Characterization of architectural distortion in mammograms. IEEE Engineering in Medicine and Biology Magazine (2005)
2. American College of Radiology (ACR): Breast Imaging Reporting and Data System BI-RADS, 3rd edn. American College of Radiology (1998)
3. Bird, R.E., Wallace, T.W., Yankaskas, B.C.: Analysis of cancers missed at screening mammography. Radiology 184, 613–617 (1992)
4. Birdwell, R.L., Bandodkar, P., Ikeda, D.M.: Computer aided detection with screening mammography in a University Hospital Setting. RSNA 236, 451–457 (2005)
5. The CADx Second Look system, `http://www.icadmed.com`
6. University of South Florida: Digital Database for Screening Mammography (DDSM), Florida, USA,
   `http://marathon.csee.usf.edu/Mammography/Database.html`
7. Dziukowared, J. (red.): Mammografia w diagnostyce raka sutka, Warszawa (1998)
8. Guo, Q., Shao, J., Ruiz, V.: Investigation of support vector machine for the detection of architectural distortion in mammographic images. Journal of Physics: Conference Series 15 (2005)
9. Ichikawa, T., Matsubara, T., Hara, T., Fujita, H., Endo, T., Iwase, T.: Automated detection method for architectural distorion areas on mammograms based on morphological processing and surface analysis. In: Medical Imaging: Image Processing, vol. 5370 (2004)
10. Koronacki, J., Cwik, J.: Statystyczne metody uczace sie. Akademicka Oficyna Wydawnicza EXIT. Wydanie drugie, Warszawa (2008)
11. Orel, S.G., Kay, N., Reynolds, C., Sullivan, D.C.: BI-RADS categorization as a predictor of malignancy. Radiology 211, 845–850 (1999)
12. Duin, R.P., Juszczak, P., Paclik, P., Pekalska, E., de Ridder, D., Tax, D.M.J., Verzakov, S.: PRTools 4 - A MATLAB Toolbox for Pattern Recognition. Version 4.1, Delft University of Technology (2007)
13. The R2 Technology's Image Checker, `http://www.r2tech.com`
14. Rangayyan, R.M., Ayres, F.J.: Gabor filters and phase portraits for the detection of architectural distortion in mammograms. In: Medical and Biological Engineering, pp. 883–894. Springer, Heidelberg (2006)
15. Rangayyan, R.M., Prajna, S., Ayres, F.J., Leo Desautels, J.E.: Detection of architectural distortion in prior screening mammograms using Gabor filters, phase portraits, fractal dimension and texture analysis. Int. J. CARS (2008)
16. Sampat, M.P., Markey, M.K., Bovik, A.C.: Computer-aided detection and diagnosis in mammography. IEEE Publication, Los Alamitos (2004),
   `e.sharif.edu/~miap/Files/MammographyReview1.pdf`
17. Sampat, M.P., Whitman, G.J., Markey, M.K., Bovik, A.C.: Evidence based detection of spiculated masses and architectural distortions. In: SPIE, Medical Imaging: Image Processing, vol. 5747, pp. 26–37 (2005)
18. Schneider, M.A.: Better detection: Improving our chances. Digital mammography. In: Proc. of the 5th Int. Workshop on Digital mamography, pp. 3–6. Medical Physics Publishing, Toronto (2000)
19. Zielinski, K.W., Strzelecki, M.: Komputerowa analiza obrazu biomedycznego. Wstep do morfometrii i patologii ilosciowej. PWN, Warszawa - Lodz (2002)

An Instrument for Monitoring Inflow and Washout of an Optical Contrast Agent into the Brain

Daniel Milej, Michał Kacprzak, Norbert Żołek, Piotr Sawosz,
Roman Maniewski, and Adam Liebert

Abstract. A time resolved method based on near infrared spectroscopy for monitoring of changes in tissue absorption and concentration of the exogenoeus chromophore concentration is presented. We constructed a setup which can be used to measure changes in oxygenation of the brain tissue by monitoring of diffuse reflectance at two wavelengths. Currently, the instrument has been modified in such a way that simultaneous measurements of diffuse reflectance and fluorescence can be carried out. We present results of measurement of diffuse reflectance and fluorescence during injection of an optical contrast agent in healthy volunteer.

1 Introduction

Methods used routinely in clinical evaluation of structure and function of human brain like computed tomography (CT), magnetic resonance imaging (MRI), and positron emission tomography (PET) are sophisticated and expensive. Moreover, their use require the transport of the patient to the brain imaging facility. Optimally, the method used in brain monitoring should allow to perform measurements at the bedside of the patient. It should be possible to use the method intraoperatively as well. Near infrared spectroscopy (NIRS) [1, 2] is an optical non-invasive method which may fulfil these requirements. This technique is based on assessment of changes in oxy- and deoxyhemoglobin by analysis of changes in attenuation of light measured at several wavelengths and utilization of differences in spectral properties of hemoglobins in near infrared wavelength region. The method can be also applied for assessment of perfusion of human brain by combined application of NIRS technique and the injection of optical contrast agent. Indocyanine green (ICG) is a dye

Daniel Milej · Michał Kacprzak · Norbert Żołek · Piotr Sawosz · Roman Maniewski · Adam Liebert
Institute of Biocybernetics and Biomedical Engineering, Polish Academy of Sciences, 4. Ks. Trojdena Str., 02-109 Warsaw, Poland
e-mail: dmilej@ibib.waw.pl

which have high absorption in near infrared spectral region, is relative non-toxic [3] and it can be safely injected intravenously in patients. The dye found application in several fields of medicine [4, 5, 6, 7, 8, 9]. In experiments carried out on animals it was shown that ICG allows for evaluation of cerebral blood volume [10].

For monitoring of the inflow and washout of the dye different optical techniques can be applied: (i) continuous wave spectroscopy [11, 12], (ii) frequency domain technique [13] and (iii) evaluation of broadening of picosecond laser pulse during its penetration through the tissue [14, 15]. In recent publications, it was reported that fluorescence light from ICG can be excited with the use of near infrared light during circulation of the dye in the human brain. This light can be detected on the surface of the head using the time-resolved optical setup [16, 17]. Theoretical analysis of light propagation show that changes of moments of distributions of times of arrival of fluorescence photons can be explained considering faster inflow of the ICG to the intracerebral brain tissue and delayed inflow to extracerebral overlaying tissue layers (skin, skull) [18, 19].

2 Methods

The constructed setup allows for simultaneous measurement of distributions of times of flight of diffusely reflected photons and times of arrival of fluorescence photons. Single channel of that setup is schematically presented in Fig. 1. Technical details of the setup were presented in more detail elsewhere [20].

The setup is equipping with a semiconductor laser heads operating at a wavelength of 760 nm which allowed to excite fluorescence of the dye. The laser light
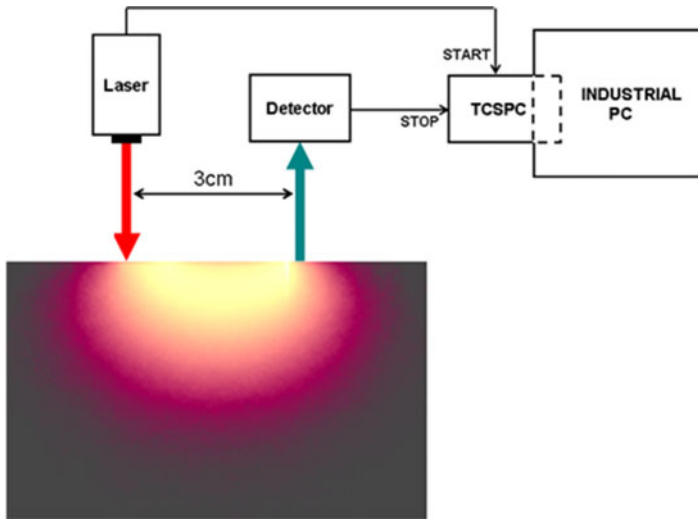
Fig. 1 Diagram of the measurement system during the *in-vivo* experiments

is delivered to the surface of the tissue with the use of four optical fibers. The light remitted from the medium is transmitted to the photodetectors with the use of four bifurcated fiber bundles. The acquisition of distributions of times of flight of photons is carried out with the use of photomultiplier tubes and eight time correlated single photon counting (TCSPC) PCI cards divided into four reflectance and four fluorescence channels. Appropriate filters applied in each channel allow to easily configure the system for measurement of distributions of times of flight (DTOF) of diffusely reflected photons and distributions of times of arrival (DTA) of fluorescence photons. Additionally, in all channels rotating film filters were applied which allow to adjust intensity of light transmitted to the photodetectors. The TCSPC cards were mounted in an industrial PC. During data analysis, statistical moments, i.e., number of photons, mean time of flight and variance of the DTAs and DTOFs were calculated.

For fixation of the source fibers and detecting boundless a flexible pad made of thermoplastic material and plastic foam was used (see Fig. 2). The distance between source fiber position and detection bundle was fixed at 3 cm for all source-detector pairs. For this source-detector separation the laser light may penetrate for the depth of 1.5 cm, i.e. it reaches the cortex of the brain.
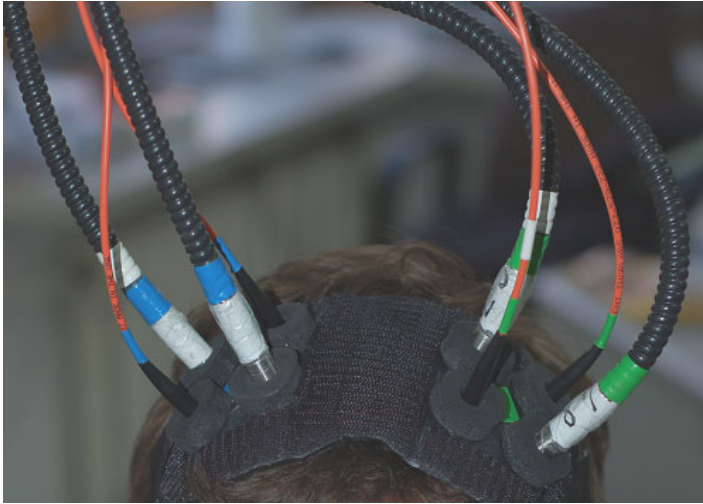
Fig. 2 Optode fixation on both sides of the head

3 Results

Example of signals measured in-vivo in a healthy volunteer in diffuse reflectance and fluorescence channels is presented in Fig. 3. Changes in number of photons N/N0 and mean time of flight $< t >$ are presented. In both signals change is clearly visible at the moment of appearance of the dye in the volume between source and detector. Larger amplitudes of changes can be noted in fluorescence channel. Specific changes of the mean time of flight of DTA of florescence photons were noted. This pattern, consisting of early increase of $< t >$ was reported previously and explained by theoretical analysis of the fluorescence light excitation and propagation in layered optically turbid medium.

4 Discussion and Conclusions

In this paper we present construction of an optical setup for simultaneous measurement of time-resolved diffuse reflectance and fluorescence. The instrument allows to measure optical signals at 4 spots on every hemisphere of the brain. The aim of further development is to construct an instrument which will be mobile and simple in operation. Laboratory tests on physical phantoms of the tissue [21] and preliminary *in-vivo* tests confirmed potential effectiveness of the technique in clinical brain assessment. The setup can be potentially easily re-configured for double-wavelength operation, monitoring of diffuse reflectance or fluorescence or combination of these quantities. Development of optimal procedure for fixation of the optodes on the head
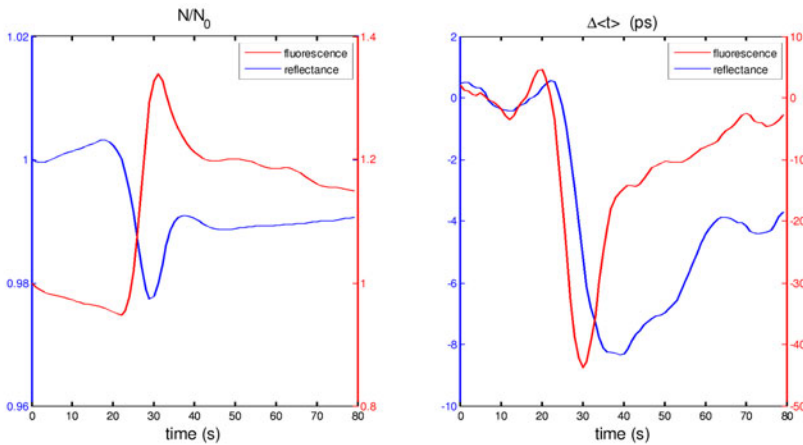
Fig. 3 Changes in number of photons N/N0 and mean time of flight $< t >$ of diffusely reflected photons and times of arrival of fluorescence photons obtained during *in-vivo* experiment. Injection of the ICG at $t = 0$.

still remains a serious challenge. The distribution of the fibers and bundles on the surface of the patient's head must be well defined and size of the optode holder must fit to different shapes of the skulls. Additionally, it should be possible to fix and adjust the optodes on the head in very fast way.

References

1. Jobsis, F.F.: Noninvasive, infrared monitoring of cerebral and myocardial oxygen sufficiency and circulatory parameters. Science 198(4323), 1264–1267 (1977)
2. Villringer, A., Chance, B.: Non-invasive optical spectroscopy and imaging of human brain function. Trends In Neurosciences 20(10), 435–442 (1997)
3. Hope-Ross, M., et al.: Adverse reactions due to indocyanine green. Ophthalmology 101(3), 529–533 (1994)
4. de Liguori Carino, N., et al.: Perioperative use of the LiMON method of indocyanine green elimination measurement for the prediction and early detection of posthepatectomy liver failure. Eur. J. Surg. Oncol. (2009)
5. Ishizawa, T., et al.: Real-time identification of liver cancers by using indocyanine green fluorescent imaging. Cancer 115(11), 2491–2504 (2009)
6. Sheng, Q.S., et al.: Indocyanine green clearance test and model for end-stage liver disease score of patients with liver cirrhosis. Hepatobiliary Pancreat. Dis. Int. 8(1), 46–49 (2009)
7. He, Y.L., et al.: Measurement of blood volume using indocyanine green measured with pulse-spectrophotometry: its reproducibility and reliability. Crit. Care Med. 26(8), 1446–1451 (1998)
8. Ishihara, H., et al.: Does indocyanine green accurately measure plasma volume early after cardiac surgery? Anesth. Analg. 94(4), 781–786 (2002) (table of contents)
9. Guenette, J.A., et al.: Human respiratory muscle blood flow measured by near-infrared spectroscopy and indocyanine green. J. Appl. Physiol. 104(4), 1202–1210 (2008)
10. Leung, T.S., et al.: A new method for the measurement of cerebral blood volume and total circulating blood volume using near infrared spatially resolved spectroscopy and indocyanine green: application and validation in neonates. Pediatr. Res. 55(1), 134–141 (2004)
11. Terborg, C., et al.: Bedside assessment of cerebral perfusion reductions in patients with acute ischaemic stroke by near infrared spectroscopy and indocyanine green. J. Neurol. Neurosurg. Psychiatry 75(1), 38–42 (2004)
12. Keller, E., et al.: Noninvasive measurement of regional cerebral blood flow and regional cerebral blood volume by near-infrared spectroscopy and indocyanine green dye dilution. Neuroimage 20(2), 828–839 (2003)
13. Steinbrink, J., et al.: Relevance of depth resolution for cerebral blood flow monitoring by near-infrared spectroscopic bolus tracking during cardiopulmonary bypass. J. Thorac Cardiovasc. Surg. 132(5), 1172–1178 (2006)
14. Liebert, A., et al.: Time-resolved multidistance near-infrared spectroscopy of the adult head: intracerebral and extracerebral absorption changes from moments of distribution of times of flight of photons. Applied Optics 43(15), 3037–3047 (2004)

15. Liebert, A., et al.: Bed side assessment of cerebral perfusion in stroke patients based on optical monitoring of a dye bolus by time resolved diffuse reflectance. Neuroimage 24(2), 426–435 (2005)
16. Steinbrink, J., et al.: Towards noninvasive molecular fluorescence imaging of the human brain. Neurodegener. Dis. 5(5), 296–303 (2008)
17. Liebert, A., et al.: Non-invasive detection of fluorescence from exogenous chromophores in the adult human brain. Neuroimage 31(2), 600–608 (2006)
18. Liebert, A., et al.: Monte Carlo algorithm for efficient simulation of time-resolved fluorescence in layered turbid media. Opt. Express 16(17), 13188–13202 (2008)
19. Liebert, A., et al.: Bed side assessment of cerebral perfusion in stroke patients based on optical monitoring of a dye bolus by time resolved diffuse reflectance. Neuroimage 24(2), 426–435 (2005)
20. Kacprzak, M., et al.: Time-Resolved Optical Imager for Assessment of Cerebral Oxygenation. Journal of Biomedical Optics 12, 034019 (2007)
21. Milej, D., et al.: Advantages of fluorescence over diffuse reflectance measurements tested in phantom experiments with dynamic inflow of ICG. Opto-electronics Review (2010) (accepted for publication)

4D Segmentation of Ewing's Sarcoma in MR Images

Joanna Czajkowska, Pawel Badura, and Ewa Pietka

Abstract. This paper presents the first stage of a semi-automatic method for the segmentation of nodules of the skeleto-muscular system from magnetic resonance (MR) imaging. The method suggested is efficient irrespective of the tumour location in human body. It is based on Fuzzy C-Means clustering (FCM), Gaussian Mixture Models (GMM) and Fuzzy Connectedness analysis applied to the dataset consisting of T1W and T2W series. In this study a method of transforming the results between planes is also presented. The suggested algorithm has been evaluated on the examinations of different parts of the body, where Ewing's sarcomas have been indicated by a radiologist.

1 Ewing's Sarcoma Segmentation Problem

Ewing's sarcoma is a highly malignant tumour usually found in children and young adults [1]. It occurs in bone tissue and it may also spread to muscles and soft tissues surrounding the bone. In this study an application is created, that assists the radiologists with comparative analysis of consecutive follow-up MR studies and evaluation of tumour size changes. The detection and staging of bone and soft tissue tumours is usually based on T2W images and contrast enhanced T1W images in different planes, both with fat saturation applied. Merging and transposing the results from one plane to another is of great diagnostic value for the radiologists. Fig. 1 shows the examples of the T2W as well as contrast enhanced T1W, fat saturated images. The Ewing's sarcoma is visible on the pinky in the coronal plane and on the right leg in the axial and coronal planes. It is the high-density area in both imaging series around the shinbone, on the shinbone and on the kneecap. However, the tumour area has different density on the slices, which is the main difficulty in this task.

Joanna Czajkowska · Pawel Badura · Ewa Pietka
Silesian University of Technology, Akademicka 16 st., 44-100 Gliwice, Poland
e-mail: jczajkowska@polsl.pl, pbadura@polsl.pl, epietka@polsl.pl
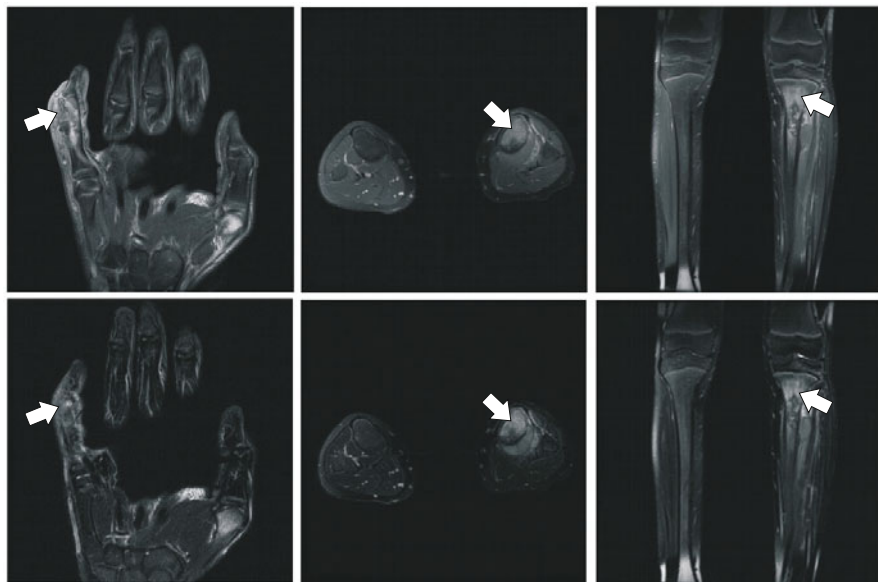
Fig. 1 An example of T2W (top) and T1W (bottom) MR images with Ewing's sarcoma visible on the pinky (coronal plane) and the right leg (axial and coronal planes). The arrows indicate the lesion.

Before the image analysis starts, one pixel belonging to the tumour area has to be indicated by the radiologist on any chosen slice and plane. For further stages of the algorithm, it does not matter on which series or slice the pixel will be indicated. It entirely depends on the radiologist's decision and preferences. The pixel indicated is transformed into all the series and planes. The further analysis is performed simultaneously on both T1W and T2W series in the same plane. Afterwards, on the basis of the kernelised version of the Fuzzy C-Means (FCM) clustering, the region of interest (ROI) is found. It is then divided into three classes using a Gaussian Mixture Model and the class with the highest mean value creates the seed points area for Fuzzy Connectedness (FC) analysis. The fuzzy membership level, which restricts the segmented area, is also calculated on the basis of the FCM clustering. The independent series analysis is followed by multiseries processing. The results previously obtained are transformed from one plane to another. On this basis the new seed points area on the target series is calculated and FC analysis as well as FCM clustering are repeated, yielding the final segmentation results.

2 ROI Detection, Fuzzy C-Means Clustering

FCM is a clustering method based on the minimisation of an objective function [4] [2]. It divides a finite set of elements into k clusters with respect to some given criterion. The number of clusters k is usually predefined. The standard FCM objective function for partitioning a dataset $\{\mathbf{x}_i\}_{i=1}^N$ into k clusters can be written as

$$J_\beta = \sum_{k=1}^c \sum_{i=1}^N u_{ki}^\beta \|\mathbf{x}_i - \mathbf{v}_k\|^2, \tag{1}$$

β being a weighted exponent on each fuzzy membership. In each iteration of the FCM algorithm, for each cluster k, the fuzzy cluster centre

$$\mathbf{v}_k^t = \frac{\sum_{i=1}^N u_{ki}^\beta \mathbf{x}_i}{\sum_{i=1}^N u_{ki}^\beta} \tag{2}$$

is calculated using a membership function $\mathbf{U}^{(t)}$. In the first iteration $\mathbf{U}^{(1)}$ is set to random values. In the next steps

$$u_{ki}^{(t+1)} = \frac{1}{\sum_{j=1}^c (d_{ki}/d_{ji})^{\frac{2}{(\beta-1)}}}. \tag{3}$$

If $\|\mathbf{U}^{(t+1)} - \mathbf{U}^{(t)}\| \leq \varepsilon$, the algorithm is finished and the analysed data $\mathbf{x}_i$ belongs to the class k with the maximum u_{ki} value.

However, the algorithm presented above is sensitive to artefacts and noise. The authors of [2] and [3] suggested some modifications, which deal with this problem. One of them - the Kernel based Fuzzy C-Means (KFCM) is used in this work. The algorithm proposed in [3] uses a kernel-induced distance metric to replace the square one applied in FCM. In this modification, the objective function is given as [3]

$$J_\beta = \sum_{k=1}^c \sum_{i=1}^N u_{ki}^\beta \|\phi(\mathbf{x}_i) - \phi(\mathbf{v}_k)\|^2, \tag{4}$$

where ϕ is a nonlinear transformation into a higher dimensional feature space F and

$$\|\phi(\mathbf{x}_i) - \phi(\mathbf{v}_k)\| = K(\mathbf{x}_i, \mathbf{x}_i) K(\mathbf{v}_k, \mathbf{v}_k) - 2K(\mathbf{x}_i, \mathbf{v}_k). \tag{5}$$

In the software presented, on the basis of the pixel indicated and after the application of the 2D KFCM algorithm, the ROI is found. The pixel intensities in the T1W and T2W series are subjected to the 2D KFCM clustering. Two regions of interest are found. The first one is the 3D bounding box ROI circumscribing the object that includes the selected pixel with its 6-neighbourhood. The second one, denoted as ROI$_C$, includes the object itself (Fig. 2).
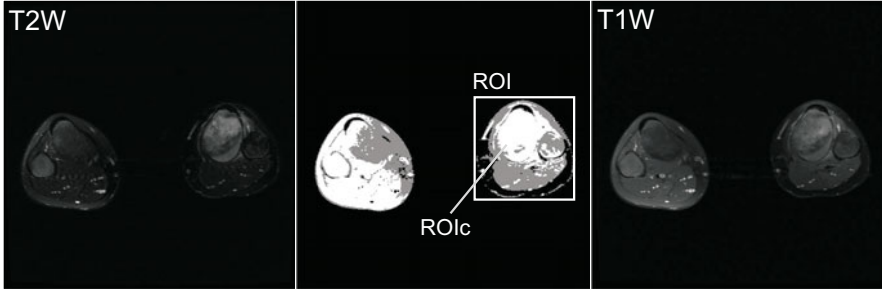
Fig. 2 ROI detection using the KFCM algorithm. A slice selected from the T2W series (left), the corresponding slice from the T1W series (right) and the clustering result with the ROI found (middle).

3   Gaussian Mixture Model

In the following step a clustering method based on the histogram of the ROI_C in two whole series, using a 2D Gaussian Mixture Model (GMM) with three Gaussian components, is applied. As a result, the seed points are obtained inside the tumour area for a 4D FC analysis described in section 4.

The mixture model assumes that each group of the data is generated by a normal probability distribution [4]. The probability density of the mth component is given as

$$p(\mathbf{x}/\theta_m) = \frac{1}{\sqrt{2\pi}^n |\mathbf{C}_m|^{\frac{1}{2}}} exp(-\frac{1}{2}(\mathbf{x}-\mu_m)^T \mathbf{C}_m^{-1}(\mathbf{x}-\mu_m)), \tag{6}$$

μ_m denoting the mean values vector and $\mathbf{C}_m$ the covariance matrix.
For the mixture model with M components in the feature space R^n for $n \geq 1$ dimensions

$$p(\mathbf{x}) = \sum_{m=1}^{M} \alpha_m p(\mathbf{x}/m), \tag{7}$$

where $\alpha_m \in [0,1](\bigvee m = 1,2,...,M)$ and

$$\sum_{m=1}^{M} \alpha_m = 1. \tag{8}$$

α_m denotes the mixing proportion coefficient.

Then, to get $\theta = (\alpha_1,...,\alpha_M,\theta_1,...,\theta_M)$, where $\theta_m = (\mu_m, \mathbf{C}_m)$, equation (7) can be written as follows

$$p(\mathbf{x}/\theta) = \sum_{m=1}^{M} \alpha_m p(\mathbf{x}/\theta_m). \tag{9}$$

The model parameters are estimated by the expectation maximisation (EM) algorithm [4].

As a result the ROI_C is divided into three subregions (Fig. 3). The subregion with the highest values in the mean values vector makes up the seed points for the next processing step. The mixture parameters calculated for this subregion, namely the covariance matrix $\mathbf{C}$ and the mean values vector $\mathbf{M} = \{\mu_1, \mu_2\}$, are also used in the following step.
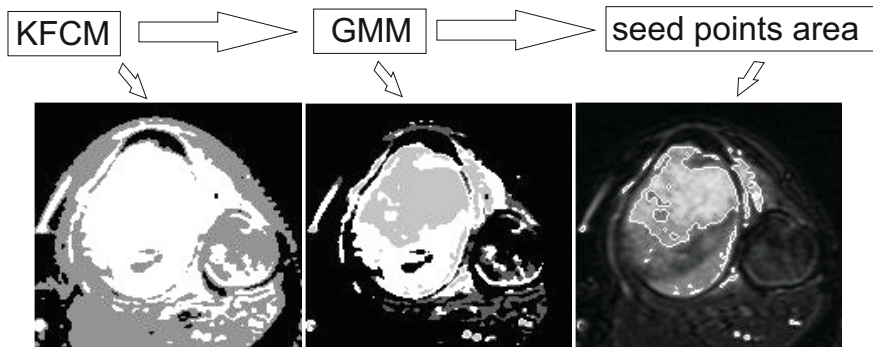
Fig. 3 Seed points selection. KFCM clustering results (left). Subregions obtained with GMM clustering (middle). Seed points area selected (right).

4 Fuzzy Connectedness

The Fuzzy Connectedness (FC) analysis focuses on fuzzy relations between two image points[1]. Specifically, a mutual and symmetric relation called fuzzy affinity $\mu_\kappa(\mathbf{c}, \mathbf{d}) \in \langle 0, 1 \rangle$ connects two neighbouring points, ie. is nonzero only if $\mathbf{c}$ and $\mathbf{d}$ are spatially adjacent (here, the hard 3D 6-adjacency relation is used). Several forms of the fuzzy affinity function have been discussed [5, 7], most of them taking the intensities $f(\mathbf{c})$ and $f(\mathbf{d})$ of $\mathbf{c}$ and $\mathbf{d}$ as arguments. The value of μ_κ may depend on either the mean intensity or the absolute difference between $f(\mathbf{c})$ and $f(\mathbf{d})$, according to

$$\mu_\kappa(\mathbf{c}, \mathbf{d}) = \mu_\alpha(\mathbf{c}, \mathbf{d}) \cdot g(\mu_\phi(\mathbf{c}, \mathbf{d}), \mu_\psi(\mathbf{c}, \mathbf{d})), \tag{10}$$

where μ_α stands for a spatial adjacency relation, and $g(\cdot)$ is a function of the mean intensity based (μ_ϕ) and intensity gradient based (μ_ψ) affinity components.

In this study a multifeature approach has been proposed. As mentioned above, two corresponding series, namely T1W and T2W, are taken into consideration. Each point $\mathbf{c}$ under FC investigation is then described by two features: $f_1(\mathbf{c})$ and $f_2(\mathbf{c})$, being its intensities in both series. Fuzzy affinity function takes advantage of four intensities, two of them describing each of the points $\mathbf{c}$ and $\mathbf{d}$. In this study only the mean intensity component is considered, which leads to

---

[1] More details can be found in [5, 6].

$$\mu_\kappa(\mathbf{c},\mathbf{d}) = \mu_\alpha(\mathbf{c},\mathbf{d}) \cdot e^{-\frac{1}{2}(\mathbf{f}-\mathbf{M})^T \mathbf{C}(\mathbf{f}-\mathbf{M})}, \tag{11}$$

where each value of the vector $\mathbf{f}$ and of the mean intensity vector $\mathbf{M}$ relates to a single series

$$\mathbf{f} = \begin{bmatrix} \frac{f_1(\mathbf{c})+f_1(\mathbf{d})}{2} \\ \\ \frac{f_2(\mathbf{c})+f_2(\mathbf{d})}{2} \end{bmatrix}, \qquad \mathbf{M} = \begin{bmatrix} \mu_1 \\ \\ \mu_2 \end{bmatrix}.$$

The μ_1, μ_2 and $\mathbf{C}$ parameters are obtained from the GMM step.

At the preprocessing step the images are prepared for the FC analysis. The pixel intensities f_1 and f_2 above the mean values μ_1 and μ_2, respectively, are replaced with the corresponding mean value.

The body of the FC algorithm remains unchanged [8]: the FC scene is computed in a 3D space over the GMM-selected seed points. The Dijkstra's algorithm is used after setting the affinity values to 1 for all the seed points. A slice chosen from the fuzzy affinity scene is shown in Fig. 4 (left).

The fuzzy affinity value restricting the finally segmented area is calculated on the basis of FCM clustering with two clusters (Fig. 4).

Fig. 4 Results of the fuzzy connectedness analysis for a chosen slice (left). Thresholding on the basis of the FCM algorithm (middle). Final segmentation results (right).

5 Transformation

During a single MR examination, several series are typically acquired (e.g. T1W, T2W, contrast enhanced T1W, etc.) in three basic planes: axial, sagittal and coronal. In radiological assessment all these series may be relevant for the final diagnosis. For the analysis of the whole examination the indirect transformation T is employed. First, all the already segmented points are transformed into the target series, using DICOM positioning information [9]
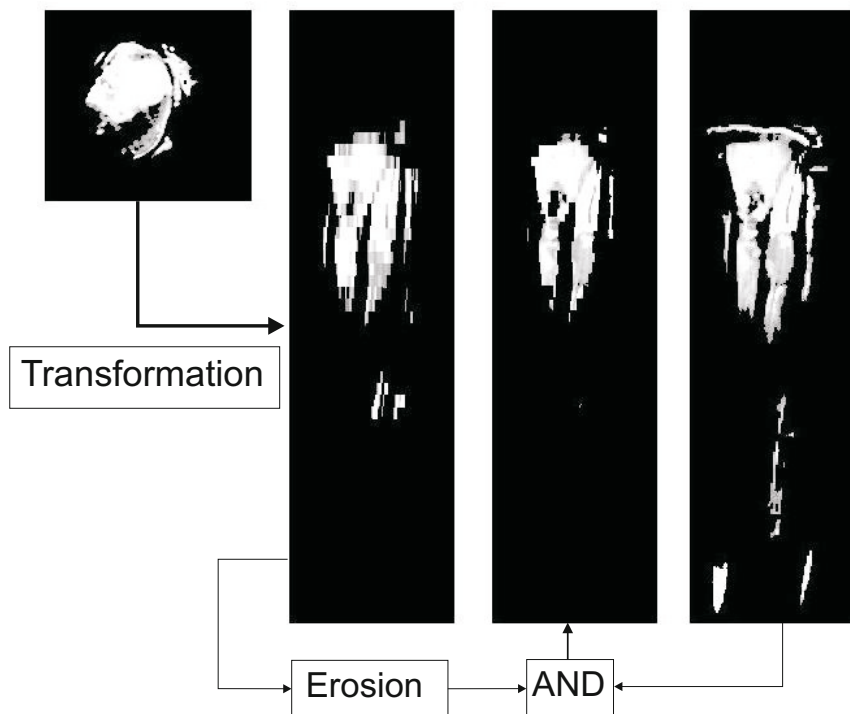
Fig. 5 An example of transformation and new seed points selection

$$\begin{bmatrix} P_x \\ P_y \\ P_z \\ 1 \end{bmatrix} = \begin{bmatrix} X_x\Delta i & Y_x\Delta j & 0 & S_x \\ X_y\Delta i & Y_y\Delta j & 0 & S_y \\ X_z\Delta i & Y_z\Delta j & 0 & S_z \\ 0 & 0 & 0 & 1 \end{bmatrix} \begin{bmatrix} i \\ j \\ 0 \\ 1 \end{bmatrix} = M \begin{bmatrix} i \\ j \\ 0 \\ 1 \end{bmatrix}$$

$P.$ - the coordinates of the voxel (i,j) in the frame's image plane in units of [mm]. $S.$ - the three values of the Image Position (Patient) (0020,0032) attributes. It is the location in mm from the origin of the RCS.

$X.$ - the values from the row (X) direction cosine of the Image Orientation (Patient) (0020,0037) attribute.

$Y.$ - the values from the column (Y) direction cosine of the Image Orientation (Patient) (0020,0037) attribute.

i, j - column and row index to the image plane.

$\Delta i, j$ - column or row pixel resolution of the Pixel Spacing (0028,0030) attribute in units of [mm].[2]

---

[2] More details about the DICOM coordinate system can be found in [9].
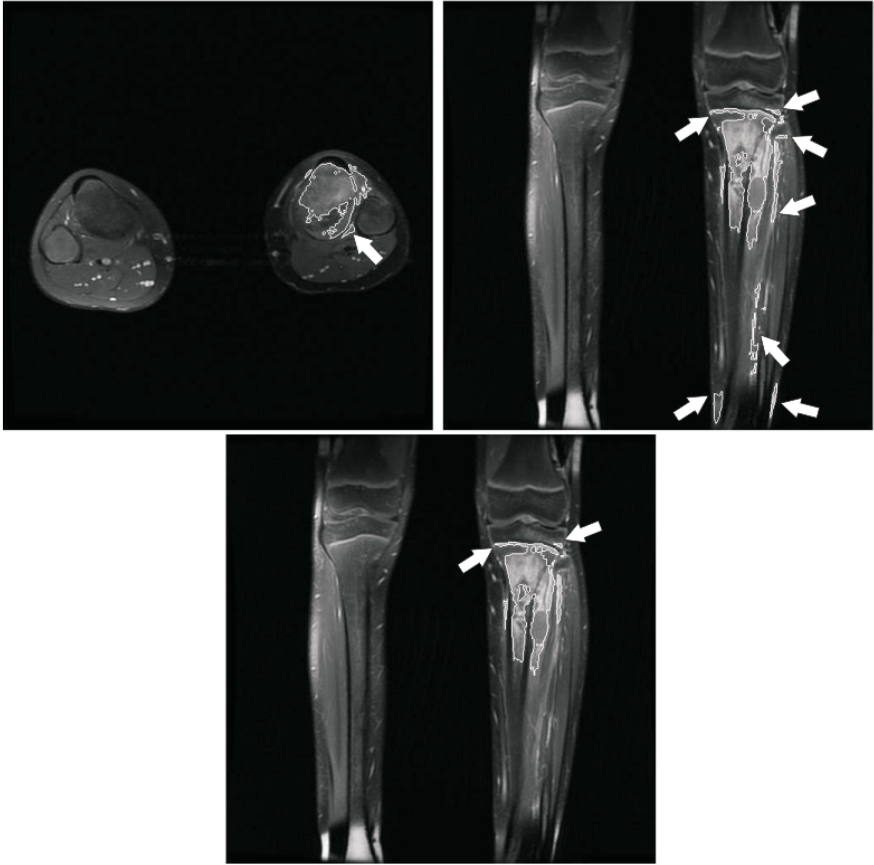
Fig. 6 Results of a single plane multiseries analysis in the axial plane (upper left). Results of a single plane multiseries analysis in the coronal plane (upper right). Results of a multiplane multiseries analysis in the coronal plane (bottom). The arrows indicate the false positives.

The transformation is defined in such a way that it maps the 3D row-column-slice (RCS) space into a 3D xyz space

$$P^{xyz} = P^{RCS} \cdot T. \tag{12}$$

Multiple series can be transformed into the same xyz coordinate system. With the inverse transformation T^{-1} the mapping from one series into another may be performed by using this xyz coordinate system.

The steps described in sections 2, 3 and 4 are independently performed for all the planes. The results of applying the FC step are transformed to the desired plane from the other planes. Next, the transformed masks are subjected to morphological erosion and the common area of the resulting masks and the mask originally obtained in the desired plane is found (Fig. 5). The new seed points area is thus obtained for
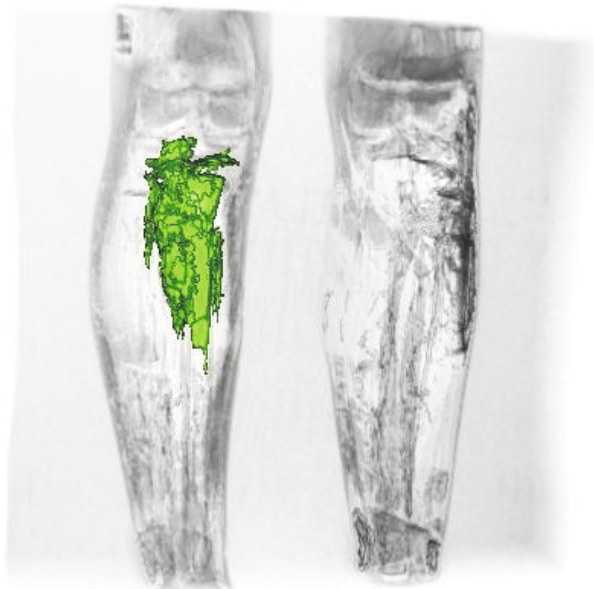
Fig. 7 Final results - a 3D view

a renewed FC analysis (as described in section 4), yielding the final tumour areas mask.

A comparison of results obtained for single plane and multiplane processing is shown in Fig. 5.

6 Results

Studies of two patients have been used for the initial evaluation of the suggested algorithm. The analysed Ewing's sarcomas arose in two different parts of the body. Each of the studies consists of T1W and T2W series, in two planes, the series containing between 10 and 30 slices. The series also differ in the size of images. In total 134 images have been analysed. Each study was earlier described by a radiologist. The achieved segmentation results (Fig. 5) are comparable to those obtained by a doctor. All the tumour areas are included in the segmented regions. However, in some cases false positive areas appeared. They constitute at most 5% of the whole volume of the segmented structure. It should be underlined that the testing results are repeatable. Moreover, from medical point of view, an over 20% change in the volume of tumour tissue between subsequent examinations is relevant. The obtained 5% accuracy will thus not hinder the diagnosis. Furthermore, the CAD workstation will enable the user to remove semi-automatically these regions from the segmented areas.

7   Conclusions

An effective method for semi-automated 4D segmentation of Ewing's sarcoma tumours has been presented. FCM clustering, its kernelised version, GMM analysis and FC algorithm have been used. The two different planes coming from one examination are combined on the basis of DICOM header information. The segmentation method has been tested on medical examinations and consulted with a radiologist. The results obtained are satisfactory, which encourages to further develop this method. As a result, the efficiency of the suggested algorithm should enhance. It is also planned to use this methodology in the segmentation of other types of cancer and anatomical structures. The CAD workstation will assist radiologists in the diagnosis and could also be useful for education and training.

References

1. University of California, San Francisco Children's Hospital, Medical Service, Sarcomas,
   `http://www.ucsfhealth.org/childrens/medical_services/`
   `cancer/sarcomas/conditions/ewings/signs.html`
2. Chen, S., Zhang, D.: Robust Image Segmentation Using FCM With Spatial Constraints Based on New Kernel-Induced Distance Measure. IEEE Transactions on Systems, Man and Cybernetics-part B, Cybernetics 34(4) (August 2004)
3. Zhang, D.-g., Chen, S., Pan, W.-S., Tan, K.-R.: Kernel-Based Fuzzy Clustering Incorporating Spatial Constrains for Image Segmentation. In: Proceedings of the IMCL 2003, Wan, November 2-5 (2003)
4. Mekhalfa, F., Goumeidane, A.B.: Unsupervised Algorithm for Radiographic Image Segmentation Based on the Gaussian Mixture Model. In: EUROCON 2007 Int. Conf. on Computer as a Tool, Warsaw, September 9-12 (2007)
5. Udupa, J., Samarasekera, S.: Fuzzy connectedness and object definition: Theory, algorithms, and applications in image segmentation. Graphical Models and Image Processing 58(3), 246–261 (1996)
6. Udupa, J., Saha, P.: Fuzzy connectedness and image segmentation. Proceedings of the IEEE 91, 1649–1669 (2003)
7. Saha, P., Udupa, J., Odhner, D.: Scale-Based Fuzzy Connected Image Segmentation: Theory, Algorithms, and Validation. Computer Vision and Image Understanding 77(9), 145–174 (2000)
8. Badura, P., Pietka, E.: Semi-Automatic Seed Point Selection in Fuzzy Connectedness Approach to Image Segmentation. Advances in Soft Computing: Computer Recognition Systems 2(45), 679–686 (2007)
9. Digital Imaging and Communications in Medicine standard.
   `http://medical.nema.org/` (Cited February 11, 2010)

Segmentation of Stained Lymphoma Tissue Section Images

Urszula Neuman, Anna Korzynska, Carlos Lopez, and Marylene Lejeune

Abstract. In order to obtain supporting tool for the pathologists who are investigating prognostic factors in folicular lymphoma a new method of color images segmentation is proposed. The method works on images acquired from immunohistochemically stained thin tissue sections of lymph nodes coming from patients with folicular lymphoma diagnosis. The proposed method of segmentation consists of: pre-processing, adaptive threshold, watershed segmentation and post-processing. The method is tested on a set of 50 images. Its results are compared with results of manual counting. It has been found that difference between the traditional method results and the proposed method is small for images with up to 100 nuclei while in more complicated images with more then 100 nuclei and with nuclei clusters this difference increases.

1 Introduction

Lymphoma is a cancer caused by an abnormally fast proliferation of lymphoid cells. There are more than 20 different types of lymphoma cancer, more or less aggressive [1]. In the current practice of pathology, the identification of specific clinical markers and particular molecular alterations represents an indispensable routine for diagnostic, predictive and therapeutic purposes. Follicular lymphoma (FL) is the prototype of indolent lymphoma characterized by long median survival, even without therapy, and rare spontaneous remissions. The inconsistency of the disease

Urszula Neuman · Anna Korzynska
Nalecz Institute of Biocybernetics and Biomedical Engineering, PAS, ul. Ksiecia Trojdena 4, 02-109 Warszawa, Poland
e-mail: `udlubak@ibib.waw.pl`

Carlos Lopez · Marylene Lejeune
Molecular Biology and Research Section, Hospital de Tortosa Verge de la Cinta, C/ Esplanetes 14, Tortosa 43500, Tarragona, Spain
e-mail: `jjaen.htvc.ics@gmail.com`

course makes it difficult to gain a clear consensus about the usefulness of the different treatment options proposed for these patients. In the search of new prognostic and predictive factors, different studies have demonstrated that an exclusively genetic model may not be sufficient to explain the pathogenesis of FL. Therefore, other growth and progression supports, like the inflammatory/immune microenvironment response to the tumor, have been proposed. Recent studies have defined follicular regulatory T cells as independent predictors of overall survival in these patients [2, 3, 4]. The T cells seems to be able to reduce tumor-driven immune suppression with clinical benefit for patients. The presence of this specific subset of immune cells with immunosuppressive activities can be detected by the fact that they express a high level of the forkhead transcription factor box protein P3 (FOXP3).

Immunohistochemistry (IHC) is a technique for identifying cellular or tissue constituents (antigens) by means of antigen-antibody interactions, the site of antibody binding being identified either by direct labelling of the antibody, or by use of a secondary labelling method. IHC has found numerous applications in medicine, especially in cancer diagnosis and prognosis. Lymphomas are among the cancers that most dependent on IHC for treatment decisions. In the evaluation and quantification of positively immunostained cells, the most prevalent method is the manual counting performed by the pathologist using a conventional microscope. To avoid subjectivity, a number of automated image analysis programs suitable for use in histopathology are recently under investigation of various research groups.

Several successful applications of supporting diagnosis, prognosis therapy evaluation processes based on immunohistochomically stained samples using image processing and analysis are reported in prostate [5], glands [6] or cervical [7], breast cancers [8], lymphomas [9] and others neoplasms [10, 11, 12]. Previous results obtained with automated or semi-automated segmentation of immunohistochemically stained digital images have used available commercial programs such as Photoshop [13], Image-Pro Plus [14], Visilog [15] or ACIS [16]. Moreover, due to increase of physicians' need of evaluating their diagnosis and calculations an internet platform software EAMUS has been arranged. The software is dedicated for general measurement of various features from immunohistochemistry and deals with various stains and colors in images [17].

Many studies, regardless of the type of cancer and affected organs, are related to color space changes and try to find the best space in which a color image segmentation can be performed [18, 19, 20]. Some of them even propose self generated spaces which are constructed as an optimized space to contrast specific colors [21, 22]. The studies give contradictory conclusions about usefulness of various color spaces [23, 24, 25]. Typically a conventional color segmentation is applied to each component of a color space and results are combined in some way to obtain the final result. Study presented in this paper is based on modified B channel from the RGB color space [26].

Some of the methods are based on color-based thresholds or on clustering with fixed number of classes [27, 28]. However, if there is inhomogenity in color and in light distribution across an image one global threshold is not a good solution. In our study an adaptive threshold [29, 30] is used because of big tone variation observed

in each image and from one image to another. Typically as a result of image segmentation the image maps are constructed. In many studies those maps are processed by morphological operation to obtain final results for example quantification of specific area or objects in the image [21, 17, 31]. Presented in the paper study also uses morphological operations, morphological filtering and watershed [32] to process results and prepare maps to count number of nuclei. Investigation presented in the paper uses Gaussian pyramid [33, 30], which is commonly used in image processing, to reduce size of image. Advantages coming from this method are described further in the text.

Digital images of immunohistochemically indirectly stained histological samples prepared to show location and a number of T regulatory cells are used in this paper. Nuclei with positive immunoreactivity against the protein FOXP3 became brown during the staining process due to 3,3'-Diaminobenzidine (DAB). Other nuclei with negative immunoreactivity become blue because of a hematoxilin counterstaining. Details of staining process are described further. The method proposed in this paper localises and counts T regulatory cells (the brown nuclei) inside the neoplastic follicles (in the image).

2   Materials

Images of lymphoma immunohistochemically stained tissue differ in tones, number and dispersion of objects. There are two basic sources which amplify the variation in the images: a staining process and the image capturing process. In the staining process the variation is connected with variation of tissue features and humane action variability in processing [34, 35]. While in the image capturing process the variation depends on visual system of a person who acquires the images and properties of microscope and camera used during image capturing. Moreover, even one person can choose various settings depending on his/her mood and trim.

(a) A part of an original image   (b) After color filtering
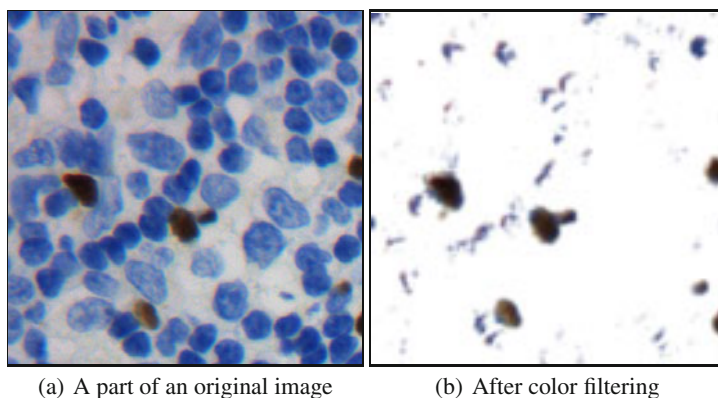
Fig. 1 Smudges in background: an original image and the image after color filtering

Each image consists of background, blue stained nuclei and brown stained nuclei. The bright background fills space between nuclei usually with light blue color. In some specimens smudges, which are fragments of positive nuclei destroyed during tissue cutting, can be locally observed in the background (see Fig. 1). These fragments depend of the position of the nuclei in the section and the level of the cut. Color of the smudges is non-uniform, it is bright brown up to yellow mixed sometimes with blue.

Blue stained nuclei distribution is very dense and the blue nuclei fill majority of each image area. Size and shape of those nuclei vary in each image. The variation of size comes from fact that spherical and ellipsoidal nuclei are cut into thin slices in various positions. Also the shapes of the blue nuclei in image are changing due to cutting process from round to elongated. Intensity of the blue color is significantly different for the various images, there are both pale (see Fig. 2(a)) and intensively blue images (see Fig. 2(c)). Inside brighter blue nuclei a texture (brighter and darker nucleus fragments) can be observed.

| (a) A weak stain | (b) A normal stain | (c) An intensive stain |
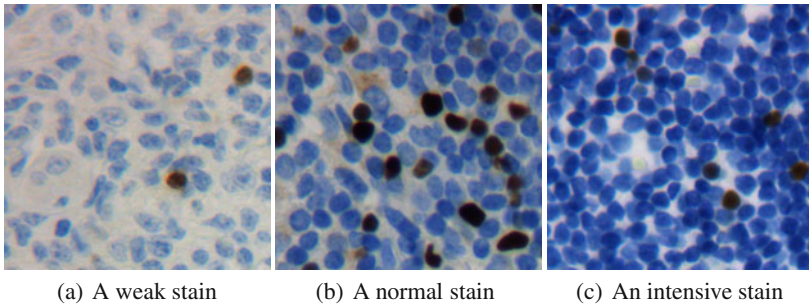
Fig. 2 Variation of intensity of blue in images of stained specimens

The brown stained nuclei are usually surrounded by the blue nuclei. Distribution of the brown nuclei is usually homogeneous but sometimes in specimens with high density of the brown nuclei, clusters created by several neighbouring cells can be observed. Objects in the clusters are very difficult to segment because they are touching or overlapping. Shapes of the brown nuclei are usually round, sometimes elliptical. A brown nuclei color variation is bigger than blue nuclei color variation observed in one image (see Fig. 2(b)). The brown color can change from bright brown (yellowish or grayish) to near black brown. In the bright brown nuclei a small texture can be observed (see Fig. 2(a)).

3 Methods

Task of the proposed algorithm is counting brown color stained nuclei in described above images.

3.1   Algorithm Description

The algorithm consists of: (1) pre-processing, (2) two-level segmentation and (3) post-processing.

Pre-processing: Before applying the main segmentation process each image is pre-processed by two consecutive steps: color separation and rescaling.

| (a) An original image | (b) Color separation | (c) Adaptive threshold |

| (d) Morphological filtering | (e) Watershed | (f) Original plus result borders |
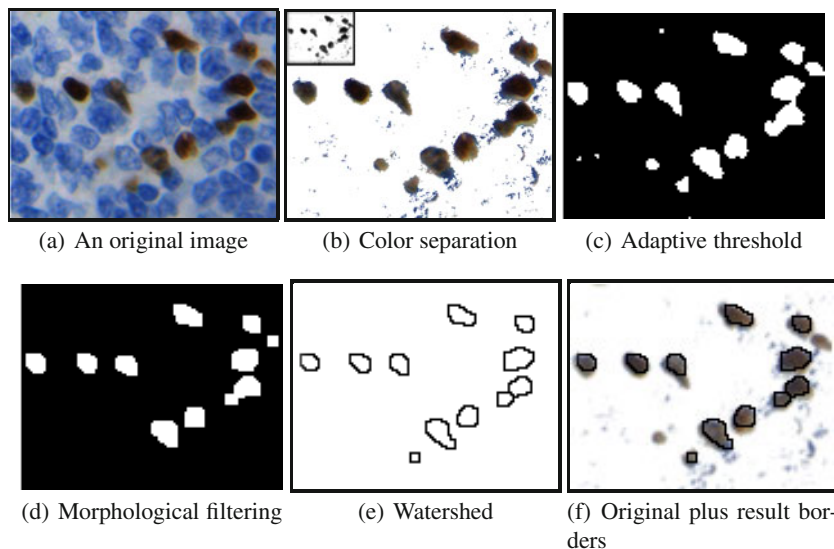
Fig. 3 The algorithm's steps

Firstly brown color in an image is separated by replacing with white pixels all the pixels which are out of defined range of brown color (see Fig. 3(b)). The brown color definition has been adjusted experimentally by establishing proper range for each of three color channels from the RGB color space. Unfortunately a dark blue color is included in the defined range of brown color. Shrinking the range in order to eliminate the dark blue color excludes some nuclei with positive colors. Hopefully the blue color nuclei are textured structures and the dark blue structures preserved in an image after color separation are shaped as small spots. Those small spots are removed later using morphological operations.

Secondly the image is rescaled with Gaussian pyramid [33, 30]. Size and resolution of the image become 16 times smaller (see Fig. 3(b), upper left, black box). Objects after such rescaling are smooth and compact what is visible in Fig. 3(c). Moreover the time of algorithm proceeding visibly decreases.

Two-level Segmentation: In the main segmentation process two steps of image processing are performed. The first step is an adaptive threshold [29, 30] and the second step is a watershed segmentation [36, 37].

Adaptive Threshold: As it has been earlier described a big tone variation in image and from image to image is observed. The adaptive threshold is flexible and quite resistant to this type of variation so it is introduced in the algorithm. It has been observed that the blue channel of the pre-processed image has the most contrasting boundaries of separate nuclei so the threshold is calculated for this channel. The adaptive threshold uses window - a square (30x30 px) which is moved through the image. For each position of the window the algorithm calculates mean value of pixels (T) and difference between maximal and minimal value (D) in the window. Having D it is possible to decide if the window contains edges. It is assumed that for the value of D smaller than 6% of the maximal possible value of the image (here 255) there are no edges inside the window. If there are no edges the middle point of the window is compared with mean value T and classified as background or foreground. If there are edges inside it is necessary to recognise if the middle point of the window is an object or not. This part of image processing produces a binary map containing white objects on black background (see Fig. 3(c)). Noise, which comes from dark blue spots is removed from the map by morphological opening filter (see Fig. 3(d)). The filter uses disc-shaped strel element with radius 3.

Watershed Segmentation: As the white objects in the adaptive threshold map are sometimes related to more then one nuclei the second step of segmentation - watershed [32, 38] is introduced to separate the nuclei. In order to use the watershed as a shape based segmentation a distance transform of the map is calculated [39]. Additionally a morphological reconstruction on the distance transform image is introduced to simplify it and to eliminate small shape disturbances. The morphological reconstruction is made using as markers image which is result of constant value (in our case it is 0.3) subtraction from the distance transform image. So the brightest parts of the distance transform are used as markers [40, 41, 36, 39]. After the reconstruction the distance transform is less complicated and results of its watershed are more proper. The result of the watershed are boundaries of single nuclei (see Fig. 3(e)). The watershed segmentation works very well by separation two round objects connected with "bottle neck" but it has problems with detection of other types of nuclei connections (e.g. tree cells creating flower-shaped object).

Post-processing: The last step of the algorithm is increase of the image to the original size using invert Gaussian pyramid. In the Fig. 3(f) rescaled boundaries imposed on an original image are shown.

In the Fig. 4 part of other original image with results of the proposed method is shown in a context of the results of traditional counting (Fig. 4(b)). It can be observed that most of the found by the method objects are marked also by an operator, expect of two objects by the border of the image and two shown by the white boxes.
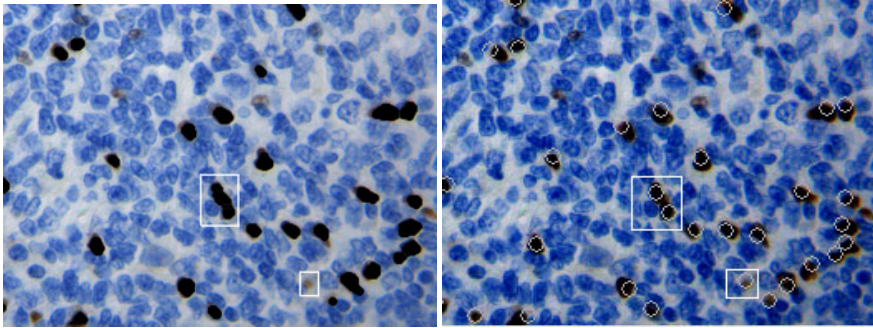
(a) An original image with results of the proposed method shown as black spots

(b) Marks on original image made by pathologist

Fig. 4 An original image with results of the proposed method and results of the traditional method

3.2 Algorithm Implementation

The algorithm is implemented in MATLAB and C. The most time consuming operations (adaptive threshold) are written in C. The implementation of the algorithm does not have any graphical user interface jet.

3.3 Evaluation of the Proposed Method

To evaluate quality and an average time of performance of the proposed algorithm a comparison with a traditional method of counting of nuclei in immunohistochemically stained specimens is made. The traditional quantification of specimens made by pathologists is always subjective but we have no other method at ours command to compare. The traditional method bases on manual counting of visually selected objects. In this paper the manual counting is made interactively with software ImagePro Plus 5.0 which allows operators to mark counted objects with circles. This interactive procedure counts objects marked by operator. To reduce inter observer variability one operator (pathologist) has made the manual calculation three times to obtain an average number of objects for each image and to prepare a counting maps (see Fig. 4(b)). An error of the automatic method for one image is defined as:

$$ERR = (\frac{|AUTO - MAN|}{MAN}) \cdot 100\% \qquad (1)$$

where:
ERR - an error of the automatic method,
AUTO - a number of nuclei detected by the automatic method,
MAN - a reference number from the averaged traditional counting.

A mean error of the automatic method is mean value of error obtained for the set of all investigated images.

In order to show structure of the error done by the automatic method a correspondence between results of the proposed method and results of the manual counting is examined for 5 chosen images. During this examination not only an absolute difference between the results (ABS) but also elements which creates the error are calculated. To these elements belong:

1. NOV - number of nuclei counted by the pathologist as one object and by the proposed method as more than one,
2. NM - a number of objects found by the method as one object and by the pathologist as more than one nuclei,
3. NEX - a number of objects found by the proposed method but rejected by the pathologist,
4. NUM - a number of nuclei not found by the proposed method but found by the pathologist.

The mean time of one image processing is precisely measured by computer while the time of the traditional counting is estimated from notes.

3.4 Sample and Image Acquisition

During the method evaluation process a biological material from Hospital "Verge de la Cinta" in Tortosa prepared by several technicians according a standard procedure is used. They cut a formalin-fixed paraffin- embedded tissue parts into 3μm thin sections. The section are dried, deparaffinized in xylene, rehydrated in graded ethanol and washed in water and PBS. Antigen retrieval is achieved by heat treatment in pressure cooker or pronase digestion. Samples ware incubated with the appropriate dilution of the primary antibody FOXP3-236A/E7 (monoclonal antibody, Monoclonal Antibodies Unit, CNIO, Madrid, Spain). The immunohistochemical indirect staining is made using a Horizon TechMate (Dako) devise. During the staining process nuclei that have positive immunoreactivity against FOXP3 become brown while all other become blue because of counterstaining with hematoxylin. Staining intensity can change a little bit every day depending of different external factors. Positive and negative controls are introduced every day in the series.

One person makes the image acquisition, so there is no error connected with changing of a personal visual system. As the images are taken during several sessions the settings of the camera can change according to external factors like sun or artificial light conditions. Obviously the settings depend on density of tissue and number of brown nuclei in field of the image.

A Leica DM LB2 upright light microscope (Leica Microsystems Wetzlar GmbH, Wetzlar, Germany) with a 40x plane apochromatic objective with a numerical aperture of 0.63 and a digital camera Leica DFC320 (Leica Microsystems Digital Imaging, Cambridge, UK) controlled by Leica DFC Twain software 6.3.0

(Leica Microsystems Digital Imaging) are used during the acquisition process. Size of acquired images is 2088x1550 pixels. Each single pixel corresponds to about 0.5μm. That means that each image shows 3.8mm x 2.8mm rectangle part of a specimen. According to information from The Hospital in Tortosa up to 293 of nuclei can be expected in one image and the mean value of the number of nuclei is about 65.5$\pm$ 57.3 [2].

The proposed method has been tested on a randomly chosen set of 55 images coming from The Hospital in Tortosa. 5 of them have been excluded from investigation due to different color ton.

4 Results

Results presented in following section had been obtained based on set of 50 images acquired according to the above description.

Results of evaluation of the proposed method are shown in two tables. Table 1 compares mean result of the method and mean result of the traditional counting. The table shows also the mean time of one image proceeding. The time of processing of one image is significantly shorter than the time needed for the traditional counting. Table 2 presents correspondence an differences between the results of the proposed method and the results of the traditional counting for 5 chosen images.

Table 1 Mean result of the proposed method versus the mean manual counting

Kind of counting	Mean amount of nuclei per image	Mean error [%]	Mean time of one image proceeding
The manual count	94	-	few minutes
The proposed method	88	11	18 sec

Table 2 shows how many objects are classified similarly in bought methods (from 83% to 100%) and how many of them are missclassified. An analyse of those errors is presented in the following section.

5 Discussion

Mean error of the proposed method which equals 11% has several sources. In order to investigate a structure of the error the Table 2 is introduced. Images from the Table 2 can be divided into two main groups: 'dense images' with a number of nuclei more then 100 (last two rows of the Table 2) and 'slack images' with a smaller number of nuclei (three first rows in the Table 2).

Table 2 Detailed results obtained for 5 chosen images: IM - an image number, NEQ - a number of nuclei similarly classified by proposed method and by pathologist (given also in percents as reference to the traditional count), other designations in the table columns according to section 3

IM	MAN	AUTO	ABS	NEQ	NOV	NM	NEX	NUM
1	43	42	1	39 (91%)	2	1	0	2
2	42	37	5	37 (88%)	0	0	0	5
3	31	32	1	31 (100%)	0	0	0	1
4	103	119	16	85 (83%)	20	5	9	0
5	119	114	5	102 (86%)	2	4	6	5

In the 'slack images' the main source of error are the nuclei undetected by automated method. It is caused by the variation of image color tone. The results obtained from the image 1 (first row of the Table 2) show that sometimes absolute difference gives lower error then it really is. In this case the number of over-segmented nuclei is compensate with the number of under-segmented objects containing more than one nucleus.

The 'dense images' are hard to segment. The number of objects with extra segments and the number of objects which consist of more then one nucleus are significant. As mentioned in section Images Characteristic in 'dense images' brown nuclei touch and overlap forming clusters which are difficult to divide into single nuclei. The watershed segmentation works well for groups of nuclei forming long ribbons but for other shapes of clusters it produces incorrect segmentation but overall error is still in acceptable range.

The traditional counting is especially hard in case of 'dense images' so the manual counting results are less reliable then for images with small number of nuclei.

6 Conclusions

The results show that the proposed method can be useful in supporting of a pathologist, because the difference between the traditional method results and the proposed method results is small for 'slack images' while in more complicated 'dense images' with nuclei clusters this difference increases. Automated image analyses save time consumed by boring counting of nuclei and decrease intra and inter operator variability in nuclei counting. Using proposed method physicians would concentrate on an examination of the other features needed to take decision about patient treatment.

In further work precision and accuracy of the method should be increased. It will be obtained by adding to the method unification of range of image tone and by preparing a special procedure for the most difficult nuclei clusters to divide it into single nuclei. It is supposed that the information about the tissue structure which is available from the histological thin section can be helpful in solution of the cluster problem.

References

1. Swerdlow, S.H., Campo, E., Harris, N.L., Jaffe, E.S., Pileri, S.A., Stein, H., Thiele, J., Vardiman, J.W.: WHO Classification of Tumours of Haematopoietic and Lymphoid Tissues. IARC (2007)
2. Alvaro, T., Lejeune, M., Salvado, M.T., et al.: Immunohistochemical patterns of reactive microenvironment associated with the clinico-biological behavior in follicular lymphoma patients. J. Clin. Oncol. 24(34), 5350–5357 (2006)
3. Farinha, P., AlTourah, A., Gill, K., Klasa, R., Connors, J.M., Gascoyne, R.D.: The architectural pattern of foxp3-positive t cells in follicular lymphoma is an independent predictor of survival and histologic transformation. Blood 115(2), 289–295 (2010)
4. Wahlin, B.E., Aggarwal, M., Montes-Moreno, S., et al.: A unifying microenvironment model in follicular lymphoma: outcome is predicted by programmed death-1–positive, regulatory, cytotoxic, and helper t cells and macrophages. Clin. Cancer Res. 16(2), 637–650 (2010)
5. Bartels, P.H., Montironi, R., da Silva, D.V., Hamilton, P.W., Thompson, D., Vaught, L., Bartels, H.G.: Tissue architecture analysis inprostate cancer and its precursore: An innovative approach to computerized histometry. Rur. Urol. 35, 484–491 (1999)
6. Hamilton, P.W., Bartels, P., Wilson, R.H., Sloan, J.M.: Nuclear measurements in normal colorectal glands. Anal. Quant. Cytol. Histol. 17, 397–405 (1995)
7. Wied, P.B.G.: Automated screening for cervical cancer: Diagnostic decision procedures. Acta. Cytol. 41, 6–10 (1997)
8. Minot, D.M., Kipp, B.R., Root, R.M., et al.: Automated cellular imaging system iii for assessing her2 status in breast cancer specimens: development of a standardized scoring method that correlates with fish. Am. J. Clin. Pathol. 132(1), 133–138 (2009)
9. Zhang, K., Prichard, J.W., Yoder, S., De, J., Lin, F.: Utility of skp2 and mib-1 in grading follicular lymphoma using quantitative imaging analysis. Hum. Pathol. 38, 878–882 (2007)
10. Elhafey, A.S., Papadimitriou, J.C., El-Hakim, M.S., El-Said, A., Ghannam, B.B.: Silverberg sg. computerized image analysis of p53 and proliferating cell nuclear antigen expression in benign, hyperplastic, and malignant endometrium. Arch. Pathol. Lab Med. 125, 872–879 (2001)
11. Franzen, L.E., Hahn-Stromberg, V., Edvardsson, H., Bodin, L.: Characterization of colon carcinoma growth pattern by computerized morphometry: definition of a complexity index. Int. J. Mol. Med. 22, 465–472 (2008)
12. Hannen, E.J., van der Laak, J.A., Kerstens, H.M., et al.: Quantification of tumour vascularity in squamous cell carcinoma of the tongue using card amplification, a systematic sampling technique, and true colour image analysis. Anal. Cell. Pathol. 22, 183–192 (2001)
13. Lehr, H.A., van der Loos, C.M., Teeling, P., et al.: Complete chromogen separation and analysis in double immunohistochemical stains using photoshop-based image analysis. J. Histochem. Cytochem. 47, 119–126 (1999)
14. Carai, A., Diaz, G., Cruz, S.R., et al.: Computerized quantitative color analysis for histological study of pulmonary fibrosis. Anticancer Res. 22, 3889–3894 (2002)
15. Loukas, C.G., Wilson, G.D., Vojnovic, B., et al.: An image analysis based approach for automated counting of cancer cell nuclei in tissue sections. Cytometry A 55, 30–42 (2003)

16. Wang, S., Saboorian, M.H., Frenkel, E.P., et al.: Assessment of her-2/neu status in breast cancer. Automated cellular imaging system (acis)-assisted quantitation of immunohistochemical assay achieves high accuracy in comparison with fluorescence in situ hybridization assay as the standard. Am. J. Clin. Pathol. 116, 495–503 (2001)

17. Kayser, K., Radziszewski, D., Bzdy, P., et al.: E-health and tissue-based diagnosis: The implementation of virtual pathology institutions. In: Workshop E-health in Com. Euro. (2004)

18. Schulerud, H., Kristensen, G.B., Liestol, K., et al.: A review of caveats in statistical nuclear image analysis. Analit. Cell. Pathol. 16, 63–82 (1998)

19. Markiewicz, T., Osowski, S., Patera, J., Kozlowski, W.: Image processing for accurate cell recognition and count on histologic slides. Analyt. Quant. Cytl. Histol. 28(5), 281–291 (2006)

20. Markiewicz, T., Wisniewski, P., Osowski, S., et al.: Comparative analysis of methods for accurate recognition of cells through nuclei staining of ki-67 in neuroblastoma and estrogen/progesterone status staining in breast cancer. Analyt. Quant. Cytl. Histol. 31(1), 49–62 (2009)

21. Hyun-Ju, C., Ik-Hwan, C., Nam-Hoom, C., Choi, H.K.: Color image analysis for quantifying renal tumor angiogenesis. Analyt. Quant. Cytl. Histol. 27, 43–51 (2005)

22. Vandenbroucke, N., Macaire, L., Postaire, J.G.: Color image segmentation by pixel classification in an adapted hybrid color space. Comput. Vis. Image Und. 90, 190–216 (2003)

23. Park, S.H., Yun, I.D., Lee, S.U.: Color image segmentation based on 3d clustering. morphological approach. Pattern Recognition 31, 1061–1076 (1998)

24. Koprowski, R., Wróbel, Z.: The cell structures segmentation. Advances in Soft Computing, pp. 569–576. Springer, Heidelberg (2005)

25. Cha, S.H.: A fast hue-based colour image indexing algorithm. MG&V 11, 285–295 (2002)

26. Brey, E.M., Lalani, Z., Johnston, C., et al.: Automated selection of dab-labeled tissue for immunohistochemical quantification. J. Histochem. Cytochem. 51, 575–584 (2003)

27. Fu, K.S., Muib, J.K.: A survey on image segmentation. Pattern Recogn. 13, 3–16 (1981)

28. Pham, L.D., Xu, C., Prince, J.L.: Current methods in medical image segmentation. Annu. Rev. Biomed. Eng. 02, 315–337 (2000)

29. Sezgin, M.: Survey over image thresholding techniques and quantitative performance evaluation (2004)

30. Lee, C.K., Li, C.H.: Adaptive thresholding via gaussian pyramid. In: International Conference on Circuits and Systems (1991)

31. Koprowski, R., Wróbel, Z.: Automatic segmentation of biological cell structures based on conditional opening or closing. MG & V 14, 285–307 (2005)

32. Vincent, L., Soille, P.: Watersheds in digital spaces: An efficient algorithm based on immersion simulations. IEEE Trans. Pattern Anal. Mach. Intell. 13, 583–598 (1991)

33. Adelson, E.H., Anderson, C.H.: Pyramid methods in image processing. RCA Engineer 29(6), 33–41 (1984)

34. Seidal, T., Balaton, A.J., Battifora, H.: Interpretation and quantification of immunostains. Am. J. Surg. Pathol. 25, 1204–1207 (2001)

35. Leong, A.S.: Quantitation in immunohistology: fact or fiction? a discussion of variables that influence results. Appl. Immunohistochem. Mol. Morphol. 12, 1–7 (2004)

36. Serra, J., Vincent, L.: An overview of morphological filtering. Circuits, Systems, and Signal Processing 11, 47–108 (1992)

37. Nieniewski, M.: Morfologia matematyczna w przetwarzaniu obrazów. PLJ Warszawa (1998)

38. Kan, J., Qing-Min, L., Dai, S.Y.: A novel white blood cell segmentation scheme using scale-space filtering and watershed clustering. In: 2003 International Conference on Machine Learning and Cybernetics, vol. 5, pp. 2820–2825 (2003)
39. Iwaruski, M.: Metody morfologiczne w przetwarzaniu obrazów cyfrowych. Akademicka Oficyna Wydawnicza EXIT (2009)
40. Vincent, L.: Morphological grayscale reconstruction in image analysis: Applications and efficient algorithms. IEEE Transactions on Image Processing 2, 176–201 (1993)
41. Iwanowski, M., Pierre, S.: Morphological Refinement of an Image Segmentation. In: Gagalowicz, A., Philips, W. (eds.) CAIP 2005. LNCS, vol. 3691, pp. 538–545. Springer, Heidelberg (2005)

Anterior and Posterior Cruciate Ligament – Extraction and 3D Visualization

Piotr Zarychta and Anna Zarychta-Bargieła

Abstract. This paper shows successive steps in extraction and 3D visualization process of both anterior and posterior cruciate ligaments. In the first stage a region of interest including cruciate ligaments (CL) is outlined. The automatic method of location of the CL on the T1W MR knee images is based on fuzzy C-means (FCM) algorithm with median modification. The next step of that process is an extraction of the cruciate ligament structure using the fuzzy connectedness approach. In the last stage a 3D structures of the anterior cruciate ligament and posterior cruciate ligament are built. These spatial structure is created through layer composition of the base images by using a linear interpolation.

1 Introduction

Anterior and posterior cruciate ligaments (ACL and PCL) are main stabilizers of the knee joint in the sagittal plane. Likewise, they contribute to the stabilisation in two remaining plans: coronal and transverse. Cruciate ligaments (CL) together with the shape of articular surface, muscles and contact forces ensure proper arthrokinematics. They play an important role in both active and passive motion. During active motion CL resist translations and reduce shear forces, whereas during passive motion CL help to change rolling into sliding movements [1]. The amount of forces loading the ligaments depends of actual knee position, knee moment and tibiofemoral joint compression forces. During open kinetic chain extension ACL strain increases while flexion angle decreases (from 40° of flexion). The bigger knee extension moment, the higher is ACL strain. During open kinetic chain flexion PCL

Piotr Zarychta
Silesian University of Technology, Akademicka 16 st., 44-100 Gliwice, Poland
e-mail: piotr.zarychta@polsl.pl

Anna Zarychta-Bargieła
Hospital in Dąbrowa Górnicza, ul. Szpitalna 13, 41-300 Dąbrowa Górnicza, Poland
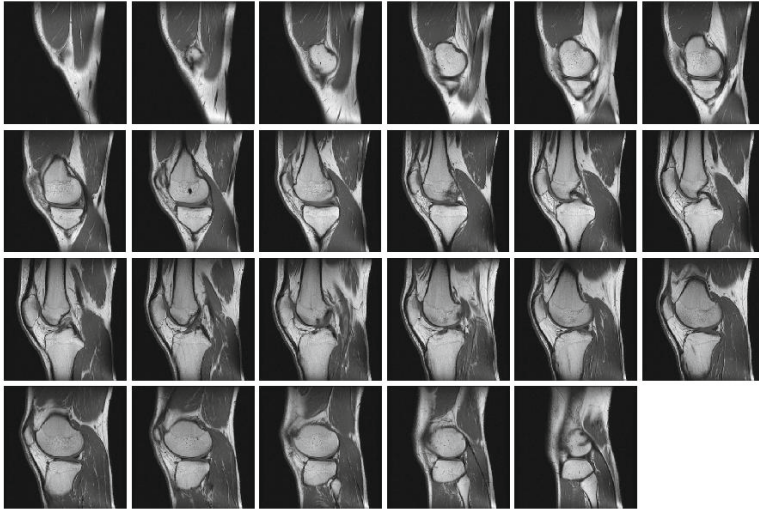
Fig. 1 T1W MR series - signal from data base clinical hospital

strain increases rapidly above 30° and reaches the maximum above 90° of flexion. In closed kinetic chain motion (like sqatting), tibio-femoral joint compression forces and contraction of muscles stabilising the joint, reduce shear forces and decrease ligament strain. Cruciate ligaments control rotational movements in the flexed knee and together with collateral ligaments ensure rotational stability of the extended knee [4].

For that reason cruciate ligaments belong to the group of anatomical structures, which are frequently susceptible to injuries, especially in the athletes. Ligamentous injuries of the knee are a very important and complex medical problem. The manual examination and after that the MR methods remain the basic approach to the injured knee. Appositely performed clinical evaluation plus additional MR slices of the knee joint determine the proper clinical way and gives information about therapy should be ordered. The MR series of the knee joint have two elementary advantages: the first precise level of knee insufficiency and the second make possible extracting and next show a three-dimensional cruciate ligament model. In this study a segmentation methodology has been developed, that extracts the anterior and posterior cruciate ligaments from T1W MR series (Fig. 1). The result is displayed in 3D.
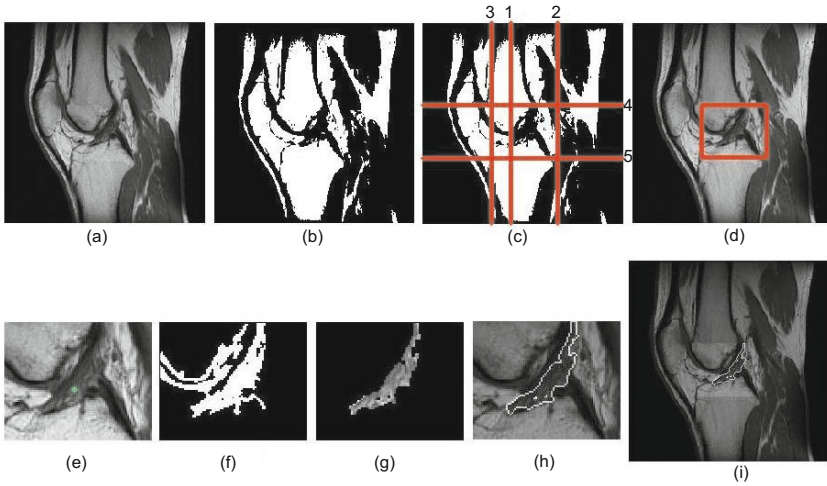
Fig. 2 Stages in the location (a)-(d) and extraction (e)-(i) process of the anterior cruciate ligament

2 Location of the Cruciate Ligament Structure on the T1W MR Series

The T1W MR knee images, which were analysed, have size 256×256 pixels. The average length of the side of a rectangle enclosing the CL structure is equal about 80 pixels. In order to increase efficiency of computational procedures, it is very important to reduce the size to the region of interest (ROI 2D) including cruciate ligament structure. The proposed automatic method of location of the CL on the T1W MR knee images is based on fuzzy C-means (FCM) algorithm with median modification. Standard FCM algorithm is widely used in many clustering approaches. Its advantages include a conceptual and computational simplicity and the ability to model uncertainty within the data. FCM has also several weaknesses. It does not incorporate spatial context information which makes it sensitive to noise and image artifacts.

In this paper a modified method of FCM is used for the clustering. The FCM objective function is modified by adding a second term, which formulates a spatial constraint based on the median estimator. Then, the final formula for FCM median modified can be expressed as

$$J(\mathbf{U},\mathbf{V}) = \sum_{k=1}^{K} \sum_{n=1}^{N} u_{kn}^{r_f} \left(\|\mathbf{x}_n - \mathbf{v}_k\|^2 + \alpha \|MedF(\mathbf{x}_n,Z) - \mathbf{v}_k\|^2 \right). \tag{1}$$

where $MedF(\mathbf{x}_n,Z) = median(S)$, $S = neighbourhood(\mathbf{x}_n,Z)$ and Z determines the size of the mask. The processed clinical T1W MR knee by the FCM median modified is shown in the Fig. 2b.

On the basis of the analysis of each profile in every slice of the T1W MR knee after fuzzy clustering, a main axis (no.1 in the Fig. 2c) running along the thighbone and tibia is determined. The main axis is determined according to following formula

$$th = \max_k \left[L_{pr}(k)\right], \; for \; each \; L_{pr}(k) \neq 0, \tag{2}$$

where $L_{pr}(k)$ denotes number of nonzero values of the pixel intensity in the k profile. When several profiles meet condition (2), the profile of the lowest nonzero pixel value is chosen. In the next step edges of a ROI 2D containing the anterior and posterior cruciate ligaments are found according to following rules:

- **Upper edge** (axis 4 in the Fig. 2c)

$$\max_u \left[d_u\right] \tag{3}$$

  where d_u - distance between main axis (no.1) and right edge of thighbone for u-profile,
- **Lower edge** (axis 5 in the Fig. 2c)

$$\max_p \left[d_p\right] \tag{4}$$

  where d_p - distance between main axis (no.1) and right edge of tibia for p-profile,
- **Right edge** (axis 2 in the Fig. 2c) has been determined on the basis of the axis 1 shifted by (4).
- **Left edge** (axis 3 in the Fig. 2c) has been determined on the basis of the axis 1 shifted by following formula:

$$\max_p \left[d_{pleft}\right], \tag{5}$$

  where d_{pleft} - distance between main axis (no.1) and left edge of tibia for p-profile.

The region of interest ROI 2D including both ACL and PCL structures determined according to above rules is shown in the Fig. 2d.

3 Extraction of the Cruciate Ligament Structure from the T1W MR Series

In order to increase the efficiency of computational procedures, ROI 2D including CL structure has been outlined. The next step of that process is an extraction of the cruciate ligament structure using the fuzzy connectedness approach.

A generalized definition of fuzzy connectedness [5] is based on the fuzzy affinity relation and introduces an iterative method, that permits the fuzzy connectedness to be determined with respect to the chosen image pixel - seed point (the green point in Fig. 2e). This paper bases on a simplified graph-based view for Z^2 [2],

that uses a digital topology approach. Let $z_i = (z_{i1}, z_{i2})$ denote an image pixel, and $f(z_i)$ its signal intensity. Let all the image pixels z_i constitute nodes of a graph. In the practical approach, within the graph, each pixel is interconnected with all its spatially adjacent pixels. The adjacency may be defined in terms of a fuzzy 2-ary relation, but usually an intuitive [2] hard relation of 9-, or 25-connectedness is used. Every direct z_i-z_j link in the graph has a strength assigned to it, that is equal to the value of a reflexive and symmetric fuzzy affinity relation for the two connected nodes $\mu_{K_v}(z_i, z_j)$. The fuzzy affinity relation models the similarity of adjacent pixels. Within the graph, for each two pixels z_k, z_l, a path consisting of zero or more links can be found. A set of all existing path from z_k to z_l is denoted as $P_{z_k z_l}$. To each path p from $P_{z_k z_l}$, the strength $\mu_N(p)$ is assigned as the strength of its weakest link, i.e. the lowest value of affinity for two constituting nodes ([0,1]). The fuzzy connectedness can be then defined as a fuzzy relation:

$$\forall z_k z_l : \mu_K(z_k, z_l) = \max_{p \in P_{z_k z_l}} [\mu_N(p)]. \qquad (6)$$

The object segmentation is possible by thresholding the fuzzy connectedness relation (FC-based labeling and object extraction) or by comparing the fuzzy connectedness determined with respect to the given segmentation seed points belonging to the object and background (relative FC approach) [3].

In both direct, and relative FC-based segmentation tasks, the fuzzy affinity μ_{K_v} is used to model the notion of similarity of adjacent pixel within the extracted object. Usually [5] the membership function is employed, that depends on the signal level of compared pixels, the local signal gradient, and the properties of the extracted object (defined in terms of mean and standard deviation parameters):

$$\mu_K(z_k, z_l) = \begin{cases} 1 & \text{if } z_k = z_l \\ \omega \cdot G_1(z_k, z_l) + (1 - \omega) \cdot G_2(z_k, z_l) & \text{if } z_k \neq z_l \text{ and adjacent} \\ 0 & \text{otherwise} \end{cases} \qquad (7)$$

where $\omega \in [0, 1]$, and G_1, G_2 are selected from (8), (9), (10) or (11).

$$g_1(z_k, z_l) = exp\left((-1) \cdot \frac{1}{2s_1^2}\left(\frac{f(z_k) + f(z_l)}{2} - m_1\right)^2\right), \qquad (8)$$

$$g_2(z_k, z_l) = exp\left((-1) \cdot \frac{1}{2s_2^2}(|f(z_k) - f(z_l)| - m_2)^2\right), \qquad (9)$$

$$g_3(z_k, z_l) = 1 - g_1(z_k, z_l), \qquad (10)$$

$$g_4(z_k, z_l) = 1 - g_2(z_k, z_l), \qquad (11)$$

where function $f(z_k)$ and $f(z_l)$ denoting signal level of z_k and z_l [3].

In the first step of the fuzzy connectedness approach is requisited to choose image pixel - seed point. That point has to be included in the extracted anatomical
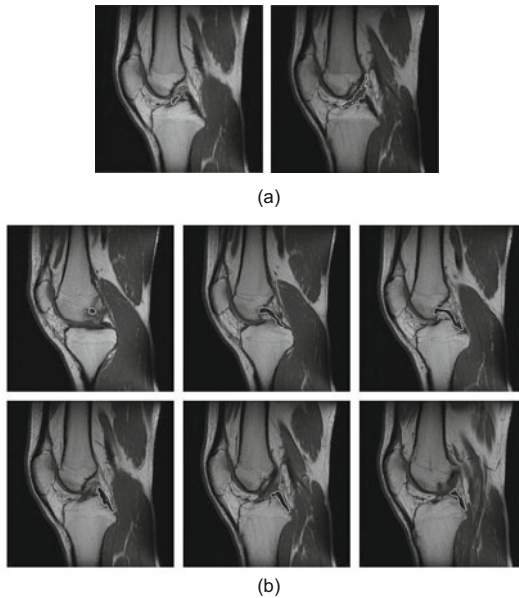
Fig. 3 Extracted (a) ACL and (b) PCL structures superimposed over the original T1W MR series (Fig. 1)

structure - anterior or posterior cruciate ligament (Fig. 2e). In the next step the above described calculates are executed. The result of the fuzzy connectedness approach is shown in Fig. 2f, where we obtained unwanted structures besides the ACL structures. In order to remove unwanted structures the morphological operations: erosions, dilation and opening have been implemented. It breaks narrow links of ligament and unwanted structures. The latter are then removed (Fig. 2g). The result is superimposed over the original image (Fig. 2h,i). The extracted ACL structures are shown in Fig. 3a. The same methodology is applied to extract the posterior cruciate ligament (Fig. 3b) and bones of the knee joint (Fig. 5). These images allowed a 3D model of both PCL (Fig. 4) and knee bones (Fig. 6) to be built. This spatial structure is created through layer composition of the base images by using a linear interpolation.

4 Numerical Results and Conclusion

The algorithm has been tested using MRI slices of the knee joint with both injured and normal anterior cruciate ligament. For all cases the segmentation process based on fuzzy connectedness has been repeated for each MR slice including the anterior and posterior cruciate ligament separately. The methodology has been tested on 24 (11 injured and 13 normal anterior cruciate ligament) clinical T1W MR knee studies. In 21 cases the proposed method location of the cruciate ligament on the T1W

Fig. 4 3D visualization of the PCL structures obtained for T1W MR series (Fig. 1)
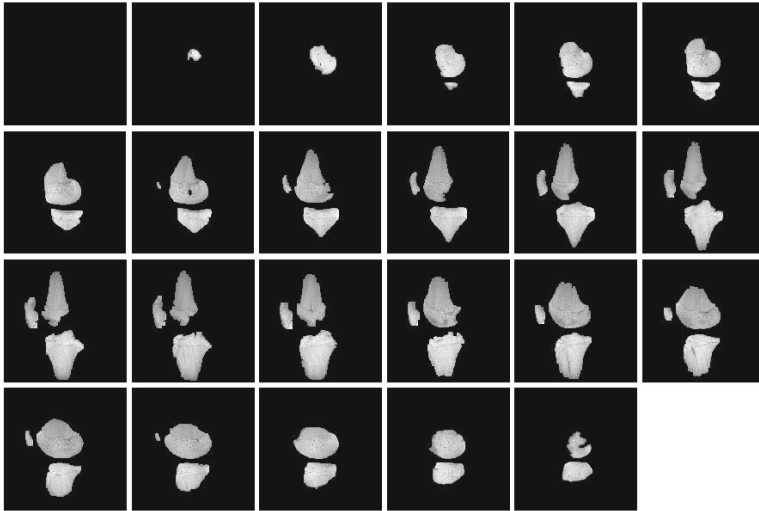
Fig. 5 Extracted bones of the knee joint from the original T1W MR series (Fig. 1)

MR knee images has been executed correctly. Errors connected with localization process have been caused by the following factors: a ligament is broken together with the thighbone, a lack of the location of thighbone and tibia along the same axis, and a location of the knee joint in the extreme part of the slice. In 19 cases the anterior cruciate ligament structure has been extracted correctly whereas posterior cruciate ligament has been extracted correctly in all cases. In two cases of serious injuries anterior cruciate ligament a modification of the methodology is required. The fuzzy connectedness procedure is completed by the fuzzy c-means function.

On the basis of the described methodology a software application has been built. This application is dedicated for the knee joint diagnosis and it makes possible the registration process of the T1W and T2W MR series ([6], [7], [8]) and the three-dimensional visualization process of following structures: ACL, PCL (Fig. 4) and bones (Fig. 6) of the knee joint.
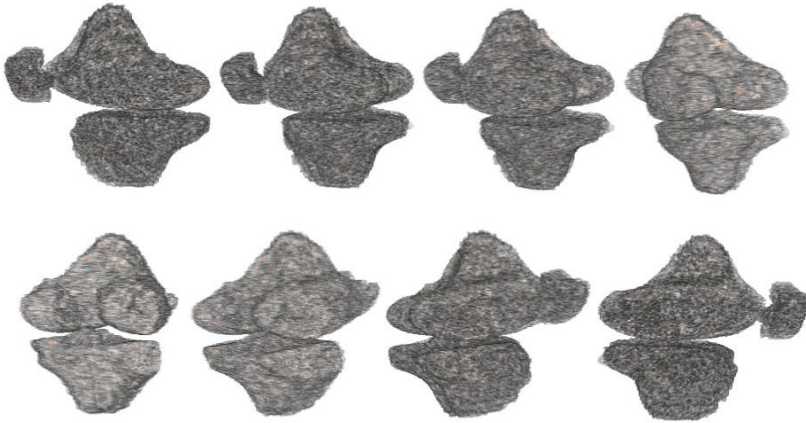
Fig. 6 Bones' 3D visualization obtained for T1W MR series (Fig. 1)

Application of the fuzzy connectedness and fuzzy c-means in the anterior and posterior cruciate ligament segmentation, and obtained results seem to be a very promising method in the three-dimensional visualization of that structures. Segmentation and three-dimensional visualization of the cruciate ligament is the initial stage in building a computer aided diagnosis of the knee joint, including the three-dimensional visualization and quantitative analysis.

References

1. Ciszkowska-Łysoń, B.: Anatomia więzadeł krzyżowych w badaniu rezonansu magnetycznego. Acta Clinica 4(1), 321–330 (2001)
2. Eckhardt, U., Latecki, L.J.: Topologies for the digital spaces Z^2 and Z^3. Computer Vision and Image Understanding 90, 295–312 (2003)
3. Kawa, J., Piętka, E.: Automated Fuzzy-Connectedness-Based Segmentation in Extraction of Multiple Sclerosis Lesions. In: Information Technologies in Biomedicine, ITIB 2008, pp. 149–156 (2008)
4. Pasierbiński, A., Jarząbek, A.: Biomechanika więzadeł krzyżowych. Acta Clinica 4(1), 284–293 (2001)
5. Udupa, J.K., Samarasekera, S.: Fuzzy connectedness and object definition: Theory, algorithms, and applications in image segmentation. Graph. Models Image Processing 58, 246–261 (1996)
6. Zarychta, P.: Automatic Registration of the Medical Images - T1- and T2-weighted MR Knee Images. In: International Conference Mixed Design of Integrated Circuits and Systems, MIXDES 2006, pp. 741–745 (2006)
7. Zarychta, P.: Location and 3D visualization of the cruciate ligament in the MR knee images on the basis of fuzzy logic. PhD Thesis, Silesian University of Technology, Gliwice (2006)
8. Zarychta, P.: Posterior Cruciate Ligament - 3D Visualization. In: V International Conference on Computer Recognition Systems, CORES 2007, pp. 695–702 (2007)

Computerized Evaluation of Abnormal Hand Bone Patterns in Skeletal Dysplasias

Arkadiusz Gertych, Morgan Clond, Ralph Lachman, and David Rimoin

Abstract. Assessment of bone disproportion is one of the routine radiological procedures frequently performed at a skeletal dysplasia diagnosis center. The existing knowledge on skeletal dysplasia patterns is more qualitative than quantitative, and the commonly applied diagnostic procedure is the manual, atlas-based evaluation of radiographs (including the hand) by an expert. A computer-aided diagnosis package (CAD) for bone age assessment was improved to analyze hand radiographs of skeletal dysplasia subjects with manifested hand bone abnormalities. The CAD software can automatically measure the lengths of phalangeal bones, compare them with those obtained from normal subjects collected in the Digital Hand Atlas (DHA), and recognize selected abnormality patterns. We have tested our method based on brachydactyly type A cases from the skeletal dysplasia diagnosis center that were matched with subjects from DHA in the age range of 2-12 years. New quantitative results obtained from this study have the potential to enrich the qualitative criteria currently utilized in the manual evaluation of abnormal bones, and thereby improve the performance of the diagnostic procedure.

Arkadiusz Gertych
Department of Surgery, Cedars-Sinai Medical Center, 8700 Beverly Blvd, Los Angeles, CA 90048
e-mail: `gertycha@cshs.org`

Morgan Clond
Cedars-Sinai Graduate Program in Biomedical Science and Translational Medicine, 8700 Beverly Blvd, Los Angeles, CA 90048
e-mail: `Morgan.Clond@cshs.org`

Ralph Lachman
International Skeletal Dysplasia Registry, Medical Genetics Institute, Cedars-Sinai Medical Center, 8700 Beverly Blvd. PACT 4, Los Angeles, CA 90048

David Rimoin
Medical Genetics Institute, Cedars-Sinai Medical Center, 8700 Beverly Blvd. PACT 4, Los Angeles, CA 90048

1 Introduction

Skeletal dysplasias (SDs) are uncommon diseases classified into more than 300 disorders of bone and cartilage growth resulting in abnormal shape and development of the skeletal system. In most cases, SDs are caused by a genetic mutation and are often detected in the newborn period or during infancy, however some disorders may not manifest until later in childhood.

Conventional radiographic examination remains the most useful mean of studying the dysplastic skeleton. The diagnostic procedure is in general time consuming, complicated and requires an expert (a pediatric radiologist or medical geneticist) with long term experience who evaluates a series of radiographs of different parts of the skeleton, including the hand. To properly classify a case, the reading is often supported by dysplasia atlases and as part of the routine, the subject's bone age is also assessed. Since the availability of experts capable of reading such radiographs is very limited, the examinations are often sent to referral centers to obtain the best possible diagnostic opinion (Fig.1). It is important to give the specific diagnosis in each case, so that an accurate prognosis can be given and proper genetic counseling provided [1].

The brachydactylies are a group of skeletal dysplasia disorders (classified into several patterns: A1, A2, A3, A4, B, C, D, and E) in which the affected individuals may have short stature and short or stubby fingers and toes [2, 3, 4, 5]. The type A brachydactylies have the shortening restricted mainly to the middle phalanges. Another anomaly is the development of a cone shape epiphysis with the apex protruding into the adjacent metaphysis. These epiphyses close prematurely, leading to short tubular bones. Such radiological findings result in abnormal bone age assessment during the diagnostic procedure.

Although the radiological description of brachydactyly patterns and other SDs have been documented based on individually classified and published cases, the present scientific knowledge in this field is rather qualitative. There is still no sufficient quantitative evidence about the range of abnormalities affecting individual bones within the scope of a particular disorder or pattern, especially if compared with standards (normal hand bone patterns). Availability of such data will not only increase the knowledge in the relevant domains but can also constitute a valuable component in the current diagnostic workup of SDs. The capabilities of computerized evaluation of abnormal hand radiographs can be enriched by automatic classification of phalangeal bones which is suitable for the recognition of SD cases throughout the methodology we propose (Fig.1).

2 Materials

The International Skeletal Dysplasia Registry (ISDR) at our institution has the largest collection in the world of cases and specimens dedicated for research, diagnosis, management and studies of etiology of the SDs [6]. From the collection of
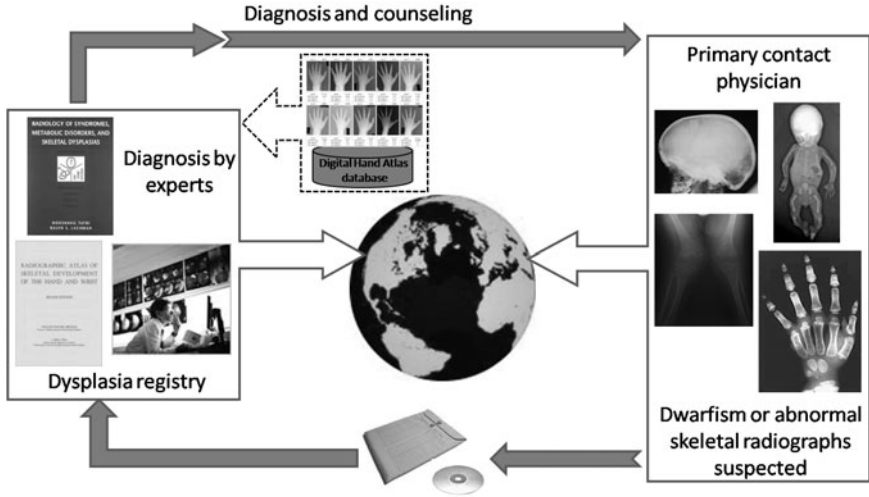
Fig. 1 A typical workflow in the diagnosis of a skeletal dysplasia case with a newly proposed component (dashed lines). Multiple radiographs of a subject's skeleton and other supporting documentation are sent to the International Skeletal Dysplasia Registry for diagnosis and counseling. The diagnostic report is sent back to the ordering institution. The Digital Hand Atlas together with CAD can augment current qualitative knowledge by incorporating quantitatively described standard bone patterns.

125 cases of brachydactylies at ISDR, several hand X-rays of subjects with brachydactyly type A, including patient demographic data, were initially selected and digitized on a DICOM compliant scanner with 16bit/pixel gray scale resolution. Private patient information was anonymized. A group of reference hand radiographs of normally developed Caucasian subjects between 2-12 years of age was selected from the DHA [7, 8] to closely match and compare with the abnormal cases. An example of a hand image of a brachydactyly A subject with an age and sex matching radiograph of a normal subject is shown in Fig. 2.

3 Methods

A CAD for bone age assessment has already been developed [9, 8]. The package includes: unsupervised procedures for localization, segmentation and feature extraction of ossification centers in distal and middle phalanges of IInd-IVth finger [10, 11, 12], radius and ulna bones [13], and an engine for automated bone age evaluation utilizing quantitative features extracted from ossification centers [14, 8]. In order to test the usefulness of this CAD in quantitative characterization of selected types of brachydactylies, some new capabilities including: a) localization and tracing of axes through Ist (thumb) and Vth finger, b) length measurement of the middle phalangeal bones in II-Vth finger, and c) length measurement of the proximal bone
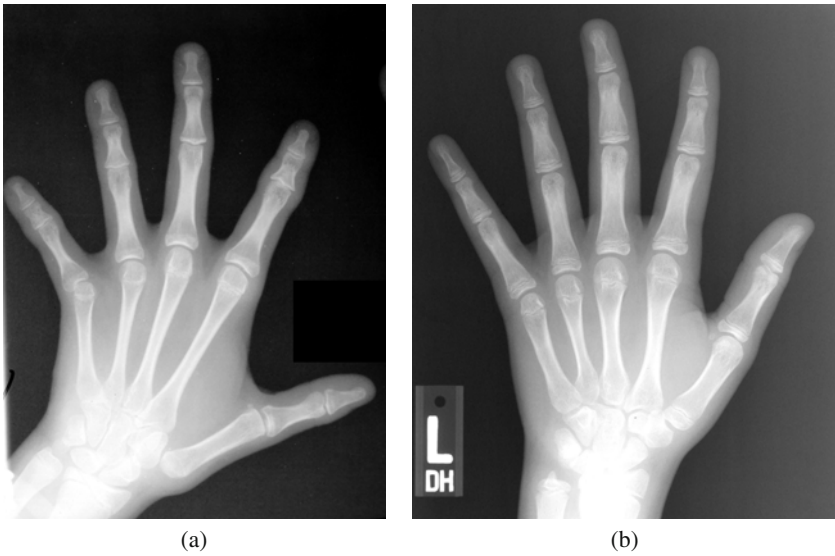
Fig. 2 Example hand radiographs of 12 year old female Caucasian subjects: a) brachydactyly type A4 from ISDR, and b) normal matching subject from DHA

of the Ist finger were supplemented to our CAD package. Although several other papers have been dedicated to hand radiograph analysis [15, 16, 17] the parameters measured through b) and c) have not been reported so far.

For the localization and tracing of the Vth finger axis we extended the approach described in [11] which has been successfully applied to the detection of II, III and IVth finger. Middle phalanges of IInd-Vth finger can be directly measured utilizing points of interest found during routine analysis of distal and middle phalanx growth plate regions [10, 14] that are mapped back onto the original image Fig. 3a In order to locate the proximal bone of the thumb a new procedure is proposed. The binary hand image is first scanned row-wise from the right side Fig. 3b A minimal distance between right border of the image and the hand object marks the thumb's tip p_{thb}. Row-wise scanning continues from the tip downward along the left and right sides of the thumb's contour. The scanning procedure is interrupted if two points are reached: p_{ra} - the upper border of the radius and ulna region on the right side, and p_{II} - the contour of the IInd finger on the left side, respectively. Next, the thumb thickness t_{thb} is approximated as a horizontal distance between points of its contour at the level of p_{II}. Then a profile is traced, starting from p_{thb} until the level of p_{ra} is reached. The position of the profile is controlled by two factors: the contour of thumb recorded during scanning and its distance from the right side border of the image, slightly varying along the profile according to t_{thb} value. Finally, the profile is analyzed using the method presented in [11] to isolate and measure the proximal bone of thumb. In the last step, lengths of middle phalanges of IInd-Vth finger and Ist finger proximal bone are automatically collected in this way.

Hand radiographs of brachdactyly A1-A4 subjects selected from ISDR and radiographs of normal subjects from DHA were analyzed by our modified CAD. Next individual measurements were normalized (expressed as ratios) and compared to respective ratios from group of age and sex matched normal subjects. Furthermore to prove feasibility of the study we implemented a rule-based strategy utilizing normalized measurements (ratios) of IInd-Vth middle phalanges and length of proximal bone of thumb to detect brachydactyly type A1-A4 abnormality. The evaluation is based on a logical decision tree implemented in the CAD software (Fig. 4).

(a) (b)
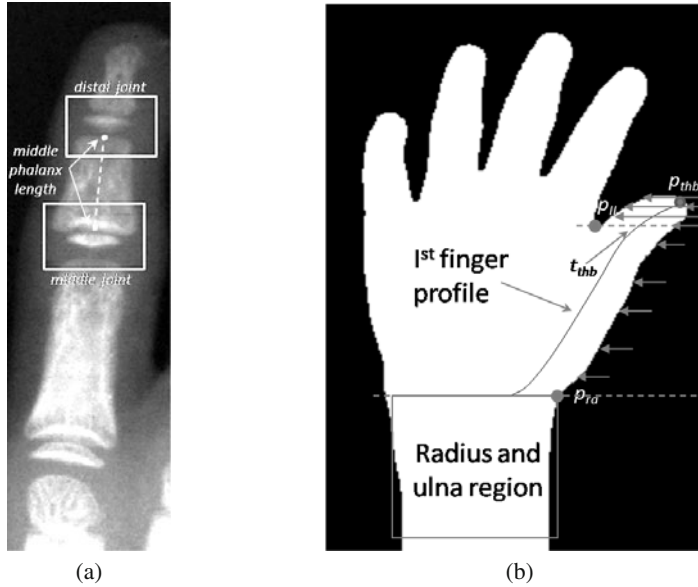
Fig. 3 New processing steps implemented into the CAD: a) measurements of middle phlanageal bones, and b) a strategy of tracing a profile through the Ist finger

4 Results

A new module offering automated and quantitative analysis of middle phalanges in hand radiographs was implemented into our CAD software (Fig.5). Bone measurements from the reference DHA data (Caucasian subjects) were performed first. Mean values and standard deviations were calculated to define ranges of normal bone deviation within all age groups for males and females. Next, measurements from abnormal radiographs were extracted, and mapped onto the data from normal subjects to validate the rule-based evaluation of brachydactyly type A patterns (Fig.6 and Fig.7) . The results are included in Tables 1 and 2, respectively. In the case of a 12 year old female with brachydactyly type A4, the ratio of $IInd^{middle}/IIIrd^{middle}$ is located 6.25 standard deviations outside of the range of matching normals. The
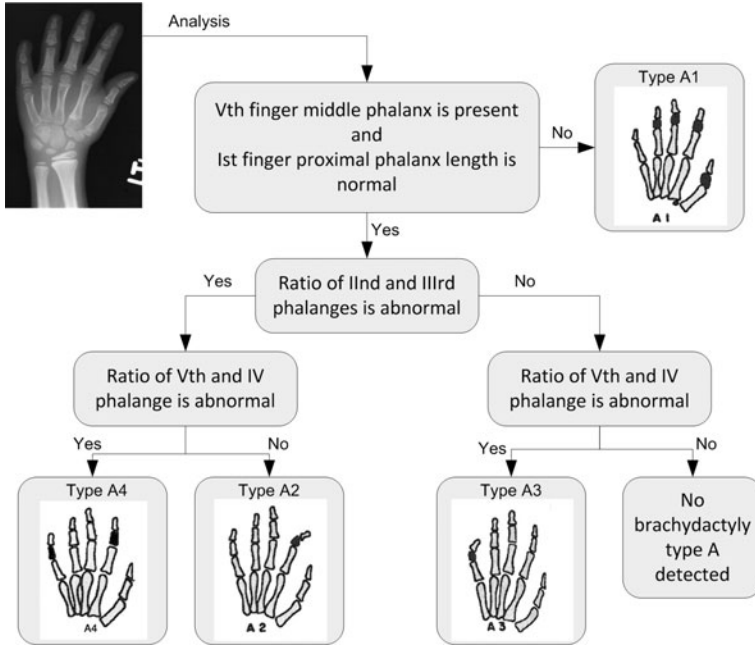
Fig. 4 Rule-based strategy in the automated evaluation of barachydactyly type A (A1, A2, A3 and A4) patterns implemented on the CAD platform

2 year old male case is solved in the first level of the decision tree (Fig. 4) due to the missing middle phalanx of the Vth finger. Furthermore, the length ratio between $IInd^{middle}/IIIrd^{middle}$ deviates from the mean value in the normal group of subjects by 5.63 standard deviations. The third case (4 year old male) is less straightforward because the formation of the skeleton is delayed compared to normal radiographs in the 4 year old age group. Moreover, the ratios of $IInd^{middle}/IIIrd^{middle}$ and $Vth^{middle}/IVth^{middle}$ are within the distance of 9 and 4 standard deviations from the mean values in the respective categories of normal ratios. The last two cases represent the brachydactyly A1 pattern.

The software's graphical user interface displays the image being analyzed with superimposed radiological findings and the regions of interest that are automatically extracted. Numerical results CAD automated assessments are exported to a file.

5 Conclusions

This study is the first of its kind to combine quantitative statistical information, use of automated hand feature detection software, and real world radiographs for the quantitative diagnosis of skeletal dysplasias. For the purpose of proving the concept of computerized evaluation of bone abnormalities, we implemented automated
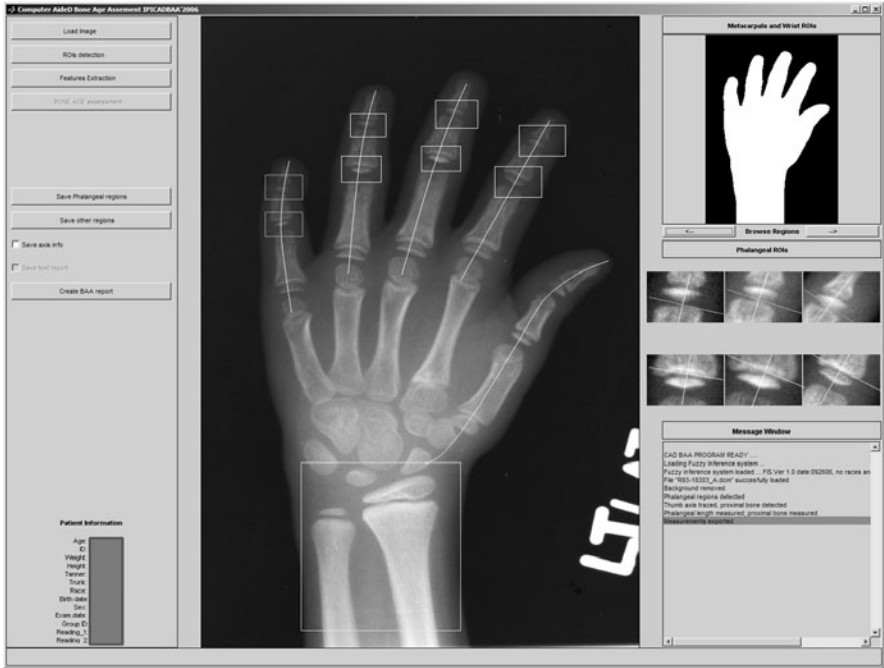
Fig. 5 CAD window with superimposed phalangeal regions and Ist-Vth finger axes and radius and ulna region
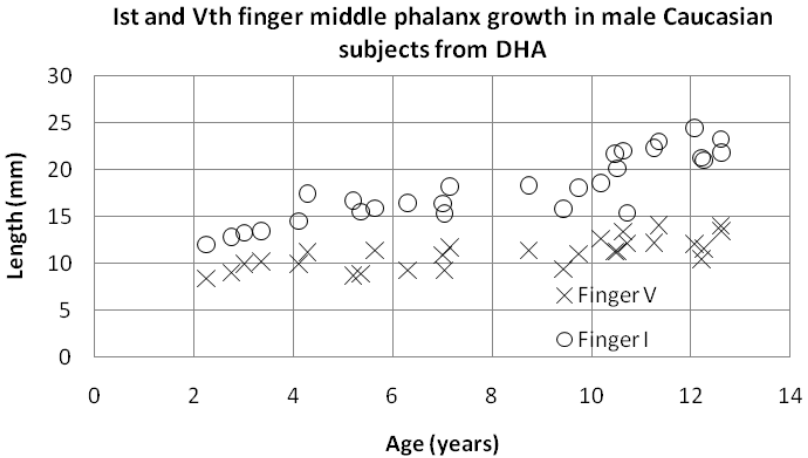
Fig. 6 Examples of normal phalange growth in male Caucasian subjects
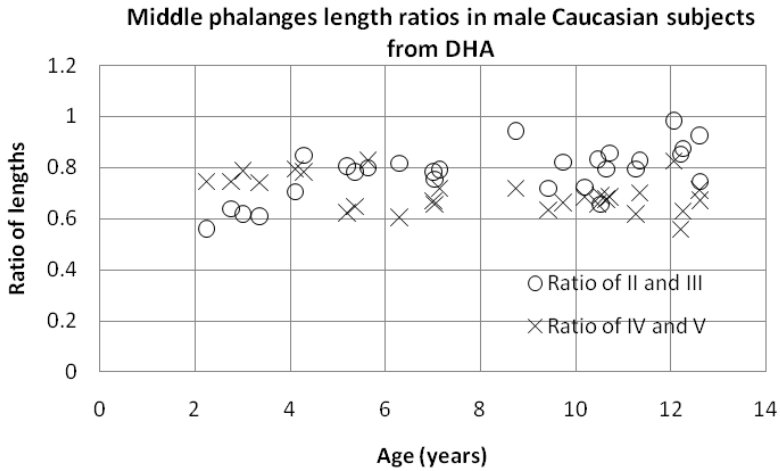
Fig. 7 Examples of finger length ratios maintained throughout development of male Caucasian subjects

Table 1 Ranges of proximal and middle bone measurements (*mean* ± *std*) obtained in three age groups of normal subjects matched to our case study subjects

Age, sex	Ist^{proximal}	IInd^{middle}	IIIrd^{middle}	IVth^{middle}	Vth^{middle}
-	*mm*	*mm*	*mm*	*mm*	*mm*
12y Female	23.9 ± 2.0	18.5 ± 2.2	23.0 ± 2.4	21.8 ± 2.2	14.9 ± 2.1
2y Male	13.5 ± 1.0	10.0 ± 1.0	12.6 ± 0.8	12.2 ± 1.0	8.47 ± 1.0
4y Female	15.5 ± 1.0	11.5 ± 0.4	14.8 ± 0.9	14.3 ± 1.0	9.22 ± 1.1

Table 2 Comparison of measurement ratios of abnormal bones (type of brachydactyly pattern) vs. ranges in matching groups of normal subjects from Table 1

Ratio	IInd^{middle}/IIIrd^{middle}		Vth^{middle}/IVth^{middle}	
Age, sex	abnormal (pattern)	normal	abnormal (pattern)	normal
12y Female	0.55 (A4)	0.8 ± 0.04	0.48 (A4)	0.68 ± 0.05
2y Male	0.35 (A1)	0.8 ± 0.08	0.00 (A1)	0.69 ± 0.03
4y Female	1.04 (A1)	0.77 ± 0.03	0.80 (A1)	0.64 ± 0.04

quantification of brachydactyly type A and its four major subtypes. Our CAD can automatically perform hand radiograph evaluation in selected SD cases via extraction of new quantitative features that can be considered in the diagnosis making process. We also established a framework to further enhance the diagnostic capabilities of CAD to work with a larger data collection from the ISDR center.

Our study elucidates some key points and potentials for the future of CAD in assessing skeletal pathologies. The measurements extracted from phalanges may be used in the detection of certain SDs, but first of all they provide a quantitative reference which can augment and improve the current clinical standard in the diagnostic workup at a skeletal dysplasia registry center. Besides the large variety of SDs, the possible combinations of their manifesting features is on a level of complexity that makes them extremely time consuming to diagnose using the standard approach, which is using the reference books and atlases. On the other hand these tasks can be facilitated by software-based solutions automatically performing measurements, utilizing databases and classifiers to arrive at quantitated hand radiograph analysis. In addition, improved speed and objectivity can also be achieved through CAD.

Although our approach was successfully applied to the analysis of a small set of cases, we also conclude that the automated analysis of the image data from patients with manifested skeletal abnormalities is very challenging. The difficulties lie in the large tolerance of the radiograph acquisition parameters among institutions. This mainly includes acquisition techniques (film-based or computed radiography), different exposure settings resulting in significant contrast discrepancy in the analyzed images. A nonstandard hand placement on the image poses additional difficulties. To this end, the implementation of digital radiography will become essential in the radiograph standardization process.

It is clear that continued input and support from radiologists and medical geneticists will be essential to improving accuracy of this CAD software and the range of computer detectable dysplasias. The widespread use of CAD could ultimately contribute to identification and more specific quantitative classification of skeletal abnormalities, and the automated accrual of epidemiological information to ultimately increase the knowledge in relevant fields.

References

1. Rimoin, D.L., Lachman, R.S.: Genetic disorders of the osseous skeleton. In: Beighton, P. (ed.) McKusick's Heritable disorders of connective tissue, ch. 14, 5th edn. (1992)
2. Spranger, J.W., Brill, P.W., Poznanski, A.K.: Bone Dysplasias, 2nd edn. Oxford University Press Inc., New York (2002)
3. Fitch, N.: Classification and identification of inherited brachydactylies. Journal of Med. Genet. 16(1), 36–44 (1979)
4. Temtamy, S.A.: Classification of hand malformations as isolated defects: an overview. J. Genet. Hum. 30(4), 281–290 (1982)
5. Lachman, R.: Taybi and Lachman's Radiology of Syndromes. Metabolic Disorders and Skeletal Dysplasias, 5th edn., Mosby Philadelphia (2006)
6. Rimoin, D.L., Cohn, D., Wilcox, W., Krakow, D., Lachman, R.: The International Skeletal Dysplasia Registry. In: 6th International Skeletal Dysplasia Society Meeting, Warrenton, VA (2003)

7. Cao, F., Huang, H.K., Pietka, E., Gilsanz, V.: Digital hand atlas for web-based bone age assessment: system design and implementation. Comput. Med. Imag. Grap. 24, 297–307 (2000)

8. Gertych, A., Zhang, A., Sayre, J., Pospiech-Kurkowska, S., Huang, H.K.: Bone age assessment of children using a digital hand atlas. Comput. Med. Imag. Grap. 31(4-5), 322–331 (2007)

9. Pietka, E., Pospiech, S., Gertych, A., Cao, F., Huang, H.K., Gilsanz, V.: Computer automated approach to the extraction of epiphyseal regions in hand radiographs. J. Digit. Imaging 4(4), 165–172 (2001)

10. Pietka, E., Gertych, A., Pospiech, S., Cao, F., Huang, H.K., Gilsanz, V.: Computer assisted bone age assessment: image processing and epiphyseal/metaphyseal ROI extraction. IEEE T Med. Imaging 20, 715–729 (2001)

11. Pietka, E., Pospiech, S., Gertych, A., Cao, F., Huang, H.K., Gilsanz, V.: Computer automated approach to the extraction of epiphyseal regions in hand radiographs. J. Digit. Imaging 14(4), 165–172 (2004)

12. Gertych, A., Pietka, E., Liu, B.J.: Segmentation of regions of interest and post segmentation edge location improvement in computer aided bone age assessment. Pattern Anal. Appl. 10(2), 115–123 (2007)

13. Tsao, S., Gertych, A., Zhang, A., Liu, B.J., Huang, H.K.: Automated bone age assessment of older children using the radius. In: Andriole, K.P., Siddiqui, K.M. (eds.) Proceedings of the SPIE Medical Imaging 2008: PACS and Imaging Informatics, vol. 6919, pp. 69190E–69190E-9 (2008)

14. Pietka, E., Pospiech-Kurkowska, S., Gertych, A., Cao, F.: Integration of computer assisted bone age assessment with clinical PACS. Comput. Med. Imag. Grap. 27(2-3), 217–228 (2003)

15. Hsieh, C.-W., Jong, T.-L., Tiu, C.-M.: Bone age estimation based on phalanx information with fuzzy constrain of carpals. Med. Bio. Eng. Comput. 45, 283–295 (2007)

16. De Luis-Garcia, R., Martin-Fernandez, M., Arribas, J., Alberola-Lopez, C.: A fully automatic algorithm for contour detection of bones in hand radiographs using active contours. In: Proceedings of the IEEE International Conference on Image Processing (ICIP 2003), vol. 3, pp. 421–424 (2003)

17. Tiu, C.-M., Liu, T.-C., Hsieh, C.-W., Niu, D.-M., Chen, J.-D., Jong, T.-L.: Turner syndrome phalangeal screening based on a two-stage linear regression concept. Pediatr. Int. 4(51), 453–459 (2009)

Method of Brain Structure Extraction for CT-Based Stroke Detection

Aleksandra Rutczyńska, Artur Przelaskowski, Magdalena Jasionowska, and Grzegorz Ostrek

Abstract. A fully automated method for extracting brain structures from computed tomography images by employing adaptive filtering and finite Gaussian Mixture Modeling (GMM) with context-based enhancement is proposed. Generally, the method is composed of two phases. First, adaptive partial mean filter for noise removal and edge sharpening is used. The second phase is the multistage segmentation. Initial segmentation step concerning brain extraction from skull and non-brain tissue defines a region of interest (ROI) for further processing. Each pixel in ROI is assigned to one of three semantically fundamental classes - white matter (WM), gray matter (GM) and cerebrospinal fluid (CBF) and two extended classes of specific tissue. GMM with expectation-maximization algorithm (EM) is employed to assign initial class labels to image pixels and followed by context information modeling through Contextual Bayesian Relaxation Labeling (CBRL). The CBRL algorithm incorporates local neighborhood information and iteratively refines the outcome of GMM classification. The results of proposed approach have been verified by extracting susceptible-to-stroke regions (SSR) processed for hypodensity distribution estimation. The extracted structures are more smooth and reliable in comparison to region growing segmentation results.

1 Introduction

Stroke is the third leading cause of death and leading cause of disability in developing countries [1]. However, ischemic stroke imaging with instant visualization of acute symptoms is still a challenging problem. Computed tomography (CT) is

Aleksandra Rutczyńska · Artur Przelaskowski · Magdalena Jasionowska · Grzegorz Ostrek
Institute of Radioelectronics, Warsaw University of Technology, Nowowiejska 15/19,
00-665 Warszawa, Poland
e-mail: {arachock,artur,mjasiono,gostrek}@ire.pw.edu.pl

a method of choice in stroke imaging. Some advantages of CT over magnetic resonance imaging (MRI) can be pointed. Amongst them, the following facts opt for CT: widespread availability (CT devices outnumber MRI equipment), short imaging times (vital with unconscious patients) and fewer limitations, e.g. CT is irreplaceable in case of patients with implanted biomedical devices (such as cardiac pacemakers) or ferromagnetic materials. CT helps to distinguish ischemic from hemorrhagic stroke or other brain diseases. Unfortunately, early signs of ischemic stroke in acute phase (up to 6 hours from onset), which are extremely useful for successful thrombolytic treatment, are hardly visible on CT scans. This was a motivation for the development of computed-aided diagnostics in the field of stroke imaging [2, 3, 4, 5].

An important role of susceptible-to-stoke region (SSR) extraction was proven in earlier research on stroke imaging. A tool for computer assisted support of acute stroke diagnostics was developed. The software used data hypodensity mapping and would be referred to as Stroke Monitor (SM) [6]. Proper segmentation of brain structures, especially delimitation of CBF structures (brain ventricles and cerebral sulci), played crucial role in reducing false indications of SM method. SSR extraction was based on region growing segmentation with adaptively selected thresholds. In some cases, segmented CBF structures were rough, ill-defined, spread out or too compact. Optimization of SSR segmentation was the general purpose of our research.

First of all, SSR segmentation as a first step of hypodensity map estimation has to be more accurate, flexible and reliable for all test cases. Unlike research on brain segmentation from MRI data, CT literature is very scarce. In [7] comparison of manual and semiautomatic methods with thresholding was performed. Region-based methods in [8] were used to brain structures segmentation in MRI. Fuzzy C-means (FCM) algorithm was used in [9] and [10] for brain hemorrhagic analysis. In [11] modified FCM was proposed, it incorporates context information. Segmentation using Bayesian classifier in CT is proposed in [12].

In this paper we proposed the method for white/gray matter and CBF structure segmentation. In the preprocessing stage adaptive filtration is used to denoise the image and enhance structures. Motivation to use implementation of Adaptive Partial Averaging Filter (APAF) [5, 13] was generally low signal to noise ratio (SNR) of CT scans, possible presence of artifacts and unclear structure delimitation in source data. Next, deskulling the brain tissue based on adaptive algorithm of 3D region growing was determined. Fundamental stage of SSR segmentation was based on stochastic image modeling. Incorporating context information revealed high potential of designed method. Input image is subject to tissue-of-interests extraction method based on sequence of selected concepts implemented and adjusted to perform efficient stroke detection. Experimental verification of the method were concluded.

2   Method

Stochastic image modeling is defined as a partitioning of the image into distinctive meaningful regions based on the statistical properties of global and local gray-level pixel dependencies. Suitable model selection depends on the pixel value distribution and characteristics of pixel contexts, i.e.: a) regional data distributions related to image data distribution, b) statistical characteristics of the nearest pixel neighborhood associated with different regions. Such components of image model are possibly justified in terms of imaging physics, acquisition limitations, visualized object properties, etc. Context data dependencies correctly redefine the membership of the pixel to each of the regions present in the image [14].

We assumed that each pixel belongs to one of three fundamental classes: cerebrospinal fluid (CBF), white matter (WM) and gray matter (GM) and two additional classes of deep hypodensity and bone artifacts. Pixel image refers to gray level distribution associated with finite Gaussian Mixture Model (GMM) used for image analysis. Moreover, contextual Bayesian relaxation model incorporates statistical properties of pixel neighborhood. Fig.1 shows flow chart of the proposed method.
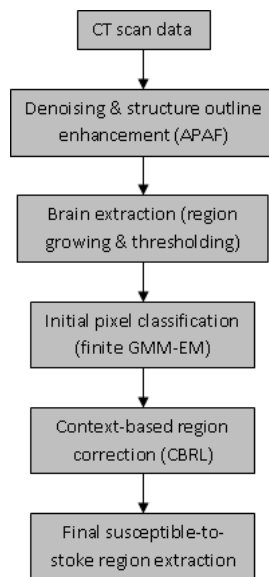
Fig. 1 Flow chart of proposed method of susceptible-to-stoke region extraction for CT-based stroke detection

Firstly, noise[1] removal operation was performed on a original CT data. Implemented APAF method outlined structure contours and enhanced subtle regional distinctions, additionally. Then brain region was determined – bones and non-brain tissue were excluded from the images. Key stage of the method, i.d. initial SSR extraction, was based on GMM region segmentation with the parameters selected

---

[1] Approximately of 4 Hounsfield Units [HU].

according to *a priori* analysis of stroke detection requirements and optimized with maximum likelihood estimation by expectation-maximization (EM) algorithm. To simplify the calculations initial regions were estimated based on the assumption that all pixels are independent. In further steps, in order to make the segmentation more reliable and accurate, segmentation refinement was performed based on CBRL algorithm [15], which incorporates local neighborhood information.

The assumptions and fundamental rules implemented in the key stage of presented SSR extraction method were shortly discussed in the following subsections.

2.1 Stochastic Image Modeling

Relationships between neighboring pixels are well described by Bayesian conditional probabilities of m-order Markov model with memory (i.e. conditional source model). However, classification rules based on conditional data dependencies of higher order models are overly complicated, number of probabilities increases exponentially for enlarged context resulting in a problem of limited statistical reliability of the model (i.e. context dilution).

To simplify image model and make it computationally acceptable, finite mixture model of regions was used with assumption that the whole image can be approximated by an independent and identically distributed random field. Local data dependencies were complied as follows: GMM was initialized by grouping-classification procedure of k-means and k-nearest neighbor classifier and followed by complementary context image modeling taking into consideration labels assigned to the pixels in the nearest neighborhood.

More precisely, we assume that image contains K regions (classes) and pixel labels are random variables. Thus, a whole image of N pixels can be modeled by independent and identically distributed (iid) random field $\mathbf{X}$, given the joint probability density function:

$$P(\mathbf{x}) = \prod_{i=1}^{N} \sum_{k=1}^{K} \pi_k P_k(x_i) \tag{1}$$

where $\mathbf{x} = [x_1, \ldots, x_N]$ and $\mathbf{x} \in \mathbf{X}$, π_k is a weighting factor and $P_k(x_i)$ is conditional region probability density function (pdf) of k class (region), i.e. $P_k(x_i) = P(x_i/R_k)$. Given image is a concrete realization of $\mathbf{X}$.

Considering statistical image properties, generalized Gaussian pdf was used:

$$P_k(x_i) = \frac{\alpha \beta_k}{2\Gamma(1/\alpha)} \exp[-\mid \beta_k(x_i - \mu_k) \mid^\alpha], \alpha > 0, \beta_k = \frac{1}{\sigma_k} \left[\frac{\Gamma(3/\alpha)}{\Gamma(1/\alpha)} \right]^{1/2} \tag{2}$$

where μ_k is the mean, σ_k is the standard deviation, $\Gamma(\cdot)$ is the gamma function and α defines distribution shape.

Because of physical conditions and statistical estimates of CT scan data, we assumed $\alpha = 2$, i.e. Gaussian pdf with two parameters μ_k and σ_k, for all regions. Therefore, we have

$$P_k(x_i \mid \mu_k, \sigma_k^2) = \frac{1}{\sqrt{2\pi}\sigma_k} \exp\left(-\frac{(x_i - \mu_k)^2}{2\sigma_k^2}\right) \tag{3}$$

Moreover, other global parameter K was set to 5 based on stroke detection requirements and experimental verification. Because of precise CBF structure segmentation, we decided to define two classes of hypodensity: weak and deep. Subsequently, two classes of white and grey matter were extended by additional class of marginal tissue distorted by bone artifacts.

Next, image model was optimized by effective estimation of regional parameters of distributions, i.e. π_k, μ_k and σ_k. Finally, pixels were labeled and image regions were determined according to Bayesian classification rule based on fixed local parameters and regional memberships of the image pixels.

2.1.1   Expectation – Maximization Algorithm

The objective of model identification (parameter estimation) is maximizing likelihood function or minimizing relative entropy between image histogram $P_F(f)$ and estimated pdf $P_X(f)$ of the image model $P(\mathbf{x})$, where f is a gray level of source alphabet. To perform maximum likelihood estimation we used the most popular approach - expectation-maximization algorithm (EM). The EM first calculates Bayesian posterior probabilities and obtains parameter estimates (E step), then updates these estimates using mean ergodic theorem (M step). The successive iterations of the E and M steps increase the likelihood of the model parameters. Used criterion is minimization of relative entropy expressed by Kullback-Leibler distance:

$$H(P_F \| P_X) = \sum_f P_F(f) \log \frac{P_F(f)}{P_X(f)} \tag{4}$$

The EM algorithm proceeds as follows

1. assumed global parameters are $K = 5$, $\alpha = 2$
2. $m = 0$ iteration with parameter set $\mathbf{g}^{(0)} = \{\pi_k^{(0)}, \mu_k^{(0)}, \sigma_k^{(0)}, k = 1, \ldots, K\}$, according to initial k-nearest neighbor classification
3. E step: for $i = 1, \ldots, N$, $k = 1, \ldots, K$ count probabilistic membership

$$z_{ik}^{(m)} = \frac{\pi_k^{(m)} P_k(x_i)}{\sum_{k=1}^{K} \pi_k^{(m)} P_k(x_i)} \tag{5}$$

4. M step: for $k = 1, \ldots, K$ update parameter estimates

$$
\begin{cases}
\pi_k^{(m+1)} = \frac{1}{N} \sum_{i=1}^{N} z_{ik}^{(m)} \\[2ex]
\mu_k^{(m+1)} = \frac{1}{N\pi_k^{(m+1)}} \sum_{i=1}^{N} z_{ik}^{(m)} x_i \\[2ex]
\sigma_k^{2(m+1)} = \frac{1}{N\pi_k^{(m+1)}} \sum_{i=1}^{N} z_{ik}^{(m)} (x_i - \mu_k^{(m+1)})^2
\end{cases}
\tag{6}
$$

5. When condition $|H^{(m)}(P_F||P_X) - H^{(m+1)}(P_F||P_X)| > \varepsilon$ is satisfied increment $m = m+1$ and go to E step; otherwise save optimal **g**.

We used GMM-EM implementation from PRTools 4 [16] with slight modification to make it more flexible.

2.1.2 Bayesian Classifier

Classification problem consists of prediction of the pixel label $k \in K$ (i.e. to predict its membership to one of the image classes) based on feature vector **x**. The classifier $d : \mathbf{x} \to K$ with accurate prediction needs to be found. Bayes theorem is a conditional probability of event A given event B. Bayes classifier is based on a Bayes rule

$$
P(A \mid B) = \frac{P(B \mid A)P(A)}{P(B)}
\tag{7}
$$

Bayes rule is used to determine posterior probabilities for pixel to be a member of each of the classes present in the image. The rule for each pixel indexed i, $i = 1, \ldots N$ classified to class k, $k = 1, \ldots K$ is given by

$$
P(k \mid x_i) = \frac{\pi_k P_k(x_i)}{\sum_{j=1}^{K} \pi_j P_j(x_i)}
\tag{8}
$$

where $P(k \mid x_i)$ is *a posteriori* probability (also referred to as regression function) that pixel belongs to class k given x_i; π_k – *a priori* probability that pixel belongs to class k (class frequency) with assumption $\sum_{i=1}^{K} \pi_i = 1$; $P_k(x_i)$ – pdf of the feature vector **x** in k-th class. Bayesian classifier form of pixel labeling is as follows

$$
d_B(x_i) = \arg\max_k P(k \mid x_i) = \arg\max_k \pi_k P_k(x_i)
\tag{9}
$$

where $P(k \mid x_i)$ is given in equation 8.

2.1.3 Context Modeling

In GMM we assumed that pixels in the image are independent to simplify calculations. To refine estimated regions and to make them more accurate, context information should be included in the model. Modified CBRL method incorporating local neighborhood information was used as compliment of GMM model.

Let ς_i be a neighborhood of the i-th pixel while $m \times m$ defines size of this neighborhood. Factor π_k is estimated locally for each pixel as

$$\pi_k^i = p(l_i \mid \mathbf{l}_{\varsigma_i}) = \frac{1}{m^2 - 1} \sum_{j \in \varsigma_i, j \neq i} I(k, l_j) \qquad (10)$$

where l_i denotes label of pixel i and $\mathbf{l}_{\varsigma_i}$ is labels set of its neighbors, I stands for indicator function

$$I(k, l_j) = \begin{cases} 1 \text{ if } l_j = k \\ 0 \text{ otherwise} \end{cases}$$

Algorithm CBRL can be summarized as follows

1. Iteration $m = 0$ with GMM-EM based pixel classification $\mathbf{l}^{(0)}$
2. Update pixel labels

   - Randomly order all image pixels for $i = 1, \ldots, N$
   - Visit successive pixel according to random selection and update its label as follows
   $$l_j^{(m)} = \arg\{\max_k \pi_k^{i(m)} P_k(x_i)\} \qquad (11)$$

   complied with $\pi_k^{i(m)}$ modification according to equation 10.

3. If less than 1% pixels changed its label algorithm stops; otherwise increment $m = m + 1$ and go to step 2.

Final SSR extraction is binarization of region map with two hypodensity classes included into non-SSR class and the rest segmented regions classified as SSR.

3 Results

Presented method of brain structure extraction was optimized and verified on a set of 21 scans of selected test CT examinations. Chosen set consisted of difficult to segment cases indicated and analyzed by radiologist. Marked regions, especially CBF structures, were gold standard for efficiency assessment. Test set contained 265 CBF structures to be segmented correctly for stroke detection application. Two statistical measures - sensitivity and number of false positives per scan were calculated to assess the reliability and accuracy of the segmentation. We reached the sensitivity of 97% with 0.3 false positives per scan. Lower sensitivity was a result of omitting small, subtle sulci close to bone order which were misclassified as a white matter. False positives occurred in brain top scans for middle brain line.

The detailed results of segmentation procedures were presented in the following figures. Results of APAF filtering in a context of less sophisticated methods were shown in Fig. 2. APAF performs better comparing to other filtration methods in terms of high noise reduction rate with simultaneous edge preserving as well as structures extraction.

Fig. 2 CT scan filtering
effects: source image (top
left) is confronted with
average filtering (top right),
median filtering (all of
which use kernel size 5x5)
and APAF filtering
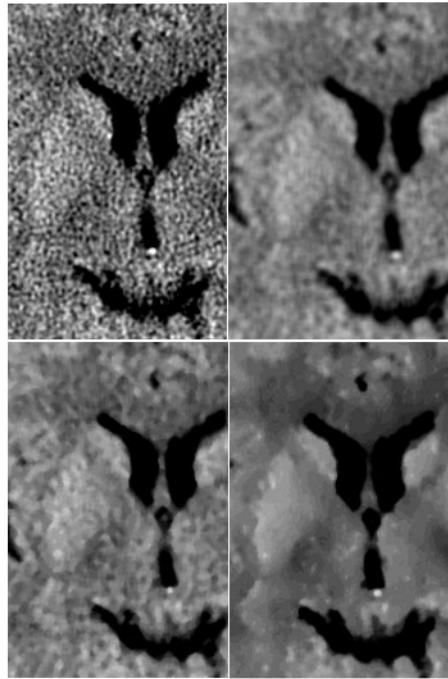
In the next figure (Fig. 3) the positive role of APAF filtration in CT image segmentation is presented. Segmentation performed on the non-enhanced CT data (without any filtration) depicts regions disturbed by the noise and significantly deviates from our expectations. Incorporating APAF-based processing results in segmentation that is coherent with the anatomy of imaged brain.
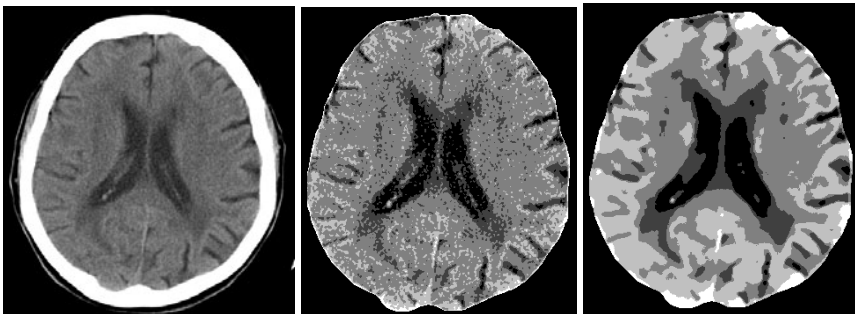
Fig. 3 The segmentation results influenced by APAF: source CT scan, effects of segmentation without APAF and the segmentation based on APAF-based image enhancement, respectively

Results of segmentation of the regions non susceptible to stroke (i.e. CBF class) are compared with reference image (Fig. 4). Gold standard image was prepared by a radiologist who selected brain structures, which should be excluded from image as they can produce false positives indications in stroke detection procedure. Binarized image is the final result of SSR extraction for that case.
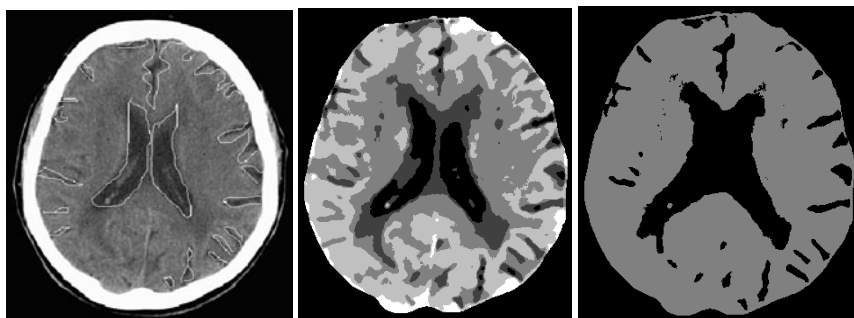
Fig. 4 Segmentation results for exemplar CT scan: reference image with marked regions, effects of 5 class segmentation and binarization for SSR extraction, respectively

An example of comprehensive 5 class segmentation output was presented in Fig. 5 and in Fig. 6. Selected scans of CT examination reflects diversity of achieved results for analyzed data set.

On the last figure (Fig. 7) follow-up CT with visible stroke is confronted with classified image. Segmentation of the stroke area from the follow-ups could be beneficial in stroke size assessment for estimated pathology progression and therapy planning.

4   Conclusions

Our method exhibits satisfactory results. Main advantage of the proposed algorithm is the fact that it has flexible parameter of the class numbers which could be adjusted to application requirements. Moreover, binarization procedure is susceptible to semantic image characteristics and *a priori* knowledge models (ontology). General method scheme was not fitted only to a specific CT data. It gives good results by employing statistical nature of the images. In future research we would further explore the efficiency level which is now degraded mainly by the artifacts (beam hardening artifacts). Better brain segmentation (ROI defining) method should be researched to remove the fifth class, which is now reserved for the artifacts from the bones. Context information in the third dimension should also be included.
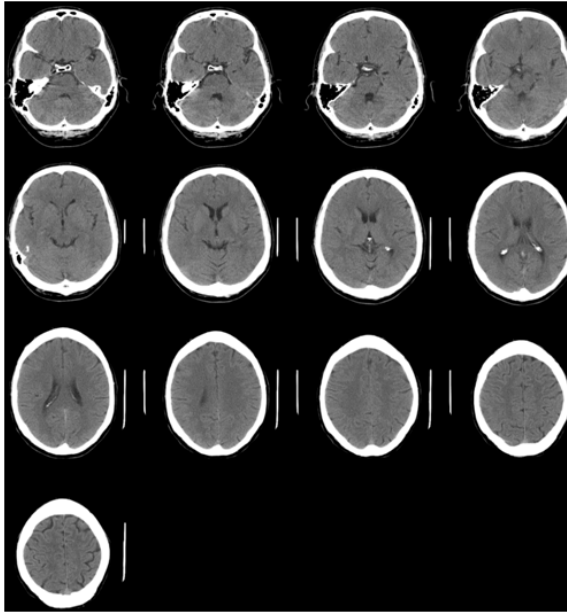
Fig. 5 Exemplar test CT data of successive source scans
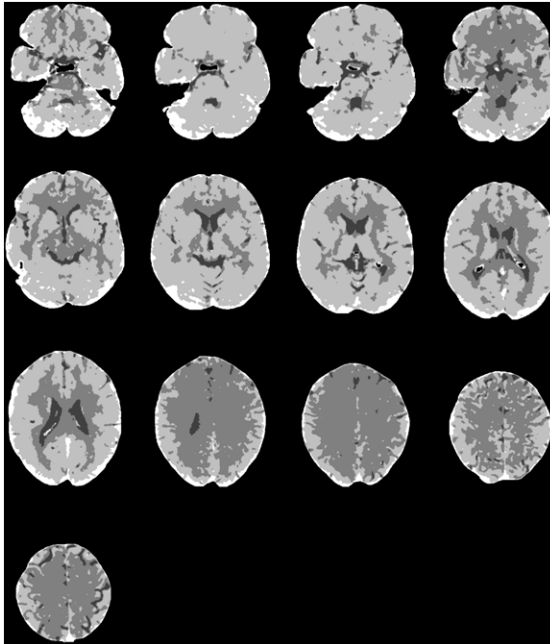
Fig. 6 The effect of segmentation of CT scans presented in Fig. 5
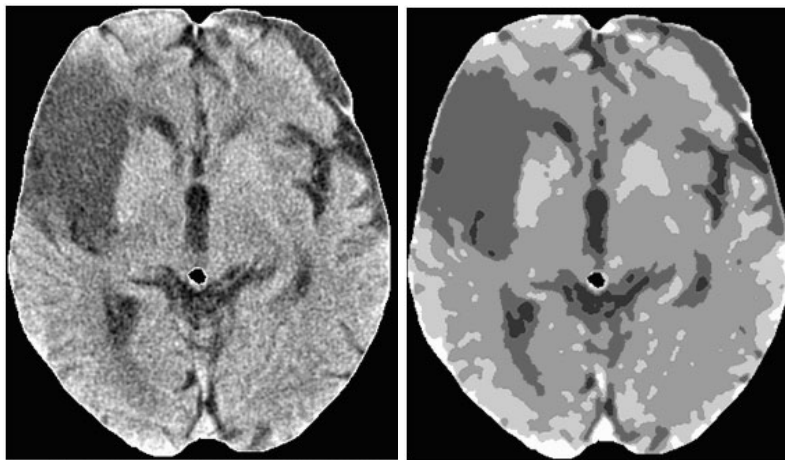
Fig. 7 Stroke area assessment for follow-up CT scan: source image and effects of proposed segmentation procedure, respectively

References

1. Chalea, J.A., Merino, J.G., Warach, S.: Update on stroke. Current Opinion in Neurology 17, 447–451 (2004)
2. Bendszus, M., Urbach, H., Meyer, B., et al.: Improved CT diagnosis of acute middle cerebral artery territory infarcts with density difference analysis. Neuroradiology 39(2), 127–131 (1997)
3. Maldjian, J.A., Chalela, J., et al.: Automated CT segmentation and analysis for acute middle cerebral artery stroke. AJNR Am. J. Neuroradiol. 22, 1050–1055 (2001)
4. Grimm, C., Hochmuth, A., Huppertz, H.J.: Voxel-based CT analysis for improved detection of early CT signs in cerebral infarction. Eur. Radiol., ECR European Congress of Radiology, B315 (2005)
5. Lee, Y., Takahashi, N., Tsai, D.-Y., Ishii, K.: Adaptive partial median filter for early CT signs of acute cerebral infarction. Int. J. CARS 2, 105–115 (2007)
6. Przelaskowski, A., Bargiel, P., Sklinda, K., Zwierzynska, E.: Ischemic Stroke Modeling: Multiscale Extraction of Hypodense Signs. In: An, A., Stefanowski, J., Ramanna, S., Butz, C.J., Pedrycz, W., Wang, G. (eds.) RSFDGrC 2007. LNCS (LNAI), vol. 4482, pp. 171–181. Springer, Heidelberg (2007)
7. Joe, B.N., Fukui, M.B., Meltzer, C.C., Huang, Q -s., Day, R.S., Greer, P.J., Bozik, M.E.: Brain Tumor Volume Measurement: Comparison of Manual and Semiautomated Methods. Radiology (1999)
8. Xuan, J., Adali, T., Wang, Y.: Segmentation of magnetic resonance brain image: integrating region growing and edge detection. In: Proc. International Conference on Image Processing, vol. C (1995)
9. Cheng, D.C., Cheng, K.-s.: Multiresolution based fuzzy c-means clustering for brain hemorrhage analysis. In: International Conference on Bioelectromagnetism
10. Loncaric, S., Cosic, D., Dhawan, A.P.: Hierarchical segmentation of ct head images. In: 18th Annual Conference of the IEEE Engineering in Medicine and Biology Society (1996)

11. Mohamed, N.A., Ahmed, M.N., Farag, A.: Modified fuzzy c-mean in medical image segmentation. In: IEEE International Conference on Acoustics, Speech, and Signal Processing (1999)
12. Lauric, A., Frisken, S.: Soft segmentation of CT brain data. Tufts University
13. Takahashi, N., Lee, Y., Tsai, D.-Y., Ishii, K.: Novel noise reduction filter for improving visibility of early computed tomography signs of hyperacute stroke: evaluation of the filter's performance-preliminary clinical experience cerebral infarction. Radiat. Med. 25, 247–254 (2007)
14. Tulay, A., Wang, Y.: Image Analysis and Graphics for multimedia presentation, ch. 8
15. Hummel, R.A., Zucker, S.W.: On the foundations of relaxation labeling processes. IEEE Trans. Pattern Anal. Machine Intell. 5(3) (1983)
16. Duin, R.P., Juszczak, P., Paclik, P., Pekalska, E., de Ridder, D., Tax, D.M.J., Verzakov, S.: PRTools 4 - A MATLAB Toolbox for Pattern Recognition. Version 4.1, Delft University of Technology (2007)

Combined DICOM and HL7 Viewer in Support of a Bridge from Content-Based Image Retrieval to Computer-Aided Diagnosis

Petra Welter, Fatih Topal, Sebastian Jansen, Thomas M. Deserno,
Jörg Riesmeier, Christoph Grouls, and Rolf W. Günther

Abstract. Content-Based Image Retrieval (CBIR) is a field of rising interest for the application in Computer-Aided Diagnosis (CADx). Exploiting the visual information hidden in the images for retrieval, it facilitates the identification of similar past examinations, thereby providing a second opinion. Still, CBIR is not an integral part of a radiologist's daily work. A comprehensive representation of CBIR results in a standard format utilizing established clinical infrastructure together with all referenced comparable examinations will support a bridge from CBIR to CADx. In this paper, we introduce the general IRMACON viewer, a system that represents results from CBIR systems encoded as a DICOM Structured Reporting document in a layout adjusted for CADx. IRMACON also allows the insight into identified similar examinations for convenient comparison by accessing patient's information and diagnostic findings from the Hospital Information System (HIS) using HL7 messages. Our system is embedded into the clinical setting and the radiologist's workflow. We applied the IRMACON viewer to the Image Retrieval in Medical Applications (IRMA) framework.

1 Introduction

Content-Based Image Retrieval (CBIR) [1] relates to the identification of images from a database using the visual information hidden in the images instead of attached textual annotations. Computer-Aided Diagnosis (CADx) can generally be defined as "a diagnosis made by a radiologist who uses the output of a

Petra Welter · Fatih Topal · Sebastian Jansen · Thomas M. Deserno
Department of Medical Informatics, RWTH Aachen University, Aachen, Germany
e-mail: pwelter@mi.rwth-aachen.de

Jörg Riesmeier
ICSMED AG, Oldenburg, Germany

Christoph Grouls · Rolf W. Günther
Department of Diagnostic Radiology, RWTH Aachen University Hospital, Aachen, Germany

computerized scheme for automated image analysis as a diagnostic aid" [2]. Physicians usually refer in their decision making of a diagnose to already closed cases with verified diagnostic results. In the context of CADx, the typical application of CBIR supports differential diagnosis, i.e. the distinguishing between two or more diseases by systematical comparison. The aim of CBIR is to provide the radiologist with a diagnostic aid by automatically identifying relevant past cases along with their diagnosis and other suitable information. This provides the radiologist with a second opinion, thereby enhancing the diagnostic assessment.

CBIR has a high potential of improving the quality and efficiency of clinical care processes [3] and entails proved high benefits for CADx [4, 5, 6]. There are promising CBIR based CADx systems, the majority concentrating on a particular application area, e.g., lung cancer [7], mammography [8], computed tomographic images of the chest [9]. However, CBIR is not established yet in clinical routine. CAD schemes using CBIR approaches face a number of challenges and this technology needs more research work [10].

One essential factor is the seamless and robust integration into Picture Archiving and Communication Systems (PACS) and the radiologist's workflow. This includes a comprehensive and integrative representation of the CBIR results along with all corresponding evidences adapted to the physicians needs. The appropriate and contextualized preparation of necessary data required for differential diagnosis delivers an indispensable brick in the bridge from CBIR to real CADx.

A substantial requirement is the use of open standards and the integration with a hospital-wide communication structure [4]. Digital Imaging and Communications in Medicine (DICOM) Structured Reporting (SR) [11, 12] is an approved standard format for exchanging CADx results in clinical environments, e.g., for mammography [13, 14], which can be stored to and retrieved from PACS. Because of the many advantages [15, 12], the Integrating the Healthcare Enterprise (IHE) employs DICOM SR in several integration profiles [16]. There are several proposals for the general integration of CAD or CBIR systems into clinical environments, also based on DICOM SR documents, e.g., [17, 18]. That motivated us to apply DICOM SR encoded CBIR results in our concept presented in this paper.

There are viewers capable of interpreting SR documents and producing a generic layout, but they are not adjusted to the special needs of CBIR for CADx. Diagnostic findings from different clinical departments, e.g. pathology, laboratory or endoscopy, are usually archived centrally by the Hospital Information System (HIS), utilizing the Health Level Seven (HL7) [19] protocol. Clinical viewers for diagnostic findings are usually not capable of integrating CBIR results or even CADx results in general. We close this gap and present in this paper the novel IRMACON viewer, a combined viewer for CBIR SR documents together with referenced diagnostic findings from HIS.

2   Materials and Methods

We first analyzed the general CBIR-based CAD scheme, in which we embedded our IRMACON viewer. Our proposed IRMACON viewer system makes use of DICOM SR and HL7. Relevant information on both is explained in the following. Thereafter, we analyzed requirements concerning a successful data capturing.

2.1   CBIR-Based CADx Scheme

CADx systems with CBIR approaches incorporate the following workflow in principle: The physician examines medical images to make a diagnosis. Either, the CADx request is done automatically, e.g., by configuring an internal mechanism inside of the PACS, or the physician manually demands the CADx request. Data from the current patient's context is then transferred to the CBIR system. The CBIR system processes the query input and generates a SR document from the CBIR results which is stored in PACS. The DICOM archive holds all SR documents and delivers requested CBIR results to the physician at his diagnostic workstation, who is awaiting the CBIR support for his diagnosis. The CBIR SR document lists identified images with a certain minimum similarity to the current examination image. Normally, the physician then requests diagnostic details of selected similar images from HIS manually to collect all relevant information for his decision making.

2.2   DICOM SR Encoded CBIR Results

DICOM provides by means of the SR format a standard encoding of structured data. Templates define valid contents and value types to restrain different encoding of the same content in order to simplify the processing of SR documents. They facilitate an automated processing and interpretation of SR documents [20]. DICOM standard templates do not cover the CBIR application for CADx. We proposed a template adapted to the special requirements of CBIR [21]. It comprises the query image, identified similar images along with their similarity score, and a description of the applied CBIR system. Our template is applicable by any CBIR system and the resulting SR document may be stored to PACS.

2.3   Query of HL7 Diagnostic Findings

HIS generally archives diagnostic findings from radiology, laboratories and other affiliated departments in a clinical repository. Reports may be plain text or encoded as, e.g., Portable Document Format (PDF), Microsoft Word. Communication regarding documents exchange is accomplished by HL7 messages. Message type QRYˆR02, "Query For Results Of Observation", requests diagnostic findings, which are returned by message type ORFˆR04. A HL7 query message is composed by a message header ("MSH"), followed by a query definition ("QRD") and a query filter ("QRF").

In clinical environments, HIS are usually configured to manage communication by a dedicated communication server. This implies that all HL7 messages are sent

to this central point, specified by an IP address and a port. The header of the HL7 message contains the final destination, given in the field named "Receiving Application". The communication server forwards the message to its addressee.

The following small fragment of an examplary ORFˆR04 message is taken from a response to a QRYˆR02 message and contains requested diagnostic findings. Parts denoted by "..." have been ommitted to simplify the example. HL7 messages are divided into mandatory and optional segments and fields, depending on the particular message type. Each message begins with a header segment, introduced by the keyword "MSH". The header of this example names "EKG" as "Sending Application" and our viewer "IRMACON" as "Receiving Application" of the message. Date of this message is 2010-02-18 and message type is "ORFˆR04". The segment starting with "OBX" contains the actual diagnostic information and is of value type "TX", which stands for text, followed by the "Observation Identifier" and the textual diagnostic information.

```
MSH|^~\&|EKG||IRMACON||201002180944||ORF^R04|...
...
OBX|1|TX|79000&ADT^EKG COMM||<diag info>|...
```

The actual diagnostic information has to be extracted from the message and to be displayed to the radiologist.

2.4 *Mapping of DICOM and HL7 Identifiers*

The IRMACON viewer queries diagnostic findings by HL7 protocol that relate to patients and examinations whose medical images have been retrieved by the CBIR system. This requires a mapping of identifiers between the DICOM and the HL7 domain. Relevant keys are patient and order which are used in the HL7 query message to query particular diagnostic findings. There is no official standard that defines a mapping. But based on generally applied principles, e.g., by [16, 22], we decided to use the following mapping:

- PACS Order Number
    - DICOM: (0008,0050) Accession Number
    - HL7: OBR-3 Filler Order Number
- Patient Identifier
    - DICOM: (0010,0020) Patient ID
    - HL7: PID-3 Patient ID

2.5 *Analysis of Data Capture Process*

We investigated the appropriate design of a viewer of similar medical cases and their corresponding diagnostic findings used in CADx. The following requirements have to be fulfilled in order for the radiologist to benefit from the viewer [23]:

Fig. 1 Overview of the
IRMACON system
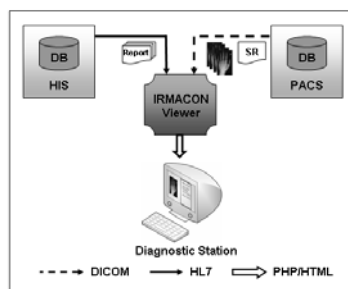
- (R1) Presentation and arrangement of information must promote an easy and quick comprehension. This includes an appropriate structuring according to semantics and interrelations of data. Furthermore, the limitation on only relevant data and the provision of details only on demand helps to accelerate data capturing.
- (R2) Handling of the viewer must be intuitive and simple. This allows a quick inital training and instant functionality recognition by the radiologist.
- (R3) Presentation of data must be adapted to the particular application. For example, the identified similar images retrieved by the CBIR system are captured easily when presented pictorially. The corresponding DICOM identifiers are of little use in the context of CADx.
- (R4) Data retrieval must not slow down the radiologist's work. Otherwise, the physician will hardly be willing to use a CADx system.

3 Results

3.1 System Design

Our proposed architecture is illustrated in Figure 1:

1. The radiologist at his diagnostic workstation starts the webpage of the IRMA-CON viewer, which is integrated into the PACS client as a plug-in by utilizing PACS' application programming interface (API). The current patient's context is passed to IRMACON.
2. The IRMACON viewer retrieves the SR document and all referenced images from PACS by DICOM C-MOVE messages. The images along with basic information are presented to the physician.
3. The physician may choose reports of diagnostic findings that are requested from the HIS by the IRMACON viewer.
4. The IRMACON viewer starts an appropriate application associated with the retrieved report to facilitate the display of the report's content.

Our system design is based on using the already established infrastructure by PACS and HIS. Data is transferred by DICOM and HL7 protocol. DICOM SR documents containing CBIR results are managed by PACS. Assuming that PACS and HIS are

balanced systems configured for high performance and reliability, our design meets the requirement (R4).

3.2 Implementation of IRMACON Viewer

The IRMACON viewer is a web-based application implemented in Hypertext Preprocessor (PHP) that dynamically generates output in Hypertext Markup Language (HTML) format. OFFIS DCMTK [24] is used for realizing DICOM commands from within IRMACON. HL7 messages are implemented using HAPI (HL7 Application Programming Interface) [25]. SR documents are converted to Extensible Markup Language (XML) by DCMTK and then parsed by the XML extension of PHP. The retrieved DICOM images are converted to Portable Network Graphics (PNG) in order to have an image format suitable for the representation in web browser.

We created a testbed for our viewer limiting PACS and HIS to their relevant functionalities needed in our scenario. It includes a DICOM database accomplished by DCMTK configured with an DICOM Application Entity Title (AET) for accessing DICOM images and SR documents. Further, the HIS is simulated by a simple HL7 application. Our CBIR system of choice is the Image Retrieval in Medical Applications (IRMA) framework [26]. It has a Simple Object Access Protocol (SOAP) interface for transferring input data and results. CBIR output is created according to our SR template.

3.3 Layout of IRMACON Viewer

The layout is illustrated in Figure 2:

Fig. 2 Exemplary output of CBIR results in the IRMACON browser

1. At the top border, the query or examination image for diagnosis is shown. The identified similar images by the CBIR system are listed below in descending order of their similarity for easy comparison. This structures the information according to their semantics and interrelation, as postulated in (R1). Presenting on the main page images instead of textual data simplifies the capturing of the information (R3).

2. Selecting an image opens a new window giving details on this image, namely examined body part, date of birth and sex. Furthermore, a button for retrieval of reports from the HIS is supplied. Providing further details only on demand meets (R1).
3. The navigation through the viewer is enabled by arrows pointing to the left for switching to images more similar or to the right to images less similar. Details are shown on pressing the field named "Select" on the bottom of the thumbnail. This enables an intuitive and easy handling as postulated by (R2).

4   Conclusions

The introduced IRMACON viewer provides a comprehensive and consistent representation of CBIR results integrated into the clinical setting of a radiologist's every day work. It assembles evidences sourced from CBIR, PACS and HIS necessary for diagnostic analyses. Hence, it follows the principal goal in health systems, "the right information, in the right place, at the right time" [27]. IRMACON establishes an essential link between CBIR systems and applied CADx. We hope that our proposal will contribute to the widespread use of CBIR for CADx in daily radiological routine. Our ongoing work comprises (i) the extension of our testbed and (ii) the processing of specified regions of interest for restricting the CBIR to a certain phenomenon.

References

1. Smeulders, A.W.M., Worring, M., Santini, S., et al.: Content-based image retrieval at the end of the early years. IEEE Trans. Pattern Anal. Mach. Intell. 22(12), 1349–1380 (2000)
2. Doi, K.: Overview on research and development of computer-aided diagnostic schemes. Semin Ultrasound CT MR 25, 404–410 (2004)
3. Müller, H., Rosset, A., Garcia, A., et al.: Informatics in radiology (Inforad): Benefits of content-based visual data access in radiology. Radiographics 25(3), 849–858 (2005)
4. Müller, H., Michoux, N., et al.: A review of content-based image retrieval systems in medical applications – Clinical benefits and future directions. Int. J. Med. Inform. 73, 1–23 (2004)
5. Deselaers, T., Deserno, T.M., Müller, H.: Automatic medical image annotation in Image CLEF 2007: Overview, results, discussion. Pattern Recognit. Lett. 29(15), 1988–1995 (2008)
6. Nakayama, R., Abe, H., et al.: Potential usefulness of similar images in the differential diagnosis of clustered microcalcifications on mammograms. Radiology 253, 625–631 (2009)
7. Li, Q., Li, F., Shiraishi, J., et al.: Investigation of new psychophysical measures for evaluation of similar images on thoracic computed tomography for distinction between benign and malignant nodules. Med. Phys. 30(10), 2584–2593 (2003)
8. Muramatsu, C., Li, Q., et al.: Investigation of psychophysical measure for evaluation of similar images for mammographic masses: Preliminary results. Med. Phys. 32(7), 2295–2304 (2005)

9. Aisen, A.M., Broderick, L.S., Winer-Muram, H., et al.: Automated Storage and Retrieval of Thin-Section CT Images to Assist Diagnosis: System Description and Preliminary Assessment. Radiology 228, 265–270 (2003)

10. Zheng, B.: Computer-Aided Diagnosis in Mammography Using Content-Based Image Retrieval Approaches: Current Status and Future Perspectives. Algorithms 2, 828–849 (2009)

11. National Electrical Manufacturers Association, DICOM Part 16: Content Mapping Resource, `http://medical.nema.org/medical/dicom/2009/09_16pu.pdf` (Cited February 23, 2010)

12. Clunie, D.A.: DICOM Structured Reporting. PixelMed., Bangor PA (2000)

13. Philips Medical Systems, Integration of digital mammography on PACS (2007), `http://www.healthcare.philips.com/phpwc/main/shared/assets/documents/about/events/2009/ecr/pdf/hi/integration_of_digital_mammography_on_pacs.pdf` (Citied February 23, 2010)

14. Eastman Kodak Company, Make mammography work flow (2006), `http://www.carestreamhealth.com/mammoPACS_brochure_N1-102.pdf` (Cited February 23, 2010)

15. Noumeir, R.: Benefits of the DICOM Structured Report. J. Digit. Imaging 19, 295–306 (2006)

16. Integrating the Healthcare Enterprise, IHE Technical Framework, vol. I: Integration Profiles (2008), `http://www.ihe.net/Technical_Framework/upload/ihe_tf_rev9-0ft_vol1_2008-06-27.pdf` (Cited February 23, 2010)

17. Le, A., Mai, L., et al.: The workflow and procedures for automatic integration of a computer-aided diagnosis workstation with a clinical PACS with real world examples. In: Procs. SPIE, vol. 6919 (2008)

18. Welter, P., Deserno, T.M., et al.: Integration of CBIR in radiological routine in accordance with IHE. In: Procs. SPIE, vol. 7264 (2009)

19. Health Level Seven, Inc., HL7, Health Level 7 Standards (2010), `http://www.hl7.org/implement/standards/index.cfm` (Cited February 23, 2010)

20. Hussein, R., Engelmann, U., Schroeter, A., et al.: DICOM Structured Reporting: Part 1. Overview and characteristics. RadioGraphics 24(3), 891–896 (2004)

21. Welter, P., Deserno, T.M., et al.: Exemplary Design of a DICOM Structured Report Template for CBIR Integration into Radiological Routine. In: Procs. SPIE Medical Imaging, vol. 7628 (2010)

22. Kinsey, T.V., Horton, M.C., Lewis, T.E.: Interfacing the PACS and the HIS: Results of a 5-year Implementation. RadioGraphics 20, 883–891 (2000)

23. Dayhoff, R., Kirin, G., Pollock, S., et al.: Medical data capture and display: the importance of clinicians' workstation design. In: Procs. Annu. Symp. Comput. Appl. Med. Care, pp. 541–545 (1994)

24. OFFIS, DICOM Toolkit DCMTK (2010), `http://dicom.offis.de` (Cited February 23, 2010)

25. University Health Network, HAPI (HL7 application programming interface) (2010), `http://hl7api.sourceforge.net` (Cited February 23, 2010)

26. Lehmann, T.M., Güld, M.O., Thies, C., et al.: Content based image retrieval in medical applications. Methods Inf. Med. 43(4), 354–361 (2004)

27. Winter, A., Lagemann, A., Budig, B., et al.: Integration of health professional workstation in hospital information systems. In: Procs. MIE, pp. 685–689 (1996)

3D Diagnostic System for Anatomical Structures Detection Based on a Parameterized Method of Body Surface Analysis

Wojciech Glinkowski, Jakub Michonski, Robert Sitnik, and Marcin Witkowski

Abstract. Features of trunk and postural deformations are clinically observed to detect related musculoskeletal disorders, namely scoliosis, kyphosis or other thoracic deformities. High variability and controversial reliability of results of postural screening require new solutions to be employed. Standardized criteria for correct body posture are needed for further studies. The aim of this work was to present the current status of development of the 3D diagnostic system for anatomical structures detection. The designed system is based on a parameterized method of body surface analysis for automated measurement of the three-dimensional shape of patient's trunk. This system uses structured light to measure patient's body in 3D space by projection of a set of raster images on its surface. A unique feature of the presented system is the ability to operate on remote sites and carry out measurement interpretation by telemedicine utilizing a data warehouse. The system comprises of three independent modules which deal with measurement, data archiving and its analysis. Communication between modules is performed over the TCP/IP protocol, incorporating two different channels for each client, dedicated to two kinds of data - text channel, for transmission of XML documents used for delivering commands and information and binary channel for the transfer of large binary data, such as clouds of points or photographs. Presented modules altogether allow to measure the full shape of subject's 3D surface along with measurement data storage and analysis for support of screening and diagnosis.

Wojciech Glinkowski
Medical University of Warsaw, Department of Orthopaedics and Traumology of Locomotor System, Center of Excellence "TeleOrto", Warsaw, Poland
Medical University of Warsaw, Department of Descriptive and Clinical Anatomy, Warsaw, Poland
Polish Telemedicine Society, Warsaw, Poland
e-mail: w.glinkowski@gmail.com

Jakub Michonski · Robert Sitnik · Marcin Witkowski
Warsaw University of Technology, Institute of Micromechanics and Photonics, OGX, Warsaw, Poland

1   Introduction

Features of trunk and postural deformations are clinically observed to detect related musculoskeletal disorders, namely scoliosis, kyphosis or other thoracic deformities. Adolescent idiopathic scoliosis (AIS) is characterized by a complex lateral shift of the spinal curve in the frontal plane, associated with a complex 3D deformity of the trunk [28, 14]. Czech study by Kratenova et al. [15] performed on the group of children aged 7, 11, and 15 years has shown poor posture was diagnosed in 38.3% of children, more frequently in boys. Scapular protrusion (50%), hyperlordosis of lumbar spine (32%) and round back (31%) were found most frequently among cohort of children . A study performed on a group of students [4] has shown common presence of lumbar hypolordosis (71.0%, 48.1%F and 97.8%M), thoracic hyperkyphosis (round back) (58.0%, 53.7%F and 63.0%M) and very high prevalence of scoliosis (54.0%, 50%F and 58.7%M). These results require focusing on that problem having in mind high probability of postural deterioration in elderly. Among older adults and elderly aged 55-80 years, who had a Debrunner kyphometer measurement of kyphosis and supine lateral spine radiographs, the manual and digitized Cobb angle was 45 degrees (range 18 degrees-83 degrees), and the mean Debrunner kyphometer reading was 48 degrees (range 17 degrees-83 degrees) [12]. Saggital angles should be seriously considered because in older women with previous vertebral fractures hyperkyphosis is associated with an increased risk of mortality. The measurements of children and teenagers [30] have shown only 0.60% children aged 12 to 15 with correct body posture that requires consideration of standardized criteria required for further studies interpretation. Recent methods turning toward Evidence Based Medicine require meeting validity, reliability and quantitativity criteria. Previously described methods simplified measurements. Simple measurement of a number of 1.7 cm blocks required to place under patient's head while lying flat to reduce hyper extension of cervical spine was practical allowing to define hyperkyphosis as requiring the use of one or more blocks [12, 13]. Other methods like inclinometry by simple reading may create no particular image to store for further monitoring. Considering both accurate measurement and data storage a combined method was developed to meet all the requirements.

The aim of this work was to develop a 3D diagnostic system for anatomical structures detection based on a parameterized method of body surface analysis for automated measurement of the three-dimensional shape of the trunk in patients with deformations related to scoliosis, kyphosis and others.

There are existing 3D measurement techniques with accompanying diagnostic algorithms. Moire photo-topography [24] was found in early 1980's as the method suitable for 3D chest assessment. Fortin et al. used a structured light projection system to reconstruct a 3D surface of patient's trunk to design a customized spinal brace [5]. Single-directional assessment of back curvatures screening has been elaborated in previous studies [25]. Poncet at al. reported that thoracic outline cross-sections can be measured based on 3D data representing patient's body surface captured with an optical measurement system [23]. However, the analysis method presented by them requires operator's interaction and may imply human factor

errors that depend on experience in 3D measurement data analysis or in clinical knowledge about pectus excavatum assessment. The clinicians are usually less familiar with new topographic surface shape measurements [15, 22]. In the last decades the equipment and software for surface measurements has evolved and turned into reliable 3 dimensions and high precision. The technology is approaching to meet clinical teams for further combined elaboration of a good consensus for surface measurements, a supplement for clinical studies. New multimodal evaluation with surface and radiological imaging shall bring new diagnostic dimension for future studies. Currently, direct comparison of radiological two-dimensional angular measurements (i.e. Cobb angle) and three-dimensional surface measurements may not show high correlation. Unequal back deformations may follow the Cobb angle [8, 10, 28] because surface measurements and x-rays do not measure the same aspect of the deformity. Gold standard parameters for surface topography require elaboration based on cooperation between engineers and clinicians to unify the parameters. Based on this principle the developed system uses structured light to measure 3D surface shape of patient's body by projection of a set of raster images on its surface. Back shape only can also be subtracted from the exam to achieve comparable data to previous systems. Accurate 3D surface topography can help the clinician to measure spinal deformity at baseline and monitor changes over time. It can help to turn the patients and their families' awareness to the deformity problem.

2   Telescreening Diagnostic System

Remote screening was described for a few disorders in otology, ophthalmology, and endoscopy but rarely for musculoskeletal problems [3, 5, 7, 11, 14, 19, 27]. The firstly reported screening for scoliosis begun in 1963 in Aitken, Minnesota, USA [18]. Screening of postural deformations is discussed in the literature frequently. Review of screening methods and policies was published recently [9]. School screening to identify children at risk for scoliosis is mandated in many countries. However, there exists some controversy on the effectiveness of routine scoliosis screening [9]. Orthopaedic societies (AAOS, SRS, POSNA, and AAP) in 2007 recognized that support for scoliosis screening has limitations, but the potential benefits that patients with idiopathic scoliosis receive from early treatment of their deformities can be substantial. Scoliosis screening, whether in the physician's office, nurses' clinics, or school environment, provides the opportunity to diagnose the condition and make referral for appropriate medical care. Females should be screened for scoliosis twice, at the age of 10 and 12, and boys once, at the age of 13 or 14. School screening personnel should be educated in the detection of spinal deformity. No single test is completely reliable for screening scoliosis but the forward bending test should be always included. Considerable screening judgment should avoid unnecessary referrals. Deformities screening among elderly may achieve a stronger feedback due to rise of mortality rate among hyperkyphotic fallers with osteoporotic fractures. In United States the total costs of medical care of scoliosis rise from one monetary unit per child screened, to 122,05 per identified case, 439,39

per child treated. Optical methods used for clinical screening attract investigators in concern of radiation exposure that the children may have undergone following clinical screening. Approaching toward the general trend of reliable screening the 3D diagnostic system is developed. Proposed solution consists of three main modules: four one-directional measurement systems, a database and a set of numerical tools for medical diagnosis support. The measurement system is designed to measure full patient body shape in a specialized laboratory by four measurement heads but also it can work in screening mode where two measurement heads can be easily transported and calibrated in any location. Authors plan to measure 20 000 children in Polish schools in screening mode and selected cases will be re-measured using the laboratory system.

The system consists of three independent modules (Fig. 1). Each of the modules has a certain type of input and output and together they form a complete data processing path. The measurement module returns a generalized measurement in the form of cloud of points, the archiving module can be customized arbitrarily to store information characteristic for specific application and the analysis module can be programmed to get all the necessary features from the data. The modules communicate with each other using a TCP/IP network.

Fig. 1 Modular structure of the system

The system allows working in on-line and off-line mode. Off-line mode is used when there is no Internet connection available in remote location. In this case the measurement data and patient information are stored locally and synchronized automatically just after establishing connection with the database. Parameters supporting medical diagnosis are calculated from measurement data representing surface shape of patient's body. First the curvature maps are calculated and on the base of their values distribution required anatomical structures are localized. Finally, from the positions of the anatomical structures final parameters are extracted [1, 2, 20, 21].

2.1 Measurement System

The measurement system consists of four modules which simultaneously measure patient's skin surface from four directions. Each directional module is an optical full-field 3D scanner based on structured light projection method. The main components of each module are: projection unit, which is a Digital Light Processing (DLP) projector, detection unit which is a Charge Coupled Device (CCD) or a

Complementary Metal-Oxide-Semiconductor (CMOS) camera and a PC-class computer (Fig. 2(a), 2(b)). During the measurement process the patient is placed inside a calibrated measurement volume while a series of patterns is projected onto his or her body surface. These patterns include sinusoidal fringes and modified binary Gray codes. The shape of body surface is calculated based on the raster deformation according to the Temporal Phase Shifting (TPS) method [27]. Dataset produced by the measurement system is in the form of a set of (x, y, z) points that represent the sampled surface of patient's body.

(a) (b)
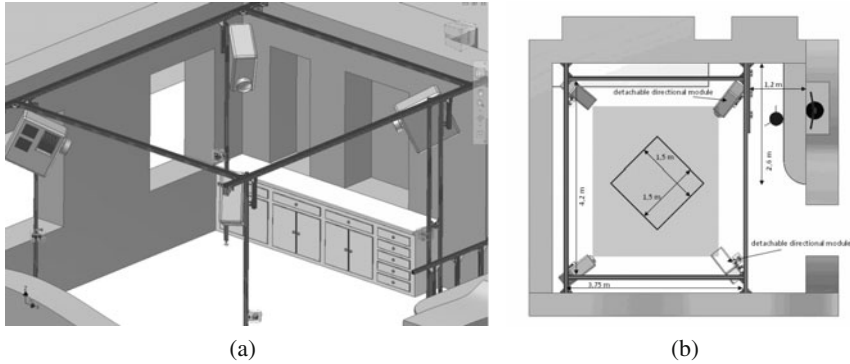
Fig. 2 A visualization of the measurement system (a) and the measurement volume (b)

The electro-optical hardware setup utilizes TDP-MT700 projectors by Toshiba Corp. and Flea B&W cameras by Point Grey Research Inc. (Fig. 3(a)). In order to avoid interferences caused by the overlapping of raster images originating from adjacent projectors spectral filters are mounted on projector and detector lenses. This allows to project raster images simultaneously (Fig. 3(b), 3(c)) and conduct measurements using all modules at the same time.

The metrological values of the measurement system are as follows:

- measurement volume size: scalable from 1.0m x 1.0m x 1.0m to 1.5m x 1.5m x 2.0m,
- accuracy: 0.2mm to 0.4mm (depending on the measurement volume size),
- data acquisition time: 0.7s (all modules simultaneously),
- maximum number of points: 4 million.

Depending on the size and position of the calibrated measurement volume the resulting point cloud may represent patient's thoraco-abdominal region or the whole body surface (Fig. 4).

Measurement data acquired with use of the measurement system along with patient's textual data are stored in a dedicated database.

| (a) | (b) | (c) |
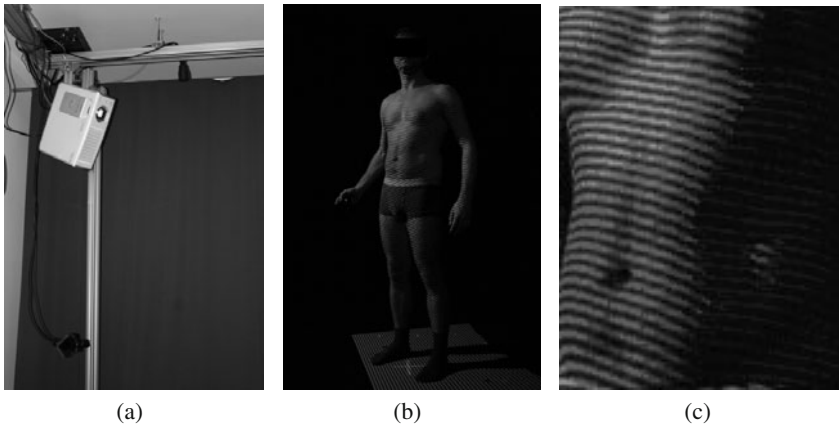
Fig. 3 The measurement setup built: (a) a directional measurement module fixed to a stand, (b) a healthy individual illuminated with fringe patterns, (c) magnified fringes projected by two adjacent measurement modules

Fig. 4 A three-dimensional point cloud representing body surface measured with the four-directional measurement system

2.2 *Database*

The database is the heart of the system and serves two main purposes - archiving of data and guarding it from unauthorized access. All operations on the database are performed using a specially designed XML interface, which makes the system independent of the underlying database implementation. The interface fulfills different functions, including user authentication, data import and user queries. Moreover, the structure within the database can be in full defined using XML without any necessary knowledge about the system itself and can be extended on the fly in case any additional information or data is required.

Data can be assigned to three main groups - objects, which are the core entities keeping data universal during system's lifetime, data elements, which are supposed to be assigned to each object, keeping information variable in time, and additional

elements which are all kinds of data derived from the original data elements. The elements can further be linked with each other in an arbitrary way, thus creating a hierarchical structure. The structure (division into groups and linkage of elements) used in this case is shown in Fig. 5.
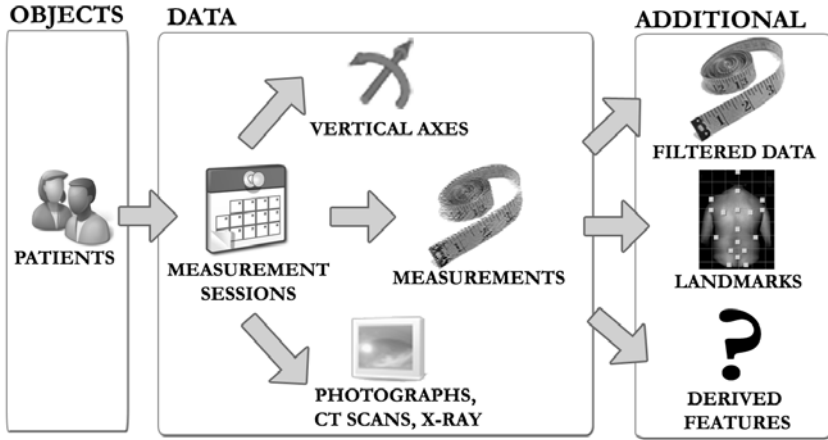
Fig. 5 Structure of elements within the database

The XML standard also provides a very robust yet easily-definable way for the construction of user queries for the data, including different types of value and linkage constraints and requests for any part of each element.

Communication between modules is performed over the TCP/IP protocol, incorporating two different channels for each client, dedicated to two kinds of data - text channel, for transmission of the XML documents and binary channel for the transfer of large binary data, such as clouds of points or photographs (Fig. 6). Such a structure is asynchronous and allows performing traffic inexpensive operations such as user logon or querying for text data independently of binary transmission, very costly in terms of network transfer. To further decrease this cost data compression was implemented and was also incorporated in data storage.
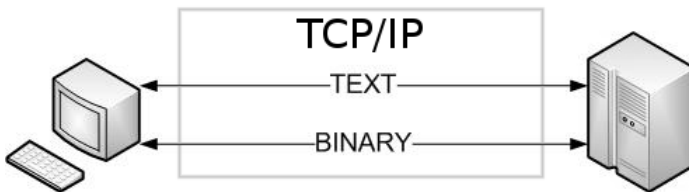
Fig. 6 Communication between modules

A user account system was also created, providing not only authentication, but also authorization of users, which allows to limit some of them to a read-only mode, even on a per element or per field basis.

These features altogether form a complete system which can be securely used over any network, be it a local area network (LAN) or the Internet.

2.3   Calculation and Diagnosis Support

The data gathering and analysis module provides a complete interface for the database, allowing the user to manage the information and perform certain operations on the archived measurements. It supports automatic analysis - so called pattern calculation - a series of operations that can be automatically performed on a subset of data according to a predefined scheme.

The module is constructed in a way which assures that no data becomes overwritten - any number of derived information can be saved in the database and linked to the parent measurement, thus keeping it consistent and easy to browse. It also makes it possible to compare different measurements, allowing the estimation of patient's improvement in time. This requires good repeatability of measurement and a method to correlate two measurements of the same patient in space. System's vertical, additionally measured every time an examination is carried out and assigned to measurement, and two points within the measurement are sufficient for absolute alignment. Since fine alignment uses two landmarks (dimples of pelvis) for accurate positioning, it is preceded by a coarse operation which detects the general position of the body.

Analysis can be carried out in two ways - discrete, based on a set of landmarks on the surface of the body or on a more global shape analysis. The discrete analysis itself can be performed either using manual indication of points or an algorithm of automatic landmark detection.

Such algorithms are currently under development, at the moment the landmarks are acquired from a team of trained physicians, which will help in the development process and provide the assessment of algorithms' reliability. Additionally, the points provide interesting information about the interobserver and intraobserver reliability for evaluated measurements.

A preliminary algorithm for automatic landmark extraction is built upon a modified back diagram for a number of predefined landmarks, of which starting positions are precalculated using an averaged set of manually selected points, scaled for each measurement with respect to a simple bounding box generated around it (Fig. 7). Such a processing path is easily extendable to an arbitrary number of characteristic points, thus providing a versatile detection method.

The method assigns an area to each landmark, within which the exact position of the landmark is searched for. The 3D shape contained in each cell is analyzed based on maps of parameters C1 and C2, which give general information about surface shape.
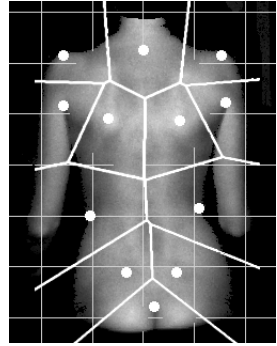
Fig. 7 A visualization of a modified back diagram generated for 12 back landmarks

These parameters were developed in order to describe surface shape of full 3D point clouds [31]. The C1 parameter describes how much the surface in the neighborhood of the considered point deviates from a plane, its values are positive for convex areas, negative for concave areas and zero for planes (Fig. 8(a)). The C2 parameter describes the distribution of normal vectors in the neighborhood of the considered point in a way allowing distinguishing areas of unidirectional curvature, such as cylindrical areas, and omnidirectional curvature, such as spherical areas and takes values equal to zero for planes and cylindrical surfaces and positive for other surface types. The highest values of C2 are obtained for sphere and for saddle shapes (Fig. 8(b)).

(a)   (b)
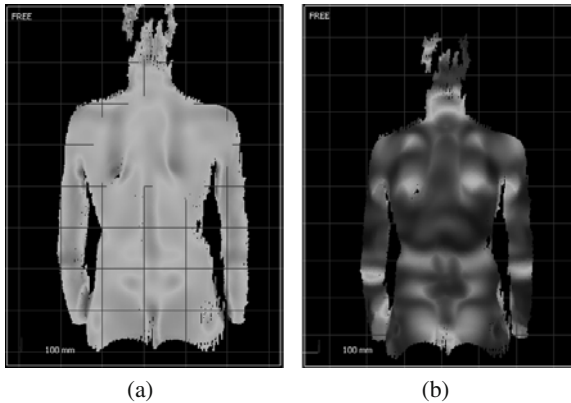
Fig. 8 A distribution map of (a) C1 (b) C2 parameter over body surface (real measurement data)

The analysis of distribution of C1 and C2 parameter values allows discrimination of various surface types in a way similar to used with mean and Gaussian curvatures, yet the former are faster to calculate and more resistant to noise in the analyzed dataset.

Division of the back into subregions makes it possible to avoid global analysis of the back surface. Moreover, the landmarks are not exactly points, but are regarded as certain regions on the surface of various scales and as such require computation of the C1 and C2 maps with different input parameters.

Each landmark also exhibits specific properties depending on the type of posture which implies the use of different detection paths and an algorithm which would provide some general, coarse information about the posture of the patient, or possibly an adaptive path of detection which would modify its parameters based on some overall properties of the shape of the back.

An additional potentially interesting feature is the possibility of comparison of the 3D shape with volumetric data, such as a CT scan.

3 Conclusions

In this paper a complex solution for diagnostic and screening of three-dimensional assessment of human body, mostly trunk and its postural deformities has been described. It allows to measure full shape of subject's body 3D surface along with measurement data storage and analysis for support of screening and diagnosis. Described system is still in the development stage, especially in the areas of final automated data analysis and clinical validation. However, for selected cases some clinical validation has proved that author's concept is correct.

Future works will be focused on the following tasks:

- Further optimization of anatomical landmarks localization and its verification for different subject types in whole population (males, females, children, elderly),
- Comparison of existing anatomical parameters versus specialist votes,
- Continuous extending of diagnosis scenarios along with its clinical validation.

References

1. Bujakiewicz, A., Krześniak, L.M., Majde, A., Zawieska, D.: Use of the moire technic in diagnosis and treatment control. Pol. Tyg. Lek. 37(23), 669–673 (1982)
2. Bujakiewicz, A., Krześniak, L.M., Zawieska, D.: The moire technic in epidemiological studies of spinal curvatures. Pol. Tyg. Lek. 40(35), 1002–1005 (1985)
3. Cikajlo, I., Matjacic, Z.: Directionally specific objective postural response assessment tool for treatment evaluation in stroke patients. IEEE Trans. Neural Syst. Rehabil. Eng. 17(1), 91–100 (2009)
4. Czakwari, A., Czernicki, K., Durmala, J.: Faulty posture and style of life in young adults. Stud. Health Technol. Inform. 140, 107–110 (2008)
5. Eikelboom, R.H., Mbao, M.N., Coates, H.L., Atlas, M.D., Gallop, M.A.: Validation of teleotology to diagnose ear disease in children. Int. J. Pediatr. torhinolaryngol. 69(6), 739–744 (2005)

6. Fortin, D., Cheriet, F., Beauséjour, M., Debanné, P., Joncas, J., Labelle, H.: A 3D visualization tool for the design and customization of spinal braces. Comput. Med. Imaging Graph. 31(8), 614–624 (2007)

7. Givens, G.D., Blanarovich, A., Murphy, T., Simmons, S., Blach, D., Elangovan, S.: Internet-based tele-audiometry system for the assessment of hearing: a pilot study. Telemed. J. E Health 9(4), 375–378 (2003)

8. Goldberg, C.J., Kaliszer, M., Moore, D.P., Fogarty, E.E., Dowling, F.E.: Surface topography, Cobb angles, and cosmetic change in scoliosis. Spine 26, E55–E63 (2001)

9. Grivas, T.B., Wade, M.H., Negrini, S., O'Brien, J.P., Maruyama, T., Hawes, M.C., Rigo, M., Weiss, H.R., Kotwicki, T., Vasiliadis, E.S., Sulam, L.N., Neuhous, T.: SOSORT consensus paper: School screening for scoliosis. Where are we today? Scoliosis 2, 17 (2007)

10. Hackenberg, L.: Evaluation of three-dimensional correction of idiopathic scoliosis by Zielke instrumentation surface measurement using videorasterstereography. Stud. Health Technol. Inform. 59, 258–261 (1999)

11. Huis in 't Veld, M.H., van Dijk, H., Hermens, H.J., Vollenbroek-Hutten, M.M.: A systematic review of the methodology of telemedicine evaluation in patients with postural and movement disorders. J. Telemed Telecare 12(6), 289–297 (2006)

12. Kado, D.M., Christianson, L., Palermo, L., Smith-Bindman, R., Cummings, S.R., Greendale, G.A.: Comparing a supine radiologic versus standing clinical measurement of kyphosis in older women: the Fracture Intervention Trial. Spine (Phila Pa 1976) 31(4), 463–467 (2006)

13. Kado, D.M., Huang, M.H., Barrett-Connor, E., Greendale, G.A.: Hyperkyphotic posture and poor physical functional ability in older community-dwelling men and women: the Rancho Bernardo study. J. Gerontol. A Biol. Sci. Med. Sci. 60(5), 633–637 (2005)

14. Kim, C.Y., Etemad, B., Glenn, T.F., Mackey, H.A., Viator, G.E., Wallace, M.B., Mokhashi, M.S., Cotton, P.B., Hawes, R.H.: Remote clinical assessment of gastrointestinal endoscopy (tele-endoscopy): an initial experience. In: Proc. AMIA Symp., pp. 423–427 (2000)

15. Kotwicki, T., Negrini, S., Grivas, T.B., Rigo, M., Maruyama, T., Durmala, J., Zaina, F., Members of the International Society on Scoliosis Orthopaedic and Rehabilitation Treatment (SOSORT): Methodology of evaluation of morphology of the spine and the trunk in idiopathic scoliosis and other spinal deformities - 6th SOSORT consensus paper. Scoliosis 4, 26 (2009)

16. Kratenová, J., Zejglicová, K., Malý, M., Filipová, V.: Prevalence and risk factors of poor posture in school children in the Czech Republic. J. Sch. Health 77(3), 131–137 (2007)

17. Kuo, Y.L., Tully, E.A., Galea, M.P.: Video analysis of sagittal spinal posture in healthy young and older adults. J. Manipulative Physiol. Ther. 32(3), 210–215 (2009)

18. Lonstein, J.E.: Screening for spinal deformities in Minnesota schools. Clin. Orthop. Relat. Res., 33–42 (1977)

19. Mendelson, Y., Duckworth, R.J., Comtois, G.: A wearable reflectance pulse oximeter for remote physiological monitoring. In: Conf. Proc. IEEE Eng. Med. Biol. Soc., vol. 1, pp. 912–915 (2006)

20. Mínguez, M.F., Buendía, M., Cibrián, R.M., Salvador, R., Laguía, M., Martín, A., Gomar, F.: Quantifier variables of the back surface deformity obtained with a noninvasive structured light method: evaluation of their usefulness in idiopathic scoliosis diagnosis. Eur. Spine J. 16(1), 73–82 (2007)

21. Nowotny, J., Gaździk, T., Zawieska, D., Podlasik, P.: Photogrammetry: myths and reality. Ortop. Traumatol. Rehabil. 4(4), 498–502 (2002)

22. Petit, Y., Aubin, C.E., Labelle, H.: Three-dimensional imaging for the surgical treatment of idiopathic scoliosis in adolescents. Can. J. Surg. 45, 453–458 (2002)

23. Poncet, P., Kravarusic, D., Richart, T., Evison, R., Ronsky, J.L., Alassiri, A., Sigalet, D.: Clinical impact of optical imaging with 3-D reconstruction of torso topography in common anterior chest wall anomalies. J. Pediatr. Surg. 42(5), 898–903 (2007)
24. Shochat, S.J., Csongradi, J.J., Hartman, G.E., Rinsky, L.A.: Moiré phototopography in the evaluation of anterior chest wall deformities. J. Pediatr. Surg. 16(3), 353–357 (1981)
25. Sitnik, R., Glinkowski, W., Licau, M., Załuski, W., Kozioł, D., Glinkowska, B., Górecki, A.: Screening Telediagnostics of spinal deformities based on optical 3D shape measurement system and automated data analysis - Preliminary report. In: Piętka, E., łęski, J., Franiel, S. (eds.) Proceedings of the XI International Conference Medical Informatics & Technology, pp. 241–245. MIT, Cambridge (2006)
26. Sitnik, R., Kujawińska, M., Woźnicki, J.: Digital fringe projection system for large-volume 360 deg shape measurement. Opt. Eng. 41(2), 443–449 (2002)
27. Taleb, A.C., Böhm, G.M., Avila, M., Wen, C.L.: The efficacy of telemedicine for oph-thalmology triage by a general practitioner. J. Telemed. Telecare 11(suppl. 1), 83–85 (2005)
28. Thulborne, T., Gillespie, R.: The rib hump in idiopathic scoliosis. Measurements, analysis and response to treatment. J. Bone Joint Surg. 58-B, 64–71 (1976)
29. Weinstein, S.L., Dolan, L.A., Cheng, J.C., Danielsson, A., Morcuende, J.A.: Adolescent idiopathic scoliosis. Lancet 371(9623), 1527–1537 (2008)
30. Wilczyński, J.: Lateral spinal curvature measured among children and teenagers as a health problem of future employees (pol.). Med. Pr. 58(5), 419–422 (2007)
31. Witkowski, M., Sitnik, R., Kujawińska, M., Rapp, W., Kowalski, M., Haex, B., Mooshake, S.: 4D measurement system for automatic location of anatomical structures. In: Proc. SPIE, vol. 6191, 61910H, pp. 131–141 (2006)

Reconstruction of the Pelvic Region Based on the Statistical Shape Modeling

Pawel Skadlubowicz, Zdzislaw Krol, Zygmunt Wrobel,
Fritz Hefti, and Andreas Krieg

Abstract. Up until now the reconstruction of the pelvis defects after bone tumor resection has typically been by autologous or allogenous grafts. These approaches were highly unsatisfied because of large shape differences between the harvested transplant and the site to be reconstructed. There exists a huge demand for patient-specific and anatomically shaped implants. In this paper we propose a new pelvis reconstruction planning approach based on the statistical shape modeling. For generation of the statistical pelvis shape model a large data pool of CT datasets has been collected. Afterwards, the CT data segmentation and surface processing methods delivered the required pelvis geometries. Via Procrustes analysis of the collected pelvis surfaces the parameterized pelvis shape mean model has been calculated and the principal component analysis (PCA) [4] applied for estimating the anatomically optimal graft or implant geometry. In this work we demonstrate on a clinical pelvis reconstruction case that the using of statistical shape models in the oncologic surgery planning is a robust and very promising method. A quantitative evaluation of the matching quality and the convergence process is given.

1 Introduction

The pelvis oncologic surgery is beside the radiotherapy the most common treatment of malignant bone tumors. Pelvis is one of the principal components of the human locomotor system therefore its reconstruction after resection of malignant

Pawel Skadlubowicz · Zygmunt Wrobel
Department of Biomedical Computer Systems, Faculty of Computer Science and Materials Science, University of Silesia, Sosnowiec, Poland
e-mail: pawel.skadlubowicz@us.edu.pl, zygmunt.wrobel@us.edu.pl

Zdzislaw Krol · Fritz Hefti · Andreas Krieg
Pediatric Orthopedic Department, University Children's Hospital Basel (UKBB),
Basel, Switzerland
e-mail: zkrol@uhbs.ch, fritz.hefti@ukbb.ch,
andreas.krieg@ukbb.ch

pelvic tumors presents a highly complex and challenging problem. One of the main problems is the shape definition of artificial implants or autologous transplants for anatomically optimal reconstruction of the resected osseous part. The analysis of the anatomical shape and statistical shape modeling is a wide area of investigation. In the past many authors have developed statistical shape models for different anatomical structures (see for instance [5, 6, 11] and [13]). The objective of this paper is to investigate the use of statistical shape models in the preoperative surgery planning for pelvis reconstruction. In the following a new reconstruction methodology based on the deformable pelvis statistical shape model including a novel optimization approach based on the genetic algorithms [8] will be described and explained. A quantitative analysis of a clinical planning case will be given.

2 Methods

Among many planning approaches for reconstruction of the resected part of the pelvis the mirroring method is the most widely used computer-aided surgery planning procedure in the reconstructive surgery. It is based on the preoperatively acquired computed tomography (CT) dataset of the patient. After segmentation of the unaffected side a mirrored surface is aligned with the defected region. It enables fast generation of an anatomically similar model of the target region. The disadvantage of this method is the natural asymmetry in human anatomy and the fact that the existing osseous structures on the unaffected side are often malformed due to increase of load on the healthy side. The additional limitation is that this method can be applied to unilateral defects only. The bilateral defects still remain a challenging problem in the reconstructive pelvic surgery planning.
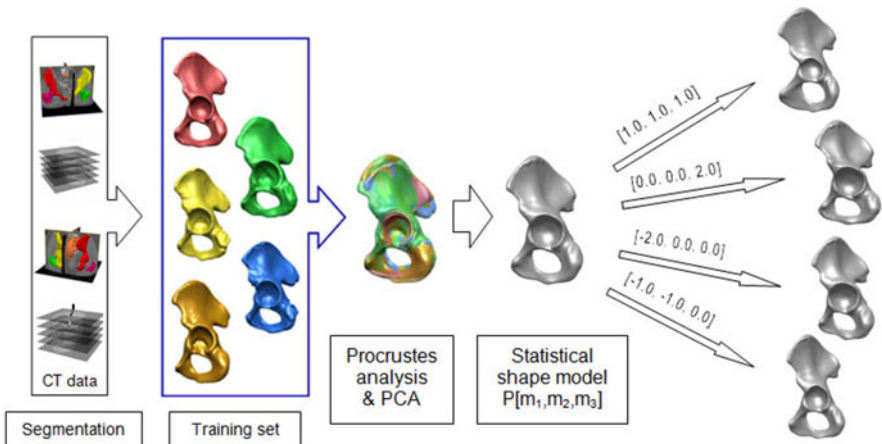
Fig. 1 The data processing pipeline for generation of our statistical pelvis shape model

The proposed new planning approach is based not only on the patient single CT dataset for the fitting the designed implant shape to the existing osseous structures but uses the statistical pelvis shape model for the optimal reconstruction of the morphological region of interest (ROI). For generating the statistical pelvis shape model one need a large data pool of pelvis CT datasets. The required pelvis geometries (called training set [2]) are obtained via segmentation and surface processing methods. Different stages of the data processing pipeline for generation of the statistical pelvis shape model are presented in Fig. 1. In the following section a brief overview of the statistical shape model generation process will be presented. We will explain the main stages of the method: segmentation, surface mesh processing, data alignment and the principal component analysis.

Our training set for the pelvis statistical shape model has been generated using a CT data pool (n = 20) collected at our hospitals. In our approach the pelvis shapes are described by triangular mesh surfaces. The generation of the training set is done via segmentation of all the CT data. Various segmentation methods implemented in our self developed segmentation, visualization and modeling system SeVisMo [10] has been used for generation of the training set. Various region growing segmentation methods like for example: connected threshold, neighborhood connected, confidence connected and isolated connected one; flood fill methods, mask operations as well as the manual segmentation tools were required to identify and separate the all required osseous structures in the pelvis region (left pelvis, right pelvis, sacrum, right femur and left femur) from all acquired CT datasets (see Fig. 2). In Fig. 3 are presented five different left pelvis bones segmented using the mentioned above methods and belonging to our pelvis shape training set. Notice the noticeable shape variability in the ilium and acetabulum regions.
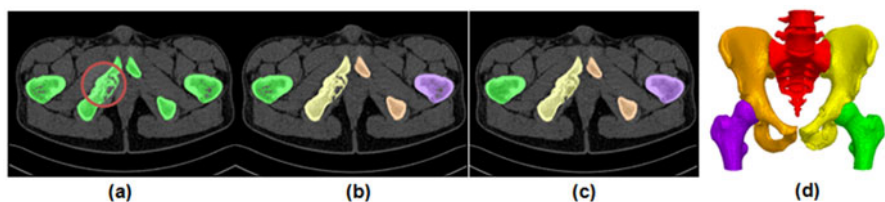
Fig. 2 Segmentation stage of the patient CT data with a tumorous lesion at the left ischiopubic ramus (red circle): (a) oseous structures (green) segmented using the connected threshold method, (b) manually separated bones, (c) masks with filled internal structure of bones, final stage of the segmentation process, (d) color coded surface mesh representation of the segmented bones, generated using the marching cubes algorithm [7]

Upon the segmentation stage and still before the incorporation into the training set the triangular mesh surfaces are undergone special processing and optimization. The surface mesh representation of the segmented bones is generated by the marching cubes algorithm [7]. Because the CT data sets are noisy and could contain different imaging artifacts the following surface mesh processing methods are
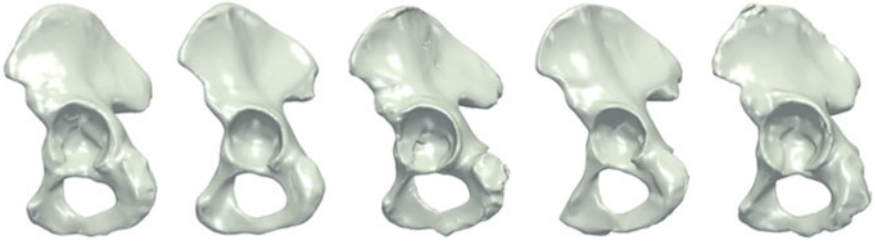
Fig. 3 Five triangular mesh surfaces of the left part of pelvis bone segmented from our pelvis CT datasets and belonging to our training set. One can observe for instance different shapes and sizes of the acetabulum.

required for improving the surface mesh quality: cleaning, smoothing, remeshing and decimating.

The next stage in our data processing pipeline is the establishing of correspondence between different pelvis shapes for statistical analysis. First and foremost, the same number of nodes in all anatomically corresponding meshes of the training set must be achieved. In our approach it will be assured by using the thin plate spline transformation [1]. We choose from the training set the surface mesh which is the best anatomical representation of the pelvis. This base surface mesh is then elastically matched with each of the pelvis surfaces from the training set. In this way we obtain approximated copies of the original pelvis surfaces but they all have now the same number of nodes. In Fig. 4 below are presented the effects of the thin plate spline transformation applied to one of the surfaces from our training set. After
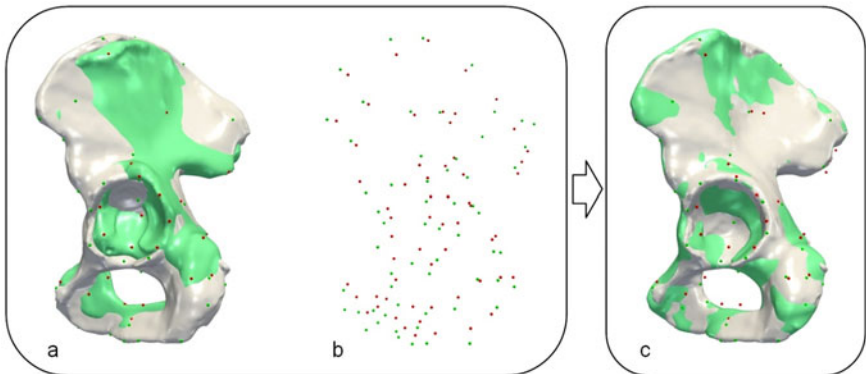
Fig. 4 Two instances of the left pelvis bone from the training set before alignment. The grey bone surface is the target surface and the green one is the source surface (a), the corresponding landmarks for both surfaces (pre-match status) are colored red and green (b), the aligned surfaces after applying the thin plate spline transformation (the green surface has been deformed) (c).

establishing the correspondence between different shapes from the training set, a Procrustes analysis and the PCA [3, 4] method are performed, resulting in a mean pelvis shape model and in the most dominant modes of variation. Our pelvis statistical shape model P is defined in the following way:

$$P = P_0 + \sum_{k=1}^{n} \lambda_k D_k \qquad (1)$$

where P_0 is the mean pelvis shape model representation and λ_k is the eigenvector matrix characterizing the prior information. Changing the deformation parameters D_k, allows us to get a model instance, which is a deformed version of the mean model P_0. Our statistical hemi-pelvis shape model has been built from the twenty training pelvis mesh surfaces. In Fig. 5 the shape changes corresponding to the first three principal modes of variation are presented. In the following we will demonstrate on a clinical case how the generated pelvis statistical shape model allows estimating the optimal morphological target geometry for arbitrary region of interest to be reconstructed.

The implementation of the described approach in the SeVisMo [10] is based in part on the Vtk library [12]. For the establishing of the correspondence between different instances of the pelvis in the training set two Vtk classes has been used: *vtkIterativeClosestPointTransform* and *vtkThinPlateSplineTransform*. Vtk also includes classes dedicated for generation of the statistical shape model. *vtkProcrustesAlignmentFilter* and *vtkPCAAnalysisFilter* are filters making possible the application of PCA to 3D surface meshes. These two methods have been implemented in our application too. The described above surface matching method (using the thin plate spline transformation) plays also a crucial role in the reconstruction of the resected pelvis defect. An automatic optimization method delivering the anatomically best shape for the pelvis reconstruction uses the genetic algorithms as the optimization engine [9]. This powerfull aproach has been choosen because of limitations of the classical optimization methods. The limitations are mostly connected with target function. Particularly an analytic form is required and in many cases first and even second derivative as well.

3 Results and Discussion

The explained above surgery planning approach based on the statistical shape model has been applied to find the anatomically optimal bone shape for reconstruction of the pelvis after tumor resection (see Fig. 6). The estimation of the optimal matching transformation parameters has been done by applying the non-deterministic optimization method: genetic algorithms.

The demonstrated application of the surgery planning method based on the statistical shape model shows that the reconstruction of the resected pelvis bone is successful and strongly correlates with the anatomical shape of the region of interest. The presented in Fig. 5 pelvis models also demonstrate the robustness of the
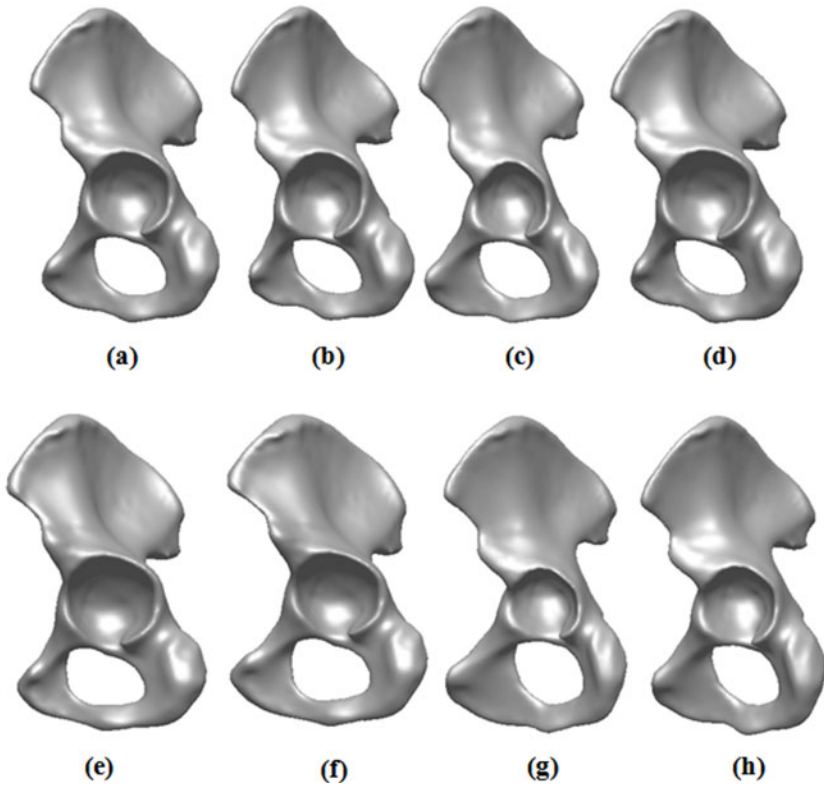
Fig. 5 Demonstration of the shape changes corresponding to the first three principal modes of variation The left pelvis bone generated using our pelvis statistical shape model for different values of variation modes: 0.0, 0.0, 0.0 (a), -1.0, -1.0, 0.0 (b), -2.0, 0.0, 0.0 (c), 0.0, -1.0, 0.0 (d), 0.0, 0.0, 2.0 (e), 1.0, 1.0, 1.0 (f), 0.0, 1.0, -2.0 (g), 0.0, 0.0, -2.0 (h).
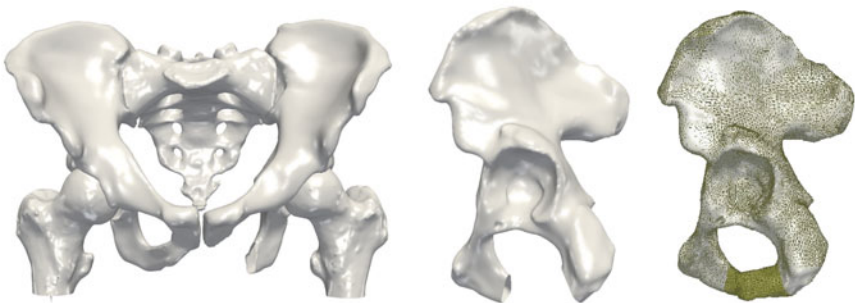
Fig. 6 Application of the planning approach for the clinical data (tumorous lesion at the left ischiopubic ramus). Virtual resection of the bone tumor (left and center). Statistical shape model matched with the patient pelvis model (right).
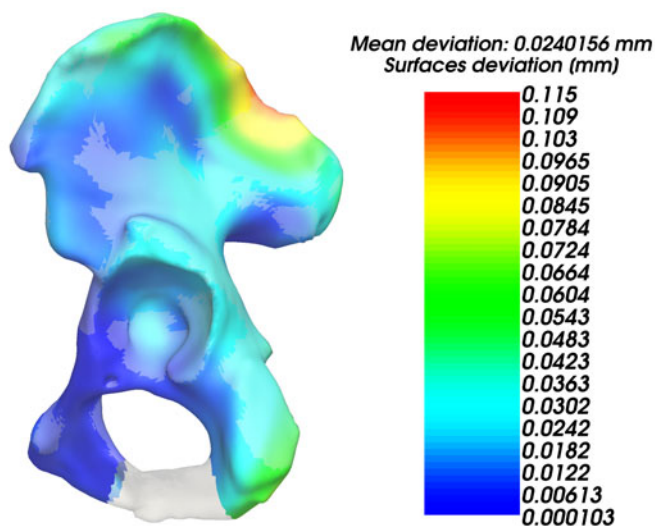
Fig. 7 Color coded deviation [mm] of the matched surface from the target surface
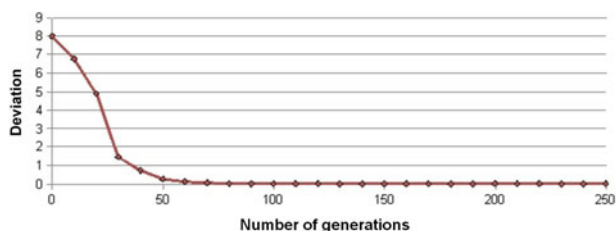
Fig. 8 Convergence of the aligning in the mean model surface and target surface matching process. Objective function value (deviation) as function of the generation number in the genetic algorithms optimization approach.

statistical shape model approach in generation of huge spectrum of pelvis shapes, which can be in an easy way aligned with an arbitrary clinical pelvis data. It is a valuable tool for the reconstructive surgery planning. It has been shown that even few datasets in the training set can be enough to create a clinically applicable statistical shape model and give satisfactory results. In Fig. 7 has been shown the excellent sub-millimeter matching quality in this case (color coded mean distance deviation between the two surfaces is 0.024 mm). Fig. 8 illustrates the convergence behavior of the genetic algorithms during the optimization phase.

4   Conclusions and Future Work

In this work a novel framework for pelvis reconstruction planning approach based
on the statistical shape model has been presented. For generation of the statistical
pelvis shape model a CT data pool consisting of twenty pelvis CT datasets has
been collected. The data segmentation and surface processing methods delivered the
required pelvis geometries. Via Procrustes analysis of the collected pelvis surfaces
the parameterized pelvis shape mean model has been calculated and the principal
component analysis method applied for estimating the anatomically optimal graft
or implant geometry. As demonstrated the generated pelvis statistical shape model
allows estimating the optimal morphological target geometry for a given clinical
region of interest in the pelvis reconstructive surgery. In the future we are planning
to extend the training set to 50 different pelvis geometries.

References

 1. Bookstein, F.L.: Principal warps: thin-plate splines and the decomposition of deforma-
    tions. IEEE Transactions on Pattern Analysis and Machine Intelligence 1(6), 567–585
    (1989)
 2. Cootes, T.F., Taylor, C.J., Cooper, D.H., Graham, J.: Training Models of Shape from Sets
    of Examples. In: British Machine Vision Conference, pp. 9–18. Springer, Heidelberg
    (1992)
 3. Dunteman, G.H.: Principal Components Analysis. Sage Publications, Newbury Park
    (1989)
 4. Jolliffe, I.T.: Principal Component Analysis. Springer, New York (2002)
 5. Lamecker, H., Kamer, L., Wittmers, A., Zachow, S., Kaup, T., Schramm, A., Noser, H.,
    Hammer, B.: A method for the three-dimensional statistical shape analysis at the bone
    orbit. In: Freysinger, W., et al. (eds.) Proc. Computer Aided Surgery around the Head
    (CAS-H), pp. 94–97. Pro Business Verlag (2007)
 6. Lamecker, H., Zachow, S., Haberi, H., Stiller, M.: Medical Applications for Statistical
    3D Shape Models. In: Computer Aided Surgery around the Head, vol. 17 (2005)
 7. Lorensen, W.E., Cline, H.E.: Marching Cubes: A high resolution 3D surface construction
    algorithm. Computer Graphics 21(4), 163–169 (1987)
 8. Osyczka, A.: Evolutionary Algorithms for Single and Multicriteria Design Optimization.
    Physica-Verlag, Berlin (2002)
 9. Shark Machine Learning Library,
    `http://shark-project.sourceforge.net/EALib/index.html` (Cited
    March 2009)
10. Skadlubowicz, P.: Statistical shape models for bone reconstruction in the craniofacial
    and orthopedic surgery, Diploma thesis, University of Silesia (2008)

11. Skoglund, K.: 3D face modeling & analysis, IMM-THESIS-2003-43, Department of Informatics and Mathematical Modelling (IMM), Technical University of Denmark (2003)
12. Schroeder, W.J., Avila, L.S., Hoffman, W.: Visualizing with VTK: A Tutorial. IEEE Computer Graphics and Applications 20, 20–27 (2000)
13. Zachow, S., Hecht, H.G., Croft, B.Y., Otsu, N.: Reconstruction of mandibular dysplasia using a statistical shape model. In: Computer Assisted Radiology and Surgery. International Congress Series, vol. 1281 (2005)

Automatic Measuring of the Iridocorneal Angle in the Optical Coherence Tomographic Image of the Anterior Segment of the Eye

Robert Koprowski, Zygmunt Wrobel, Anna Nowinska, and Edward Wylegala

Abstract. The article proposes a new automatic method of the iridocorneal angle analysis in the anterior segment of the eye, using an original algorithm proposed by the authors. Results of analysis of a several tens of thousands images are shown in the later part of the article. There is also a proposal of a new method of measuring the iridocorneal angle, based directly on the image analysis and image processing methods. The algorithms have been implemented in the Matlab computing environment.

1 Introduction

Optical coherence tomography (OCT) is a modern, noninvasive method of imaging cross-sections of tissue, in this case: iris of the eye, which uses light scattered on several distinct layers of the examined tissue. The spectral domain OCT, compared to previous solutions such as time-encoded domain OCT, offers a much higher resolution. The elimination of the moving mirror, needed for scanning the depth of the object, also allows for reduction of the scanning time roughly one hundred times. The shorter scanning time, sequentiality of the scanning and the constant offset allows to obtain three-dimensional images [3, 4, 5].

Robert Koprowski · Zygmunt Wrobel
University of Silesia, Institute of Computer Science, 41-200 Sosnowiec,
Bedzinska 39, Poland
e-mail: `koprow@us.edu.pl`, `wrobel@us.edu.pl`

Anna Nowinska · Edward Wylegala
Department of Ophthalmology, District Railway Hospital, 65 Panewnicka St.,
40-760 Katowice, Poland

The iridocorneal angle (Fig. 1, 2) is a structure responsible for the drainage of aqueous humour from the eye's anterior chamber. The correct production of aqueous humour by the ciliary body, as well as correct speed of drainage through the iridocorneal angle are the conditions of healthy intraocular pressure. Any anatomical anomalies like narrowing or closure of the angle cause difficulties in the drainage and heightening of the pressure. Gonioscopy is an examination which allows us to check the width of the iridocorneal angle. Based on the width of the angle, glaucoma can be categorized as open angle or closed angle.
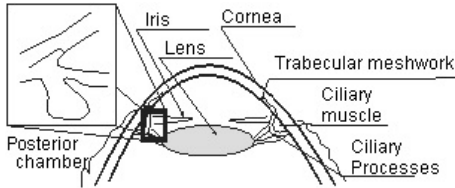
Fig. 1 Cross-section of the anterior chamber of the eye, with locations of characteristic areas
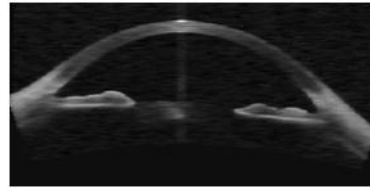
Fig. 2 Sample view of the anterior segment of the eye

Practical methods of measuring the iridocorneal angle, shown on Fig.3 have many inaccuracies and faults, letting the physician choose the method individually. As a consequence, the results are not dependable and hard to verify and compare with other physicians' results and patterns. Relatively: the AOD method (Fig. 3) measures the distance; TIA method (Fig. 3) measures the angle, and the TISA method (Fig. 3) measures the surface [1, 2, 6, 7]. All of these measures are performed manually, by finding specific characteristic points. In cases of pathology or individual variability, the methods have various accuracy and reproducibility,
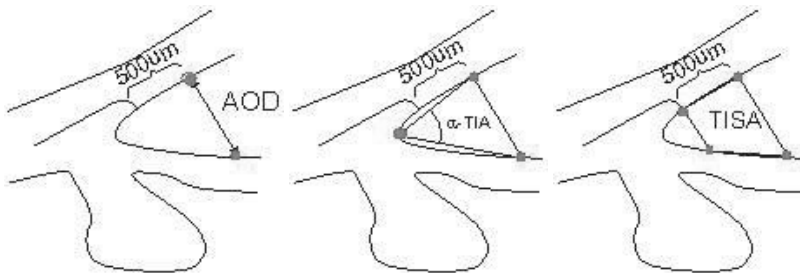
Fig. 3 Methods of measuring the iridocorneal angle: AOD (Angel Opening Distance), TIA (Trabecular-Iris Angle), TISA (Trabecular-Iris Space Area)

resulting from their character and differences in measured values. Fig. 4 shows the anterior chamber with various levels of pathology, with distances in various points measured by the AOD method. As can be seen (Fig. 4), the AOD method is not very
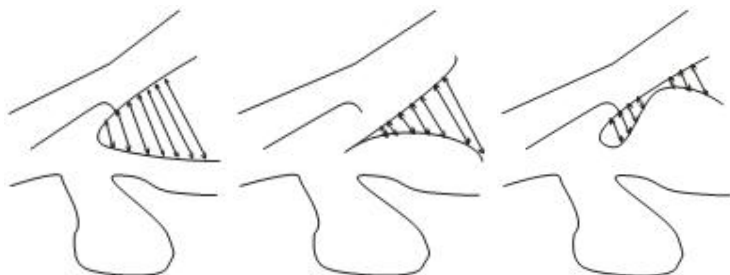
Fig. 4 Anterior chamber of the eye with various levels of pathology, showing distances measured by the AOD method

efficient in pathological cases, and the obtained results are not diagnostically reliable. What's worse, the physician using this method consciously makes a potentially large (depending on the level of pathology) error in choice of method. Therefore, we propose an automatic method of measuring the iridocorneal angle and an original method of measuring (based on above-mentioned AOD, TISA and TIA methods) free of the above-mentioned errors.

2 Image Acquisition

The algorithms described below have been tested on images acquired in the following medical institutions:

- Okręgowy Szpital Kolejowy w Katowicach,
- Wojewodzki Szpital Specjalistyczny Nr 5 im. św. Barbary,

on the following devices:

- OCT COPERNICUS produced by Optopol,
- VISANTE OCT Carl Zeiss Meditec.

The acquired images have the resolution of $256x1024$ pixels, within measuring range of $8mm$ x $16mm$, which allows for resolution of $0.0313mm$ per pixel. In total, above seventy thousand images of anterior segment of the eye were obtained by the above-mentioned devices, the major part of which were used for testing the accuracy of the described algorithm. Image analysis was implemented with the Matlab software package with Image Processing and Signal Processing toolboxes; the code was further optimized in C language.

3   Existing Methods of the Iridocorneal Angle Analysis

Existing methods of the iridocorneal angle analysis are easy to evaluate, because all software included with both of used tomographs uses the manual methods. The user sets the reference points characteristic for a given measuring method (Fig. 5, Fig. 6). They are prone to errors resulting both from the user's mistakes and the chosen method. The lack of reproducibility of measures is particularly troublesome in statistical analysis. In sum, the available software has the following disadvantages:

- lack of 3D reconstruction, and therefore the possibility of measuring the volume of selected sections of the anterior segment of the eye,
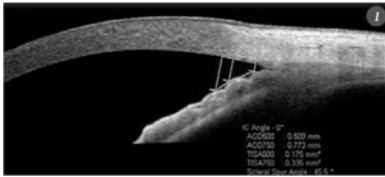
Fig. 5 Examples of operations on commercial software included with OCT Visante devices
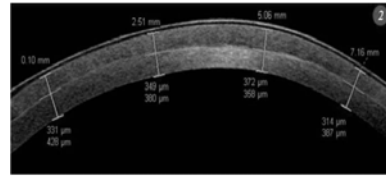
Fig. 6 Examples of operations on commercial software included with OCT Visante devices

- lack of full automatization,
- manually performed operations provide only local information,
- significant errors in case of iridocorneal angle analysis of pathological cases.

4   Results Obtained by Existing Algorithms

The necessity of using a custom-made algorithm is justified by unsatisfactory results of using other, existing algrithms used for line or area detection on images:

- the Hough transform allows for line detection on images with pre-set shapes,
- the wavelet analysis gives incorrect results when the objects are not clearly visible or interfering,
- the methods of elongated objects analysis also are not applicable because of possibilities of significant changes in size of the object and its width, and division of the object into multiple parts,
- the approximation methods are hard to implement without pre-processing of the image.

Because of this, and with regard to the medical premises mentioned below, we propose a custom-made algorithm of analysis and processing of the image of anterior segment of the eye.
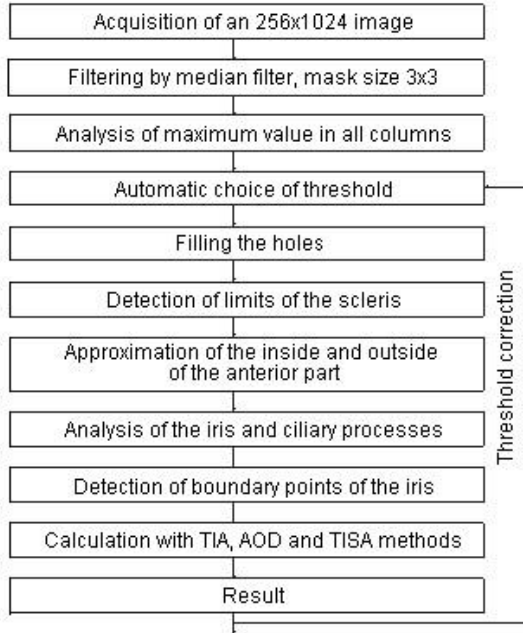
Fig. 7 Flowchart of the algorithm

Fig. 8 Binary image obtained by binarization of the original image with a threshold of 90% of maximum value

Fig. 9 Binary image after the hole-filling operation

Input image of resolution 256x1024 and averagely 0.313 mm per pixel, in DICOM format, is entered into the Matlab space. Filtering with a median filter (mask size 3x3) and analysis of subsequent columns is performed. For each column, a binarization threshold (the images are calibrated) of 10% of the brightest pixel is calculated (Fig. 10). Next, in order to eliminate minor inclusions and separations, the hole-filling method is employed. On this pre-processed image, we perform the detection of limits of the scleris, and approximation of the detected values with a fourth degree polynomial (Fig. 11). After the analysis of the iris and ciliary processes, we perform the analysis of the boundary points of the iris, using the
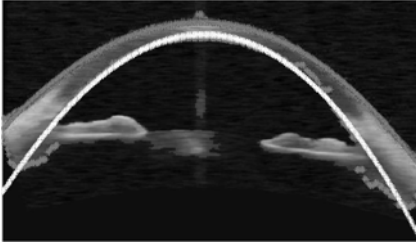
Fig. 10 Input image with detected limits of the anterior segment
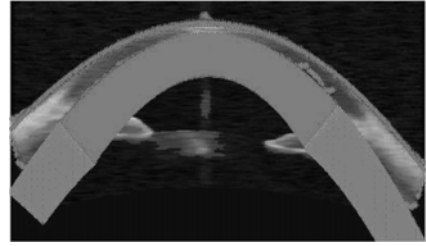
Fig. 11 OCT image (and magnification) of the anterior segment with area of the analysis

information obtained from the areas near the limits of the scleris (Fig. 12). Subsequent phases of the algorithm are shown on figures: Fig. 10- Fig. 12. Based on intrascleral analysis, we can evaluate the position of iridocorneal angles and calculate the values of AOD, TISA and TIA in about 3 seconds, on a system with an Intel Core Quad 2.5 GHz CPU, 2GB RAM and 64-bit operating system (Fig. 13).
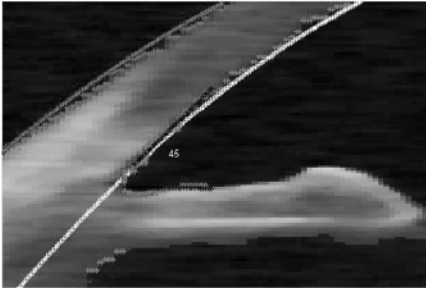
Fig. 12 Results of the automatic measuring of the iridocorneal angle
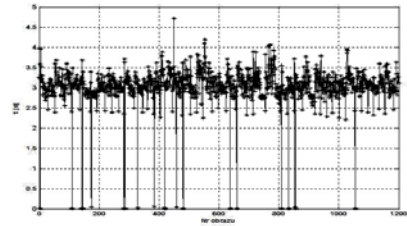
Fig. 13 Operation time of the algorithm for subsequent images, calculated on a system with an Intel Core Quad 2.5 GHz CPU, 2GB RAM

The AOD, TISA and TIA methods have difficulties coping with high levels of pathology. Such situations take place in case of partial narrowing of the iridocorneal angle. Therefore, we propose the analysis of distance between specific points according to Fig. 14. The results obtained with this original method are much more efficient in case of high levels of pathology (Fig. 4), as shown by the graph of distance changes shown on Fig. 15.
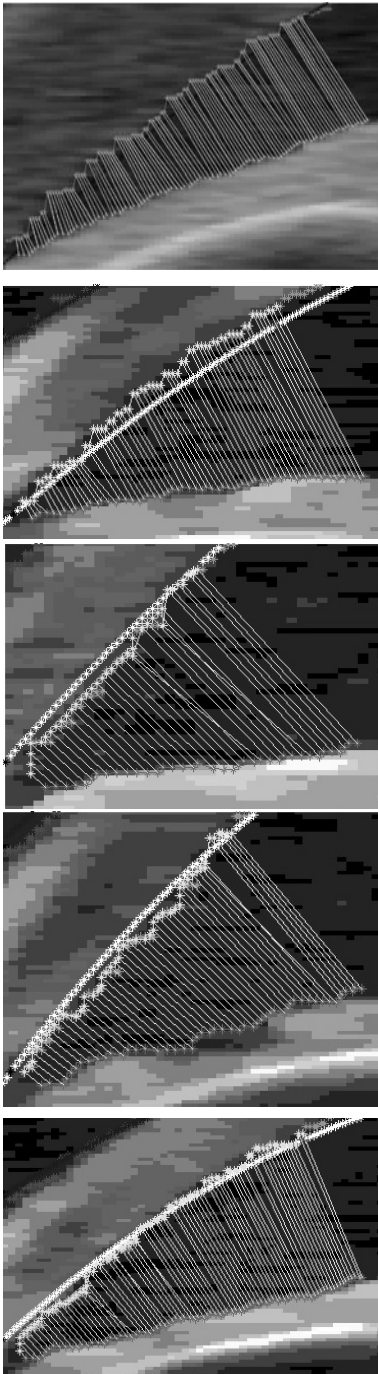
Fig. 14 Results of the automatic measuring of the iridocorneal angle
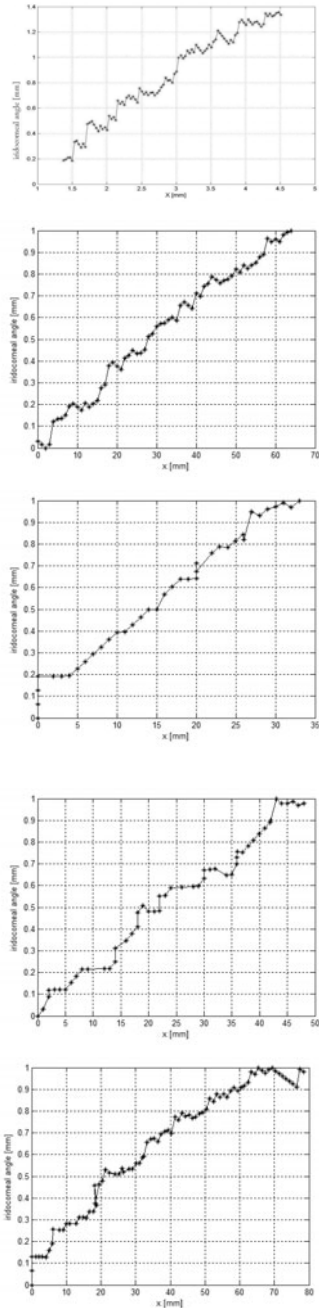
Fig. 15 Results of the automatic measuring of the iridocorneal angle

5 Conclusion

- Automatic analysis of the anterior segment of the eye allows for obtaining reliable results in under 3.5 seconds.
- Evaluation of the algorithm's sensitivity to parameters change, specifically the area of the search for the iridocorneal angle, indicates the greatest dependence on the size of area of the search for the size of iris in pathological cases.
- For 70.736 images, correct results were obtained in about 55.000 cases. Approximate number of correct measures is the consequence of difficulties in evaluation and proposing of the correct operation of the algorithm.
- The greatest error in measuring, excluding errors in choice of method and its sensitivity, appeared for the AOD and TIA methods.
- Based on the obtained experience in measuring the iridocorneal angle, an original method of measuring was proposed.

References

1. Ishikawa, H., Schuman, J.S.: Anterior segment imaging: ultrasound biomicroscopy. Ophthalmol. Clin. North Am. 17(1), 7–20 (2004)
2. Kai-shun, L.C., Li, H., Neal, W.R., Liu, J., Yim, L.C., Yiu, K.L.R., Pui, P.C., Shun, C.D.: Anterior Chamber Angle Measurement with Anterior Segment Optical Coherence Tomography: A Comparison between Slit Lamp OCT and Visante OCT IOVS, vol. 49(8), pp. 3469–3474 (August 2008)
3. Koprowski, R., Wrobel, Z.: Hierarchic approach in the analysis of tomographic eye image, sent to International Fuzzy Systems Association. In: 2009 IFSA World Congress, Lizbona, Portugalia, July 20-24 (2009)
4. Koprowski, R., Wrobel, Z.: Layers recognition in tomographic eye image based on random contour analysis. In: Computer Recognition Systems 3. Advances in Intelligent and Soft Computing, vol. 57, pp. 471–478. Springer, Heidelberg (2009)
5. Koprowski, R., Wrobel, Z.: Identification of layers in a tomographic image of an eye based on the Canny edge detection. In: Conference on Information Technologies in Biomedicine (2008)
6. Radhakrishnan, S., See, J., Smith, S.D., Nolan, W.P., Ce, Z., Friedman, D.S., Huang, D., Li, Y., Aung, T., Chew, P.T.K.: Reproducibility of Anterior Chamber Angle Measurements Obtained with Anterior Segment Optical Coherence Tomography IOVS, vol. 48(8), pp. 3683–3688 (August 2007)
7. Yoo, C., Hyun, O.J., Yeon, K.Y., Hai, R.J.: Peripheral Anterior Synechiae and Ultrasound Biomicroscopic Parameters in Angle Closure Glaucoma Suspects. Kor. J. Ophthalmol. 21(2) (2007)

Parametric Curves in Liver Deformation for Laparoscopic Purposes

Monika Bugdol and Jan Juszczyk

Abstract. An increasing number of conducted endoscopic procedures results in inventing new computer systems, that would be a helpful tool in this kind of medical examinations. In this paper the need of evaluating algorithms describing the deformation of internal organs for laparoscopic surgery purposes is presented. A possible solution to the problem of visualising such deformations has been suggested. Furthermore, the way of collecting data by studying the liver reaction to an external force was described. A model of the liver deformations based on Bézier curves has been developed and compared with the shape of the real liver deformation.

1 Introduction

The technological progress makes us eager to take advantage of the modern world benefits. This applies also to medicine. The laparoscopic surgery, chosen more and more enthusiastically, features qualities that are difficult to overestimate. First of all, the incision is much smaller than during a traditional surgery and results in significantly shorter recovery time and inconspicuousness of the scar. Especially the latter, as an esthetic factor, becomes nowadays more and more important. Secondly, medical consequences are also less troublesome. Reduced haemorrhaging decreases the probability of the need of a blood transfusion. The patient is able to leave the hospital and get back to his everyday activity faster. The post-operative pain is much lower, thus the convalescent takes less medication. Moreover, the risk of acquiring infections is reduced since internal organs are not as much exposed to external contaminants as during a conventional surgery.

Nevertheless, there are still some inconveniences, that could be reduced. The most important of them is the visualisation issue. Currently, a small section of the

Monika Bugdol · Jan Juszczyk
Silesian University of Technology, Akademicka 16st., 44-100 Gliwice, Poland
e-mail: monika.bugdol@polsl.pl, jan.juszczyk@polsl.pl

abdomen can be seen by using the laparoscope camera, which often turns out to be insufficient. That is the reason, why attempts are made to create a computer system, which would solve the problem. The camera display can be supported by a 3D patient model, built on the basis of CT scans of the subject. However, since the pre-operative patient model does not reflect changes of shape of the anatomical structure during the surgical procedure, one of the tasks is to superimpose the deformations of the internal organs caused by the trocar movements and pressure. An algorithm estimating the organ shape change is expected to be both very efficient, so that real-time model deformations are possible, as well as very realistic [1]. Many methods hava been implemented to simulate soft tissue deformations: spring-mass models [2], free form deformations [4], various finite element methods (FEM) [6, 7, 8, 9] and combinations of the finite element method with other methods like linear [5] or non-linear elasticity [1]. The FEM method is very popular because of its high accuracy in organ deformations [10, 11, 12, 13, 14], yet it is very time-consuming. Various methods have been introduced to reduce the computational cost of the FEM, yet the insufficient efficiency still remains an unsolved problem [12, 13, 14].

While evaluating a new algorithm, conditions of a real laparoscopic surgery are assumed - the abdomen is considered being filled with carbon dioxide gas after insufflation, the liver lies naturally on the stomach, is linked to the diaphragm and its physical properties differ in various places. The main goal of this study is to simulate the liver deformation under the pressure of an external force.

2   Data Collecting

The liver deformation has been observed using a pig liver extracted from the animal body 10 minutes before the experiment started (Fig. 1). The liver has been taken out of the abdomen taking precautions not to injure the organ. The diaphragm has not been removed to minimise the risk of making any damage to the coronary ligament.

The applied force has been measured by Biopac MP36 - a biomedical data acqui-sition system. The dynamometer included in the original set has been adapted to the

Fig. 1 The tested liver

study by adding a cylindrical tip that imitates a trocar (Fig. 2). It has been assumed, that the angle between the external force vector and the surface normal of the plane tangential to the liver surface at the contact point of the trocar and the organ is no more than 45 degrees.

Fig. 2 The used dynamome-
ter

While studying the size and shape of the organ deformation the radius and the depth of the strain are tested. The measuring accuracy for both radius and depth values has been 1 mm. Since the liver physical properties change due to the presence of blood vessels, the measurements have been performed in different lobe parts as well as on the coronary and falciform ligament. Photos have been taken from several perspectives on each experiment. Moreover, several plaster casts of the liver deformation have been made to improve the accuracy of the deflection measurement.

3   Deformation Modelling

Let W be the set of all points forming the liver:

$$W = \left\{ w : w \in \mathbb{R}^3 \wedge w \in \text{liver} \right\}. \tag{1}$$

While evaluating the deformation model it has been assumed, that the vector of the external force $\mathbf{F}$ acting on the organ and the contact point X are given as:

$$\mathbf{F} = [f_1 \ f_2 \ f_3], \tag{2}$$

$$X = (x_1, x_2, x_3). \tag{3}$$

F is the length of the force vector $\mathbf{F}$:

$$F = \| \mathbf{F} \| \quad [\text{N}] \tag{4}$$

and will be called force from now on.

The experiment has shown that the deflection depth h and the force F are directly proportional and the dependence can be approximated as:

$$h \approx \begin{cases} 10 \cdot F & \text{if} \quad X \in \text{coronary ligament} \\ 20 \cdot F & \text{if} \quad X \in \text{falciform ligament} \\ 40 \cdot F & \text{if} \quad X \in \text{the remaining part of the liver} \end{cases} \quad [\text{mm}]. \quad (5)$$

Furthermore, the studies have revealed that the dependence between the deflection depth h and the radius r might be described as:

$$r \approx 1.5 \cdot h. \quad (6)$$

The location U, reached by the the trocar tip after the pressure, is defined as:

$$U = (x_1 + m \cdot f_1, x_2 + m \cdot f_2, x_3 + m \cdot f_3). \quad (7)$$

RR is a set of points whose Euclidean distance ρ between X and r differ less than a fixed threshold t. In other words it is a set of those surface points that build a circle inside which all points will change their position:

$$RR = \{w : w \in W \wedge \rho(w, X) < t\}, \quad (8)$$

$$s = \overline{\overline{RR}}, \quad (9)$$

Since it is assumed, that the average angle between the neighbour curves is not smaller than 10 degrees, the number of curves l, on which the deflection surface is built is given as:

$$l = \min(s, 36). \quad (10)$$

If l is equal to or less than 36, all the elements from RR will be curve endings. Otherwise 36 elements should be chosen evenly:

$$R = \{r_1, r_2, \ldots, r_l : \forall i \ r_i \in RR\}. \quad (11)$$

Splines of cubic Bézier curves are employed to model the deflection surface since they are enough complex to accurately project the deformation shape yet their computional cost is acceptably small. The set R contains points that will be the first control points in the first Bézier curve. Each of the l curves is a spline of two Bézier curves of degree three:

$$\forall i \in \{1.2, \ldots, l\} \quad C_i = C_{1i} \oplus C_{2i}, \quad (12)$$

where:

$$C_{1i} = r_i(1-t)^3 + 3q_{1_i}(1-t)^2 t + 3q_{2_i}(1-t)t^2 + p_i t^3, \quad t \in \{1.2, \ldots, l_1\} \quad (13)$$

$$C_{2i} = p_i(1-t)^3 + 3s_{1_i}(1-t)^2 t + 3s_{2_i}(1-t)t^2 + Ut^3, \quad t \in \{1.2, \dots, l_2\} \quad (14)$$

where $p_i, q_{1_i}, q_{2_i}, s_{1_i}, s_{2_i}$ are control points which are calculated as explained below and l_1, l_2 are the numbers of points for which the curve values are computed.

Parameters of the Bézier curve have been estimated by applying curves which precisely reflect the shape of the plaster cast slope. The inflection point p_i as well as $q_{1_i}, q_{2_i}, s_{1_i}, s_{2_i}$ in the model are calculated by minimasing the sum of the square euclidean distances between them and the corresponding point from the casts. A line parallel to the vector $\mathbf{U} - \mathbf{X}$ is computed and the point where it crosses the line segment $\overline{Ur_i}$ can be on the one hand defined as $\mathbf{U} + (\mathbf{r_i} - \mathbf{U}) \cdot a$, on the other as $\mathbf{q_{1_i}} + (\mathbf{U} - \mathbf{X}) \cdot b$. Using the values of $p_i, q_{1_i}, q_{2_i}, s_{1_i}, s_{2_i}$ obtained from the casts, for each of them a and b are calculated. Since the only points known are X, U and for every curve another r_i is given, all parameters describing the deformation have to be defined by the means of them. Fig. 3 shows the q_{1_i} value defined by U, X, r_i. While calculating the control points in the model, first the point on the line segment $\overline{Ur_i}$ is computed and then translated by the vector $\mathbf{U} - \mathbf{X}$ multiplied by an appropriate proportion factor b (Fig. 3).
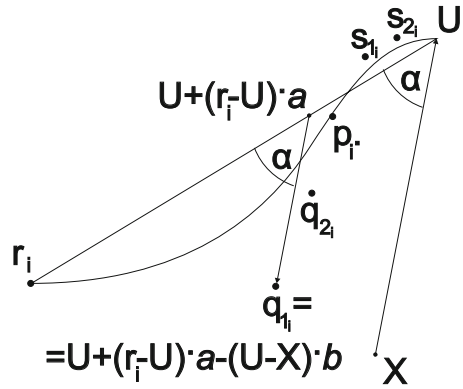
Fig. 3 Estimating the model parameters

On the basis of r_i, U and X the following parameters can be computed:

$$\forall i \; p_i = U + (r_i - U) \cdot 0.15 - (U - X) \cdot 0.23, \quad (15)$$

$$\forall i \; q_{1_i} = U + (r_i - U) \cdot 0.53 - (U - X) \cdot 0.47, \quad (16)$$

$$\forall i \; q_{2_i} = U + (r_i - U) \cdot 0.32 - (U - X) \cdot 0.70, \quad (17)$$

$$\forall i \; s_{1_i} = U + (r_i - U) \cdot 0.09 - (U - X) \cdot 0.07, \quad (18)$$

$$\forall i \; s_{2_i} = U + (r_i - U) \cdot 0.1 - (U - X) \cdot 0.1. \quad (19)$$

4   Results

Negative plaster casts of the liver surface being deflected in different points were made (Fig. 4 a)). Next, pictures of the casts were taken so that the sagittal cross-section is visible. For chosen images thresholding and edge detection were performed. This curve was compared to the one obtained using the model by computing the area between them. It ranges between 10 mm^2 and 15 mm^2 for various plaster casts. It has not exceeded 10% of the overall area above the dotted line in Fig. 4b. In the model the following values were fixed: l_1=10 and l_2=4. In Fig. 5 a) and b) an example of a liver deformed using the new model can be seen.

a)

b)
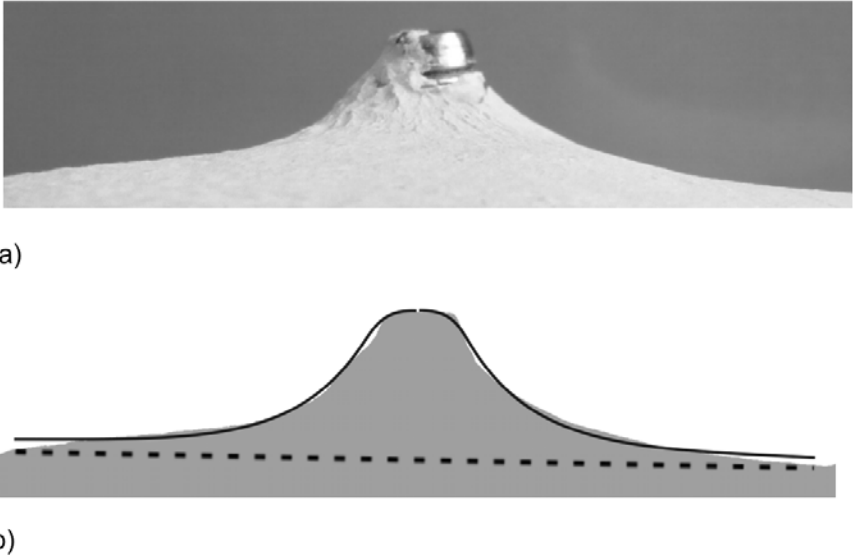
Fig. 4 a) Plaster cast b) Comparison of the cast shape and the model curve

a)   b)
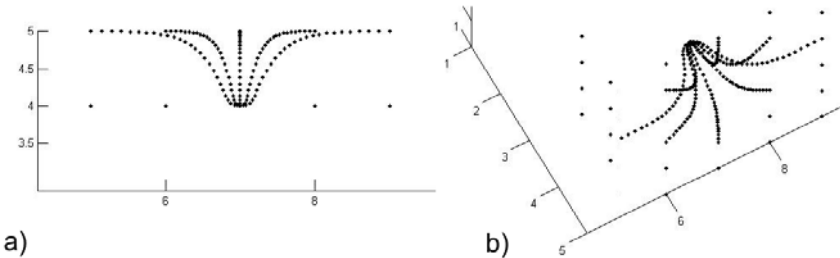
Fig. 5 An example of liver surface deformation

5 Future Works

Studies on the liver deformation will be continued. Various shape pressure tools will be used in order to examine the reaction of the organ to different instruments. The model is going to be supplemented with the possibility of piercing the tissue and visualisation of the tumour movement inside the liver.

References

1. Picinbono, G., Delingette, H., Ayache, N.: Nonlinear and anisotropic elastic soft tissue models for medical simulation. In: IEEE International Conference on Robotics and Automation, vol. 2, pp. 1370–1375 (2001)
2. de Casson, F.B., Laugier, C.: Modeling the dynamics of a human liver for a minimally invasive surgery simulator. In: Taylor, C., Colchester, A. (eds.) MICCAI 1999. LNCS, vol. 1679, pp. 1156–1165. Springer, Heidelberg (1999)
3. Lamy, D., Chaillou, C.: Design, implementation and evaluation of an haptic interface for surgical gestures training. In: International Scientific Workshop on Virtual Reality and Prototyping, pp. 107–116 (1999)
4. Basdogan, C., Ho, M., Srinivasan, S., Small, D., Dawson, S.L.: Force interaction in laparoscopic simulation: haptic rendering soft tissues. In: MMVR, ch. 6, pp. 28–31 (1998)
5. Debunne, G., Desbrun, M., Barr, A., Cani, M.-P.: Interactive multiresolution animation of deformable models. In: CAS 1999 (1999)
6. Bro-Nielsen, M., Cotin, S.: Real-time volumetric deformable models for surgery simulation using finite elements and condensation. In: Eurographics 1996, pp. 57–66 (1996)
7. Cotin, S., Delingette, H., Ayache, N.: Real-time elastic deformations of soft tissues for surgery simulation. IEEE Transactions on Visualization and Computer Graphics 5, 62–73 (1999)
8. Cotin, S., Delingette, H., Ayache, N.: A hybryd elastic model for real-time cutting, deformations and force feedback for surgery training and simulation. The Visual Computer 16, 437–452 (2000)
9. Picinbono, G., Lombardo, J.C., Delingette, H., Ayache, N.: Improving realism of a surgery simulator: linear anisotropic elasticity, complex interactions and force Extrapolation. Journal of Visualization and Computer Animation (2001)
10. Debunne, G., Desbrun, M., Cani, M., Barr, A.: Dynamic real time deformations using space an time adaptive sampling. In: SIGGRAPH, pp. 31–36 (2001)
11. Wu, X., Downes, M.S., Goktekin, T., Tendick, F.: Adaptive nonlinear finite elements for deformable body simulation using dynamic progressive meshes. In: Eurographics, vol. 20, pp. 349–358 (2001)
12. Muller, M., Dorsey, J., McMillan, L., Jagnow, R., Cutler, B.: Stable real-time deformations. In: ACM SIGGRAPH, pp. 49–54 (2001)
13. Nakaguchi, T., Tagaya, M., Tamura, N., Tsumura, N., Miyake, Y.: Real-time deformations of organ based on structural mechanics for surgical simulators. In: SPIE, pp. 2A1–2A6 (2006)
14. Ushiki, S., Matsuguma, C., Koishi, T., Nakaguchi, T., Tsumura, N., Miyake, Y.: Real-time deformation model of liver based on structural mechanics for medical training systems and its accuracy evaluation. Asian Forum on Medical Imaging 2007, IEICE Technical Report 106, 77–80 (2007)

15. Gibson, C.G.: Elementary geometry of algebraic curves: an undergraduate introduction. Cambridge University Press, Cambridge (1998)
16. Goldman, R.: On the algebraic and geometric foundations of computer graphics. ACM Transactions on Graphics 21, 1–35 (2002)
17. Kiciak, P.: Podstawy modelowania krzywych i powierzchni. Zastosowania w grafice komputerowej. Wydawnictwa Naukowo-Techniczne (2000)
18. Jackowski, B.: Co ma Bézier do B-spline'a? Biuletyn GUST 17, 3–12 (2001) (in Polish)

Fractal Analysis of Dental Radiographic Images in the Irregular Regions of Interest

Edward Oczeretko, Marta Borowska, Izabela Szarmach, Agnieszka Kitlas, Janusz Szarmach, and Andrzej Radwański

Abstract. The irregularity or "roughness" of medical images is quantified by means of fractal dimension D. For medical images diagnostically important information often lies in the texture. In this paper we describe the application of the intensity difference scaling method for assessment of the fractal dimension D in the irregular regions of interest (irregular ROI-s). Near boundary between different tissues or structures the values of fractal dimensions changed significantly. It is difficult to fit entire regular region of interest within the examined organ with simultaneous inclusion of the relevant fragment, and at the same time to avoid the influence of boundaries.

1 Introduction

Fractals, a concept of the last decades have been successfully applied in many areas of science and technology. One of the most prominent applications is fractal analysis in medicine, especially in modelling of tissues and organs constitution, analysis of different kinds of images and time sequences [13, 16]. Medical images can be treated as surfaces with the intensity at each pixel. For radiological, magnetic

Edward Oczeretko · Marta Borowska · Agnieszka Kitlas · Andrzej Radwański
Department of Medical Informatics, University of Białystok, Sosnowa 64,
15-887 Białystok Poland
e-mail: eddoczer@ii.uwb.edu.pl, mborowska@ii.uwb.edu.pl,
akitlas@ii.uwb.edu.pl, ara2n@wp.pl

Izabela Szarmach
Department of Orthodontics, Medical University of Białystok, Waszyngtona 15A,
15-274 Białystok Poland
e-mail: izaszarmacgr@gmail.com

Janusz Szarmach
Department of Maxillofacial Surgery, Medical University of Białystok,
M. Skłodowskiej-Curie 24A, 15-274 Białystok Poland
e-mail: zchs@umwb.edu.pl
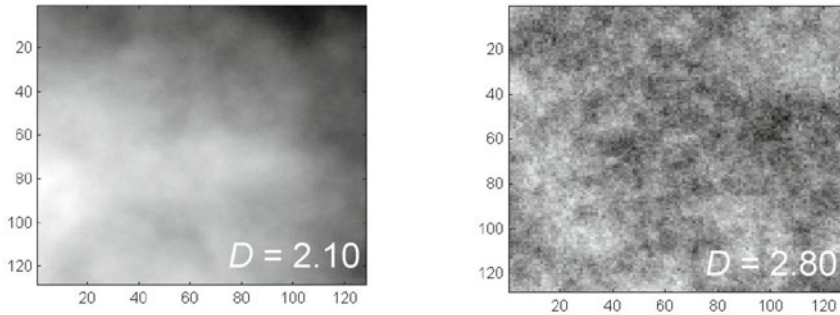
Fig. 1 Synthetic fractal textures with fractal dimension $D = 2.10$ and 2.80. These surfaces were generated by means of Matlab function **synth2**, that is a part of FracLab, a Fractal Analysis Software (www.scilab.org).

resonance or ultrasonic images the grey levels estimate the intensity. For different surfaces the values of the fractal dimension are in the range between 2 and 3. The smooth surface is characterized by fractal dimension of about 2; the rougher surfaces have higher fractal dimensions. The fractal dimension may be used as an index of heterogeneity (Fig. 1). Generally, fractals are the sets for which the Hausdorff–Besicovitch dimension, or the fractal dimension D are greater than topological dimension. The fractal dimension may be calculated in many ways since Hausdorff–Besicovitch's definition is too complicated for practical estimation [9, 2]. Hausdorff definition is a mathematical foundation of various methods of the fractal dimension estimating. Thus, according to various algorithms, there are various kinds of fractal dimension. Thus we can use various algorithms to assess the fractal dimension of medical images. For all the methods, the relationship between selected parameters is governed by a power-law:

$$M(\varepsilon) = C \cdot \varepsilon^{exponent}, \tag{1}$$

where $M(\varepsilon)$ is a result of measurements, ε is a scale, C — is a constant, *exponent* — there is a direct relationship between the exponent and the value of the fractal dimension. Among the algorithms for the calculation of fractal dimension of surfaces are:

- rectangular prism surface area method [4];
- triangular prism surface area method [7];
- power spectral density method [8];
- methods based on mathematical morphology: flat structuring element method [10], and cover blanket method [11];
- dispersion analysis [1];
- variogram analysis [3];
- intensity difference scaling method [5];
- box dimension [6].

These methods were applied in the analysis of various kinds of medical images [12, 13, 14]. In all the cases the studies were performed in regular regions of interest (regular ROI-s) — mostly square regions. Calculation of fractal dimension in irregular regions of interest was described two times in the literature [17, 18]. We showed that in the case of the lung scintigrams, $D = 2.23$ in the region containing the boundary of the organ and $D = 2.59$ within the organ. In order to avoid the influence of the boundaries, and other structures it would be proper to calculate the fractal dimensions in irregular ROI-s. The aim of this study was to show the validity of assessment of fractal dimension in irregular regions of interest, where D can be calculated by means of the intensity difference scaling method.

2   Practical Assessment of Fractal Dimension

In this chapter three methods of calculations of fractal dimension are presented: rectangular prism surface area method ("skyscraper method"), triangular prism surface area method, and intensity difference scaling method.

2.1   Rectangular Prism Surface Area Method — "Skyscraper Method"

Medical images can be treated as surfaces with the intensity $I(x,y)$ at each point (x,y). For nuclear medicine images, the intensity is a number of counts of gamma radiation quantum, whereas for radiological or ultrasonic images the gray levels estimate the intensity. Fig. 2a shows this idea of the "skyscraper" model of medical image [4]. For each element of image matrix (x,y) there is a rectangular prism $\varepsilon \cdot \varepsilon \cdot I(x,y)$, where ε is the length of pixels creating a single element of image matrix. Assuming $\varepsilon = 1$ is more convenient for our calculation. The area $S(\varepsilon)$ of such "skyscraper" surface is expressed by the sum of the areas of the roofs plus the sum of the exposed walls of the rectangular prisms:

$$S(\varepsilon) = \sum_{x,y} \varepsilon^2 + \sum_{x,y} \varepsilon[|I(x,y) - I(x+1,y)| + |I(x,y) - I(x,y+1)|] \qquad (2)$$

$S(\varepsilon)$ was calculated for $\varepsilon = 1$. Afterwards the numbers of counts were averaged for adjacent four elements of the image matrix ($\varepsilon = 2$) to form a new image matrix and $S(\varepsilon)$ was computed. Repeating this averaging process we calculated $S(\varepsilon)$ for $\varepsilon = 4, 8, 16$ and so on. The matrix of the investigated image must be square. The empirical relationship between $S(\varepsilon)$ and ε is:

$$S(\varepsilon) = C \cdot \varepsilon^{2-D}, \qquad (3)$$

where C is a constant, D is the fractal dimension. Values of D can be obtained using least-squares linear regression to estimate the slope of line of $S(\varepsilon)$ versus ε in ln-ln scale.
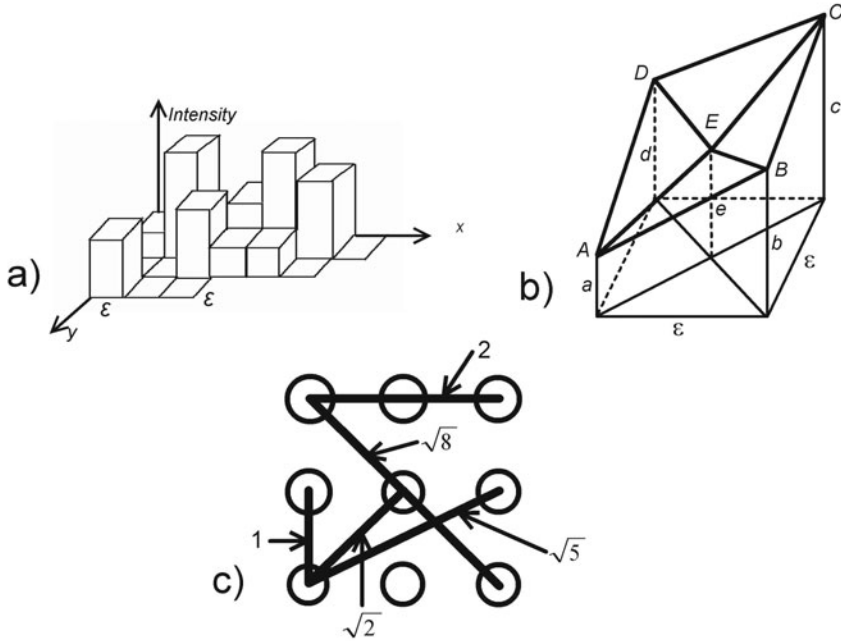
Fig. 2 a) The "skyscraper" model of medical image, b) Creation of triangular prism, c) 3×3 image. There are 5 possible scales. The total number of pixel pairs for these scales is 38.

2.2   Triangular Prism Surface Area Method

The idea of triangular prism surface area method is presented on Fig. 2b. Let a, b, c and d represent the number of counts in four adjacent pixels, e is the mean, $e = (a + b + c + d)/4$. The area of surface $S(\varepsilon)$ is the sum of areas of triangles DCE, DAE, ABE and CBE [7]. We calculate the $S(\varepsilon)$ for all image. By repeating this for different size of squares, the relationship (3) between the total area and the spacing of squares is used to estimate the fractal dimension. Here the image matrix must have the shape of a square.

2.3   Intensity Difference Scaling Method

For given $M \times M$ image the multi-scale intensity difference vector IDV is defined as follows [5]:

$$MIDV = [id(1), id(2), id(3), \ldots, id(smax)], \tag{4}$$

where $smax$ is the maximum possible scale, $id(s)$ is the average of the absolute intensity difference of all pixel pairs with scale s.

$$cd(s) = \frac{1}{N_S} \sum_{x_1=0}^{M-1} \sum_{y_1=0}^{M-1} \sum_{x_2=0}^{M-1} \sum_{y_2=0}^{M-1} |I(x_2, y_2) - I(x_1, y_1)|, \qquad (5)$$

where $I(x_1, y_1)$ and $I(x_2, y_2)$ are two pixels in the image with intensity values between 0 and 255; N_S is the number of pixel pairs for scale s, scale s (distance between two pixels):

$$s = \sqrt{(x_2 - x_1)^2 - (y_2 - y_1)^2} \qquad (6)$$

Fig. 2c shows 3×3 image. There are 5 possible scales, 5 possible distances between pixels. The total number of pixel pairs analyzed for these scales is 36. For 27×27 images the number of all scales is 314, for 63×63 images the number of all scales is 1529, and the total number of pixel pairs analyzed for these scales is 31505922. To reduce the number of elements of *MIDV* vector, normalized *NMIDV* vector was used in which only integer scales occurred. Non-integer scales were not lost. For example, information from scales: $\sqrt{5}$, $\sqrt{8}$, $(2.2361, 2.8284)$ was included in scale 2. For fractal surfaces the relationship between *MIDV* and scale s is governed by a power-law:

$$MIDV = C \cdot s^{3-D} \qquad (7)$$

3   Irregular Regions of Interest

By means of the intensity difference scaling method we could assess the values of fractal dimension in irregular ROI-s, which is impossible by means of other algorithms. Fig. 3a shows the 5×5 image with 25 pixels and 14 possible scales. The total number of pixel pairs analyzed for these scales is 300. Fig. 3b illustrates manually drawn irregular region of interest **R** with 11 pixels and 9 possible scales. In calculation only pixels belonging to regions **R** were used.
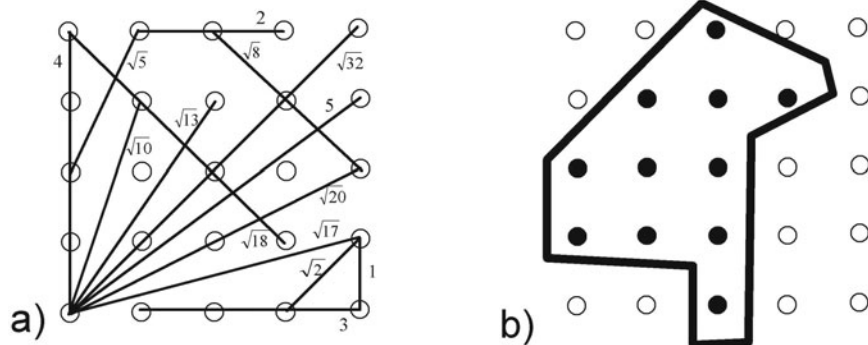
Fig. 3 a) 5×5 image. There are 14 possible scales. The total number of pixel pairs analyzed for these scales is 300. b) Manually drawn irregular region of interest with 11 pixels and 9 possible scales.
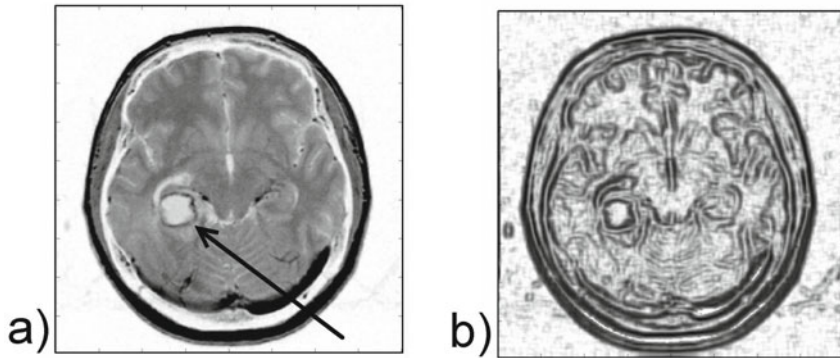
Fig. 4 a) Original MR images (the arrow shows the tumor), b) Transformed images in which the value of each pixel is the fractal dimension

4 Experiments – Intensity Difference Scaling Method

Program for fractal analysis was written in Visual Basic (Microsoft .NET Framework 3.5).

4.1 *Magnetic Resonance Image*

Magnetic resonance (MR) image of the brain was obtained using 1.5T MR scanner (Picker Edge Eclipse) with standard circulatory polarized head coil. We calculated fractal dimension over the whole 512×512 image in each pixel by calculating the dimension of a 9×9 pixel block centered on that pixel. In the obtained images the value of each pixel was the fractal dimension. Fig. 4a illustrates an original 512×512 image (the arrow shows the tumour). Fig. 4b shows transformed image in which the value of each pixel is the fractal dimension. The tumour is more obvious. The edges of other structures were enhancement too.

By means of the fractal analysis we can detect and enhance edges in the analyzed image, which may a diagnostic significance. Near boundary between different tissues or structures the values of fractal dimensions changed significantly, which enables edge enhancement.

4.2 *Pantomogram (Panoramic Radiograph)*

Pantomogram is a panoramic radiographic record obtained by a pantomograph. It shows maxillary and mandibular dental arches and their associate structures. Pantomograms were digitized with an Umax Alpha Vista II scanner (LaserSoft Imaging Inc., USA), interfaced through a scan software program (SilverFast Applications) to a computer. Fig. 5a shows the pantomogram with two marked regular regions. Figures 5b and 5c show the regular regions of interest from Fig. 5a. Inside of these
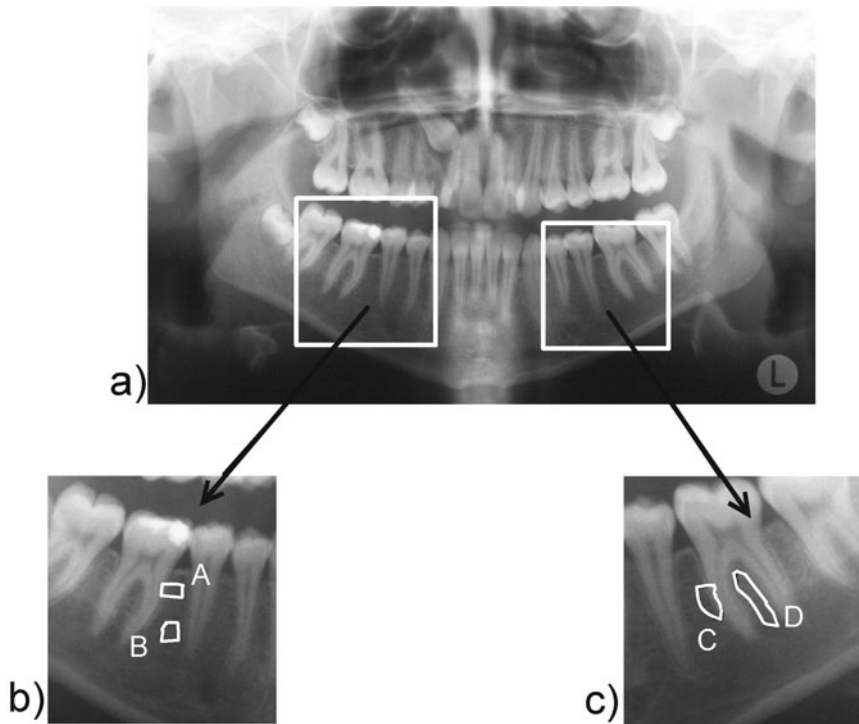
Fig. 5 a) Panoramic radiograph with marked two regular regions, b, c) Regular regions with marked irregular ROI-s

Table 1 Results of fractal analysis in irregular regions of interest (Fig. 5b and Fig. 5c)

Irregular Regions	Fractal dimension D	Number of scales	Number of pixel pairs
A	2.461	1891	2377290
B	2.848	4005	8110378
C	2.313	3160	4286846
D	2.777	6903	7689081

regions irregular ROI-s A, B, C and D were marked. Table 1 shows the results of fractal analysis in the irregular regions. When the irregular ROI contain the boundaries and fragment of the teeth the value of fractal dimension is relatively low.

4.3   Dental Radiovisiographic Image

The study was based on the analysis of radiovisiogram of patient treated with prosthetic implants in a private dental practice due to a missing tooth. In the patient,

Table 2 Results of fractal analysis in irregular regions of interest (Fig. 6)

Irregular Regions	Fractal dimension D	Number of scales	Number of pixel pairs
A	2.306	7626	265054121
B	2.596	10878	31541653
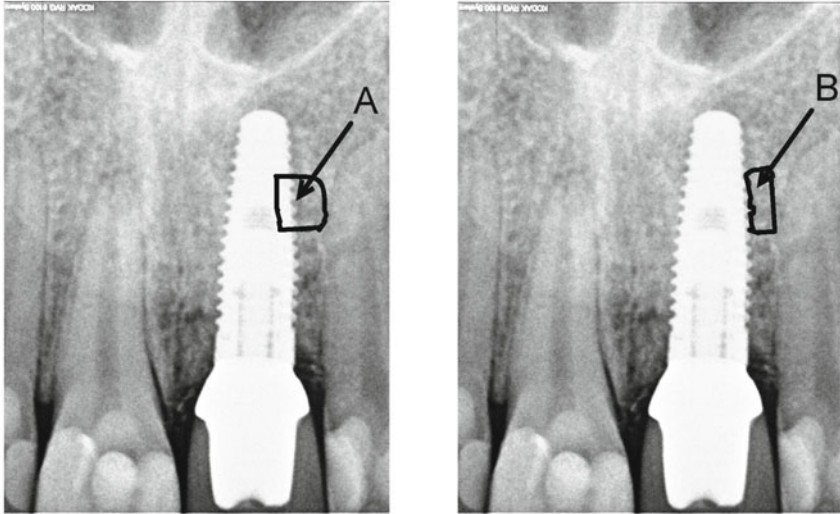
Fig. 6 Radiovisiographic images with marked two irregular regions A and B. Irregular region B was drawn close to the implant, but it did not contain the elements of the implant.

Nobel Biocare implant was used — intraosseous, screw-type, made up of pure titanium (99.75% titanium, 0.05% iron, 0.1% oxygen, 0.03% nitrogen, 0.05% carbon, 0.012% hydrogen). X-ray picture was obtained using a KODAK RVG 6100 set. Radiovisiogram was done after 6 months after implantation. Table 2 summarizes the results of fractal analysis of irregular region of interest (Fig. 6). When the irregular ROI contain the boundary and fragment of the implant the value of fractal dimension is low ($D = 2.306$).

5 Conclusions

Medical images are often complex, irregular and noisy. The diagnostic information often lies in the texture. In the case of dental radiographic images the boundaries of the analyzed structures change significantly the values of fractal dimension. It is difficult to fit the entire regular region of interest within the examined organ with simultaneous inclusion of the relevant fragment avoiding the influence of boundaries

and other kinds of unnecessary structures at the same time. Our method of assessment of fractal dimension in irregular regions of interest solves these difficulties.

References

1. Bassingthwaighte, J.B.: Physiological heterogeneity, fractals link determinism and randomness in structures and functions. News Physiol. Sci. 3, 5–10 (1988)
2. Besicovitch, A.: On the fundamental properties of linearly measurable plane sets of points. Math. Ann. 98, 422–464 (1928)
3. Bianchi, F., Bonetto, R.: FERimage: an interactive program for fractal dimension, d(per) and d(min) calculations. Scanning 23, 193–197 (2001)
4. Caldwell, C.B., Moran, E.L., Bogoch, E.R.: Fractal dimension as a measure of altered trabecular bone in experimental inflammatory arthritis. J. Bone Miner Res. 13(6), 978–985 (1998)
5. Chen, C.C., Daponte, J.S., Fox, M.D.: Fractal feature analysis and classification in medical imaging. IEEE Trans. Med. Imaging 8, 133–142 (1989)
6. Chen, S.S., Keller, J.M., Crownover, R.M.: On the calculations of fractal features from images. IEEE Trans. Patt. Anal. Machine Intell. 15(10), 1087–1090 (1993)
7. Clarke, K.C.: Computation of the fractal dimension of topographic surfaces using the triangular prism surface area method. Comp. Geosci. 12, 713–722 (1986)
8. Dennis, T.J., Dessipris, N.G.: Fractal modelling in image texture analysis. IEEE Proc.-F 136, 227–235 (1989)
9. Hausdorff, F.: Dimension und äußeres Maß. Math. Ann. 79, 157–179 (1918)
10. Maragos, P., Sun, F.-K.: Measuring the fractal dimension of signals: morphological covers and iterative optimization. IEEE Trans. Signal Process. 41(1), 108–121 (1993)
11. Peleg, S., Naor, J., Hartley, R., Avnir, D.: Multiple resolution texture analysis and classification. IEEE Trans. Pattern Anal. Mach. lntell. 6(4), 518–523 (1984)
12. Losa, G.A., Merlini, D., Nonnemacher, T.F., Weibel, E.R.: Fractals in Biology and Medicine, vol. II. Birkhäuser Verlag, Basel (1998)
13. Losa, G.A., Merlini, D., Nonnemacher, T.F., Weibel, E.R.: Fractals in Biology and Medicine, vol. III. Birkhäuser Verlag, Basel (2002)
14. Losa, G.A., Merlini, D., Nonnemacher, T.F., Weibel, E.R.: Fractals in Biology and Medicine, vol. IV. Birkhäuser Verlag, Basel (2005)
15. Umbaugh, S.E.: Computer vision and image processing: A practical approach using CVIP tools. Prentice Hall PTR, Upper Saddle River (1998)
16. Oczeretko, E.: Wymiar fraktalny w analizie sygnałów i obrazów biomedycznych. Wydawnictwo Uniwersytetu w Białymstoku, Białystok (2006) (in Polish)
17. Oczeretko, E., Rogowski, F., Jurgilewicz, D.: Fractal analysis of nuclear medicine scans. In: Losa, G.A., Merlini, D., Nonnemacher, T.F., Weibel, E.R. (eds.) Fractals in Biology and Medicine, vol. II. Birkhäuser, Basel (1998)
18. Oczeretko, E., Borowska, M., Kitlas, A., Borusiewicz, A., Sobolewska-Siemieniuk, M.: Fractal analysis of medical images in the irregular regions of interest. In: 8th IEEE International Conference on Bioinformatics and BioEngineering, Athens, CD, October 8–10 (2008), ISBN: 978-1-4244-2845-8

Computer-Assisted Navigation in Brain Tumor Surgery

Zbigniew Kotwica and Agnieszka Saracen

Abstract. Despite a great advancements in brain tumor diagnosis and surgery, a precise intraoperative location and removal of the neoplasmatic tissue remains difficult in many patients. For these reasons different navigation systems were developed. For the last several years neuronavigation has become widely used in brain tumor surgery. Surgical removal remains difficult in patients with small and deep seated brain lesions, multiple tumors, or location in important functional areas of the brain. Neurosurgeon faces the problem of causing severe neurological deficit as well as can have problems with finding and removing the lesion. Use of key hole procedures and surgical microscopes minimizes an operation field what forces to have a perfect orientation in the operation area, as well as precise data about the actual position of the instruments and their distance from the lesion. GOAL AND PURPOSE: Basing on their own surgical experience of 30 patients with brain tumors, the authors show the advantages and limitations of neuronavigation in surgical removal of brain tumors. MATERIAL AND METHODS: 30 patients with brain tumors located deeply in the hemispheres, skull and posterior fossa were analyzed. All patients were treated surgically with the use of neuronavigation equipment (Stryker Intellect Cranial Navigation System). Microsurgical technique with the use of magnification was introduced in all patients. After surgery, controlled CT examinations were performed in order to check the extension of tumor removal. RESULTS: Total surgical removal had been achieved in all patients. In all but one clinical result was excellent, the last patient died 2 weeks after removal of giant hypophyseal adenoma because of heart failure. CONCLUSIONS: Neuronavigation is an easy to use system which brings efficiency to surgical procedures. It allows to get a proper orientation in the operation field resulting in safe and accurate removal of intracranial neoplasms.

Zbigniew Kotwica
Department of Neurosurgery, WestPomorian District Hospital, Niechorska 27,
Gryfice, 72-300 Poland
e-mail: zbigniew.kotwica@neostrada.pl

Agnieszka Saracen
Institute of Health Sciences, Technical University of Radom, Malczewskiego 20a,
26-400 Radom, Poland
e-mail: saracena@op.pl

1   Introduction

Brain tumors present certain challenges in terms of kind of surgical treatment, sur-gical strategies, and the extension of removal [2, 7, 9, 13]. Presence of benign lesion is almost always an indication for surgical removal, and in glioma patients at some point during the course of the disease surgical treatment becomes a necessity, at least in order to perform a biopsy [2, 10]. It is also known that glioma patients ben-efit from surgical cytoreduction, however, it should be performed with a maximal safe in order to avoid eventual postoperative neurological deficits [2, 10]. In order to reduce surgical morbidity, different types of neronavigation systems have been developed. The most common is computed tomography - CT or magnetic resonance imaging - MRI guided navigation, which bases on the previously loaded examina-tion performed with several markers attached to the skin of the head. During sur-gical procedure special pointers are recorded by the machine and show the actual position of the instrument in the operation field using previously loaded pictures [4, 6, 8, 9, 13]. In last years, real time neuronavigation systems were developed, basing on intraoperative, real-time performed MRI studies [5, 7, 9, 11]. It also al-lows to integrate actual pictures with brain mapping - magnetoencephalography or positron emission tomography, what allows to recognize precisely the location of important functional areas [1, 3, 11, 15].
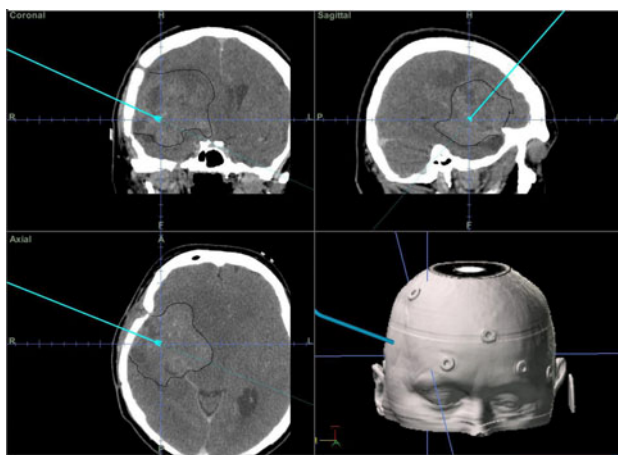
Fig. 1 Large glioma of the right hemisphere infiltrating deep structures. The mass of the tumor is outlined. CUSA tube is seen within the pathological mass.

Neuronavigation also brings precise information about surrounding structures, the most important are vessels, what helps to avoid severe damage to the brain. A precise location of the instruments is especially helpful in patients with deep-seated lesions [1, 3, 4], in sellar -suprasellar area [14], where it allows to avoid damage to important neurovascular structures located in the vicinity of tumors [1, 11], in skull

base surgery [7, 13] and in ventricular area [2, 10]. Integration with functional magnetic resonance imaging, positron emission tomography or magnetoencephalography brain mapping allows to perform functional neurosurgical procedures [4, 11] used in surgical treatment of epilepsy [1, 2, 15], or some psychotic diseases [6, 9]. It also allow to implement precisely different brain tissue stimulators, used for epilepsy or pain treatment [8, 15]. Development of microsurgical techniques has allowed to operate small, deeply located intracerebral lesions in clinically asymptomatic patients, and thus minimally invasive approach is extremely important in order to avoid brain damage, which could produce neurological deficits.

A perfect orientation in the operation field allows to minimize the extension of craniotomy, leading to key hole surgery. It also shortens the time of surgery [2, 3, 6].

In brain tumor surgery, navigation is especially helpful in tumors infiltrating deep structures, in parasellar region and in patients with multiple lesions. In tumors of the skull base, the most of them are situated in sellar and parasellar area, the neurosurgeon faces the problem of potential damage to optic chiasm, anterior arteries and anterior communicating artery [2, 8]. In patients with multiple tumors, often located near vital areas neuronavigation allows to remove all tumors or safely perform a biopsy [1, 3].

2 Clinical Material

The authors revealed the files of 30 consecutive patients treated in Neurosurgical Department of WestPomorian District Hospital for cerebral tumors. 16 tumors were located in cerebral hemispheres, deeply in the brain or infiltrating deep structures. 5 patients had large hypophyseal tumors and 9 lesions located deeply in the cerebellum, nearby the cerebral trunk. All patients were treated surgically by one of the authors (ZK).

2.1 Procedures Performed

All the surgical procedures were performed with the use of microsurgical technique and operating microscope – magnification 5 to 10 times. We routinely use surgical laser - Aura XP (AMS, USA) and cerebral ultrasound aspirator (CUSA) for cerebral tumors extirpation. During surgery Stryker Intellect Cranial Navigation System was used. CT studies were previously imported and approaches to the lesions were planned. Tumors as well as the borders of planned excisions were highlighted for easier orientation. Stryker navigation software package is easy to use, especially because it works with PC-based platform, and is friendly to the most users.

With tumors infiltrating the deep structures of the brain the depth of surgery is vital to avoid severe brain damage. Fig. 1 shows a large glioma of the right cerebral hemisphere (outlined). The picture in the right down corner shows the location of the skin markers. The pointer is put on the ultrasound suction tube and shows the location of the instrument within the tumor. It allows the surgeon to avoid too deep removal of the tumor what could result in severe neurological deficit – left-sided hemiplegia.
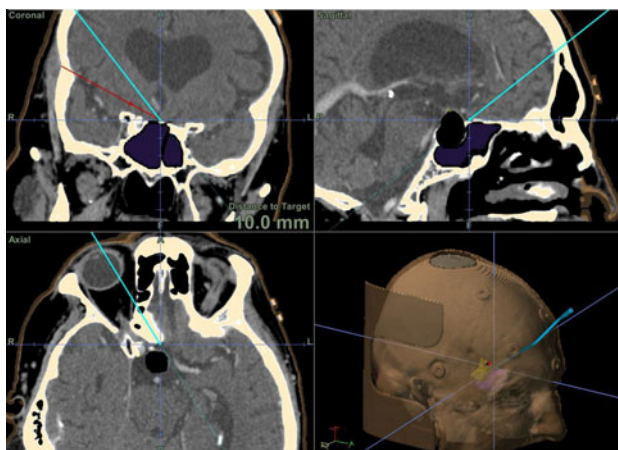
Fig. 2 The pointer shows the border of planned extirpation. Extensive shift of the ventricular system is noted.

Figure 2 shows the pointer situated deeply in the hemisphere. Cytoreduction of the glioma mass has to be stopped in order to avoid postoperative left-sided hemiplegia. Black areas show the left-sided shift of ventricular system caused by the tumor mass.

In tumors of the skull base, the most common of them are located in the sellar area, a distance to the border of the tumor is an important information for a surgeon and such information allows to remove the tumor totally, what can result in a perfect outcome. Fig. 3 shows a large hypophyseal adenoma with a significant extension
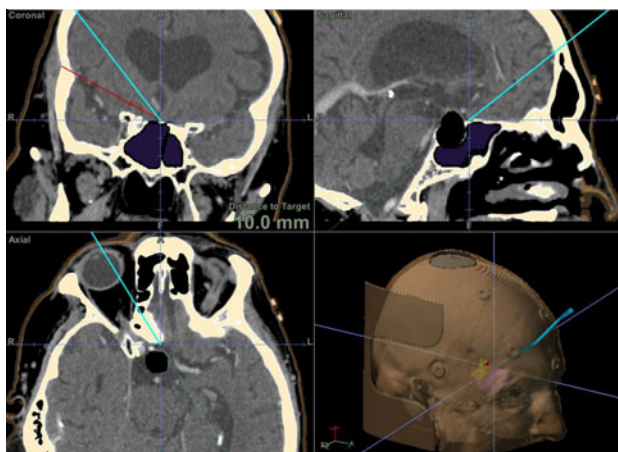
Fig. 3 Large hypophyseal adenoma (marked in black). The end of laser device is on the anterior wall of the lesion.
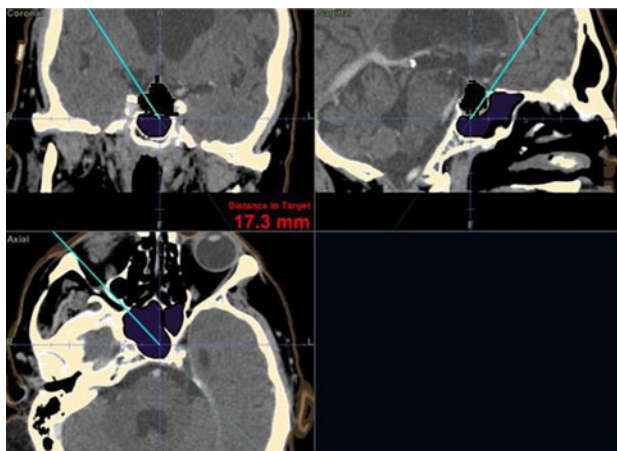
Fig. 4 The end of resection of giant hypophyseal adenoma. The pointer achieves the bottom of the sella, which is free of neoplastic tissue.

above the sellar edge (marked in black). Such an expansion implies subfrontal approach, tumor cannot be removed totally via transphenoidal approach. Navigation pointer is located on the tip of the microsurgical laser device and strictly shows the position of the anterior wall of the tumor.

Figure 4 shows the position of the instrument after removal of tumor. The tip of the instrument has strict contact with the bottom of sella turcica, proving total removal of the adenoma. In subfrontal approach, neurosurgeon faces a problem of visual control of the bottom of the sella, because clinoid processes cover the view of the bottom, not allowing to see it in an operating microscope. Postoperative CT reveals total extirpation of the lesion - Fig. 5.

With multiple and deeply situated lesion the approach to the lesion should be planned precisely and during operation procedure it is necessary to observe the position of the instruments, because it is easy to pass over tumor. Figure 6 shows three deeply located cerebellar tumors 10 to 30 mm in diameter. Tip of the suction tube directly touches the tumor located in the left cerebello-pontine angle. Removal of tumor can be made safely, it also proves, that the tissue given to neuropathological examination has been taken from the tumor mass, not from the surrounding tissues.

After surgery all patients had good clinical result without new neurological deficits. However, one of the patients, with large hypophyseal adenoma, who before surgery complained of severe heart insufficiency, developed vascular complications and died of heart failure 2 weeks later. Postoperative CT scan revealed total extirpation in 24 patients, and subtotal removal in 6 patients. In this last group we did not plan to remove the whole mass in order to avoid severe damage to deep brain structures.

Figure 7 shows the main steps in brain tumor surgery with the use of neuronavigation.

Fig. 5 Postoperative CT. Sella turcica is free of tumor mass.
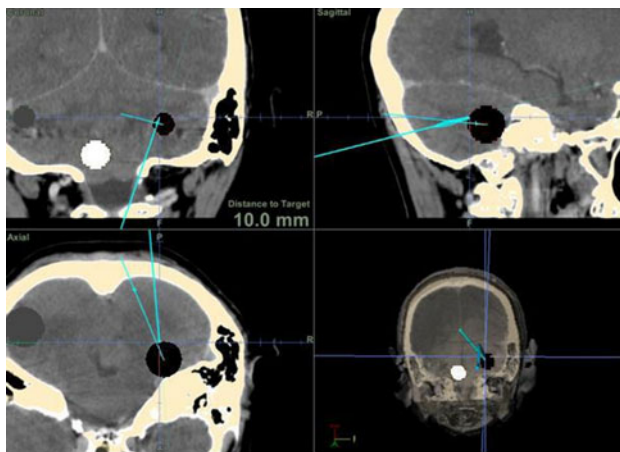
Fig. 6 Three deeply seated cerebellar metastatic tumors. The tip of CUSA is in the mass of the tumor located in the cerebello-pontine angle.
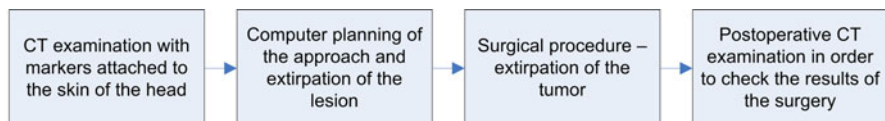
Fig. 7 Main steps in brain tumor surgery

3 Discussion and Conclusions

The figures shown above prove the advantages of computer assisted neuronavigation in brain tumors surgery. It allows to have a good orientation in the actual position of the surgical instruments, shows surrounding areas, gives information about the distance to the borders of the lesion, as well as gives important information about the extension of the tumor removal. Previous planning of the approach to the brain lesion, before starting surgical procedure, allows to minimize an operation field and diminish the possibility of eventual damage of the important structures. However, this type of neuronavigation has important limitations and disadvantages. It does not show the real-time pictures of the brain, and thus, does not give absolutely reliable information. Deviation of the exact location of the instruments usually does not exceed 2-3 millimeters, but we do not obtain real time information. For this reason instrumentation does not give precise information in the bordering areas. It depends on neurosurgeon only when to stop the removal of the lesion and where are the margins of the tumor. In this situation neuronavigation has limitations and does not give any advantages. However, each neurosurgeon who have experience with all conventional techniques can afford this problems, even with a very limited operation field. With the use of laser and CUSA, two tools, which significantly improved the safety of brain surgery, neuronavigation allows to attack lesions, which could not be safely removed without this instrumentation. Limitations of this type of neuronavigation disappear with new types of navigation systems, by means of real time CT or MRI navigation with studies performed at the operation theatre, during surgery [5, 7, 12]. It seems to be a future way to make brain tumor surgery more safe and more effective. Actually the main limit is a very high cost of equipment and only several centers can afford it. The authors actually start to work with a real-time intraoperative MRI guided neuronavigation (Pole Star system) what should give us further experience in the use of neuronavigation in brain tumor surgery.

References

1. Air, E.L., Leach, J.L., Warnick, R.E., McPherson, C.M.: Comparing the risks of frameless stereotactic biopsy in eloquent and noneloquent regions of the brain: a retrospective review of 284 cases. J. Neurosurg. 111, 820–824 (2009)
2. Berger, M.S., Hadjipanayis, C.G.: Surgery of intrinsic cerebral tumors. Neurosurgery 61, 279–304 (2007)
3. Dammers, R., Haitsma, I.K., Schouten, J.W., et al.: Safety and efficacy of frameless and frame-based intracranial biopsy techniques. Acta Neurochir (Wien) 150, 23–29 (2008)
4. Fahlbusch, R., Samii, A.: A review of cranial imaging techniques: potential and limitations. Clin. Neurosurg. 54, 100–104 (2007)
5. Fuji, M., Wakabayashi, T.: Image-guided neurosurgery using intraoperative MRI. Brain Nerve 61, 823–834 (2009)
6. Ganslandt, O., Behari, S., Gralla, J., et al.: Neuronavigation: concept, techniques and applications. Neurology India 50, 244–255 (2002)

7. Iseki, H., Nakamura, R., Muragaki, Y., et al.: Advanced computed aided intraoperative technologies for information-guided surgical management of gliomas: Tokyo Women's Medical University experience. Minim. Invasive Neurosurg. 51, 285–291 (2008)

8. Johnson, R.D., Stacey, R.J.: The impact of new imaging technologies in neurosurgery. Surgeon 6, 344–349 (2008)

9. Jung, T.Y., Jung, S., Kim, I.Y., et al.: Application of neuronavigation system to brain tumor surgery with clinical experience of 420 cases. Minim. Invasive Neurosurg. 49, 210–215 (2006)

10. Simon, M., Schramm, J.: Surgical management of intracranial gliomas. Recent Results Cancer Res. 171, 105–124 (2009)

11. Tanaka, Y., Nariai, T., Momose, T., et al.: Glioma surgery using a multimodal navigation system with integrated metabolic images. J. Neurosurg. 110, 163–172 (2009)

12. Tirakotai, W., Sure, U., Benes, L., et al.: Image guided transsylvian, transinsular approach for insular cavernous angiomas. Neurosurgery 61, 423–430 (2007)

13. Willems, P.W., van der Sprenkel, J.W., Tulleken, C.A., et al.: Neuronavigation and surgery of intracerebral tumours. J. Neurol. 253, 1123–1136 (2006)

14. Xue-Fei, S., Yong-Fei, W., Shi-Qi, L., et al.: Microsurgical treatment for giant and irregular pituitary adenomas in a series of 54 consecutive patients. Br. J. Neurosurg. 22, 636–648 (2008)

15. Zhou, H., Miller, D., Schulte, D.M., et al.: Transsulcal approach supported by navigation-guided neurophysiological monitoring for resection of paracentral cavernomas. Clin. Neurol. Neurosurg. 111, 69–78 (2009)

Computer Aided Alternative Methods of Dental Implants Placement

Jarosław Żmudzki

Abstract. Final product of computer aided dental implants placements is an object created by means of Rapid Prototyping (RP) – surgical template. An essential condition that makes utilization of this special technique possible is computer tomography (CT), which has to be carried out first. Radiation might be in some cases inadvisable, not possible or not necessary. In this work presented are possibilities of using standard CAD techniques for the purposes of planning and assisting of dental implantology treatment based on introduced into a CAD software prosthetic foundation topography and a standard panoramic radiograph.

1 Introduction

Development of computer assisted dental implantology leads to increased number of successful treatments [1]. Virtual models not only support analysis and choice of the most favorable implantological treatment plan, but also makes it possible to achieve a direct support during the phase of surgical bed drilling and implant placement. This support is constituted by surgical templates, thanks to which the accuracy of implant placement is no longer dependant only on prosthodontist's dexterity varying among people but also changing due to some psychophysical factors. Even in case of a safe distance between implant and anatomical nervous system structures or tooth roots, appropriate implant placement decides about successfulness of bone tissues adaptation processes, and hence the possibility of an early implant loading and therefore also rehabilitation. It has also significant influence on the final result's aesthetics. In case, in which higher number of implants are placed under complete overdentures, without a template, it is very hard to achieve satisfying implants parallelism, which directly influences usage (wear) characteristics of solitary attachments joining dentures with implants.

Jarosław Żmudzki

Department of Materials Technology, Silesian University of Technology, 40-019 Katowice, Poland

e-mail: `Jaroslaw.Zmudzki@polsl.pl`

Primary stage in spatial planning systems is imaging of particular area by means of a CT scan and three-dimensional (3D) reconstruction of tissues structures [1, 2]. Finally, achievement of the designed individual template requires placing a chargeable order and creation of template by technology owner [3]. Hence, implantological clinic itself is not able to lower prices of treatments utilizing templates. In a lot of cases there is a contraindication regarding a CT scan [4]. Branch literature tries to convince prosthodontists to avoid such a dose of radiation [5], especially if exposed are younger organisms. As an alternative, implantology point out other implants planning techniques that are based on standard X-ray procedures and gypsum diagnostic models [4, 6, 7, 8, 9]. As opposed to computer assisted techniques, in this case a template can be created in an ordinary dental lab. In spite of labor that they require, manual methods look to be very competitive and they are commonly used. Especially, because they belong to the more comfortable ones and do not cause mucosal membrane flapless [3].

Nevertheless, the basic disadvantages of manual methods are difficulties and limits regarding accuracy of spatial analysis of implant position related to tissues of foundation. Most of the above mentioned difficulties in implants planning can be avoided by inputting the geometry of prosthetic foundation to a standard CAD software, that enable creation of templates by any numerically controlled machining tool. In such case, computer assistance of manufacturing of the template is free from limits imposed in specialized implantologic software, in which after designing a template, manufacturing of such template on our own is not possible as software producers disabled possibility to record the data necessary to control numerical machining tools.

In this work presented are possibilities of improving alternative manual techniques of manufacturing surgical templates by means of CAD/CAM computer support, making it possible to replace manual activities carried out by dental technician, as well as to replace the gypsum diagnostic model with a virtual model.

2   Materials and Methods

Presented is planning of implants placement for lower overdentures. Placement of implants for such dentures requires specially accurate parallelism. Lack of implants parallelism leads to an inappropriate distribution of occlusion loads. Proposed method of computer-assisted implants placement planning requires inputting geometrical data (topography) of prosthetic foundation into the CAD software. Geometrical data has been achieved by tactile scanning of prosthetic foundation gypsum model, by means of scanner-milling machine Roland Modela MDX-20 (Fig. 1). It has to be mentioned here that use of a laser scanner would significantly accelerate this process.

After importing scanned foundation topography to CAD software, it is possible to spatially plan the orientation of implants in relation to mucous surface, by means of relatively simple 3D modeling options. Taking into account bone foundation structure during planning requires inputting into the program all information about their geometry. In case if there is no data related to 3D construction (i.e. 3D
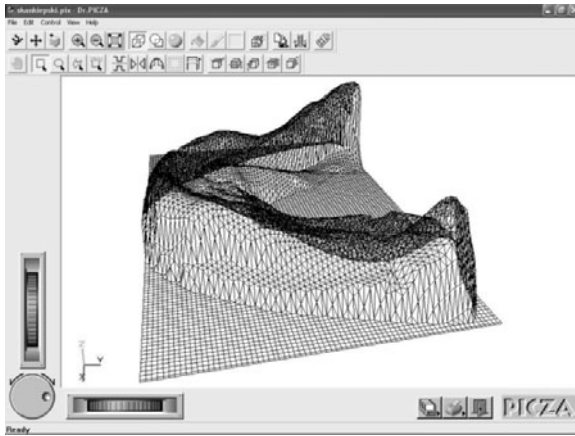
Fig. 1 Prosthetic foundation topography achieved by scanning a model by a Roland scanner

Fig. 2 Implants placement planning based on panoramic radiograph, which is placed and calibrated in the front plane
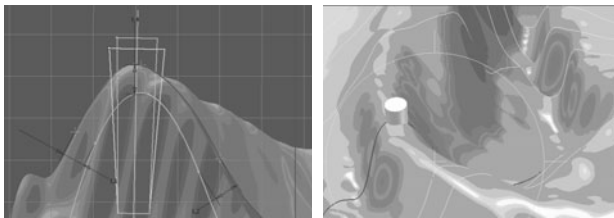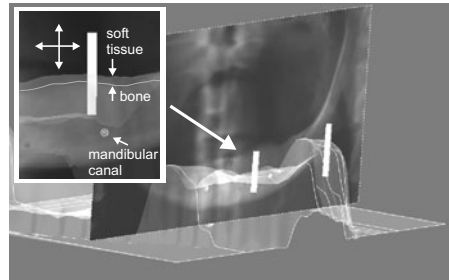
Fig. 3 Estimation of available bone tissue for implant placement

reconstruction from a CT scan) planning can be carried out based on a panoramic radiograph, according to standard procedures of planning implantological treatment. Further implant placement planning stages have been presented on Fig. 2-4. In order to achieve template stability on its foundation there are used fixed pins [10]. Procedures of their location however, has not been presented in this work. Possibilities of the elaborated methodology have been presented in paragraph 3: *Results*.
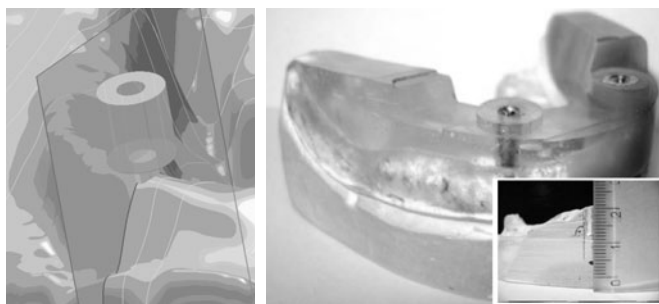
Fig. 4 Designed cylindrical surfaces, necessary in template to fix sleeves, replaced during treatment according to surgical procedure and initial verification of template viability at dental model

3 Results

Standard implant placement planning procedures are based on matching of transparent implant templates (outlines) to foundation, which is represented by a panoramic radiograph [9]. Then, prosthodontist in collaboration with technician has a possibility to analyze and set the final location of implants in a gypsum model. Navigation is based on drilling and slicing of diagnostic gypsum models [4, 9]. Creating a section makes it possible to mark the width of alveolar process [4, 9] measured while pressing soft tissues by means of e.g. caliper [11, 12]. In case of residual dentition, outline of teeth roots is to be marked on gypsum model on the base of a radiograph [6].

In presented work, gypsum model of prosthetic foundation has been replaced with a virtual model, which improved manual methods. Implants placement points are located in relation to foundation spatial topography in a similar way to manual methods carried out on gypsum models. Commonly available level of scanning preciseness [13] makes us believe that differences between real and virtual positions are not bigger than error resulting from the procedure of bed marking and drilling under implant's analog on gypsum model. As it has been already mentioned in methodology description, searching for an ideal location for implants can be carried out not only in relation to foundation surface, but also in parallel, taking into account information regarding bone foundation. Here, presented is planning of implants placement in case when available is only a panoramic radiograph made with appropriate markers, thanks to which such radiograph can be located and adapted to appropriate scale in relation to the scanned foundation topography. A line drawn through implant placement point creates its axis. Revolving of implant profile makes it possible to achieve implant outline.

Model orientation in front view onto the front plane with a radiograph makes it possible to plan placement of implants in a safe distance to mandibular canal. Movement of implants placement points and their axes automatically results in change of location of whole implants bodies. In case if there is known the thickness of soft

tissue, in a relatively simple way in CAD model bone surface outline can be controlled, by means of control dimensions as shown on Fig. 3.

Achieved is then a significant improvement of analysis and adjustment of implants location in comparison to manual techniques. Main limitation of manual techniques in this respect is the necessity of drilling gypsum models [4, 6, 7, 9]. Virtual planning also gives a freedom of analyzing implants diameter and length. Based on presented method for chosen implants in CAD software, designed is location of nests for replaceable sleeves. Sleeves inner diameters reflect sequence of tools used in order to prepare the bed under implant and its final screw in. In fact, determining of nests location ends planning process and constitutes a starting point for creation of template [14]. Although, the way, in which template is created differs from stereolithographic techniques, on which based are commercial navigation systems, and is much closer to manual techniques, where in polymerized mass on diagnostic model there is located a nest for replaceable sleeves. Nevertheless, in manual methods, use of wires for the purposes of nests fixing under sleeves is very inconvenient [6]. In fact, it is sufficient to mill cylindrical surfaces to fix the nest for replaceable sleeves. As it has been shown, designing required cylindrical surfaces for sleeves' nests on virtual model is not problematic. Cylindrical surfaces can be achieved by revolving the contour, as well as by extruding circular profile to the required height. Milling of the designed cylindrical surface in polymer mass along with creation of sleeves belong to operation that are competitive as far as prices [2] are concerned as compared to ordering a template in companies representing rapid prototyping technologies. Described method supports achievement of implants parallelism for overdenture implants retained by solitary attachments, as well as assists procedure in case of oblique implants, e.g. splinted with bars.

In this work error analysis of the presented method has not been shown. At this point of time, such surveys have not been done. Nevertheless, described method has been presented as a way of increasing effectiveness of manual methods, which are commonly used [9] and the achieved precision level is satisfactory in indicated clinical cases [8]. As it has been shown, using the described method does not require very developed CAD skills, they are in fact limited to a few basic functions. Many technicians and prosthodontist are already acquainted with CAD and virtual method enough to carry out such operations. An encouragement to create templates by means of alternative methods might be the common availability and very competitive price of laser data acquisition and CAD software.

4   Conclusion

Possibility to increase effectiveness of the already known alternative methods of manual planning and preparation of surgical templates by means of computer assisted ways has already been presented. Elaborated methodology makes it possible to avoid all disadvantages of manual methods, i.e. eliminates mechanical treatment (slicing and drilling) of diagnostic gypsum models during spatial analysis of implant position. In virtual space it is incomparably more convenient to analyze

various implantological solutions. Designing a template in CAD software creates the possibility to use any of numerically controlled milling machines. Hence, creation of a template in the described way is very competitive as it is free from exclusiveness enforced by specialized commercial technologies.

References

1. Ozan, O., Turkyilmaz, I., Ersoy, A.E., MmGlumphy, E.A., Rosenstiel, S.F.: Clinical accuracy of 3 different types of computed tomography-derived stereolithographic surgical guides in implant placement. J. Oral. Maxillofac. Surg. 67, 394–401 (2009)
2. Winder, J., Bibb, R.: Medical rapid prototyping technologies: state of the art and current limitations for application in oral and maxillofacial surgery. J. Oral. Maxillofac. Surg. 63(7), 1006–1015 (2005)
3. Azari, A., Nikzad, S.: Flapless implant surgery: review of the literature and report of 2 cases with computer-guided surgical approach. J. Oral. Maxillofac. Surg. 66, 1015–1021 (2008)
4. Pesun, I.J.: Fabrication of a guide for nonradiographic evaluation of bone contour. J. Prosthet. Dent. 77(6), 621–623 (1997)
5. Loubele, M., Van Assche, N., et al.: Comparative localized linear accuracy of small-field cone-beam CT and multislice CT for alveolar bone measurements. Oral. Surg. Oral. Med. Oral. Pathol. Oral. Radiol. Endod. 105(4), 512–518 (2008)
6. Stumpel, L.J.: Cast-based guided implant placement: A novel technique. J. Prosthet. Dent. 100, 61–69 (2008)
7. Meitner, S.W., Tallents, R.H.: Surgical templates for prosthetically guided implant placement. J. Prosthet. Dent. 92, 569–574 (2004)
8. Kuzmanovic, D.V., Waddell, J.N.: Fabrication of a self-retaining surgical template for surgical placement of dental implants for the partially edentulous patient. J. Prosthet. Dent. 93(1), 95–96 (2005)
9. Surgical Instructions 10, 16–17 (2006), http://www.dentaurum.de (Cited March 11, 2010)
10. Yeh, S., Monaco, E.A., Buhite, R.J.: Using transitional implants as fixation screws to stabilize a surgical template for accurate implant placement: a clinical report. J. Prosthet. Dent. 93(6), 509–513 (2005)
11. Van Den Bergh, J.P., Ten Bruggenkate, C.M., Tuinzing, D.B.: Preimplant surgery of the bony tissues. J. Prosthet. Dent. 80(2), 175–183 (1998)
12. Perez, L.A., Brooks, S.L., Wang, H.L., Eber, R.M.: Comparison of linear tomography and direct ridge mapping for the determination of edentulous ridge dimensions in human cadavers. Oral. Surg. Oral. Med. Oral. Pathol. Oral. Radiol. Endod. 99(6), 748–754 (2005)
13. Persson, A., Andersson, M., Oden, A., Sandborgh-Englund, G.: A three-dimensional evaluation of a laser scanner and a touch probe scanner. J. Prosthet. Dent. 95(3), 194–200 (2006)
14. Kopp, K.C., Koslow, A.H., Abdo, O.S.: Predictable implant placement with a diagnostic/surgical template and advanced radiographic imaging. J. Prosthet. Dent. 89(6), 611–615 (2003)

An Idea of Human Voice Reaction Measurement System under the Aspect of Behavioral Biometric

Andrzej W. Mitas and Marcin D. Bugdol

Abstract. A proposition of the human's reaction measurement system focused on the voice is presented in the paper. The main idea of this system is to test the human behavior under the influence of sound and visual stimulations. In order to evaluate the human reaction, the signal of speech is examined. This signal is acquired in strict conditions using external device which have a high measurement accuracy.

1 Behavioral Biometric – Introduction

Nowadays the most often used identity verification systems are those which base on the physiological features like fingerprint, iris or face recognition. There are few reasons of this state. First is that the physiological features have been the subject of study for many years. Dactyloscopy has over 80 years history and signature recognition reaches ancient times (e.g. royal stamps). Additionally, physiological features are easily perceptible and thanks to this they can be easily acquired and analyzed. However, this group of features has also some disadvantages, of which the most important is that the patterns are absolutely disposable. A feature which has been lost once (e.g. fingerprint) cannot be restored and thus it cannot be used again.

The behavioral biometric, which is related to the behavior of a person, does not have the disadvantage mentioned above. The behavioral patterns are formed during our adolescence and they are determined by many factors like the environment, upbringing or education. Moreover, our behavior is constantly changing as we are gaining more and more life experience. It can be considered as a fault, because it is difficult to extract one invariable pattern from such fuzzy sample. On the other hand it is a huge advantage - in case of pattern loss, new habits can be developed

Andrzej W. Mitas · Marcin Bugdol
Silesian University of Technology, Krasińskiego 8 St., 40-019 Katowice, Poland
e-mail: `andrzej.mitas@polsl.pl, marcin.bugdol@polsl.pl`

and used to verify ones identity. In this group of biometric are such methods as keystroke dynamics, gait or speaking. An extensive survey of currently considered behavioral biometric methods can be found in [1].

2 Structure of the Measurement System

The research is focused on measuring the human reaction in response to the stimulations generated by a software stimulator (Fig. 1). On the presented schema a feedback loop between verification and stimulation is omitted. In this case it is realized by the computer but in everyday life the human together with his senses creates the feedback loop.
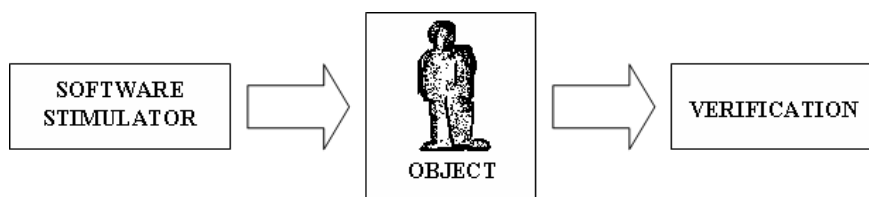
Fig. 1 General idea of the system

The general idea is a development of previous studies on the biometrical strengthening of the digital signature which have been presented in [2, 3, 4, 5]. The purpose of the research is not only to verify the user's identity but also to extract from his biometrical pattern an invariable sequence. This sequence can be next used as an initial value (seed) of the pseudo-random number generator such as realized using the linear register [6].The analysis of the distribution of the behavioral feature is an individual research problem. In the context of the research idea and the structure of the measurement system it is necessary to assume that this feature has an uniform distribution in contrast to physiological features. Employment of the behavioral test results to program the linear register provides the linearity of the operation and finally the uniform distribution of digital signature which is the aim of the proposed method of biometric cryptography. The schema of the system for biometrical strengthening of digital signatures is presented in Fig. 2.
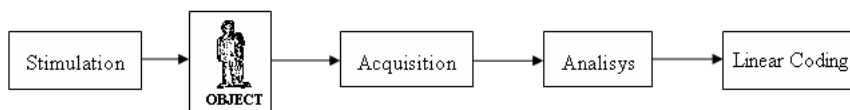
Fig. 2 The schema of the system for biometrical strengthening of digital signatures

Computer, opposite to human, does not have so many and so sensitive senses, which could be used to identify people. That is why there is a need to select such signal that would allow to measure a human's reaction and identifying him based on it. In this study the human voice has been chosen. It contains the information about the physiological features as well as the information about the behavioral ones. Especially the second group of features is important because the reaction on the stimulation is a behavioral feature. Moreover, measuring the voice is completely non-invasive and commonly accepted [7]. Additionally it was assumed that the signal will be acquired in very strict conditions using devices with high accuracy and all external distortions will be eliminated during the acquisition phase. The detailed information about the used devices and created software is presented in the next subsection.

2.1 Hardware and Software

External devices are employed to measure the human voice, among which there is a high quality microphone, ultra low noise microphone preamplifier and A/D converter that is connected to the computer by a USB interface (Fig. 3).
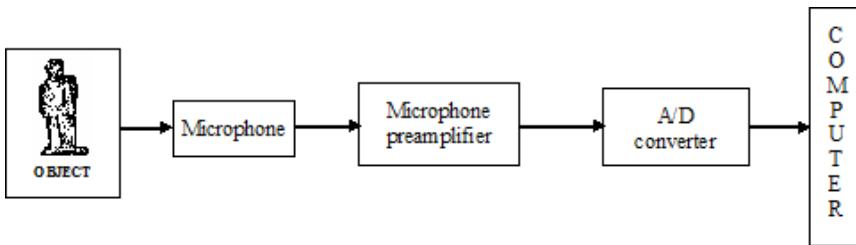
Fig. 3 The schema of the samples register

As can be noticed, the standard integrated sound card was not used because its parameters are insufficient for such accurate measurements. The most important parameters of every analog-to-digital conversion are differential non-linearity and integral non-linearity which are responsible for the accuracy of this conversion. If the values of this parameters are high then the digital output does not refer exactly to the analog input. The influence of the non-linearity is presented in Fig. 4. Moreover there is no possibility to reduce the noise using hardware, so the filtration has to be done by software what is more time-consuming and causes partial data loss.

The used microphone Tonsil MD 268 has a characteristic that reduces the acoustic noise that comes from the environment.

The ultra low noise microphone preamplifier is based on integrated circuit LM2209 that has the dynamic over 100dB and harmonic distortions below 1%. It was closed in a metal case what effectively protects the circuit from the influence of the external electromagnetic field. The gain of the circuit has been set so as the output voltage would not exceed $\pm$ 5V, which is the highest input value of the A/D converter analog inputs.
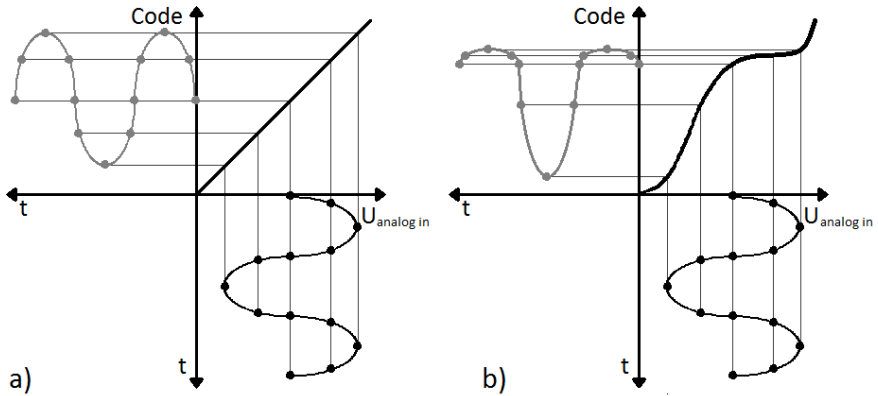
Fig. 4 The influence of the linearity on the digital output a) ideal linearity, b) non-linearity

The Labjack UE9 A/D converter has integral linearity error $\pm 0.02\%$ of full scale, differential linearity error for 12-bit is ± 1 count and typical absolute accuracy error is $\pm 0.025\%$ of full scale (± 0.05 maximally). The other parameters like sampling speed and resolution are high enough to accurately convert the sound signal.

The measurement system has also a reference circuit in which the ECG monitor is used. The additional measurement circuit has been interposed to observe the biomedical signal which gives an unambiguous information about the human's emotional state [8]. Thanks to it there is the possibility to compare the changes in the ECG signal and in the speech signal. Moreover, the ECG is an additional source of biometrical features, what is proved by publications [9, 10, 11]. The whole system, completed with the comparative circuit, is presented in the figure below (Fig. 5).
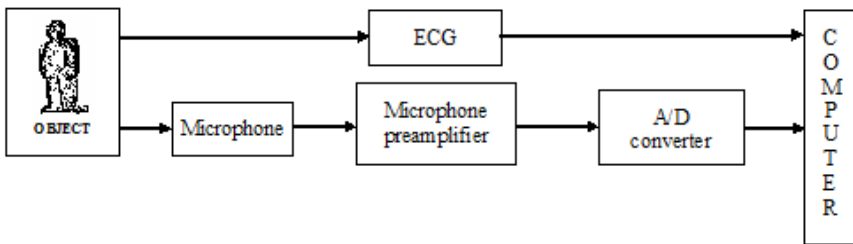
Fig. 5 The schema of the samples register with ECG

The software created for the measurement system has to allow the experiments to be carried out. It has the following functionality:

1. generate sound and visual stimulations;
2. acquire and save on the hard disk samples of sound signal and ECG wave;
3. present and analyze the registered results.

The ECG samples are recorded in 8 bits quality with sapling rate at 100Hz. The sound signal is recorded in 12 bits quality with 44.1 kHz sampling rate. Moreover, some additional information are stored, which are the time of: the begin of the stimulation, the begin of the response (singing) and the end of trial.

3   Experiment

The block scheme of the algorithm of the experiment is presented in Fig. 6.
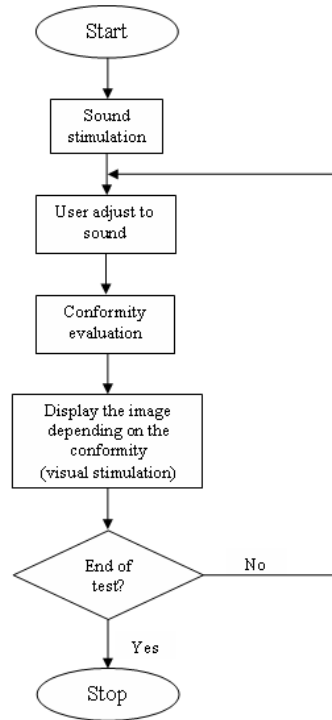
Fig. 6 The algorithm of the experiment

Before the beginning of the experiment the ECG electrodes are connected to the person, and then the ECG wave is being registered for 30 second in order to define the user state before the stimulation. Next, the stimulator generates a single sound that comes from a real instrument (particularly from an electric piano). The task of the tested person is to match to the exemplary sound by singing a single sound on a given pitch. Previous research showed that in such tasks vowels (especially the vowel "a") give the best results [12]. The program acquires uttered sounds and evaluates the match degree in real time. The fundamental frequencies are compared and depending on the result of matching, a proper image is presented on the screen. These images are the second type of user stimulation - visual.

The presented picture is a square of uniform color that changes depending on the degree of the match between the emitted sound and the exemplary sound (Fig. 7). The colors of this pictures are: green, dark green, yellow, orange, dark red and red; they mean respectively from almost perfect match (green) to completely lack of match (red).
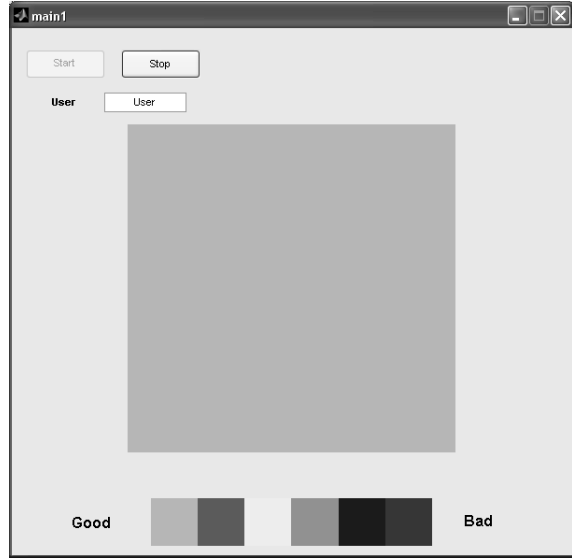
Fig. 7 Main window of the samples acquisition program

The ranges have been defined basing on the difference between the fundamental frequencies of the emitted and the exemplary sound ($f_{exemp} - f_{sign}$) and they are given by the following formula:

$$
color = \begin{cases}
green & \text{for } |f_{exemp} - f_{sing}| \in [0, \frac{1}{4}\text{tone}] \\
dark\,green & \text{for } |f_{exemp} - f_{sing}| \in (\frac{1}{4}\text{tone}, \frac{3}{4}\text{tone}] \\
yellow & \text{for } |f_{exemp} - f_{sing}| \in (\frac{3}{4}\text{tone}, \frac{5}{4}\text{tone}] \\
orange & \text{for } |f_{exemp} - f_{sing}| \in (\frac{5}{4}\text{tone}, \frac{7}{4}\text{tone}] \\
dark\,red & \text{for } |f_{exemp} - f_{sing}| \in (\frac{7}{4}\text{tone}, \frac{11}{4}\text{tone}] \\
red & \text{for } |f_{exemp} - f_{sing}| > \frac{11}{4}\text{tone}
\end{cases}
$$

The duration of a single trial (without the preliminary ECG measurement) is about 7 seconds. Within the confines of single experiments 5 trials are carried out.
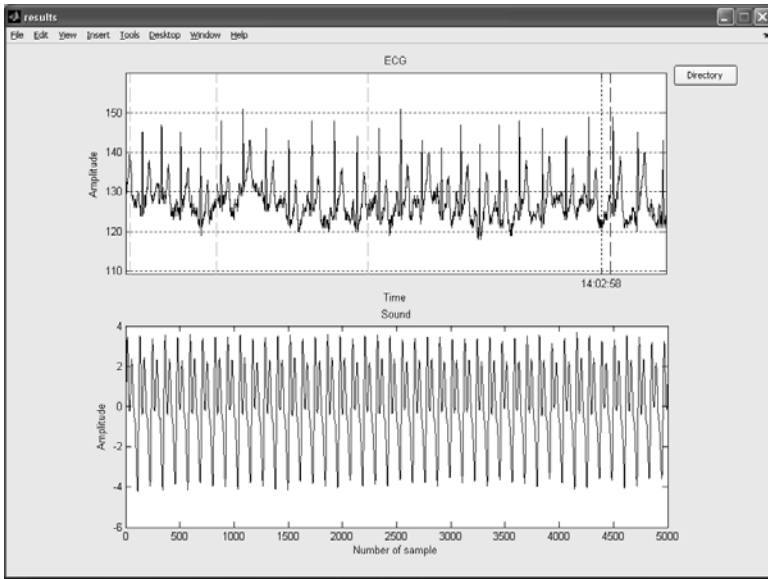
Fig. 8 Main window of the results analyzing module

The preliminary measurements have been carried out in order to verify the correctness of the designed system. Samples from 10 people of different sex, age and having different musical education have been taken. None of the examined persons did have any problems to understand the goal of the task what proves the simplicity of the system. The results of the measurements can be initially analyzed in a proper module of the system. In Fig. 8 the measurement window is presented. It allows to define the initial and ending points which specify the interval of user's visual evaluation of possible correlation between the signals: speech signal parameters and the distortion in the ECG wave.

The example of obtained results is presented in Tab 1.

Table 1 Example of experiment results

Sound					
Trial No.	FQ	Start time	Sign start time	Stop time	U_{in}
1	277 Hz	15:44:33:099	15:44:35:562	15:44:40:241	0.454361 V
					0.416913 V
					0.396942 V
					0.384459 V
					0.364487 V
					0.349508 V
					⋮
2	493 Hz	15:44:45:447	15:44:47:908	15:44:52:585	0.057420 V
					0.049930 V
					⋮
…	…	…	…	…	…
ECG					
Start time			Sample value		
15:43:46			138		
			139		
			139		
			⋮		

4 Conclusion

The preliminary results of the conducted experiment make the statement, that the designed system fulfills all guidelines, true. The omission of the integrated sound card allows the external noise to be eliminate. Acquisition and initial analysis of the correctness of the registered date is possible using the created software.

Further studies will be focused on searching the correlations between the stimulations and the human reactions to the stimuli. The found correlation will be used to extract the characteristic features. Not only the physiological features will be searched but also the behavioral ones.

The changes of the signals are evident in behavioral biometry. The main problem of developing image recognition system is (as usual) to create an automatic algorithm. This algorithm has to be able to replace the polisensoric and intuitive human's reactions, who can easily recognize the voice timbre and also judge whether the uttered words are true or false. In the presented measurement system the ECG

signal is tentatively treated as a source of model information. Such reference signal (containing, in the sense of biocybernetics, so many details that from the point of view of the biometric cryptography there is a problem of information overflow) is employed in attempts of automatic evaluation of starting and ending moments of measurement window for biometrical voice analysis, obviously with biocybernetics feedback using test images.

The information about human's physiological features or about his behavior, regardless if they are instinctive reactions or learned ones, is undoubtedly one of many derivatives of genotype and in this meaning can be used in biometrics. Several problems from the domain of biometrics seem to have crucial influence on the encode quality in biometric cryptography. Especially the distribution of biometrical feature. Apart from numerous utility advantages of behavioral biometry (especially a real safety of user - owner of the biometric feature) it should be pointed out the possibility of real influence on the linearity of the marker distribution, which parametrize in linear dependency the digital code of signature in biometric cryptography (Fig. 9).
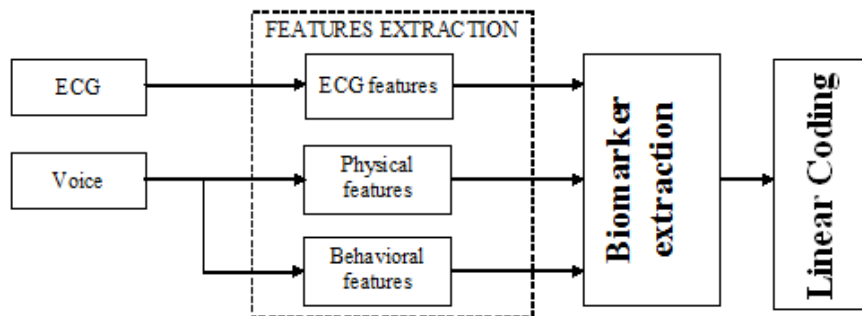
Fig. 9 Schema of the analyzer

References

1. Yampolskiy, R.V., Govindaraju, V.: Behavioural biometrics: a survey and classification. Int. J. Biometrics 1(1), 81–113 (2008)
2. Mitas, A.W., Bugdol, M.D., Plucińska, M.: Biometry and e-signature - a study of application. Elektronika - konstrukcje, technologie, zastosowania 12, 160–163 (2008) (in Polish)
3. Mitas, A.W., Bugdol, M.D., Plucińska, M.: Biometrical strengthening of the digital signature - technical aspects of use. Elektronika - konstrukcje, technologie, zastosowania 12, 164–167 (2008) (in Polish)
4. Mitas, A.W., Mostowski, D., Bugdol, M.: Biometric cryptography in the aspect of biometric hardening of the digital signature. Techniki Komputerowe, Special monographic edition 42(1), 71–81 (2008) (in Polish)
5. Mitas, A.W.: Digital signature. Biometrical parametrization of digital signature. In: Biometria - wybrane zagadnienia, Warszawa, Cieszyn, pp. 85–88 (2004)

6. Mitas, A.W., Hryńków Statkiewicz, K.: Psudo random generators in MVL technique under the aspect of biometrical application. Techniki Komputerowe, Naukowy Biuletyn Informacyjny Instytutu Maszyn Matematycznych 36(1) (2002) (in Polish)
7. Jain, A.K., Ross, A., Prabhakar, S.: An introduction to biometric recognition. IEEE Trans. on Circuits and Sys. for Video Tech. 14 (2004), doi:10.1109/TCSVT.2003.818349
8. Mitas, A., Bugdol, M., Ryguła, A.: Simultaneous analysis of driver's physiological and behavioural parameters under the aspect of transport safety. J. of Med. Inf. & Tech. 12, 241–248 (2009)
9. Biel, L., Pettersson, O., Philipson, L., Wide, P.: ECG analysis: a new approach in human identification. IEEE Tran. on Instrumentation and Measurement (2001), doi:10.1109/19.930458
10. Kyoso, M., Uchiyama, A.: Development of an ECG Identification System. In: Proc. 23rd Annual International IEEE Conference on Engineering in Medicine and Biology Society, vol. 4, pp. 3712–3723 (2002)
11. Israel, S.A., Irvine, J.M., Cheng, A., Wiederhold, M.D., Wiederhold, B.K.: ECG to identify individuals. Pattern Recognition 38 (2005), doi: 10.1016/j.patcog.2004.05.014
12. Bugdol, M.D., Bugdol, M.N.: Vowels in speaker verification. In: Int. Conf. on Biometrics and Kansei Engineering (2009), doi:10.1109/ICBAKE.2009.39

Biomedically Aided Car Driver Safety System

Andrzej W. Mitas and Artur Ryguła

Abstract. The article presents some behavioural measurements, together with the results of some biomedical research experiments and the assumptions underlying them. In order to determine the behavioural characteristics driving style was analysed, which was estimated using data recorded by a tachometric device. Biomedical measurements were made with using an ECG holter and infrared camera to record heart rate changes and the image inside the cab of the vehicle. On the basis of the results obtained, the assumption of a biomedically aided driver safety system is presented.

1 Introduction

The problem of road safety has come into prominence with the advent of motor vehicles in our daily lives. Growing number of cars is causing a continuously increased risk to the life and health of drivers, passengers and third parties who are connected with road traffic (pedestrian, cyclist, etc.). The dynamic development of the automotive industry has allowed the use of more advanced technologies, which offer users faster, more convenient and seemingly more secure vehicles. This apparent safety results from covering increasingly longer distances, spending more time behind the wheel and thus increasing pressure on the driver and his psychomotor performance. In addition, the ubiquitous stress of contemporary life and the constant pursuit of ever newer objectives, radically reduce the human condition, making it the weakest link in a complex system: driver-vehicle-road.

Andrzej W. Mitas · Artur Ryguła

Silesian University of Technology, Department of Transport Informatics Systems, Krasińskiego St. 8, 40-019 Katowice, Poland

e-mail: `andrzej.mitas@polsl.pl`, `artur.rygula@polsl.pl`

2 Standardization of Driver's Road Behaviours

Analysis of driver's road behaviour has been the subject of research and observation for many years. Already by the beginning of the twentieth century, the first tacho-metric device had been invented, which recorded basic information about speed and driving time. Conducted over many years, observations and statistical data on road accidents led to the normalization of unsafe driving behaviours, indicating a set of standards and rules, for examples, limiting speed, the use of telecommunications equipment or normalizing driving time (in the case of professional drivers). Manda-tory medical examinations were also introduced for learner-drivers, and additional psycho-technical tests for people working as professional drivers. However, these standards in general based on statistical assumptions that determine traffic safety, which does not take into account the personal attributes and the current psychomo-tor condition of the driver [6]. Moreover, the use of only biomedical research such as ECG, EEG, GSR, eye closure and facial temperature distribution measurements [1, 2, 3], which allow the recognition of reactions while driving can also point the general standard of critical values which indicating whether dangerous traffic situa-tions are more likely. Only combining the behavioural indicators with the biomed-ical measurement of a driver's psychophysical condition offers the possibility of identifying the exact causes of abnormal road behaviours and relating them to the individual characteristics of particular drivers.

3 The Analysis of Driver's Behaviours

Previous studies [9, 10] have pointed out that driving characteristic (especially the number of acceleration sign changes over particular distance of road) are an im-portant indicator of driver's road behaviours. The research used digital recordings of professional truck drivers' driving parameters as input data. The analysis took into account the records of more than 50 drivers who had covered a total distance of about 35 thousand km, and in addition the driving records in the cases of a few road accidents. According to the assumptions described in work [10], the function of accelerations sign changes was calculated as:

$$f(a_i) = \begin{cases} 1 \text{ if } a_i a_{i+1} < 0 \wedge v_i > 20km/h \\ 0 \text{ if } a_i a_{i+1} < 0 \wedge v_i \leq 20km/h \\ 0 \text{ if } a_i a_{i+1} \geq 0 \end{cases} \tag{1}$$

where: a_i -acceleration in the ith meter of travelled distance; v_i-speed in the ith meter of travelled distance.

Knowing the value of function $f(a_i)$, the parameter was defined as:

$$n(k_i) = \sum_{i=k \cdot 10000+1}^{(k+1) \cdot 10000} f(a_i) \tag{2}$$

where:k-number of brackets; k_i-ith distance bracket.

On the basis of $n(k_i)$ was determined $p(k_i)$ function:

$$p(k_i) = \begin{cases} n_k^2 & \text{if } k < 1 \\ n_k^2 + p_{k-1} & \text{otherwise} \end{cases} \qquad (3)$$

where: n_k-value of the function in the kth bracket; p_k-value of the function in the kth bracket.

The next step was to calculate the value of the $p(k)$ function for each driving record. The results obtained presented graphically in Fig. 1a. The curves which represent road accidents are indicated using bold lines.
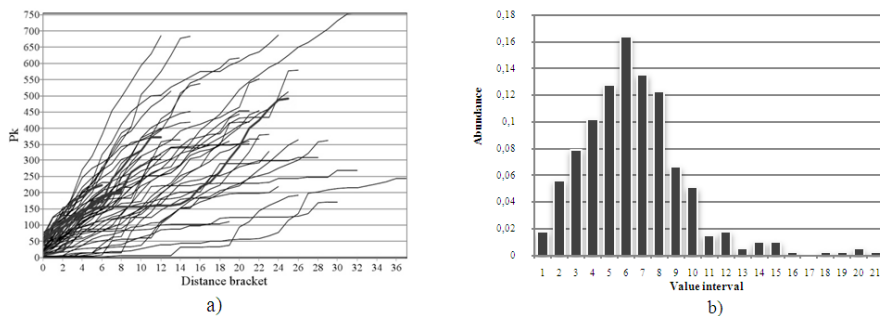
Fig. 1 a) The $p(k)$ value for particular driving intervals b) The value distributions of the slope of the curves

In order to present the distribution of $p(k)$ changes graphically, regression analysis was used to estimate the average and normalized value of the slope of the curves:

$$\alpha = \frac{k \sum k_i p_k - \sum k_i \sum p_k}{k \sum k_i^2 - (\sum k_i)^2} \qquad (4)$$

Distribution of the determined values shown in Fig. 1b. As can be seen, the distribution of selected parameters is similar to the normal distribution. On the basis of this, the critical values can be determined beyond which there is an increased likelihood of a dangerous situation. However, safety systems based on this kind of compound are suitable only for the overall analysis owing to the fact that they are not taking into account the individual driving parameters of a driver. It is noteworthy that the curves accident (bold lines) in the overall analysis did not differ substantially from the average value of the distribution of driving style changes. Therefore, the next step of the research was to determine the driver's individual characteristics.

Figure 2 shows that the accident curves (bold lines) clearly differ from typical driving characteristics, which allow the putting forward of proposal that each driver has his own unique and distinctive style of driving. In addition, the location of the accident curves can be a indicator of a driver's psycho-physiological state limitation. The lines above the average values may provide information about the driver's increased aggression, while the curves located below the average may be a sign the
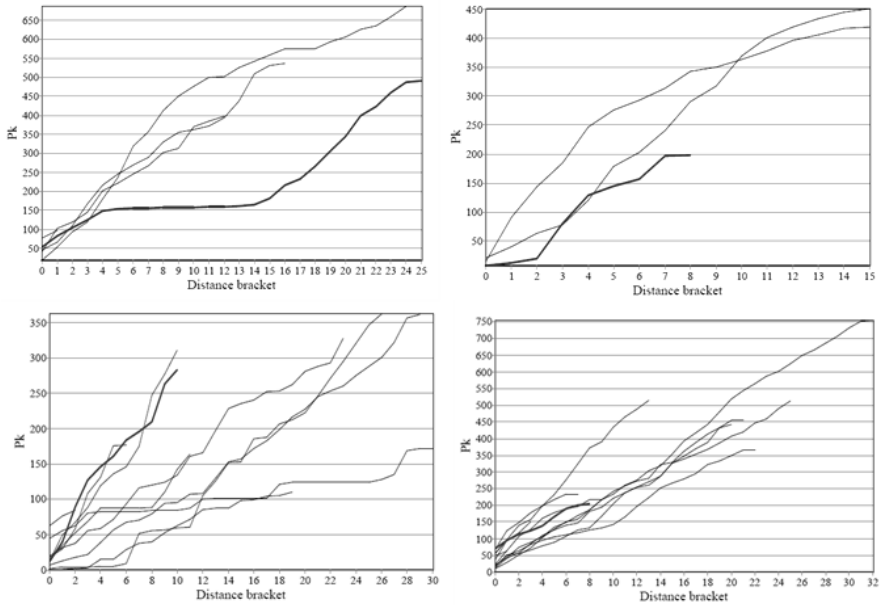
Fig. 2 The individual $p(k)$ value distribution

occurrence of fatigue or weariness. Detailed analysis, however, requires additional information about the current state of a driver at particular stages of driving, which is indicating the need for the monitoring of biomedical parameters.

4 Biocybernetics System of Driving Behaviours Analysis

As shown in previous chapters, an effective system of driver behaviour-analysis requires the use of additional indicators to assess the work of the driver. In order to identify indicator of individual driving style and to correlate changes occurring in the driver's psychophysical state, the biocybernetics measuring system is proposed as applying. According to the definition of biocybernetics [11] in the system, there is feedback between the behaviour of the driver (the research object) and his mental and physical state (the biological process).

If the model is referred back to live observations, it seems fairly certain that the driver himself is the optimal regulatory system. The driver is an object which is recording and controlling external signals , processing information on the current state of the environment and taking heuristically optimal decisions. A high danger state occurs only in the case of system disorders. Therefore, monitoring system parameters should in principle record and distinguish states different from the normal behaviour of the driver. According to the system presented (Fig. 3), the signal of derogation from the normal working person-vehicle system is the alteration in driver behaviour, recorded on changes in driving parameters and the driver's
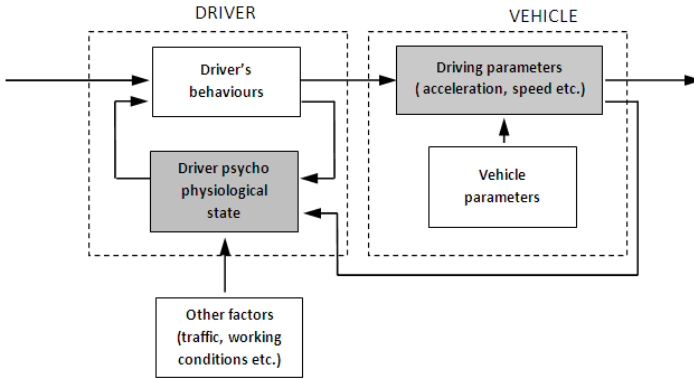
Fig. 3 Biocybernetics model of analysis

psycho-physical movements. As presented in chapter three, relative measures minimize the influence of the vehicle's technical parameters (type of vehicle, technical efficiency, etc.) and focus on changes at driving style in various stages of the road.

4.1 Psycho-physiological State Determination

The issue of driver psycho-physical research has been the subject of earlier experiments. Works [5, 8] presented the design of early warning systems, taking into account measurements of the driver's emotions. Research attempts, however, have shown the difficulties of automatic evaluation of facial expressions, but have drawn attention to degree of eye-opening as an important signal of the negative emotional state of the driver. Research [4, 12] has helped to demonstrate that the estimator of eye-closure (PERCLOS) is one of the most effective parameters in assessing the condition of the driver. However, the determination of this indicator, owing to changing conditions of illumination in the vehicle cabin, requires the use of appropriate recording equipment [7]. The experiments results demonstrated the desirability of the use of an infrared camera. The camera was constructed by modifying a typical webcam. The modifications consisted of replacing the optical filter and using of infrared LEDs. Figure 4 shows examples of images recorded in the car under different lighting conditions.

Fig. 4 Image of driver's face by: a) day, b) night, c) night with side illumination

As shown in the attached images, the application of an infrared lighting source placed close to the axis of the camera allows the obtaining of the bright pupil effect. This phenomenon of the reflex has been used for eye-detection and eye-closure determination. An essential element in determining the PERCLOS values is setting the threshold of the opening and closing of the eye. These values are individual and must be determined dynamically, depending on the object of observation and the prevailing environmental factors (increased light intensity, etc.).
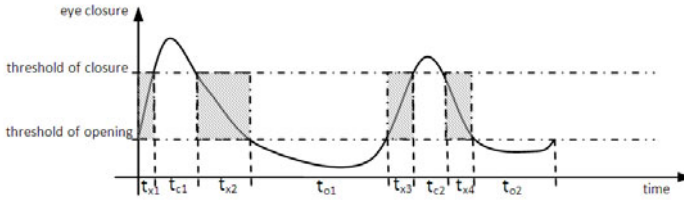
Fig. 5 Curve of eye-closure/opening

Figure 5 schematically shows the limits of the opening and closing of the eye and the undefined intermediate states (shaded area). Given the definition of the PERCLOS as a percentage of eyelid closure over the pupil over time, the coefficient can be written as:

$$PC = \frac{\sum t_{c_i}}{\sum t_{c_i} + \sum t_{o_i} + \sum t_{x_i}} \tag{5}$$

where: t_{c_i}-ith time interval of closed eyes; t_{o_i}-ith time interval of opened eyes; t_{x_i}-ith time interval of undefined state.

Owing to the as yet not fully determined impact of infrared light on the human body (in particular an account of the risk of thermal damage to the eye), an additional reference measurement is proposed. This element will have the task of setting and minimizing the exposure time to infrared light. For this purpose it is proposed to use heartbeat measurements, which, according to research are a reliable indicator of changes in the driver's emotional state [5]. A simple research experiment involving the recording of the pulse during sleep can easily show the characteristic changes in the pulse of pre-sleep, sleep and waking.

In the first stage of falling asleep (I) can be seen a significant drop of the pulse-rate associated with calmness and introspection. The transition from the first phase to the stage of sleep (II), is characterized by further drop in heart activity which reached an average pulse-rate of about 48 beats per minute. In the third stage, there is a visibly distinct increase in heart-rate associated with the waking-up process.

Fig. 6 Experiment results: heart-rate graph during pre-sleep (I), sleep (II) and waking (III)
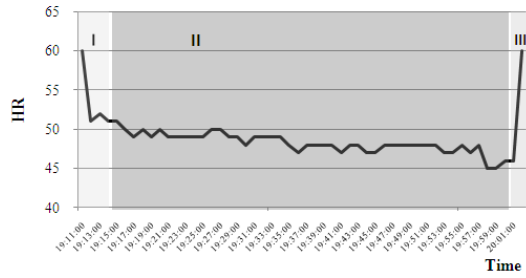
4.2 Proposition of Measurement System

The proposed measurement system is the result of the modification of earlier works [5, 8]. The system is based on three-path measurement.
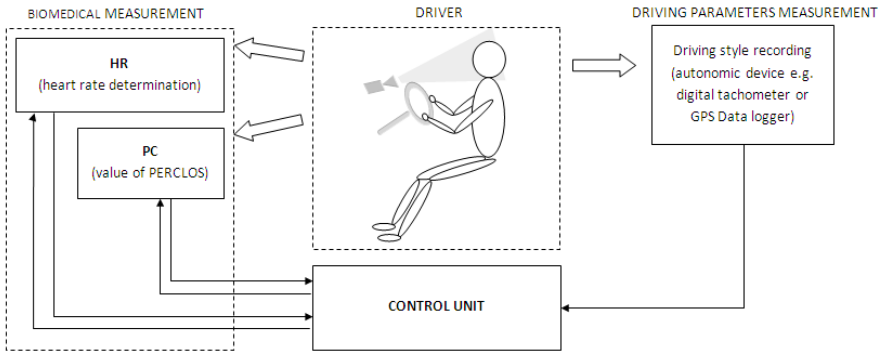
Fig. 7 Proposition of biomedical measurement system

The measurement of the vehicle position as a function of time (using a tachometer or GPS logger) is used to designate the changes in driver's driving style. Measurement of heart-rate (using a pulsometer) and recording of PERCLOS (using an IR camera) are used to determine the person's biomedical status and to correlate the parameters of the vehicles with the driver's psychophysical state. The control unit has the task of setting the interval measurement of the IR lighting (on the basis of the pulse-rate) and of recording particular parameters of the system.

5 Conclusions

The presented results and assumptions of the experiments show the advantages of multi-modal measurements, taking into account the behavioural and biomedical research. Monitoring only driving parameters does not provide sufficient information about the current conditions in the cabin of the vehicle, and other factors directly

affecting psychomotor efficiency. Biomedical research, in particular, measurements of eye closure and cardiovascular efficiency, complement the proposed system with necessary information about the current physical and emotional state of the driver. The recorded data are a key indicator in the diagnosis and classification of causes of risk. Future work will focus on extensive surveys of drivers in real road conditions, taking into account all the aforementioned measurements of biomedical state and the recording of the external parameters of driving (acceleration, speed etc.).

References

1. Lal, S.K.L., Craig, A.: Driver fatigue: Electroencephalography and psychological assessment. Psychophysiology 39(3), 313–321 (2002)
2. Healey, J.A., Picard, R.W.: Detecting Stress During Real World Driving Tasks Using Physiological Sensors. IEEE Transactions on Intelligent Transportation Systems 6(2), 156–166 (2005)
3. Healey, J., Seger, J., Picard, R.: Quantifying Driver Stress: Developing a System for Collecting and Processing Bio Metric Signals in Natural Situations. In: Proceedings of the Rocky Mountian Bio-Engineering Symposium, April 16-18 (1999)
4. Igarashi, K., Miyajima, C., Itou, K., Takeda, K., Itakura, F., Abut, H.: Biometric identification using driving behavioural signals. In: Proc. 2004 IEEE International Conference on Multimedia and Expo. (2004)
5. Mitas, A., Bugdol, M., Rygula, A.: Simultaneous analysis of driver's physiological and behavioural parameters under the aspect of transport safety. Journal of Medical Informatics and Technologies 13, 241–247 (2009)
6. Mitas, A., Bugdol, M., Rygula, A.: The psychophysiological conditionings of driver's work under the aspect of traffic safety. Transport Problems 4(1), 87–94 (2009)
7. Mitas, A., Bugdol, M., Rygula, A.: Computer aid assessment of driver's fatigue during driving based on eye movement analysis. Journal of Medical Informatics and Technologies 12, 195–200 (2008)
8. Mitas, A., Czapla, Z., Bugdol, M., Rygula, A.: Recording and evaluation of driver's biometrics parameters for a traffic safety improvement. Scientific Papers of Silesian University of Technology, Katowice (2009) (in printing)
9. Rygula, A., Mitas, A.: Numeric tools for tachogram analysis. Transport Problems 2(4), 73–80 (2007)
10. Rygula, A.: Driving style identification method based on speed graph analysis. In: Proceedings of 4th International Conference on Image Analysis and Biometrics and International Conference on Kansei Engineering and Affective Systems, Cieszyn, June 25-28 (2009)
11. Tadeusiewicz, R.: Problems of biocybernetics, 2nd, revised edn., PWN, Warszawa (1993)
12. Wierwille, W., Ellsworth, L., Wreggit, S., Fairbanks, R., Kirn, C.: Research on vehicle based driver status/performance monitoring: development, validation, and refinement of algorithms for detection of driver drowsiness. National Highway Traffic Safety Administration Final Report: DOT HS 808 247 (1994)

Myriad Filter Computation with 2nd Order Approximation Polynomial

Tomasz Pander

Abstract. The myriad filter is a robust filter which is very useful in suppressing impulsive noise. It belongs to the family of the robust m-filters and is controlled with one parameter only. The myriad filter is defined as a running window filter whose output is the sample myriad of elements in the window. In this paper, a fast and simple method of the myriad filter computation is presented. It performs the 2nd order polynomial fitting and the next *x*-coordinate of the parabola top is searched. The proposed method can operate on different types of impulsive noise, requires less computational time and is equally robust as the fixed point method or the branch-and-bound search method. The presented method is applied to process a chirp signal in the impulsive environment. The obtained results are compared to the fixed-point algorithm and the branch-and-bound searching method.

1 Introduction

The robust filters are applied in many different fields of digital signal processing, particularly in the impulsive noise environment which can occur in a radar clutter, ocean acoustic noise, wireless communication systems, biomedical signal and image processing, industrial process control, etc. [3, 16, 19, 20, 22].

The linear filtering techniques are commonly used in different applications of digital signal processing, thanks to their mathematical simplicity and efficiency in the Gaussian environment. The usual assumption that different types of noise are normally distributed can be justified with the use of Central Limit Theorem. For this assumption a reasonable model for any physical phenomena can be made [18]. However, there are many signals that are not well-described by the Gaussian model. A large variety of noise processes have impulsive nature.

Tomasz Pander
Institute of Electronics, Silesian University of Technology,
Akademicka St. 16, 44-100 Gliwice, Poland
e-mail: `tpander@polsl.pl`

The process of a noise suppression should be the first step of each biomedical signal processing system. The accuracy of further signal processing steps like detection, measurement or classification depend on the quality of reduction noise algorithms [21]. There exists many different biomedical signals, for example the electrocardiogram (ECG signal), the electrooculogram (EOG), and others. For instance, the muscle noise contaminations in ECG signals distort low-amplitude ECG wave components and hence lower the accuracy of computer-aided measurements of various morphological characteristics [12]. The most popular model of EMG noise is a Gaussian model, but the muscle noise shows frequently an impulsive nature. One of the most disadvantage of linear filters are their sensitivity to outliers samples, which can appear as an impulsive noise or sudden change of signal's morphology. In these cases the linear filtering techniques performance can dramatically deteriorate and disturb further signal processing steps like detection, measurement or classification [5, 21].

The family of α-stable distributions was recently often used to model the impulsive phenomena mentioned above [13, 16, 17]. In this work, the symmetric α-stable distribution is applied. A class of symmetric α-stable distributions (SαS) is described by their characteristic function

$$\varphi(t) = \exp(j\mu t - \gamma |t|^{\alpha}) \tag{1}$$

where α is the characteristic exponent restricted to the $0 < \alpha \leq 2$ range, μ is the real-valued location parameter and γ - the dispersion of the distribution ($\gamma > 0$) [3, 5, 16].

The signal smoothing, enhancing or shape preserving in cases when the impulsive noise appears, involves an application of the robust method as the only alternative for the linear filtering. In the presence of a heavy tailed noise, linear filters tend to blur sharp edges, destroy lines and other fine image or signal details. However, there is an important class of smoothing applications that require careful treatment and preservation of signal edges [1, 6, 11].

The myriad filter has recently been proposed as a robust filtering and an estimation technique in impulsive environments. This filter is a non-linear robust filter. It represents a wide class of maximum likelihood type estimators (M-estimators) of location, which were developed in the theory of robust statistics [19]. The basis for filters is the simple myriad which is defined as the maximum likelihood estimation of location of the Cauchy distribution [13].

The aim of this paper is to present a new method of estimation the myriad filter output with the 2nd order polynomial fitting. In order to ensure the proper operation of the proposed algorithm, the method of selection of parameters like filter window length is shown. The organization of the paper is as follows. It begins with introducing the myriad filter theory. The presentation of the new method of the myriad filter output estimation is introduced in the next section. Finally, a number of results and conclusions are presented.

2   The M-Estimator and the Myriad Filter

The M-estimator technique is one of the most popular methods to solve the problem of robust parameter estimation. The principle of M-estimators can be formulated in the following way. Let us choose a set of N data samples $x_1, x_2, \ldots, x_N$, where $x_i = \beta_i + v_i$ and $1 \le i \le N$, the problem is to estimate the β_i location parameter under noise component v_i. This parameter identifies the position of the probability density function (*pdf*) on the real line of data samples. The distribution of v_i in not assumed to be exactly known. The only basic assumption is that $v_1, \ldots, v_N$ obey a symmetric, independent, identical distribution (symmetric i.i.d.) [9, 10].

The M-estimate or maximum likelihood-type estimator (MLE) was originally proposed to improve robustness of statistical estimators subject to the small deviations mentioned above. The M-estimator of $\hat{\beta}$ is defined as the minimum of a global energy function:

$$\hat{\beta} = \arg\min_{\beta} \sum_{i=1}^{N} \rho(x_i - \beta). \tag{2}$$

The $\rho(\cdot)$ is called the penalty or the cost function. An M-estimator of location is defined as the parameter $\hat{\beta}$ that minimizes the expression in (2). The behavior of the M-estimator is entirely characterized by the shape of ρ function [2, 7, 10]. Let $\rho(z)$ be a function of a single variable $z \equiv (x_i - \beta)$.

Given the Cauchy distribution with scaling factor $K > 0$,

$$f(z) = \frac{K}{\pi} \frac{1}{K^2 + z^2}, \tag{3}$$

its associated cost function has a form:

$$\rho(z) = \log(K^2 + z^2). \tag{4}$$

The maximum likelihood estimator of location (M-estimator) associated with this cost function is called a *sample myriad*. The scaling factor K is also called linearity parameter and controls the impulse-resistance (outlier-rejection capability) of the estimator. For details see in [4, 7, 13, 14, 15]. The optimal selection of K parameter is also described in [23].

The myriad filter is also defined as the weighted myriad filter by assigning weights to the sample in the maximum likelihood of the location estimation. The weights reflect the different levels of reliability of the observed samples [13, 14, 15]. Let us consider a set of observations $\{x_i\}_{i=1}^{N}$ and a set of filter weights $\{w_i\}_{i=1}^{N}$. The output of the weighted myriad filter is defined as

$$\begin{aligned} \hat{\beta} &\triangleq myriad(x_1 \circ w_1, x_2 \circ w_2, \ldots, x_N \circ w_N; K) = \\ &= \arg\min_{\beta} \prod_{i=1}^{N} [K^2 + w_i(x_i - \beta)^2] = \\ &= \arg\min_{\beta} \sum_{i=1}^{N} \log[K^2 + w_i(x_i - \beta)^2] \end{aligned} \tag{5}$$

where $x_i \circ w_i$ denotes the weighting operation and the weights are restricted to be non-negative: $w_i \geq 0, i = 1, \ldots, N$, N is the window length. The weighted myriad filter may use negative weights, which results in potential instability of the filter (the output can sometimes be $+\infty$ or $-\infty$) [13]. When all weights equal 1 ($w_i = 1$ for $i = 1, \ldots, N$), the sample myriad depends on the linearity parameter K only.

It is important to realize that the location estimation problem being considered in this paper is related to the problem of filtering a time-series $x(n)$ using a sliding window. The output $y(n)$ can be interpreted as an estimate of location based on input samples:

$$y(n) = myriad\{x(n-N_1), \ldots, x(n), \ldots, x(n+N_2); K\} \tag{6}$$

where N is window length (if N is even then $N_1 = \frac{N}{2}$ and $N_2 = N_1 - 1$, if N is odd then $N_1 = \frac{N-1}{2}$ and $N_2 = N_1$).

In this work, to make it more simple, $w_i = \frac{1}{N}$ for $i = 1, \ldots, N$ and a further analysis of the weights value is not considered in the present work.

The main algorithm of estimation of the myriad filter output is the fixed-point method presented in [5, 14, 15]. Recently in [20] a new way of estimation of the myriad filter output using the branch-and-bound algorithm was presented.

3   Estimation of the Output Myriad Filter Using 2nd Order Approximation Polynomial

The method proposed in this paper is based on the simple idea of application the least squares approximation with the 2nd order polynomial.

Finding the best fit function $f(x)$, that is close to the data samples: (x_1, y_1), (x_2, y_2), ..., (x_n, y_n), is the main problem in the least squares numerical approximation. In order to obtain the best fit a total square error between the data values and the approximation is minimized. The total square error is defined as:

$$e = \sum_{i}^{N} (y_i - f(x_i))^2, \tag{7}$$

where $f(x)$ is the approximation polynomial.

The upper plot of Fig. 1 illustrates the shape of the myriad cost function as the function of β. The lower plot presents the sorted data $\mathbf{x}$ and corresponding the myriad cost function values $\mathbf{y}$ from eq. (4). According to eq. (5) β is such a value for which the expression at right side of eq. (5) reaches the minimum value. The main problem is that there can exist many local minima (see upper plot of Fig. 1). The fixed-point method from [4, 5] calculates iteratively this optimal β value, but requires at least 10 iterations to find it.

The idea of the proposed method is based on the observation that the sorted data samples in the filter window and their corresponding myriad cost function values are placed on a parabolic. Then coefficients of the 2nd order polynomial are calculated
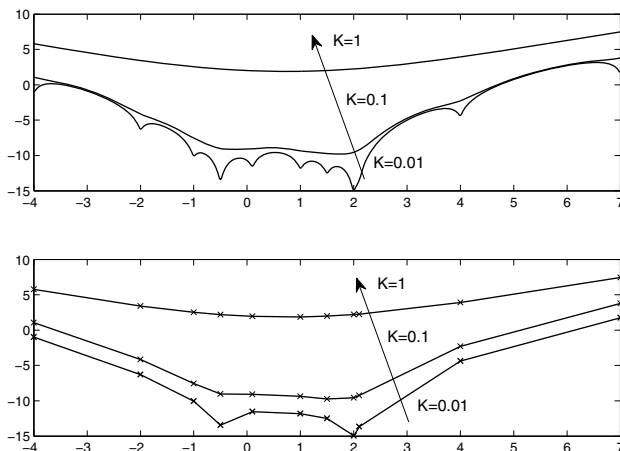
Fig. 1 Degree of nonconvexity in the slide window for the myriad filter cost function calculated for data vector (-2 1.5 1 2.1 -0.5 -1 4 2 -4 2 -.5 0.1 7). In the lower plot the sorted x data and corresponding values of the myriad cost function are presented.

using the least square approximation. And the location of the peak of parabola is estimated. This value corresponds to the optimal β from eq. (5).

The first step of this method is to sort in ascending order samples $(x_1, x_2, \ldots, x_N)$ in the sliding window of the myriad filter:

$$x_{(1)} \leq x_{(2)} \leq \ldots \leq x_{(N)}. \tag{8}$$

The next step is to calculate the cost function of the myriad filter for each sample x_i in the window:

$$y_i = \sum_{j=1}^{N} \log[K^2 + w_j(x_j - x_i)^2]. \tag{9}$$

In order to prevent the approximation from outliers in the filter window, the cut-off process is made in the following way:

$$\forall_{i=1,\ldots,N} |x_{(i)}| < \varepsilon. \tag{10}$$

If inequality (10) is true, then the filter window is cut down on a sample $x_{(i)}$ and a new filter window is created which consists of samples $(x_{(1)}, x_{(2)}, \ldots, x_{(N_1)})$, where N_1 is the new filter window length. Thus, N has a new value $N = N_1$. The set of the cost function values is also cut down on a sample $y_{(i)}$, hence the set of values is the following: $(y_{(1)}, y_{(2)}, \ldots, y_{(N_1)})$. Value of ε is chosen in an empirical way and in this work $\varepsilon = 5$. Such value guarantees that further operations are correct.

Now, the coefficients c_0, c_1, c_2 of the 2nd order polynomial are estimated using the least square approximation:

$$f_{myrappr}(\beta) = c_0 + c_1\beta + c_2\beta^2. \tag{11}$$

To solve this problem the following matrix $\mathbf{S}$ and vector $\mathbf{T}$ are created:

$$\begin{cases} S_0c_0 + S_1c_1 + S_2c_2 = T_0 \\ S_1c_0 + S_2c_1 + S_3c_2 = T_1 \\ S_2c_0 + S_3c_1 + S_4c_2 = T_2 \end{cases} \tag{12}$$

where:

$$S_i = \sum_{j=1}^{N} x_j^i \tag{13}$$

and $i = 0, 1, \ldots, 2m$,

$$T_k = \sum_{j=1}^{N} x_j^k y_j \tag{14}$$

and $k = 0, 1, \ldots, m$, and for quadratic polynomial approximation $m = 2$. The Gauss elimination is applied to find coefficients c_0, c_1 and c_2.

The coordinate x of the parabola top corresponds to β value for which eq. (5) gets the minimum value:

$$\hat{\beta} = -\frac{c_1}{2c_2}. \tag{15}$$

The illustrations of the proposed protection against outliers are shown in the Fig. 2. The obtained solution with the correction is much closer to the fixed-point estimation.

myriad output: FP = –0.91798 AppCor = –0.91 App = –1.878
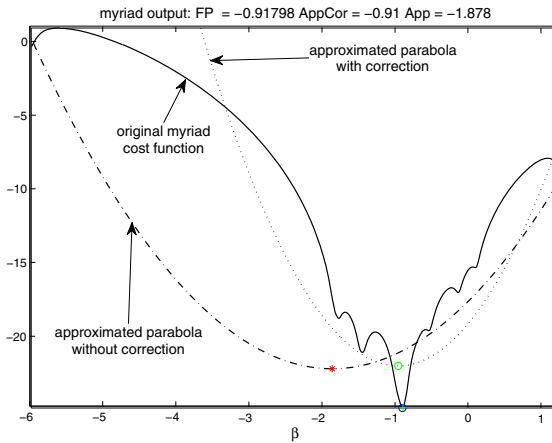
Fig. 2 The shape of approximated parabola without (dashed-dot line) and with (dotted line) the correction as well as the original myriad cost function (solid line) and the solution for data vector (-0.91 -1.0 -1.79 -1.85 1.23 0.1 -1.5 -0.93 -6 -0.87 -0.145 -0.54 -1.45). The linear parameter $K = 0.01$ and $\varepsilon = 3$.

In order to ensure the condition that solution belongs to the range:

$$x_{(1)} \leq \hat{\beta} \leq x_{(N)} \tag{16}$$

it is checked if for the obtained value $\hat{\beta}$ inequalities

$$\hat{\beta} < x_{(1)} \text{ or } \hat{\beta} > x_{(N)} \tag{17}$$

hold true. If inequality (17) is, true then the solution $\hat{\beta}$ is selected from the samples of $x_{(i)}$:

$$\hat{\beta} \equiv x_{(i)}|_{y_{min}=\min(y_1,y_2,...,y_N)} \tag{18}$$

4 Filtering Procedure

Filtering a signal in the time-domain results in a change of the signal's original spectral component. This change usually consists in decreasing of unwanted components of the input signal. The filtering process should not deform the signal, but there exists a group of filters which may introduce inadmissible deformations of the signal. The nonlinear filters belong to this group. For those reasons, the presented filters are evaluated using the mean absolute error (MAE) defined as $\text{MAE} = \frac{1}{M}\sum_{i=1}^{M}|s_i - y_i|$, where: M - is the signal's length, y_i is the output of the evaluated filter, s_i is the deterministic part of signal, without a noise. The MAE factor allows to measure the absolute mean error of the additive residual distortions introduced by the nonlinear filtering. Signals y_i and s_i are aligned and they have the same time index.

For the testing requirements chirp signals (see Fig. 3) are used as the same deterministic component with added different realization of random impulsive noise. Each tested chirp signal cycle is of a length of 2000 samples at sampling frequency 2000 Hz. The chirp signal and the frequency bandwidth were chosen for their similarity to the ECG signal processing troubles. The desired signal $s(n)$ is obtained by passing the $s_{chirp}(n)$ signal through the FIR filter of length 70 with the cut-off frequency 30 Hz. Such signal was corrupted by the simulation of the α-stable noise with the known value of α and *Geometric Signal-to-Noise Ratio* (G-SNR) defined as [8]:

$$\text{G-SNR} = \frac{1}{2C_g}\left(\frac{A}{S_0}\right)^2, \tag{19}$$

where $C_g = e^{C_e} \approx 1.78$ is the exponential of the Euler constant, A is the amplitude of a modulated signal in an additive-noise channel with noise geometric power S_0. The normalization constant $2C_g$ is used to ensure that the definition of the G-SNR corresponds to that of the standard SNR if the channel noise is Gaussian [8]. The geometric power definition is the following [8]:

$$S_0 = \left(\prod_{i=1}^{M}|x_i|\right)^{1/M}. \tag{20}$$
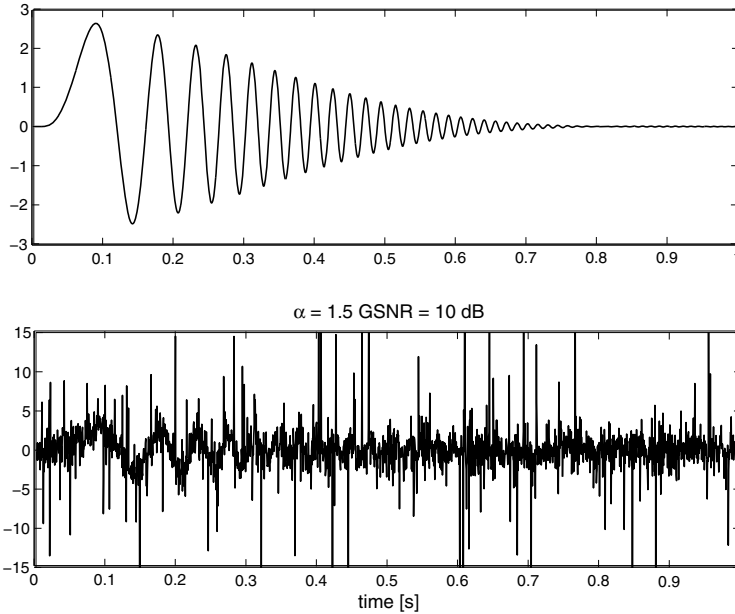
Fig. 3 An example of chirp signal corrupted with simulated impulsive noise modeled with SαS process for $\alpha = 1.5$ and G-SNR= 10 dB (upper plot - clean signal, lower plot - noisy signal)

The results are obtained for one value of GSNR, i.e. 10 dB. For each value of α (from 1 to 2 with step 0.1) and $\gamma = 1$, 100 different realizations of impulsive noise were generated with known value of GSNR. Afterwards the averaged MAE$_{ave}$ value is calculated as:

$$\text{MAE}_{ave} = \frac{1}{100} \sum_{i=1}^{100} \text{MAE}_i. \tag{21}$$

Linear parameter K of the myriad filter is varying (0.01, 0.1, 1) and the MAE factor is calculated for each value of K.

Three variants of the myriad filtering were analyzed:

1. the original myriad filter with the fixed-point method, the initial value in each running filter's window is the selection weighted myriad (fixed-point search weighted myriad algorithm II [14]), this is the first reference filter, denoted as **FP** myriad filter,
2. the myriad filter with the branch-and-bound algorithm according to [20], this is the second reference filter, denoted as **BB** myriad filter,
3. the proposed 2nd order approximation myriad filter, denoted as **Appr** myriad filter.

The efficiency of the proposed method to filter chirp signals in impulsive environment was stated for the constant filter's window length and $N = 21$.

The average MAE factors are shown in tables 1, 2 and 3.

Table 1 MAE for different computation algorithms of myriad filter and K=0.01

α	FP myriad filter	BB myriad filter	Appr myriad filter
1.0	0.4215	0.4170	0.3540
1.1	0.4360	0.4334	0.3468
1.2	0.4509	0.4476	0.3552
1.3	0.4585	0.4584	0.3378
1.4	0.4694	0.4693	0.3328
1.5	0.4789	0.4783	0.3325
1.6	0.4849	0.4855	0.3232
1.7	0.4890	0.4901	0.3146
1.8	0.4967	0.4980	0.3137
1.9	0.4972	0.4992	0.3061
2.0	0.5078	0.5104	0.2986

Table 2 MAE for different computation algorithms of myriad filter and K=0.1

α	FP myriad filter	BB myriad filter	Appr myriad filter
1.0	0.3298	0.3306	0.3338
1.1	0.3390	0.3400	0.3267
1.2	0.3546	0.3557	0.3356
1.3	0.3588	0.3602	0.3176
1.4	0.3641	0.3658	0.3113
1.5	0.3736	0.3749	0.3123
1.6	0.3769	0.3785	0.3024
1.7	0.3787	0.3806	0.2937
1.8	0.3867	0.3885	0.2938
1.9	0.3874	0.3893	0.2868
2.0	0.3952	0.3973	0.2785

Table 3 MAE for different computation algorithms of myriad filter and K=1

α	FP myriad filter	BB myriad filter	Appr myriad filter
1.0	0.3435	0.4557	0.3651
1.1	0.3296	0.4385	0.3475
1.2	0.3313	0.4269	0.3475
1.3	0.3098	0.3897	0.3220
1.4	0.2993	0.3659	0.3102
1.5	0.2988	0.3497	0.3076
1.6	0.2855	0.3259	0.2917
1.7	0.2758	0.3014	0.2794
1.8	0.2742	0.2899	0.2767
1.9	0.2669	0.2733	0.2671
2.0	0.2575	0.2576	0.2555
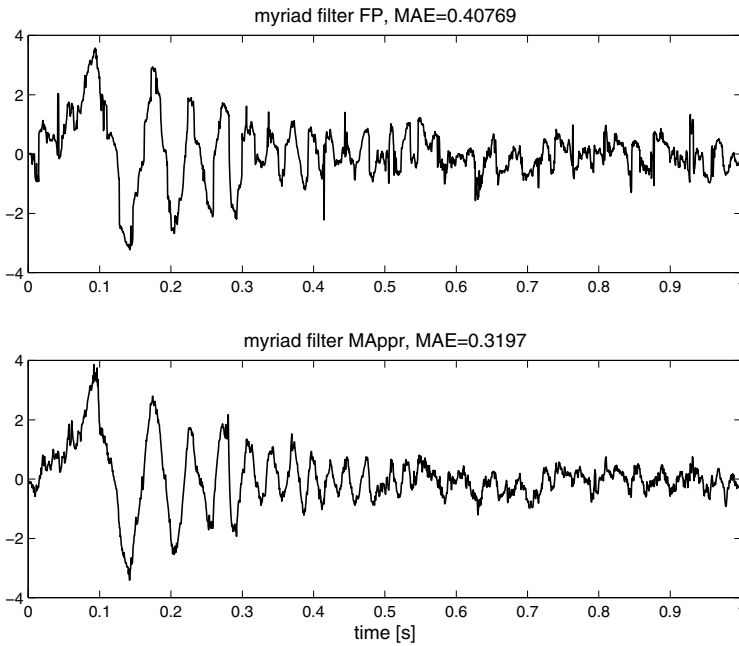
Fig. 4 The example of filtering signal with the FP myriad (upper plot) and the Appr myriad (lower plot) filters

5   Results of Filtering

The proposed algorithm for the myriad filter output estimation leads to obtaining the comparative or even better results with the reference output estimation methods of the myriad filter. For all values of α investigated methods lead to obtaining the smallest value of MAE. When $1.0 \leq \alpha \leq 2.0$ and for $K = 0.01$ and $K = 0.1$ the Appr myriad filter leads to obtaining the smallest value of MAE in comparison to the FP and BB myriad filters. It can be seen in tables 1, 2. In these cases the proposed Appr myriad filter shows the highest accuracy of filtering. When $K = 1$ MAE values obtained for the Appr filter are a little greater than MAE values obtained for the FP myriad filter, but smaller than for the BB myriad filter.

The BB myriad filter for $K = 0.01$ and $K = 0.1$ tends to obtain comparable results to the FP myriad filter, but when $K = 1$, the MAE values are greater than the rest of investigated filters.

The Fig. 4 presents results of using myriad filters with FP and Appr computation methods to suppress the noisy signal from Fig. 3.

6   Conclusion

The new method of computation of the myriad filter output is proposed. This method is based on the least square approximation with the 2nd order polynomial. Knowing

the coefficients of the approximation polynomial the top of parabola is calculated. Obtained coordinate x corresponds to the output of myriad filter in the running window of the length N. In order to prevent algorithm from outliers the filter window length is reduced. One condition is described which should be checked for correct use of the proposed computation method. This condition allows to find an accurate value of the output of running window. The proposed polynomial approach to computation of the output of myriad filter can effectively operate in wide range of the linear parameter K and the characteristic exponent α. The proposed method offers the comparative or better results of filtering signals in an impulsive environment than the reference myriad filter with the fixed-point searching method or the branch-and-bound method.

References

1. Barr, R.E., Chan, E.K.Y.: Design and implementation of digital filters for biomedical signal processing. J. Electrophysiol. Tech. (13), 73–93 (1986)
2. Chan, S., Zou, Y.: A Recursive least M-estimate algorithm for robust adaptive filtering in impulsive noise: fast algorithm and convergence performance analysis. IEEE Trans. on Signal Processing 52, 975–991 (2004)
3. Georgiou, P.G., Tsakalides, P., Kyriakakis, C.: Alpha-stable modeling of noise and robust time-delay estimation in the presence of impulsive noise. IEEE Trans. on Multimedia 1, 291–301 (1999)
4. Gonzalez, J.G., Arce, G.R.: Optimality of the myriad filter in practical impulsive-noise environments. IEEE Trans. on Signal Processing 49, 438–441 (2001)
5. Gonzalez, J.G., Griffith, D.W., Arce, G.R.: Matched myriad filtering for robust communications. In: Proc. Conf. Inform. Sci. Syst., Princeton, NY, USA (March 1996)
6. Gonzalez, J.G., Lau, D.L., Arce, G.R.: Towards a general theory of robust nonlinear filtering: selection filters. In: IEEE International Conference on Acoustics, Speech, and Signal Processing (ICASSP 1997), Munich, Germany, April 21-24, pp. 3837–3840 (1997)
7. Gonzalez, J.G., Arce, G.R.: Statistically-Efficient Filtering in Impulsive Environments: Weighted Myriad Filters. EURASIP Journal on Applied Signal Processing 1, 4–20 (2002)
8. Gonzalez, J.G., Paredes, J.L., Arce, G.R.: Zero-order statistics: a mathematical framework for the processing and characterization of very impulsive signals. IEEE Trans. on Signal Processing 54, 3839–3851 (2006)
9. Hong, X., Chen, S.: M-estimator and D-optimality model construction using orthogonal forward regression. IEEE Trans. on Systems Man and Cybernetics 35, 1–7 (2005)
10. Li, S.Z.: Robustizing robust M-estimation using deterministic annealing. Pattern Recognition 29, 159–166 (1996)
11. Hamza, B.A., Krim, H.: Image denoising: a nonlinear robust statistical approach. IEEE Trans. on Signal Processing 49, 3045–3054 (2001)
12. Hu, X., Nenov, V.: A single-lead ECG enhancement algorithm using a regularized data-driven filter. IEEE Trans. on Biomedical Eng. 2, 347–351 (2006)
13. Kalluri, S., Arce, G.R.: Adaptive weighted myriad filter algorithms for robust signal processing in a-stable noise environments. IEEE Trans. on Signal Processing 46, 322–334 (1998)

14. Kalluri, S., Arce, G.R.: Fast algorithms for weighted myriad computation by fixed point search. IEEE Trans. on Signal Processing 48, 159–171 (2000)
15. Kalluri, S., Arce, G.R.: Robust frequency-selective filtering using weighted myriad filters admitting real-valued weights. IEEE Trans. on Signal Processing 49, 2721–2733 (2001)
16. Shao, M., Nikias, C.L.: Signal processing with fractional lower order moments: stable processes and their applications. Proc. of the IEEE 81, 986–1009 (1993)
17. Pander, T.: An application of a weighted myriad filter to suppression an impulsive type of noise in biomedical signals. TASK Quartarly 2, 199–216 (2004)
18. Kim, K., Shevlyakov, G.: Why Gaussianity? IEEE Signal Processing Magazine 3, 102–113 (2008)
19. Aysal, T.C., Barner, K.E.: Meridian Filtering for Robust Signal Processing. IEEE Transactions on Signal Processing 55, 3939–3962 (2007)
20. Núñez, R.C., Gonzalez, J.G., Arce, G.R.: Fast and Accurate Computation of the Myriad Filter via Branch-and-Bound Search. IEEE Transactions on Signal Processing 56, 3340–3346 (2008)
21. Łęski, J.: Robust Weighted Averaging. IEEE Transactions on Biomedical Engineering 49, 796–804 (2002)
22. Surender, V.P., Ganguli, R.: Adaptive Myriad Filter for Improved Gas Turbine Condition Monitoring Using Transient Data. Journal of Eng. for Gas Turbines and Power 127, 329–339 (2005)
23. Lim, H.S., Chuah, T.C., Chuah, H.T.: On the Optimal Alpha-k Curve of the Sample Myriad. IEEE Signal Processing Letters 14, 545–548 (2007)

Electrophysiology-Based Monitoring System for a Human in Motion

Joanna Jaworek and Eliasz Kańtoch

Abstract. This paper proposes an electrophysiological wireless patient monitoring system which integrates a Wireless ECG signal transmitter, GPS device and a mobile phone to acquire physiological signals and transmit them to a local server via Bluetooth wireless technology. Four kinds of monitor units were specially designed for a wireless communication, including a control center , a local monitor unit, mobile devices (personal digital assistant; PDA), and a Web page (for both patient and doctor). The use of various monitor units is created to fulfill different medical personnel requirements and wishes. This application was developed to promote the mobility and flexibility for the patients and also for the medical personnel, which further will improve both the quality of health care and lifestyle of the patient.

1 Introduction

Electrophysiology has achieved a significant degree of medical success in the last 30 years. In this project autors concentrate on the combination of electrocardiological systems and pulso oxymetry to monitor human in motion. Electrocardiological systems allow us to record and analyze the electrical currents produced by the human heart and instruments commonly called electrocardiographs have been devised to receive these electrical impulses and record them on an electrocardiogram. There is a growing trend in electrophysiology toward remote, home monitoring systems of implantable cardioverter defibrillators (ICDs), pacemakers and cardiac resynchronization therapy (CRT).

Pulse oximetry is a non-invasive method allowing the monitoring of the oxygenation of a patient's hemoglobin. A patient's need for oxygen is the most essential

Joanna Jaworek · Eliasz Kańtoch
Katedra Automatyki, Al. Mickiewicza 30; 30-059 Kraków
e-mail: jaworek@agh.edu.pl, kantoch@agh.edu.pl

element to life; no human life thrives in the absence of oxygen (cellular or gross). Although pulse oximetry is used to monitor oxygenation, it cannot determine the metabolism of oxygen, or the amount of oxygen being used by a patient. For this purpose, it is necessary to also measure carbon dioxide (CO_2) levels. However, pulse oximetry data is necessary whenever a patient's oxygenation is unstable and can detect hypoventilation. Remote monitoring systems that include electrocardiological systems and pulse oximetry as well, can help alleviate the volume of in-office patient follow-ups, can give early warning of cardiac problems that appear at home, allow physicians to monitor more effectively patients, makes follow-up rehabilitation easier.

2 Monitoring Aspects

The ECG records is the electrical activity that appears when the heart muscle cells in the atria and ventricles contract. A general ECG signal of the heartbeat consists of waves and intervals that are described below. The heart's electrical axis refers to the general direction of the heart's depolarization wavefront.

2.1 Waves and Intervals

In an ECG signal we can distinguish: P wave, a QRS complex, ST segment, PR interval, QT interval, a T wave, and a U wave which is normally visible in 50 to 75 percent of ECGs. Below in the table are listed the most important and significant features with the Clinical specification [10].
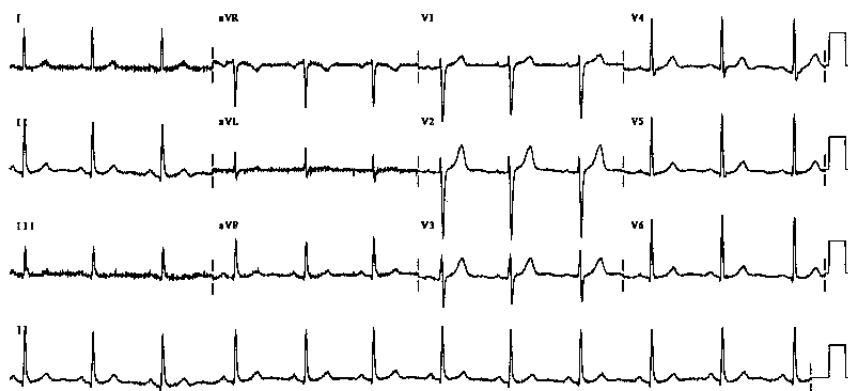
Fig. 1 A 12-lead ECG signal

Table 1 Important and significant features with the Clinical specification

Feature	Clinical specification
P wave	Left atrial enlargement can accompany mitral stenosis. P wave with increased amplitude can indicate hypokalemia. P wave with decreased amplitude can indicate hyperkalemia. Absence of the P wave may indicate atrial fibrillation. A saw tooth formed P wave may indicate atrial flutter.
QRS complex	The analysis of QRS complex allows us to diagnose: cardiac arrhythmias, conduction abnormalities, ventricular hypertrophy, myocardial infarction, electrolyte derangements, and other disease states.
PR interval	An abnormal PR interval can indicate first degree heart block, hypokalemia or acute rheumatic fever.
QT interval	A prolonged QT interval is a risk factor for ventricular tachyarrhythmias and sudden death.
T wave	The calculation of the T wave can diagnose: coronary ischemia, Wellens' syndrome, left ventricular hypertrophy, CNS disorder or hypokalemia.

2.2 *Mean Electrical Axis*

The mean electrical axis is the average of all the instantaneous mean electrical vectors occurring sequentially during depolarization of the ventricles. The mean electrical axis is the sum of all of the mean electrical vectors. To calculate the mean electrical axis from the ECG signal, the algorithm chooses two leads that are perpendicular ($90°$) and the vectorial sum of the deflections of the QRS complex give us the result in degrees [2, 10]. The mean electrical axis for the heart normally lies between -30 and $+90°$. Primary conduction abnormalities can cause an electrical axis shift. Less than $-30°$ (or less than $0°$) is termed a left axis deviation and greater than $+90°$ is termed a right axis deviation [10].

2.3 *Respiration Signal*

It is worth mentioning that analysis of the ECG signal allows us to assess not only the heart function but also the respiration signal that is presented on Fig. 2.

The method that is used to calculate the respiration signal has been described by G.B. Moody et al. in the [5] and bases on the changes of the heart position inside the chest when the diaphragm lowers during an inspiration [6]. The changes of the direction of the main cardiac electrical axis can be observed during breathing. The direction of the main cardiac electrical axis is calculated as: $\arctan(AI/AaVF)$, where leads AI and AaVF are perpendicular. To estimate the correctness of the respiration waveform we have done the next few steps [6]:

Table 2 Important and significant features with the Clinical specification

Feature	Clinical specification
Northwest axis, Northwest territory	- emphysema - hyperkalaemia - lead transposition - artificial cardiac pacing - ventricular tachycardia
Right axis deviation	- normal finding in children and tall thin adults - right ventricular hypertrophy - chronic lung disease even without pulmonary hypertension - anterolateral myocardial infarction - left posterior hemiblock - pulmonary embolus - Wolff-Parkinson-White syndrome - left sided accessory pathway - atrial septal defect - ventricular septal defect
Left axis deviation	- normal finding in children and tall thin adults - left anterior hemiblock - Q waves of inferior myocardial infarction - artificial cardiac pacing - emphysema - hyperkalaemia - Wolff-Parkinson-White syndrome - right sided accessory pathway - tricuspid atresia - ostium primum ASD - injection of contrast into left coronary artery

- analyze the respiration waveform with the FFT (Fast Fourier Transform)
- filtrate the signal with the high pass filter based on IFFT (Inverse Fast Fourier Transform)
- Cut-off frequency set to 0.1Hz
- Analyze the breathing frequency in time with the Short-Time Fourier's Transform
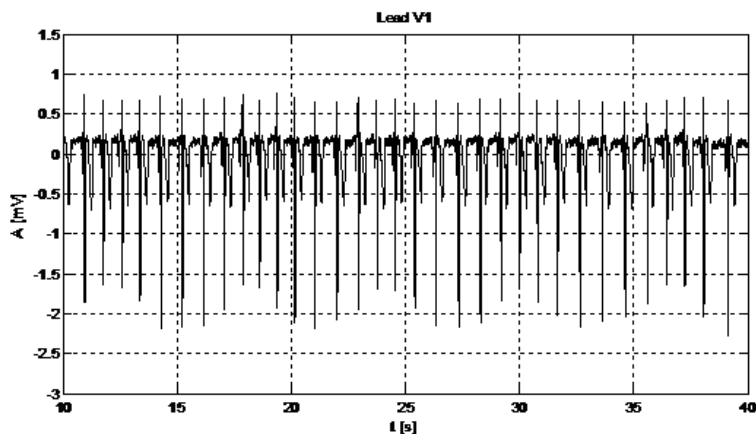
Fig. 2 Respiration signal

The described above algorithm allows us to assess parameters like: number of breaths in defined period of time or the time between the inspiration and the expiration.

2.4 Oxygen Saturation

A pulso oximeter measures the oxygen saturation of a patient's blood and changes in blood volume in the skin, producing a photoplethysmograph. It has been attached to the medical monitoring system to help diagnosing many heart diseases that are invisible in the ECG signal. Because of its simplicity, versatility and speed, pulse oximeters are of critical importance for patients with respiratory and cardiac problems, for diagnosis of some sleep disorders such as apnea and hypopnea. Acceptable normal ranges are from 90 to 100 percent.

3 System Design

In this paper we propose a mobile wireless electrocardiograph monitoring system. It includes Aspel Aspekt 500 ECG monitoring device GPS module and PC computer or laptop with constructed software for collecting and analyzing medical examination data. The system overview is presented on the Fig. 3.

3.1 Hardware Setup

A medical system is based on wireless ECG sensor (Fig. 4) and GPS module which transmits data to PC via Bluetooth wireless network technology.
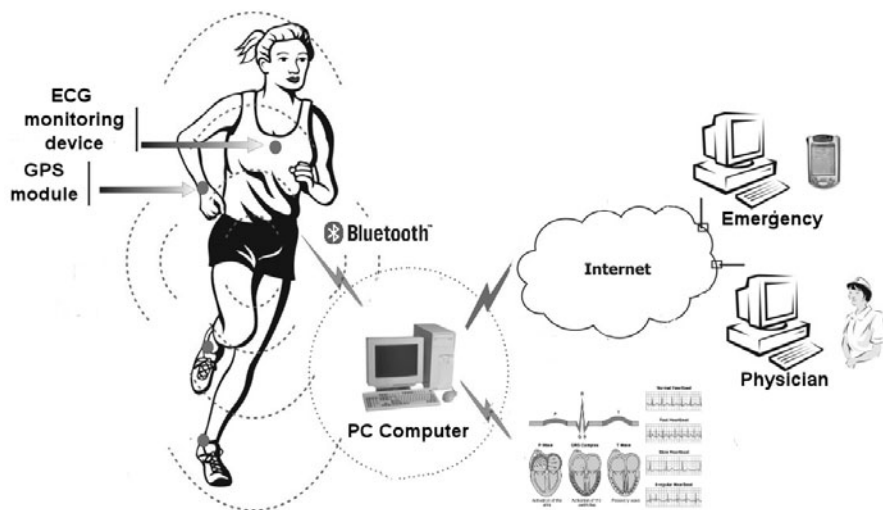
Fig. 3 Wireless ECG monitoring system

Fig. 4 Aspekt 500 ECG
wireless monitoring device

The main idea of this work was to construct system that is easy to use even for old and disabled people. Therefore, user needs only to perform tree simple steps to start the system:

1. Put on and switch on ECG monitoring device and pulso oxymeter.
2. Switch on GPS module.
3. Run PC control application.

PC application will automatically connect and download data form monitoring devices. Moreover, a proper dialog box will be show in case of connection or hardware problems.

3.2 Connection Modes and Data Flow

The ECG sensor, GPS module and PC computer exchange data using Bluetooth wireless network. At first PC application initiates connection with ECG sensor

Fig. 5 Patient's examination data flow

using PC Bluetooth COM port and sets connection parameters. When connection is established PC application sends to ECG sensor "start code" which starts transmission. Computer application collects and analyze transmitted data. Furthermore, PC software automatically connects to GPS module every 30s using Bluetooth wireless network and reads patient's GPS position. Finally, patient's examination data can be transmitted via Internet to the physician on duty. Patient's data flow in ECG monitoring system is shown on Fig. 5.

3.3 Data Format

One of the major application task was the correctly interpretation of the obtained data. Data is transmitted between computer and ECG monitoring device using AS-PEL protocol [1]. Data is divided into packets which contain information about 7 following samples and additional information which describe device status(battery state, frame number and connection state). Correct packet is presented below:

```
80 81 e1 11 14 08 a7 04 cd e1 f7 f1 97 04 2f e4 05 fd
80 05 28 11 38 f3 08 04 1b e8 86 f8 9f 04 3e eb 5f fc
80 64 ce 0f 66 dd d9 02 88 ef b0 02 e0 05 e0 ef f9 fa
80 00 57 10 10 e1 2c 03 cb ee 0f 06 7c 05 3e eb 77 fb
80 ff 41 11 98 eb 21 04 b0 ec d4 06 0f 05 76 e6 85 fc
80 53 b6 10 6d 00 99 03 48 e6 14 00 ea 04 79 df e5 fb
80 04 f7 0f f6 15 c1 02 ee de cb f5 92 05 d4 da 05 fb
```

The length of correct packet is 18 bytes. First two bytes ex. 80 81 are information bytes followed by 16 bytes from sensors.

The data line from the packet can be interpreted as following:

```
marker  I     II      V1      V2     V3      V4    V5      V6
80 81 e1 11 14 08 a7 04  cd e1  f7 f1 97 04 2f e4 05 fd
```

Where

- I - Lead I is the voltage between the (positive) left arm (LA) electrode and right arm (RA) electrode.

- II - Lead II is the voltage between the (positive) left leg (LL) electrode and the right arm (RA) electrode.
- V1 - V6 - The electrodes for the precordial leads (V1, V2, V3, V4, V5, and V6) are placed directly on the chest(close proximity to the heart).

For ECG analysis we need 12 channels. However, during examination we obtain 8. Addition 4 channels can be calculated [2].

- Lead III is the voltage between the (positive) left leg (LL) electrode and the left arm (LA) electrode and may be calculated as following:

$$III = II - I \qquad (1)$$

- Lead augmented vector right (aVR) has the positive electrode (white) on the right arm. The negative electrode is a combination of the left arm (black) electrode and the left leg (red) electrode, which "augments" the signal strength of the positive electrode on the right arm and may be calculated as following:

$$aVR = -\frac{I + II}{2} \qquad (2)$$

- Lead augmented vector left (aVL) has the positive (black) electrode on the left arm. The negative electrode is a combination of the right arm (white) electrode and the left leg (red) electrode, which "augments" the signal strength of the positive electrode on the left arm and may be calculated as following:

$$aVL = I - \frac{II}{2} \qquad (3)$$

- Lead augmented vector foot (aVF) has the positive (red) electrode on the left leg. The negative electrode is a combination of the right arm (white) electrode and the left arm (black) electrode, which "augments" the signal of the positive electrode on the left leg and may be calculated as following:

$$aVF = II - \frac{I}{2} \qquad (4)$$

4 Software

The computer software application was written in C++ with Qt library. It is easy to use and intuitive. At first, ECG signal is pre-processed. In the next step an elaborated algorithm measures ECG parameters, calculates breathing frequency from the ECG signals and evaluates patient motion from the GPS module in the real time. Finally, monitoring system makes a decision about patient state changes based on calculated parameters and in case of appearance of dangerous situation sends the warning signal to doctor, informs the patient about his condition and analyzed results are

transmitted to physician on duty. With the help of this Wireless ECG monitoring system patients are supervised at home with no necessity for staying in hospital.

5 Experimental Database

Testing of correct implementation of the algorithm was carried on several ECG data records performed in The Independent Laboratory of Biocybernetics. The ECG records were judged by a doctor and could be used to check not only the monitoring system and transmission but also communication with the base station. The tests were divided into few main parts:

- Verifying the technical correctness of data transmitted between the monitor units,
- Data saving and displaying in the Web pages,
- Communicating alarm system (between PDA, GPRS and mobile phone)
- Correctness of the interpretation of the received data (ECG, pulso oxymetry)

6 Future Tests

A promising perspective is to broaden the amount of function and the use of new methods for automatically detection of pathological ECG signals. In the future, instead of using well known parameters, it could be interesting to find out and use different ones, more related to the flow of electrical impulses of the heart (vectocardiography).

7 Discussion

Remote medical monitoring systems have developed very fast in recent years. In order to predict complications before patient cause serious harm, we need a wearable, wireless and low power patient device to monitor their electrical charges at real time. Wireless electrocardiograph monitoring system integrated with GPS was designed for home care patients with cardiac risk.

There are several system limitations including the effective range of Bluetooth devices (about 10 meters) and battery operated time. The major advantage of the system is an application of wireless technologies in order to monitor patient 24h a day and react in case of emergency. Moreover, remote monitoring system is a chance for number of patients who suffer from protracted diseases who can be supervised at home with no necessity for staying in hospital.

References

1. Description of ASPEL Standard Serial Transmission Protocol
2. Augustyniak, P.: Przetwarzanie sygnałów elektrodiagnostycznych, UWND AGH, Krakow (2001) (in Polish)
3. Manual for wireless ECG monitoring device AsPEKT 500
4. Mikrut, Z., Augustyniak, P.: Mobilny system zdalnego nadzoru kardiologicznego: aspekty implementacyjno - techniczne, Automatyka Tom 10 Zeszyt 3, UWND AGH, Kraków (2006)
5. Moody, G.B., Mark, R.G., Zoccola, A., Mantero, S.: Derivation of Respiratory Signals from Multi-lead ECG. Computers in Cardiology 12, 113–116 (1985)
6. Augustyniak, P., Kikta, A.: Comparing methods of ecg respiration signals derivation based on measuring the amplitude of QRS complexes. Journal of Medical Informatics and Technologies 11, 155–163 (2007)
7. Dorfman Furman, G., Shinar, Z., Baharav, A., Akselrod, S.: Electrocardiogram Derived Respiration during Sleep. Computers in Cardiology 32, 351–354 (2005)
8. Ludwin, W. (ed.): Bluetooth. Nowoczesny system łączności bezprzewodowej, Uczelniane Wydawnictwa Naukowo-Dydaktyczne, Krakow (2003) (in Polish)
9. Daniluk, A.: RS 232C - praktyczne programowanie. Od Pascala i C++ do Delphi i Buildera. Wydawnictwo Helion (2002)
10. Garcia, T.B., Holtz, N.E.: EKG Sztuka interpretacji, Medipage, Warszawa (2007)

Analysis of Major Adverse Cardiac Events with Entropy-Based Complexity

Tuan D. Pham, Cuong C. To, Honghui Wang, and Xiaobo Zhou

Abstract. Major adverse cardiac events (MACE) are referred to as unsuspected heart attacks that include death, myocardial infarction and target lesion revascularization. Feature extraction and classification methods for such cardiac events are useful tools that can be applied for biomarker discovery to allow preventive treatment and healthy-life maintenance. In this study we present an entropy-based analysis of the complexity of MACE-related mass spectrometry signals, and an effective model for classifying MACE and control complexity-based features. In particular, the geostatistical entropy is analytically rigorous and can provide better information about the predictability of this type of MACE data than other entropy-based methods for complexity analysis of biosignals. Information on the complexity of this type of time-series data can expand our knowledge about the dynamical behavior of a cardiac model and be useful as a novel feature for early prediction.

1 Introduction

The emerging concept of personalized medicine [1] has placed an important role in studying methods for disease prediction and biomarker discovery. The gain of new knowledge of the molecular basis of disease is expected to make it possible a

Tuan D. Pham · Cuong C. To

School of Engineering and Information Technology, University of New South Wales, Canberra, ACT 2600, Australia

e-mail: `t.pham@adfa.edu.au`, `c.to@adfa.edu.au`

Honghui Wang

Clinical Center, National Institutes of Health, Bethesda, MD 20892, USA

e-mail: `hwang2@cc.nih.gov`

Xiaobo Zhou

Center for Biotechnology and Informatics, The Methodist Hospital Research Institute, Weill Cornell Medical College, Houston, TX 77030, USA

e-mail: `xzhou@tmhs.org`

revolution of pharmacogenomics where drug discovery will no longer be a linear process but an integrated approach. This new approach will involve the use of modern biological data and computational methods for the selection and validation of drug targets, molecule screening, and preclinical assessment of compounds.

While genomic technologies can be applied for identification of drug targets and co-regulated genes that can be potential surrogate biomarkers for use in preclinical and clinical studies; proteomic technologies including two-dimensional gel electrophoresis, mass spectrometry, and computational prediction programs offer a promising high-throughput platform for identifying proteins, mapping their interactions, and enabling the discovery of new biomarkers [2].

Prediction of major adverse cardiac events (MACE) has recently been a focus of biomedical research including the use of protein biomarkers [3, 4], fractional flow reserve [5], mass-spectrometry protein data [6], adenosine stress magnetic resonance [7], and percutaneous coronary intervention [8]. On recent applications of proteomic technologies, proteomic patterns have recently been utilized for early detection of cancer progressions [9]. In particular, methods for classification of normal and disease states using mass spectrometry data have been progressively developed [10].

The study of biosignal complexity for understanding disease mechanisms has been attracting attention of the biomedical research community [11, 12]. Another perspective of analysis of time-series biosignals for clinical diagnosis and disease classification is by studying the predictability of the signal variability using the concept of approximate entropy (ApEn) [13] and sample entropy (SampEn) [14]. In this study, a low value of the entropy indicates the time series is deterministic (low complexity); whereas a high value indicates the data is subject to randomness (high complexity) and therefore difficult to predict. In other words, lower entropy values indicate more regular time series; whereas higher entropy values indicate more irregular time series. Both ApEn and SampEn estimate the probability of the subsequences of a pattern that are initially closely related remain within a tolerated similarity on the next incremental comparison. ApEn differs from SampEn in that its calculation involves counting a self-match for each sequence of a pattern, which leads to bias in ApEn. SampEn is precisely the negative natural logarithm of the conditional probability that two sequences similar for m points remain similar at the next point, where self-matches are not included in calculating the probability. Thus a lower value of SampEn also indicates more self-similarity in the time series. In addition to eliminating self-matches, the SampEn algorithm is simpler than the ApEn algorithm, requiring approximately one-half as much time to calculate. SampEn is largely independent of record length and displays relative consistency under circumstances where ApEn does not.

However, it has been realized that standard application of this type of entropy measures has limitations. For example, approximate entropy measure of atrial fibrillation, which is the twitching of the upper chambers of the heart that produce highly erratic rate fluctuations, is similar to that in healthy hearts [15]. Therefore, other attempts to improve the framework of the entropy are necessary to distinguish the difference between physiological and pathological states. As an attempt to add

a new quantity to the sample entropy, multiscale entropy (MSE) [16] has been introduced to quantify the complexity or predictability of physiological time-series data at different scales. MSE measures complexity of time series data by taking into account multiple time scales, and uses SampEn to quantify the regularity of the data.

All ApEn, SampEn and MSE methods depend on the selection of the two control parameters known as m and r: parameter m is used to determine the sequence length, whereas parameter r is the tolerance threshold for computing pattern similarity. Results are sensitive to the selections of these two parameters and it has recently been reported that good estimates of these parameters for different types of signals are not easy to obtain [17].

This paper addresses the analysis of the complexity of mass spectral based MACE data using entropy-based methods. The rest of this paper is organized as follows. Section II presents entropy methods including approximate entropy, sample entropy, multiscale entropy, and the geostatistical entropy. Section III involves the study of the complexity of MACE and control subjects using mass spectrometry data where the entropy-based features can also be used for disease classification. Section IV is the conclusion of the findings of the application of entropy methods for the analysis of clinical proteomics for major adverse cardiac events.

2   Geostatistical Entropy (GeoEn)

The principle of geostatistical entropy, denoted as GeoEn, is developed based on the theory of regionalized variables. We present the conceptual framework of GeoEn as follows [18].

Let $z(X)$ be a regionalized variable which has characteristics in a given region $\mathscr{D}$ of a spatial or time continuum [19]. In the setting of a probabilistic model, a regionalized variable $z(X)$ is considered to be a realization of a random function $Z(X)$. In such a setting, the data values are samples from a particular realization $z(X)$ of $Z(X)$. We now consider n observations: $z(X_\alpha)$, $\alpha = 1, \ldots, I$; taken at locations or times α. Thus, the sampled objects in $\mathscr{D}$ is considered as a small subset of a larger collection of objects. Many more observations may be made but because of the further cost, effort, or experiments involved this collection has been not allowed. If the objects are points in time or space, the possibility of infinite observations of the same kind of data is introduced by relaxing the index α. The regionalized variable is therefore defined as $z(X)$ for all $X \in \mathscr{D}$, and $\{z(X_\alpha), \alpha = 1, \ldots, I\}$ is viewed as a collection of a few values of the regionalized variable. The study of a regionalized variable concerns with at least two aspects: 1) the domain $\mathscr{D}$ in which the regionalized variable is defined, and 2) the geometry or time dependent support for which each sample of the regionalized variable is defined.

We now consider that each measured value in the dataset has a geometrical or time point in the respective domain $\mathscr{D}$, which is called a regionalized value. The regionalized values at all points in $\mathscr{D}$, $\{z(X), X \in \mathscr{D}\}$, can be viewed as one set of values drawn from an infinite set of random variables. The family of random variables $\{Z(X), X \in \mathscr{D}\}$, is called the random function. Thus, a regionalized variable

$z(X)$ is one realization of a random variable $Z(X)$, and a regionalized value at a specific location or time is a realization of a random function which is itself a member of an infinite family of random variables. The variability of a regionalized variable $z(X)$ at different scales can be measured by calculating the dissimilarity between pairs of data values, denoted by $z(X_\alpha)$ and $z(X_\beta)$, located at geometrical or time points α and β in a spatial or time domain $\mathcal{D}$, respectively (from now on we address point/domain to imply either geometrical or time point/domain). The measure of this semi-dissimilarity, denoted by $\gamma_{\alpha\beta}$, is computed by taking half of the squared difference between the pairs of sample values (the term *semi* is used to indicate the half difference) as

$$\gamma_{\alpha\beta} = \frac{1}{2}(X_\alpha - X_\beta)^2 \tag{1}$$

The two points x_α and x_β in space or time can be linked by a space or time lag $h = X_\alpha - X_\beta$ (we use h here as a scalar but its generalized form is a vector to indicate various spatial orientations). Now let the semi-dissimilarity depend on the lag h of the point pair, we have

$$\gamma_\alpha(h) = \frac{1}{2}[(z(X_\alpha + h) - z(X_\alpha)]^2 \tag{2}$$

Expression (2) indicates that the dissimilarity is a function of a squared quantity, in which the order of the points X_α and X_β are not considered, and symmetric with respect to h: $\gamma(h) = \gamma(-h)$. Using all samples pairs in a dataset, a plot of the $\gamma(h)$ against the separation h is called the semi-variogram. The function $\gamma(h)$ is referred to as the semi-variance and defined as

$$\gamma(h) = \frac{1}{2N(h)} \sum_{(\alpha,\beta)|h_{\alpha\beta}=h} [z(X_\alpha) - z(X_\beta)]^2 \tag{3}$$

where $N(h)$ is the number of pairs of data points whose locations are separated by lag h.

The semi-variance defined in (3) is known as the experimental semi-variance and its plot against h is called the experimental semi-variogram, to distinguish it from the theoretical semi-variogram that characterizes the underlying population. The theoretical semi-variogram is thought of a smooth function represented by a model equation; whereas the experimental semi-variogram estimates its form. The behavior of the semi-variogram can be graphically illustrated by the theoretical semi-variogram using the spherical or the Matheron model which is defined as [20]

$$\gamma(h) = \begin{cases} s\left[1.5\frac{h}{g} - 0.5(\frac{h}{g})^3\right] & : \quad h \le g \\ s & : \quad h > g \end{cases} \tag{4}$$

where g and s are called the *range* and the *sill* of the theoretical semi-variogram, respectively.

The concept of regionalized variables and its modeling of variability in space continuum by means of the semi-variogram have been described. What can be

observed is that the range g of the semi-variogram presents an idea for capturing the auto-relationship of the time-series data: within the range g, the data points are related; when $h > g$, information about relationship between the data points becomes saturated and not useful. Based on this principle of the semi-variogram, the length of the sub-sequences of the time-series data X can be appropriately chosen to be the range g, which ensures an optimal study of self-similarity of the signal, that is $m = g(X)$. To address the criterion of similarity/dissimilarity between the sub-sequences, we can establish its lower bound as the absolute difference between two consecutive interval of the semi-variance or the absolute one-step semi-variance difference: $r = |\gamma(h) - \gamma(h+1)|$, or multi-step semi-variance difference: $r = |\gamma(h) - \gamma(h+c)|$ where c is a positive constant. Having defined the subsequence length m and the similarity criterion r, determination of GeoEn can be obtained using the principle of either ApEn or SampEn.

GeoEn algorithm for calculating the complexity of time-series data is outlined as follows.

1. Compute the semi-variance of X_N and its range $g(X_N)$
2. Set vector length $m = g(X_N)$
3. Construct vectors of length m, X_1 to X_{N-m}, defined as

$$X_i = (x_i, x_{i+1}, \ldots, x_{i+m-1}), \ 1 \le i \le N - m$$

4. Set semi-variance lag $h = 1, \ldots, \min_i[g(X_i)]$
5. Compute distance between X_i and X_j as

$$d(X_i, X_j) = |\gamma_{X_i}(h) - \gamma_{X_j}(h)| \tag{5}$$

6. Set the criterion of similarity r as follows.

$$r = |\gamma_{X_i}(h) - \gamma_{X_i}(h+1)| \tag{6}$$

7. Calculate either ApEn or SampEn for each h to obtain multiscale $GeoEn(X_N, h)$.

3 Analysis of Major Adverse Cardiac Events

3.1 Data

Six-hundred and four patients presented in emergency room with chest pain and their blood samples were collected at the presentation of the emergency room and the protein level of MPO (myloperoxidase) and other known cardiovascular biomarkers were measured [3]. The patient's outcome (any cardiovascular event) was monitored for 6 months. The study showed the MPO to be a new biomarker for the prediction of MACE risk in 30 days after the presentation of chest pain in emergency room with accuracy about 60%. The plasma samples used in our study are the same as those used in the original work previously described [3]. We used a portion of the available SELDI (Surface-Enhanced Laser Desorption/Ionization)

dataset in this study. MPO levels were measured with FDA approved assay and were provided by Cleveland Clinic Foundation. In this study, the data processing is limited to MACE and control experiments which were originally described in [4].

Protein spectra were obtained on IMAC ProteinChip arrays (PCA) coupled to copper (IMAC30-Cu21, Ciphergen Biosystems, Inc., Fremont, CA) and weak cation exchange (CM10, Ciphergen Biosystems, Inc.) PCAs. Fractions were subsequently profiled on both IMAC30-Cu21 and CM10 protein arrays. Fraction 2 was not analyzed since experiments have shown that it contains little protein (data not shown). Samples from MACE and control, as well pooled samples from both groups and blank cases were randomly distributed to the spots of PCA in Group A or B. All spectra were acquired in duplicate using two Bioprocessors, Bioprocessor 1 and 2, which were processed at the same time using the same aliquot sample plate. The remaining portions of the samples were stored at 2807C and were never re-used for other PCAs. PCAs were analyzed using a ProteinChip Reader, model PBSIIc (Ciphergen Biosystems Inc.). Protein spectra were externally calibrated using the All-in-One Protein Standard II (Ciphergen Biosystems, Inc.) consisting of seven calibrants between 7 and 147 kDa. Data was collected between 0 and 200 kDa with the region between 2 and 20 kDa optimized. Spectra were generated by averaging 130 laser shots with a laser intensity (215-220) and a detector sensitivity (5-8) optimized for each fraction.

For the control group, the dataset consists of 60 patients who presented in emergency room with chest pain and the patients' troponin T test was consistently negative. These patients lived in the next 5 years without any major cardiac events or death. The total 166 plasma samples, 24 reference samples and 6 blanks were fractionated into 6 fractions using two 96-well plates containing anion exchange resin (Ciphergen, CA). For the MACE group, the dataset was designed to comprise 60 patients who presented in emergency room with chest pain but the patients' troponin T test was negative. However, the patients in this group had either a heart attack, died or needed revascularization in the subsequent 6 months.

3.2 Results

As a preliminary analysis of the times series data under study, the mass spectrometry signals were standardized to have zero mean and unit standard deviation by subtracting each value of the data with the mean and then dividing it by the standard deviation in order to isolate and remove periodicity and noise. For the entropy estimates using MSE, the constant values of $m = 2$ and $r = 0.15$. Fig. 1 shows the plots of the mean entropy values of the MACE and control groups using MSE. By observation, the difference between the MACE and control curves is not clearly distinguished. The MSE-based entropy values of the two groups exhibit similar fluctuating values at scales after 9.

Applying the experimental semi-variogram, we obtained the range about 8 for both MACE and control populations and set this value to be the value of m for the geostatistical entropy calculation. We then applied GeoEn analysis, where r is

Fig. 1 Mean entropy values of MACE and control groups using MSE
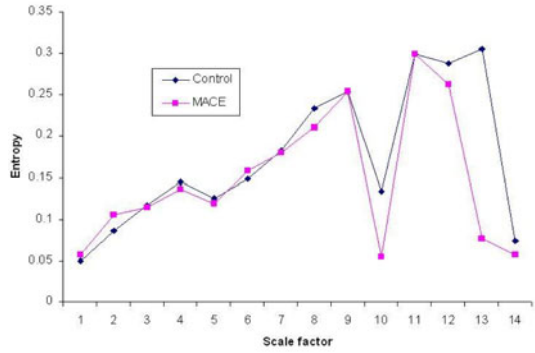
Fig. 2 Mean entropy values of MACE and control groups using SampEn-based GeoEn
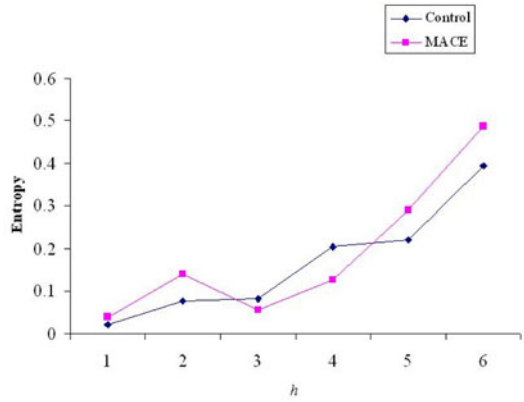
Fig. 3 Mean entropy values of MACE and control groups using ApEn-based GeoEn
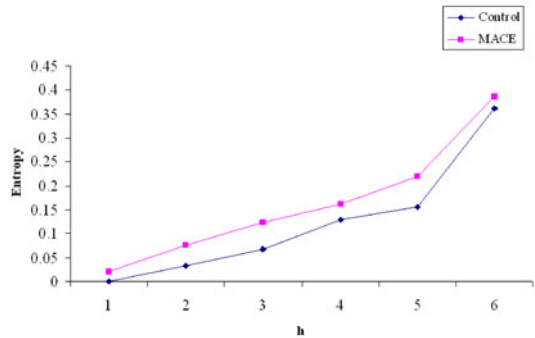
Fig. 4 Typical mass spectrometry data of MACE and Control subjects, where solid lines indicate MACE and dotted lines indicate Control, showing strong signal similarity.
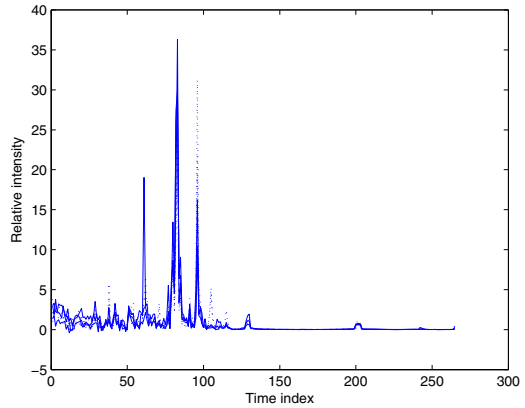
locally calculated to check the similarity between the subsequences. Fig. 2 shows the entropy profiles of the MACE and control groups using SampEn-based GeoEn. Fig. 3 shows the entropy profiles of the MACE and control groups using ApEn-based GeoEn. By setting maximum value of lag h to be equal to the minimum of the semi-variogram ranges of the time series data, the entropy values of the MACE and control groups were truncated at $h=6$, showing positive slopes. The GeoEn-based entropy profiles show better separations between the two groups, particularly the ApEn-based GeoEn profile. Variances of the entropy values obtained from differentS methods are shown in Table 1, in which the variances of GeoEn are smaller than those of MSE.

With the MSE-based results shown in Fig. 1, it is difficult to observe which group, MACE or control, has higher entropy values from scale 1 to 8; but there appear higher entropy values for the control group from scales 10 onward, except at scale 11. It can be seen that entropy values obtained from GeoEn approach are higher for the MACE group, particularly those given by the ApEn-based GeoEn. Both GeoEn and MSE analyses suggest similar patterns for MACE and control subjects since the mass spectrometry data of the two groups are similar to each other because the MACE data used are the early onset of the cardiac events. As an example, Fig. 4 shows the plots of typical MS samples of the two groups which can be appreciated that the identification of the two patterns is a difficult task as the signals of the control and MACE subjects are similar to one another. The results obtained from GeoEn approach provide more meaningful and consistent interpretations of the dynamic behaviors of the two groups, whereas it is harder with the MSE approach as the entropy values are overlapping at the smaller scales and become erratic at the larger ones.

To illustrate the usefulness of the complexity-based features we have presented. These features were then utilized for classification between MACE and control samples. We have recently developed a spectral matching method for classifying MACE and control samples [6]. However, this method is applicable when the feature vectors are of sufficient length to guarantee the reliable estimate of the prediction

coefficients. The multiscale values expressed in form of vectorized features we investigate here are expected to be of length much shorter than the forementioned vectors of the prediction coefficients. We therefore applied a strategy of a single-class classification scheme based on the concept of a hyperplane for data transformation [21] to classify the entropy-based features. This single-class classification method tries to map each training vector into a hyperplane: $\sum_{1=1}^{n} u_i x_i = v$, where $u_1, u_2, \ldots, v \in \mathcal{R}$ to be determined with at least one of u_i is non-zero, and $\mathbf{x} = (x_1, x_2, \ldots, x_n)$ is a training feature vector. The hyperplane $H = \{\mathbf{x} \in \mathcal{R}^n : \mathbf{u}^T \mathbf{x} = v\}$. This classifier finds a hyperplane H by using an objective function that minimizes the total distances from all training patterns to H. The distance between an unknown sample $\mathbf{y} = (y_1, y_2, \ldots, y_n)$ and the hyperplane H of the training set is calculated as: $d(\mathbf{y}, H) = |\mathbf{u}^T \mathbf{y} - v| / ((\sum_{i=1}^{n} u_i^2)^{1/2})$. The classification decision rule is that $\mathbf{y}$ is assigned to the same class of $\mathbf{x}$ if $d(\mathbf{y}, H)$ is less than or equal to the maximum distance between a training vector and the training hyperplane H.

In previous work [4], we used the MPO value, five selected biomarkers by T-test, five selected biomarkers by the sequential forward floating search (SFFS), five selected biomarkers by standard genetic algorithm (GA), and five selected biomarkers by an improved genetic algorithm (IGA) to carry out the prediction. In another recent work [6], we used a kriging scheme to extract MACE and control features and the applied its spectral distortion measure for classyfying the subjects with the same mass-spectrometry dataset presented in this study. The results obtained from the recent work were found more favorable than those reported in [4]. Using the GeoEn-based features with the single-class classifier, we were able to further improve the classification rates. Sensitivity is the percentage of the MACE (diseased) samples that are correctly identified, whereas specificity is the percentage of the control (non-diseased) samples that are correctly identified. We then run fifty different tests with different ratios of training and testing data, which were randomly selected, to compute the sensitivity and specificity of the classification. The average sensitivy and specificity results are shown in Table 2. The average validation results of different methods are presented in Table 3. Results from both Tables 2 and 3 show the best performance given by the entropy-based classification. In particular, the GeoEn-based classification model was found to be more robust in various designs of training and testing datasets with the lowest average classification rate of 93.55% (average of sensitivity and specificity where training and testing data sets were equally divided) and as high as 95.71% for the total average result in compasrion with the distortion method giving 90.50% and 92.97%, respectively.

To measure the strength of the evidence against the claims of the average results on the sensitivity and specificity given in Table 2, we randomly selected other ten training and testing datasets for each training-testing ratio design and applied the z-test, where a 5% significance level is adopted. The p-values obtained from the z-tests of the 50%, 60%, 70%, 80%, and 90% training sets are 0.823, 0.837, 0.842, 0.866, and 0.875, respectively. All the results of the hypothesis tests indicated that the average performance data are statistically significant at the 5% significance level, which suggest the average performance data would occur just by chance no more than 5% of the time in repeated samples.

Table 1 Variances of entropy values

Methods	Control	MACE
MSE	0.00057	0.00048
SampEn-based GeoEn	0.00021	0.00020
ApEn-based GeoEn	0.00009	0.00001

Table 2 Sensitivity (SEN) and specificity (SPE) using distortion-based and GeoEn-based classification methods

Training (%)	SEN		SPE	
	Distortion	GeoEn	Distortion	GeoEn
50	0.952	0.961	0.858	0.910
60	0.964	0.982	0.879	0.921
70	0.970	0.985	0.900	0.935
80	0.972	0.990	0.908	0.938
90	0.976	0.997	0.918	0.952

Table 3 Average MACE prediction rates by different methods

Method	Average accuracy (%)
MPO value	55.25
T-test	62.23
Standard genetic algorithm	69.05
Sequential forward floating search	71.92
Improved genetic algorithm	75.16
Statistical distortion measure	83.34
Geostatistical distortion measure	97.10
GeoEn-based classification	99.08

4 Conclusion

The disease subjects are at the early onset having similar signal statistics with the healthy, they exhibit similar dynamic behaviors. The results obtained from GeoEn provide better separations between the entropy-based complexity profiles of the two groups, which would be useful for further computational analysis for early detection and discovery of cardiac biomarkers. Being similar to MSE, GeoEn is multiscale entropy. Its multiscale measure can be obtained by computing GeoEn for each lag h and therefore this computational process results in a vector of geostatistical entropies that can be utilized as vectorized feature for pattern classification. We have also applied an effective classification scheme using the concept of hyperplane mapping for single-class classification to maximize the discriminant power

of the entropy-based feature vectors where considered not being appropriate for the application of the spectral distortion measure in our previous study.

The use of both high-throughput genome-scale and proteome-scale screening is emerging as powerful tools for identifying and classifying novel regulators of diverse cell and protein behaviors based on which results new biomarkers and better treatments for complex diseases can be discovered. The conceptual framework of the entropy methods for capturing signal characteristics appears to be promising for automated data analysis of such biosignals.

References

1. Ginsburg, G.S., McCarthy, J.J.: Personalized medicine: revolutionizing drug discovery and patient care. Trends in Biotechnology 19, 491–496 (2001)
2. Yarmush, M.L., Jayaraman, A.: Advances in proteomic technologies. Annu. Rev. Biomed. Eng. 4, 349–373 (2002)
3. Brennan, M.L., Penn, M.S., Van Lente, F., Nambi, V., Shishehbor, M.H., Aviles, R.J., Goormastic, M., Pepoy, M.L., McErlean, E.S., Topol, E.J., Nissen, S.E., Hazen, S.L.: Prognostic value of myeloperoxidase in patients with chest pain. The New England Journal of Medicine 13, 1595–1604 (2003)
4. Zhou, X., Wang, H., Wang, J., Hoehn, G., Azok, J., Brennan, M.L., Hazen, S.L., Li, K., Wong, S.T.C.: Biomarker discovery for risk stratification of cardiovascular events using an improved genetic algorithm. In: Proc. IEEE/NLM Int. Symposium on Life Science and Multimodality, pp. 42–44 (2006)
5. Klauss, V., Erdin, P., Rieber, J., Leibig, M., Stempfle, H.-U., König, A., Baylacher, M., Theisen, K., Haufe, M.C., Sroczynski, G., Schiele, T., Siebert, U.: Fractional flow reserve for the prediction of cardiac events after coronary stent implantation: results of a multivariate analysis. Heart 291, 203–206 (2005)
6. Pham, T.D., Wang, H., Zhou, X., Beck, D., Brandl, M., Hoehn, G., Azok, J., Brennan, M.L., Hazen, S.L., Li, K., Wong, S.T.C.: Computational prediction models for early detection of risk of cardiovascular events using mass spectrometry data. IEEE Trans. IT in Biomedicine 12, 636–643 (2008)
7. Chan, W.S., Luk, C.H., Tse, H.F.: Abstract 3091: Prediction of major adverse cardiac events in patients presenting with chest pain in outpatient clinic by adenosine stress magnetic resonance. Circulation 116, II_693 (2007)
8. Madan, P., Elayda, M., Lee, V., Wilson, J.: Predicting major adverse cardiac events after percutaneous coronary intervention: The Texas Heart Institute risk score. American Heart Journal 155, 1068–1074 (2008)
9. Conrads, T.P., Zhou, M., Petricoin III, E.F., Liotta, L., Veenstra, T.D.: Cancer diagnosis using proteomic patterns. Expert Rev. Mol. Diagn. 3, 411–420 (2003)
10. Tibshirani, R., Hastie, T., Narasimhan, B., Soltys, S., Shi, G., Koong, A., Le Sample, Q.-T.: classification from protein mass spectrometry by peak probability contrasts. Bioinformatics 20, 3034–3044 (2004)
11. Goldberger, A.L., Peng, C.-K., Lipsitz, L.A.: What is physiologic complexity and how does it change with aging and disease? Neurobiology of Aging 23, 23–26 (2002)

12. Goldberger, A.L., Amaral, L.A.N., Hausdorff, J.M., Ivanov, P.C., Peng, C.-K., Stanley, H.E.: Fractal dynamics in physiology: alterations with disease and aging. Proc. Natl. Acad. Sci. USA 99(suppl. 1), 2466–2772 (2002)

13. Pincus, S.M.: Approximate entropy as a measure of system complexity. Proc. Natl. Acad. Sci. USA 88, 2297–2301 (1991)

14. Richman, J.S., Moorman, J.R.: Physiological time series analysis using approximate entropy and sample entropy. Amer. J. Physiol. Heart Circ. Physiol. 278, H2039–H2049 (2000)

15. Chialvo, D.R.: Unhealthy surprises. Nature 419, 263 (2002)

16. Costa, M., Goldberger, A.L., Peng, C.K.: Multiscale entropy analysis of complex physiologic time series. Phys. Rev. Lett 89, 068102-1–068102-4 (2002)

17. Lu, S., Chen, X., Kanters, J.K., Solomon, I.C., Chon, K.H.: Automatic selection of the threshold value r for approximate entropy. IEEE Trans. Biomedical Engineering 55, 1966–1972 (2008)

18. Pham, T.D.: GeoEntropy: a measure of complexity and similarity. Pattern Recognition 43, 887–896 (2010)

19. Matheron, G.: Estimating and Choosing. Springer, Berlin (1989)

20. Isaaks, E.H., Srivastava, R.M.: An Introduction to Applied Geostatistics. Oxford University Press, New York (1989)

21. To, C., Pham, T.D.: Analysis of massive data in biology using hyperplane-based genetic algorithms. Int. J. Trans. Mass-Data Analysis of Images and Signals 1, 76–88 (2009)

Adaptive Time-Varying Frequency Characteristic Filtering of ECG Signal

Alina Momot and Michał Momot

Abstract. The primary diagnostic tools allowing the detection of cardiovascular system diseases through the study of bioelectric activity of the heart are the electrocardiographic systems. The low amplitude ECG signal is usually disturbed by various types of noise, particularly by power line interference, which should be reduced without distortion of useful signal component. Since the amplitude (sometimes also frequency) of such noise varies in time, the adaptive approach may be applied to construct time-varying frequency characteristic filter.

This paper presents an approach to adaptive filtering based on set of infinite impulse response (IIR) bandpass filters, which responses are base for noise amplitude and frequency estimation. These values are used to adjust parameters of notch filter originally proposed by Mortara. The performance of the new method is numerically evaluated using the artificial ECG signal from CTS database combined with simulated power line noise with varying amplitude and frequency.

1 Introduction

The primary diagnostic tools allowing the detection of cardiovascular system diseases through the study of bioelectric activity of the heart are the electrocardiographic (ECG) systems. Clinicians can evaluate the conditions of a patient's heart from the ECG and perform further diagnosis. ECG records are obtained by sampling the bioelectric currents sensed by several electrodes, known as leads.

Alina Momot
Silesian University of Technology, Institute of Computer Science,
16 Akademicka St., 44-100 Gliwice, Poland
e-mail: alina.momot@polsl.pl

Michał Momot
Institute of Medical Technology and Equipment, 118 Roosevelt St., 41-800 Zabrze, Poland
e-mail: michal.momot@itam.zabrze.pl
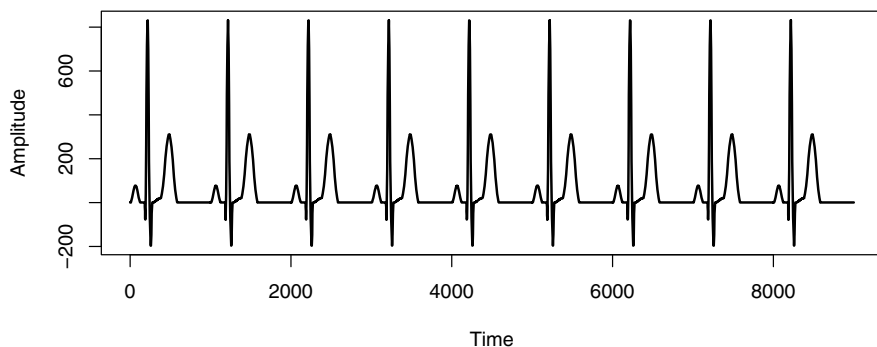
Fig. 1 An example of ECG signal

The ECG signals (see Fig. 1) are often corrupted by electrical noise from different sources such as adjacent electrical supply and power lines in the neighborhood of used equipment. Because the useful component of ECG signal has usually very low voltage, it is highly susceptible to noise introduced from these sources.

To reduce the power line noise in a disturbed ECG signal (see Fig. 2), narrow band notch filters are often used. Such a notch filter must be very selective, having a very thin bandwidth in order to avoid filtering any of the desired components of the ECG signal. However, the use of narrow band notch filters is of limited utility because the frequency of a power line noise may vary around 50 Hz (or 60 Hz in some countries).

Although in some countries the power line frequency is relatively fixed and stable at its nominal frequency, the power line frequency in other countries can vary substantially. For example, in Poland the power line frequency may vary from 49 Hz to 51 Hz [7]. That is why a narrow band filter having a fixed notch frequency has to be relatively broad banded to reduce the noise induced by the power line.

Another solution of power line noise reduction problem is an adaptive filtering technique. An example of an adaptive filtering is presented in [4], where finite
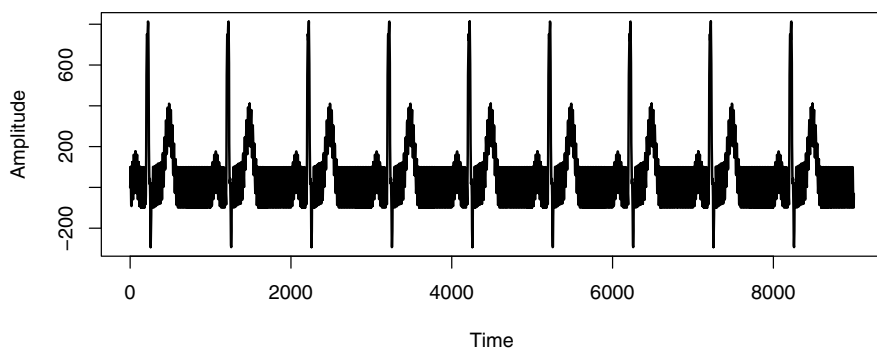
Fig. 2 An example of ECG signal disturbed by power line noise with frequency 50Hz

impulse response (FIR) filter has adaptive parameters which modify the frequency of the signal being filtered based on some feedback. The feedback adjusts the parameters of FIR filter so that undesired noise in the output signal is minimized and a filter with large stopband damping can be provided with minimal damping in the passband. Furthermore the frequency of the noise makes no difference, so that adaptive filtering finds some use in the case where power line frequency varies considerably. Other examples of adaptive filtering are presented in [6], [2] and [3].

This paper presents another approach to adaptive filtering based on set of infinite impulse response (IIR) bandpass filters, which responses are base for noise amplitude and frequency estimation. These values are used to adjust parameters of notch filter originally proposed by Mortara in [5]. The performance of the new method is numerically evaluated using the artificial ECG signal from CTS database [8] combined with simulated power line noise with varying amplitude and frequency.

2   Adaptive Filtering Method

The main idea of the proposed new approach to adaptive filtering is using infinite impulse response (IIR) bandpass filters [1] as a set of auxiliary filters. The passband centers of these filters are arranged symmetrically around the nominal frequency of the power line, for example: 49Hz, 49.5Hz, 50Hz, 50.5Hz and 51Hz.

In noise parameters (amplitude and frequency) estimation procedure there are computed the sample standard deviations of output samples for each auxiliary filter. The estimates of amplitude and frequency of noise are set as linear combinations of these standard deviations with constant coefficients. The estimates (amplitude and frequency) are used to adjust the notch filter parameters, which perform the actual noise reduction in input ECG signal using Mortara method [5] as it is depicted in Fig. 3.
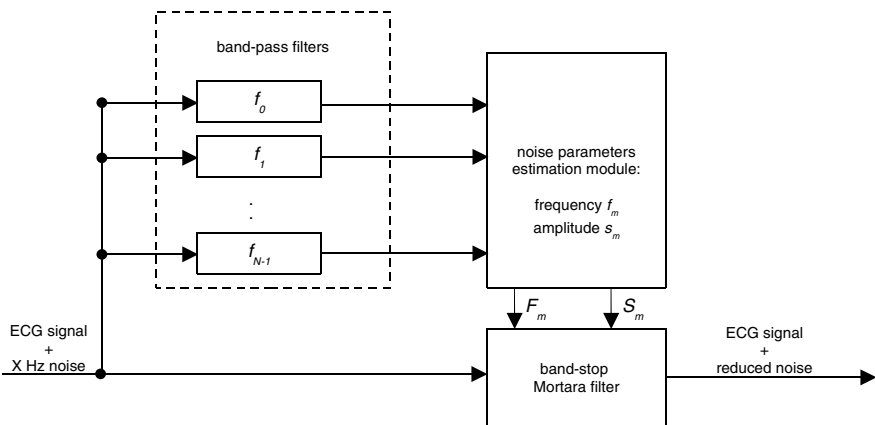
Fig. 3 Operation scheme of the proposed adaptive filter

For positive integer M, there are $2M+1$ auxiliary bandpass IIR filters with passband centers given by

$$f_j = f_m + \frac{j}{M} R, \tag{1}$$

where $j \in \{-M,\ldots,0,\ldots,M\}$, f_m is nominal power line frequency, i.e. 50Hz (or 60Hz) and R is maximal deviation of power line frequency from the nominal value (for example in Poland, where the power line frequency may vary from 49Hz to 51Hz, R may be set as 1Hz). The transfer function of jth filter is given by

$$H_j(z) = 1 - \frac{1 - \alpha\beta z^{-1} + \alpha^2 z^{-2}}{1 - \beta z^{-1} + z^{-2}}, \tag{2}$$

where α is arbitrarily chosen parameter which controls the width of passband and β is given as follows

$$\beta = 2\cos\left(2\pi\frac{f_j}{f_s}\right), \tag{3}$$

where f_s is sampling frequency of the input signal.

The noise amplitude and frequency are estimated based on computed sample standard deviations of output samples for each auxiliary filter. These sample standard deviations are calculated periodically every N input samples, i.e.:

$$\widehat{\sigma}_j(n) = \sqrt{\frac{1}{N-1} \sum_{i=0}^{N-1} \left(y_j(n-i) - \frac{1}{N} \sum_{k=0}^{N-1} y_j(n-k) \right)^2}, \tag{4}$$

where $y_j(n)$ is nth output sample of jth auxiliary filter. The estimate of noise amplitude is given by

$$\widehat{\sigma}_m(n) = \frac{1}{2M+1} \sum_{j=-M}^{M} \widehat{\sigma}_j(n) \tag{5}$$

and the estimate of noise frequency is given by

$$\widehat{f}_m(n) = \frac{\sum_{j=-M}^{M} \gamma^{|j|}\widehat{\sigma}_j(n)f_j}{\sum_{j=-M}^{M} \widehat{\sigma}_j(n)}, \tag{6}$$

where γ is arbitrarily chosen parameter which differentiates influence of auxiliary filter frequencies on resulting estimate (for $\gamma = 1$ each frequency has the same impact).

The actual noise reduction in input ECG signal is performed using Mortara method, which requires defining two additional parameters:

$$\theta(n) = 2\cos\left(2\pi\frac{\widehat{f}_m(n)}{f_s}\right) \tag{7}$$

and

$$\eta(n) = \xi\,\widehat{\sigma}_m(n), \tag{8}$$

where ξ is arbitrarily chosen positive-value parameter (usually significantly less than 1), which controls dependency of notch filtering single step on estimated noise amplitude. Besides these two parameters the notch filter uses following variables: $x(n)$ - the input sample of ECG signal with noise, $t(n)$ - the estimated noise and $z(n)$ - the estimated ECG signal. The notch filtering of single input sample is performed by following formulas:

$$t(n) = \theta(n)t(n-1) - t(n-2), \tag{9}$$
$$z(n) = x(x) - t(n). \tag{10}$$

Additionally after above calculations the estimated noise $t(n)$ is modified by adding value $\eta(n)\,\mathrm{sgn}[z(n) - z(n-1)]$.

Since the estimated parameters $\widehat{\sigma}_j(n)$, $\widehat{\sigma}_m(n)$, $\widehat{f}_m(n)$, $\theta(n)$, $\eta(n)$ are updated periodically every N input samples, their values for n between consecutive multiplicities of N remain constant, i.e.:

$$\widehat{\sigma}_j(n) = \widehat{\sigma}_j\left(\left\lfloor\frac{n}{N}\right\rfloor N\right), \ldots, \eta(n) = \eta\left(\left\lfloor\frac{n}{N}\right\rfloor N\right). \tag{11}$$

3 Numerical Experiments

Below there are presented results of numerical experiments which empirically evaluate performance of the presented adaptive filtering. As input data there were taken pure synthetic power line noise (with time-varying amplitude or time-varying both amplitude and frequency) as well as artificial ECG signal disturbed by these types of noise. This ECG signal (the signal amplitude was expressed in μV) is depicted in Fig. 1 and it was created as 9 consecutive identical copies of ANE20000 taken from database CTS [7]. The preset parameters, which are needed to perform adaptive filtering described above, were set as follows:

- $f_s = 1000\mathrm{Hz}$, where f_s is sampling frequency of the input signal;
- $f_m = 50\mathrm{Hz}$, where f_m is nominal power line frequency;
- $R = 1\mathrm{Hz}$, where R is maximal deviation of power line frequency from the nominal value;
- $M = 1$, i.e. there were three auxiliary bandpass IIR filters;
- $\alpha = 0.995$, where α is parameter which controls the width of passband;
- $N = 200$, i.e. update of selected parameters in filtering was made every 200 input samples;
- $\gamma = 1.035$, where γ is parameter which differentiates influence of auxiliary filter frequencies on resulting estimate;
- $\xi = 0.001$, where ξ is parameter which controls dependency of notch filtering single step on estimated noise amplitude.
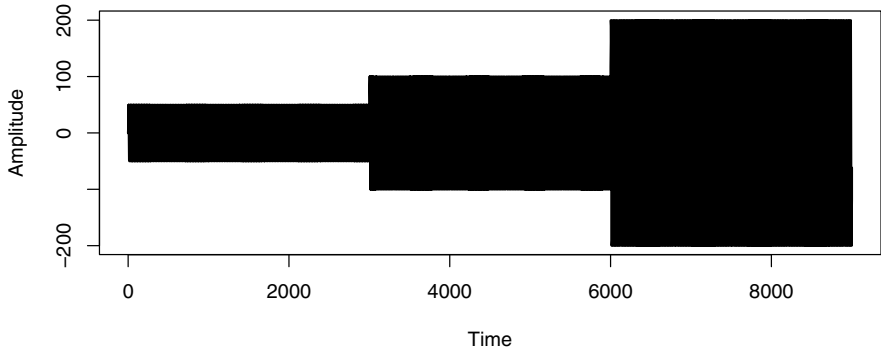
Fig. 4 The pure synthetic power line noise with time-varying amplitude

All experiments were run on the PC platform using implementation in the C++ language.

Figure 4 presents the pure synthetic power line noise simulated as sinus function

$$x(n) = a(n) * \sin\left(\frac{2\pi f(n)}{f_s}n\right),$$
(12)

where $a(n)$ is piecewise-constant ("stair") function (its values are 50μV, 100μV and 200μV respectively) and $f(n)$ is constant and equal 50Hz.

For the input signal depicted in Fig. 4 there was performed the adaptive filtering and the output signal, which was the result of the filtering, is presented in the Fig. 5. As it could be seen the adaptation time did not exceed one second (1000 samples).
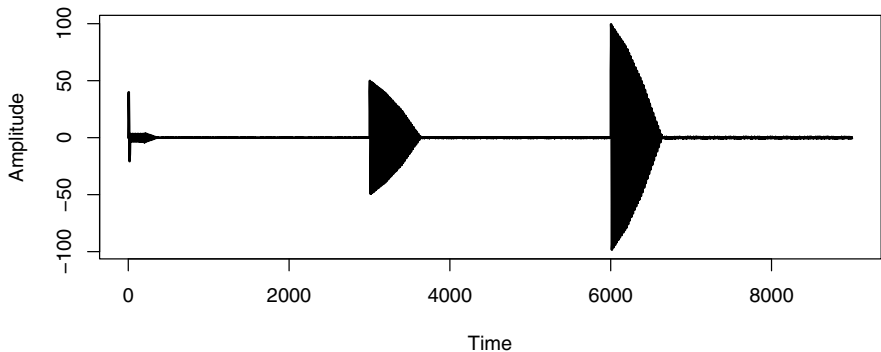
Fig. 5 Result of filtering the noise with time-varying amplitude

Next there was simulated noise with time-varying amplitude and frequency defined by equation (12). The amplitude function $a(n)$ was set as previous and the frequency $f(n)$ was also piecewise-constant function (its values were 50Hz, 49.25Hz,

50.75Hz respectively and they were changing at the same sample indexes as amplitude function). This noise is not depicted in separate figure because (for presented scale) it would look like the one in Fig. 4. For this input signal there was also performed the adaptive filtering and the output signal, which was the result of the filtering, is presented in the Fig. 6. As it could be seen the adaptation time was a little longer in this case but it did not exceed two seconds.
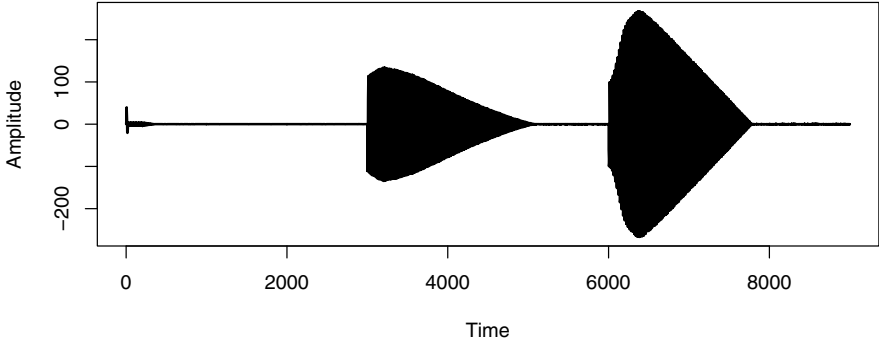
Fig. 6 Result of filtering the noise with time-varying amplitude and frequency

Figure 7 presents the described above ECG signal disturbed by time-varying amplitude noise simulated as sinus function in equation (12), where amplitude function was set as previously.
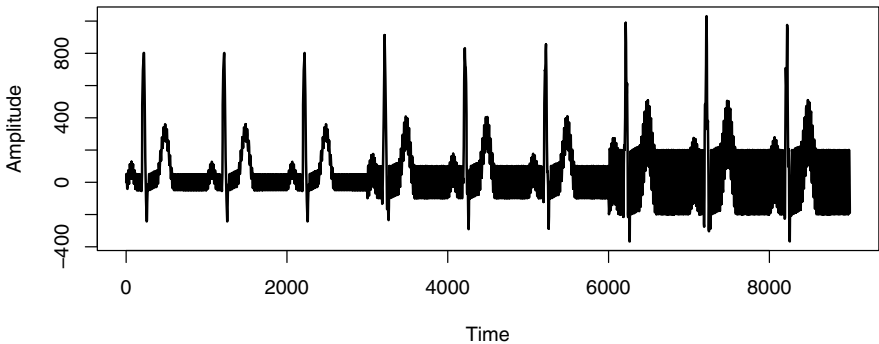
Fig. 7 The ECG signal disturbed by time-varying amplitude noise

For such disturbed ECG signal there was performed the adaptive filtering and the output signal, which was the result of the filtering, is presented in the Fig. 8. As it could be seen the adaptation time was similar to the adaptation time in case of pure time-varying amplitude noise and it was about one second.
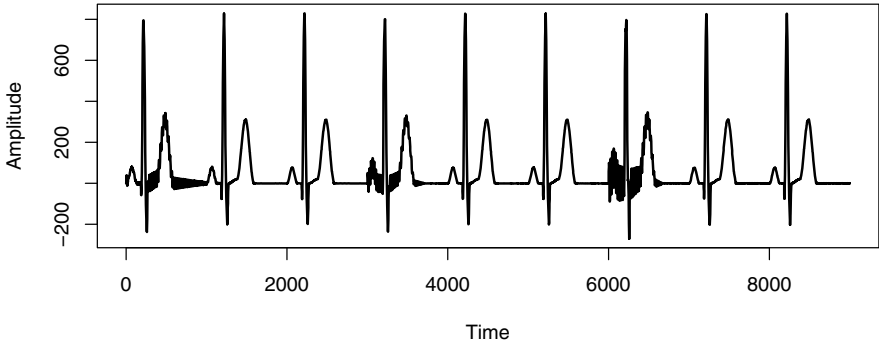
Fig. 8 Result of filtering the ECG signal disturbed by time-varying amplitude noise

Similarly there was performed the adaptive filtering of the ECG signal disturbed by time-varying amplitude and frequency noise (described above) and the output signal, which was the result of the filtering, is presented in the Fig. 9. As it could be seen the adaptation time was similar to the adaptation time in case of pure time-varying amplitude and frequency noise and it was about two seconds.
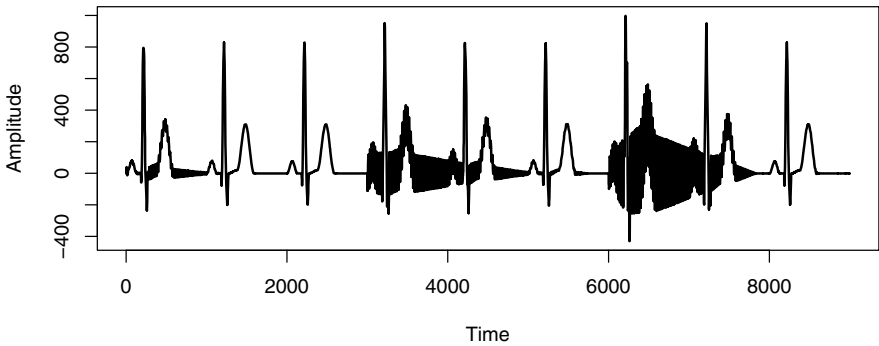
Fig. 9 Result of filtering the ECG signal disturbed by time-varying amplitude and frequency noise

Based on 900 output samples taken after the filter reached the stable state there were calculated the values of root mean-square error between the original (undisturbed) signal samples and the filtered samples. These calculation were repeated for each combination of the noise amplitude and frequency values used in experiments described earlier and Table 1 presents the obtained results.

In presented experiments the number of auxiliary filters was only three, but increasing this number did not improve performance of filtering. However for different set of data this rule does not necessarily apply. For example in other experiments (not described here), where sampling frequency was equal 250Hz the minimal number of the auxiliary filters needed to obtain satisfactory results was five.

Table 1 Root mean-square error for performed experiments

frequency [Hz]	amplitude [μV]	pure noise [μV]	ECG + noise [μV]
50	50	0.0753	0.5329
50	100	0.1521	0.9346
50	200	0.3011	1.7175
50	50	0.0753	0.5329
49.25	100	0.1559	4.1828
50.75	200	0.2878	1.5122

4 Summary

During the history of the electrocardiographic signal processing there were proposed many methods for the removal of power line interference. They can be categorized into non-adaptive and adaptive filtering. The non-adaptive filtering approach usually employs a sharp notch filter and is easy to implement at low cost. However its performance depends on the frequency stability of the power line. Adaptive filtering, on the other hand, is able to effectively remove time-varying power line frequency, but requires considerable computational power.

In this paper there was presented the new approach to adaptive filtering based on set of infinite impulse response (IIR) bandpass filters, which responses are base for noise amplitude and frequency estimation. The results of numerical experiments show that the proposed method gives relatively small root mean-square error (not exceeding 4μV in the worst case) for simulated power line noise with varying amplitude and frequency.

Authors believe that it is worth investigating using other auxiliary filters, for example with different transfer function, or even using whole different sets of filters for estimate power line noise amplitude and frequency to improve the quality of the proposed method. This will be the subject of a further research.

References

1. Antoniou, A.: Digital Filters: Analysis, Design, and Applications. McGraw-Hill, New York (1993)
2. Ferdjellah, M., Barr, R.E.: Adaptive digital notch filter design on the unit circle for theremoval of powerline noise from biomedical signals. IEEE Transactions on Biomedical Engineering 41, 529–536 (1994)
3. Levkov, C., Mihov, G., Ivanov, R.: Removal of power-line interference from the ECG - a review of the subtraction procedure. BioMedical Engineering Online 2005, 4–50 (2005)
4. Lofgren, N., Karlsson, P., Lundahl, G., Lundqvist, F.: Adaptive filtering system and method. United States Patent 6487295 (2002)

5. Mortara, D.A.: Digital Filters for ECG Signals. Computers in Cardiology, 511–514 (1977)
6. Van Alste, J.A., Schilder, T.S.: Removal of base-line wander and power-line interference from the ECG by an efficient FIR filter with a reduced number of taps. IEEE Transactions on Biomedical Engineering 32, 1052–1060 (1985)
7. Medical electrical equipment. General requirements for basic safety and essential performance. Polish Norm PN-EN 60601-1:2006. Polish Committee for Standardization (2006)
8. International Electrotechnical Commission Standard 60601-3-2 (1999)

Heart Rate Analysis in the EGG Examination

Stanislaw Pietraszek and Dariusz Komorowski

Abstract. This paper presents a novel method for synchronous recording and analyzing both the electrogastrographic signal (EGG) and the heart rate variability signal (HRV). The four channel signals are non-invasively captured by six electrodes placed on the surface of the stomach. The EGG and electrocardiographic (ECG) signals, recorded simultaneously using the same electrodes and an amplifier, are separated by digital filtration. In our work the EGG and ECG analysis is limited to the calculation the most frequently used parameters: the dominant frequency (DF), dominant power (DP) of the power spectrum for the EGG, and LF/HF ratio of the HRV power spectrum for the ECG signals.

1 Introduction

The electrogastrographic examination can be considered a noninvasive method for investigating the propagation the slow waves in the stomach [1] [2]. The classic surface EGG signals are captured by six disposable electrodes, placed on the surface of patient's stomach. During the signal registration process the standard protocol is applied according to the EGG Task Force recommendations [3]. The registration process usually includes a 30-minute period before meal (preprandial period), a short meal period (5 - 10 minute) for a standardized meal, and several (2 - 4) 30-minute periods after the meal (postprandial periods). For more detailed analysis, each period is split into segments of 60 or 256 seconds length.

The signals collected from the stomach surface include not only the EGG signal but also ECG signals that may be separated by proper band-pass filtration.

Stanislaw Pietraszek · Dariusz Komorowski
Institute Electronics, Division of Biomedical Electronics,
Silesian University of Technology, Gliwice, Poland
e-mail: stanislaw.pietraszek@polsl.pl,
dariusz.komorowski@polsl.pl

For the EGG signal we calculated the power spectrum density (PSD) of each individual segment, based on which, we obtained dominant frequencies (DF) and the dominant power for each segment and for the entire periods (overall dominant frequencies (ODF)). Next the distributions of the dominant frequency and dominant power for periods are obtained. Investigation of the heart rate variability (HRV) is one of the most common methods used for the analysis of long term ECG records (for example from Holter recorders). The HRV analysis is based on RR intervals and require the detection of QRS complexes in single channel ECG signal. According to the Task Force Rapport [4], frequency analysis of RR intervals is performed in 256 seconds long segments. Finally we calculated LF/HF ratio in power spectrum of RR intervals for segments and periods [1].

2 Method

The signals were recorded in the department of clinical sciences in the medical university by means of a four-channel amplifier (gain=5000, signal amplitude range $\pm$2mV, resolution - 12 bits, sampling rate 200Hz per channel) with galvanic isolation of the patient's side. During the signal registration process standard electrodes were applied according to the standard [3] [5], including four signal electrodes (A1 - A4), a reference electrode (R) and the ground electrode (U). An example of the electrodes placement is shown in Fig.1.
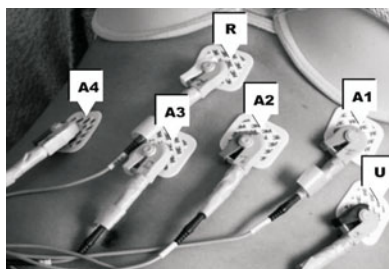
Fig. 1 The standard placement of the EGG electrodes [2]

An example of one-minute snapshot recorded signal (one channel) is shown in Fig. 2. Note that, a relatively high sampling frequency allows to capture both the EGG and the ECG signal. From the recorded data the EGG and the ECG signals were extracted using proper preprocessing.

2.1 The EGG Preprocessing

The EGG signal extraction was performed by an application of the band-pass filter covering the range 0.015Hz - 0.15Hz [3]. The lower cutoff frequency results from the high-pass, first-order RC filter applied in the amplifier hardware and digital the fourth-order high pass Butterworth filter. The upper cutoff frequency results from
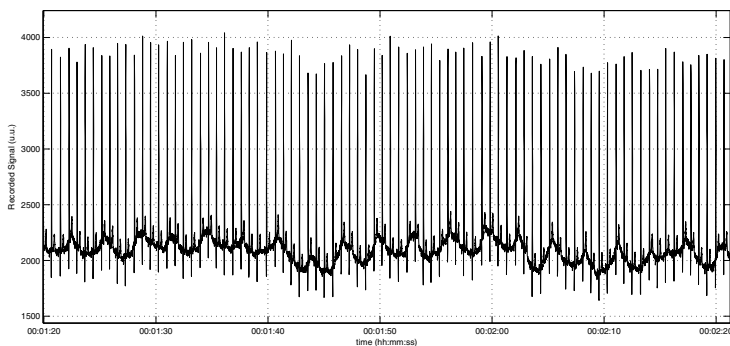
Fig. 2 An example of the recorded signal from A1 electrode

the application of the digital the fourth-order Butterworth filter. Next the EGG signal has been resampled to 4Hz.

2.2 The ECG Preprocessing

The ECG signal required for the purpose of the HRV analysis was extracted from the recorded signal using a band-pass filter, tuned in the range 1 to 35Hz. For the QRS detection one channel with the most prominent QRS complex (usually the A1 channel) is sufficient. Next the standard cascade of digital filters, tuned to the spectral characteristics of the average QRS complex was applied. The filtered signal was rectified and averaged to obtain a single-peak detection function, for each QRS complex. To improve the detector noise tolerance, the detection function is calculated separately in each channel and subsequently averaged. Fiducial points were found in the maximum of detection function [6]. Since the RR intervals are non-uniformly sampled, so for further analysis, we interpolated and resampled RR intervals with the frequency of 4Hz. The resampled HRV signal for the entire record was separated into segments of 1024 samples (256 seconds). In some cases, segments for the time of taking the meal were excluded, when motion artifacts occurred.

2.3 Calculation of Power Spectrum Density

Power spectrum density of given time series may be calculated by means of periodogram or autoregressive modeling. The second technique has been applied in presented work for both EGG and HRV signals.

A time series $x[n]$ can be modeled as an AR process. The AR model is given by input-output difference equation (1)

$$x[n] = -\sum_{k=1}^{p} a_k x[n-k] + e[n] \qquad (1)$$

where $x[n]$ is the output of the model, $e[n]$ is the input of the model, and the a'_ks are its coefficients, and p is the order of the model. The input $e[n]$ is a zero mean white noise process with unknown variance σ. This model is usually abbreviated as an $AR(p)$. The power spectrum density of the $AR(p)$ is given by (2)

$$P_{AR}(f) = \frac{\sigma^2}{\left|1 + \sum_{k=1}^{p} a_k e^{-j2\pi fk}\right|^2} \qquad (2)$$

If the coefficients ak and the noise variance (of the $AR(p)$ model are identified, the power spectrum density $P_{AR}(f)$ can be calculated. After some mathematical manipulation and simplification of Eq. (1), the Eq.(3) for $k > 0$ is obtained.

$$E(x[n]x^*[n-k]) = -\sum_{l=1}^{p} a_1 E(x[n-l]x^*[n-k]) + E(e[n]x^*[n-k]) \qquad (3)$$

where *means the complex conjugate and E is the expectation. The Eq.(3) is often written by the following expressions and known as the Yule-Walker equations Eq.(4):

$$r[k] = \begin{cases} -\sum_{l=1}^{p} a_l r[k-l], & k > 0 \\ -\sum_{l=1}^{p} a_l r[k-l] + \sigma^2, & k = 0 \end{cases} \qquad (4)$$

where the $r[k]$ is the autocorrelation function of the process realization. The estimation of the p unknown al coefficients from Eq.(4) requires at least p equations as well as the estimates of the appropriate autocorrelations. The equations that requires the estimation of the minimum number of correlation lags are given by the following formulas:

$$\hat{R}a = -\hat{r} \qquad (5)$$

where is the matrix

$$\hat{R} = \begin{bmatrix} \hat{r}[0] & \hat{r}[-1] & \hat{r}[-2] & \cdots & \hat{r}[-p+1] \\ \hat{r}[1] & \hat{r}[0] & \hat{r}[-1] & \cdots & \hat{r}[-p+2] \\ \vdots & \vdots & \vdots & \vdots & \vdots \\ \hat{r}[p-1] & \hat{r}[p-2] & \hat{r}[p-3] & \cdots & \hat{r}[0] \end{bmatrix} \qquad (6)$$

and

$$\hat{r} = [\hat{r}[1]\hat{r}[2]\cdots\hat{r}[p]]^T \qquad (7)$$

The parameters a are estimated by

$$\hat{a} = -\hat{R}^{-1}\hat{r} \qquad (8)$$

and the noise variance can be found from

$$\hat{\sigma}^2 = \hat{r}[0] + \sum_{k=1}^{p} a_k \hat{r}^*[k] \tag{9}$$

The power spectrum density estimate is obtained if and are substituted in Eq. (2) [7].

In AR modeling techniques the most important issue is choosing the proper model order. In presented paper the model order was chosen by using the information criterion (AIC) due to Akaike. According to the AIC criterion, the best model is the one that minimizes the function AIC(k) over k defined by

$$AIC(k) = N \log \hat{\sigma}_k^2 + 2k \tag{10}$$

where k is the order of the model, and $\hat{\sigma}_k^2$ is the estimated noise variance, and N is the number of data samples The selected order of the model substantially influences on the PSD shape [7] [8].

2.4   Calculation of Dominant Frequency for Segments

The dominant frequency is defined as a value of frequency of the highest peak of the PSD of EGG, in the range 0cpm - 9cpm. The maximum amplitude of power spectrum density is called dominant power (MPSD). The spectrum analysis of the EGG signal was performed by the means of identification parameters of AR model and estimation of the power spectrum density. In some segments when the peak of PSD lies in or near 0, algorithm tries to find the next peak and if the difference in peaks height is less than 2.5 dB, the dominant frequency is corrected. The examples spectra of one minute length EGG signals are presented in Fig.3 and Fig. 4. The PSD for all preprocessed segments was calculated and the dominant frequencies were found.
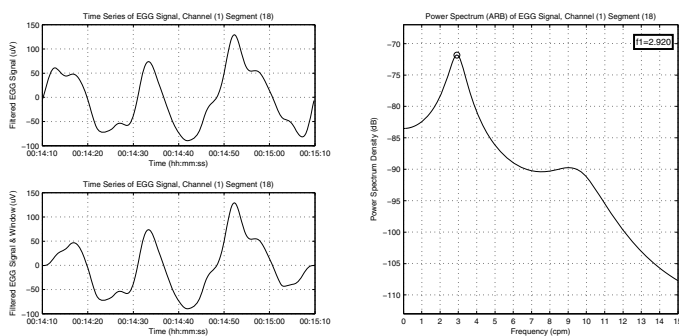
Fig. 3 The spectrum of one-minute EGG signal with marked DF
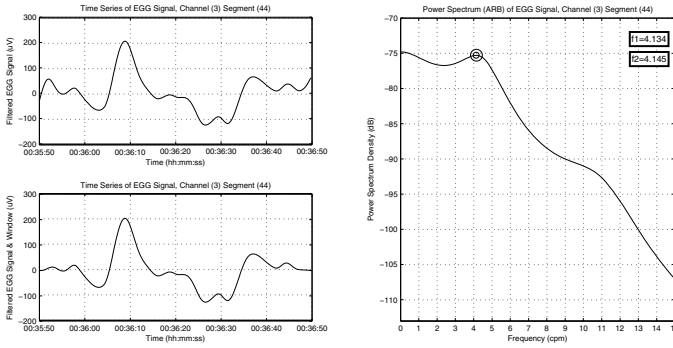
Fig. 4 The spectrum of one-minute EGG signal with DF correction marked

2.5 Calculation of LF/HF Balance for Segments

The signal of resampled RR intervals for entire record was split into 1024-sample segments, similarly to EGG segments. For all segments the power spectrum density of HRV was calculated by means of the Welch method. The comparison between the PSD of HRV obtained using autoregressive modeling (Welch method) and periodogram is presented for comparison in Fig.5 (boundaries of LF and HF bands are
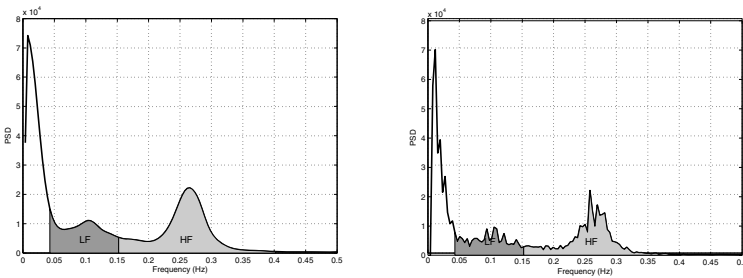
Fig. 5 The PSD of HRV, Welch method (left), periodogram method (right)

marked). Next the value of ratio LF/HF was calculated for each of 4 minute length segment using PSD calculated be means of Welch method, Eq. (11) [4].

$$BAL = \frac{LF}{HF} \qquad (11)$$

In Fig.6 an example of LF/HF ratio, calculated for whole examination is presented. Dotted line shows the best interpolation of presented data. The meal period is passed over.
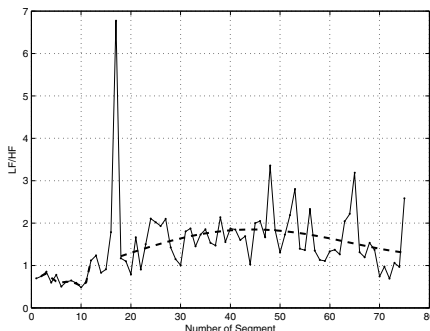
Fig. 6 An example of BAL for all segments

3   Results

EGG examinations were done for three types of standardized meals:

1. liquid acaloric load - 400 ml of still mineral water - 0 kcal,
2. liquid caloric meal - 400 g of fruity yogurt - 378 kcal,
3. solid meal - 2 egg pancake (fat (5 g), flour (30 g), strawberry jam(50 g)), 200 ml of mineral water - 355 kcal.

For all segments, values of LF/HF and DF were calculated. The examples results (for three persons) of LF/HF, MPSD and DF are presented in Fig.7 - 15.
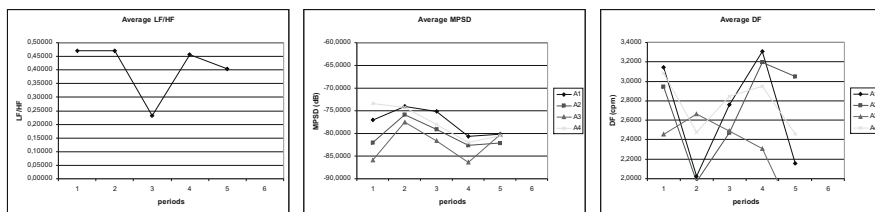
Fig. 7 The Average LF/HF, average MPSD and DF for four channels EGG examination (acaloric load, person one)
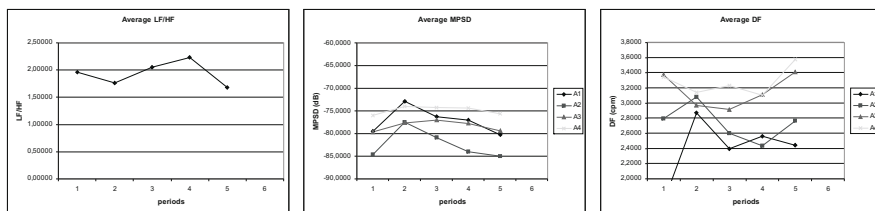
Fig. 8 The Average LF/HF, average MPSD and DF for four channels EGG examination (acaloric load, person two)
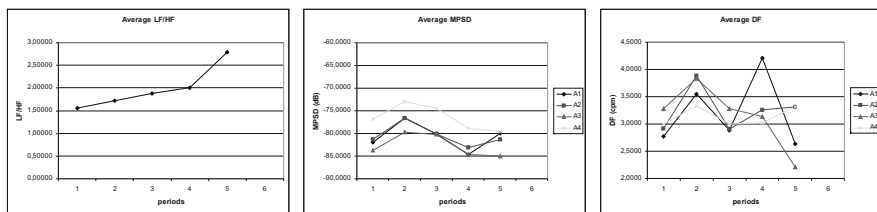
Fig. 9 The Average LF/HF, average MPSD and DF for four channels EGG examination (acaloric load, person three)
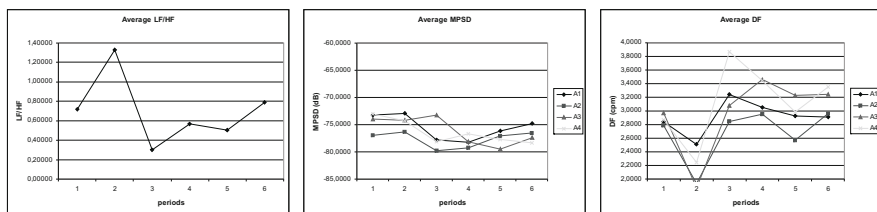
Fig. 10 The Average LF/HF, average MPSD and DF for four channels EGG examination (liquid caloric meal, person one)
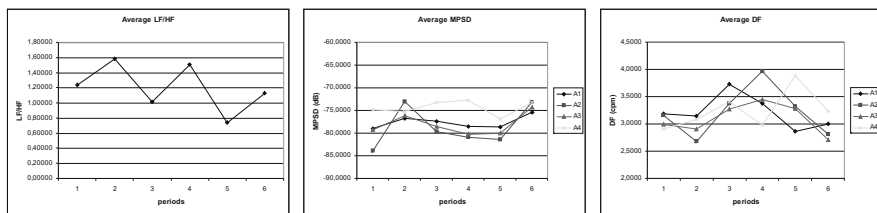
Fig. 11 The Average LF/HF, average MPSD and DF for four channels EGG examination (liquid caloric meal, person two)
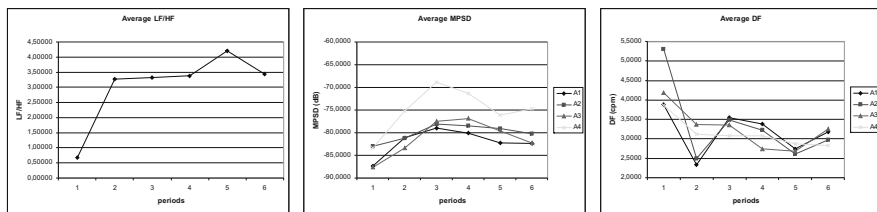
Fig. 12 The Average LF/HF, average MPSD and DF for four channels EGG examination (liquid caloric meal, person three)
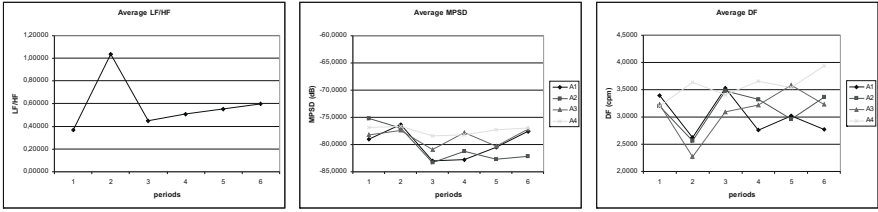
Fig. 13 The Average LF/HF, average MPSD and DF for four channels EGG examination (solid meal, person one)
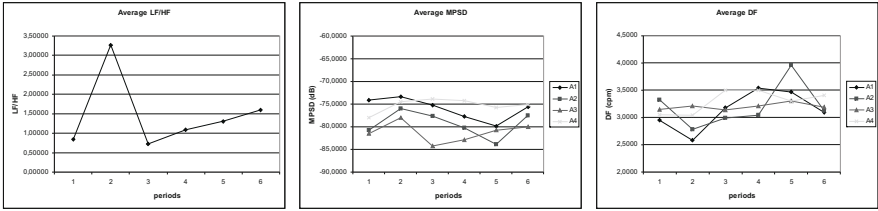
Fig. 14 The Average LF/HF, average MPSD and DF for four channels EGG examination (solid meal, person two)
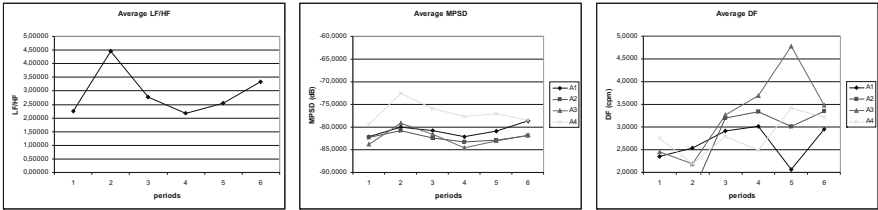
Fig. 15 The Average LF/HF, average MPSD and DF for four channels EGG examination (solid meal, person three)

The results show similar influence of the digestion to LF/HF and MPSD, while DF shows greater changes between channels.

4 Conclusions

Presented work explains that more physiological signals may be extracted from standard EGG recording, with the slight increase of the sampling frequency. Preliminary analysis of simultaneously recorded EGG and HRV signals and computed basic parameters shows similar pattern of LF/HF and MPSD changes caused by the standard

types of meal. In multichannel DF plots this influence is not so clear. The present method do not require using any additional equipment for simultaneously recording of the EGG and the ECG signals, and is fully implemented in software. Because of relatively small group of EGG records some conclusions and analysis of mutual connections between EGG and HRV may require further investigations.

References

1. Alvarez, W.C.: The electrogastrogram and what it shows. JAMA 78, 1116–1119 (1922)
2. Tomczyk, A., Jonderko, J.: Multichannel electrogastrography as a non-invasive tool for evaluation of the gastric myoelectrical activity a study on reproducibility of electrogastrographic parameters before and after a meal stimulation. Ann. Acad. Med. Siles. 61, 5 (2007)
3. Parkman, H.P., Hasler, W.L., Barnett, J.L., Eaker, E.Y.: Electrogastrography: a document prepared by the gastric section of the American Motility Society Clinical GI Motility Testing Task Force. Neurogastroenterol. Motil. 15, 89–102 (2003)
4. Task Force of The European Society of Cardiology and The North American Society of Pacing and Electrophysiology (Membership of the Task Force listed in the Appendix), Heart rate variability Standards of measurement, physiological interpretation, and clinical use. European Heart Journal 17, 354–381 (1996)
5. Medtronic A/S: Polygram NetTM Reference Manual. Skovlunde, Denmark (2002)
6. Pan, J., Tompkins, W.J.: A real-time QRS detection algorithm. IEEE Transactions on Biomedical Engineering 32, 230–236 (1985)
7. Madisetti, V.K., Williams, D.B. (eds.): Digital Signal Processing Handbook. CRC Press LLC, Boca Raton (1999)
8. Soderstrom, T., Stoica, P.: System Identification. Prentice Hall International (UK) Ltd., Englewood Cliffs (1994)

Convergence Improving in Evolution–Based Technique for Estimation and Separation of Electrooculography and Blinking Signals

Robert Krupiński and Przemysław Mazurek

Abstract. Estimation of electrooculography (EOG) and blinking signals could be done by using numerous algorithms. The separation of EOG and blinking signals is hard if the blinking pulses occur in the neighborhood of saccades. The appropriate estimation and signals separation could be obtained by using the optimization algorithm and a proper signals model. The proposed method improves the convergence of evolution–based technique and reduces the optimization time by using the additional algorithm for the estimation of possible positions of blinking pulses, the saccades positions and the EOG levels. A median filter based estimator is used for the initialization of optimization algorithm of blinking pulses. A differential filter based detector is used for the initialization of saccades position and the EOG signal level values between them. The proposed method reduces the computation time a few times what is important for the possibility of real–time implementation.

1 Introduction

The electrooculography (EOG) is one of the occulography methods used for the estimation of eyes orientation [10]. The obtained estimates could be used mainly for medical purposes [10, 22] such as electronystagmography, polysomnography [2], but in the last decade a new applications area arose. Nowadays, the EOG is used in the ergonomics, the advertisement analysis [27], the human–computer interaction (HCI) systems (e.g. a virtual keyboard [31], the vehicle control [4], the wearable computers [8]), the video compression driven by eye–interest [14], and the motion–capture systems for further eyes animation [10, 6, 26]. The increase of EOG applications areas stimulated the wider interest in research related to such systems.

Robert Krupiński · Przemysław Mazurek
West–Pomeranian University of Technology, Szczecin, Chairs of Signal Processing and Multimedia Engineering, 26-Kwietnia 10 st., 71-126 Szczecin Poland
e-mail: `robert.krupinski@zut.edu.pl`,
`przemyslaw.mazurek@zut.edu.pl`

Advances in the acquisition hardware and non–linear filtering techniques improved the quality of recorded data. Even using an old hardware a new algorithm could be applied and much better performance of available systems could be obtained.

There are alternative occulography techniques based on the near infrared light reflection (IROG) [25], the video tracking techniques (VOG) and other specific, but the EOG is still utilized [2, 10]. Every occulography method has its own specific disadvantages and advantages so there are no the best one for all purposes.

The EOG is a skin contact–based method, and the Ag/AgCl electrodes are used for the measurements of biopotentials from the retina–cornea constant voltage source [24, 28]. This source has about $\pm 1 [mV]$ [29], which is a very high value in comparison to other biosignals, but it also depends on the numerous factors, for instance, the light conditions [9], the contact between electrodes and skin, which is the source of amplitude instability [15, 2]. For the proper signal processing a low–pass measurement systems should be employed because a DC signal should be also measured.
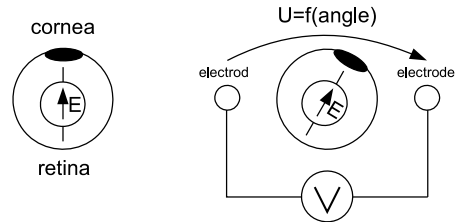
Fig. 1 Model of retina–cornea voltage source and the method of measurement [18]

The EOG measurements are based on the voltage amplitude modulation of voltage between two electrodes placed around an eye and this voltage depends directly on the angle of the eye. Such a technique appears to be simple, but it is more complicated in the case of real measurements due to the noise disturbance, the external interference and the need of good skin contact. There are a few typical electrodes placements for the measurement of EOG biosignals [7]. The detailed information about the eyes orientation could be obtained [30] by using the 7/8 electrodes placed around both eyes. This configuration uses seven electrodes for measurements and one additional electrode as a voltage reference. The simpler configuration uses the 3/4 electrodes (Fig. 2) what is useful for most applications.
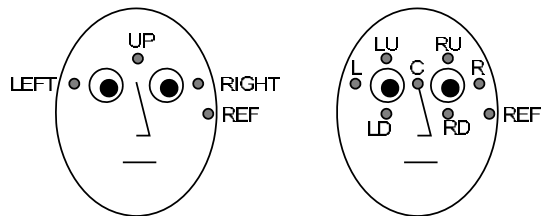
Fig. 2 3/4 and 7/8 electrodes measurement systems

The LEFT–UP and RIGHT–UP channels are used for differential measurements in the 3/4 system and such system is considered. Unfortunately, not only the EOG signals are measured, but also the 50/60Hz interference from a power line is observed [28]. Additionally, the interference from the incandescent lamps is also recorded. The analog and digital filtering techniques are used for the suppression of such signals [28]. There is also another and very important source of the EOG signals distortion, which is a blinking signal. During the eyelid movement there are significant amplitude modulations of the EOG signal and for typical fast blinking it could be observed as a pulse (similar to the Gaussian pulse). The blinking signal could be treated as a distortion, necessary to remove, but in some applications it is a useful signal – for example in the HCI systems it is an additional degree–of–freedom for interaction. The EOG and blinking signals should be separated from each other in more general approach.

There are numerous methods for the separation of both signals, where the linear filtering techniques do not work correctly, because even if the blinking pulses are removed (the high–frequency part of a signal) the saccades of EOG signal are significantly disturbed (they also contain the high–frequency components). The saccades are the rapid changes of eyes orientations [10, 11, 12, 5, 16] and they should not be influenced by the separation algorithm so the linear filtering is useless. The median based filters are proposed in the last decade for the separation of both signals with less disturbance of saccades [3, 13, 17, 20, 23]. This non–linear filter class is usefully for a pulse removal and after subtraction from an original signal the blinking signal could be also obtained (Fig.3).
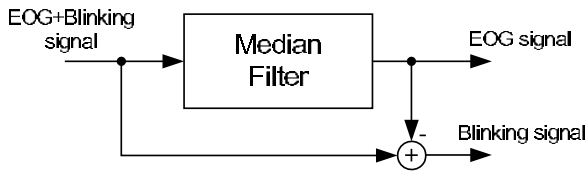
Fig. 3 Processing scheme for the separation of EOG and a blinking signal using a median filter

The median filters give quite good separation if the blinking pulses are not in the neighborhood of saccades. For such cases the blinks are not adequately recognized and the position of saccade is not correctly estimated, therefore, this was motivation for the authors for developing another more reliable algorithm. Because the EOG and blinking signals are well described in the time–domain a Matching Pursuit algorithm [19] seemed to be a promising solution. The analyzed signal could be reconstructed by using the set of signal atoms and the inverse operation (the composition of original signal) is possible by using the optimization algorithm. Unfortunately, this approach by the direct implementation of Matching Pursuit algorithm is non–optimal and requires a long computation time and the representative set of atoms is required too.

Because the EOG and blinking signals could be modeled by the signal models it was possible to achieve the signal decomposition (the estimation and also separation) by using the evolution-fit algorithm. The subject of optimization is a set of variable model parameters corresponding to the appropriate characteristic of EOG and blinking signals. The proposed and tested algorithm analyzes a signal by using a non–overlapping window approach. The obtained results allow the estimation of saccades position and the EOG signal levels between saccades directly.

2   Model-Based Optimization Approach

The optimization approach proposed in [18] is based on the simplified model described in [17] and uses a set of optimization algorithms. This approach uses different optimization techniques dependent on the optimized parameters. The number of parameters is also a subject of optimization and is optimized by a non–gradient method. The position of saccades, the blink pulses, the level value of EOG signal between the saccades and the height of blink pulses are estimated by using the non–gradient and gradient methods. The operations related to the parallel modification of time–domain neighborhood components for improving convergence are also combined. For example, the modification of saccade position together with the modification of constant values of time periods are recommended for the local minima omitting. The overall processing scheme for a single optimization step is shown in Fig. 4 and is detailed explained in[18]. From the evolutionary programming point–of–view [21] it is a kind of mutation with a single child and a single parent. Each iteration in the algorithm contains four sections, which are processed serially. In each section, there is performed up to one adjustment. First two sections are related to the saccades positions and the EOG levels and next two are related to the blinks parameters. The type of adjustment can be based on the random changes or gradient one. The modification can include: the changes of dimensionality, the saccades positions, the EOG levels, the blinking position and amplitudes.

The optimized parameters are divided into two groups: the EOG and blinking signal descriptors. The EOG signal is modeled by the time periods t_i and a constant level value between two saccades s_i. The blinking signal is estimated as a set of blink pulses located at a position b_j and with a corresponding pulse height h_j. The approximated reconstruction of a signal is given by the following formula:

$$\hat{Y} = \sum_i f_S(S,i) + \sum_j f_B(B,j) \tag{1}$$

The synthesis of intervals between two saccades is the f_S function and the synthesis of blink pulse is the f_B function. Two indexes i and j correspond to the number of both functions, and they are also a subject to optimization.

The example results of separation for the synthetic EOG and blinking signals are shown in Fig. 5. Even if a blinking pulse is near to the saccade it is possible to separate such signals. This is not possible by using only a median filter.
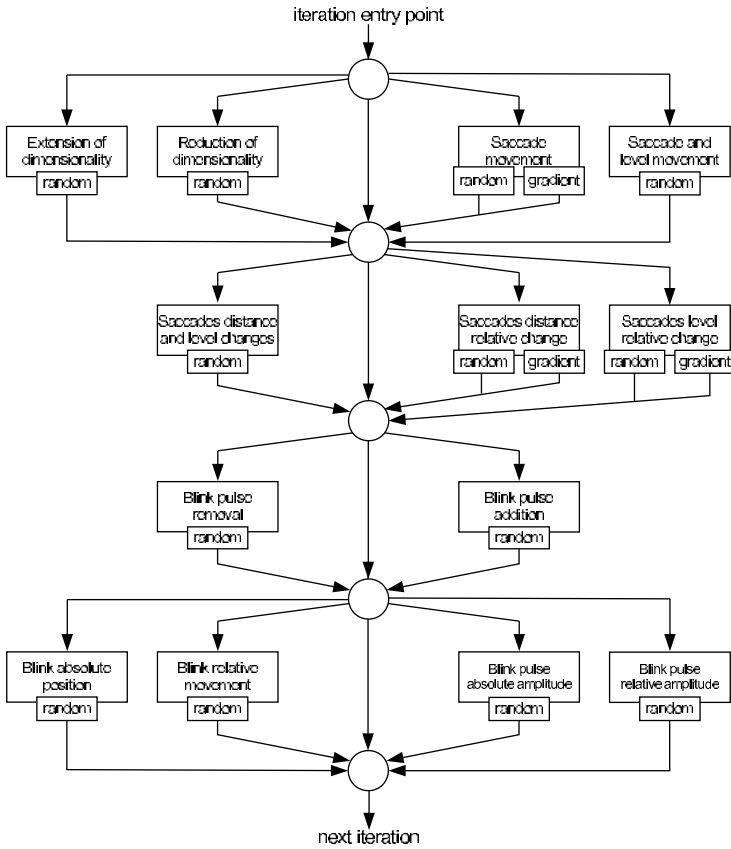
Fig. 4 Processing scheme in the optimization approach [18]

The optimization approach uses a single instance of parameters initialized by the random values. The optimization algorithm uses the minimization of Mean Squared Error (MSE) criteria:

$$MSE = \frac{1}{N} \sum_{n=1}^{N} \left(Y_n - \hat{Y}_n\right)^2 \qquad (2)$$

where n is the sample number of a signal window that has the size N. The Y is a given signal and $\hat{Y}$ is the reconstruction of this signal (the EOG and blinking signal after summation). The optimization process is stopped after the arbitrary selected number of iteration steps (e.g. 10^5) or if the MSE is bellow an arbitrary selected threshold value.

The proposed algorithm in [18] uses a processing scheme shown in Fig. 4. In this paper a more advanced processing (the modification of more parameters before testing an error value) is incorporated. The algorithm is processed twice according to Fig. 4 and then an error for proposed parameters is calculated. Such an approach
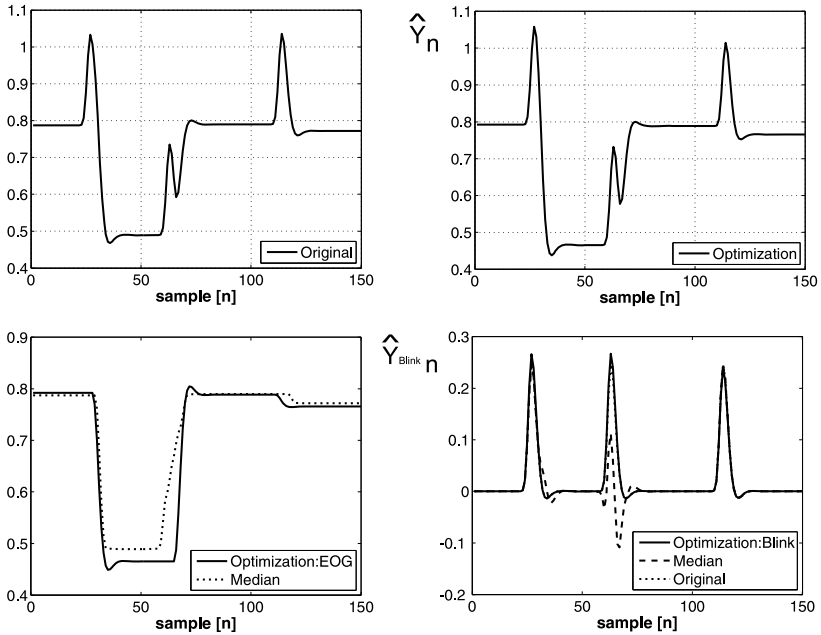
Fig. 5 Example of EOG and blinking pulses separation: the original signal, the reconstructed signal after optimization, the separated EOG signals (for the optimization and median approach), and the separated blinking signals (for the optimization and median approach)

gives a better convergence in the comparison to the original method and as a reference for the next proposed algorithm based on the initialization is used.

The processing time is rather long and takes typically a few minutes for 200 samples on the single core of Intel Q6600 (2.4GHz) processor and Matlab 2009b. Although, the median filters could process data in real–time and could be implemented in a typical embedded microcontroller, but they are less reliable for this type of data processing. The reduction of computing time is possible by parallel implementation, a more advanced processing architecture, a compiled code instead of a scripting language and what is more important by improved algorithm.

3 Improving Convergence by Initialization

There are numerous techniques for improving the convergence of evolution–based technique and one of the most important is the proper initialization of algorithm. A good starting point for the optimization can lead to the reduction of iteration steps and the computing time. The overall problem is non–linear and there are numerous local minima, which could be observed during the detailed analysis of algorithm behavior during processing. A non–gradient parts of the algorithm are used for escaping from the local minima, but it is a time consuming task.

The proper initialization is a very important approach and well known median filters for the EOG and blinking signal separation could be used for this step. The estimation of blink position and its height by a median filter. Even if some pulses are missed or false detected then some of them may be correctly estimated.

The detection of blinking pulses uses the following separation formula of EOG and blinking signals [16]:

$$w = LPF(x) - MED(LPF(x)) \tag{3}$$

where:
x – an input signal,
w – the output signal from the first stage,
LPF – a lowpass filter,
MED – the median filter.

The peak detector returns the sum of five neighboring samples $\{n-2,\ldots,n+2\}$ if a center sample n is detected as a peak one. The following formula is used by the detector:

$$v_n = \left\{ \begin{matrix} \sum_{i=n-2}^{n+2} z_i : z_n \geq z_{n-1} \bigvee z_n \geq z_{n+1} \\ 0 \qquad : \qquad otherwise \end{matrix} \right\} \tag{4}$$

The parameters estimation of blinking pulses is not enough for the significant improvement of convergence and the additional EOG signal estimation is necessary. In the context of MSE value, most part of this error in the beginning iterations corresponds to the EOG signal, not to the blinking signal. Such an effect is dependent on the random initialization of EOG signal parameters and should be suppressed by the correct estimation of EOG signal too. The proposed processing scheme for the EOG estimation initialization is shown in Fig. 6. The saccades create two pulses after the differential filtering and after calculating an absolute value. The Peak Detector is identical to one used in the blinking estimator but now it is used for the estimation of saccade position. The Peak Distance Filter removes a false pulse (the false saccades) and measures the distance between two neighborhood peaks (corresponding to the saccades) $\{P_n, P_{n+1}\}$. A smaller pulse is removed if a distance between them is smaller than minimal allowable D_{min}:

$$P_{n+1} - P_n < D_{min} \tag{5}$$

The segmentation algorithm is necessary for the optimization process and if a distance between two pulses (saccades) is longer than allowable, then such a time
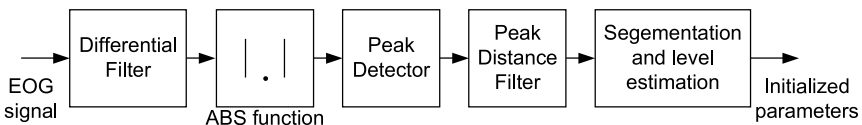
Fig. 6 Proposed initialization scheme for the saccades and a level signal between the saccades

period is divided into smaller segments. For each segment the mean value of signal is calculated and used as an initialization value for a EOG signal level. This approach allows to divide time period to the smaller segments with the similar level values between two real saccades.

4   Results for Proposed Optimization Method

The Monte Carlo tests could be used for testing the algorithm performance. 500 tests were calculated by using the proposed initialization (Initialized) and with the random initialization (Normal) for an identical input signal. The mean value for all tests is depicted in Fig. 7.
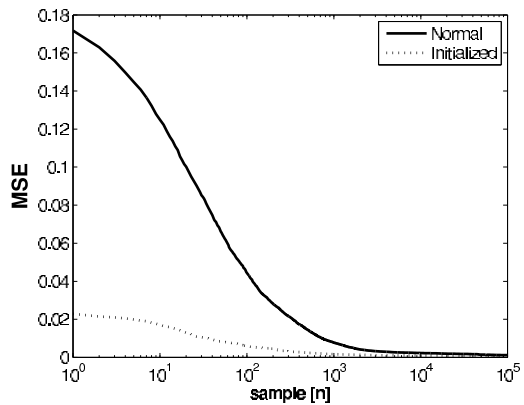
Fig. 7 Comparison of error (MSE) reduction for the reference algorithm (Normal) and algorithm with proposed initialization (Initialized)

This performance test shows the reduction of MSE and depicts that the initialization gives the faster reduction of error in comparison to the normal reference algorithm.

For both algorithms the error is reduced to a similar value, but the convergence of the initialized version is much faster (7.5 times higher reduction for the first 1000 steps).

Moreover, the initialization of blinking values reduces the blink detection errors (false and missing detection) to 2.6% in comparison to the original algorithm 4.1% after 10^5 iteration steps. The obtained errors (MSE) are 0.082 and 0.115 respectively.

5   Conclusions

The evolution–based technique gives the possibility of detection blinking pulses not only for the flat EOG signal parts but also in the neighborhood of saccades. This is very important for improving the confidence of estimated signals.

This algorithm uses only a single measurement channel of 3/4 system. If there are more channels available (especially in the 7/8 systems) similar technique could be employed with possible better results, due to the correlation of blinking signal between multiple channels.

The proposed method of initialization based on the estimation of EOG and blinking signal gives the significant reduction of computation time what is useful especially for further real–time implementation. The real–time processing is possible using the high performance computing devices with a fixed latency and it will be considered in further research and development.

References

1. Augustyniak, P., Mikrut, Z.: Task Dependent Parameters of Attention Measured by Two Eyetrackers. J. of Med. Inf. and Techn. (2), MI59–MI66 (2001)
2. Augustyniak, P.: Przetwarzanie sygnałów elektrodiagnostycznych, 244 pages, Uczelniane Wydawnictwa Naukowo–Dydaktyczne AGH, Kraków (2001) (in Polish)
3. Bankman, I.N., Thakor, N.V.: Noise reduction in biological step signals: application to saccadic EOG. Med. Biol. Eng. Comput. 28(6), 544–549 (1990)
4. Barea, R., Boquete, L., Mazo, M., López, E.: Wheelchair Guidance Strategies Using EOG. Journal of Intelligent and Robotic Systems 34, 279–299 (2002)
5. Becker, W.: The Neurobiology of Saccadic Eye Movements. In: Wurtz, R.H., Goldberg, M.E. (eds.) 1989 Metric, pp. 13–67. Elsevier Science Publishers BV (Biomedical Division) (1989)
6. E.O.G Beowulf DVD 2'nd disc, Warner Brothers (2008)
7. Brown, M., Marmor, M., Vaegan, Zrenner, E., Brigell, M., Bach, M.: ISCEV Standard for Clinical Electro–oculography (EOG). Doc. Ophthalmol. 113, 205–212 (2006)
8. Bulling, A., Roggen, D., Tröster, G.: Wearable EOG goggles: Seamless sensing and context awareness in everyday environments. Journal of Ambient Intelligence and Smart Environments (JAISE) 1(2), 157–171 (2009)
9. Denney, D., Denney, C.: The eye blink electro oculogram. British Journal of Ophthalmology 68, 225–228 (1984)
10. Duchowski, A.: Eye Tracking Methodology: Theory and Practice. Springer, Heidelberg (2007)
11. Fleming, B., Dobbs, D.: Animating Facial Features & Expressions. Charles River Media, Hingham (1999)
12. Gu, E., Lee, S.P., Badler, J.B., Badler, N.I.: Eye Movements, Saccades, and Multiparty Conversations. In: Deng, Z., Neumann, U. (eds.) Data Driven 3D Facial Animation, pp. 79–97. Springer, Heidelberg (2008)
13. Juhola, M.: Median filtering is appropriate to signals of saccadic eye movements. Computers in Biology and Medicine 21, 43–49 (1991)
14. Khan, J.I., Komogortsev, O.: Perceptual video compression with combined scene analysis and eye–gaze tracking. In: Duchowski, A.T., Vertegaal, R. (eds.) ETRA 2004 – Proceedings of the Eye Tracking Research and Application Symposium, San Antonio, Texas, USA, March 22–24, p. 57 (2004)

15. Krogh, E.: Normal values in clinical electrooculography. 1. Material, method, methodological investigations and distribution of the potential and time parameters. Acta Ophthalmol. (Copenh) 53(4), 563–575 (1975)
16. Krupiński, R., Mazurek, P.: Estimation of Eye Blinking using Biopotentials Measurements for Computer Animation Applications. In: Bolc, L., Kulikowski, J.L., Wociechowski, K. (eds.) ICCVG 2008. LNCS, vol. 5337, pp. 302–310. Springer, Heidelberg (2009)
17. Krupiński, R., Mazurek, P.: Median Filters Optimization for Electrooculography and Blinking Signal Separation using Synthetic Model. In: 14th IEEE/IFAC International Conference on Methods and Models in Automation and Robotics, MMAR 2009, Miedzyzdroje (2009)
18. Krupiński, R., Mazurek, P.: Optimization–based Technique for Separation and Detection of Saccadic Movements and Eye blinking in Electrooculography Biosignals. In: Software Tools and Algorithms for Biological Systems. Advances in Experimental Medicine and Biology. Springer, Heidelberg (2010)
19. Mallat, S.G., Zhang, Z.: Matching Pursuits with Time–Frequency Dictionaries. IEEE Transactions on Signal Processing, 3397–3415 (December 1993)
20. Martinez, M., Soria, E., Magdalena, R., Serrano, A.J., Martin, J.D., Vila, J.: Comparative study of several Fir Median Hybrid Filters for blink noise removal in Electrooculograms. WSEAS Transactions on Signal Processing 4, 53–59 (2008)
21. Michalewicz, Z.: Genetic Algorithms + Data Structures = Evolution Programs. Springer, Heidelberg (1996)
22. Mosimann, U.P., Müri, R.M., Burn, D.J., Felblinger, J., O'Brien, J.T., McKeith, I.G.: Saccadic eye movement changes in Parkinson's disease dementia and dementia with Lewy bodies. Brain 128(6), 1267–1276 (2005), doi:10.1093/brain/awh484
23. Niemenlehto, P.H.: Constant false alarm rate detection of saccadic eye movements in electro oculography. Computer Methods and Programs in Biomedicine 96(2), 158–171 (2009), doi:10.1016/j.cmpb.2009.04.011
24. Northrop, R.B.: Noninvasive Instrumentation and Measurement in Medical Diagnosis. CRC Press, Boca Raton (2002)
25. Ober, J., Hajda, J., Loska, J., Janicki, M.: Application of eye movement measuring system Ober2 to medicine and technology. In: Proc. of SPIE, vol. 3061(1), pp. 327–332 (1997)
26. Sagar, M., Remington, S.: System and method for tracking facial muscle and eye motion for computer graphics animation, Patent US, International Publication Number WO/2006/039497 A2 (April 13, 2006), Sony Pictures Entertainment, Sony Corporation
27. Poole, A., Ball, L.J.: Eye Tracking in Human–Computer Interaction and Usability Research: Current Status and Future Prospects. In: Ghaoui, C. (ed.) Encyclopedia of Human Computer Interaction, pp. 211–219. Idea Group, USA (2005)
28. Prutchi, D., Norris, M.: Design and Development of Medical Electronic Instrumentation. Wiley, Chichester (2005)
29. Schlgöl, A., Keinrath, C., Zimmermann, D., Scherer, R., Leeb, R., Pfurtscheller, G.: A fully automated correction method of EOG artifacts in EEG recordings. Clinical Neurophysiology 118, 98–104 (2007), doi:10.1016/j.clinph.2006.09.003
30. Thakor, N.V.: Biopotentials and Electrophysiology Measurement. In: Webster, J.G. (ed.) The Measurement, Instrumentation, and Sensors Handbook, vol. 74. CRC Press, Boca Raton (1999)
31. Usakli, A.B., Gurkan, S., Aloise, F., Vecchiato, G., Babiloni, F.: On the Use of Electrooculogram for Efficient Human Computer Interfaces. Computational Intelligence and Neuroscience 2010, Article ID 135629, 5 pages (2010), doi:10.1155/2010/135629

Classification of DNA Microarray Data with Random Forests

Tomasz Stokowy

Abstract. The article includes information about the advantages of Random Forests in DNA microarray data classification. The experiment presented as a background for the publication was performed on the data devoted to Barrett's Esophagus and two types of Reflux Disease - Erosive and Nonerosive. An original idea of estimation of a quality of the classification evolved during studies on the problem and resulted in many interesting conclusions. There are presented topics such as advantages of Random Forests in supervised DNA microarray analysis, application of bootstrap resampling used for calculation of average quality results and comparison of classification quality for Random Forests, Support Vector Machines and Linear Discriminant Analysis. Proposed solutions are said to be a good measure of quality of classification with Random Forests method.

1 Random Forests in Microarray Data Classification

Random Forests have become very popular classifier since there appeared many scientific publications which prooved its high accuracy. There are many advantages which make RF a perfect algorithm for the supervised decision making, such as large number of inputs handling and fast learning process. Growing a forest structure for the aim of the classification was proposed by Leo Breiman, University of California, Berkeley and the general idea is as follows:

1. If the number of cases in the training set is N, sample N cases at random - but with replacement, from the original data. This sample will be the training set for growing the tree.
2. If there are M input variables, a number $m \ll M$ is specified such that at each node, m variables are selected at random out of the M and the best split on these

Tomasz Stokowy
Silesian University of Technology, Institute of Automatic Control
ul. Akademicka 16, 44-100 Gliwice
e-mail: tomasz.stokowy@polsl.pl

     m is used to split the node. The value of m is held constant during the forest
     growing.
3. Each tree is grown to the largest extent possible. There is no pruning [1].

According to this learning algorithm a computer program for DNA microarray classification was implemented. It gives an opportunity to generate a ranking of genes which classify a given testing set in the best way and estimate the accuracy of classification of particular data set.

2   Data Used in the Experiment

During the experiments there were two data sets used. The first of them came from Institute of Oncology, Warsaw and it was described as set of 115 patients with different reflux diseases. Classes in this set were described as follows:

$$D_{reflux} = \begin{cases} 1 \text{ for patients with Barrett's Esophagus diagnosed (57 samples)} \\ -1 \text{ for patients with ERD or NERD diagnosed (58 samples)} \end{cases} \quad (1)$$

The second data set was used for the second analysis of quality of classification methods. The microarrays came from Institute of Oncology, Gliwice and they described two most frequently met thyroid cancer types - papillary and follicular [4]. Classes in this set were described as follows:

$$D_{thyroid} = \begin{cases} 1 \text{ for patients with PTC diagnosed (64 samples)} \\ -1 \text{ for patients FTC diagnosed (21 samples)} \end{cases} \quad (2)$$

Both sets were scanned from Affymetrix HGU133A microarrays and normalized with GCRMA method. Other normalization methods tested - MAS5 and RMA did not influence the accuracy significantly (the differences were below 1%), so the simplest bioconductor GCRMA method was chosen. The data sets were published for the workshop on Data Analysis for Functional Genomics, which took place in Gliwice, 16-17 june 2007.

3   Description of the Classification System

For the aim of estimation of the general error and splitting of the data into training and testing sets, bootstrap 0.632 was used [3]. Generation of many pseudo experiments gives an opportunity to calculate an average error of the method, determine its variance and draw a histogram of accuracies reached in each iteration. The reasonable number of iterations should be set at least to 200, so the histogram could be approximated by the normal distribution function. For the aim of increasing the probability of finding the best genes, gene preselection procedure is applied. This task is realized by modified Sebestyn criterion which gives a measure of

separation between classes. Another important feature of Random Forests classification system was setting the criterion for splitting the tree node. For this task Gini diversity index was chosen. It is similar to fraction of wrong classifications or entropy. The only difference is that it is applied when observations in the node are not classified with given earlier rule, but they are classified to desired set with p_{mc} probability. Formula for the index is given:

$$Q_m(T) = \sum_{n=1}^{q} p_{mc}(1 - p_{mc}), \qquad (3)$$

where $Q_m(T)$ is an index dscribing particular gene importance at given node T and q is the number of genes selected to split the node [2].

4   Quality of Random Forests DNA Microarray Classification

The best way to describe quality of the classification system is to draw a histogram of accuracies reached in each bootstrap iteration. Average accuracy and width of the histogram are the factors that inform about the quality. Unfortunately for each microarray data set the qualities of classification are different, since there are sets that classify very well and ones which are very hard to be properly classified by any of known methods of unsupervised analysis. In case of Random Forests histogram generated by number of iterations i >100 can be well approximated with normal distribution function. Such approximation can be observed in the Fig. 1.

Comparison of the classification methods is a difficult task, due to many ways it can be done. Some classifiers have different parameters than others, sometimes even the inputs to the methods are not the same. Some methods generate the model of gene classifier which is used for prediction, other measure the distance between the samples, Random Forests use only some of selected genes to grow particular trees used for classification. For three different methods the proposed histograms were generated for two data sets. The results are stored in the Table 1.

Fig. 1 Random Forests quality histogram for 500 iterations of bootstrap, 200 trees used to grow the forest and 200 genes selected
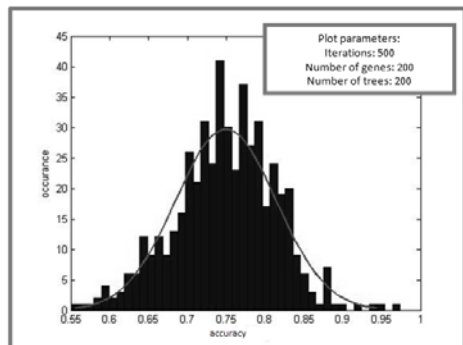
Table 1 Table of average qualities calculated for different methods of supervised classification

Supervised classifacation method[1]	Average accuracy for i=500	
	BE vs ERD, NERD data set[%]	FTC vs PTC data set [%]
Random Forests	78.85	91.13
Support Vector Machines	80.11	89.20
Linear Discriminant Analysis	76.48	84.05

[1] (Accuracies were calculated with Matlab Statistics Toolbox and Bioconductor).

5 Final Conclusions

Random Forests method is a very good solution for the supervised DNA microarray data analysis. Accuracy of classification with Random Forests which is close to 80% for the data set that was used in the experiments can be treated as a very good one. The quality reached by the method strictly depend on the microarray data, sometimes it is worse, but often it is better than quality of methods like SVM, and LDA. The conclusion is, that Random Forests are competition for other methods of supervised learning, what is more they are a great tool which can be successfully used when other classifiers fail. Their great advantage is that classification is made on the base of Euclidean distance between the samples and they run efficiently with large sets of microarray data.

References

1. Breiman, L., Cutler, A.: Random Forests. Machine Learning, 5–32, doi:10.1023/A:1010933404324
2. Koronacki, J., Cwik, J.: Statystyczne systemy uczące sie. Oficyna wydawnicza EXIT, Warszawa, p. 136, pp. 162–164 (2008) (in Polish)
3. Hastie, T., Tibshirani, R., Friedman, J.: The Elements of Statistical Learning: Data Mining, Inference, and Prediction, July 30. Springer, Heidelberg (2003) (Corrected edition), ISBN-13:978-0387952840
4. Jarzab, B., et al.: Gene expression profile of papillary thyroid cancer: Sources of variability and diagnostic implications. Cancer Res. 65, 1587–1597 (2005)
5. Efron, B., Tibshirani, R.J.: Improvements on cross-validation: the 632+ bootstrap method. J. American Statistical Association 92, 548–560 (1997)
6. Diaz-Uriarte, R., Alvarez de Andres, S.: Gene selection and classification of microarray data using random forest. BMC Bioinformatics 7, 3 (2006)
7. Liaw, A., Wiener, M.: Classification and Regression by random Forest. R News 2(3), 18–22 (2002), http://CRAN.R-project.org/doc/Rnews/

Homogeneity Assessment of Cell Populations for High Content Screening Platforms

Arkadiusz Gertych and Jian Tajbakhsh

Abstract. The main thrust of this work is to develop a bioinformatics tool for the automated evaluation of cell population homogeneity, which can be implemented on high content screening platforms. For that we employed Kullback-Leibler (K-L) divergence as a measure of similarity of multidimensional DNA codistribution patterns extracted from cell nuclei, and assigned analyzed cells into four categories. The resulting cell population homogeneity is determined as the ratios of cell quantities in the respective similarity categories. We evaluated our approach on human prostate cancer cells treated with an anticancer drug in comparison to untreated cells. A difference in homogeneities measured in these two populations was influenced by strong changes induced into DNA distribution patterns by treatment process vs. the occurrence of naturally more diverse groups of DNA patterns in the naïve cells.

1 Introduction

Large quantities of three-dimensional (3-D) image data delivered by modern cellular imaging systems necessitate a machine vision support to determine, extract, and classify a variety of cellular features for the evaluation of cell structure changes through communication with their native environment or through experimental conditions. High content screening (HCS) platforms are being developed to offer complex analyses of individual cells in populations - typically in a high-throughput fashion. These platforms usually delineate structures at the cellular and subcellular resolution and quantify relevant signals captured from multicolor,

Arkadiusz Gertych · Jian Tajbakhsh

Translational Cytomics Group, Department of Surgery, Cedars-Sinai Medical Center, 8700 Beverly Blvd. Los Angeles, CA 90048

e-mail: gertycha@cshs.org, tajbakhshj@cshs.org

fluorescence-labeled targets including nucleic acids, proteins, lipids, carbohydrates and complexes thereof. Primary applications in which modern HCS is used are the early phases of pre-clinical drug discovery, cytopathology, and basic research in systems cell biology. The latter area may particularly benefit from HCS platforms as these integrate imaging devices with unified and scalable bioinformatics tools to automatically analyze biological sample *in situ* or extract structure-function information retrieved from processed and archived data of thousands of cells.

A systems cell biology profile is defined as the cells systemic response measured by means of reporters. Currently immunofluorescent reporters are widely used to delineate cellular targets for their localization and quantification [1, 2]. The need to understand and model complexity of temporal and spatial processes in cells has led to the development of numerous computational techniques that are used to elucidate biological mechanisms from the tissue level down to the subcellular level. The cell nucleus has traditionally been one of the most frequent objects studied in disease diagnosis and treatment. Numerous applications related to cancer diagnosis and therapy utilize the load and distribution of one or more proteinaceous and nucleic acid components as multidimensional patterns [2, 3, 4] through which a systems cell biology profile can be approximated. Such analytical approaches with HCS platforms typically require the segmentation of nuclear regions of interest (ROI) followed by the extraction of residing patterns, and their recognition using one of the following techniques: (i) comparison of a known or unknown pattern with a reference using statistical tests; (ii) classification of patterns through supervised learning, support vector machines and neural networks; or (iii) clustering, in which the distance between points in feature space is used as a discriminating factor [5]. Ultimately, all of these methods require a reference pattern to evaluate unknown nuclear patterns or those being tested for changes.

Similarity measured between two patterns is a useful tool to express proximity between objects in a multi-dimensional space of attributes. Although definitions of similarity vary from one application to another, in most cases, the concept of similarity is based on distances, however the distance functions are not always sufficient in capturing correlations among the objects. Ultimately, similar objects are required to have close values in at least one subset of dimensions. Pairwise object similarity perceived from a global perspective is associated with homogeneity of objects to characterize a whole set of patterns.

Automated homogeneity assessment is highly valuable for a HCS setting, in which a quick evaluation of large number of cells is required. Isolation of cells, which display a common (similar) pattern under certain criteria, or those that can be flagged as outliers, is usually the primary purpose of screening. A typical HCS scenario involves studying several cellular targets in conjunction, and thus, multiple fluorescence-based reporters are simultaneously applied and measured. In these cases the homogeneity assessment is challenged as more than one significant target is available for screening and therefore the most significant codistribution of targets needs to be determined.

In this paper a new similarity-based homogeneity assessment method in cell populations is presented. Our approach employs Kullback-Leibler divergence to first

calculate similarity between cells within a population based on multidimensional patterns of DNA-specific signals extracted from 3-D images of nuclei. We developed a bionformatics software that displays immediately readable statistics including the population's homogeneity value and a pseudo-color map of cells according to their quantified similarity. The results and properties of our approach are discussed in this article.

2   Materials

DU145 prostate cancer cells were used in this study as a model. The cells were divided into two groups: (i) a control population that was not treated for 72 hrs, and (ii) a subpopulation of cells treated with an anticancer drug for 72 hrs. Cells were fixed on glass coverslips for immunofluorescence. 4,6-diamidino-2-phenylindole (DAPI) (M_1) to delineate global DNA, and antibody specific to methylcytosine (M_2) was applied to visualize methylated DNA in nuclei. Imaging of cells was performed using a confocal supercontinuum laser scanning microscope (Leica TCS SP5 X) that allows for excitation within the continuous range of 470-670nm in 1nm increments. DAPI was excited with an external diode laser at 405nm. Optical sections of cells were recorded separately in channels capturing M_1- and M_2-specific fluorescence in the ranges of 411-497nm and 498-575nm, respectively. Typical image size was $2048 \times 2048 \times 35$, with a voxel size of $116 \times 116 \times 230$nm, and 12bit/pixel resolution. Three such image cubes were acquired per each cell group. More details on immunofluorescnce and imaging can be found in [7, 6].

3   Methods

3.1   HCS Platform Components

HCS platforms are designed to identify and quantify specific aspects of images with as little human intervention as possible and involve optical imaging and image analysis embedded into a bioinformatics application software. In this article we focus on the latter component which is used to extract the quantitative information. The data flow starts at the level of image acquisition (Fig. 1). First, immunofluorescently labeled cells are scanned and signals from different cellular channels are recorded. Such an image reflects the spatial distribution of multiple fluorescent targets. Next, an image processing procedure delivers statistical analysis and high-level interpretation of results performed on the basis of knowledge of the experimental variables - the DNA patterns. Finally cell similarities are measured and the homogeneity of the entire population is calculated. The respective values are obtained and displayed numerically as well as pseudo-colored maps. Our software offers these yields as key quantitative readouts for HCS.
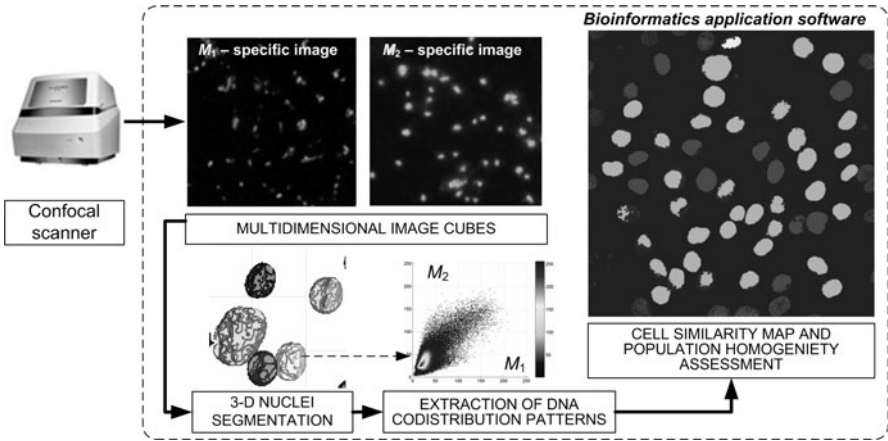
Fig. 1 Implementation of a bioinformatics software on a HCS platform. Fluorescent signals (reporters) recorded in channels of a confocal scanner are used to detect nuclei, compose DNA codistribution patterns, and assess cell population homogeneity.

3.2 Image Preprocessing and Extraction of Intensity Patterns

As shown in (Fig.1) the analysis of individual cells is performed within a multichannel image cube. 3-D ROIs of cell nuclei are automatically outlined [7]. Each ROI receives a unique label and is mapped back onto the original M_1- and M_2-specific images in order to extract individual nuclear patterns for further analysis. Codistributions of voxels outlined by an ROI in channels M_1 and M_2 are represented as a scatter plot and form a pattern in which the variables are the various classes of nuclear DNA targets [6, 7]. In Fig. 2 example patterns are displayed. The respective scatter plots are distinct in appearance and codistribution of M_1 and M_2 - the DNA-specific signals. A joint distribution pattern (explained later) is created as a superposition of individual patterns from all nuclei.

3.3 Pattern Similarity Analysis via Kullback-Leibler Divergence

Commonly applied similarity measures fall into three groups: (1) point-based, including Euclidean and Minkowski distances, (2) set-based including Jaccard's, Tanimoto's, and Dice's indices, and (3) probabilistic with Kullback-Leibler divergence, Bhattacharyya, and Mahalanobis distances. The latter one is the most frequently used criterion in multivariate outlier detection tasks. On the other hand, Kullback-Leibler divergence is considered as a generalization of the Mahalanobis distance to data with a mixture of nominal, ordinal and continuous variables [8], and in its basic form is expressed as information linked to two probability distributions $p = \{p_i\}$ and $q = \{q_i\}$ [9]:
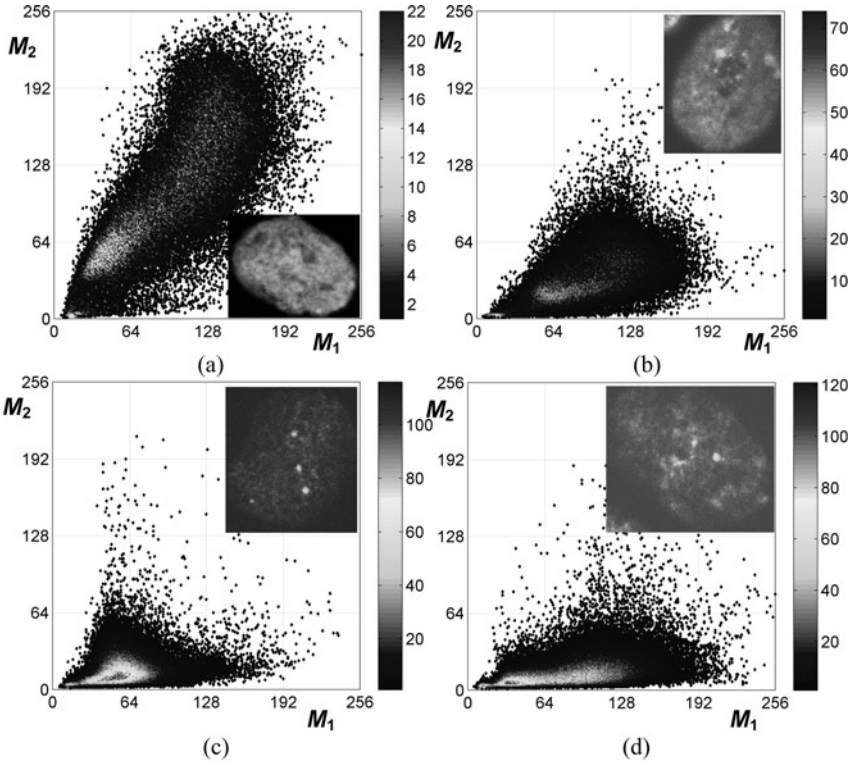
Fig. 2 Scatter plots as DNA-based signatures of prostate cancer cell nuclei: (a, b) untreated, and (c, d) drug-treated populations. The patterns in a) and b) are visually more distinct than the patterns in c) and d), which appear more similar. The nuclei are the extreme entities (according to appearance of their patterns) that were found in the entire population.

$$KL(p||q) = H(p) - K(p,q) =$$
$$\sum_i p_i \log(p_i) - \sum_i p_i \log(q_i) = \sum_i p_i \log(p_i/q_i), \quad (1)$$

where: $H(p)$ is the negative Shannon's entropy and $KL(p,q)$ is the measure of information referred to as inaccuracy. $KL(p||q)$ is nonnegative and constrained by: $\lim_{\substack{p_i \to \infty \\ q_i \neq 0}} p_i \log(p_i/q_i) = 0$ and $\lim_{\substack{q_i \to \infty \\ p_i \neq 0}} p_i \log(p_i/q_i) = \infty$.

Typically, p_i represents data, observations, or a precisely calculated probability distribution, and q_i represents an *arbitrary* distribution, a model, a description or an approximation of p_i. Following [9] it is assumed that: $0 \log(0/q_i) = 0$ and terms in Equ.1 where the denominator is zero are treated as undefined and thus neglected in order to provide continuity of p_i with q_i.

For two multivariate d-dimensional Gaussian densities p and q the Kullback-Leibler divergence is expressed by:

$$KL_G(\mu_p, \Sigma_p; \mu_q, \Sigma_q) = \frac{1}{2}\left(\log\left(\frac{|\Sigma_q|}{|\Sigma_p|}\right) + \text{tr}(\Sigma_q\Sigma_p)\right) +$$

$$\frac{1}{2}\left((\mu_p - \mu_q)^T \Sigma_q^{-1}(\mu_p - \mu_q) - d\right), \quad (2)$$

where: μ are vectors of means, the Σ are covariance matrices, tr is the trace function, and $|(.)|$ is the determinant of a matrix.

Substitution of two one-dimensional univariate normal distributions into Equ. 2 – $p_G(x) = N(x; \mu_p, \sigma^2)$ and $q_G(x) = N(x; \mu_q, \sigma^2)$ with x as the random variable – yields the K-L divergence as:

$$KL_G = (\mu_p, \sigma_p; \mu_q, \sigma_q) = \frac{1}{2}\left(\log\left(\frac{\sigma_q^2}{\sigma_p^2}\right) + \frac{(\mu_q - \mu_p)^2}{\sigma_q^2} + \frac{\sigma_q^2}{\sigma_p^2} - 1\right). \quad (3)$$

For our application we chose to utilize Kullback-Leibler divergence because of its properties such as the invariance to translation, and applicability to various kinds of distributions [9, 10]. It has been also shown that the K-L divergence between two bivariate normal densities is a function of Pearson's correlation coefficient [10].

The K-L divergence values $\in [0, \infty)$. In order to categorize patterns based on K-L measure the whole range can be split. Utilizing Equ.3 and assuming that $\sigma_p \approx \sigma_q$, and that a σ can be substituted instead of σ_p and σ_q in Equ.3 we obtain:

$$KL_G(\mu_p, \mu_q, \sigma) = \left(\frac{\mu_q - \mu_p}{\sqrt{2}\sigma}\right)^2, \quad (4)$$

where the numerator reflects the distance between the peaks of the two Gaussian distributions.

The KL_G in the simplified formula can be also related to the area yielded by the intersection of Gaussian distributions and thus used as another way to articulate the degree of dissimilarity (Fig.3a). Additionally, expressing the numerator in Equ.4 as $\mu_p - \mu_q = n\sigma$ (as a multiple of σ), the KL_G value becomes solely dependent on the standard deviation in the evaluated distributions and reduces to $KL_G(n\sigma) = (n/\sqrt{2})^2$. In this notion, the more distant the distribution peaks are the higher the divergence value will be. For this constraints the area of distributions overlap (Fig.3a) can be calculated from:

$$A_{p \cap q}(n\sigma) = 1 - \text{erf}\left(\frac{n\sigma}{2\sqrt{2}}\right), \quad (5)$$

where: erf is the Gauss error function, and n is the multiple of σ.

Based on the relationship between KL_G and $A_{p \cap q}$ (Tab. 1) a set of similarity categories can be defined, which nonlinearly maps $A_{p \cap q}$ onto KL_G (Fig. 3b). In our case four categories: *similar* KL_G [0,0.5), *likely similar* KL_G [0.5,2), *unlikely similar* KL_G [2,4.5), and *dissimilar* for KL_G [4.5,∞) are utilized. They express the similarity degree of KL_G divergence between two one-dimensional Gaussian distributions with equal σ and the distance between the peaks of the distributions expressed as

Table 1 Relationship between $A_{p \cap q}$ and KL_G as a function of $n\sigma$

$n = (\mu_q - \mu_p)/\sigma$	$A_{p \cap q}$	KL_G
0	1	0
0.5	0.82	0.125
1	0.62	0.5
1.5	0.45	1.125
2	0.32	2
2.5	0.21	3.125
3	0.13	4.5
∞	0	∞

(a)   (b)
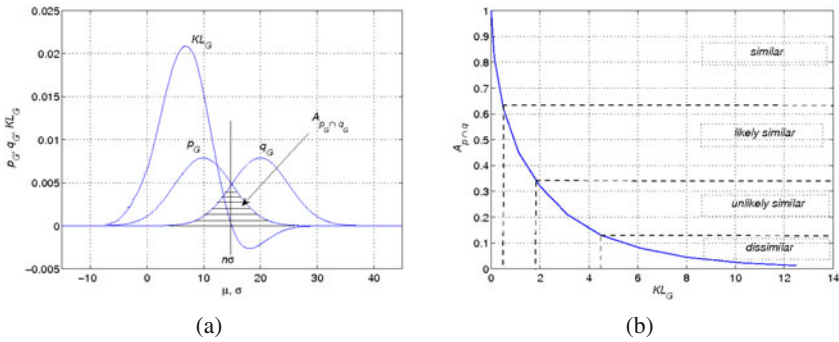
Fig. 3 Mapping of KL_G and $A_{p \cap q}$ and cell similarity categories: a) two example Gaussian distributions $p_G = N(\mu_p, \sigma^2)$ and $p_Q = N(\mu_q, \sigma^2)$ with $\mu_q = 10$, $\mu_p = 20$ and $\sigma = 5$ of and the respective Kullback-Leibler divergence. The overlap between p_G and q_G is used to express four degrees of similarity in b). They are defined using $A_{p \cap q}$ and KL_G which are functions of $n\sigma$.

$n\sigma$ ($n \in R^+$). Using these categories we performed similarity analysis between DNA codistribution patterns of cell nuclei considering an individual pattern distribution of each cell nucleus as $\{p_i\}$ and a reference pattern distribution as $\{q_i\}$ in Equ.1. In our case the reference pattern is the normalized sum of all individual patterns in the entire cell population.

3.4   Homogeneity Assessment Based on Similarity Measure

In [11] homogeneity has been described as a function of optical densities of chromatin measured for a single nucleus. Three categories of pixels: white (N_w), black (N_b), and gray (N_g) have been constructed according to the relationship between

each pixel value and the mean value of all pixels. If the pixel value was within the $(80\% \div 120\%)$ range of the mean a pixel was assigned to N_g category. If the difference was higher than 120% or lower than 20%, a pixel received white or black label respectively. According to this distance-based categorization a *homogeneity* and *heterogeneity* have been defined as the following ratios: $N_g/(N_b + N_w + N_g)$, $(N_w + N_b)/(N_b + N_w + N_g)$. Here we propose to extend the original definition of homogeneity from [11] by introducing quantities yielded by our divergence-based measure of similarity:

$$Homogeneity = \frac{N_{SI}}{N_{SI} + N_{LS} + N_{US} + N_{DS}}, \qquad (6)$$

where: N_{SI}, N_{LS}, N_{US} and N_{DS} are the number of cells in *similar*, *likely similar*, *unlikely similar* and *dissimilar* categories respectively.

The quantity in Equ. 6 was then implemented and applied to the two (treated and untreated) DU145 cancer cell populations. The reference patterns were obtained apart as the sum of all nuclear patterns for each population type.

4 Results

We developed a software module, which automatically processes 3-D images of fluorescently labeled cells according to the workflow in Fig. 1. Our re-defined homogeneity assessment approach can be outlined in the following steps: (i) each cell receives a K-L divergence-based similarity value measured between the pattern of DNA-specific signals of its nucleus and a reference pattern that is constituted by the combined patterns of the entire cell population. These DNA-specific signals are mapped as 2-D intensity codistribution patterns and converted to probabilities; (ii) each cell is assigned into one of the predefined similarity categories, and (iii) two statistics are provided: a homogeneity value and a similarity-based false-colored map of nuclei for an immediate and visual quantitative readout. We tested our approach on two populations of fluorescently stained human prostate cancer cells; a naïve population and a subpopulation of the same cells that was treated with an anticancer drug. The respective statistics are presented in Fig. 4 and Table 2.

Table 2 Results of homogeneity assessment in untreated and treated human prostate cancer cells

Cell type	No. of cells in each category					Homogeneity
DU145	*similar*	*likely similar*	*unlikely similar*	*dissimilar*	Total	%
untreated	54	88	6	2	150	36
treated	58	65	7	0	130	44

(a)   (b)
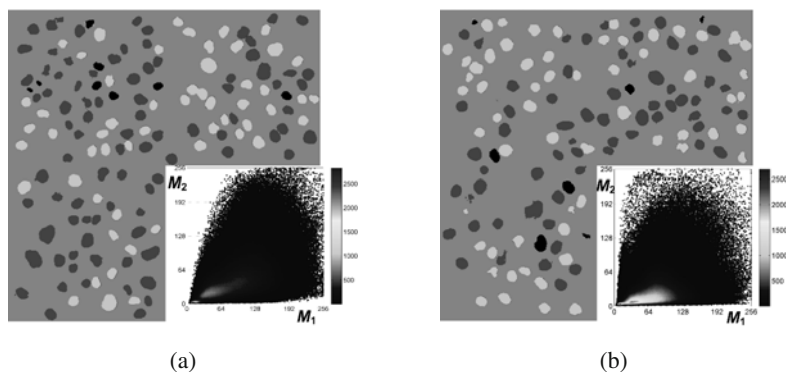
Fig. 4 Homogeneity assessment in two DU145 cancer cell populations and their reference patterns: a) untreated population ($n = 150$), b) population treated with an anticancer drug ($n = 130$). Two pseudo-colored maps superimposed onto original images visualize statistics of the four represented cell categories: *similar* (bright areas), *likely similar* (gray), *unlikely similar* and *dissimilar* (black). Each sub-figure consists of three separate 3-D image cubes of cells.

5 Conclusions and Discussion

Measuring cellular response to drugs is a principal task of HCS platforms with the objective to assess drug efficacy through the quantification of relevant cellular structures. This process leads to the identification of groups of cells with different responses, including outlier cells, and determines population response homogeneity based on targeted structure similarity. The quantities of similar and dissimilar cells can be considered as relevant measurable indicators of cellular response to external conditions or restricted for the assessment of a cell's state in certain disease processes. The key to HCS is the automation of image analysis through: (i) primary object identification and counting, (ii) measurement of dominant object properties, (iii) identification of associated cellular targets, and (iv) analysis of raw measurements to address specific biological mechanisms and disorders. A HCS platform should ideally offer standardization, objectivity, speed and accuracy of the analysis regardless of cell line, cell morphology, type of drug, treatment schedules, and other experimental conditions applied. In fact, these requirements are difficult to be met in reality. Therefore, we propose a more universal and unified cell population homogeneity assessment technique that would add a valuable feature to existing HCS platforms.

According to our definition of homogeneity (Equ.6) we found that the untreated population renders itself less homogeneous than the treated population. In our experimental study a biological explanation would be that the applied drug introduced changes into the higher organization of nuclear DNA (chromatin) creating a larger number of similar DNA distribution profiles than originally present in the naïve population (Fig.2). The method presented here is sensitive to such changes. This fact emphasizes that the drug screening meant to evaluate drug effects on DNA topology

benefits from homogeneity measurement and would constitute a considerably valuable HCS upgrade. Our technique inherits all properties of the Kullback-Leibler divergence. In addition it possesses the following advantages: (1) can operate on multidimensional histograms as vectors, (2) allows for processing of intensity patterns of arbitrary shapes and sizes, (3) is not restricted by cardinality of analyzed objects and targets, (4) any reference pattern can be flexibly substituted, (5) is more general than the one shown in [11] and (6) is computationally inexpensive.

For this work we arbitrarily selected four classes of divergence-based similarities, however the number of classes as well as the respective K-L ranges can be flexibly adjusted according to screening purposes and restrictions in outlier identification (*dissimilar* cells). These properties are well suited for applications on a variety of bioinformatics and HCS platforms, in which the identification of homogeneous subsets of cells as well as outliers is followed by high-level data interpretation. HCS methods can benefit from this approach, especially when cell population homogeneity is difficult to assess due to the lack of standardized references and unknown number of objects. Furthermore, our concept of homogeneity assessment can be flexibly adjusted for topological studies of other nuclear entities, where multidimensional patterns are targeted in different medical or biological context that goes beyond the HC screening.

References

1. Herceg, Z., Hainauta, P.: Genetic and epigenetic alterations as biomarkers for cancer detection, diagnosis and prognosis. Mol. Oncol. 1, 26–41 (2007)
2. Evans, J., Matsudaria, P.: Linking microscopy and high content screening for large scale biomedical research. In: Taylor, L., Haskins, J., Guiliano, K. (eds.) High content screening. Humana Press, Totowa (2007)
3. Conrads, T., Zhou, M., Petricoin, E., Liotta, L., Veenstra, T.: Cancer diagnosis using proteomic patterns. Expert Rev. Mol. Diagn. 4, 411–420 (2003)
4. Castelli, C., Losa, G.: Ultrastructural complexity of nuclear components during early apoptotic phases in breast cancer cells. Anal. Cell. Pathol. 23, 1–9 (2001)
5. Glory, E., Murphy, R.F.: Automated subcellular location determination and high throughput microscopy. Dev. Cell 12, 7–16 (2007)
6. Tajbakhsh, J., Wawrowsky, K., Gertych, A., Bar-Nur, O., Vishnevsky, E., Lindsley, E., Farkas, D.: Characterization of tumor cells and stem cells by differential nuclear methylation imaging. In: Proc. SPIE, vol. 6859, p. 68590F (2008)
7. Gertych, A., Wawrowsky, K., Lindsley, E., Vishnewsky, E., Farkas, D., Tajbakhsh, J.: Automated quantification of DNA demethylation effects in cells via 3D mapping of nuclear signatures and population homogeneity assessment. Cytom Part A 75A, 569–583 (2009)

8. de Leon, A.R., Carriere, K.C.: Generalized Mahalanobis distance for mixed data. J. Multivariate Anal. 92, 174–185 (2005)
9. Kullback, S., Leibler, R.: On information and sufficiency. Ann. Math. Stat. 22, 79–86 (1951)
10. Kullback, S.: Information theory and statistics. Dover Pub., New York (1997)
11. Young, I., Verbeek, P., Mayall, B.: Characterization of chromatin distribution in cell nuclei. Cytom 7, 467–474 (1986)

Automated Cell Nuclei Segmentation in Breast Cancer Fine Needle Biopsy Smears

Marek Kowal and Andrzej Obuchowicz

Abstract. Reliable segmentation of cell nuclei from microscopic images is an important task in many medical studies. This paper present a novel method for the segmentation of cell nuclei from microscopic images based on fuzzy clustering and ellipse fitting algorithm. It was designed specifically to segment nuclei in breast cancer FNB (Fine Needle Biopsy) cytological images. The segmentation approach takes both the color information and the spatial information into account during detecting the cell nucleus. Because of the presence of the elliptic shape function dissimilarity measure is able to differentiate the pixels with similar color but located in in different regions of the image. Moreover, it is very easy to extract morphometric parameters of the cell nuclei based on parameters of detected ellipses. Simulations and experimental results are provided to demonstrate the performance and generality of the proposed method. The proposed algorithm is able to segment cell nuclei obtained from microscopy imaging with reasonable accuracy.

1 Introduction

Breast cancer is the most common cancer among women. The prognosis in breast cancer is strongly dependent on the disease development before any treatment is applied so the chance of recovery is a function of time of the detection of cancer. Modern medicine does not provide one hundred percent reliable, if possible cheap and at the same time non-invasive diagnostic methods for the diagnosis of breast pathology. As a result, in practice the important function acting in breast cancer diagnosis is the so-called triple-test, which is based on the summary of results of three medical examinations with different degrees of sensitivity and it allows to achieving high confidence of diagnosis. The triple-test includes self examination (palpation), mammography or ultrasonography imaging and fine needle biopsy [11]. Fine needle

Marek Kowal · Andrzej Obuchowicz
University of Zielona Góra, Institute of Control and Computation Engineering
e-mail: M.Kowal@issi.uz.zgora.pl, A.Obuchowicz@issi.uz.zgora.pl

biopsy is collecting nucleus material directly from tumor for microscopic verification. Next, the material (collected cells) is examined using microscope in order to confirm or exclude the presence of cancerous cells. The present approach requires a deep knowledge and experience of the cytologist responsible for diagnosis. In short, some pathologists can diagnose better than others. In order to make the decision independent of the arbitrament factor, morphometric analysis can be applied. Objective analysis of microscopic images of cells has been a goal of human pathology and cytology since the middle of the 19th century. Early work in this area consisted of simple manual measurements of cell and nuclear size. Along with the development of advanced vision systems and computer science, quantitative cytopathology has become a useful method for the detection of diseases, infections as well as many other disorders [10, 5]. In this work, we present a method that allows recognizing the malignancy and distinguish cancerous cells from the normal and benign cells. The classification of the tumor is based on morphometric examination of nuclei cells. In contrast to normal and benign nuclei, which are typically uniform in appearance, cancerous nuclei are characterized by irregular morphology that is reflected in several parameters. Morphometric measurements characterizing the shape and size have been mainly used for feature extraction. Features of the nuclei can be extracted from the image after the nuclei are correctly segmented and labeled. This work concentrates mainly on the segmentation phase because this stage of image processing is critical for correct diagnosis and treatment. Taking into account the specificity of the problem, the segmentation task is used to distinguish nuclei from the background and next label all nuclei. One of more often used methods for image segmentation is fuzzy clustering in the form of the Fuzzy C-Means algorithm (FCM). Unfortunately, the algorithm is useless in the case considered because it makes it possible to distinguish the brighter background from darker groups of cell nuclei and it is required to separate each single nuclei from the image in order to measure its morphometric parameters. Finally, the fuzzy c-means with shape algorithm has been adopted to tackle the mentioned problem [7, 12]. The original version of the FCMS algorithm was prepared to determine two clusters only (background and demanded objects). The work proposes a modified iterative algorithm in order to overcome the mentioned problem and allows determining all nuclei in the image as separate objects.

The paper is divided into three sections. Section 1 gives an overview of breast cancer diagnosis and fine needle biopsy imaging techniques. Section 2 describes the idea of the FCMS algorithm. Section 3 deals with modifications applied to the original algorithm. Section 4 shows the experimental results obtained using the proposed approach. The last part of the work includes a summary, conclusions and references.

2   Fuzzy Clustering with Shape Constraints

The idea of the segmentation of images using a clustering algorithm usually boils down to a search for natural clusters of pixels represented in color space. With this

approach, it is possible to find objects characterized by similar colors, and by applying the fuzzy clustering algorithm the method is more robust against disturbances and image inaccuracy [1]. Taking into account the fine needle biopsy images of nuclei, the task of segmentation reduces to searching separate objects (cell nuclei) in order to determine their morphometric parameters. Unfortunately, the application of fuzzy clustering in the form of the FCM algorithm allows us to separate two interesting objects only: the background and all cell nuclei viewed as one big object. In order to solve the problem, a modified FCM algorithm is used, which was originally developed in the work [7, 13] and used in lip segmentation from the face image.

The FCMS algorithm, similarly to the original FCM algorithm, is based on finding the local minimum of the nonlinear cost function using the Picard iteration through first-order conditions for stationary points [2, 1]. In the case of the FCMS algorithm, the cost function is defined by the following expression:

$$
J(\boldsymbol{U},\boldsymbol{V},\boldsymbol{\theta}) = \sum_{x=1}^{X} \sum_{y=1}^{Y} \sum_{k=1}^{C} \left[\mu_{x,y,k}^{m} \left(f_c(\boldsymbol{c}_{x,y},\boldsymbol{v}_k) + \right. \right.
$$
$$
\left. \left. + \alpha f_d(x,y,\boldsymbol{\theta},n_k) \right) \right], \tag{1}
$$

where the matrix $\boldsymbol{U} \in \mathbb{R}^{X \times Y \times C}$ contains the membership degrees of pixels to the defined clusters, $\boldsymbol{V} = [\boldsymbol{v}_1,\boldsymbol{v}_2,\ldots,\boldsymbol{v}_C], \boldsymbol{v}_i \in \mathbb{R}^{C \times q}$ is a matrix which defines the centers of the clusters, $\boldsymbol{\theta}$ is a vector of parameters describing the preferred shape of the objects searched in spatial domain, X and Y defines the size of the analyzed image, f_c is a function used to determine the distance between the data points and cluster centers, f_d is a function to evaluate the belong rate of the pixel to the ellipse associated with the tested cluster, $\mu_{x,y,k}$ is the membership of the (x,y)-th pixel in the fuzzy cluster k, $m \in (1,\infty)$ is the fuzziness of the clustering procedure, $\boldsymbol{c}_{x,y}$ is a vector of (x,y)-th pixel parameters which describes its color, $\boldsymbol{v}_k \in \mathbb{R}^q$ is a vector of the coordinates of the k-th cluster center, n_k is an exponent of elliptic function associated with the k-th cluster, α is a weighting parameter.

The function f_c defines dissimilarity measures based on the distance between the data points and cluster centers:

$$
f_c(\boldsymbol{c}_{x,y},\boldsymbol{v}_k) = \|\boldsymbol{c}_{x,y} - \boldsymbol{v}_k\|^2 =
$$
$$
= (\boldsymbol{c}_{x,y} - \boldsymbol{v}_k)^T \boldsymbol{A}(\boldsymbol{c}_{x,y} - \boldsymbol{v}_k). \tag{2}
$$

The matrix A which occurs in the expression (2) is used to tune the shape and orientation of the clusters in space. In the simplest approach, the matrix $\boldsymbol{A}$ is unitary, thus the distance measure $f_c(\boldsymbol{c}_{x,y},\boldsymbol{v}_k)$ is an Euclidean norm. In this case, the study metric is defined as a Euclidean distance which measures color dissimilarity in RGB or HSV color space. The function f_d incorporates the shape function in the objective function and measures the spatial distance. As the nuclei are more like an ellipse, it was decided to chose the shape function f_d as elliptic function described by the following expression:
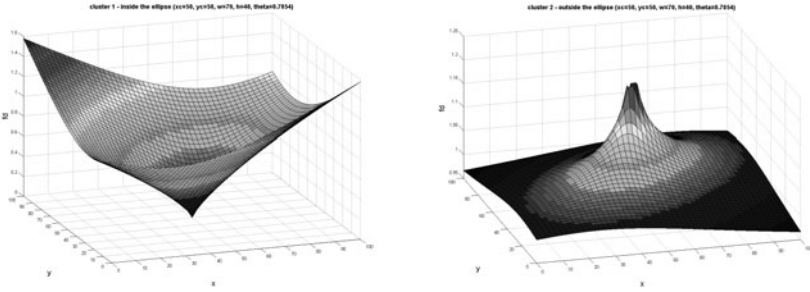
Fig. 1 Sample elliptic function for two clusters

$$f_d(x,y,\boldsymbol{\theta},n_k) = \left(\frac{\left((x-x_c)\cos\phi + (y-y_c)\sin\phi\right)^2}{w^2} + \right.$$
$$\left. + \frac{\left((x-x_c)\cos\phi - (y-y_c)\sin\phi\right)^2}{h^2} \right)^{n_k}, \tag{3}$$

where $\boldsymbol{\theta} = [x_c, y_c, w, h, \phi]$ denotes the set of parameters that describes the elliptic function, (x_c, y_c) is the center of the ellipse, w and h are respectively the semi-major and semi-minor axis, and ϕ is inclination angle, exponent n_k ensures a small function values within the ellipse and large vales for the pixels outside the ellipse. Figure 1 shows values of the sample elliptic function f_d for two clusters. Taking into account that each cluster has identical parameters $\boldsymbol{\theta}$ but with a different exponent n_k, it is possible to determine two clusters only. The first one represents the background and the second one represents the cell nuclei found in the image.

The idea of the proposed fuzzy clustering is to minimize the objective function (1):

$$(\boldsymbol{U}^*, \boldsymbol{V}^*, \boldsymbol{\theta}^*) = \arg\min_{(\boldsymbol{U}, \boldsymbol{V}, \boldsymbol{\theta})} J(\boldsymbol{U}, \boldsymbol{V}, \boldsymbol{\theta}). \tag{4}$$

The minimum of the objective function is calculated by an iterative algorithm using the following expressions for the updating matrices $\boldsymbol{U}$ and $\boldsymbol{V}$:

$$\mu_{x,y,k} = \left[\sum_{j=1}^{C} \left(\frac{f_c(\boldsymbol{c}_{x,y}, \boldsymbol{v}_k) + \alpha f_d(x,y,\boldsymbol{\theta},n_k)}{f_c(\boldsymbol{c}_{x,y}, \boldsymbol{v}_j) + \alpha f_d(x,y,\boldsymbol{\theta},n_j)} \right)^{\frac{1}{m-1}} \right]^{-1}, \tag{5}$$

$$\boldsymbol{v}_k = \frac{\sum_{x=1}^{X} \sum_{y=1}^{Y} \mu_{x,y,k}^m \boldsymbol{I}_{x,y}}{\sum_{x=1}^{X} \sum_{y=1}^{Y} \mu_{x,y,k}^m}, \tag{6}$$

where $\boldsymbol{I}_{x,y} \in \mathbb{R}^q$ represents a single pixel. The parameters of the ellipse $\boldsymbol{\theta}$ are updated in each step of the FCMS algorithm by the gradient descent algorithm using the following general expression:

$$\theta_i(t+1) = \theta_i(t) - \gamma \frac{\partial J(\boldsymbol{U}, \boldsymbol{V}, \boldsymbol{\theta})}{\partial \theta_i}, \tag{7}$$

where

$$\frac{\partial J(\boldsymbol{U}, \boldsymbol{V}, \boldsymbol{\theta})}{\partial \theta_i} =$$
$$= \alpha \sum_{x=1}^{X} \sum_{y=1}^{Y} \sum_{k=1}^{C} \mu_{x,y,k}^{m} n_k f_d(x, y, \boldsymbol{\theta}, n_k)^{n_k - 1} \frac{\partial f_d(x, y, \boldsymbol{\theta}, n_k)}{\partial \theta_i}. \tag{8}$$

Equations (5), (6) and (7) are iterated as a Picard iteration to obtain the segmentation of the image. Detailed expressions for updating the parameters of the ellipse can be found in the paper [7].

Figure 2 shows a sample image with two cell nuclei and a corresponding objective function calculated for two parameters x_c and y_c (for simplicity, the rest of the ellipse parameters are frozen). Two local minima present in Fig. 2 represent two cell nuclei present in the original image. Hence, the gradient descent method can be applied to find the local minima and thus the centers of cell nuclei.

It can be noticed that the objective function is continuous in $(\boldsymbol{U}, \boldsymbol{V}, \boldsymbol{\theta})$ and $\boldsymbol{I}_{x,y}$ is bounded in $\mathbb{R}^q$. Moreover, the second partial derivative of the objective function with respect to $(\boldsymbol{U}, \boldsymbol{V})$ is a positive diagonal matrix for any feasible $\boldsymbol{\theta}$. Following the proof of convergence for FCM in [2] and FCMS in [7] respectively, the objective function value of the i-th Picard solution $(\boldsymbol{U}^i, \boldsymbol{V}^i)$ is less than that of $(\boldsymbol{U}^{i-1}, \boldsymbol{V}^{i-1})$:

$$J(\boldsymbol{U}^i, \boldsymbol{V}^{i-1}, \boldsymbol{\theta}^{i-1}) < J(\boldsymbol{U}^{i-1}, \boldsymbol{V}^{i-1}, \boldsymbol{\theta}^{i-1}), \tag{9}$$

and

$$J(\boldsymbol{U}^i, \boldsymbol{V}^i, \boldsymbol{\theta}^{i-1}) < J(\boldsymbol{U}^i, \boldsymbol{V}^{i-1}, \boldsymbol{\theta}^{i-1}). \tag{10}$$

While using the gradient descent method for solving $\boldsymbol{\theta}^i$, the objective function $(\boldsymbol{U}^{i-1}, \boldsymbol{V}^{i-1})$ is decreasing until $\boldsymbol{\theta}^i$ falls to a local minimum or reaches the
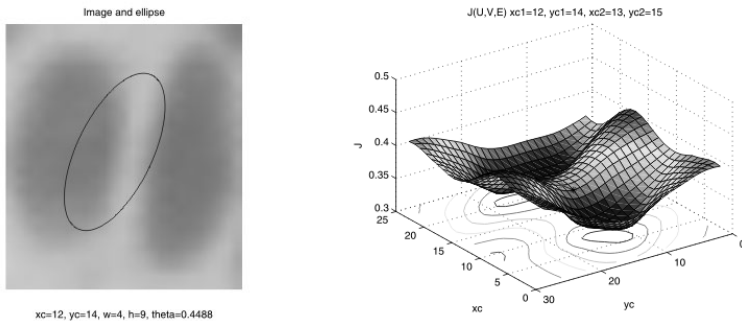
Fig. 2 Original image and the corresponding objective function

boundary of the $\boldsymbol{\theta}$-vector space. Taking this into account, the following inequality can be formulated:

$$J(\boldsymbol{U}^i, \boldsymbol{V}^i, \boldsymbol{\theta}^i) < J(\boldsymbol{U}^i, \boldsymbol{V}^i, \boldsymbol{\theta}^{i-1}). \tag{11}$$

Therefore, the Picard iteration is shown to give a local minimum solution. Unfortunately, in the presented approach the update of the parameter vector $\boldsymbol{\theta}$ is computationally very expensive and the solution is extremely dependent upon the initial vales of the calculated parameters. Figure 5 shows the result of fuzzy segmentation applied to find cell nuclei with random initialization of ellipse parameters. It can be observed that the optimization procedure very often leads to the detection of spurious cell nuclei corresponding to the local minimum of the objective function.

The next section tackles the presented problems and finally solves them by applying some modifications to the segmentation procedure presented in this section.

3   Cell Nuclei Segmentation

The fuzzy segmentation method presented in the previous section is able to differentiate the objects with different colors, but what is more significant in the case considered it is also designed to differentiate objects with the same color but located in different regions of the image. Such a feature of the algorithm is very useful in the segmentation of cell nuclei. Unfortunately, the original FCMS algorithm [7, 13] has a few drawbacks and limitations when applied to the segmentation of cell nuclei. The main problem arises from the fact that the algorithm is able to find only two clusters, the first one corresponding to the object with an elliptic shape and the second one corresponding to the rest of the image, while it is required to discover as much as possible of cell nuclei in order to make reliable diagnosis based on cell nuclei parameters.

In Section 2 it was mentioned that the FCMS algorithm is computationally very expensive due to gradient descent optimization applied to solve the parameters of the ellipse in each iteration of the whole FCMS procedure. Moreover, the results obtained using such a procedure are very problematic because the objects found are usually not cell nuclei but rather groups of cell nuclei or parts of cell nuclei (Fig. 5).

The mentioned limitations and drawbacks are weakened by changes proposed to the original approach. The first one is to divide the whole process of segmentation into two phases. The first phase is reduced to preprocessing the input image using the FCM algorithm in order to find the color of the cell nuclei and the color of the image background. The second phase is an iterative procedure applied to find cell nuclei in the preprocessed image. The developed modification arises from the observations that computing the parameters of the ellipse in each step of the FCMS algorithm is useless. While the matrices $\boldsymbol{U}$ and $\boldsymbol{V}$ do not represent precisely the proper clusters (cell nuclei and the background), the optimization procedure used to compute the parameters of the ellipse usually leads to finding spurious cell nuclei. Taking into account this fact, it was decided to solve the ellipse parameters optimization problem only once after the FCM algorithm has preprocessed the original image by minimizing (12). So, the modified segmentation procedure can be viewed

Fig. 3 Determining initial parameters for ellipses
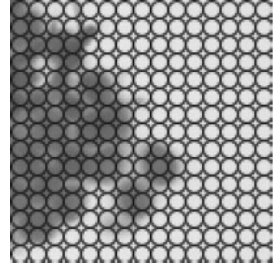
as minimizing the objective function (12) and afterwards minimizing the objective function (13) with respect to $\boldsymbol{\theta}$.

$$J_1(\boldsymbol{U},\boldsymbol{V}) = \sum_{x=1}^{X} \sum_{y=1}^{Y} \sum_{k=1}^{C} \left[\mu_{x,y,k}^{m} f_c(\boldsymbol{c}_{x,y}, \boldsymbol{v}_k) \right], \tag{12}$$

$$J_2(\boldsymbol{\theta}) = \sum_{x=1}^{X} \sum_{y=1}^{Y} \sum_{k=1}^{C} \left[\mu_{x,y,k}^{m} f_d(x,y,\boldsymbol{\theta},n_k) \right]. \tag{13}$$

It was observed during the experiments that the standard FCMS algorithm usually requires about 15 iterations to detect separate cell nuclei and the whole segmentation procedure must be repeated for each cell nuclei present in the image, so the introduced modification dramatically decreased the number of computations required to segment the image.

Unfortunately, the developed method does not solve all of the mentioned problems because, similarly like standard FCMS, it often gets stuck in an inappropriate minimum (Fig. 5). This problem arises from the fact that the parameters of the initial ellipse were generated randomly and the gradient descent method converges to the nearest local minimum. To overcome the problem, it was decided to limit the initial values of ellipses using knowledge about a typical size of the cell nuclei and the multi-start gradient method (Fig. 6). The method allows us to reduce false segmentation of cell nuclei; however, finally the best results was obtained using the Hough like transform to initialize the ellipse. Such an approach proposes systematic generation of a series of ellipses arranged in the form of grids covering the whole image (Fig. 3). Next, the objective function is calculated for each ellipse and the ellipse with the smallest value of the objective function (13) becomes a starting point for the gradient descent tuning procedure. Of course, such a procedure was time consuming, so in order to reduce the complexity, the grids of ellipses was sparse and the parameters w and h were limited by the knowledge about a typical size of the cell nuclei, the parameter ϕ was constant to simplify the exploration. The proposed initialization greatly improved the quality of the segmentation and accelerated the convergence of the gradient method. In order to reduce the number of steps required to reach the minimum by the gradient method even more, an adaptive learning rate was applied to control the level of parameter updates.

Fig. 4 Segmentation approach using FCM and the gradient descent method

Original image

FCM clustering in color space

Deleting nuclei from image

FCMS clustering

Segmented image
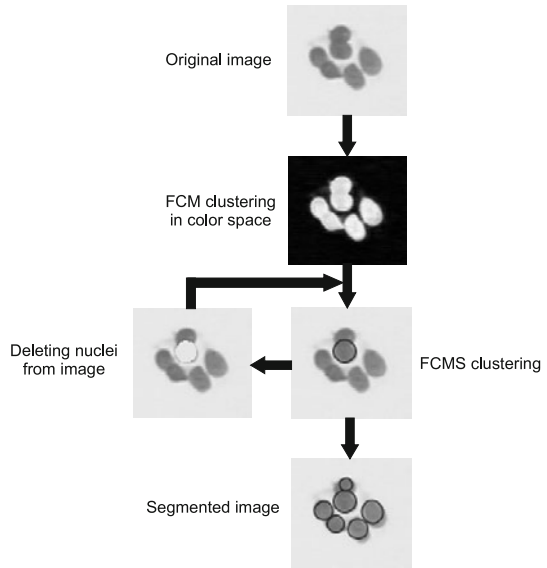
The scheme of the final version of the algorithm is presented in Fig. 4. It consists of three steps. In the first one, the original image is preprocessed by the FCM method to find the color of cell nuclei and the background. Next, the parameters of ellipses are initialized using the developed approach. Finally, the gradient method is used to tune the parameters of ellipses in the following iterations. The ellipse found a single algorithm iteration represents a single cell nucleus. In order to facilitate the searching procedure, cell nuclei already detected and described by the corresponding ellipse are erased from the original image by filling in the ellipses using the background color. The stop criteria for the gradient descent algorithm are defined in the form of a minimal value of objective function change and a maximum number of tuning steps. The stop criteria for global algorithm iterations are defined as the maximum number of ellipses found and the minimum objective function value (13). Choosing right values for stop criteria requires some kind of experience from the user. The next section presents some sample results of segmentation using the developed approach.

4 Experimental Results

Testing existing and newly developed algorithms requires to have databases at disposal, on which tests and benchmarks can be realized, especially in the domain of image analysis, where in many problems a domain knowledge needs to be taken into account. In our study we decided to design a new data set that could be applied to a completely automatic process of image analysis. The segmentation of cell nuclei was carried out on cytological material obtained by FNB. Biopsy without aspiration was performed under the control of ultrasonography with a needle of a diameter of

Table 1 Dataset

Feature	Value
Number of samples (malignant)	50 (25)
Number of images	500
Format of files	BMP
Resolution	704x578
Number of colors	256^3

0.5 mm. Smears from the material were fixed in spray fixative (Cellfix by Shandon) and dyed with hematoxylin and eosin (h+e). The time between the preparation of smears and their preserving in fixative never exceeded three seconds. The smears were derived from 25 FNB of benign and 25 of malignant lesions collected from 50 patients of the out-patient clinic ONKOMED in Zielona Góra . All cancers were histologically confirmed and all patients with benign disease were either biopsied or followed for a year. The image for digital analysis was generated by a SONY CCD IRIS color video camera mounted at top of AXIOPHOT microscope. The slides were projected into a camera with $10\times$ and $160\times$ objective and a $2.5\times$ ocular. One image was generated for $100\times$ enlargement and nine for $400\times$ enlargement.

Most of the criteria of malignancy are seen in the nuclei of the cells. Therefore, it is essential to isolate the nuclei from the rest of the image. It can be observed that malignant cells in contrast to normal and benign cells are characterized by irregular morphology that is reflected in several morphometric parameters. Morphometric measurements characterizing the shape and size have been mainly used for feature extraction. The extracted features are: size, circularity, perimeter, compactness, lengths of the axis of the ellipse circumscribing the nuclei and the eccentricity of the ellipse circumscribing the nuclei. Details about these features can be found in [14, 6, 9]. However, from previous research in the subject it is known that there are big differences in size between benign and malignant cases, and shape factors do not have good discriminative properties . Hence the proposed segmentation approach seems to be very promising in this case due to simplicity in calculating crucial features. In order to test the effectiveness of the proposed segmentation method, a set of 50 manually binary-segmented images was prepared. The result of automatic segmentation was compared to that of manual segmentation using the error measure based on the Hamming distance between manually segmented image and automatic segmented image. Since the developed segmentation method produces as a result of segmentation a set of ellipses, it was needed to convert ellipses which represent cells to a binary image by filling in the ellipses. The results of the comparison are summarized in Table 2, where EF stand for ellipse fitting phase. Following error measures were used to demonstrate the performance of segmentation:

$$E_{ave} = \sum_{i=1}^{N} \frac{e_i}{n_i N}, \qquad (14)$$

Table 2 Segmentation results

Segmentation method	E_{ave}	E_{max}	E_{min}
FCMS (RGB)	132	25670	29
FCM (RGB), EF with random init.	127	22198	32
FCM (HSV), EF with grid init.	78	17011	15
FCM (RGB), EF with grid init.	81	16210	14
FCM (RGB) clustering	102	14129	23
K-mean (RGB) clustering	125	16509	28

$$E_{min} = \min_{i=1...N} \frac{e_i}{n_i}, \tag{15}$$

$$E_{max} = \max_{i=1...N} \frac{e_i}{n_i}, \tag{16}$$

where e_i is a Hamming distance between the i-th manually segmented binary image and the i-th automatically segmented binary image, n_i is the number of cell nuclei in the i-th image and N is the number of test images. It must be noticed that although FCM and KM clustering achieved better segmentation results with respect to defined
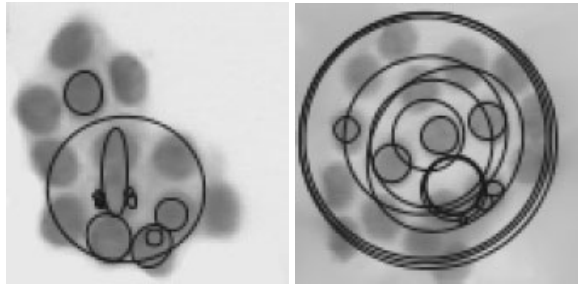
Fig. 5 Segmentation using standard FCMS
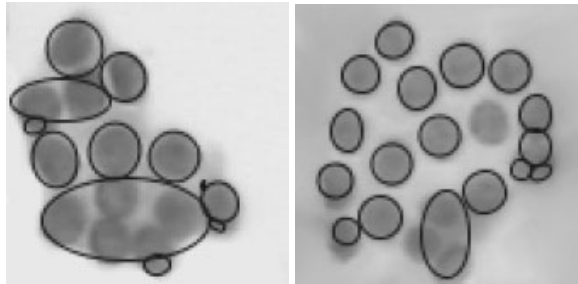
Fig. 6 Segmentation using FCM clustering and gradient descent with random initialization
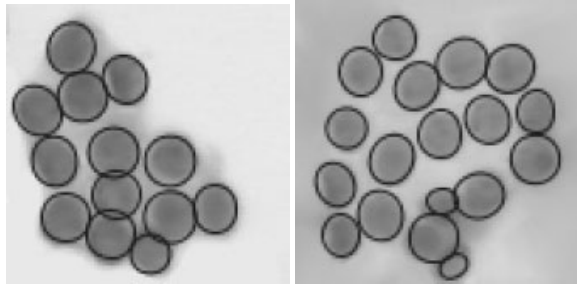
Fig. 7 Segmentation using FCM clustering and gradient descent with grid initialization

criteria than FCMS and two stage FCMS with random initialization, their usage is strongly limited due to the fact that they are not able to determine separated cell nucleus. In order to compare the segmentation results visually, some segmented parts of images are shown in Figs. 5, 6 and 7.

The software to realize the segmentation initially was prepared in the Matlab environment; unfortunately, time consuming computations make this software applicable to parts of the original images only. Hence the final version of the software was prepared in the Java environment using the Java Advanced Imaging (JAI) library. In order to accelerate the computations , the segmentation algorithm was written as a JAI operator and was prepared to work in a multi-threaded environment.

5 Conclusions

The work presents a cell nuclei segmentation method based on fuzzy-c means clustering with a shape function. The results achieved in the experiments seem to be very promising. The main advantage of the method is that the results of the segmentation can be directly used to calculate the morphometric parameters of the cells. Modifications proposed in the work to the original FCMS algorithm allow decreasing significantly the cost of computations. This achievement is very important due to the fact that nowadays colonoscopes are able to produce images with the resolution of 50000x50000 or even higher. Of course, the presented approach is not able to segment all cases properly so there are a few challenges for the near future. The first one concerns the segmentation of overlapped cell nuclei. The second one regards the adaptation of FCMS clustering to deal with more complex shapes. This will allow calculating parameters of cell nuclei more precisely, and possibly the algorithm can gain more general applications due to the ability to detect objects with different shapes [4, 16, 3]. However, it must be pointed out that the present accuracy of segmentation is so high that the future research will concentrate on the feature extraction and classification stages. The recognition rate in malignancy classification will be a true test for the quality and effectiveness of the developed segmentation method [15].

References

1. Babuska, R.: Fuzzy Modelling for Control. Kluwer, London (1998)
2. Bezdek, D.: Pattern Recognition with Fuzzy Objective Function Algorithms. Plennum Press, New York (1981)
3. Chatzis, S.P., Buhmann, T.A.: A fuzzy clustering approach toward hidden Markov random field models for enhanced spatially constrained image segmentation. IEEE Trans. on Fuzzy Systems 15(5), 1351–1361 (2008)
4. Gong, L., Pathak, S.D., Haynor, D.R., Cho, P.S., Kim, Y.: Parametric shape modelling using deformable superellipses for prostate segmentation. IEEE Trans. on Medical Imaging 22(3), 340–349 (2004)
5. Hrebień, M., Steć, P., Obuchowicz, A., Nieczkowski, T.: Segmentation of breast cancer fine needle biopsy cytological images. Int. J. Appl. Math. and Comp. Sci. 18(2), 159–170 (2008)
6. Jeleń, Ł., Fevens, T., Krzyżak, A.: Classification of breast cancer malignancy using cytological images of fine needle aspiration biopsies. Int. J. Appl. Math. and Comp. Sci. 18(1), 75–83 (2008)
7. Leung, S.-H., Wang, S.-L., Lau, W.-H.: Lip image segmentation using fuzzy clustering incorporating an elliptic shape function. IEEE Trans. on Image Processing 13(1), 51–62 (2004)
8. Liew, A.W., Leung, S.-H., Lau, W.-H.: Segmentation of Color Lip Images by Spatial Fuzzy Clustering. IEEE Trans. on Fuzzy Systems 11(4), 542–549 (2003)
9. Obuchowicz, A., Hrebień, M., Nieczkowski, T., Marciniak, A.: Computational intelligence techniques in image segmentation for cytopathology. In: Smoliński, T.G., Milanova, M.G., Hassanien, A.-E. (eds.) Computational intelligence in biomedicine and bioinformatics, pp. 169–199. Springer, Berlin (2008)
10. Suri, J.S., Setarehdan, K., Singh, S.: Advanced Algorithmic Approaches to Medical Image Segmentation. Springer, London (2002)
11. Underwood, J.C.E.: Introduction to Biopsy Interpretation and Surgical Pathology. Springer, London (1987)
12. Wang, S.-L., Lau, W.-H., Liew, A.W.C., Leung, S.-H.: Robust Lip Region Segmentation for Lip Images with Complex Background. Pattern Recognition 40(12), 3481–3491 (2007)
13. Wang, S.-L., Lau, W.-H., Leung, S.-H.: Automatic Lip Contour Extraction From Color Images. Pattern Recognition 37, 2375–2387 (2004)
14. Wolberg, W.-H., Street, W.-N., Mangasarian, O.-L.: Breast cytology diagnosis via digital image analysis. Analytical and Quantitative Cytology and Histology 15, 396–404 (1993)
15. Zhang, Y.J.: A Survey on evaluation methods for image segmentation. Pattern Recognition 29(8), 1335–1346 (1996)
16. Zoller, T., Varvarigou, T.A.: Robust image segmentation using resampling and shape constraints. IEEE Trans. on Pattern Analysis and Machine Intelligence 29(7), 1147–1164 (2007)

Model of Optical Sectioning by Using Structured Light in a Conventional Microscope

Jan Juszczyk

Abstract. Mathematical and physical principals of optical sectioning by using structured light in a conventional microscope are expanded. Assumptions and structure of a model of optical sectioning by using structured light are presented. The results of this model are discussed and compared with a reference method.

1 Introduction

Like computed tomography or magnetic resonance, microscopy is an important section of diagnostic imagining and research. Advanced and specialized techniques allow to show the specimen under a microscope more and more precisely. Marvin Minsky patented in 1955 the first confocal microscope. This microscope was the first one allowing the optical sectioning - a clear look into the specimen [1]. Confocal microscopy has become nowadays exceptionally well developed and popular [2]. This is the most important and the best, yet expensive, method of optical sectioning, therefore it is not available for many research centers. Neil, Juskaitis and Wilson published in 1997 a new simple method of optical sectioning by using structured light in a conventional microscope [4]. Since then only one manufacturer has constructed a device using this method [3, 6]. The method is based on projecting various patterns onto the object, where we would like to obtain optical sectioning. However, if we project the grid pattern only, the sectioned image will be unsettled by the view of this pattern. The sectioned image of a 3D structure, which is in the specimen, will be disordered and we will not be able to use it e.g to measure the structure size. In this method we need a three phase-modulated image of the same region to obtain optical sectioning. This method is not as good as confocal microscopy, but it

Jan Juszczyk
Silesian University of Technology, Akademicka 16 st., 44-100 Gliwice, Poland
e-mail: `jan.juszczyk@polsl.pl`

is the simplest and also permits obtaining a much better image than with a conventional wide-field microscope. We will try to approach this system by using a simple model.

2   Principals of the Method

We define a function of an optical system without pattern illumination

$$A(t_0, w_0, t, w) = \left| \iint h_1(t_0 + t_1, w_0 + w_1) \times \tau(t_1, w_1) h_2(t_1 + t, w_1 + w) dx_1, dx_2 \right|^2 , \tag{1}$$

where: h_1 and h_2 represent the amplitude point-spread functions of the two lenses and $\tau(t_1, w_1)$ is the amplitude transmittance of the object which we are imaging. Variables (t, w) are optical coordinates, defined as

$$(t, w) = \frac{2\pi}{\lambda}(x, y) n \sin \alpha \tag{2}$$

Where $n \sin \alpha$ is the numerical aperture (NA) and λ denotes the wavelength.
The mask is defined as

$$S(t_0, w_0) = 1 + m \cos(v t_0 + \phi_0), \tag{3}$$

where m is the modulation depth and ϕ_0 is the spatial phase. We can choose ϕ_0 arbitrarily. It is clear that the mask is dependent only on one variable. If we combine equations (1) and (3) we can write the image intensity as

$$I(t, w) = \iint S(t_0, w_0) A(t_0, w_0, t, w) dt_0, dw_0. \tag{4}$$

Explicitly substituting mask eq. (3) into eq. (4), we obtain

$$I(t, w) = \iint (1 + m \cos(v t_0 + \phi_0)) A(t_0, w_0, t, w) dt_0, dw_0. \tag{5}$$

Next, by simply modifying this equation, we will see that the image intensity consists of three parts

$$I(t, w) = \iint A(t_0, w_0, t, w) dt_0, dw_0 \tag{6}$$

$$+ m \cos \phi_0 \iint \cos(v t_0) A(t_0, w_0, t, w) dt_0, dw_0$$

$$+ m \sin \phi_0 \iint \sin(v t_0) A(t_0, w_0, t, w) dt_0, dw_0.$$

The first part is a conventional wide-field image, the second and third ones are images modulated by a grid pattern. Without the first part eq. (6) is an SSB modulated

(*Single Side Band*) signal, where $\cos(vt_0)$ and $\sin(vt_0)$ denote the phase shift [5]. We can write further

$$I = I_0 + m\cos(\phi_0)I_{mod} + m\sin(\phi_0)I^*_{mod}. \tag{7}$$

If we treat the image intensity I as an SSB signal, we can write the demodulation as

$$I_p = m\alpha\sqrt{I^2_{mod} + I^{*2}_{mod}}\,^1 \tag{8}$$

[8, 7] (where α is the parameter countering the modulation depth), yet only if we can rewrite the equation removing I_0. It is easy to show that

$$I_p = m\alpha\sqrt{I^2_{mod} + I^{*2}_{mod}} = m\sqrt{(I_1 - I_2)^2 + (I_1 - I_3)^2 + (I_2 - I_3)^2}, \tag{9}$$

with $\alpha = \frac{3\sqrt{2}}{2}$, where I_1, I_2, I_3 are image intensities I with the spatial phase $\phi_1 = 0, \phi_2 = \frac{2\pi}{3}, \phi_3 = \frac{4\pi}{3}$. It is important only for these spatial phases that the unwanted intensity I_0 be erased from eq. (7).

3 Model

We can reduce the optical setup to two lenses, if the modulated light will be transmitted through the specimen. In this setup only the space in the black rectangle in Fig. 1 is interesting for us. The intensity of illumination in the black rectangle is constant over time, unless the specimen is moving, for each $I_{1,2,3}$. The model computes 2D-table intensity of illumination in the space between two lenses for a selected w. We abandoned creating the 3D model, because the results would be a 4D-table, which would be difficult to represent and analyze. On the basis of the definition of the stationary system in [9] we can state that a system of optical sectioning is a stationary system. The model simulates the intensity of illumination in each point in the black rectangle. First we designed a table containing intensity of illumination for each point in the 2D space between two lenses (t, i) (Fig. 1) for one point source. We called it „peak". The integrated intensity of illumination has to be constant for each i.
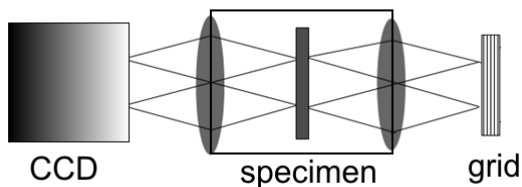
Fig. 1 Reduced optical set

---

[1] We can skip the module, because I is real and positively defined.

$$\int I(t,i)\,dt = \int C(i)\cdot(1+\cos(\omega(i)\cdot t))\,dt = D = const, \qquad (10)$$

where $\omega(i) = \frac{\pi}{i}$, the solution being

$$C(i) = \frac{D}{i} \qquad (11)$$

This condition stems from a simple assumption that the intensity of illumination farther from the source cannot be greater than the intensity closer to it. If D is constant, the ith optical set has the transmittance $\tau_{opt} = 1$, that means it is lossless.
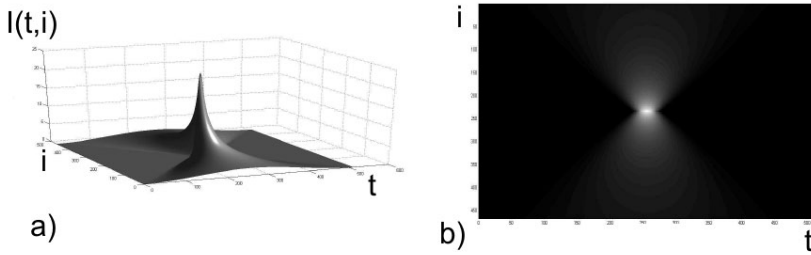
Fig. 2 The peak and the resolution of illumination intensity in a a) 3D visualization b) 2D visualization

The model consists of a table containing illumination intensities for each point in the 2D space between two lenses and it was built on the basis of a few simple assumptions:

1. Intensity of infocus illumination is given by eq. (3).
2. The model is built by adding single peaks. [2]. The resultant intensity of illumination is calculated by adding the intensity of illumination for all the peaks. We called this structure „mask".
3. The interaction between the specimen and the mask is modeled by multiplication.
4. The resultant image consists of the function

$$M(t) = \int I(t,i)\,di. \qquad (12)$$

We can split the mask (Fig. 3) into two parts: a homogeneous field outside the focus and a highly modulated infocus space. Only the center field is useful for sectioning. On the brink artifacts appear and sectioning is impossible. In fact first part - *homogenous field* - is not really flat. We observe stripes and lines with descending amplitude in the outer direction of i. These stripes cause quality aggravation of the optical sectioning (Fig. 5).

---

[2] It is a correct assumption for „white", incoherent light.
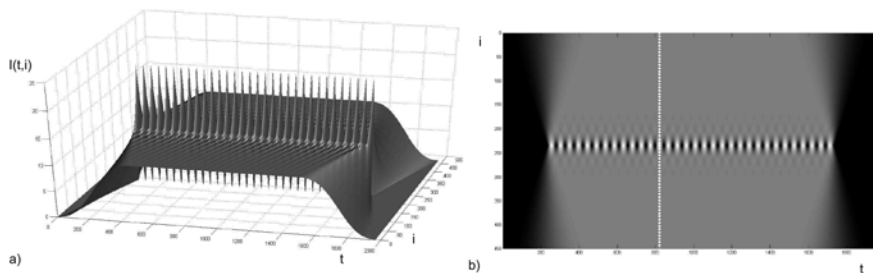
Fig. 3 The mask and resolution of illumination intensity in a a) 3D visualization b) table

4   Results

We present the results of image sectioning $M(t)$ as a thin image (Fig. 4d)), yet we can also show the full resolution of illumination intensity for all the 2D space (Fig. 4 b)). If we compare a sectioned image (Fig. 4 d)) with a classic image (Fig. 4 d)) the differences are obvious. In Fig. 4 c) we cannot determine how many object we can see, because their transmittances are similar and we can determine their shapes only. After the sectioning the image is sharper, because we see the *infocus* space with a small margin only. Most of the *homogeneous field* was damped, yet not all of it.

In Fig. 5 we see illumination intensity from the interaction of the specimen with the mask after the sectioning. Intensity of the *infocus* field is more than ten times greater than that of the field outside the focus, yet we observe the integrated
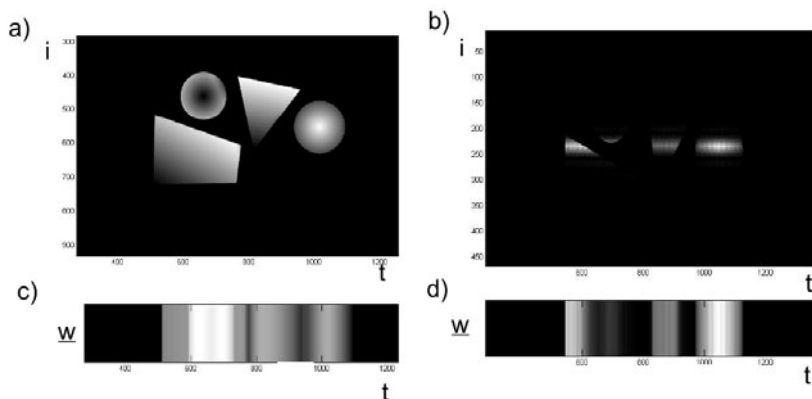
Fig. 4 Specimen, a) Table of intensity of illumination without sectioning, b) Table of intensity of illumination after sectioning, c) Real image of the specimen without sectioning, d) Real image of the specimen after sectioning
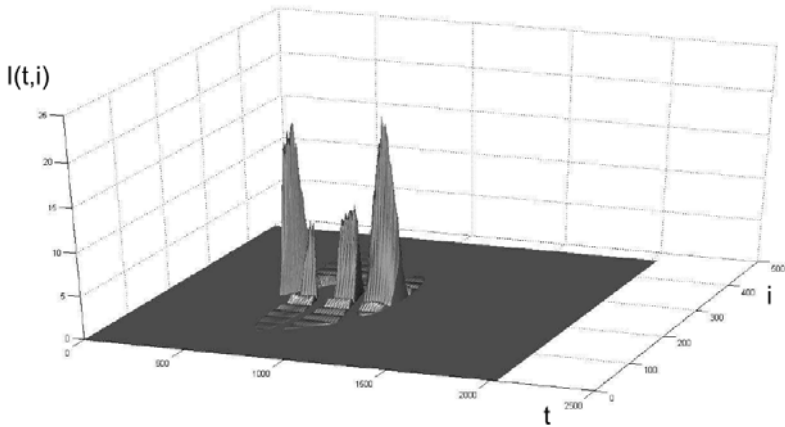
Fig. 5 Sectioning of one slice, intensity of illumination - 3D visualization

illumination intensity, therefore the effect of the field outside the focus can be greater and image sectioning will be worse. We should remember we cannot see the full field of illumination intensity. For this reason, in the algorithm implemented, the optical sectioning is based on modulated images $I_{1,2,3}$ of the specimen (Fig. 4 c)) and not on the full table of illumination intensity (Fig. 4 a) b)).

We can compare confocal microscopy to a situation with only one peak, where there is no modulation in the field *outside the focus*. The illumination intensity after sectioning is similar to the illumination intensity for the same slice without sectioning, so after sectioning we can make measurements of the specimen density.

We compared axial responses of the received illumination intensity with axial responses from [4] and [2], the results being similar (Fig. 6) and received illumination intensity ideal. It means that the axial responses symmetrical maximum has been achieved. It is not a real situation and there is no dispersion. The shape of the obtained curve is the same type as in [4] and [10].
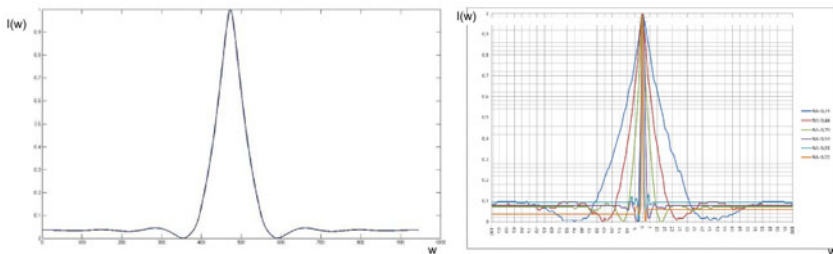
Fig. 6 Axial responses of the system
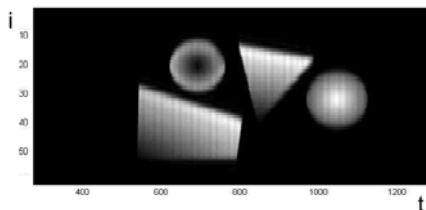
Fig. 7 Reconstruction of the specimen

Having sectioned all the slice of the specimen, we reconstructed a 2D (Fig. 7) image of the specimen and we compared it with the original specimen. The reconstruction has two types of artifacts, namely related with direction (i) and direction (t). The artifacts in direction (i) are related with the thickness of the sectioned slice. The thinnest possible slice depends on the NA and a greater gap does not have sense. As far as the second type of artifacts, related with the phase mismatch, is concerned we observed vertical stripes growing with the phase mismatch. During testing, we observed that the size of the grid pattern (related with v in eq. (3)) does not affect the vertical resolution. The vertical resolution depends only on the magnitude of optical system.

5 Conclusion

We simply explained the presented system of optical sectioning with signal analysis and we proved that algorithm (eq. 9) is correct. The effects of presented model show the resolution of illumination intensity in the 2D space between two lenses at each step of optical sectioning. We can explore the influence of changing the NA, which is the only parameter related with the optical system. That means this model is universal because it is not related with any special optical system. We can explore the effects of phase mismatch on the quality of optical sectioning and we proved that only for $\phi_1 = 0, \phi_2 = \frac{2\pi}{3}, \phi_3 = \frac{4\pi}{3}$ phases the optical sectioning is correct. We presented how the resultant image is created at each step of optical sectioning. We reconstructed the resolution of the specimen transmission analog and showed that is similar to the original one.

References

1. Minsky, M.: Double focussing stage scanning microscope (1955)
2. Semwogerere, D., Weeks, E.: Confocal microscopy. Encyclopedia of Biomaterials and Biomedical Engineering (2005), doi:10.1081/E-EBBE-120024153
3. Bauch, H., Schaffer, J.: Optical sections by means of stuctured illumination: background and application in fluorescene microscopy. Photonik International (2006)
4. Neil, M.A.A., Juskaitis, R., Wilson, T.: Method of obtaining optical sectioning by using structured light in a conventional microscope. Optics Letters 22(24) (1997)

5. Lathi, B.P.: Systemy telekomunikacyjne. Wydawnictwa Naukowo-Techniczne, Warszawa (1972)

6. Conchello, J.-A., Lichtman, J.W.: Optical Sectionin Microscopy. Nature Methods 2(12) (2005)

7. Wong, C.H., Chen, N.G., Sheppard, C.J.R.: Study on potential of structured illumination microscopy utilizing digital micromirror device for endoscopy purpose. IEEE, Los Alamitos (2006)

8. Papir, Z.: Podstawy Modulacji i detekcji Cz. I. Wydawnictwa AGH, Kraków (1992)

9. Wilk, I., Wilk, P.: Optyka fizyczna Cz. I, Politechnika Wrocławska (1995)

10. Török, P., Wilson, T.: Rigorous theory for axial resolution in confocal microscopes. Optics Communications 137 (1997)

Evaluation of Antibacterial Agents Activity

Igor Buzalewicz, Katarzyna Wysocka-Król,
Katarzyna Kowal, and Halina Podbielska

Abstract. The novel computer aided image processing analysis presented in this paper is used to evaluate the number of bacteria colonies. Proposed algorithm exploits the computer-aided calculations of optical transforms and it is implemented to the analysis of CCD recorded images of bacteria colonies. The diffraction patterns were approximated by the Fourier spectrum and additionally, the Mellin transform was applied to omit the problem of bacteria colonies sizes fluctuations. This approach exploits the properties of Fourier and Mellin transforms for scale and spatial locations invariant analysis. The significant correlation between parameters characterizing the Mellin spectrum and the number of bacteria colonies, was observed. Presented method was used for characterization of sterilization efficiency of antibacterial nanomaterials.

1 Introduction

The problem of bacterial infections is currently an important issue in many fields of life science, as well as in health safety and food protection. Generally, Quality of Life is in focus of many international and national initiatives. The continuously increasing bacteria resistance to commonly used antibacterial chemicals (antibiotics, sterilization agents etc.), is worldwide observed. Especially, antibiotics resistance is frequently discussed in the medical literature [3, 11, 15, 19]. For example, it was observed that the 50% of *Staphylococcus aureus* species isolated from leg ulcers were resistant to oxacillin and 36% of isolated bacteria *Pseudomonas aeruginosa* to ciprofloxacin [11]. Comparison of current antibiotics resistance profiles with data collected in 1992 revealed the increase of bacteria resistance to oxicillin and cipofloxacin in leg ulcers from 24% to 50% for *Staphylococcus aureus* and from

Igor Buzalewicz · Katarzyna Wysocka-Król · Katarzyna Kowal · Halina Podbielska
Wroclaw University of Technology, Institute of Biomedical Engineering and Instrumentation
Wybrzeże Wyspiańskiego 27, 50-370 Wrocław, Poland
e-mail: igor.buzalewicz@pwr.wroc.pl

9% to 24% for *Pseudomonas aeruginosa*, respectively. Moreover, the resistance to macrolide, linosamide and streptogramin antibiotics is observed, as well [19]. The National Institute of Allergy and Infectious Diseases - NIAID warns that over 70% of various bacteria species, most often causing hospital infections, are already completely resistant to at least one kind of antibiotics commonly used for treatment [15]. Simultaneously, NIAID points out a need to carry out studies towards novel techniques of bacteria characterization that can be applied in microbiological diagnosis. Therefore, the broad spectrum of currently performed research is focused on obtaining more effective antibiotics and various antibacterial agents. In standard microbiological procedures, the characterization of antibacterial efficiency of different agents is based on the determination of the number of bacteria colonies (so called bacteria colony forming units - CFU). However, in a routine microbiological examination, it is mostly performed manually, what is time-consuming and may affect the validity.

Some attempts were made to improve quality and efficiency of this process, whereas various semi-automated and automated algorithms have been proposed. Image processing techniques for microbiological examination may be exploited as well, since they provide a useful tool for improving the screening and analysis of the bacterial samples by eliminating observer bias and reducing the analysis time. Image recording may be realized by means of various optoelectronics systems; e.g. classical microscopes, confocal laser scanning microscopes, fluorescence microscopes, CCD cameras etc. and then, various image processing algorithms, are applied [6, 17, 18, 25]. These methods are widely used in a computer-assisted identification of bacteria species and characterization of susceptibility to antimicrobial agents [9]. Some attempts were made to use these techniques for bacteria identification. For example, tuberculosis bacteria were examined basing on the combined use of some invariant shape features along with a simple threshold operation on the chromatic channels [13]. *Methanospirillum hungatei* and *Methanosarcina mazei* were analyzed by means of pattern recognition and edge detection [12]. Computer aided image processing techniques are often exploited for counting the number of CFU, as well.

Various approaches and computer algorithms were applied to solve the problem of evaluation of bacteria colonies number. Digitized microscopic images of the yeast were analyzed using the watershed algorithm for cell number determination and a morphological edge detection for colony size evaluation [24]. Other approaches include PC-based techniques for the automated counting of digitized images of Petri dishes [22], a distance-transform techniques for the segmentation of monochromatic images of colonies grown on membrane filters [20] or more complex techniques, including detecting dish/plate regions, identifying colonies, separating aggregated colonies, and finally, their counting [29]. Moreover, some dyes are applied to increase bacteria colonies visibility and in a consequence to facilitate counting procedures [16].

The proposed method is based on image processing analysis by means of computer aided calculations of Fourier and Mellin spectra of bacteria colonies grown in Petri dishes. Recently published results demonstrated that the scattering patterns

of bacteria colonies may be exploited for identification of various bacteria species [4, 5, 23, 27]. The forward light scattering by bacteria colonies, generally associated with diffraction effects, exhibits some specific features suitable for bacteria species characterization in context of inverse scattering problem. Our approach exploits the correlation between the Fourier spectrum, which can be considered as far-field diffraction pattern (Fraunhofer pattern), and the amount of analyzed objects - bacteria colonies. In previously performed experiments, we demonstrated that it may be used to evaluate the efficiency of APDT (antimicrobial photodynamic therapy) against *Staphylococcus aureus* and *Escherichia coli* by means of Fourier spectra correlation [7]. However, validity of this analysis was limited to the samples, which contained bacteria colonies with the same size, since size fluctuations are significantly affecting the extraction of desired information from the Fourier spectrum.

Presented in this paper analysis is enhanced by the additional application of Mellin transform, which eliminates the influence of bacteria colonies size fluctuation on Fourier spectrum pattern. Combing the properties of Fourier and Mellin spectra for image processing analysis of bacteria colonies grown on solid nutrient medium, enables the realization of shift, scale and rotation invariant evaluation of bacteria colonies number. Although Mellin transform was already applied in microbiological studies, however, it was used to identify the Vibrio cholerae O1 bacteria by image correlation and it was based on a different computational algorithm [1, 2]. The novelty of our approach rely on the characterization of Fourier and Mellin spectra in order to retrieve an information about the efficiency of antibacterial activity against *Escherichia coli* of examined nanomaterials: Ag silica-based nanoparticles.

2 Theoretical Concepts of Proposed Image Processing Analysis of Bacteria Colonies

Previous theoretical consideration demonstrated that the Fourier spectrum $S(f_x, f_y)$, assumed as a magnitude of Fourier transform, is highly correlated with the number of objects with the same size and shape [8]. This relation can be expressed as follows

$$S(f_x, f_y) = |F_o(f_x, f_y)| [N + \mathrm{mod}(f_x, f_y)], \qquad (1)$$

where f_x, f_y are spatial frequencies, $|F_o(f_x, f_y)|$ is the Fourier spectrum of an one single object of the objects set, N is a modulation factor associated with the objects number n and $\mathrm{mod}(f_x, f_y)$ is correlated to the spatial configuration of objects. According to this notation, N is so-called modulation background corresponding to objects number n, however N is not linearly proportional to n. In the case of objects with same size, it is possible to analyze normalized Fourier spectrum:

$$S_{output}(f_x, f_y) = \frac{S(f_x, f_y)}{|F_o(f_x, f_y)|} = [N + \mathrm{mod}(f_x, f_y)] \qquad (2)$$

from which one may determine directly the modulation background as a constant component of $S_{output}(f_x, f_y)$, while the factor $mod(f_x, f_y)$ is an additional cosinusoidal modulation. Determination of modulation background value can be used to evaluate the unknown number of objects. However, if the random fluctuations of objects sizes appear, normalization of the Fourier spectrum in the described above manner leads to significant errors, which are affecting the correctness of the analysis, since the Fourier transform does not assure the scale invariant approach (see Fig. 1).

(a)   (b)
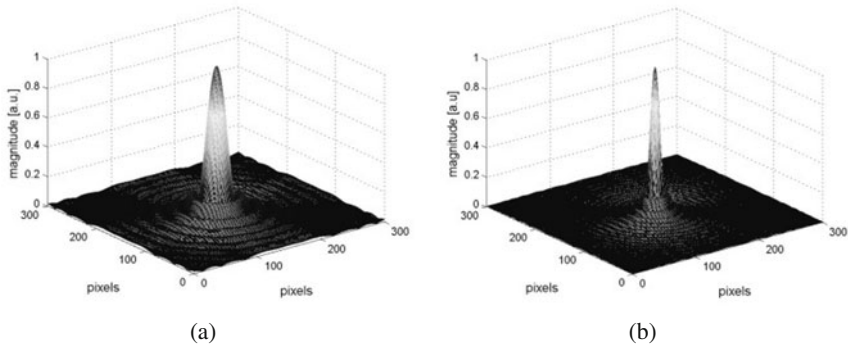
Fig. 1 Fourier spectra caused of circular apertures: (a) Fourier spectrum of the circular aperture with the radius of 7 pixels, (b) Fourier spectrum of the circular aperture with the radius of 14 pixels

Therefore, the Mellin transform, which is scale invariant, will be applied in further analysis [14]. In one-dimensional case, the Mellin transform of the function $g(\xi)$ can be described as:

$$M(s) = \int_0^\infty g(\xi)\xi^{s-1}d\xi \tag{3}$$

where in general, s is a complex variable. If the complex variable s is associated with imaginary axis $s = i2\pi f_x$, the Mellin transform is reduced to the Fourier transform by the substitution of variables: $\xi = e^{-x}$, what results in the following equation:

$$M(i2\pi f_x) = \int_{-\infty}^\infty g(e^{-x})e^{-i2\pi x f_x}dx \tag{4}$$

We see that the Mellin transform can be obtained from the Fourier transform of an exponentially stretched function. The Mellin transform is scale and rotation invariant, but it depends on the object localization. Therefore, the main advantage of the Fourier transform as shift invariance, is completely lost. To omit this problem, we proposed to combine the properties of Fourier and Mellin transforms. The algorithm

described in [10], will be exploited. The concept of our analysis is shown on Fig. 2. The core of the adapted algorithm is log-polar transformation, which reduces the two-dimensional Fourier spectrum scale changes in frequency domain caused by bacteria colonies size fluctuations, to one-dimensional change along radial coordinate.
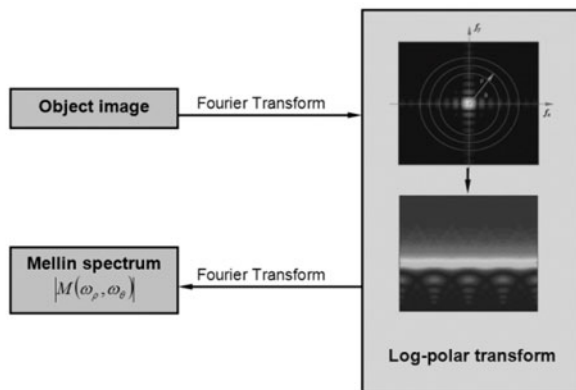
Fig. 2 Schema of the proposed algorithm

Therefore application of our image processing algorithm enables realization of position, scale and rotation invariant analysis. Presented approach was already numerically verified and the results of numerical simulations confirmed the high correlation between maximal values of the Mellin spectrum and the number of analyzed objects for various objects numbers, spatial configurations and sizes fluctuations [8].

3   Antibacterial Efficiency Evaluated by Means of Optical Transforms

The correlation between appropriate parameters characterizing the Mellin spectrum and the number of objects of the same shape, but with various sizes and spatial locations, justifies the application of proposed algorithm to the analysis of bacteria colonies samples for examination of antibacterial activity. Calculation of the number of bacteria colonies - CFU is a standard procedure in microbiology. Therefore, presented above method will be used to examine the interaction between bacteria cells and silica-based Ag nanomaterials. The antibacterial activity of Ag nanoparticles was already demonstrated [28].

3.1 Materials and Methods

The proposed above method will be used to evaluate the antibacterial activity of Ag doped silica nanospheres. The results will be compared with these obtained by manually counting of bacteria colonies.

The silica nanoparticles were prepared by modified Stöber synthesis, which comprises the base catalyzed hydrolysis of TEOS (Tetraethoxysilane) in water-ethanol mixture [26]. The silica nanoparticles were prepared by the successive addition of ethyl alcohol (95%, Polish Chemicals), ammonium water (25%, Polish Chemicals), hydrofluoric acid (35%, Polish Chemicals), TEOS (from Aldrich) at room temperature. Next, silica nanoparticles sediment was washed in methyl alcohol, and dried at 70°C for 24 hours. Tollen's method for silica silver doped nanospheres production. was applied [21]. As the result, colloidal solutions of Ag-doped SiO_2 nanoparticles, were produced.

The bacterial cultures of *Escherichia coli* were obtained from the microbiological laboratory of the Department of Epizootiology and Veterinary Administration with Clinic of Infectious Diseases of the Wroclaw University of Environmental and Life Science. Bacteria suspensions were incubated for 24 hours at the temperature of 37°C and then seeded on the MacConkey agar in Petri dishes. The samples were incubated for next 24 hours. Three various concentrations were tested: 0.25:1 (0.25 ml of colloid on 1 ml bacteria suspension), 0.5:1 and 1:1. As a control, the bacteria samples not treated by antimicrobial agent, were used. Additionally, some of the samples were irradiated for 4 minutes by the laser light (wavelength 410 nm, output power 50mW).

The images (768×768 pixels) of bacteria colonies samples were recorded by means of CCD camera (see Fig. 3). Then, the central part, corresponding to the circular shape of Petri dish, was extracted and Fourier transforms were calculated by means of FFT (Fast Fourier Transform) in the MatLab environment. The computer-aided analysis is schematically depicted on the Fig. 4.

(a)   (b)
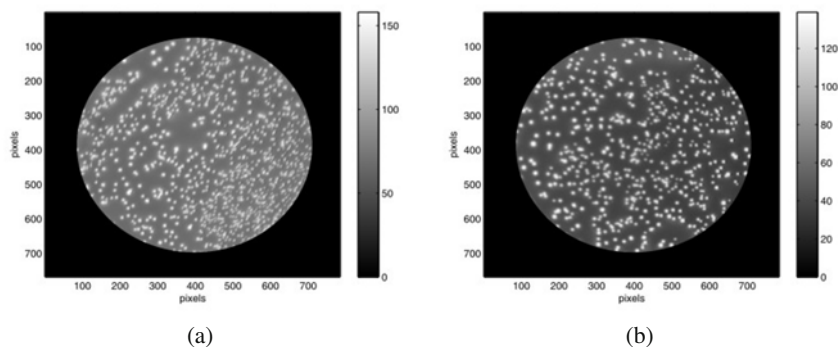
Fig. 3 Exemplary images of bacteria colonies treated by Ag doped nanomaterials in concentrations: (a) 0.25:1, (b) 0.5:1
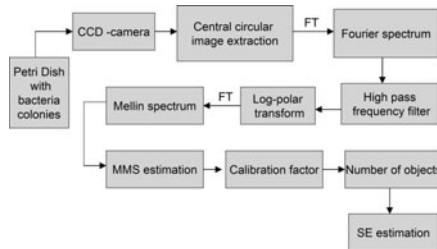
Fig. 4 Schematic representation of computer-aided bacteria colonies analysis (explanations in text)

The high frequencies pass filter (high-pass filter) was applied to eliminate zero-order maximum of the Fourier spectrum. Next, the log-polar transformation of modified Fourier spectrum was performed (see Fig. 5). Both, angular and logarithmic components of the radius were sampled by 768 points in the range from 0 to 360 degree and from $\ln\rho_{min}$ to $\ln\rho_{max}$, respectively. Number of sampling points was associated with the size of the input image of bacteria colonies.
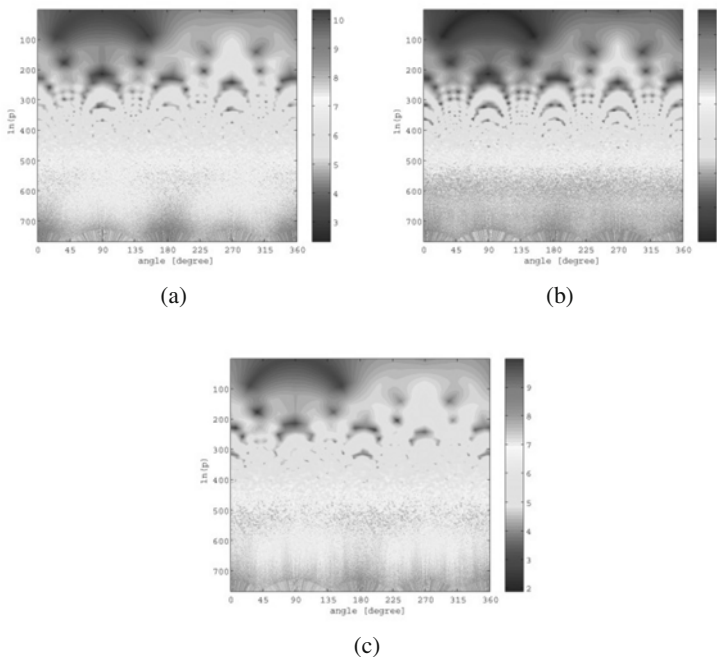
Fig. 5 Exemplary log-polar representations of Fourier spectra of bacteria colonies, where vertical axis represents natural logarithm of radial coordinate $\ln\rho$ and horizontal axis represents angular coordinate. Material concentration: (a) 0.25:1, (b) 0.5:1, (c) 1:1.

Table 1 Correlation (non-linear) between maximum value of Mellin spectrum (MMSsample) and amount of bacteria colonies (CFU)

Sample description antibacterial agent [ml]/bacteria suspension [ml]	Amount of CFU	MMS_{sample} $[\times 10^8 a.u.]$
treated with Ag-doped silica nanoparticles 0.25:1 non-irradiated	887	5.4
treated with Ag-doped silica nanoparticles 0.5:1 non-irradiated	664	5.2
treated with Ag-doped silica nanoparticles 1:1 non-irradiated	572	4.6
treated with Ag-doped silica nanoparticles 0.25:1 irradiated	519	4.52
treated with Ag-doped silica nanoparticles 0.5:1 irradiated	445	4.1
treated with Ag-doped silica nanoparticles 1:1 irradiated	295	2.9

In the last step, the Fourier transform calculation of log-polar modified spectrum, was performed. This transformation is an equivalent to the Mellin transform of the input bacteria colonies image. Obtained maxima of Mellin spectra, were further analyzed in order to evaluate the antibacterial efficiency. Basing on achieved results, which are presented in Table 1, the high correlation between parameter characterizing the Mellin spectrum - maximum value of Mellin spectrum (MMS) and the number of bacteria colonies was observed.

3.2 The Evaluation of Antibacterial Agents Activity

Let us to describe the sterilization efficiency in term of difference between the number of bacteria colonies in the control sample and in the antibacterial treated samples. In the case of manually counted bacteria colonies, the sterilization efficiency SE_{MC} is described by the following formula:

$$\text{SE}_{MC} = \frac{\text{CFU}_{control} - \text{CFU}_{sample}}{\text{CFU}_{control}} \cdot 100\% \tag{5}$$

where MC denotes: manually counted.

SE_{EV} is the sterilization efficiency, which was obtained from the analysis of Mellin spectra: maximum value of 2D Mellin spectrum of the control sample $\text{MMS}_{control}$ and treated sample MMS_{sample}. The sterilization efficiency SE_{EV} can be described as:

$$\text{SE}_{EV} = \left(\frac{\text{MMS}_{control} - \text{MMS}_{sample}}{\text{MMS}_{control}} \cdot 100\% \right) \cdot \text{CF} \tag{6}$$

Table 2 Sterilization efficiency

Sample number	Sample description antibacterial agent [ml]/bacteria suspension [ml]	SE_{EV} (%)	SE_{MC} (%)	$\|SE_{EV} - SE_{MC}\|$ (%)
1	treated with Ag-doped silica nanoparticles 1:1, irradiated	65.6	65.7	0.01
2	treated with Ag-doped silica nanoparticles 1:1, irradiated	62.4	61	1.6
3	treated with Ag-doped silica nanoparticles 0.5:1, irradiated	56	54	2
4	treated with Ag-doped silica nanoparticles 0.25:1, irradiated	44.9	43	1.9
5	control sample, non treated, no laser	0	0	0

where CF is a calibration factor, describing the correlation between MMS values and the number n of bacteria colonies: $n = f(MMS; CF)$. One has to remember that MMS values are not linearly proportional to n.

4 Conclusion

The Fourier spectrum of objects set with the same shape and size may be exploited for retrieving the information about objects number. If the objects in the input plane do not have the same sizes, such analysis cannot be performed. However, the log-polar transformation of initial Fourier spectrum and performance of an additional one-dimensional Fourier transform as an equivalent to the Mellin transform, assures the spatial orientation and scale invariance. Therefore, it may be applied to perform quantitative analysis of bacteria colonies number CFU. This algorithm, can be used for comparative evaluation of changes in bacteria colonies number due to antimicrobial materials. It was demonstrated that differences between the sterilization efficiency counted manually and obtained from Mellin spectra, are insignificant and they do not exceed 2%. Moreover presented method can be used for evaluation of the number of other biological objects with the same shape as for example cells in colloidal solution or on solid mediums based on pictures recorded by different microscopic techniques e.g. optical microscope or scanning electron microscope. Presented image processing method in significant way can improve counting process of cells by elimination of the manual procedures and reduction of the analysis time.

References

1. Alvarez-Borrego, J., Mouriño-Pérez, R., Cristóbal, G., Pech-Pacheco, J.: Invariant optical color correlation for recognition of Vibrio cholerae O1. In: Proceedings of International Conference on Pattern Recognition, vol. 2, p. 2283 (2000)
2. Alvarez-Borrego, J., Mouriño-Pérez, R., Cristóbal, G., Pech-Pacheco, J.: Invariant recognition of polychromatic image of Vibrio Cholerae O1. Optical Engineering 14(4), 827–833 (2002)
3. Amyes, S.G.B.: The rise in bacterial resistance. BMJ 320, 199–200 (2000)
4. Bae, E., Banada, P.P., Huff, K., Bhunia, A.K., Robinson, J.P., Hirleman, E.D.: Biophysical modeling of forward scattering from bacterial colonies using scalar diffraction theory. Applied Optics 46(7), 3639–3648 (2007)
5. Bae, F., Banada, P.P., Huff, K., Bhunia, A.K., Robinson, J.P., Hirleman, E.D.: Analysis of time - resolved scattering from macroscale bacterial colonies. J. of Biomedical Optics 13(1), 014010-1-8 (2008)
6. Bloem, J., Veninga, M., Shepherd, J.: Fully automatic determination of soil bacterium numbers, cell volumes, and frequencies of dividing cells by confocal laser scanning microscopy and image analysis. Appl. Environ. Microbiol. 61, 926–936 (1995)
7. Buzalewicz, I., Wieliczko, A., Podbielska, H.: Evaluation of antibacterial photodynamic activity by optical diffraction methods. In: Proceedings of the IX International Conference Symbiosis, pp. 63–65 (2008)
8. Buzalewicz, I., Wysocka, K., Podbielska, H.: Exploiting of optical transforms for bacteria evaluation in vitro. In: Proceedings of the SPIE, vol. 7371, pp. 73711H–73711H-6 (2009)
9. Cantón, R., Pérez-Vázquez, M., Oliver, A., Sánchez Del Saz, B., Gutiérrez, M.O., Martínez-Ferrer, M., Baquero, F.: Evaluation of the Wider System, a New Computer Assisted Image Processing Device for Bacterial Identification and Susceptibility Testing. Journal of Clinical Microbiology 38(4), 1339–1346 (2000)
10. Casasent, D., Psaltis, D.: Position, rotation and scale invariant optical correlation. Applied Optics 15(7), 1795–1799 (1976)
11. Colsky, A.S., Kirsner, R.S., Kerdel, F.A.: Analysis of antibiotic susceptibilities of skin wound flora in hospitalized dermatology patients: The crisis of antibiotic resistance has been come to the surface. Arch. Dermatol. 134, 1006–1009 (1998)
12. Dubuisson, M.P., Jain, A.K., Jain, M.K.: Segmentation and classification of bacterial culture images. Journal of Microbiological Methods 19(4), 279–295 (1994), doi:101016/0167-7012(94)90031-0
13. Forero, M.G., Sroubek, F., Cristóbal, G.: Identification of tuberculosis bacteria based on shape and color. Real Time Imaging 10(4), 251–262 (2004), doi:101016/jrti200405007
14. Goodman, J.W.: Introduction to Fourier Optics, 3rd edn. Robert & Company Publishers, Colorado (2005)
15. http://www.cdc.gov/drugresistance/actionplan/ 2007_report/ann_reptpdf
16. Hyo Kim, K., Yu, J., Nahm, M.H.: Efficiency of a pneumococcal opsonophagocytic killing assay improved by multiplexing and by coloring colonies. Clinical & Diagnostic Laboratory Immunology 10(4), 616–621 (2003)
17. Jansen, G.J., Wildeboer-Veloo, A.C., Tonk, R.H., Franks, A.H., Welling, G.W.: Development and validation of an automated, microscopy based method for enumeration of groups of intestinal bacteria. J. Microbiol. Methods 37, 215–221 (1999)

18. Kuehn, M., Hausner, M., Bungartz, H.J., Wagner, M., Wilderer, P.A., Wuertz, S.: Automated Confocal Laser Scanning Microscopy and Semi automated Image Processing for Analysis of Biofilms. Applied and Environmental Microbiology 64(11), 4115–4127 (1998)

19. Leclercq, R.P., Courvalin, P.: Bacterial resistance to macrolide, linosamide and streptogramin antibiotics by target modification. Antibacterial Agents and Chemotherapy 35(7), 1267–1272 (1991)

20. Mukherjee, D.P., Pal, A., Eswara Sarma, S., Dutta Majumder, D.: Bacterial colony counting using distance transform. International Journal of Bio Medical Computing 38(2), 131–140 (1997)

21. Peterson, M.S.M., Bouwman, J., Chen, A., Deutsch, M.: Inorganic metallodielectric materials fabricated using two single step methods based on the Tollen's process. J. Colloid and Interface Science 306, 41–49 (2007)

22. Putman, M., Burton, R., Nahm, M.H.: Simplified method to automatically count bacterial colony forming units. J. Immunol. Methods 302, 99–102 (2005)

23. Rajwa, B., Venkatapathi, M., Ragheb, K., Banada, P.P., Hirleman, E.D., Lary, T., Robinson, J.P.: Automated classification and recognition of bacterial particles in flow by multi angle scatter measurement and a support-vector machine classifier. Cytometry A 73A, 369–379 (2008)

24. Robinson, A., Sadr-kazemi, N., Dickason, G., Harrison, S.T.L.: Morphological characterization of yeast colonies growth on solid media using image processing. Biotechnology Techniques 12(10), 763–767 (1998)

25. Selinummi, J., Seppälä, J., Yli-Harja, O., Puhakka, J.A.: Software for quantification of labeled bacteria from digital microscope images by automated image analysis. BioTechniques 39(6), 859–862 (2005), doi:102144/000112018

26. Stöber, W., Fink, A., Bohn, E.: Controlled growth of monodisperse silica spheres in the micron size range. J. Colloid and Interface Science 26, 62–69 (1968)

27. Venkatapathi, M., Rajwa, B., Ragheb, K., Banada, P.P., Lary, T., Robinson, J.P., Hirleman, E.D.: High speed classification of individual bacterial cells using a model-based light scatter system and multivariate statistics. Applied Optics 47(5), 678–686 (2008)

28. Wysocka, K., Buzalewicz, I., Wieliczko, A., Kowal, K., Stręk, W., Podbielska, H.: Biomaterials with antibacterial activity. Engineering of Biomaterials 81-84, 117–119 (2008)

29. Zhang, C., Chen, W.H., Liu, W.L., Chen, C.B.: An Automated Bacterial Colony Counting System. In: IEEE International Conference on Sensor Networks, Ubiquitous and Trustworthy Computing (2008), doi: 101109/SUTC200850

Discrete Nonlinear Control of the Diagnostic Quality in Distributed Telemedical Systems

Piotr Augustyniak

Abstract. This paper addresses principles of discrete nonlinear control performed towards the diagnostic quality-based interpretive software optimization for cardiology-based monitoring system. Thanks to the pervasive access to wireless digital communication, distributed biosignal interpretation networks may not only optimally solve difficult medical cases, but also adapt the data acquisition, interpretation and transmission to the variable patient's status and availability of technical resources. The adaptation is based on the innovative use of results from the automatic ECG analysis to the seamless remote modification of the interpreting software. This paper focuses on the static properties and control accuracy and dynamic properties of the ECG processing optimization. It provides also details on the automatic scoring of the performance of ECG interpretation procedures. Testing of the prototype, despite its limited scale, yields significant quantitative benefits and improvement of diagnostic quality.

1 Introduction

The easy-to-use technical surrounding of a human, created mainly with the software, is in today's information society an often-referenced quality-of-life estimator. A prominent example is the remote surveillance and heart diagnostic, benefiting from wearable computers and wireless digital communication [9, 10]. Besides cardiovascular off-hospital patients [5, 7, 8], this technique concerns also seamless monitoring of vital signs from sportsmen, elderly people living on their own or members of military or civil services exposed to danger. Wearable recorders do not limit the everyday subject activity while the embedded intelligence simulates well the continuous assistance of medical experts.

Piotr Augustyniak

AGH University of Science and Technology, 30 Mickiewicza Ave. 30-059 Kraków Poland
e-mail: august@agh.edu.pl

Our approach postulates that the interpretation process is performed as a network-distributed computing task. Particular subtasks of the interpretation process are flexibly shared between the remote recorder and the central server and automatically controlled via bi-directional digital wireless transmission channel. The adaptivity of data interpretation and transmission is based on the quality of diagnostic parameters, continuously estimated in context of the patient's status by a procedure mimicking the human performance. The adaptation is modulated by several technical constraints.

An interesting issue is the discrete and non-uniform nature of the adaptation. In regular control systems, the control signal is linearly proportional to the error value accordingly to the feedback transmittance. In discrete systems, this proportion is modulated by discrete steps, usually having the uniform size. In the proposed system, the available procedures are attributed by their inherent performance and requirements factors and a linear response to the diagnostic error cannot be expected.

The remote adaptation of selected procedures for automatic interpretation of electrocardiogram has been recently proposed [2, 4] as a remedy for the unnecessary remote computing and data transmission. Besides the significant reduction of the datastream, the advantage of the method is a patient-oriented optimization of the processing, opening fields for improvement of diagnosis quality and patient's comfort. The economical aspect of the software flexibility-based approach also cannot be neglected, since the patient's units may be mass-produced as general-purpose biosignal recorders and their desired functionality may be remotely programmed upon request.

The non-uniform adaptation of the software is the main topic considered in this paper. Chapter 2 presents theoretical principles of the non-uniform control, chapter 3 reveals implementation details and chapter 4 includes test results and discussion.

2   Principles of Non-uniform Control

The remote adaptation of automatic ECG interpretation is driven by two sources:

- changes of the patient's status (objective - by diagnostic parameters values or subjective - by the event button), where existing interpretation setup is no longer optimal,
- changes of the environment including alteration of diagnostic goals, recording conditions or data transmission quality.

As in a regular control system, the processing error is compared to a reference which is a procedure running on the server and re-interpreting a selected ECG strip on a virtually unlimited platform. The value of difference in diagnostic parameters values plays the role of error signal and triggers actions towards alteration of the remote processing statements or code. The results of that action in the form of updated diagnostic parameters values are next evaluated with respect to two aspects:

- is the direction of changes appropriate to approach the reference values?
- is the amount of changes sufficient to meet diagnostic quality criteria?

The iterative and error-based nature of this adaptation justifies the control theory approach developed in following subsections.

2.1   Components of the Control Loopback

The idea of on-the-run software adaptation comes from the availability of different-grade procedures designed for the same computational purpose, but with different prerequisites for the resources requirements and result quality. Standardized data gateways enable the commutation between procedures while the interpretation is running, aiming at optimization of the remote interpretation process. Each subroutine is described by attributes of quality, resources requirements and external dependency, specifying its relations with other components in the signal interpretation tree. The optimization loopback is composed of three elements (see Fig. 1):

- error verification procedure, issuing the error vector of values proportional to divergence between actual and expected remote system output,
- adaptation management procedure, selecting in the repository the most appropriate executable code, corresponding to control signal,
- software transport and relinking mechanism, being the analogy of summation node.

Unlike in regular control systems, the control signal has a form of selectable software code characterized by inherent features not possible to be precisely defined. In the domains of particular features, the values corresponding to subsequent procedures are thus discrete and non-uniform, moreover, no intermediate values can be achieved.
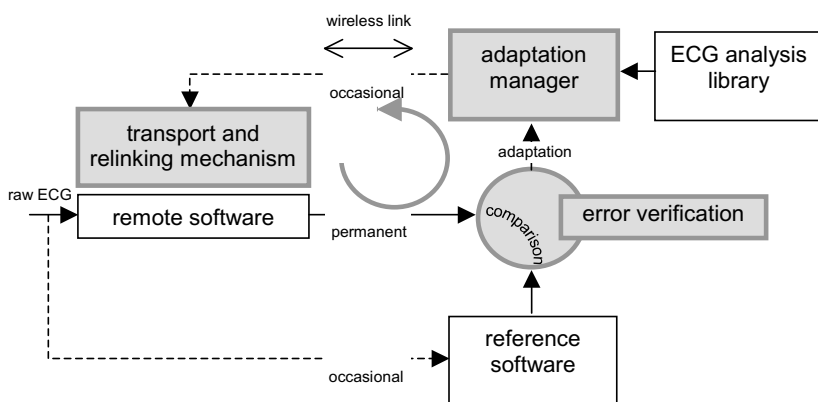
Fig. 1 Block diagram of the ECG processing optimization loopback

Table 1 Expert-derived individual thresholds of measurements and diagnostic result tolerance

parameters group	procedure example	relative accuracy threshold RAT [%]
1	heart rate	2
2	wave limits detection	5
3	morphology classification	10
4	QRS electrical axis reconstruction	20

The verification is performed occasionally in predefined time intervals, or is asynchronously triggered as a result of data consistency check or by external (e.g. patient-activated) events. It begins with sending a short strip (8s) of raw electrocardiogram from the recorder's buffer along with the results of remote interpretation. This signal is next re-interpreted by the server and the values received from the remote recorder are individually compared to this reference. Based on the guidelines for required calculation accuracy [11] are specific values of tolerance thresholds *RAT* (see tab. 1) applied to the individual evaluation of measurement parameters differences (1).

$$\Delta v_i = \frac{v_i^{meas} - v_i^{ref}}{v_i^{ref}} \tag{1}$$

Excessive dissimilarity values trigger the decision on the automatic modification of the remote recorder interpretation software. Besides the diagnostic parameter-specific measure, we use also a global estimate of diagnostic quality. It is issued automatically by the server and used to assess the efficiency of the remote ECG interpretation. The disease-dependent global dissimilarity measure *DSm* (2) uses differences Δv_i between respective values of measurement parameters *i* weighted by corresponding relevance value w_i derived from the pursuit of knowledge expressed involuntarily by the human expert during the ECG interpretation [3].

$$DSm = \sum_{i=1}^{I} \Delta v_i \cdot w_i \quad where \sum_{i=1}^{I} w_i = 1 \tag{2}$$

2.2   *Static Properties and Control Accuracy*

Besides technical constraints (e.g. limitation of available memory) limiting the procedures availability in specific conditions, the selection of the most appropriate replacement procedure is based on the values Δv_i of error vector and subroutine description. For each procedure, the requirements of resources, restricting the range of procedure replacements, are derived from the code analysis. This method, however, is not applicable to the evaluation of algorithm quality, nor to the prediction of expected interpretation improvement. We used the expert system to estimate the performance improvement based on analysis of the usage history and past

quality scores. Each procedure i is attributed by quality indicators AA_i and RA_i unified within the interpretation-oriented library, being a background of replacement decisions and improvement expectations. As the indicators are in fact experimental values, its non-uniform nature is intrinsic.

At a given time point the description of the commutable procedures may be considered as constant. For a given diagnostic parameter i (i.e. the one which value is found most outstanding from the reference), the *adaptation manager* expert system uses the corresponding series of $AA_i(c_m)$ where c_m is the identifier of m^{-th} $m \in M_i$ commutable procedure for the parameter i, as stepwise (i.e. discrete, with irregular steps) forecast of the absolute accuracy, determining the selection of replacing code. From the viewpoint of a particular diagnostic parameter, the commutable procedures are thus temporarily ordered by their quality expressed by the $AA_i(c_m)$ value. The *adaptation manager* uses this hierarchy to propose the software upgrade or downgrade, when necessary.

In case of sudden changes of the patient status or recording conditions, selection of the next better or next worse replacement procedure may not be optimal and result in an iterative, time consuming approach. This impacts the system response time for the possibly life-threaten events and requires longer storage of buffered raw ECG signal, particularly when data link quality is weak. Therefore in cases where diagnostic error suddenly exceeds the tolerance threshold, the radical change of interpreting software is alleged and the *adaptation manager* expert system uses the relative quality descriptors RA_i. For each diagnostic parameter i they are stored in a triangular matrix $RA_i(c_1, c_2)$ which facilitates the selection of a procedure better (or worse) than the current by an extent closest to the given factor.

The management of the commutable procedures aims at limiting the unsuccessful software replacement, however it should be considered that:

- the procedures hierarchy is history-dependent,
- the quality estimators are historical values with limited predictive value.

Therefore, the only reliable method for evaluation of the software optimization lies in repeated interpretation and validation of results quality. Asymptotic accuracy is the absolute value of diagnostic error st the time point when the transient-evoked software adaptation is completed. Assuming no other transient is present in the subsequent input signal, the asymptotic accuracy AAc for each parameter i is expressed as (3):

$$AAc_i = \lim_{t \to \infty} \left| v_i^{meas}(t) - v_i^{ref} \right| \qquad (3)$$

where $v_i^{meas}(t)$ is the subsequent measurement outcome and v_i^{ref} is the server-calculated reference value. Although the definition of the AAc is linear, it is valid also in the particular case of discrete non-uniform adaptation and with constraints on the number of modification attempts applied in our system. Taking the analogy from the theory of control, the software adaptation plays the role of a feedback correcting the diagnoses made automatically. If the software modification decisions are correct, the outcome altered by the interpreting software modification approaches to the true value, the modification request signal is removed in consequence of

decreasing error and the system is stable. Incorrect decisions lead to the growth of diagnostic outcome error and imply even stronger request for modification. The outcome value may stabilize on an incorrect value or swing the measurement range in response to subsequent modification attempts. In such case the system is unstable and the diagnostic outcome does not converge to the true value.

2.3 Automatic Scoring of the Procedure Performance

Without loosing the generality, we assume here that each interpretation procedure yields a unique main outcome, the accuracy of which determines the procedure performance. Although it is not always true in real applications, procedures can be decomposed to comply with this assumption. The quality indicators for procedures are continuously updated each time the procedure outcome is evaluated. Two scenarios yield new quality values:

- absolute accuracy AA_i calculated when regular re-interpretation is made in predefined time intervals, as averaged absolute difference between the remotely-calculated result and the server-issued reference (4); this value is used to determine whether the usage of the particular procedure as replacement is sufficient to yield a result fitting within the tolerance margins for a particular parameter,

$$AA_i = \frac{1}{N_i} \sum_{n=1}^{N_i} |\Delta v_{n,i}| \tag{4}$$

  where N is the length of the usage history set individually for each parameter i,
- relative accuracy $RA_i(c)$ calculated when the procedure replacement has been decided as ratio of desired improvement between the previously used and newly applied executable code (5); this value is calculated with respect to all commutable procedures C_i and used as an estimator of expected improvement and limits the number of necessary try-and-evaluate iterations.

$$\forall c_m \in \{c_1 \cdots c_M\} \ RA_i(c, c_m) = \frac{1}{N_i} \sum_{n=1}^{N_i} \left| \frac{\Delta v_{n,i}^c}{\Delta v_{n,i}^{c_m}} \right| \tag{5}$$

where c_m is the identifier of commutable procedure $m \in M_i$ and c is the identifier of procedure currently concerned as replacement

The list of procedure attributes (see Fig. 2) contains few static values (e.g. *processing $PR_{i,c}$* and *memory requirements $MR_{i,c}$*) filled in at the moment of code analysis and experimental quality indicators AA_i and RA_i varying with the time in context of patient needs. It is noteworthy here, that the notions of "better" or "worse" procedure became patient-relative and the processing adaptation in particular case is performed with regard to the patient's history.
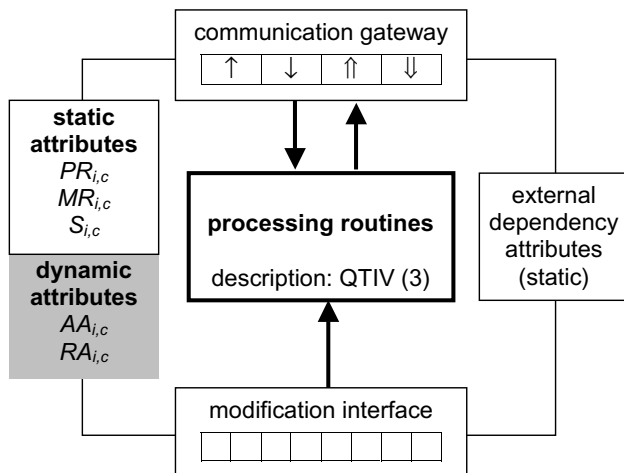
Fig. 2 Attributes of the commutable procedures

2.4 Dynamic Properties of the ECG Processing Optimization

In an early version of the prototype, due to the limitation of program memory write cycles, all libraries were permanently implemented in the recorder's ROM. The working version of the interpretation software was adaptively build up with use of the flags system selecting libraries to be linked. Different approach was selected in the last prototype with unlimited program memory write cycles. The agile software of the remote recorder consists of 9 facultative interpretive components. For each of them the working code can be selected by the management expert system from specialized library containing 2 to 5 mutually commutable subroutines precompiled for the remote platform. Selected procedures are downloaded from the server each time before linking. Although the adaptation using software upgrade needs considerable more time, the range of alternative procedures is not limited at the recorder's manufacturing stage. The volume of largest single procedure is 17kB, and the download time is 3,4s assuming the use of full bandwidth of the GPRS downlink (40 kbps). Memory requirements specified for each procedure in tab. 2 includes maximum declared memory amount for local variables and are significantly larger than the volume of executable code. The volume of the 8s signal strip is considerable (48kB), resulting in the upload time of 24s (GPRS uplink bandwidth 16 kbps). As a compromise between the control response time and additional occupation of the wireless channel, the redundant re-interpretation interval is set to four minutes (average data stream of 1kbps). The particular signal strip is sent once for the control or adaptation purpose, while alternative procedures may be replaced several times approaching the reference results in the remote recorder. For practical reasons,

Table 2 Inventory of interpreting procedures with respective CPU/memory requirements [%]/[kB]

procedure name	version number				
	1	2	3	4	5
heartbeat detector	7/25	8/32	10/38	15/42	16/48
heartbeat classifier	15/18	17/26	20/35		
wave delimitation procedure	35/22	65/26			
ST-segment assessment	10/10	12/17	13/25		
arrhythmia detector	5/7	8/10	13/12	19/15	
heart rate variability analyzer	30/25	51/38	68/44		
electrical axes calculator	7/8	27/21			
rhythm identification procedure	5/12	6/18	8/26		
QT-segment assessment	13/20	17/31	33/35		

however, the count of replacement iterations was limited to four per a single adaptation attempt.

This approach results in presence of an additional time factor delaying the adaptation of the remote software and justifying additional studies of dynamic behavior of the control loopback. The adaptation time depends on the size of the replacing executable code and can be roughly estimated from the indicator of link quality. Adaptation delay is defined by (6) as the time period from the transient occurrence t_0 to the moment t_D when the diagnostic outcome altered by the interpreting software modification starts falling into a given tolerance margin ε around its final value.

$$D = t_D - t_0 : \forall t > t_D \; v(t) \in (v(\infty) - \varepsilon, v(\infty) + \varepsilon) \tag{6}$$

The device status message describing basic technical conditions of the remote recorder, independently or within the diagnostic report, provides the estimate of wireless link quality. Together with the static procedure attribute *code size* $S_{i,c}$, this value is used to calculate the expected adaptation delay caused by the procedure code transmission. The delay exceeding a given threshold (e.g. in bad transmission conditions) inhibits the upgrade of interpreting software. In relation to the length of remote recorder raw signal buffer (64 s), this threshold is given to 30 s.

3   Experiments and Results

3.1   Prototype Details

The prototype remote recorder was based on a development kit of the PXA-270 CPU [12] running GNU/Linux operating system with the Aspect-500 (Aspel) ECG acquisition module (8 channels, 12 bits, 500 sps) and bi-directional GPRS connection [14]. The prototype server was based on a PC with Linux OS and the 100Mbps static IP Internet connection. The largest partition of the remote system memory

(512kB) is allocated for the raw ECG circular buffer of the capacity of 64 s. The second largest memory block is allocated for the variables and the executable code of the interpretive software. The prototype software provided options for selective disabling the adaptation.

3.2 Experimental Setup

In all the experiments we used 2751 artificially combined signals originating from 58 records of Common Standards for quantitative Electrocardiography (CSE) Multilead Database [13]. Cardiologists annotated the CSE records since the database does not directly disclose the pathology information. In each test signal the appearance of a single pathology was simulated by the concatenation of a record annotated as normal followed by a pathology-specific record. The count of samples was adjusted accordingly to the precedent RR interval in the vicinity of the border point. Also the baseline level of the subsequent record was corrected for each lead independently. Such test records simulate the abrupt cardiac changes and facilitate the technical analysis of the adaptive system behavior. A multi-channel arbitrary generator reproduced the analog signals of the total duration of 1-1.5 hour. Reference values of wave borders for the assessment of interpretation in the distributed system were calculated as the mean of CSE results.

3.3 Static Accuracy of the Processing Optimization

The test procedure was focused on the following aspects:

- Efficiency of the iterative software adaptation expressed by the required number of iterations,
- Convergence of the remotely computed diagnostic parameters to the server-computed reference values.

In case the remote software is modified in result of the data inconsistency, the iterative interpretation of the buffered ECG is repeated up to four times, until the values of the remotely calculated diagnostic results are out of the tolerance margins (see tab. 1). Main results of the test are presented in tab. 3. In the medical aspect, the correctness of the single attempt of software optimization was measured by the

Table 3 Results of remote diagnostic results convergence test after the consecutive steps of interpretation software modification

software modification steps	converging [%]	non-converging [%]
first	63.1	36.9
second	74.5	25.5
third	79.1	20.9
fourth	80.7	19.3

Table 4 Medical correctness of software adaptation

optimization type	diagnosis improvement	diagnosis degradation
software upgrade	643 (99,4%)	4 (0,6%)
software replacement	97 (80,2%)	24 (19,8%)

percentage of cases (tab. 4) for which in result of the software adaptation new diagnostic parameters approach to the reference values and reduce the *DSm* value (see 2). The calculation of *DSm* uses the relevance of diagnostic data and thus favorizes certain procedures over others.

The medical correctness of software replacement decisions summarized in the last row of table 4 is the quality estimator of the software management expert system. For over 80% of cases, the software replacement improved the diagnostic result.

3.4 Dynamic Properties and Temporal Convergence

The delay of messages varied from 1.3s (abnormal finding message of high priority) to 6s (regular report). The diagnostic data quality and the transmission delay were measured with respect to the procedures recommended by IEC [11]. Estimation of the longest adaptation delay was performed with use of the real wireless GPRS connection (tab. 5).

Table 5 Delay to the remote recorder adaptation

optimization type	longest delay [s]	average delay [s]	standard deviation
coefficients update (CU)	17.1	4.3	1.3
software upgrade (SU)	6.0	4.4	1.5
software replacement (SR)	5.9	4.5	1.5
server-side allotment (ST)	2.4	0.8	0.3

4 Discussion

Discrete nonlinear control of the diagnostic quality in distributed telemedical system was designed, prototyped and tested. The quality control is based on the disease-specific hierarchy of diagnostic parameters and on the hierarchy of commutable diagnostic procedures. Two principal quantitative benefits measured in the system are: reduction of digital communication costs (by 5.6 times on average) and extended autonomy time (by 65% on average), both being a result of avoiding the unnecessary computation and data transmission.

Test results show a considerable improvement on the diagnosis quality against the rigid software, however further analysis of outliers is required. The adaptive processing and transmission combine the advantages of two solutions being in use today (e.g. [1]):

- Load of the transmission channel is nearly as low as when the remote interpretation was used,
- Interpretation reliability is almost as high as in the centralized interpretation architectures with an occasional assistance from human expert.

Further considerable impact to the diagnostics quality comes from the use of content-dependent data format.

Future investigations are necessary for the compatibility of the interpretive software designed for different platforms (i.e. remote recorder and central server). Designing both variants based on identical rules affects the optimization of the server interpretation thread. Consequently, the processing chain of the server thread tends to mimic the design of its remote counterpart, losing the potential benefits of efficient hardware platform.

The selection of the replacing code is based on the value of parameter-specific error Δv_i and on the reported resources availability. If the replacing procedure sufficiently ameliorates the diagnostic result, further adaptation is not performed even if the availability of resources reported after the replacement allows for a higher-grade procedure.

Technical constraints are main source of inaccuracy of the ECG interpretation made by the software of wearable remote recorder. Such limitations are not present in a server-side application using virtually unlimited resources. Therefore the diagnostic result occasionally issued by the server is accurate enough to play the role of the reference in the assessment of remote interpretation quality (see 3). The resulting similarity-based estimate of recorder-side interpretation quality is issued automatically by the server and used to adapt the remote ECG interpretation. Nevertheless, other limitations of the automatic interpretation are intrinsic for an algorithmic approach, therefore the surveillance from a human expert is indispensable for the system reliability. The role of the expert is twofold: interpreting medically difficult cases and correcting the automatic adjustment of remote interpretation software.

The system behavior in presence of outliers and the raw signal noise needs more testing in clinical conditions (in parallel to currently approved systems). The influences of the noise and propagated processing errors on the subsequent interpretation stages highly depend on the quality of interpretive procedures. Another limitation influencing the experimental results comes from relying on manufacturer-specific software resources (from Aspel S.A.), and more sophisticated software collection will improve the noise immunity of the system.

References

1. Atoui, H., Telisson, D., Fayn, J., Rubel, P.: Ambient Intelligence and Pervasive Architecture Designed within the EPI-MEDICS Personal ECG Monitor. International Journal of Healthcare Information Systems and Informatics 3(4) (2008)
2. Augustyniak, P.: Content Adaptive Signal and Data in Pervasive Cardiac Monitoring. Computers in Cardiology 32, 825–828 (2005)
3. Augustyniak, P.: Exploring the knowledge of human expert beyond his willing expression. In: Pietka, E., Kawa, J. (eds.) Information technologies in biomedicine. AISC, vol. 47, pp. 3–14. Springer, Heidelberg (2008)
4. Augustyniak, P.: Strategies of Software Adaptation in Home Care Systems. In: Kurzynski, M., Wozniak, M. (eds.) Computer Recognition Systems 3, pp. 393–400. Springer, Heidelberg (2009)
5. Bousseljot, R., et al.: Telemetric ECG Diagnosis Follow-Up. Computers in Cardiology 30, 121–124 (2003)
6. Chen, X., Ho, C.T., Lim, E.T., Kyaw, T.Z.: Cellular Phone Based Online ECG Processing for Ambulatory and Continuous Detection. Computers in Cardiology 34, 653–656 (2007)
7. Chiarugi, F., et al.: Continuous ECG Monitoring in the Management of Pre-Hospital Health Emergencies. Computers in Cardiology 30, 205–208 (2003)
8. Fayn, J., et al.: Towards New Integrated Information and Communication Infrastructures in E-Health. Examples from Cardiology, Computers in Cardiology 30, 113–116 (2003)
9. González, R., Jiménez, D., Vargas, O.: WalkECG: A Mobile Cardiac Care Device. Computers in Cardiology 32, 371–374 (2005)
10. Gouaux, F., et al.: Ambient Intelligence and Pervasive Systems for the Monitoring of Citizens at Cardiac Risk: New Solutions from the EPI-MEDICS Project. Computers in Cardiology 29, 289–292 (2002)
11. IEC 60601-2-51. Medical electrical equipment: Particular requirements for the safety, including essential performance, of ambulatory electrocardiographic systems, First edition 2003-02, International Electrotechnical Commission, Geneva (2003)
12. http://www.toradex.com (visited on March 31, 2008)
13. Willems, J.L.: Common Standards for Quantitative Electrocardiography 10th CSE Progress Report. ACCO Publ., Leuven (1990)
14. Ziecik, P.: Mobile Development Platform for Wide Area ECG Monitoring System. In: Proc. of Biosignal 2008 Conference, paper 72 (2008)

Sleep Evaluation Device for Home-Care

Magdalena Smoleń, Klaudia Czopek, and Piotr Augustyniak

Abstract. The influence of sleep conditions to human health and performance is currently well known but still underestimated and monitoring devices are not widespread. This paper describes measurement methodology and prototype design of a home-care sleep scoring device. The proposed solution is oriented towards low-cost equipment and easy-to-use data capture using contactless recording as far as possible. Unlike the regular laboratory systems, the quality of sleep is estimated from the video-recorded subject motion, audio-recorded acoustic effects and from the single-lead electrocardiogram being the only electrical signal recorded from the body surface. The presented prototype is built of consumer-grade devices working in a short-distance network and providing multimodal data. The information provided from different modes are partly redundant, giving opportunity for refinement of the accuracy, and partly complementary, widening the aspect of sleep analysis.

1 Introduction

Sleep scoring belongs currently to the most innovative multimodal diagnostic methods, and is investigated by dozens of scientists all around the World. Since during the sleep all regulatory functions are under the sole control of the autonomous nervous system, sleep scoring benefits from the absence of voluntary behavior control from the subject under investigation. A probably sole but significant drawback of this method is the requirement of advanced recording equipment and analysis software deriving diagnostic data from the polysomnogram. Sleep laboratories require expensive infrastructure and well trained laboratory staff to provide reliable patient description.

Magdalena Smoleń · Klaudia Czopek · Piotr Augustyniak
AGH University of Science and Technology, 30 Mickiewicza Ave. 30-059 Kraków Poland
e-mail: m-smolen@wp.pl, klaudia.czopek@gmail.com, august@agh.edu.pl

The alternative approach postulates a common use of consumer-grade sleep scoring devices in order to draw general attention to routine control of sleep quality. The lack of consciousness during the sleep is not a justification for neglecting the conditions in which the average human spends a third of his lifetime. Despite bad sleeping is considered among most important factors of human health and performance during the day, a commercial device for everyday control of sleep quality at home is still not available.

The aim of our research presented in this paper is to design a multimodal measurement infrastructure and analysis methods providing everyday information about the sleep quality integrated into a single coefficient. Such parameter is expected to be correlated with precedent activity (e.g. stress, alcohol intake, dormitory airing etc.) or with the subsequent day performance or feelings. The readings may be performed every morning by the subject himself or his relatives and the conclusion is expected to indicate simple means to take or events to avoid in order to improve the comfort during the night and consequently the overall feeling of living quality.

2   Measurement Modalities and Methods

The scoring of sleep and sleep-related events was developed by six task forces reviewing evidence for the scoring manual [5]. This worldwide standard, as well as other research programmes on the sleep [3] use the polysomnogram as a reliable and complete source of multimodal medical information about the patient behavior. Since the adaptation of the complete sleep scoring measurements to home care conditions is hardly feasible, the intended surveillance system has to be limited to a subset of recommended parameters. The measurements performed in polysomnography were then scored accordingly to the costs and feasibility in home care conditions:

- cost and availability of equipment,
- susceptibility for errors if operated by untrained persons (subject's relatives or the subject himself/herself),
- availability of complementary outcomes,
- automated data interpretation and integration.

These reasons led us to reduce the electrophysiological measurements, in particular the EEG and EMG, being the background of a standard polysomnography. The only direct recording we kept is the ECG, due to its lowest vulnerability to distortion and to rich informative values. The ECG signals is used to derive the respiratory wave and the pattern of heart rate variability (HRV) typical to autonomous nervous system control during the sleep. Two other measurements are:

- video-based motion estimation, which can be partly correlated with HRV,
- acoustic effects-based snore detection, which can be partly correlated with respiratory wave.

A noteworthy advantage of these methods in everyday use is no body contact requirement, the instrumentation may thus be implemented in the infrastructure of subject's house.

2.1 Analysis of Heart Rate Variability

The response of the human cardiovascular system to variations of subject's status reflects well fast changes in subject's behavior. During the sleep, the voluntary control is suppressed and the heart rate variability is solely controlled by the autonomous nervous system. During the sleep both the short-time and long-time variability indexes are low, unless the subject suffers from neurological syndromes. Long-term variability remains stable during all the sleep, whereas short-term variability may increase depending on subject's motion, respiratory obstructions or during the REM phase. Although sleep staging is not the aim of the analysis, the influence of sleep phases is noticeable in the tachogram (Fig. 1). Many other aspects of the subject's
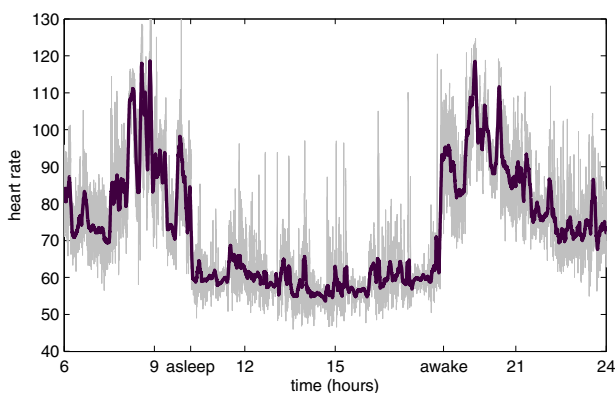
Fig. 1 Example of overnight tachogram

health status during the sleep were recently investigated by Maier [10] and Guzik [4]. It is noteworthy that the HRV-based estimation of the subject's status involves a considerable delay, thus requires support from other methods in detection of sudden status changes.

The aim of a second analysis performed on the ECG signal is derivation of the respiratory wave (also called: *Electrocardiogram-Derived Respiratory*, EDR). Three general processing methods can be distinguished corresponding to the physical measurement principle [6]:

- differences in heart axis direction depending on variation of the heart position,
- differences in R-wave amplitude representing variable electrical properties of the thorax,
- differences in RR intervals caused by common autonomous control of both: respiration and heart rate, known as respiratory arrhythmia

The assumed recording simplicity and consequently the use of a single ECG recording channel limits the EDR processing options to the latter two methods and, as
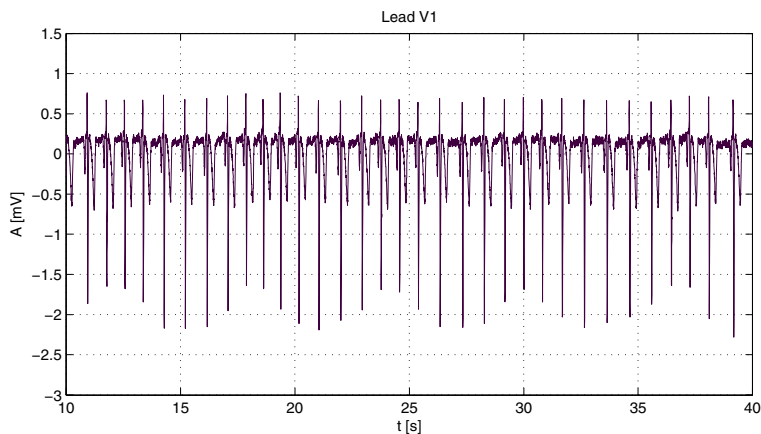
Fig. 2 Single-lead rest electrocardiogram with amplitude and interval respiratory-related effects

described in [6], their combination yields the most reliable result. The sample single-lead rest electrocardiogram with both amplitude and interval respiratory-related effects is presented in Fig. 2.

2.2 Analysis of Subject's Motion

Quantity assessment of the human body motion occurred during nightlong sleep provide supplementary information useful in a sleep quality evaluation [16]. The movement activity estimation enables success performance of the differentiation between awake and sleep stage. It is possible thanks to distinct some feature of the motion during these states. While subject is in an awake condition his or her movements patterns occur frequently, are relatively irregular and their temporal and spatial intensity achieves a greater value. Exact motion episode is taken into account in quantitative activity level while its time duration is longer than dozens seconds. Researchers in most studies assume 30 seconds period. Video sleep analysis could incorporate information not only about general volume of movement activity, but also data of precise recognition of the type and direction of motion as well as change of body postures.

Significant body motion during sleep could be a visible sequence and symptom of different sleep related disorders [14]. Parasomnias constitute a great deal of sleep disorders diagnosed in occurrence of some particular symptoms or behavior, probably because of partial awakening during sleep. Over twenty parasomnias are distinguished in the International Classification of Sleep Disorders (ICSD). The disorders occurred in children, limited to single episodes of anxiety during a night or talking during sleep should not be a cause of fear and does not necessitate any special

diagnostic proceeding. However in case of parasomnia appearance in adults requires reliable analysis, which is significant factor of avoiding serious health problems.

Due to a close relation between several sleep disorders and motion activity during sleep, analysis of subject's motion is investigated in long-term monitoring, recognitions of early symptoms of illnesses and treatments results valuation. Obviously motion activity is not an universal marker of any sleep disturbance. For instance insomnia in its initial stage does not show any type of body movements [13]. In this case earlier mentioned ECG device is a proper sensor for accurate investigations.

2.3   Analysis of Acoustic Effects

Snoring is a common sleep disorder which affects people of all ages, although it is most frequent for men and overweight people. From adults who snore occasionally about twenty five percent are habitual snores. These two kinds of snoring could have different influence on quality rest during sleep: usually an occasional snorer has good sleep and rest but a habitual snorer is often tired after all night sleep and does not have good quality rest.

Snoring is a common sleep disorder that affects people of all ages, although it is most frequent for men and overweight people. Among adults who snore occasionally about twenty five percent are habitual snores. These two kinds of snoring could have different influence on quality rest during sleep: usually an occasional snorer has good sleep and rest but a habitual snorer is often tired after all night sleep and does not have good quality rest.

Medical support is needed for subjects who snore to get a good night's sleep. This prospective study is aimed to show how sleep disorders influence a good night sleep. Acoustic characteristics of snoring sounds, which are approximately periodic waves with noise, can be analyzed by using a multidimensional voice program e.g. MDVP. Multiple protocols of MDVP can show differences between markers used in an automatic analysis e.g. peak frequency, soft phonation index (SPI), noise to harmonics ratio (NHR), and power ratio. Measurement results compared with norms are shown on polar diagrams that are very easy to interpret. At the same time snoring sounds were analyzed using the short-time Fourier transform (STFT) to determine the frequency and content of local sections of the samples [17].

Acoustic analysis techniques give information on the mechanism, loudness and intensity. Waveforms of snoring events over a period of 60s were analyzed. Depending on the snorer, there are from ten to fifteen respiratory cycles. The subjects have very regular respiratory cycles, unlike typical snoring patients. The frequency domain provides most important information from snoring sounds, enabling power analysis and three-dimensional graphs of energy-frequency-time, as evident in figures 3. The averaged spectrum shape of snoring event is represented with frequencies (Hz) of its formants. Different conditions in which subjects and patients snore can affect formants range. Examining snoring sound signal during sleep, energy was mainly concentrated in low frequencies, below 6000Hz. The main components lie in the low frequency range, at about 130Hz. The pathological signal
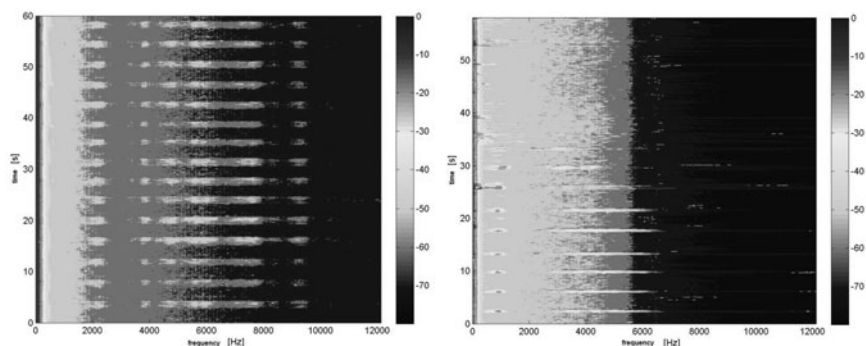
Fig. 3 left: STFT of a normal signal, right: STFT of an abnormal signal

presents weak formants, while the normal signal has more periodicity in low frequencies, and introduces stronger formants. Calculated vectors of characteristics of the abnormal sound were quantitatively compared with normal sound, which allowed drawing conclusions from available data. The most important parameters were the fundamental frequency, moments M0-M2 and formants. The pathological importance of snoring has been related to its intensity (dB), maximal and mean intensity, number of breathing per minute of sleep, snoring frequency and formants structure. As can be seen in Table 1, the mean energy is significantly higher for habitual snorers, when compared to occasional snorers.

Using the multidimensional voice program MDVP many parameters that are necessary to estimate sleep quality can be extracted, with the most useful information among them coming from the soft phonation index (SPI), noise to harmonics ratio

Table 1 Acoustic parameters of snoring sound

	Occasional snorer	Habitual snorer	Reference subject
Minimum Energy (dB)	44.92	47.20	45.56
Maximum Energy (dB)	61.02	58.67	47.88
Mean Energy (dB)	48.64	57.47	46.66
Standard Deviation (dB)	1.45	1.95	0.29
Median Energy (dB)	48.57	57.83	46.68
number of snorers/minute	7.00	10.00	0.00
number of breathing/minute	15.00	10.00	15.00
M0	426.00	2620.00	427.00
M1	44.00	72.00	44.00
M2	2939.35	6267.81	3149.44
F1	127.00	125.00	127.00
F2	2499.00	1249.00	1499.00
F3	2748.00	1874.00	2374.00
F4	3123.00	2998.00	2748.00

Table 2 Parameters vF0, SPI, NHR for habitual snorer (male)

parameters	norm(m)	STD(m)	meas.1	meas. 2	meas. 3	meas. 4	meas. 5
vF0 [%]	0,94	0,43	68,7	45,3	43,3	8,02	43,3
SPI	6,77	3,78	7,49	6,37	2,56	0,63	5,09
NHR	0,12	0,01	3,55	1,54	2,89	2,79	3,79

(NHR) and fundamental frequency variation (vF0). Table 2 shows how a snorer sound is different from normal sleep sound.

3 System Design

Considerations given in previous chapter led us to sketch the approach of the infrastructure of the home-care system for sleep scoring (Fig. 4). This system, except for the personal recorder is built of commercially available computer and peripherals. Thanks to the use of wireless connection, the subject's motion is unconstrained and the measurement device having direct electrical contact to the subject is isolated from others mains-operated system components. The measurement of time-domain
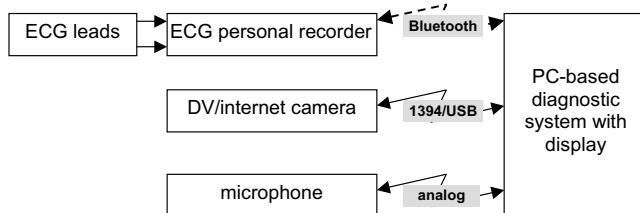
Fig. 4 Block diagram of the home care sleep scoring system

variability of the sinus node requires acquisition of a single-lead electrocardiogram. We used two disposable chest electrodes corresponding to V1 and V2 leads in bipolar mode connected to the personal recorder. This custom-built device performs real-time filter-based beat detection [7] and shape-based classification. The output datastream lying of RR intervals, corresponding R-wave amplitudes, and beat types is then transmitted to the acquisition center via short-range wireless link (Bluetooth). The missing RR intervals were interpolated by a successive procedure minimizing their short-term variability, accordingly to the guidelines in [15]. The square root of the mean squared differences of successive NN intervals (RMSSD) and the standard deviation of the average NN interval calculated over five minutes periods (SDANN) were selected from basic time-domain heart rate variability (HRV) parameters Malik [11] as representing short-time and long-time variability respectively.
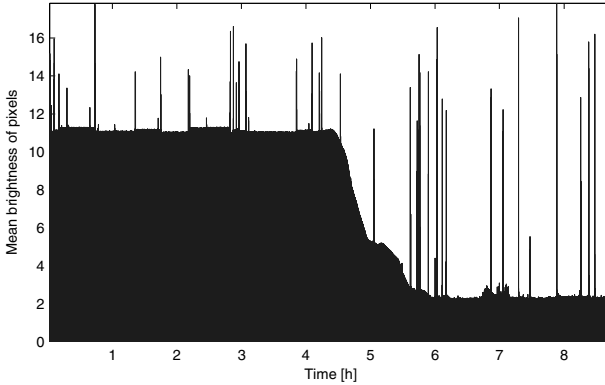
Fig. 5 General evaluation of example motion during nightlong sleep - mean brightness in dependence of sleep time

For the motion monitoring, we use black/white CCD (Charge Coupled Device) camera and additional set of nine infrared diodes placed below the camera. This kind of illuminators placement instead of location directly over the subject bed, makes possible to avoid creating non-uniformities reflected in overexposure in the center. Dependent on the room arrangement, camera could be located either in parallel either perpendicularly to the longer dim of the bed. Although the best signal to noise ratio and wider analyzed surface are obtained when a camera is put in parallel.

Basic evaluation of the general motion of the human body bases on each 250^{-th} video frame which corresponds to 10 sec. time interval. The absolute value of the difference only between those chosen frames is performed [8]. The image resolution is 720 pixels wide and 576 pixels high. From each of obtained difference images all pixels mean brightness is accumulated. Fig. 5 presents an example of mean brightness in dependence of sleep time. All sharp peaks emerging from the background noise refer to episodes with motion of the subject. To estimate the level of movements activity during nightlong sleep, noise level variations should be taken into consideration by referencing the value of proper peak with the level of noise at that time. Observed distinction between the value of noise in different time epochs stems from the different lightning during sleep (night/dawn). This first step of estimation led us to assign the threshold of noise which constrains no motion background as well. In more detailed analyses that way of activity level assessment could be over-estimated. Therefore the percentage of pixels with earlier obtained overthreshold brightness is calculated for every frame of the video recording. Fig. 6 contains a comparison diagram of pixel mean brightness and the percentage of pixels scaled to the level of the noise. The movements of different segments of the body reveal also distinct differential images pattern. Fig. 7 presents an overhead assessment of the selected common motions of the human body. Three first peaks refer to the motion during whole body posture change from one-side to another. Two next peaks
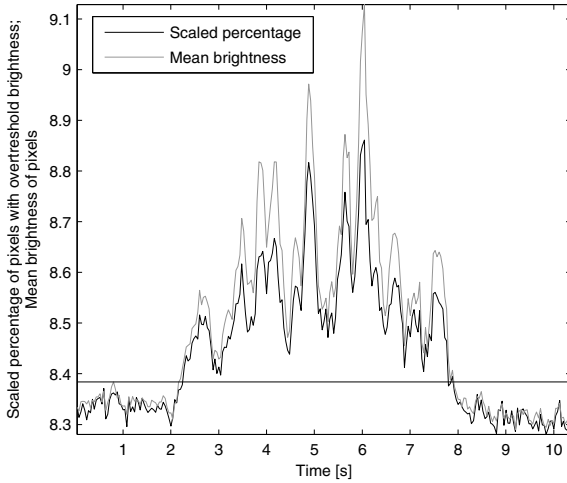
Fig. 6 Comparison of pixel mean brightness and percent of pixels scaled to the level of the noise
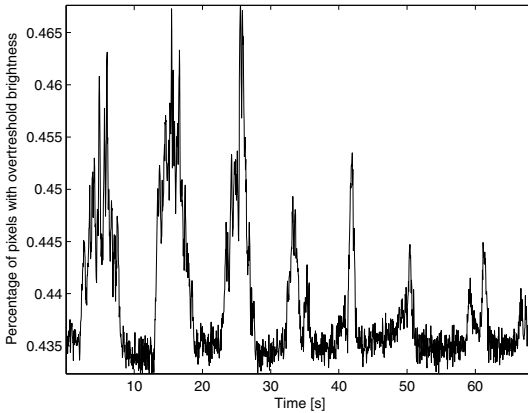
Fig. 7 General evaluation of example motion extracted from the difference of the consecutive video frames

are responsible for lower limbs movements and others correspond to upper limbs motion.

Measurement of the acoustic snoring signal is very easily performed using a microphone to record the signal in *Cool Edit Pro* with the sample rate set to 44100 Hz which is realistic enough to fool the human ear. Afterwards we analyze the signal using available equipment e.g. MDVP. Utilization of acoustic methods yields research results in a straightforward, graphical way. Proposed method of support for

snoring individuals copes with this disorder. Based on this method people can judge what kind of disorders they are dealing with. Acoustic diagnosis of sleep disorders, especially the *Obstructive Sleep Apnea Syndrome* may help find a way of snoring rehabilitation and making decisions concerning future treatment and have influence on the quality of night sleep.

4 Software Design

The variety of data provided by sensors in a multimodal system requires the appropriate software design including:

- sensor-specific software translating the acquired signal or image into a mode-specific message of unified format,
- system-specific data structures and exchange rules considering the informative properties of particular sources,
- final rule- or artificial intelligence-based decision and user messaging system.

As the subject measurement modes were selected as a compromise of at-home applicability and information completeness, the mode-specific information was easy to be defined as tokens (Table 3). The system is expected to yield a single sleep

Table 3 Subject information provided from basic sleep recording modes

recording mode	subject information	data type
electrocardiogram	stimulation degree	short-time index (RMSSD)
		long-time index (SDANN)
	breathing parameters	breathing frequency
		breathing depth
video surveillance	motion estimation	body motion index
		legs motion index
		hands motion index
audio recordings	acoustic effects analysis	snoring index
		environmental noise index

quality index simple to understand for everyone (like the *Body Mass Index*). Unfortunately, no worldwide standard of such index exists and its development is the issue for medical scientists. Since first approach has to be made in the framework of our project, we tried to quantify all events undesirable during the sleep. The integration of these information related to the laboratory sleep scoring results or to the subjective sleep evaluation made by the subject himself or herself leads to the rule-based or AI-supported sleep evaluation.

In the case of rule-based sleep evaluation, values of respective indexes (see Table 3) are compared to thresholds, weighted and integrated to a single output value. Since the contribution of specific parameters are not known, and may vary from one subject to another, it seems reasonable to use a AI-based decision system (e.g. based on an *Artificial Neural Network*) allowing for adaptation for subject and environment conditions. Such system has to learn its desirable functionality prior to be used for sleep evaluation.

5 Conclusions and Future Works

The multimodal system has been sketched in aspects of measurement methodology, hardware and software solutions. Future investigations are expected to reveal the strong and weak points of the prototype and their conclusions will lead to a prototype device. The presented approach has successfully eliminated the costly and uncomfortable measurements, preserving ca. 70% of the laboratory sleep scoring functionalities. If such limited device is used to relative scoring of the same subject's sleep in repeatable conditions of his or her home, we expect high usefulness in individual pursuit for optimal sleep conditions. Eliminating the electroencephalographic and electromiographic recordings are the most problematic compromise and impoverish the system performance.

During these studies five video recordings of nightlong sleep from five different subjects were investigated. Both the value and frequency of the movements parameter (mean brightness of pixels) were taken into consideration to draw a conclusion. Obtained data revealed significant inter-subject motion variability as well as motion variability in time of the same patient.

In order to assess precise motion activity of the particular parts of the body, human body recognition must be provided. It can be applied by means of artificial neural network processing [16]. Video motion recordings of long-term sleep provide a great amount of data. Therefore application prepared for acquisition of video frames must contain also a preprocessing stage operating in real time. Its main objective is data recording only while motion periods occur.

Correct interpretation remains a significant problem also in dealing with respiratory sounds such as snoring and/or breathing. Examining the snoring sound signal during various stages of sleep, we observed that light snorers snored evenly throughout all of them. The most interesting fact was that heavy snorers tend to snore more with maximum snoring intensity in the rapid eye movement sleep phase than in any other stage of sleep. Further conclusions can be made by comparing simultaneously gathered acoustic and electrocardiographic signals. During two thirty minute intervals starting at 130 and 300 minutes after recording initiated, a significant decrease in variation can be seen, especially short term *SDANN*, which is in accordance with *RMSSD*. In these intervals we also observe increased snoring sound intensity.

References

1. American Academy of Sleep Medicine Task Force, Sleep-related breathing disorders in adults: Recommendations for syndrome definition and measurement techniques in clinical research. Sleep 22(5), 667–689 (1999)
2. Dorfman-Furman, G., Shinar, Z., Baharav, A., Akselrod, S.: Electrocardiogram Derived Respiration During Sleep. Computers in Cardiology 32, 351–354 (2005)
3. Grube, G., Flexer, A., Dorffner, G.: Unsupervised continuous sleep analysis. Methods Find Exp. Clin. Pharmacol. 24(suppl. D), 51–56 (2002)
4. Guzik, P., Piskorski, J.: Heart Rate Assymmetry. In: Proc. International Congress on Electrocardiology (2009)
5. Iber, C., et al.: AASM Manual for Scoring Sleep. American Academy of Sleep Medicine, Westchester IL (2007)
6. Kikta, A., Augustyniak, P.: Comparing Methods of ECG Respiration Signals Derivation Based on Measuring the Amplitude of QRS Complexes. Journal of Medical Informatics and Technologies 11, 155–163 (2007)
7. Kohler, B., Hennig, C., Orglmeister, R.: The principles of software QRS detection. IEEE Engineering in Medicine and Biology Magazine 21(1), 42–57 (2002)
8. Liao, W.H., Yang, C.M.: Video-based Activity and Movement Pattern Analysis in Overnight Sleep Studies. In: Pattern Recognition, ICPR 2008 (2008)
9. Maier, C., Dickhaus, H., Laguna, P.: Amplitude Variability Extraction from Multi-Lead Electrocardiograms for Improvement of Sleep Apnea recognition. Computers in Cardiology 32, 355–358 (2005)
10. Maier, C., Roedler, V., Wenz, H., Dickhaus, H.: ECG Fingerprints of Obstructed Breathing in Sleep Apnea Patients. IEEE Eng. Medicine and Biology Magazine 28(6), 41–48 (2009)
11. Malik, M., Camm, A.J.: Heart Rate Variability. Wiley-Blackwell (1995)
12. Moody, G.B., Mark, R.G., Bump, M.A., Weinstein, J.S., Berman, A.D., Mietus, J.E., Goldberger, A.L.: Clinical Validation of the ECG-Derived Respiration (EDR) Technique. Computers in Cardiology 13, 507–510 (1986)
13. Peng, Y.T., Lin, C.Y., Sun, M.T., Landis, C.A.: Multimodality Sensor System for Long-Term Sleep Quality Monitoring. IEEE Transactions on Biomedical Circuits and System 1(3), 217–227 (2007)
14. Prusinski, A.: Parasomnie: Obraz Kliniczny. Diagnostyka i Postepowanie, Sen 1(1), 33–39 (2001) (in Polish)
15. Task Force of the ESC/ASPE, Heart rate variability: Standards of measurement, physiological interpretation, and clinical use. European Heart Journal 17, 354–381 (1996)
16. Yang, F.C., Kuo, C., Tsai, M.Y., Huang, S.C.: Image-based Sleep Motion Recognition using Artificial Neural Networks. In: Proceedings of the Second International Conference on Machine Learning and Cybernetics, Wan, November 2-5, pp. 2775–2780 (2003)
17. Zieliński, T.P.: Digital Signal Processing. WKiL, Warszawa (2005) (in Polish)

A Graph Representation of Subject's Time-State Space

Grażyna Ślusarczyk and Piotr Augustyniak

Abstract. Surveillance systems are currently the most developed branch of assisted living applications providing the disabled or elderly people with unprecedented security in their independent life. This paper presents a design of a telemedical surveillance system, where graph theory is used to describe subjects' states. Patient's states expressed by sets of medically-derived parameters and his or her daily activity (a behavioral pattern) are represented by attributed probabilistic graphs with indexed and labeled nodes. This representation provides high flexibility in a state and transient description as well as a reliable measure of behavior divergence, which is a basis for automatic alerting. The system is designed for the subject's apartment and supports a localization-dependent definition of his or her usual and unusual behavior. The apartment topology is also represented in the form of a graph determining subject's pathways and states. This approach has been found very flexible in all aspects of personalization, appropriate to work with the behavioral presumption set or with the auto-adaptive artificial intelligence recognition engine. Also the patient's state, thanks to the semantic description may be easily extended or refined if necessary by adding new, complementary data capture methods.

1 Introduction

Assisted living applications benefit from the wide range of biomedical measurements being derivatives of clinical diagnostic systems. The pursuit for simplicity of

Grażyna Ślusarczyk
The Faculty of Physics, Astronomy and Applied Computer Science, Jagiellonian University, Reymonta 4, 30-059 Kraków, Poland
e-mail: gslusarc@uj.edu.pl

Piotr Augustyniak
The Biocybernetics Lab. Institute of Automatics, AGH University of Science and Technology, 30 Mickiewicza Ave. 30-059 Kraków Poland
e-mail: august@agh.edu.pl

usage and public availability of the home care equipment often decreases the reliability of each single measurement. As a promising remedy to maintain the overall system performance in home surveillance and alerting, multimodal measurement approaches are developed worldwide [1], [3], [4], [7]. They principle benefits from several measurements performed simultaneously with the use of different methodologies, results of which are integrated on the level of a universal semantic description of the patient's status [6], [20].

Regardless of the method used, the patient's status is determined by a sorted list of symbols representing his or her conditions, attributed by the numeric value of occurrence probability. At this stage, biomedical measurements are completed by environmental variables of two kinds:

• stimuli, influencing the subject's behavior (i.e. room lighting),
• results, being consequences of subject's actions (i.e. subject's coordinates).

It is worth a remark that such a measurement infrastructure supports not only passive capturing of the subject's status, but also active interaction and stimulation aimed at subject's assessment and detection of events. Including temporal variability in the multimodal surveillance of status allow us to define the behavioral pattern as a sequence of predefined status vectors appearing in a given order and complying with specified temporal restrictions. Putting aside possible delay and inaccuracy of values of some status components, the subject's behavior may be captured and analyzed in real time in order to detect abnormalities and to warn about possible health danger. Such preventive analysis is highly welcome in general surveillance of elderly people living on their own, as well as in specific situations as car driving or similar.

A multimodal surveillance system providing a semantic description of basic subject's health parameters (e.g. heart rate), subject's motion and sounds is currently under development in Biocybernetic Lab, AGH-University of Science and Technology. Its principal purpose is the recognition of abnormalities in behavioral patterns and classification of events into one of four categories implying further actions. The recognition of alternate behavior is performed on the semantic description of the subject's status in the context of subject's habits. This step is in main focus throughout this paper.

Chapter 2 presents principles of the surveillance system and specifies the subject's state and behavior observation, chapter 3 reveals a graph-based representation of the patient's state and defines a distance measure between the 'usual' and 'unusual' behavior. Chapter 4 includes discussion and final remarks.

2   Principles of the Surveillance System

Automatic semantic summarization of human activity and detection of unusual inactivity are useful goals for video-based systems operating in a supportive home environment. Learned models of a spatial context are used in conjunction with a tracker to achieve these goals. The surveillance is oriented to detect 'unusual inactivity' an example of which is fall detection [12], [15]. Falls are a major health

hazard for the elderly and a major obstacle to independent living. The estimated incidence of falls for both institutionalized and independent persons aged over 75 is at least 30 percent per year [16].

Four various sources of behavioral signals are considered in the system: two surface-recorded vital signs, video sequences and acceleration patterns. This setup allows for the use of general-purpose consumer-grade devices as main sensors of the subject's behavior. The translation of the acquired data (signal or image) to the semantic description of the subject's status is performed by the dedicated software, which may be individually tuned accordingly to the patient's or environmental conditions.

2.1 State and Behavior Observation

Health records usually provide several organ-specific descriptors and principal global parameters describing the whole organism in aspects representing it as organ's environment influencing its functionality. For describing a subject state, we use a parameter-domain representation, in which the subject S is described by the set of diagnostic parameters $S_p = \{p_1 \cdots p_N\}$, considered as the projection of his physiological state on the modality-dependent N-dimensional state space $\mathbf{S}^N$. The projection is limited due to restrictions on the count N of values available for measurement and inaccurate due to measurement errors ε_N and additive interferences ρ_N [19]. In the proposed system, the state observation complies to the following requisites:

- the multimodal acquisition has to provide a reliable description of subject's behavior,
- the system infrastructure has to be feasible in home-care conditions and preferably to use only a customer-grade equipment.

The most visible and easily obtainable markers representing daily activity in humans are movements signals of their bodies [13]. Many previous studies proved the utility of continuous round-the-clock registration of body arrangements and motion in behavior quantitative evaluation [9], [11]. To acquire the mechanical activity of the body, the proposed system is equipped with video [8], acceleration and angular velocity sensors. Additionally, the human activity is represented well by the response of the human cardiovascular system to variations of physical burdens and psychical conditions. The main parameter used for the assessment of extracardiac influence is the *heart rate variability* (HRV) controlled by the autonomous nervous system. Continuous monitoring the value of the cardiac rhythm is an appropriate background for the support of human activity assessment [10]. The measurement of time-domain variability of the sinus node activation requires acquisition of a single-lead electrocardiogram, heart beat detection and exclusion of all beats other than sinoatrial. Accordingly to [22] these steps are usually directly followed by the statistics, interpolation of missing intervals is performed for frequency-domain analysis.

The subject's behavior is usually referenced to as changes of the state with time. The distinction of the typical human behavior is thus based on the temporal
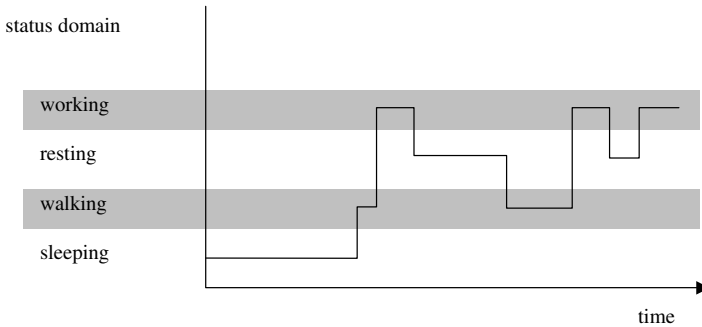
Fig. 1 Example of a behavioral pattern recorded in the morning

synchronization of the parameters' sequences. The sequence of multimodal state descriptions is known as the *behavioral pattern* (Fig. 1). Since the time is a distinctive factor of behavioral patterns, first question to be answered while designing the system is the state sampling frequency. The resulting value is a compromise between two contradictory requirements:

- technical and methodological feasibility (e.g. video system throughput [8], necessary averaging of HRV parameters [22]),
- expected temporal resolution of the system defined by the duration of the shortest events.

In the proposed system the value is set to 1 minute, however this should be verified by the prototype test. Patterns typical for the common human actions are easily separable, however, regardless the acquisition and state description accuracy, the behavior is not directly represented by behavioral patterns. This justifies the attribute of probability p_b used in the behavior representation in the system. The behavioral patterns represented in the system belong to a finite list L_p (see. Table 1).

Table 1 Examples of behavioral patterns and their acquisition modes

acquisition mode	parameter representation	state aspect	behavioral examples
single-lead electrocardiogram	heart rate variability	workload	{working, resting, sleeping}
video recording	image analysis	posture detection	{standing, sitting, lying, walking}
accelerometric recording	signal analysis	motion classification	{resting, working, walking}

2.2 *Qualification of the Behavior*

Qualification of the behavior is made by the system automatically with respect to two factors: presumptions and heuristics. First mode involves human-designed definitions of 'usual' and 'unusual' actions based on the description of subject's habits. The latter mode involves artificial intelligence (AI) to record, analyze and statistically process the everyday subject's behavior and detect whether and how the recorded pattern differs from the typical performance. The qualification of the behavior aims at issue an output token describing the subject's action as belonging to one of the following categories: {normal, suspicious, dangerous, critical}. This qualification is performed with consideration of various aspects of similarity between behavioral patterns:

- by the sequence pattern (subject is doing/undergoing an extra activity not matching to any 'usual' pattern),
- by the sequence time (subject is doing/undergoing a typical activity in unusual time),
- by the response to the stimulus (subject is not performing the action expected as a response to the stimulus).

The subject's premises are attributed with various functionalities, and therefore the behavior, is considered as 'usual' or 'unusual' with regard to the subject's positioning. The example of the behavior permitted in given rooms defined in the presumptions-based behavior qualification is presented in Table 2.

Table 2 Presumptions on the allowed subject's activities in particular rooms

room type / behavior type	living room	bedroom	kitchen	bathroom	entrance hall
working	+	-	+	+	+
resting	+	+	+	-	-
lying	+ ≤60 min	+	-	-	-
sitting	+	+	+ ≤10 min	+ ≤10 min	-
walking	+	+ ≤1 min	+	+ ≤1 min	+

As usually in case of artificial intelligence-based systems [21], the proposed system has two operation modes:

- a learning phase, in which the main task is the acquisition of behavioral patterns typical to each specific subject and the analysis of generalized results by a supervising person - on this stage the abnormalities severity and necessary actions are also defined.
- a working (or testing) phase, in which the system is expected to detect and classify specified events, and consequently to trigger a desired action.

Although formally separated, these operation modes may partially overlap: the data acquired during the testing phase may be used for refinement of system responses and to define other factors of possible danger, which have not been previously considered.

3 A Graph Representation of Subject's Behavior

As graphs provide an easy way to depict complex structures visually, they are one of the most frequently used data structures in computer science, engineering, designing, business analysis and so on [14]. To represent objects with a number of different elements related in various ways hierarchical graphs are often used [2], [5], [18].

3.1 Definition of Subject's State Graph

A typical behavioral pattern is represented by an attributed probabilistic graph with indexed and labeled nodes. Node indexes correspond to different body positions {standing, sitting, lying, walking}, while node labels represent types of activities which are possible in these positions. Graph edges represent successive changes of the positions. Each node has a random label being a set of labels together with their probabilities. The random labels reflect the different probabilities of various activities resulting from taken body positions. To each label a set of attributes corresponding to the foreseen duration of activities and to biomedical measurements specifying the person's state is assigned. The node labeling of the proposed graph is a modification of the way of labeling random IE graphs used for distorted patterns analysis [17].

Definition 3.1. An attributed probabilistic graph, called a **state graph**, is a five-tuple $G = (V, E, \Sigma, \varphi, \alpha)$, where:

1. V is a finite, nonempty set of nodes with indices ascribed in an unambiguous way,
2. $E \subseteq 2^V$ is a set of edges such that $\forall\, e \in E: |e| = 2$,
3. Σ is a finite, nonempty set of node labels,
4. $\varphi: V \to 2^{\Sigma \times [0,1]}$ is a node labeling function, where each random node label $\varphi(v)$ is a set of pairs of the form (σ, p), $\sigma \in \Sigma$, $p \in [0,1]$ is a probability of labeling a node v with σ, such that the sum of the second elements of these pairs is equal to 1,
5. $\alpha: \Sigma \to 2^A$, where A is a set of node attributes, is a node attributing function, which assigns finite subsets of A to node labels of Σ.

A state graph representing a typical behavioral pattern for a given person located in a living-room is shown in Fig. 2. This graph is composed of four nodes, where the node number 1 represents standing position, the node number 2 - walking position, while the nodes 3 and 4 represent sitting and lying positions, respectively. The elements of the set of node labels *{wrk, wlk, slp, rst}* denote the following activities:
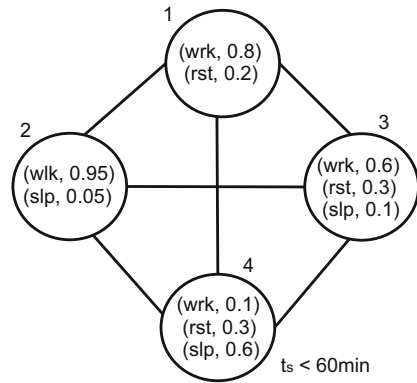
Fig. 2 A state graph of a typical behavioral pattern

working, walking, sleeping and resting, respectively. Probabilities of these activities are different for each node. Also the range of values for attributes (like the heart rate, limb acceleration etc.) assigned to labels denoting various activities can be different for each node. One of the attributes assigned to the label *slp* is t_s denoting the foreseen duration of the sleep. It is assumed that the period of this activity in the living-room should be shorter than 60 minutes.

3.2 A Graph Representation of Subject's Habits

As the behavioral pattern strongly depends on the room the person is located in, the status of the patient who is surveyed by the home care equipment will be represented by a hierarchical graph, where hierarchical nodes correspond to rooms of the apartment, while edges connecting them represent the accessibility relation between rooms. The nodes are labeled by names reflecting the functionality of rooms. In each hierarchical node a state graph describing a behavioral pattern typical for the corresponding type of room is nested.

Let G be a family of state graphs describing typical behavioral patterns.

Definition 3.2. A hierarchical graph, called a ***state-space graph***, is a five-tuple
$H = (N, E, \Gamma, \phi, \eta)$**,** where:

1. N is a finite, nonempty set of hierarchical nodes,
2. $E \subseteq 2^V$ is a set of edges such that $\forall\, e \in E: |e| = 2$,
3. Γ is a finite, nonempty set of hierarchical node labels,
4. $\phi: N \rightarrow \Gamma$ is a hierarchical node labeling function,
5. $\eta: N \rightarrow G$, is a nesting function, which assigns a state graph to each hierarchical node.

An example of a state-space graph obtained as a result of a learning phase, in which typical behavioral patterns reflecting subject's habits are determined, is shown in Fig. 3a. Different state graphs are nested in hierarchical nodes representing rooms of an apartment presented in Fig. 3b. Coming out of one room and entering the other
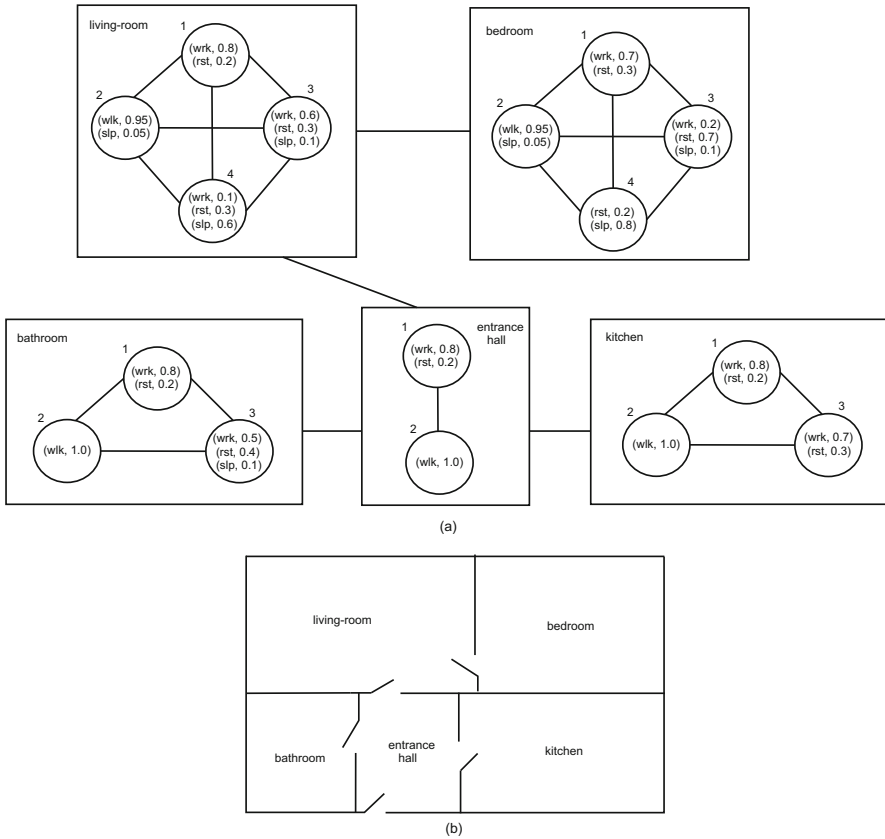
Fig. 3 a) A state-space graph of typical behavioral patterns, b) a layout of the considered apartment

according to an edge connecting hierarchical nodes representing these rooms can be treated as coming from the node number 2 (which represents walking position) of the state graph nested in one hierarchical node to the node number 2 of the state graph nested in the second hierarchical node.

3.3 Quantifying of Behavior Differences

The proposed representation of behavioral patterns allows us to specify the behavior divergence as the distance between two state graphs. The distance is computed between a state graph representing the typical behavior of the subject in a given room and a state graph corresponding to the present subject's behavior in the same room, which is obtained at the working phase of the system. On the basis of this distance the subject's state is classified.

It should be noted that the distance is computed only between two isomorphic state graphs. As state graphs used presently are complete ones, the isomorphism in this case means that both graphs have the same number of nodes with the same indices, i.e., representing the same body positions. If a state graph representing a present behavioral pattern has more nodes than the state graph of a typical behavior, the alert is triggered as it means that an unexpected body position has been found.

Definition 3.3 Let v_k be a node with the index k of a state graph G.

Let $P_k = \{(\sigma_k^1, p(\sigma_k^1)), \ldots, (\sigma_k^r, p(\sigma_k^r))\}$, where $\sigma_k^j, j = 1, \ldots, r$, is a j-th label of the node v_k and $p(\sigma_k^j)$ is a probability of the label σ_k^j, be a probability distribution of labels assigned to v_k.

Let v_i, v_l be two nodes with r labels with probability distributions P_i, P_l, respectively.

The **distance** between v_i and v_l is defined as: $\delta(v_i, v_l) = \sum\limits_{m=1}^{r} |p(\sigma_i^m) - p(\sigma_i^m)|$.

Definition 3.4 Let G_1 and G_2 be two isomorphic state graphs with n nodes.

The **distance between G_1 and G_2** is defined as $\Delta(G_1, G_2) = \sum\limits_{i=1}^{n} \delta(v_i^1, v_i^2)$, where v_i^1 and v_i^2 denote nodes of G_1 and G_2, respectively.

Let us consider a state graph G_2 representing the present subject's behavior in the bathroom (Fig. 4a). The distance between this graph and the state graph G_1 representing the typical behavior in a bathroom (Fig. 3a) is computed as $\delta(v_1^1, v_1^2) + \delta(v_2^1, v_2^2) + \delta(v_3^1, v_3^2) = 0.4 + 0 + 0 = 0.4$. The distance between a state graph G_3 (Fig. 4b) and G_1 is computed as $\delta(v_1^1, v_1^2) + \delta(v_2^1, v_2^2) + \delta(v_3^1, v_3^2) = 0 + 0 + 1 = 1$. The first result indicates that the state of the surveyed person can be suspicious as he/she rests more frequently than usually. The second result is great enough to classify the state as dangerous, because the subject does not perform their normal working activity at all.

Classification of subject's behavior as {normal, suspicious, dangerous, critical} is based on comparison of the current behavior divergence expressed by the graph distance (see def. 3.4) and the appropriate threshold value. Even in the presumptions-based system these values cannot be set arbitrarily without the
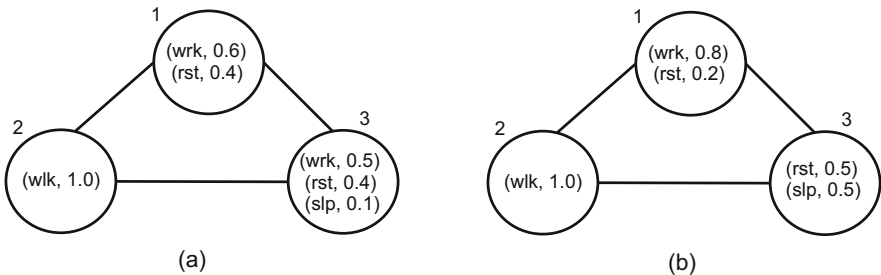
Fig. 4 Two state graphs representing different behavioral patterns

experimental verification of the tolerance margins, wide enough to cover a range of 'usual' states. The threshold values depend on several factors:

- the subject's action repetitiveness,
- state measurement methodology and accuracy,
- subject's localization (in some rooms unexpected states are more dangerous than in the others),
- the current state (some states are more precisely defined than the others).

In the AI-based surveillance system, the states selected as 'usual' during the supervised learning phase are statistically processed in order to calculate threshold values providing best sensitivity and specificity of the danger recognition. These statistics provide subject-specific threshold values $T_s(m,l,s)$ in the three-dimensional context of the measurement, localization and state.

4   Discussion

The application of the behavioral pattern analysis methodology to recognition potentially dangerous events in pursued subject was presented and designed. Three aspects of novelty are presented in this paper:

- the representation of the subject's state as an attributed probabilistic graph,
- the use of behavioral patterns considering the temporal aspect of state changes,
- the interpretation of the behavioral patterns in the context of subject's localization which considers various functionalities of rooms in subject's apartment.

The consequence of state representations using graphs, was a straightforward definition of other possible states and transients between them. This justified a quantitative measure of differences between the recorded behavioral pattern and the reference as a graph distance. The automatic classification of recorded patterns as 'usual' or 'unusual' and alerting are also based on this measure. The representation of the apartment topology by means of graphs, although rather conventional, was very useful to represent the room-specific range of expected actions.

The advantage of our approach is the unprecedented integration of multimodal data describing the subject and his environment in behavioral patterns. In the application for assisted living, the system flexibility and high degree of personalization are highly desirable.

Although the measurement of specific vital signs is not precise, the integration of data in a multimodal system provides a reliable stepwise alerting. The alerting may then be used as a trigger of a health-oriented message, on-demand medication, a nurse visit or medical intervention.

Despite of a broad representation, the available patient information may be too sparse to detect some dangerous episodes. In case the system systematically misses certain types of episodes, monitoring of other complementary parameters may be included in the integrated state description. For each new subject or in presence of false alerts, the manual review and evaluation of behavioral patterns are desirable and the appropriate threshold values are to be tuned individually.

References

1. Al-Ani, T., Le Ba, Q.T., Monacelli, E.: On-line Automatic Detection of Human Activity in Home Using Wavelet and Hidden Markov Models Scilab Toolkits. In: IEEE 22nd International Symposium on in Intelligent Control, ISIC 2007, pp. 485–490 (2007)
2. Drewes, F., Hoffmann, D., Plump, D.: Hierarchical Graph Transformation. Journal of Computer and System Sciences 64, 249–283 (2002)
3. Eklund, J.M., Hansen, T.R., Sprinkle, J., Sastry, S.: Information Technology for Assisted Living at Home: building a wireless infrastructure for assisted living. In: 27th Annual International Conference of the IEEE-EMBS, pp. 3931–3934 (2005)
4. Fayn, J., et al.: Towards New Integrated Information and Communication Infrastructures in E-Health. Examples from Cardiology, Computers in Cardiology 30, 113–116 (2003)
5. Grabska, E., Ślusarczyk, G., Papiernik, K.: Interpretation of objects represented by hierarchical graphs. In: KOSYR 2003, Wroclaw, pp. 287–293 (2003)
6. Hristova, A., Bernardos, A.M., Casar, J.R.: Context-aware services for ambient assisted living: A case study. In: First International Symposium on Applied Sciences on Biomedical and Communication Technologies, ISABEL 2008, pp. 1–5 (2008)
7. Jovanov, E., Milenkovic, A., Otto, C., de Groen, P.C.: A wireless body area network of intelligent motion sensors for computer assisted physical rehabilitation. J. Neuroengineering Rehabil. 2, 6 (2005)
8. Liao, W.H., Yang, C.M.: Video-based Activity and Movement Pattern Analysis in Overnight Sleep Studies. In: Pattern Recognition, ICPR 2008 (2008)
9. Liu, T., Inoue, Y., Shibata, K.: Development of a wearable sensor system for quantitative gait analysis. Measurement (2009), doi:10.1016/j.measurement.2009.02.002
10. Malik, M., Camm, A.J.: Heart Rate Variability. Wiley-Blackwell (1995)
11. Najafi, B., Aminian, K., Paraschiv-Ionescu, A., Loew, F., Büla, C.J., Robert, P.: Ambulatory System for Human Motion Analysis Using a Kinematic Sensor: Monitoring of Daily Physical Activity in the Elderly. IEEE Transactions on Biomedical Engineering 50(6), 711–723 (2003)
12. Nait-Charif, H., Mckenna, S.J.: Activity summarisation and fall detection in a supportive home environment. In: Proceedings of the 17th International Conference on Pattern Recognition, ICPR 2004, vol. 4, pp. 323–326 (2004)
13. Rougier, C., Meunier, J., St-Arnaud, A., Rousseau, J.: Fall Detection from Human Shape and Motion History Using Video Surveillance. In: 21st International Conference on Advanced Information Networking and Applications Workshops, AINAW 2007, vol. 2, pp. 875–880 (2007)
14. Rozenberg, G.: Handbook of Graph Grammars and Computing by Graph Transformations. Fundations, vol. 1. World Scientific, London (1997)
15. Schuldt, C., Laptev, I., Caputo, B.: Recognizing human actions: a local SVM approach. In: Proceedings of the 17th International Conference on Pattern Recognition, ICPR 2004, vol. 3, pp. 32–36 (2004)
16. Sixsmith, A., Johnson, N.: A smart sensor to detect the falls of the elderly. IEEE in Pervasive Computing 3(2), 42–47 (2004)

17. Skomorowski, M.: Syntactic recognition of distorted patterns by means of random graph parsing. Pattern Recognition Letters 28, 572–581 (2007)
18. Ślusarczyk, G.: Hierarchical hypergraph transformations in engineering design. Journal of Applied Computer Science 11, 67–82 (2003)
19. Straszecka, E., Straszecka, J.: Interpretation of Medical Symptoms Using Fuzzy Focal Element. In: Kurzynski, M., et al. (eds.) Computer Recognition Systems, pp. 287–293. Springer, Heidelberg (2005)
20. Sun, H., De Florio, V., Gui, N., Blondia, C.: Promises and Challenges of Ambient Assisted Living Systems. In: Sixth International Conference on Information Technology: New Generations, ITNG 2009, pp. 1201–1207 (2009)
21. Tadeusiewicz, R., Ogiela, L.: Selected cognitive categorization systems. In: Rutkowski, L., Tadeusiewicz, R., Zadeh, L.A., Zurada, J.M. (eds.) Artificial Intelligence and Soft Computing, pp. 1127–1136. Springer, Heidelberg (2008)
22. Task Force of the ESC/ASPE, Heart rate variability: Standards of measurement, physiological interpretation, and clinical use. European Heart Journal 17, 354–381 (1996)

Data Integration in Multimodal Home Care Surveillance and Communication System

Piotr Augustyniak, Magdalena Smoleń, Anna Broniec, and Jacek Chodak

Abstract. This paper presents the data capture methodology and design of a home care system for medical-based surveillance and man-machine communication. The proposed system consists of the video-based subject positioning, monitoring of the heart and brain electrical activity and eye tracking. The multimodal data are automatically interpreted and translated to tokens representing subject's status or command. The circadian repetitive status time series (behavioral patterns) are a background for learning of the subject's habits and for automatic detection of unusual behavior or emergency. Due to mutual compatibility of methods and data redundancy, the use of unified status description vouches for high reliability of the recognition despite the use of simplified measurements methods. This surveillance system is designed for everyday use in home care, by disabled or elderly people.

1 Introduction

Assisted living applications are commonly understood as technical environment for disabled or elderly people providing the care in the user-specific range. A considerable drawback is the equipment cost implied by the assumption of use of very reliable close-to-clinical devices in patient's home. Our proposal is based on the integration of data provided by several surveillance devices of relatively low reliability in order to provide raw diagnosis and control of the focus of detailed examinations. Additionally, the assisted living applications are not required to provide precise diagnostic information, usually the desired output is the alert message, which role is to put a feedback to the patient's behavior or medication, trigger a specialized

Piotr Augustyniak · Magdalena Smoleń · Anna Broniec · Jacek Chodak
AGH University of Science and Technology, 30 Mickiewicza Ave. 30-059 Kraków, Poland
e-mail: august@agh.edu.pl, m-smolen@wp.pl, abroniec@gmail.com, falowiec@wp.pl

diagnostic procedure or notify the medical staff. The role of assisted living applications is usually reported as twofold:

- automatic detection of health risk factors in the human organism,
- providing of an alternative way of interaction between the human and his environment.

In our approach, we assume that a common idea of these tasks is the acquisition and automatic interpretation of selected vital parameters. The particular interest is the mutually correlative information gathered with use of independent recording techniques based on various physical backgrounds. The present paper describes a concept of data integration in a multimodal system for assisted living. As far as possible the system design is based on consumer-grade equipment (computers and cameras) or simplified recorders for selected biosignals. The measurement is performed with use of method-specific software and all results are presented in a common diagnostic state-space. Considering the uniqueness of certain data or redundancy of the others, the representation of the patient's state is completed or refined. Closely related subject, also concerned in this paper, is the use of selected vital signs as an alternative way of human-computer interaction. The literature survey led us to a conclusion that any brain activity or eye movement signals are interpreted unconditionally. Consequently, the laboratory results are promising, but applications in subjects' homes usually end with ambiguity of commands interpretation. Therefore, as an efficient remedy, we propose the contextual interpretation of the human commands on the background of his or her activity, topological position and status. We assume a common approach to the physiological data measurements and processing for status and command detection. The unified description of subject's status provides a reasonable tolerance of the recognition system for unintended gesture or motion similar to the command. The interpretation of status or behavioral patterns being a status sequence, is the last stage of our project, not covered in this paper.

2 Materials and Methods

Four various sources of behavioral signals are considered in the system: two surface-recorded vital signs, video sequences and acceleration patterns. This setup allows the use of general-purpose consumer-grade devices as main sensors of the subject's behavior. The translation of the acquired data (signal or image) to the semantic description of the subject status is performed by the dedicated software, which may be individually tuned accordingly to the patient's or environmental conditions. Depending on detected condition, selected vital signs are considered for communication of the patient with his environment. The bibliographic study show, that brain and eye motion signals are particularly useful for such application. In the proposed system, we also used EEG and EOG signals, however their interpretation is made automatically in context of the subject's status. The subject's status is described by

single lead ECG measurement → heartbeats detection → heartbeats qualification → NN-interval statistics → interpretation of status
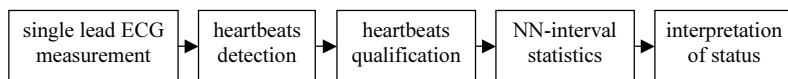
Fig. 1 Block diagram of heart rate variability signal processing

the probability attributes in a given time point. Time-domain variability of the status is often referred to as 'behavioral pattern'. Our approach assumes the extension of this notion to both status-descriptive and intention-descriptive parameters. Such extension unifies the output of measurement methods-dedicated procedures and facilitates the integration of syntactic description of the subject.

2.1 Electrical Activity of the Heart

The response of the human cardiovascular systems to variations of physical load and psychical conditions is very fast and thus reflects changes in subject's behavior. Main parameter used for the assessment of extracardiac influence is the heart rate variability controlled by the autonomous nervous system. Continuous monitoring the value of the cardiac rhythm is an appropriate background for the support of human activity assessment. The measurement of time-domain variability of the sinus node activation requires acquisition of a single-lead electrocardiogram, heart beat detection and exclusion of all beats other than sinoatrial (Fig. 1). These steps are usually directly followed by the statistics, interpolation of missing intervals is performed for frequency-domain analysis. Three patient's states are distinguished by the analysis of the human heart rate:

- sleeping - corresponding to low heart rate value and variability
- resting - represented by low or decreasing heart rate value and high short-time variability,
- loaded or anxious - represented by high or increasing heart rate value and high short-time variability.

The heartbeats are detected in the electrocardiogram with use of signal filters based on QRS-frequency, acceleration and moving window integration [4]. The custom-built beat detector was proved for compliance with IEC60601 requirements [2] when tested on MIT-BIH Arrhythmia Database [9]. The shape-based discriminator eliminated all but sinus-originated beats. The missing RR intervals were interpolated by a successive procedure minimizing their short-term variability, accordingly to the guidelines in [12]. Finally, time-domain heart rate variability (HRV) parameters were calculated following the formulas given by Malik [7] and confirmed by other researchers [11]. Two standard quantitative HRV parameters were selected as representative:

- the square root of the mean squared differences of successive NN intervals (RMSSD), for measurements of short-time variability,
- the standard deviation of the average NN interval calculated over five minutes periods (SDANN), for measurements of long-time variability,

The HRV-based estimation of the subject's status involves a considerable delay, thus requires support from other methods in detection of sudden status changes.

2.2 Mechanical Activity of the Body

The most visible and easily obtainable markers responded to daily activity in humans are movements signals of their bodies. Many previous studies proved the utility of continuous round-the-clock registration of body arrangements and motion in behavior quantitative evaluation [3], [5], [6], [10]. In context of the proposed multimodal home care surveillance it is essential to incorporate straightforward, cheap and non-limiting patient movements sensors. Therefore to acquire desirable mechanical activity of the body, we decided to use in our project both video recordings as well as acceleration and angular velocity patterns. Setting-up such kind of different equipment allows to obtain sufficiently accurate and complete conclusions about state of the object which is supervised under conditions of daily living.

General approach consists in state recognition which is possible to extract by means of motion quantification of whole human body or its selected segments, especially upper and lower limbs. In this research we determined four main types of condition and physical activity accordingly to the level of motion quantity and variability:

- sleeping and resting - when whole body motion quantity and variability in dependence of time keep on low level,
- working - correspond to increasing or moderate amount and time variability of the upper limbs motion mainly,
- walking - reflected in high quantity and time periodicity of both upper and lower limbs motion.

In calculation of two mentioned parameters of the exact human status (quantity and variability) from the video registrations we need to carry out preliminary processing of the obtained data. Fig. 2 presents principal stages of our approach. First step concerns segmentation of the human silhouette from the surrounding environment background. Then both vertical and horizontal projections histograms of segmented
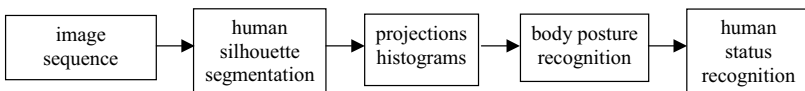
Fig. 2 Block diagram of status recognition process from the video sequence recording

subjects are performed for the purpose of preparation and extraction of the features corresponded to particular body postures. Within the specified postures owing to the numerical criteria of motion amount, the object state is estimated. If necessary more detailed report of daily limbs physical activity, block diagram from Fig. 2 can be extended with an extra model-based step referred to matching the prepared body model to the person silhouette. That kind of approach enables to determine principal parts of the body and to give the information about their movements. In context of this particular activity semantic description, accelerometers and gyroscopes could be also very useful. Sensors placed on the upper and lower limbs of the tested subject provide not only motion quantity but also precise kinematics parameters corresponded to the pattern of motion present in definite movement (sloping, crouching, sitting down and standing up from the chair, reaching some subject, etc.).

2.3 Electrical Activity of the Brain as Status Determinant

The EEG signal is a sum of oscillations with characteristic frequency and Gaussian noise, thus the simplest way to describe the EEG signal is to present frequency and amplitude of component brain waves. Most of the cerebral signal observed in the scalp EEG falls in the frequency range of 1-40 Hz interval with amplitude which does not exceed 100 μV (about 100 times less in comparison with ECG signal).

Traditionally, brain waves are named by the following letters of Greek alphabet in order of their discovery. Each wave is closely associated with the activity condition of the person subjected to an examination. Brain waves are given as follow:

- Alpha (α) is the oscillations in the frequency range from 8 Hz to 13 Hz, with amplitude from 20 to 100 μV. Alpha waves originate mainly from the occipital lobe during total and wakeful relaxation with closed eyes. Alpha waves are reduced with open eyes, mental activation, or drowsiness and sleep. They are thought to represent the activity of the visual cortex in an idle state. Occipital alpha waves during periods of closed eyes are the strongest EEG brain signals.

  There is a variant of alpha wave in the same frequency range, called mu (μ), which can be found over the motor cortex (central scalp) and is reduced with movement, or the intention of movement.

- Beta (β) is the oscillation in the frequency range from 13 Hz to about 45 Hz, with amplitude up to 20 μV. It can be detected usually on both sides of brain hemispheres in symmetrical distribution and is most evident frontally. Beta waves are associated with active, information processing, busy or anxious thinking and active concentration. Beta activity is generally attenuated during active movements. It is the dominant rhythm in patients who have their eyes open or who are alert or anxious.

- Theta (θ) is the oscillation in the frequency range from 4 Hz to 7 Hz, with amplitude up to 30 μV. Theta occurs normally in young children. It may be recorded during drowsiness or sleeping in older children and adults and it can also be seen

during meditation, trance, hypnosis, dream and creative states. The occurrence of this wave in other cases is pathological.

- Delta (δ) is the oscillation in the frequency range up to 4 Hz and amplitude from 75 to 200 μV. It is the highest in amplitude and the slowest wave. It occurs typically in adults in slow wave sleep. It is also seen normally in babies. In pathological situation delta wave may occur focally with subcortical lesions and in cases of metabolic encephalopathy hydrocephalus.
- Gamma (γ) is the oscillation in the frequency range approximately between 35-100 Hz. Gamma rhythms are thought to connect together different populations of neurons into a network for the purpose of carrying out a certain cognitive or motor function from all parts of the brain. Having high gamma wave activity is associated with high levels of intelligence, high amounts of self-control, great memory and an increased perception of reality. However, there is no agreement on the theory.

Summing up, slow waves occur with idle, calm brain activity and fast wave occur during intensive brain activity connected with information processing.

2.4 Subject's Motion Assessment and Emergency Detection in Context of the Localization

Monitoring activities of daily living of elderly and disabled people, understanding their behavior, providing life support and alarm situations detection must be undertaken with reference to their presence localization at home. It involves division of the supervised living area to smaller regions and matching with them the most common type, intensity and time duration of the human activity. Any significant deviation from the usual behavior could be the base of alerting.

In order to detect automatically anxious or dangerous situation, specific spatial or temporal assumptions and criteria has to be set up. Transitions between different body postures regarded as a physiologically essential function and a prerequisite for gait could be also a sign of emergency. Posture change is then recognized and verified whether its occurrence, localization and duration is typical or uncommon.

In multimodal home care surveillance each of functionality requires its specific zone. Therefore presence of the subject is detected inside the following main zones:

- command zone - place from which the subject is able to send commands to his or her environment (operating the computer, audio or video equipment, etc.),
- sleeping zone - region where favorite sleep-related measurements devices are added to assess and control the human sleep (bed pressure detectors, ECG and EEG sensors, accelerometers placed on the lower limbs, detector and calculator of snoring, etc.),
- health zone - special zone which is provided with dedicated health status measurements equipment (simple tactile ECG sensors, feet pressure detectors, etc.).

2.5 *Voluntary Activity of the Brain as Command Representation*

Regions of the cerebral cortex involved in the planning, control, and execution of voluntary motor functions are specified as motor cortex. This areas are typically divided into three regions which have different functional roles: primary motor cortex (M1), pre-motor area (PMA), supplementary motor area (SMA). The primary motor cortex has a somatotopic representation, which means that particular groups of muscles of different body parts correspond to motor cortex areas in an arrangement. This somatotopic representation is called a motor *homunculus*. The arm and hand motor area (lying between the leg and face area) is the largest, and occupies the part of precentral. The lateral area of the primary motor cortex is arranged from the top to the bottom in areas that correspond to the shoulder, elbow, wrist, fingers, thumb, eyelids, lips and jaw. Interior parts of the motor area correspond with the legs. All of these areas are not proportional to their size in the body. The lips, face parts (especially the tongue) and hands occupy particularly large areas as the body parts which they represent perform most complicated movements. Damage, amputation or paralysis, can shift motor areas to adopt new parts of the body.

The somatotopic organization gives possibility of decoding the movement intention of different parts of the body. The movement intention are associated with different spatiotemporal patterns of increase or attenuation of neuron amplitude oscillation and it may provide additional degrees-of-freedom for command representation and control in the noninvasive methods, as electroencephalography (EEG), mainly support the multi-state BCI. The somatotopic organization allows also to reduce the number of electrodes in EEG to those which lie over motor cortex and provides better parameters for classification, hence the electrode setup time might be reduced to minimum which is very important in brain-computer interfaces.

However ,there are few problems, which have limited the reliability and produced high rate of errors. They have to be considered when constructing the alternative way of interaction between the human and his environment based on EEG signal.

Firstly, the motor imaginary of movement where the subjects imagine the movement of only one limb of the body or for example tongue can be difficult task. It is important to imagine the limb movement properly which is essential for achieving purely mental control without involvement of muscle activity. Fatigue is a common problem during data collection which requires a relatively long time and repetitive motor tasks. Contamination of EMG artifacts from facial muscles may possibly cause serious problems in BCI development. Additionally, the task of the primary motor cortex is to connect the brain to the lower motor neurons via the spinal cord in order to tell them which particular muscles need to contract. In fact, the same muscle are often represented over quite large regions of the brain's surface, and there is an overlap in the representation of different regions of the body. The activity of a single neuron could cause contraction of more than one muscle, which suggests that primer motor cortex may not simply code the degree of contraction of individual muscles.

2.6 Voluntary Eye Movements as Command Representation

In proposed system we used three different methods for tracking eye movements. Each method differently characterizes obtained signal. The *electrooculogram* represents electric potential, the *infrared oculography* measures intensity of reflected infrared light and *video-based eye-tracking* records sequence of images of the eye. These three methods are widely described below.

Electrooculogram (EOG). The eye behaves as a single electrical dipole, the cornea of the eye is electrically positive relative to the retina, therefore this dipole is oriented form the retina to the cornea. During the eye movements the dipole also changes its position and rotating adequately, thanks to these signals measurements of the eye movements are possible.

Figure 3 presents the measure of the horizontal eye movements. Two electrodes are placed outside of the left and right eye. If the eye is at rest, the electrodes have effectively this same potential and no voltage is recorded. The movement (rotation) of the eye causes change of the potential of the electrodes. For example, if eye rotates to the right, the right electrode is relatively positive to the second (left) electrode. The opposite move gives opposite effect, as illustrated in Fig. 3. Up to rotation of ca. 30 degrees the difference of the measured potential on the electrodes can be considered as proportional to the angle rotate, but beyond this limit the linearity becomes progressively worse. In this method spatial resolution can reach about 1 degree and maximum measured eye rotation can reach 70 degrees. The EOG has advantages and disadvantages. The main disadvantage is that corneoretinal potential is not fixed and changes as a result of act of light, fatigue, and other qualities. These are reasons of frequent calibration. Signal is measured with respect to a head. This enforces stabilization of the head, or there is a need to use some other devices
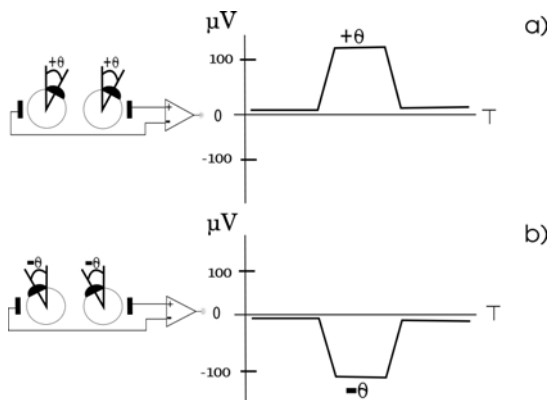
Fig. 3 Signal corresponding to the angle of eye rotation
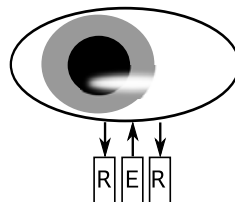
Fig. 4 Infrared light illuminated by an emitter (E) is received by phototransistor (R)

to tracking of the head movements. The measured signal is sensitive to muscle artifacts. As advantages we should classify: easy to use, even for children and patient confined to bed, the recordings may be made in total darkness and with closed eyes.

Infrared oculography. In this eye tracking method, eye is illuminated by infrared light which is reflected by the sclera (Fig. 4). A pair of sensors (phototransistor) registers reflected light and quantity of difference between sensors make possible to measure eye movements. The light source and sensors can be placed on special glasses.

The *infrared oculography* has less noise than EOG, but is more sensitive on changes of external light tension. The main disadvantage of this method is that it only works well for about 30 degree of eye deflection from the center. The advantages include ability to measure eye movements in darkness. Spatial resolution is about 0.1 degree. Setup is quick but the calibration is necessary. Like in EOG the measured signal is respected to the head, so another devices is needed to measure head movements if we want to have relatively free movements.

Video-based eye-tracking. This is the third method we used to track the eye movements. This method is base on an infrared source, which illuminates the eye and a camera for capturing an image of the eye. The result of such illumination is that the pupil is well visible and with big contrast to the rest of the eye. Beside this reflection occurs on the boundaries of the cornea. The cornea reflection center and the pupil center make a vector which is used for calculation degree of eye movements.

Usage of infrared light for illumination, makes that this method become useless for outdoors activities. During the daytime can occur too many artifacts. The main advantage is the possibility of usage of this method in remote and head-mounted systems. As presented in Fig. 5 each method of eye movements measurement has different features. These features allow to select the adequate method dependent on environmental needs.

In the proposed system, eye movements is obtained by multimodal method which choice is adequate to environmental needs. Idea of multimodal input for the system is illustrated in Fig. 7. Each method characterizes different output signal, therefore requires a specific preprocessor which yields previously defined tokens. These tokens are commands to execute for the command system (see Fig. 6 and Fig. 7).

Methods:	EOG	Infrared Oculography	Video based with infrared illumination
Spatial resolution:	1°	0.1°	1°
Temporal resolution:	500 Hz	500 Hz	25 60 Hz
Ability to record horizontal, vertical movements:	h = v = ±70°	h = ±30° v = ±20°	h = v = ±40°
Subject contact:	electrodes	glasses	head mounted or none if remote
Disadvantages:	- need preparing a skin for electrodes placement, - frequently calibration needed, - another device to measure head movements, - sensitive to muscle artifacts	- need calibration, - record small eye deflection, - sensitive on change of external light tension, - another device to measure head movements	- small temporal resolution, - useless in outdoors activities during daytime, - need another device to measure head movements (if head mounted), - subject must stay within a relatively confined area of operation (if remote)
Advantages:	+ easy to use, also for children and patient confined to bed, + recordings may be made in total darkness, + and with closed eyelids	+ fast setup, + recordings may be made in darkness, + high spatial resolution,	+ fast setup, + do not need calibration, + do not need another device to measure head movements (if remote), + no contact with subject (if remote)

Fig. 5 Comparison of features of three eyetracking methods

Command	Abbreviation
Left	L
Right	R
Up	U
Down	D
Error	E

Fig. 6 Five tokens (commands) refer to eyes movements
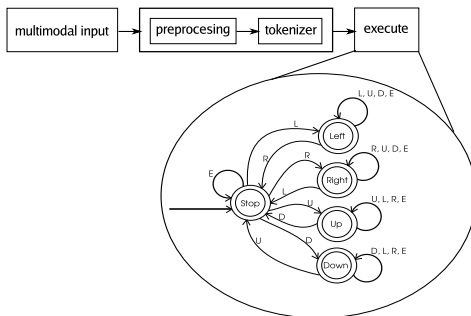
Fig. 7 Schematic diagram of selected eye movements interpretation

3 Results

Preliminary studies on detection of the subject's status and intention based on separate recording techniques led us to distinguishing of several subject-specific behavioral patterns (Fig. 8). Although the subject's status is determined with limited reliability (Table 1), thanks to the stability of everyday measurement conditions we are able to detect abnormality of subject behavior.

Table 1 Estimation of sensitivity [%] of individual methods and multimodal status recognition

recording modality vs. subject status	sleeping	walking	resting	working
Electrical activity of the heart	80	60	85	55
Mechanical activity of the body	70	90	70	75
Electrical activity of the brain	90	70	85	70
Multimodal status recognition	99.4	98.8	99.3	96.7

Fig. 8 Example of behavioral pattern recorded in the morning
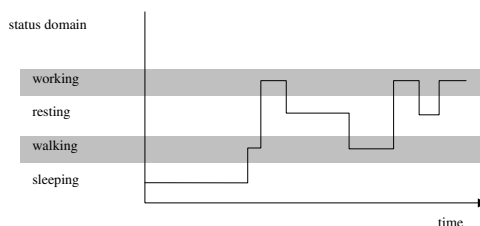
4 Discussion

The multimodal system for diagnostic and control aspects of assisted living has been sketched with consideration of the measurement method selection, their reliability, usability in home condition and costs. The novelty of our approach is twofold:

- contextual and conditional interpretation of measured parameters from multimodal acquisition,
- common status and command description at measurement and processing stages.

Expected reliability of the proposed system is still not sufficient to comply with requirements for medical-grade equipment. However in assisted living application, the main objective is to provide general information or alerts rather than precise medical data. Further tests in the prototype application are necessary to reveal weak points of this approach and to verify the usability in home condition.

References

1. Huang, D., Lin, P., Fei, D., Chen, X., Bai, O.: Decoding human motor activity from EEG single trials for a discrete two-dimensional cursor control. J. Neural Eng. 6, 046005, 12 pages (2009)
2. IEC 60601-2-51, Medical electrical equipment: Particular requirements for the safety, including essential performance, of ambulatory electrocardiographic systems, First edition 2003-02, International Electrotechnical Commission, Geneva (2003)
3. Juang, C.F., Chang, C.M.: Human Body Posture Classification by a Neural Fuzzy Network and Home Care System Application. IEEE Transactions on Systems, Man, and Cybernetics - part A: Systems and Humans 37(6), 984–994 (2007)
4. Kohler, B., Hennig, C., Orglmeister, R.: The principles of software QRS detection. IEEE Engineering in Medicine and Biology Magazine 21(1), 42–57 (2002)
5. Li, C.C., Chen, Y.Y.: Human Posture Recognition by Simple Rules. In: IEEE International Conference on Systems, Man, and Cybernetics, Taipei, Taiwan, October 8-11, pp. 3237–3240 (2006)
6. Liu, T., Inoue, Y., Shibata, K.: Development of a wearable sensor system for quantitative gait analysis. Measurement (2009), doi:10.1016/j.measurement.2009.02.002
7. Malik, M., Camm, A.J.: Heart Rate Variability. Wiley-Blackwell (1995)
8. Mensh, B.D., Werfel, J., Seung, H.: BCI Competition 2003-Data Set Ia: Combining Gamma-Band Power With Slow Cortical Potentials to Improve Single-Trial Classification of Electroencephalographic Signals. IEEE Transactions on Biomedical Engineering 51(6) (June 2004)
9. Moody, G.: MIT/BIH arrhythmia database distribution. MIT Division of Health Science and Technology, Cambridge (1993)
10. Najafi, B., Aminian, K., Paraschiv-Ionescu, A., Loew, F., Büla, C.J., Robert, P.: Ambulatory System for Human Motion Analysis Using a Kinematic Sensor: Monitoring of Daily Physical Activity in the Elderly. IEEE Transactions on Biomedical Engineering 50(6), 711–723 (2003)
11. La Rovere, M.T., Bigger Jr., J.T., Marcus, F.I., Mortara, A., Schwartz, P.J., ATRAMI Investigators: Baroreflex sensitivity and heart-rate variability in prediction of total cardiac mortality after myocardial infarction. Lancet 351(9101), 478–484 (1998)
12. Task Force of the ESC/ASPE, Heart rate variability: Standards of measurement, physiological interpretation, and clinical use. European Heart Journal 17, 354–381 (1996)
13. Wolpaw, J.R., Birbaumer, N., McFarland, D., Pfurtscheller, G., Vaughan, T.M.: Brain-computer interfaces for communication and control. Clinical Neurophysiology 113, 767–791 (2004)

Open Standards as a Basis of the Information Services Platform in Health Care Area

Kazimierz Frączkowski and Michał Szczepaniak

Abstract. Open standards and "open source" software are seen as those which are largely contribute to solving the problems of integration and interoperability in the newly-built computer information systems. In this work are presented views of the authors who propose certain conceptions and ideas about ICT in medical area based on the authors' opinions, observations and the need of introducing changes in the healthcare. The perception of XML as the information exchange format, evolution of the exchange systems and data processing in the context of building Electronic Platform to Collect, Analyze and Sharing Digital Resources about Medical Events are main issues in this work.

1 Introduction

At present, both in the development of information systems of the health care and in solving integration or interoperability problems, there are being used more and more new technologies of project production, project methods and project management. Alongside with the appearance of projects co-funded by UE financial appropriations, there occurred a requirement of interoperability as well as the requirement of durability of information solutions. It is proposed that in order to achieve these characteristics of ICT (*Informatics Communication Technology*) solutions there should

Kazimierz Frączkowski
Institute of Informatics, Wrocław University of Technology, Wyb. Wyspiańskiego 27, 50-370 Wrocław, Poland
e-mail: `kazimierz.fraczkowski@pwr.wroc.pl`

Michał Szczepaniak
e-mail: `michal.szczepaniak@hotmail.com`

be used "open source" solutions. However, in Poland and other countries, there are hundreds of hospitals and health care institutions that use applications which has been introduced and developed for the last several years by companies which not only protected their own code, but also implemented the data model. What is more, a lot of articles are being published by many authors among whom there can be distinguished Kathryn Edwards with his article from November 2009, entitled "Open Source non-panacea Health". Consequently, all these above mentioned articles tend to characterize and present the "Open Source" software as being a good pattern for the interaction in the e-Health, although this software should not be treated or considered as a panacea for all challenges appearing in the area of co-operation in the health care field.

Due to the fact that some central projects for numerous health care entities have been launched in order to co-operate with regional enterprises and local solutions already existing in ZOZs (healthcare establishments), the problem of interoperability becomes a very difficult key issue. Other countries which earlier had started to cope with this difficult matter, have their own ideas to lessen and moderate the problems; for example Malcolm Thatcher from CIO of Queensland Mather Hospital in Australia claims that one should commonly work on interoperability standards as well as standardise and propagate reference models in the area of health care processes.

It is becoming more and more doubtful to assume that the IKT technologies introduced in the health care during the last several years bring any organizational or business benefits. In fact, there is constantly being presented argumentation and evidence that is completely opposite to the one requested, expected or taken for granted [6]. Moreover, the economic cost bill of all the actions needed to provide given medical service must also include the IT infrastructure costs as well as its maintenance costs because of the fact that it is an element of costs which debit the medical benefits.

The holistic approach to the evaluation of both technology effectiveness and the mission of health care institutions effects in considering and treating the IT technologies equally with other technologies which support the therapeutic, diagnostic an other processes in the health care.

Nevertheless, so far the above mentioned approach has not been regarded as significant or taken into account due to the fact that the health care functions in a specific business environment which interprets and perceives in a different way the competition, need of continuous perfecting or the optimisation of business processes realised by other economic subjects. Central management mechanisms together with one insurer-NFZ (National Health Care) only contribute to the fact that the effectiveness and functionality of a" enterprise" are not priority features which characterize companies on the service market where there is a competition among entities. Moreover, detailed analyses of a subject's activity effectiveness possible to achieve by using the analytic systems of BI class (Business Intelligence) aim at presenting detailed information about the current business condition, results of operational activity [16].

2   Tendencies in the Development of System Integrations and Operability

Constantly increasing complexity of software, anticipation and servicing by the IS (Information Systems) generates new challenges and is the source of innovative solutions in approach to the integration and necessary changes in the IS area. Works on the 2.0 version of The European Interoperability Framework For Pan-European e Government Services were started in 2006. In the ongoing process of formation there occur considerable strains- it is mainly connected with the definition of open standards. If one kept the open standards definition proposed in the 1.0 version in the public sector, a lot of economic entities would have to adjust in order to meet given criteria, which is not a beneficial situation for them, hence there are so many attempts to exert pressure on among others: the redefinition of the open standards and their application. The 1.0 version from 2004 it is stated about the open standard that if:

- it is accepted and managed by a non-profit organization, and its development takes place through the open process of making decisions (consensus, majority of votes etc.) in which all to whom it may concern can take part.
- it is published and its specification is available for all to whom it may concern free of charge or charged only for making copies, and if it is made possible to copy, distribute and use by all to whom it may concern also free of charge or charged only for operational costs.
- all copyrights, patents or any industrial property connected with it are irrevocably available free of charge.
- the usage is not limited.

On the other hand, in the sketch of the 2.0 version, which is available at the website of Ministry of the Interior and Administration, the definition of the open standard and more specifically the definition of openness was reduced to the following three criteria:

- all individuals interested can take part in developing of the specification, and the very standard is verified publicly.
- the specification of the standard is available free of charge for everyone.
- The specification can be implemented with various models of software creators.

Thus, there were removed the notations about management of the standard by a non-profit organization as well as the notations about the copyright charges and any patents connected with it. Consequently, the document defines a new concept of "openness" instead of the formerly established "open standard" [4].

Contrary to EIF in 1.0 version, which was not officially published, 2.0 will be published in the Official Journal (pol. Dziennik Urzędowy- UE) but will only gain the status of an announcement conferred by the European Commission to the European Parliament Council. SOA (*Service Oriented Architecture*) architecture is one

of innovative solutions in approach to the integration in IS area. According to the Gartner Company, until the year 2010 there will be 80% customers using SOA architecture. Moreover, SOA is one of the 36 key technologies which according to Gartner will dominate the development of IT in the nearest future (except of it in the lead there are also Web 2.0 and Real World). Before 2011, 40% of demand for ICT infrastructure will be realised by companies in the form of services. In SOA approach, more attention should be paid to the modelling of business processes and therefore, the creation of applications and the work of computer programmers are greatly modified and changed [7]. The program code should be written in a universal way enabling a multiple use. IT experts expect reduction of the costs of information systems manufacturing and the increase of their flexibility [4].

The basis of advanced analytic systems is providing the analysts and managing personnel with the possibility of presenting forecasts, prognoses based on the data collected in given systems, e.g. financial, personnel. The success of a flexible extension of the information system is the possibility of extending it for a new service which is of new business value. The cost of hospitalization of a certain patient as an element of the analysis of procedures' cost, the number of treatments done in a given entity, the daily cost of a person in hospital etc. The evolutions of the development of analytic systems in Health Care can be basically presented in three stages as illustrated Fig. 1.

The first stage presents the manner in which the reporting and analysis of electronic medical data was conducted during the first years. First, the data existing in Hospital Information Systems were being exported to flat files like for example
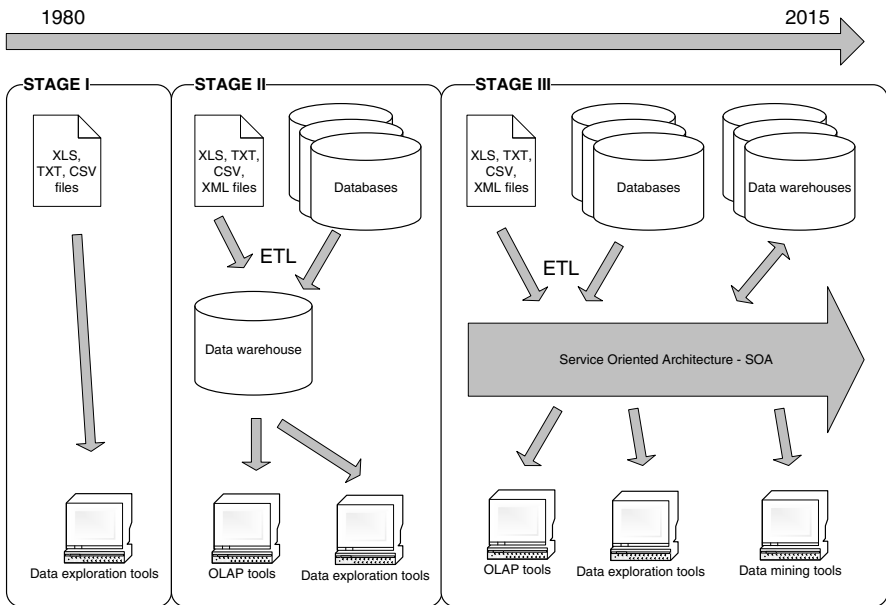
Fig. 1 The evolutions of the development of analytic systems in Health Care

TXT, CSV or above all the XLS and then opened in programs enabling operations on spreadsheets. Then, there was an arduous process of analyzing and converting of data done by the analytic departments as well as generating of specifications satisfactory for the hospital management. IT must be mentioned that this process was relatively long and determined the usage of dedicated applications. As a consequence, taking of any tactically important decision was ineffective because it was technically impossible. If one looks closer at the specifications of tenders put out to software by the departments of public orders, one will easily notice that all of those orders required from the purchased equipment the possibility of generating of the above mentioned files.

Nowadays, in the health care entities, there is constantly taking place the second stage of the development of processes of data analysis. The main cause of this situation is the fact that the NFZ (National Health Care) issued a regulation obliging all health care subjects to use the open format when exchanging statistic and billing data between the providers of services and the subjects responsible for refinancing of expenses and costs born while executing the medical procedures. The patterns of XML communicators were published, which effected in uniformity of data sent from different, heterogenic domain systems. As a consequence, information exchanged in this manner allows to a fluent and dynamic analysis of the up-to-date market, and this makes it possible to the establishment organs to manage their subsidiaries in an effective way.

The most important XML reports created by NFZ (National Health Care):

- The report of purchase invoices (FZX)
- The report of the queues of highly- specialist services (KOL)
- The report of hospital and ambulatory services
- The report of the billing of hospital and ambulatory services
- The report of the collective data about the services provided by POZ (GPs)
- The report of provision of the orthopaedic equipment and auxiliary materials
- The report referring to the waiting lists
- The report of POZ/KAOS declarations
- The report of the statistic report for chemists' [19]

The third stage of the process presents the vision of analytic systems' development, which will take place in future, and more precisely in the period between 2010 and 2015. It is a generation of analytic systems of class BI based on integration SOA bus-bar. Thanks to this approach, it will be possible to make multidimensional analyses while using countless autonomous domain systems, where the XML reports will the main data transmission media. As examples there may serve the following projects developed by the Ministry of the Interior and Administration and Ministry of Health: "e-PUAP"- electronic platform of public administration's services as well as the Electronic Platform of Storing, Analysis and Making Available of the Digital Resources of Medical Occurrences as written in the Plan of Informatization of Countries for the years 2007–2010 [14]. The concept of above mentioned systems suggests using the architecture that is focused on services, which is the ESB (*Enterprise Service Bus*) bus-bar as illustrated in the Fig. 2.
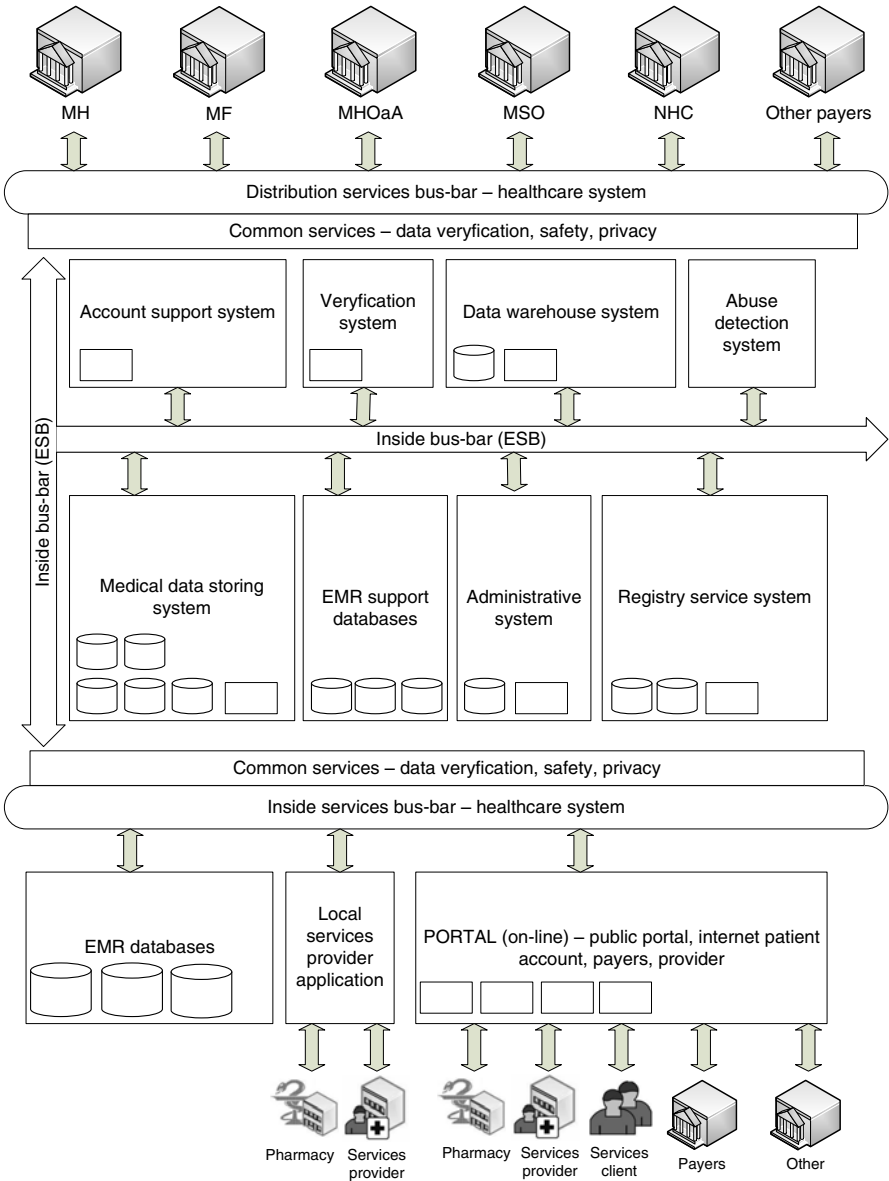
Fig. 2 The concept of above mentioned systems suggests using the architecture that is focused on services, which is the ESB (*Enterprise Service Bus*) bus-bar[based on 3]

The construction of the bus-bar consisting of open formats and web services allows to a safe and collision- free working of business systems and fluent exchange of information among them. It is worth to mention the fact that the use of web services gives countless possibilities of extending and modifying them as well as access by

means of web using any communication messages even so that the source application can be created in different technologies and working on different operation systems.

Using ESB bus will allow connecting the obsolete systems working in the health care entities with the new ones, which will appear. The very bus is the transitional, indirect layer- a broker, to which you can switch in or switch out functional modules which are part of the elements of health care. The specific characteristic of ESB makes it possible to send, transmit huge amounts of data at the same time retaining safety and homogeneity of communication mechanisms as well as the decreasing of redundancy, thanks to the opportunity of sending only the crucial data, which will contribute to the improvement of data exchange quality between medical registers, payers and the service providers.

The benefits from using the ESB will be noticeable in several years' time from the moment of implementation together with build-up and adding new business modules concurrent according to generally established standards. In the context op Polish Heath Care development, the benefits can have different dimensions depending on the type of the parts interested.

The application of homogeneous data storing rules about medical occurrences will be highly credible and reliable and that is why it will be possible to monitor and react to the dangers and emergencies appearing, for example to those of epidemic character. The billing and statistic departments will gain improved processes of billing for with payers medical services, and it all be possible thanks to introducing among others the electronic invoice service. According to this system, a Polish citizen is considered as the main beneficiary, and the range of her potential benefits is very wide.

Above all, the access to medical data will be gained by the medical personnel and will enable them to react properly in emergencies. What is more, there will be available new services which not only will improve the process of providing of the medical services but also will increase patients' awareness about their health condition. Thus, among these new services, there can be distinguished: on-line registering for medical appointments, access to the whole case history and the health condition of a patient from any place in the country (access to the Internet will only be required), storing and opening information about any referrals, medical certificates, sick leaves, prescriptions, recommendations, performed procedures, results of laboratory examinations, check-ups, vaccination plans. Moreover, thanks to a complete integration with source systems there will be implemented the electronic realization of prescriptions.

3   Open Standards – Information Exchange Format XML

There can be distinguished two types of standards: open standards and closed standards. Closed standards are the standards which are developed by a definite provider, can not be used without their author's consent and are subjected to some patent policy or protected by law. As far as open standards are concerned, they are defined in a

different manner [1, 2, 9] and among their characteristics, there can be enumerated the following: open standards created and developed through an open procedure available for all subjects; their specifications are publicly available; and their usage is completely legal and is not subjected to any technical or legal limitations. Additionally, the principal of technological neutrality is continually becoming more and more popular. As a consequence, according to this principle, the state or the government must introduce and use the open technological standards in all the areas where these standards are accessible [13, 19]. Apart from the lack of discrimination of providers, citizens gain the liberty to choose any tools that fulfil the standards available currently on the market. There are a lot of examples of application of this principle in the world. Thus, in Australia, the Australian National Archives proclaimed that the data in digital form collected by them will be saved in the Open Document form. What is more, Norway has also announced to use this principle and also successive American states have started using it.

Nowadays, disk drives of "5.25" type are not often found, and additionally an installed TAG program to read them properly, if such a program was available under e.g. Windows 7. Consequently, it means that the preservation of documents on a digital drive is not enough but the format, drive, software, which were stopped to develop in order to create documents, begin to cause many problems. The situation becomes even worse when it concerns the documentation of a project conducted for a long period of time or the data collected by the public administration. The drive on which documents have been saved turned out to be long-lived, however, its ability to be used quickly and with ease becomes limited or even impossible after some time.

In Poland, the legislator also defined the requirements concerning the manner in which the public subjects should use the open standards, e.g. in the Act on Informatization of Public Service from February 17 2005 there are notations in which the legislator declares that setting minimum standards to ensure openness of information, requirements for communication systems used to carry out public functions and for the public registers and exchange information electronically with public entities. Development of open standards in Poland is propagated by *Internet Society Poland* and *Coalition of Open Standards* [18].

One of the main factors that go hand in hand with standardization is the selection of a universal format for the exchange of information between operators, or systems. In the computer systems, in a medical environment, the most common standard for electronic exchange of information is HL7 (Health Level seven). It is used mainly for communication with hospital information systems, diagnostic systems (laboratory and radiological). Unfortunately, HL7 is a standard closed cell communication, which can not be expanded as required - same standard defines 27 types of messages [12].

Looking at the matter of closed message structure, you can attempt to state that it is one of the reasons why the XML language also enters to the health care systems. It was based on this language that the National Health Care has created the message structure which allows exchanging information, e.g. the statistic and billing information between the service providers and payers. Superiority of the XML over HL7 format primarily is that at any moment it may be expanded by adding other tags

describing the data by which the transmission is increasing and is unlimited or maybe it is limited but only by the information abundance of domain applications.

Language carries with it many features that do not restrict the choice of any sub-contractors in the construction of a computer system because it is not related to any platform or operating system. The text format of message and its internationalization makes possible the modification and reading to be done using the simplest text editor. In addition, compliance with Unicode in the form of UTF-8 allows you to use the full range of international characters, so it is possible to exchange information on a global scale. The European Union may be in the project epSOS (*European Patients Smart Open Services*)[5].

Another very important advantage is the extensibility feature of language and this extensibility can be viewed in two categories. Firstly, it is a resistance to changes in the structure of the XML message by the applications processing them. On the other hand because of the fact that XML is a meta language there is not a limited set of tags describing the data target. Data mining of medical events from the domain systems is the most important and most complicated and lengthy process occurring in the construction of analytical systems. Resistance to changes produced in the structure of the XML file, it is a feature that has a significant importance in the case of analytical systems and especially in the design and development stages of exploration, transformation and loading of data.

Combining harvesting of data from source systems and resistance to changes, we can distinguish two models of action. The first is to operate on the basis of the source database of the domain systems, the second is the action based on open formats of data exchange. The process of data mining from systems that do not support open formats is much more complicated and time consuming because it requires a careful analysis of the source database for each individual domain systems and analysis of their processes and patterns of action. An additional problem is the situation when the producer of such domain application modifies the structure of the database. This carries a need to modify the ETL scripts, otherwise the process of exploration will be stopped. This solution results in a forced necessity to make changes to the processes of exploration, transformation and loading of the data even if the changes do not influence the need for their analysis [8].

The issue of data mining looks quite different in the case of domain systems supporting the communication based on XML language, where the messages already containing the data sets are subjected to processing and not the structures without the database of given systems. Undeniable advantage is the fact that there appears an independence from changes because in the case of modification of XML message structures, the business applications continue to function, and the whole process takes place without any disturbances.

The only drawback is the lack of supporting the bran new tags by the domain applications and ETL scripts. In addition, in the case of large distributed systems, standardization of messages simplifies and unifies the form and thanks to this situation there takes place the independence from the manner of acting and domain system

building in the health care (eg, Hippocrates, Infomedica, Solmed , KS-Medis, Clin-iNet). Using open formats of data exchange brings with it another significant benefit, at the beginning barely noticeable, namely, there are significant savings associated with modifying of software when any changes in the structure take place. It is worth stressing that the medical systems used in Poland in the overwhelming majority are of heterogeneous nature, which is that they are made using various tools, languages, technology, without any developed model of the exchange of information.

4   Summary

In this work there are presented views of the authors who propose certain concep-tions and ideas about ICT in medical area based on the authors' opinions, obser-vations and the need of introducing changes in the healthcare. Therefore, the paper indicates that practical and useful dimension of ICT, which permanently entered to the stage of implementation in very large projects which have had the most out-standing budgets, execution time, number of stakeholders and the estimated number of transactions in the history of Polish. The Electronic Platform of Storing, Analy-sis and Making Available of the Digital Resources of Medical Occurrences has to handle more than 550 million prescriptions implemented at more than 10,500 phar-macies, which are printed by physicians annually in Poland. The medical events are to be of the following relationship: patient - the doctor - Health Care subjects, such as access via the Internet for approximately 38 million potential patients who are in contact with more than 340 thousand medical personnel.

According to the statistics of Standich Group and Gartner's research, projects of this class are the ones that are most threatened by failure. Spectrum of potential sources of risks that may arise is significantly different for various services to be available in projects. Taking into account e.g. a planned opening of medical data, so called EHR (Electronics Health Record) through IKP (Individual Patient's Ac-count), one should indicate the following hazards:

- Problems in communication necessary to achieve interoperability, given the am-bitions of the project stakeholders about the role of project
- encapsulation of access to information within the corporation
- Excessive focus on technology and information security problems
- Natural, non- verbalized fear of the "new"
- Bad or unconvincingly defined goals and benefits for stakeholders IKP
- Enemy interface IKP and social exclusion of older population
- Limited public confidence in the placement of data on the Internet

A separate problem within the cohesion and interoperability of the projects such as The Electronic Platform of Storing, Analysis and Making Available of the Digital Resources of Medical Occurrences will accept Medical will be the acceptance and arrangement of open formats within introduced ICT technologies and services.

References

1. Cerri, D., Fuggetta, A.: Controversy Corner: Open standards, open formats, and open source. J. Syst. Softw. 80(11), 1930–1937 (2007)
2. Edwards, K.: Open source no panacea for e-health, Comuterword (November 2009)
3. Elektroniczna Platforma Gromadzenia, Analizy i Udostępnienia zasobów cyfrowych o Zdarzeniach Medycznych. Centrum Systemów Informacyjnych Ochrony Zdrowia. Ernest &Young, Warszawa (2009)
4. European Interoperability Framework for European Public Services (EIF) Version 2.0, `http://www.mswia.gov.pl/download.php?s=1&id=10012`
5. European Patients Smart Open Services, `http://www.epsos.eu/`
6. Frączkowski, K.: Bazy danych w e-zdrowiu i telemedycynie - standardy informatyczne w regulacji UE. W: Bazy danych. Struktury, algorytmy, metody. Praca zbiorowa pod red. S. Kozielskiego [i in. T. 2]. Wybrane technologie i zastosowania. Wydawnictwo Komunikacji i łączności, Warszawa (2006)
7. Frączkowski, K., Mazur, Z.: SOA - architektura zorientowana na usługi. Prace Naukowe Instytutu Informatyki Stosowanej Politechniki Wrocławskiej. Bazy Danych. z. 7, 21–28 (2006)
8. Fryźlewicz, Z., Salamon, A.: Podstawy Architektury i Technologii Usług XML Sieci Web. PWN, Warszawa (2008)
9. Fuggetta, A.: Controversy corner: open source software-an evaluation. J. Syst. Softw. 66(1), 77–90 (2003)
10. IDABC: The European Interoperability Framework for pan-European eGovernment Services (2004), `http://europa.eu.int/idabc/en/document/3761`
11. Krechmer, K.: Open Standards Requirements. The International Journal of IT Standards and Standardization Research 4(1), 43–61 (2006)
12. Polska wersja narodowa standardu HL7. Lublin (2004), `http://www.uhc.lublin.pl/uhc/standar1.htm`
13. Rozporządzenie Ministra Zdrowia z dnia 20 czerwca 2008 r. w sprawie zakresu niezbędnych informacji gromadzonych przez świadczeniodawców, szczegółowego sposobu rejestrowania tych informacji oraz ich przekazywania podmiotom zobowiązanym do finansowania świadczeń ze środków publicznych (Dz.U. Nr 123, poz. 801). Warszawa (2008)
14. Rozporządzenie Rady Ministrów z dnia 28 marca 2007 r. w sprawie Planu Informatyzacji Państwa na lata 2007-2010 (Dz. U. z dnia 6 kwietnia 2007 r.). Warszawa (2007)
15. Sun Microsystems, JCP 2: Process document, The formal procedures for using the Java Specifications development process (2004), `http://www.jcp.org/en/procesures/jcp2`
16. Surma, J.: Business Intelligence - Systemy wspomagania decyzji biznesowych. PWN, Warszawa (2009)
17. Ustawa o systemie informacji w ochronie zdrowia - projekt. Warszawa (wrzesień 2007)
18. Ustawa z dnia 17 lutego 2005 r. o informatyzacji działalności podmiotów realizujących zadania publiczne (Dz.U.2005.64.565). Warszawa (2005)
19. Zarządzenie Nr 4/2009/DŚOZ Prezesa Narodowego Funduszu Zdrowia z dnia 9 stycznia 2009 r. w sprawie określenia szczegółowych komunikatów sprawozdawczych XML dotyczących świadczeń ambulatoryjnych i szpitalnych (I fazy) oraz rozliczenia świadczeń ambulatoryjnych i szpitalnych (II fazy). Warszawa (2009)

Application of Motion Analysis Systems in the Designing of a Rehabilitation Device

Robert Michnik, Jacek Jurkojć, Zbigniew Paszenda, Andrzej Michnik,
Michał Bachorz, Wiesław Rycerski, and Jan Janota

Abstract. The paper presents the results of kinematic analysis of the prototype of rehabilitation device for human upper limb. The aim of these measurements was to assess possibility to execute PNF movements in upper limb joints and correctness of functioning of control algorithms responsible for reproducing of assigned movements The measuring site consisted of a set of 4 digital cameras, computer workstation, a set of markers, calibrating dice and light sources. Measurements were carried out for simple and complex movements. First a man forced a motion sequence, and then the device had to repeat it. Measurements revealed necessity of changes in constructions due to unacceptable positioning inaccuracy. Exemplary results before and after these changes are presented in the paper.

1 Introduction

Daily activities, like walking, lifting, reaching, sitting down, standing up, executing by healthy people, are based on complex movements of human body. They all

Robert Michnik · Jacek Jurkojć
Silesian University of Technology, Department of Applied Mechanics, Konarskiego 18a,
44-100 Gliwice, Poland
e-mail: robert.michnik@polsl.pl, jacek.jurkojc@polsl.pl

Zbigniew Paszenda
Silesian University of Technology, Institute of Engineering Materials and Biomaterials,
Konarskiego 18a, 44-100 Gliwice, Poland
e-mail: zbigniew.paszenda@polsl.pl

Andrzej Michnik · Michał Bachorz
Institute of Medical Technology and Equipment, ITAM", Roosevelta 118, 41-8004 Zabrze,
Poland
e-mail: andrzejm@itam.zabrze.pl, Michal.bachorz@itam.zabrze.pl

Wiesław Rycerski · Jan Janota
Upper Silesian Rehabilitation Center "Repty", Śniadeckiego 1, 42-604 Tarnowskie Góry,
Poland
e-mail: wieslaw.rycerski@wp.pl

consist in the correct execution of the, correct motion standard. The correct execution of the motion depends both on the correct operation of the central nervous system, spinal cord, peripheral nerves and skeletal muscles. Loss of motion ability is caused by injury of one ore some of these elements. Restoration of health needs complicated rehabilitation. Some rehabilitation methods of such injuries base on teaching movements similar to these carried out by healthy people during daily activities. It enables patients to learn complicated movements and use them in their lives. One of the rehabilitation method, based on the described way, is the PNF method. It consisted in repeated movements, both passive and active, carried out by patient but with the help of physiotherapeutist [1, 2, 3, 4].

Because these movements must be carried out many times and in a very similar and proper way, the PNF rehabilitation method is very time consuming and tiring. That's why, within the confines of cooperation between Silesian University of Technology, Institute of Medical Technology and Equipment „ITAM" Upper Silesian Rehabilitation Center „Repty", the prototype of the device, which enables executing rehabilitation exercises of upper limb was designed. According to physiotherapeutists hints this device should enable execution of repeatable PNF exercises, reproducing motion showed by a doctor.

Spatial motions, carried out in the PNF method, impose many restrictions on the device construction. This construction should be similar to the upper limb kinematic chain, enables exercises in all planes and in the same time does not collide with patient's body. Additionally moments of forces in individual kinematic pairs force application of relatively big driving units. This heavy construction together with mass of the upper limb pose a problem for the control system. To ensure patients safety there must be permanent control of moments in kinematic pairs. System must 'know' if the moment of force is caused by the device weight or by the patient wanted to stop execution of the program because of, for example, pain. Additionally repeatability of exercises is very important both for the sake of rehabilitation method and safety of the patient. That was the reason of the necessity to carry out some measurements showing how correct and repeatable are movements conducted by the device. The way of carrying out these measurements and some results are presented in this paper.

2   Methodology

To ensure the correctness of functioning of the device prototype many measurements were carried out. One of them concerned kinematics of the motion. Authors decided to carry out experimental measurements to check:

- possibility to execute isolated movements in individual upper limb joints,
- correctness of functioning of control algorithms responsible for reproducing of assigned motions.

Kinematic quantities were determined by means of the motion analysis APAS system. On the characteristic points of the device some markers were placed (Fig. 1). The motion was recorded by four Basler digital camcorders with frequency 100 Hz.

Then recorded movies were processed in the APAS system and positions of markers were determined. This enabled calculation of trajectories of individual markers and then relative angle displacements of individual device segments. All calculations were carried out in MATLAB system by means of the program prepared by authors of this paper [5, 6, 7].
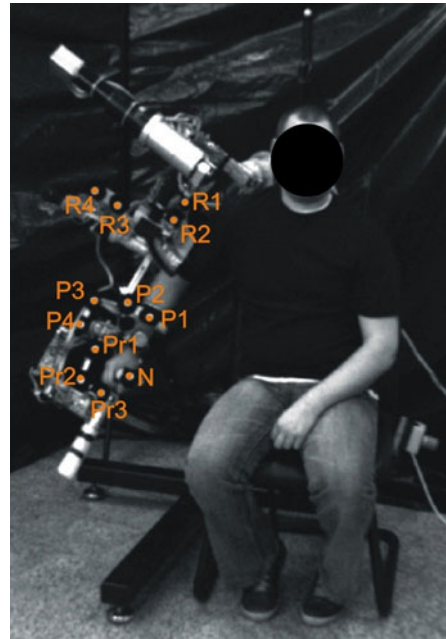
Fig. 1 Marker placement on the device

The following movements were registered and analyzed during investigation:

- simple movements
- shoulder flexion and extension (Fig. 2),
- shoulder adduction and abduction,
- shoulder rotation,
- elbow flexion and extension,
- elbow rotation,
- movements in the ankle joint,
- spatial movements similar to PNF exercises.

All registrations were carried out for movements of the device:

- forced by the upper limb motion,
- repeated by the device by means of the control system.
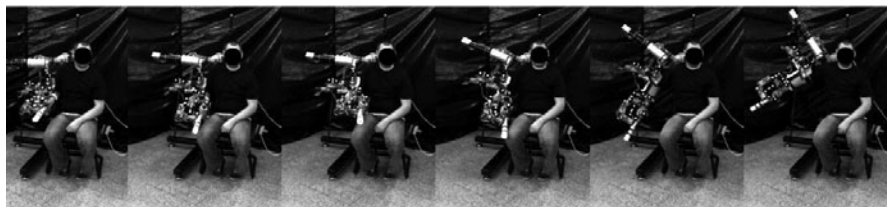
Fig. 2 Movement sequence for the shoulder flexion and extension

3 Results and Discussion

Measurements were conducted on two stages of the design process. The first stage showed that movements of some device elements is not smooth enough. Additionally slight vibrations were noticed in some movements. It was visible in the recorded movies and was confirmed by mathematical kinematic analysis. Moreover there were differences between trajectories obtained for movements forced and repeated. Analyses of markers displacement showed that differences reached even 20 cm, that was unacceptable result (Fig. 3, Fig. 4). On the basis of observations and calculations some changes in the device construction had to be conducted. Kinematic analysis showed necessity of reconstruction of some kinematic chain drives. Additionally a new function in the control system - visualization of vectors of forces acting in individual sensors - was implemented. This visualization showed that the correct sensor placement is the main problem and helped to improve the construction. After these changes the new kinematic analysis was carried out. Measurements and calculations were conducted similarly to these in the first part of verification and for the same movements. Exemplary results are showed in Fig. 5 and Fig. 6. The analysis showed that changes implemented in the device significantly improved accuracy of repeated movements in comparison with these forced by physiotherapeutist.

Fig. 3 Trajectories of the chosen markers before changes in the device construction (thick line - trajectories of the forced motion, thin line - trajectories of the repeated motion)
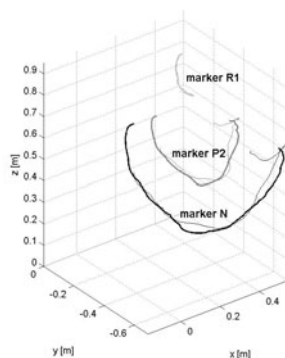
Fig. 4 Displacements of marker P2 with respect to coordinate system axes
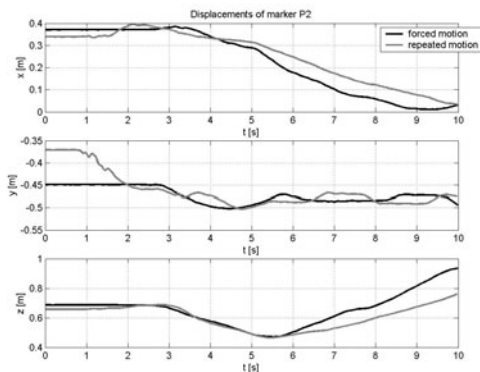
Fig. 5 Trajectories of the chosen markers after changes in the device construction (thick line - trajectories of the forced motion, thin line - trajectories of the repeated motion)
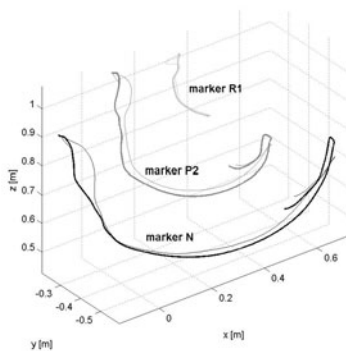
Fig. 6 Displacements of marker R1 with respect to coordinate system axes
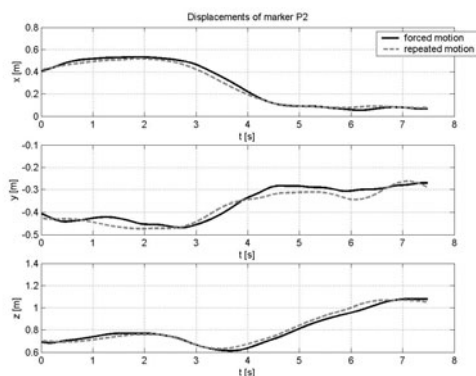
4   Conclusions

Analysis of obtained results and verification tests conducted after some changes in the device construction and control system shows significant improvement in the device positioning. The accuracy of repeated movements was much better too. Changes between trajectories obtained for movements forced and repeated decreased to only 5 cm. Also analysis of angle displacements showed good accuracy of repeated movements. But for some movements even this 5 cm can by to much what indicates the necessity of further changes in the device construction and control system.

References

1. Kokosz, M., Klukowski, K., Łoza, T., Saulicz, E., Plinta, R., Zembaty, A.: Kinezyterapia tom 1. Wydawnictwo Kasper, Kraków (2002) (in Polish)
2. Kwolka, A.: Rehabilitacja medyczna pod redakcją Andrzeja Kwolka, Tom II - Rehabilitacja Kliniczna. Wydawnictwo Medyczne Urban & Partner, Wrocław (2003) (in Polish)
3. Zembaty, A. (red.): Kinezyterapia - tom II. Wydawnictwo Kasper, Kraków (2003) (in Polish)
4. Blauth, W.: The CPM therapy with motorized exercise devices. Urban & Vogel, Munchen (1992)
5. Michnik, R., Jurkojć, J., Rak, Z., Mężyk, A., Paszenda, Z., Rycerski, W., Janota, J., Brandt, J.: Kinematic Analysis of Complex Therapeutic Movements of the Upper Limbs. In: Information Technologies in Biomedicine. AISC, vol. 47, pp. 551–558. Springer, Heidelberg (2008)
6. Robert, M., Jacek, J., Paweł, J., Agata, G., Dagmara, T.: Analysis of gait kinematics of patients after total hip or knee replacement. Journal of Vibroengineering, Vilnius 8(3), 15–18 (2006)
7. Michnik, R., Jurkojć, J., Rak, Z., Mężyk, A., Paszenda, Z., Rycerski, W., Janota, J., Brandt, J.: Analiza kinematyki ruchów kończyny górnej podczas wykonywania ćwiczeń rehabilitacyjnych metodą PNF. Modelowanie Inżynierskie 36, 243–248 (in Polish)

Control System for a Limb Rehabilitation Robot

Andrzej Michnik, Jacek Brandt, Zbigniew Szczurek, Michał Bachorz,
Zbigniew Paszenda, Robert Michnik, and Jacek Jurkojć

Abstract. Limb disability, which in many cases results from disease or injury, impairs everyday actions and limits job opportunities. Treatment consists of physical therapy that requires laborious repetition of recommended motions with the help of an experienced physiotherapist. Robot-aided exercises for repeatable rehabilitation motions would allow speeding up the rehabilitation process and reduce its costs. This work presents a concept of a control system for a rehabilitation robot constructed for this aim. The solution has been verified with the prototype robot ARM-100 for upper limb rehabilitation with the control system based on the assumptions discussed in this paper.

1 Introduction

There is an increasing number of patients in the world who require improving their limb motion, both upper and lower limbs. There are many reasons for this, which include the process of an ageing society and changes in lifestyle leading to many diseases impairing motion ability. Such diseases include: paretic limb after

Andrzej Michnik · Jacek Brandt · Zbigniew Szczurek · Michał Bachorz
Institute of Medical Technology and Equipment ITAM, Roosevelta 118, 41-800 Zabrze, Poland
e-mail: andrzejm@itam.zabrze.pl, jacekb@itam.zabrze.pl,
zbyszcz@itam.zabrze.pl, michal.bachorz@itam.zabrze.pl

Zbigniew Paszenda
Silesian University of Technology, Institute of Engineering Materials and Biomaterials, Konarskiego 18a, 44-100 Gliwice, Poland
e-mail: zbigniew.paszenda@polsl.pl

Robert Michnik · Jacek Jurkojć
Silesian University of Technology, Department of Applied Mechanics, Konarskiego 18a, 44-100 Gliwice, Poland
e-mail: robert.michnik@polsl.pl, jacek.jurkojc@polsl.pl

strokes, limb injuries, cervical spine injuries, craniocerebral traumas, osteoarthritis, reumathologic diseases, muscular dystrophies, diseases of the nervous system, and conditions after orthopaedic treatment, etc. Disabilities occurring after these diseases impair everyday actions, cause pain complaints, decrease the quality of life and limit job opportunities [1, 2].

Treatment of such diseases and elimination of disabilities caused by them is lengthy, requires much more and engages many people. At present it is impossible to imagine modern medical treatment without rehabilitation or physical therapy. One of the rehabilitation methods often used is PNF (Proprioceptive Neuromuscular Facilitation). It consists of performing with the patient repeated limb multi-plane motion sequences, so-called motion patterns. In this method, exercising engages the physiotherapist tremendously as he or she repeats the set patterns with patients, which limits the patients' access to frequent enough rehabilitation sessions [3, 4, 5].

Nowadays, for upper and lower limbs, robot-aided rehabilitation is increasingly used. The robots usually perform one-plane motions, used in the rehabilitation of single joints [6, 7, 8, 9]. For example, devices used in upper limb rehabilitation allow for rehabilitation of: fingers and the wrist joint - Kinetec 8080, elbow joint - Artromot-E, or shoulder joint - Kinetec Centura Shoulder CPM. Recently, ARMin, a device for upper limb multi-plane rehabilitation, has been developed at the Zurich University of Science and Technology with the cooperation of the company Hocoma and therapists from the Zurich Clinic in Balgrist. Initially, it had six degrees of freedom, four of which were power-driven and two of which were passive. The kinematic scheme from the shoulder joint to the forearm was provided. The next version has been added with two degrees of freedom that allow for the forearm and wrist motion. Although the device in this shape allows performing nearly all basic and complex exercises, they cannot be performed with the PNF method due to the limited range of the exercises [10]. Another example is a prototype of arm exoskeleton ARAMIS developed by S. Anna Institute and RAN - Research on Advanced Neuro-rehabilitation [12, 13].

A solution that allows increased access to the PNF rehabilitation method is the use of a robot which repeats with the patient the preset patterns which reproduce the multi-plane motions without the physical therapist [14, 15]. The physical therapist would only introduce the motion pattern to the memory of the robot connected with the rehabilitated patient's limb and set the speed and number of repetitions. This solution would enable one qualified physical therapist to perform rehabilitation for several patients at a time. This paper presents assumptions and a description of the robot control system which allows performing complex multi-plane motions: passive, active and resisted motions, of a similar range and dynamics to those used in natural activity.

2 Assumptions of the Control System

The rehabilitation robot is a mechanical frame with drives which after attaching to the patient's limb will enable rehabilitation motions and repeating them for pre-set
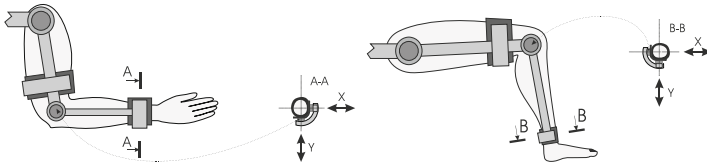
Fig. 1 General concept of the rehabilitation robot control

times. The basic issue to solve is how to connect the control system with the robot's mechanical system. Here, the system has been divided into autonomous nodes controlling the robot's drives. The node controlling one drive is connected with one or two force sensors so that the force put to the limb by the drive would be measured by the given node controller - Fig. 1. The node is understood here as a system performing a simple motion along one axis (e.g. of an elbow joint or knee joint). Dividing the control system into individual nodes enables the autonomous control of a selected drive. Such a solution facilitates the control of forces put by the limb both in the case of passive and active motion (reconstructing and performing the motion). Another crucial problem to solve is the appropriate location of the force sensors on individual construction elements of the robot for achieving the required sensitivity and selectivity of force measurement.

3 Construction of the Robot Control System

The rehabilitation robot control system consists of three elements: modules of measurement and performance nodes, communication module and a PC with the control software - Fig. 2. The idea of control is based on a cyclical information exchange between the PC controlling program and the measurement and performance modules. The PC programme allows changing the mode of each node to the motion tracing mode or position changing mode. The PC programme also makes it possible to change many settings configuring the node, e.g. settings of controllers stabilising
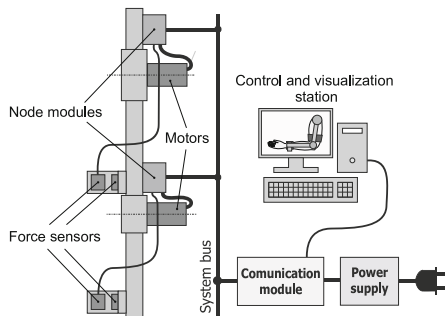
Fig. 2 Construction of the robot control system

the drive speed or position. In each cycle of the data exchange, the PC Programme sends new working settings to the measurement and performance modules, which create the information on the node working mode and settings. In response, the node modules send information on the working settings, such as: angular positions, speeds, PWM duty cycle, temperature or power supply current.

Communication of the PC based control program with measurement and performance modules of the robot nodes takes place with the use of the communication module. The communication module also acts as the drive power supply emergency cut-out. The PC with the control program enables remembering the motion trajectory of the rehabilitated limb as a training programme and for re-performing the remembered training programme through suitable control of the measurement and performance nodes. During the training session, the system operator starts recording the model training trajectory and after completion, starts performance of the recorded trajectory. The programme acts as a particular motion "recorder". Each of the recorded trajectories can be saved to the hard disc for further comparison of the rehabilitation progress.

4   Construction of the Measurement and Performance Node

The role of the measurement and performance nodes is to control the node operational settings, controlling a single drive and autonomous prevention of emergency situations to the rehabilitated patient or controlled drive. The operating element of each node is a brushless DC motor (BLDC) with Hall-effect sensors built-in. The module performs the following measurement functions:

- measurement of drive relative position on the basis of the Hall-effect sensors built in the motor,
- measurement of absolute drive position in the basis of a Hall-effect angle sensor located in the axis of the turning arm,
- measurement of the motor rotational speed on the basis of the Hall-effect sensors built in the motor,
- measurement of the pressure force from dial extensometers at the human-robot contact,
- measurement of power MOSFET temperature,
- measurement of the motor power supply current based on the Hall-effect current sensor.

The node controller enables flexible configuration from the control program level on the PC. An example of this flexibility is the measurement of force performed by the node controller. The controller has two analogue measurement inputs, while only one of them is equipped with a measuring differential amplifier for direct connection of the extensometric beam. The node controller makes it possible to select
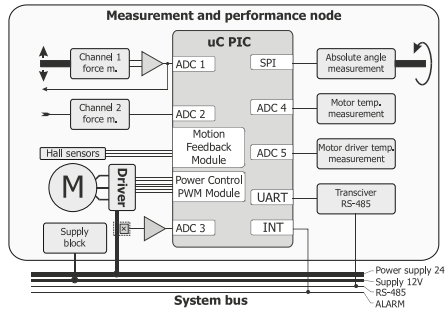
Fig. 3 Construction of the measurement and performance node

controlling the node from the force measuring input 1 or 2, to set negative value or to set a measurement which is a sum or difference between force measuring inputs - Fig. 3.

Modules of node controllers are designed to be connected in pairs and in such a configuration the signal amplified by a differential amplifier from the 1st measuring channel is connected to the 2nd channel of the second node controller module. Such a solution enables controlling two drives joined into a pair, where one drive is controlled by a sum of forces and the other by the difference between them, which can be used to control the wrist or ankle joint drives - Fig. 4. Additionally, the controller allows for individual setting of the measuring channel amplification and the insensitivity threshold, which limits the influence of the sensor system hysteresis in the modes of motion tracing on the basis of the force sensors' readings.
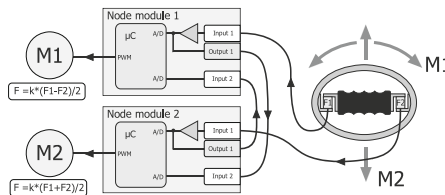
Fig. 4 Scheme of joining nodes into pairs with the example of a hand grip

Each node of the robot can operate in several operation modes but the most useful are the following two: motion tracing mode and position stabilising mode. The motion tracing mode [11] is used mainly for programming the rehabilitation trajectory but it also allows for performing active training by appropriate setting of the insensitivity threshold of the force measurement trajectory. The position stabilising mode allows for passive training during which the robot performs the previously saved rehabilitation motion pushing the robot elements to subsequent, pre-set points. Sufficiently frequent sending of a new position creates a smooth motion which precisely reproduce the motion set by the physical therapist. A simplified algorithm of
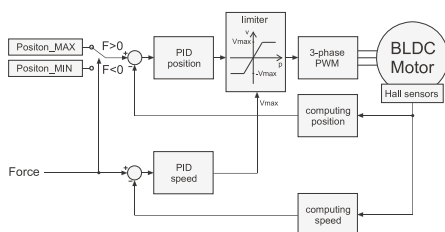
Fig. 5 Block diagram of the motion tracking algorithm

the measurement and performance module operation in the motion tracing mode is shown in Fig. 5. The main elements of the system are two PID regulators. The first regulator stabilises the drive rotational speed which is directly proportional to the force applied. The other regulator stabilises the position, which ensures limitation of the motion range within a given node. The force direction switches the position regulator between two states and changes the position to MAX or to MIN. However, the element is moved only when an appropriate force is applied which exceeds the pre-set insensitivity threshold of the force measuring trajectory. The speed of motion is directly proportional to the force applied, provided we are within the allowed motion range. The position regulator enables automatic speed reduction to zero if the moved element reaches the motion range limits.

5 Verification of the Concept of a Rehabilitation Robot Control System

The prototype robot ARM-100 with 7 degrees of freedom for upper limb rehabilitation has been constructed - Fig. 6, while work on the prototype robot for lower limb rehabilitation is at the point of defining the trajectories of complex motions required for their rehabilitation. The graph in Fig. 7 presents comparison of trajectories of selected markers located on the arm of the prototype robot ARM-100 for upper limb rehabilitation.

In the tested prototype robot ARM-100, the motion performed from the control system's memory differed from the preset motion by a maximum of 5cm. The average deviation between the preset motion displacement and the performed motion displacement did not exceed 2 cm. The main reasons of difference between preset and performed motion trajectories are gear backlash and clutch backlash, which can be corrected in the next construction. The analysis of angular displacement of each element also demonstrated quite precise motion performance. Analysis of results also indicated it is necessary to continue work on optimising the structural form of the device, particularly within the shoulder joint. Analysis of motion trajectories of the upper limb rehabilitation robot arm has revealed that the developed system to meets the design assumptions well.
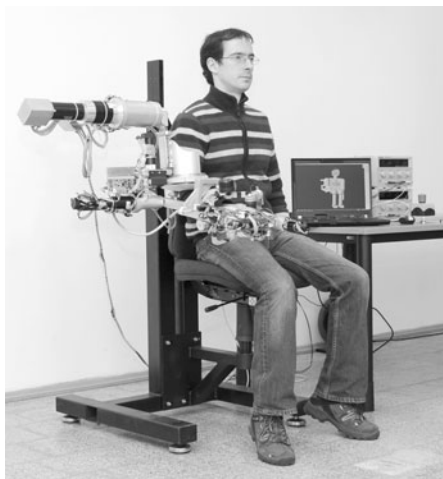
Fig. 6 Prototype robot ARM-100 for upper limb rehabilitation
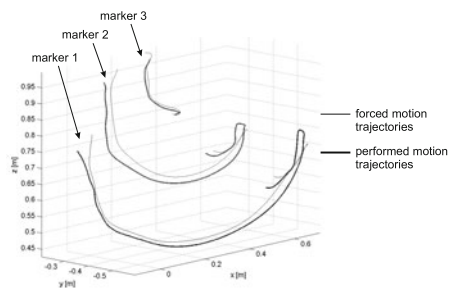
Fig. 7 Motion trajectories of markers located on the rehabilitation robot

6 Conclusions

On the basis of the aforementioned analysis, the following general conclusions may be drawn:

1. The aptness of the selected robot control concept has been confirmed by the construction of the prototype robot for upper limb construction and its testing which has demonstrated high repeatability of motion patterns.
2. Construction of a commercial version of such a robot must be preceded by work on the optimization of individual functional nodes, developing a software version adjusted to practical use, as well as a practical solution on how to fix the patient's limb to the robot's arm.

3. Experiences gained during work with the robot for leading a multi-plane motion of the upper limb have shown it is probable that after taking into consideration the specificity of the lower limb motion, in particular higher loads, the design of the robot for leading the lower limb motion should be successful.

References

1. Zambaty, A.: Kinezyterapia. Wydawnictwo Kasper, Kraków (2002)
2. Kwolek, A.: Zasady rehabilitacji szpitalnej chorych po udarze mózgu. Postępy Rehabilitacji (2004)
3. Blauth, W.: The CPM therapy with motorized exercise devices. Urban & Vogel, München (1992)
4. Blauth, W.: Übungsgeräte zur CPM-Behandlung. Grundlagen, Merkmale, Erfahrungen. Med. Orthop. Tech. 111, 178–186 (1991)
5. Blauth, W.: Gegenwart und Zukunf der CPM-Behandlung. Orthop. Prax., 684–690 (1991)
6. Milanowska, K.: Kinezyterapia. Wyd. Lek. PZWL, Warszawa (2003)
7. Marciniak, J.: Sprzęt szpitalny i rehabilitacyjny. Wydawnictwo Politechniki Śląskiej, Gliwice (2003)
8. Kiwerski, J.: Rehabilitacja medyczna. PZWL, Warszawa (2005)
9. Whyte, J., Hart, T., Borde, A., et al.: Rehabilitation of patient with traumatic injury. In: De Lisa, J.A., Gans, B.M., Bockenek, W.L., et al. (eds.) Rehabilitation medicine - principles and practice, 3rd edn. Lippincott-Raven, Philadelphia (1998)
10. Materiały firmy ETH Zentrum: Robot wspomagający terapię ruchową. Przegląd Mechaniczny, zeszyt XI, pp. 3–4 (2006)
11. Pons, J.L.: Wearable Robots: Biomechatronic Exoskeleton. In: Bueno, L., Brunetti, F., Frizera, A., Pons, J.L. (eds.) Human-robot cognitive interaction. Wiley, Chichester (2008)
12. Dolce, G., Lucca, L.F., Pignolo, L.: Robot-assisted rehabilitation of the paretic upper limb: Rationale of the ARAMIS project. J. Rehabil. Med. (2009), doi:10.2340/16501977-0406
13. Colizzi, L., Lidonnici, A., Pignolo, L.: The ARAMIS project: A concept robot and technical design. J. Rehabil. Med. (2009), doi: 10.2340/16501977-0407
14. Michnik, R., Jurkojć, J., Rak, Z., Mężyk, A., Paszenda, Z., Rycerski, W., Janota, J., Brandt, J.: Kinematic analysis of complex therapeutic movements of the upper limb. In: Information Technologies in Biomedicine. AISC, vol. 47, pp. 551–558 (2008)
15. Michnik, R., Jurkojć, J., Rak, Z., Mężyk, A., Paszenda, Z., Rycerski, W., Janota, J., Brandt, J.: Analiza kinematyki ruchów kończyny górnej podczas wykonywania ćwiczeń rehabilitacyjnych metodą PNF. Modelowanie Inżynierskie (36), 243–248 (2008)

Methodology of Examining Fracture Surfaces of Biomaterials by Means of Modelling and Multifractal Analysis

Sebastian Stach and Zygmunt Wrobel

Abstract. The aim of the study was to take advantage of a three-dimensional minimal spanning tree (3DMST) to model the crack process of materials, based on an example of a metallic biomaterial. The modelling of the crack process and its characterization were carried out on a stereometric measuring file acquired as a result of surface analyses of the biomaterial examined, using confocal microscopy.

Analysis of issues related to the crack process requires a quantitative description of the problem which frequently, due to its complexity, is difficult or impossible to solve. In a number of cases, the deficiencies of a quantitative description made using classical methods are compensated for by unconventional mathematical tools, such as the multifractal analysis, which was carried out for the obtained model of the crack path.

1 Introduction to the Problem

Biomedical materials, including metals and alloys intended for orthopaedic implantation, should be distinguished by the following properties: good corrosion resistance, appropriate mechanical properties, good metallurgical quality and homogeneity, histocompatibility, resistance to abrasion and wear, no tendency to forming blood clots, proper electrical properties and acceptable production costs.

The essential problems of implantology, when selecting the properties of biomaterials and implants, include, undoubtedly, the biomechanical issues [5, 4]. The analysis of strain and stress in anatomical structures faces considerable difficulties. Therefore, an analysis of surface properties followed by modelling desirable properties of the surface, which modelling should in the best possible way reflect the

Sebastian Stach · Zygmunt Wrobel

Department of Biomedical Computer Systems, Institute of Computer Science, Faculty of Computer and Materials Science, University of Silesia in Katowice, ul. Bedzinska 39, 41-200 Sosnowiec, Poland

e-mail: `sebastian.stach@us.edu.pl, zygmunt.wrobel@us.edu.pl`

real object and thus, its generalized properties, is becoming a topical issue on the borderline between technology and medicine.

In paper [13], computer modelling and a three-dimensional minimal spanning tree [8] were used to reconstruct the crack path on a stereometric measuring file of fracture surface. Based on the physical model so built, an attempt can be undertaken to build a mathematical model [1].

Analysis of issues related to the crack process requires a quantitative description of the problem which frequently, due to its complexity, is difficult or impossible to solve. In a number of cases, the deficiencies of a quantitative description made using classical methods are compensated for by unconventional mathematical tools. Fractal geometry is an alternative form of description of engineering surfaces and has become a popular method in the theory and applications of rough surfaces.

Self-similar fractals are characterized with that they can be described by means of one parameter which is not a natural number, D, whereas engineering surfaces are more self-affine than self-similar. Where surface properties are a function of scale, we have to do with multifractality.

In the description of surface morphology [7], a practical significance is attributed to a combination of multifractal analysis, surface stereometry and stereology of materials [11], the latter aiming at evaluation of crack resistance [10].

All analyses presented in the study are based on author's own original algorithms implemented in the engineering environment Matlab.

2 Acquisition of Stereometric Data for the Material Investigated

The research equipment consisted of a confocal microscope, LEXT 3000 by Olympus (Fig. 1), designed for precision measurements and meeting the highest accuracy and repeatability standards. To work with the LEXT microscope, a sample does not require special preparation. It can be placed directly on the microscope table. Observation and measurement in three dimensions are possible in real time.

Owing to the application of UV laser light of wavelength 408nm in a combination with a confocal scanner, LEXT exceeds the optical capacity threshold, as known for conventional equipment. A special optical system, which minimizes aberrations formed in the short-wave range, while maximizing the transmission within 408nm, allowed obtaining a unique image quality and signal transmission.

The resolution was increased through using a confocal scanning technique. In this method, the surface of a sample is scanned point by point. To detect a signal, a photomultiplier tube is used, before which a confocal diaphragm is placed. The latter cuts off the light coming from beyond the plane of sharpness and reflected from the surface. The photomultiplier tube measures the light intensity in each point.

An advanced scanner XY applied in the LEXT microscope uses a micro-electro-mechanical system, patented by Olympus (MEMS), making the scanning process faster and more accurate compared to traditional scanning systems. Control of movement in axis Z is extremely precise owing to the linear system with a 5nm

Fig. 1 Confocal microscope LEXT OLS3000
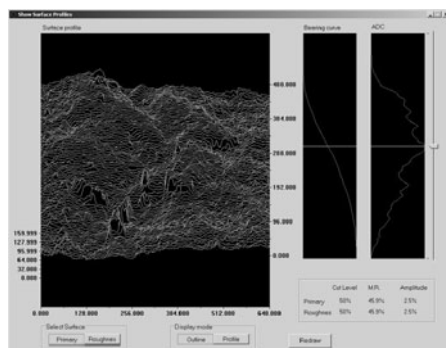
Fig. 2 Fragment of surface scanned with a confocal microscope LEXT OLS3000

increment. For each of the surfaces observed, the intensity curve called "*IZ*" is calculated. It is based on an advanced analysis of the maximum intensity value. The so formed intensity map is used to reconstruct the sample into a spatial image (Fig. 2).

The effect of these solutions is the world's best horizontal resolution of $0.12\mu m$ and $0.01\mu m$ in axis Z, all this with maintaining extraordinary repeatability of $3\sigma\ n-1 = 0.02\mu m$ in axis Z and $3\sigma\ n-1 = 0.05\mu m + 0.002L\mu m$ in the plane (L means the length measured). Credibility of the measured data has been confirmed by international control organizations, including The Japan Ouality Assurance Organization, Physikalisch-Technische Bundenanstalt and the United Kingdom Accreditation Service.

Unlike other known measuring systems, which can be operated only by experts, LEXT establishes new standards of speed and simplicity of operation thanks to its unique software. Only LEXT offers the possibility of displaying two images in real time: a conventional colour microscopic image and a confocal image, simultaneously on the same picture. It is easier and faster to focus the image on the surface observed, based on the microscopic image. Next, it is enough to define the range of confocal scanning by indicating the highest and the lowest points and afterwards, the scanning proceeds automatically.

The research material consisted of a titanium alloy used, inter alia, for orthopaedic implantation and in dental prosthetics, for implants or as a bone connector. Biocompatibility of implants and connectors made of titanium accelerates the healing process and patient's recovery [15].

The fracture surface of a material coming from a three-point static bending test was subjected to examination. A sampling step of $0.625\mu m$ was applied in directions X and Y. From the surface measured, an area of 1345×1345 points was selected, thereby obtaining a matrix of height Z, which was used for further analyses.

Details concerning the type of the biomaterial, the size of samples and the parameters of the test made are passed over on purpose in this study, so as to generalize the methodology presented here for a wide group of biomaterials.

3 The Minimal Spanning Tree Method – 3DMST

As a result of stereometric analyses, a sort of a square net was obtained consisting of 1,809,025 nods distributed evenly in a three-dimensional space.

The problem of the three-dimensional minimal spanning tree was used to model the crack path of metallic biomaterials. An appropriate algorithm was developed and then used to calculate the 3DMST from a given set of points distributed over space. The procedure starts performing by selecting any point out of the set and finding its nearest neighbour. These two points and appropriate edges form a sub-tree, $T1$. The distance to the closest neighbour with a sub-tree is added for each isolated point (a point that does not have a sub-tree yet) and referred to as the distance of the isolated point from the sub-tree. These potential MST edges are called connections. The Mth sub-tree, TM, is formed by adding the closest neighbour of the sub-tree to $TM - 1$, provided there is an isolated point, the distance of which to the sub-tree is minimal. A new connection will be updated as well, once this new point has been added to the sub-tree, i.e. the distance from each isolated point to each sub-tree vertex is calculated in order to check whether the distance is smaller than the previous distance of the point from the tree. The layout of edges that results from $TN - 1$ is a minimal spanning tree (3DMST) (Fig. 3) [14].

The so created set of data is called a graph. It consists of a set of vertices and a set of edges on a network of measuring points arranged in space, that were obtained by means of stereometric measurement of the surface area. A sequence of edges that accompany the vertex forms a path and a confined path is called a circle. A graph is called a combined one when there is a path between any pair of vertices. A combined graph which does not contain any circles is called a tree. If a tree of a combined graph includes all vertices from a vertex set, it is referred to as the spanning tree. The length of the tree is defined as the sum of constituent edges.
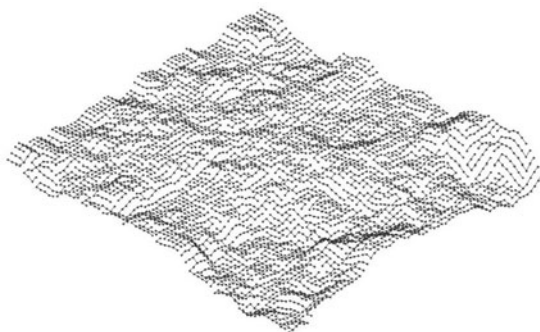
Fig. 3 Fragment of the generated 3DMST

4 Multifractal Analysis of Fracture Surface Based on 3DMST

As results from the definition, the MST is the only one and independent of the starting point. The 3DMST method unequivocally decides about the position of every point, providing at the same time information on correlations of every order. In addition, when a branch is added to the created tree, its position does not depend on the branch added to the tree before. On this basis, it can be said that the 3DMST system is delocalized. Because of the above reasons, 3DMST is particularly recommended for highlighting the main features of the global structure of distribution.

The 3DMST is a spanning tree of minimal length. This resembles a little a search for minimal covering of a set, required by the definition of the Hausdorff dimension and, in the best possible way, approximates the complexity of the crack path propagation (energy dissipation). It served as a basis for developing a new methodology of multifractal analysis of surfaces of materials.

In this study, the analysis was conducted based on an algorithm which consisted in fractal scaling (in many approximation steps) of the 3DMST generated, so as to meet the criterion of a boundary within which the "box" size in the box-counting method is approaching zero. This was achieved through simulating the changing size of boxes by changing the measuring density. By selecting every 672nd, 448th, 336th, 224th, 192nd, 168th, 112th, 96th, 84th, 64th, 56th, 48th, 42nd, 32nd, 28th, 24th, 21st, 16th, 14th, 12th, 8th, 7th, 6th, 4th, 3rd, 2nd and 1st measuring point, 27 scalings of the 3DMST were obtained, which approximate the real appearance of the crack path of the material when the distance between the measuring points decreases.

For so obtained scaling sets, an algorithm was applied consisting in the calculation of the sum of edges forming a fragment of the tree (Fig. 4a) in a given measuring field (Fig. 4b), while omitting those edges that had already been counted in the previous step.
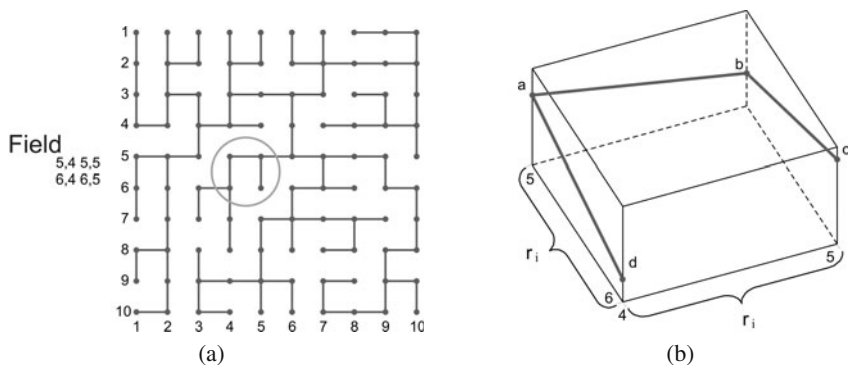
Fig. 4 Diagram of counting the edges: a) fragment of a set of measuring fields; b) enlarged, isometric view of an example of a measuring field with marked edges

Knowing this information, it is possible to determine the probability of finding the appropriate measuring field (1):

$$P_i(r) = \frac{L_i(r)}{L_T(r)} \tag{1}$$

where:

L_i in a given scale r, the sum of the lengths of edges in a particular measuring fields with disregarding the already counted edges;

L_T the total length of all edges in a given scale r;

r the size of box in a given scale.

Multifractals are expressed by generalized fractal dimensions (2), where: q is a parameter used for searching through a set and $D(q,r)$ is the spectrum of fractal dimensions for a given set:

$$D(q,r) = \frac{1}{q-1} \lim_{r \to 0} \frac{\log \sum\limits_{i=1}^{N} [P_i(r)]^q}{\log r} \tag{2}$$

Another method to present a description of multifractal measures is a spectrum $f(\alpha)$. Based on the probability values expressed by formula (1), a single-parameter family of standardized measures is built (3):

$$\mu(q,r) = \frac{[P_i(r)]^q}{\sum\limits_{i=1}^{N} [P_i(r)]^q} \tag{3}$$

next, the fractal dimensions of the subset $f(q,r)$ are determined (4):

$$f(q,r) = \lim_{r \to 0} \frac{\sum\limits_{i=1}^{N} \mu_i(q,r) \log \mu_i(q,r)}{\log r} \tag{4}$$

and indexed with exponents $\alpha(q,r)$ (5):

$$\alpha(q,r) = \lim_{r \to 0} \frac{\sum\limits_{i=1}^{N} \mu_i(q,r) \log P_i(q,r)}{\log r} \tag{5}$$

The obtained values of $\alpha(q,r)$ are called the singularity of the set investigated (5). In graphic interpretation, they are plotted on the abscissa, whereas the values of $f(q,r)$, representing entropy (4), are plotted on the ordinate (Fig. 5) [3].

From the point of view of the methodology described, the most important parameter of the multifractal analysis is the width of spacing of the multifractal spectrum arms, whose interpretation is presented in papers [9, 12].

Fig. 5 Spectrum of fractal dimensions
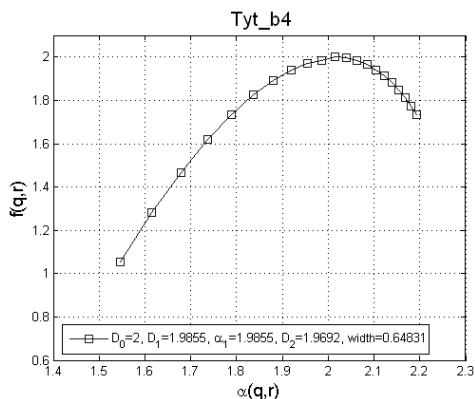
5 Conclusions and Further Work

Development of methods of a quantitative description of the microstructure and surface of materials constitutes the principal tool of a quantitative analysis in the field of materials science. It is implemented in order to modernize the production technology, improve the structure and enhance the properties of materials. Oriented to stereological and stereometric research methodologies, it uses at the same time, a computer image analysis and assistance by multifractal techniques. In the description of surface morphology, a practical significance is attributed to a combination of multifractal analysis, surface stereometry and stereology of materials, the latter aiming at evaluation of crack resistance of the materials.

The aim of the study was to take advantage of the method of modelling the crack process of materials, based on an example of a metallic biomaterial, using 3DMST. The modelling of the crack process and its characterization were carried out on a stereometric measuring file acquired as a result of analysis of a fracture surface of the material examined, using confocal microscopy.

The utilization of confocal microscopy for an evaluation of the surface topography is very well founded. With its unique observation and measuring potential, this method creates a new dimension in metrology - for better effectiveness of measurement, for better credibility and for better understanding of the surface structure. A confocal microscope shortens considerably the time of research, while maintaining very high accuracy and repeatability of measurements. In addition, it offers horizontal resolution which is one of the best in the world.

For a quantitative description of propagation of cracks in ideally brittle materials or in materials where the area of plastic deformation in the crack vertex is insignificant comparing to the sample size, the laws of the linear elastic crack mechanics are applied [16, 6, 2]. This allows determining quantitative dependencies between crack resistance of the material and the critical length of crack, the shape and dimensions of structural elements, and the type and value of load. Materials crack under stressed much lower than those determined by theoretical strength. The reason for

this discrepancy may lie in microfissures, pores or macrocracks which occur in the material and cause concentration of stresses. The ability to work of elements and engineering structures containing the above-mentioned material defects is identified by means of their crack resistance.

The 3DMST generated on a net composed of nodes very well approximates the real crack path of the material and, based on a stereometric-fractal analysis of the record of fracture surface artifacts, it will serve, in the author's future study, as a basis for developing a methodology to determine the theoretical resistance to crack of brittle biomaterials.

References

1. Blazewicz, S., Stoch, L.: Biomaterials. In: Nalecz, M. (ed.) Biocybernetics and biomedical engineering 2000, vol. 4. AOW Exit, Warszawa (2003)
2. Bochenek, A.: Elements of crack mechanics. Wydawnictwo Politechniki Czestochowskiej, Czestochowa (1998)
3. Chhabra, A., Jensen, R.V.: Direct determination of the $f(\alpha)$ singularity spectrum. Phys. Rev. Lett. 62(12), 1327–1330 (1989)
4. Glazkov, V.I.: Medicinskaja Biomechanika. Medicina, Riga, 466–480 (1986)
5. Mueller, M.E.: Biomechanishe Fehlleistungen. Langenbecks Arch. Klin Chir 329, 1144–1151 (1971)
6. Neimitz, A.: Crack mechanics. PWN, Warszawa (1998)
7. Pawlus, P.: Surface topography. Oficyna Wydawnicza Politechniki Rzeszowskiej, Rzeszów (2006)
8. Stach, S.: Fractal description of the banded structure. Thesis. University of Silesia, Sosnowiec (1999)
9. Stach, S., Cybo, J.: Multifractal description of fracture morphology: theoretical basis. Materials Characterization 51, 79–86 (2003)
10. Stach, S., Roskosz, S., et al.: Fracture surface development coefficient and sialon ceramics' bending strength. Key Engineering Materials 409, 279–282 (2009)
11. Stach, S., Roskosz, S., et al.: Properties of sialon ceramics evaluated by means of multifractal, surface stereometry and quantitative fractography techniques. Materials Characterization 60(10), 1151–1157 (2009)
12. Stach, S., Roskosz, S., et al.: Quantitative description of overlaps on sialon ceramics fractures by the multifractal method. Key Engineering Materials 409, 394–401 (2009)
13. Stach, S.: Application of a three dimensional minimal graph for reconstructing the crack path on fractures of metallic biomaterials. Powder Metallurgy and Metal Ceramic (2010) (in press)
14. Van de Weygaert, R., Jones, B.J.T., Martinez, V.J.: The minimal spanning tree as an estimator for generalized dimensions. Physics Letters A 169, 145–150 (1992)
15. Weisman, S.: Metals for implantation in the Human Body. Ann. NY Acad. Sci. 146(1), 80–101 (1986)
16. Wyrzykowski, J.W., Pleszakow, E., Sieniawski, J.: Deformation and cracking of metals. WNT, Warszawa (1999)

ACL Rehabilitation Enhanced by 3D Modeling Software

Marek Krótkiewicz, Krystian Wojtkiewicz, and Radosław Kardas

Abstract. The main purpose of this paper is to show possible positive effect of 3D modeling application in rehabilitation. Authors provide clinic example of patient with ACL reconstruction. The patient has undertaken the therapy consisting of regular rehabilitation sessions as well as those enhanced by 3D rehabilitation application. The improvement in ACL rehabilitation was significant and worth further exploration.

1 Introduction

Rehabilitation is a complex common action towards people with disabilities, both physical and psychical, aiming at recovering their either psychical or physical abilities. The main purpose for rehabilitation is to allow disabled people to take active part in social life as well as to let them work with less limitation. Rehabilitation which takes as its priority the mobility-skeletal system enhancement is the most specialized form of physical activity, just next to such activities as sport, recreation through movement or physical education. Movement rehabilitation stays in opposition to sport due to theirs participants motor and somatic abilities. Nowadays rehabilitation is not only an action of enhancing abilities but also aims at supplementing basic medical treatments. It has its great share in accelerating recovery process, preparing for surgeries, enhancing effects of surgeries as well as in basic motor system treatments.

The importance of physiotherapy is hard to challenge. It is not only a method but also a great supplement that can change life of many people. The thing that one

Marek Krótkiewicz · Krystian Wojtkiewicz
Institute of Mathematics and Informatics, University of Opole
e-mail: `mkrotki@math.uni.opole.pl, wojt@math.uni.opole.pl`

Radosław Kardas
Faculty of physical education and physiotherapy, Technical University of Opole
e-mail: `raddek0@onet.eu`

has to take under consideration is how to bring physiotherapy closer to the patient and make it easier to comprehend and fully attend. One of many possible ways is presented in this paper. Authors suggest that 3D model visualization brings an enormous gain in the whole process of physical treatment. One of the most important functionalities is the ability to show all of exercises on the model that has the same movement restrictions as the patients but also in the model that has exactly the same parameters as the patient. Basically patient can see almost him or herself doing the exercises and easily follow the example. On the other hand the tool is a great advantage for the therapist, who can easily monitor progress of his patient, prepare more suitable exercises and finally he can prepare a special exercises set for self monitoring for the patient. Following parts of this article will show how 3D virtualization can help patient before and after surgery on the example of knee surgery.

2 Traditional Approach towards Rehabilitation

One of the first who said that training and exercises have positive effect on correct development of humans was Claudius Galen (130-199 B.C.). Chinese and Japanese culture has also great tradition in propagating healthy lifestyle by physical training. Medieval brought to Europe the motion saying that anything good for body is bad for soul. It changed around XIII century after gunpowder started to be used, resulting in high number of cripple. The idea started from making metal and wood prosthesis in around XVI century. It was also the time when Francis Glisson started to promote physical exercises in treating spine and chest degeneration. "Glisson loop", one of the first therapeutic device, is still being used in to extract muscles and cervical vertebrae in their disabilities. In XVIII century Henry Ling suggested medical exercises, named after him, that are nowadays used in kinesitherapy. Since that time many have work to promote healthy life style through physical exercises. In 1981 Douglas McMurties was the first to use word *rehabilitation* to name therapy for handicapped in New York. The name was taken from Latin, *habere* - to have, *habilis* - capable, handy. The meaning evolved from just professional or social enhancement to more complex treatment.

The main advantage of rehabilitation is that it has no side effects, like for example pharmacological treatment. Another advantage is positive effect on overall psychical condition of the patient, coming from personal and conscious evolvement in the process of enhancing sick organ or the body at all. At this time one can suppose that rehabilitation will move to another level of human utility. There are serious reasons to assume that the future will bring even more people in need of rehabilitation. One of them is increasing number of newborns with disabilities that survive. Another is the shift from sicknesses with short and hard course to rather long lasting chronic diseases. Increasing number of communication collisions and their victims, as well as wider understanding for handicapped, makes another reason. The very next thing one has to take under consideration is increasing average life expectancy and what comes from this fact aging of the society. If we add the increase in number of diseases coming from the lack of movement (hypokinesis) all the factors will show that

rehabilitation will become even more needed [3]. The main purpose of rehabilitation nowadays is to help people to be capable of living for long and in luxury. For the luxury we take all improvements and enhancement mankind has brought to itself during its development. Public or private transportation instead of walking makes our motor system to fail eventually. It is the same with sitting way of life. Most of people do not know that if they work in the office and sit for many hours, they need to take breaks, not only to have a snack but what more important to have some exercises. Even 10 minutes of systematic break filled with special set of exercises may help to keep fit and healthy.

Treatment system and rehabilitation is blended with overall policy toward patients with disabilities. Ministry of Health is responsible for national disabled help program in the manner of medical treatment and rehabilitation. On the side Ministry of Labor and Social Policy is responsible for social help. All of medical, social and economical actions lead to ensure handicapped conditions comparable to those without psychical or physical limitations. Those actions penetrate all life segments, e.g. family life, education integrity, work and well organized support and social rehabilitation.

3 ACL Rehabilitation

With the development and expansion of knowledge in the fields of biology and biomechanics of the knee, and thanks to significant advances in the field of reconstruction with the use of transplants, rehabilitation rules and methods of ACL (front cross ligament) has changed. In the 70's of the twentieth century the ACL reconstruction was performed through as extensive non-joint arthrotomy, which led to disabling patient operated leg in plaster for a long period of time. In the eighties the development of arthroscopic techniques has allowed as intra-articular reconstruction using a special camera and instruments without the need of broad knee opening. This in turn allowed using planned accelerated rehabilitation and helped focus attention on fast knee joint enabling after ACL. In the next decade, since 1990, the idea of accelerated rehabilitation expanded and changed to an attempt to give sportsman a chance to recover as fast as possible. Emphases given on fast recovery slipped to the fore the problem of exercises in closed and open kinetic chain, as well as, the problem of pressure that is given on the implant after surgery, along with postoperative and functional prosthesis. The postoperative rehabilitation has also been appreciated since it helped prevent side effects o the surgery.

Ligament cross-front is the main ligaments of the knee preventing the movement of the front of the tibia. It also provides a secondary element of a restraining rotation of the tibia, also prevents the pressure in the direction of varus and valgus knees deformity. The average healthy young man ACL ligament can withstand the strength of approximately 2500 N (newtons) before it is damaged or completely severed. This value decreases together with body aging. Force acting on the healthy ligament is in the range 100 N at a passive knee extension to about 400 N while walking and 1700 N during activities that include actions triggering static forces or

fast acceleration and deceleration. Overloading this capacity in excess of the ACL occur only in unusual combinations of forces acting on the knee joint. These forces often cause twisting of the knee resulting in damage to knee ligaments and the ACL. Broken ligaments cannot be saved and the reconstruction procedure should be made only after the termination of the inflammation and swelling in the knee. At that time, the completely broken ligament dies, or even become dissolved in the joint cavity. Taken early in the reconstruction causes many postoperative complications, among other things, increases the risk of fibrosis of the knee. The material used mostly at this time for transplantation is the patellar ligament of the knee or a complex consisting of gracilis tendon and semitendinosus. The initial strength of the implant must be greater than the normal ACL, as the strength of ligaments after implantation significantly decreases. This property is essential to ensure optimal strength of the implant, despite its decline in the healing phase. Stronger graft allows safer rehabilitation and faster return to activity. Patellar ligament implant may obtain the initial strength of about 2977 N and complex gracilis tendon and semitendinosus up to 4000 N.

Inoperable treatment of knees with ACL injury might be acceptable choice for elderly or sedentary people [2, 4]. At the same time athletes or young people with high activity habits no ACL is associated with the occurrence of knee instability, which in turn leads to damage of meniscus, damage of joint and the secondary process of knee degeneration. Satisfactory knee function can be sustained over a short period of time, especially through high gracilis tendon and semitendinosus strength, but the results of such proceedings are unpredictable, and the resulting functionality of the knee far from the state before the damage. Surgery ACL reconstruction restores stability to the knee in a predictable way. It became possible to use aggressive rehabilitation programs, thanks to advances in materials used for transplants and the techniques for fixing, as well as the number of exercises with emphasis on transplant. These methods, although they appear to be safe and appropriate must be treated with caution until the ongoing study of the transplants healing process set limit to what can be "accelerated" rehabilitation after reconstruction. For this purpose, post-operative rehabilitation of ACL reconstruction, is supposed to take special care of achieving full straightening of the knee and reducing inflammation and swelling before surgery. This prevents fibrosis of the joint.

4   The Use of 3D Modeling Application in ACL Rehabilitation Process

The patient was injured on 24th of November 2008 during basketball play. As described after first examination he suffered "sprains and tears of the other, unspecified parts of the knee". Additional research showed instability of injured knee in valgus, severe pain, mediocre swelling and dried joint. X-ray scanning showed no bone injury. The patient was given plaster splint tutor and he was directed to the orthopedic clinic. On 18th December 2008 and next on 17th March 2009 he was given ultrasound examination that showed small amount of fluid in posterior lateral complex.

This showed possibility of ACL insufficiency. The ACL itself could not be examined due to small amount of fluid and swelling of posterior cruciate ligament (PCL). The MRI taken on April the 1st confirmed the proximal attachment of the ACL rapture as well as minor traumatic changes. After being referred to the Surgery Department, he had surgery on 17th of April, which consisted of left knee arthrotomy, ACL stumps cut. New ACL ligament has been made from gracilis tendon and semitendinosus. After surgery patient was formed plaster cast for 3 weeks until stitches could be taken off. After about 2 months the knee was released from immobilization and the patient was allowed to attempt self-advised walking. He was also advised to choose therapists who will guide him through rehabilitation process.

The developed 3D visualization application has been used from this point. Physiotherapist prepared set of exercises that the patient learned during the direct sessions. Exemplary exercise is shown on figures 1, 2, 3. They were prepared for him as 3D animation suited to his abilities. To do so, there had to be some measurements takes from the patient to map all of his body to the model. The body shape of the model was similar to the patient. Secondly the movement ranges and angles were mapped using muscle strength tester and joint angle counters. The application model design is showed on figure 4. Afterwards he was instructed how to conduct those exercises at home. Thanks to those exercises carried enhanced by the 3D

Fig. 1 Starting position for the exercises

Fig. 2 First exemplary exercise

(a) (b)
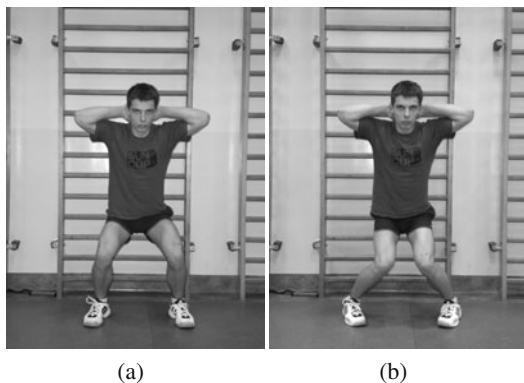
Fig. 3 Squads for ACL strengthening
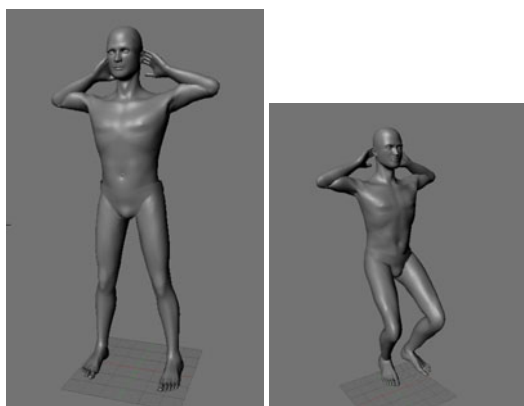
Fig. 4 3D model presenting the exercises

visualization and thanks to patient self control, which prevent overtraining, the patient has accelerated the rate of rehabilitation. With the exercises carried out at any time of the day, according to the need and possibilities of the patient, allowed obtaining faster performance. Every day after the patient took the exercises he was obligated to support the application with the information which exercises and with how many repetition he has performed. This allowed the application to compile each training toward his needs. The patient had also taken physiotherapist consultation every third week. The very summer of the year he took the surgery, he was able to run, practice martial arts and other sports including swimming and basketball. These results could not be obtained through regular rehabilitation, which consist mainly of regular visits in rehabilitation facility.

5 Computer Application

The work on the model started in MakeHuman solution. Modified mesh was then exported to the COLLADA 1.4 format and imported into blender and then administered SubSurf. The size of the grid was adopted in the scale 1 blender unit equals 1 meter. After refining the details the grid become the primary model. The base model is used to create models of every patient. The modifications are made according to the measurements taken from the patient and applied to the model. The proper modeling required creation of the shape keys, both vertex animations and morph animation. For each modification e.g. leg length, two extreme key frames were created. The mesh has been shaped in each of the frames and finally the linear interpolation between frames has been established. The interpolation rate was changed from 25FPS to 1FPS to obtain better results. Knowing the measurements of the patient, the modeling application chooses the proper frame.

The movement of the model was obtained through fittings showed on the simplified skeleton. The leading lines of the skeleton are showed on the picture 5. Even though it's simplified it allows modeling of very complicated and prices movements. At this time the work is focused on the development of the skeleton model that would be almost perfectly accurate. The last stage before export was the grid dividing on materials and determining the corresponding UV coordinates for textures. Materials has been defined by their name, all other parameters were irrelevant at that point.

The model prepared as described has been exported to OGRE format stored in xml and then converted to a binary format. OGRE technology allowed easy work on materials. Every material has a number of textures: diffuse map (colors), normal map (hollows and bulges), ambient occlusion maps (shadows) and specularity maps (light reflection). In addition diffusion maps for the skin, hair, eyes and eyebrows can have many variations. Based on the set of materials four sets were created varying in quality (2048x2048, 1024x1024, 512x512, 256x256 pixels).

The application uses OGRE library to render 2D and 3D animations, OIS library to handle mouse and keyboard, CEGUI as a user interface and Python as the main scripting language.
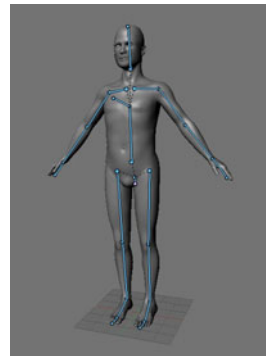
Fig. 5 Leading lines on the skin layer

The 3D modeling technology has found application to physical rehabilitation at almost all levels of presented rehabilitation proceedings [1]. A patient awaiting operation can use it in preparation for the surgery. This self preparation could also contain information about future exercises to be performed after the surgery. Interactive 3D model programmed to imitate the patient would show all the muscles and joints involved in the exercises as well as it would show how to limit the effort of rehabilitation.

6   Conclusion

Presented method shows that 3D modeling can be advantageous for enhancing rehabilitation speed. It allows patient to conduct unsupervised rehabilitation exercises at home at the most appropriate time for him. It increases patients' motivation, effectiveness of their exercises and the speed of rehabilitation process. Further work will be dedicated to enhance the model and to make it even more realistic. Authors would also like to model more precisely each and every bone, muscle and joint in the model. This eventually will lead to the possibility to model all of the movement of the body, to find its limitations. Authors believe also that 3D virtualization is the weakest point of the solution. At this point several measurements are taken to provide information how to adjust model to reflect patients body shape. There is a possibility to use stereoscopic cameras to obtain the 3D picture of patients' body. There are also plans to use laser 3D scanner to visualize patient body as the mesh that after some mapping could be directly used in the application. There is also a wide area of how to obtain information on joint movement limitations. At this point the counters used are not directly connected with the computer. The idea and prototype of automatic angle and strength counter is the subject of future work and publication.

References

1. Prystupa, W., Prystupa, E., et al.: Biological Regeneration as a Factor for Muscle Strength Optimization in Upper Limbs of Disabled Weight lifters with Cerebral Palsy. Journal of Human Kinetics 18 (2007); Katowice
2. Starosta, W.: Science of Human Movements - Meaning, Name, Directions of Development. Journal of Human Kinetics 6 (2001); Katowice
3. Plewa, M., Cieślinska-Świder, J., et al.: Effects of the Weight loss Treatment on Selected Kinematic Gait Parameters in Obese Women. Journal of Human Kinetics 18 (2007); Katowice
4. Kuszewski, M., Saulicz, E., et al.: Body Proportions and the Results of the Toe-Touch Test. Journal of Human Kinetics 16 (2006); Katowice

Numerical Analysis of Spine Stabilizers on Lumbar Part of Spine

Marta Kiel, Jan Marciniak, Marcin Basiaga, and Janusz Szewczenko

Abstract. The numerical analysis of spine stabilizers was carried out in the work. The aim of the work was determination of more favourable stabilization variant. Moreover, this analysis is the basis to determine an optimal geometry of the stabilizer as well as to select mechanical properties of metallic biomaterial. The work presents the results of biomechanical analysis of lumbar spine stabilization by plate and transpedicular stabilizer. The finite element method was applied for biomechanical characteristic of implants made of stainless steel Cr-Ni-Mo and Ti-6Al-4V alloy. Geometrical models of part of spine L3-L4 and the stabilizer were discretized by SOLID95 element. Appropriate boundary conditions imitating phenomena in real system with appropriate accuracy were established. The result of numerical analysis was calculation of displacements and reduced stresses in particular elements of system in a function of the applied loading: 700 - 1600 N. The displacements calculated for part L3-L4 show that the proposed type of stabilizer enables the correct treatment process. The obtained numerical results should be verified in "in vitro" tests.

1 Introduction

The spine is extraordinary important part of skeleton, where are performing three fundamental functions: supporting, protecting (for core and roots of a spinal nerve) and motor activity (thanks to segmental building and to muscles). Its upper part (cervical part) is connecting with braincase. The particular vertebras are connecting with each other by joints, ligaments and intervertebral discs. Movements between vertebras have limited range, however their summation (especially in cervical and lumbar part of spine) gives possibility of significant change of shape, what is very

Marta Kiel · Jan Marciniak · Marcin Basiaga · Janusz Szewczenko
Silesian University of Technology, Institute of Engineering Materials and Biomaterials, Konarskiego 18a, 44-100 Gliwice, Poland
e-mail: marta.kiel@polsl.pl

helpful for everyday life. Composed biomechanical functions of spine presents wide spectrum of loading and deformation, which are submitted during movement. Correct distribution of load ensures the proper formation of anatomical characteristic in osteo-muscular system and the correct functioning of spine [1, 2].

The spine is damageable in consequence of overload, pathological changes or injuries.It causes the dysfunctions which are the most often of pathological syndrome state. Diseases of spine may be result of activity loss in social life. Its injuries are a huge danger for health and life [1].

Increasing tendency of affections and dysfunctions of spine which result from little mobile activity of society, communication injuries, sport activity, especially extreme sports is observed in last years. This tendency is also supported by ageing of population. Medical statistics indicate that the main reason of inefficiency in middle age and older people is a spine pain. About 70 - 80 % of population are suffering from this reason [3].

Degenerative and overloaded changes are often observed in lumbar part of spine. There is the result of considerable load in this area. Human's center of gravity is located in lumbar part of spine and maximum loading forces influenced the vertebras and intervertebral discs are observed. About 62 % of pathological changes in the vertebra - intervertebral disc system refers to the L3-L4 segment [4, 5].

Post-injury and pathology state treatment of spine is realized with the use of complex, multicomponent stabilizers and complicated operating procedures [6, 7, 8, 9].

Development of stabilization of spine with the use of metallic implants is connected with the progress in medical technology.

The transpedicular stabilization system of spine enables treatment of thoracic, thoracic - lumbar and lumbar segment of spine by posterior surgical approach. The plate stabilizer system of spine enables treatment of cervical and lumbar part of spine by anterior surgical approach. Applied of plate' stabilizers in surgical treatment of diseases of spine isn't universal by difficult surgical approach (anterior surgical approach), more post-operating complications also psychical and physical loading of patient. Geometric features of stabilizers' elements match individual anthropometric features of patients [10, 11]. Implants which are used can immobilize the sick part of spine and let achieve the stable adhesion.

The numerical analysis of spine stabilizers was carried out in the work. The aim of the work was determination of more favourable stabilization variant.Moreover, in order to determine the more favourable variant of stabilization, a comparison of the plate and the transpedicular stabilizers was done.

2   Materials and Methods

Two systems of stabilization of spine in the lumbar segment was analyzed in the work: transpedicular stabilizing system by posterior surgical approach known from the patent [12] and plate stabilizing system by anterior surgical approach. The
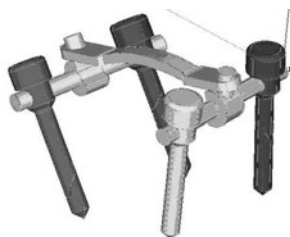
Fig. 1 Geometrical model of transpedicular stabilizer

transpedicular system consists of transpedicular screws, clamp element, nut, contact arm and supporting rod - Fig. 1.

The plate system consists of plate and bone screws - Fig. 2.
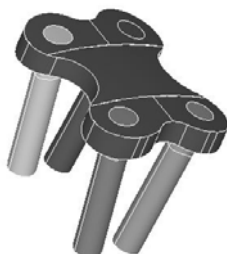
Fig. 2 Spine's plate stabilizer

Stabilization of two vertebras of lumbar part of spine was analyzed in the work - Fig. 3.
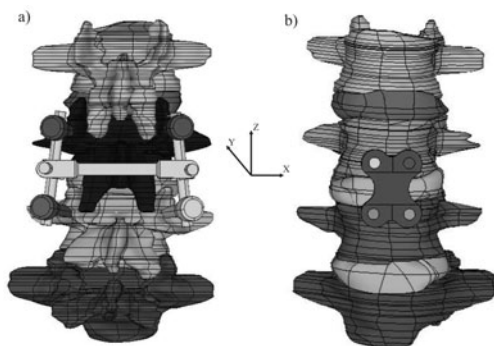
Fig. 3 Geometrical model of: a) lumbar spine - transpedicular stabilizer system, b) lumbar spine - plate stabilizer system

Models of stabilizers were modified with use of the ANSYS program for realized calculations. The mechanical properties for analysis were as follows [13, 14]:

- for Cr-Ni-Mo steel: $E = 2 \cdot 10^5$ MPa, Poisson's ratio $v = 0,33$,
- for Ti-6Al-4V alloy: $E = 1,06 \cdot 10^5$ MPa, Poisson's ratio $v = 0,33$,
- for vertebras: $E = 1,15 \cdot 10^4$ MPa, Poisson's ratio $v = 0,30$,
- for intervertebral discs: $E = 110$ MPa, Poisson's ratio $v = 0,40$.

In next step of the analysis the models were meshed. Meshing was realized with the use of SOLID 95 element - Fig. 4.

In order to carry out calculations it was necessary to evaluate and establish initial and boundary conditions which imitate phenomena in real system with appropriate accuracy. The following assumptions were established:

- the fifth vertebra of lumbar spine was immobilized (all degrees of freedom of surface nodes were taken away). It enabled displacements at last lumbar vertebrae, blocking possible rotation,
- the second lumbar vertebra was loaded with forces: 700 N, 1000 N, 1300 N, 1600 N, on whole surface,
- in third and fourth vertebra the spine stabilizer was implanted according to the operating technique.

The scope of the analysis included determination of displacements and stresses:

- in the part of lumbar spine,
- in the vertebras (L3-L4) - stabilizer system made of Cr-Ni-Mo,
- in the vertebras (L3-L4) - stabilizer system made of Ti-6Al-4V alloy.

Stresses and displacements obtained in the analysis are reduced values according to the Huber - Misses hypothesis. The muscle system of spine was omitted in settlement of boundary conditions. In the effect all the loads and displacements of the parts of spine were carried by stabilizer - vertebras - intervertebral discs system.
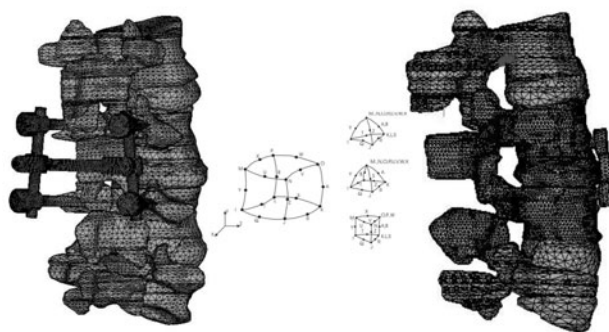
Fig. 4 Meshed models

3 Results

3.1 Results of Analysis of Lumbar Spine - Transpedicular Stabilizer System

Results of the analysis of displacements carried out for the lumbar spine - transpedicular stabilizer system are presented in Table 1 and 2 and Figs 5 and 6. On the basis of the analysis it was affirmed that maximum displacements for stabilizer made of Cr-Ni-Mo steel for the maximum forces of 1600 N were determine in the OZ axis (which is cover with axis of compression force) - 0.93 mm. For other axis OY and OX displacements were adequate 0.83 and 0.18 mm - Table 1. While the maximum displacements for stabilizer made of Ti-6Al-4V alloy for the maximum forces of 1600 N were determine in the OZ axis (which is cover with axis of compression force) too - 0.97 mm. For the other axis OY and OX displacements were adequate 0.86 and 0.19 mm - Table 1., Fig. 5.

Table 1 Relative displacements of transpedicular stabilizer for different loads and directions

Load, N	Displacements, mm					
	Stabilizer made of stainless steel Cr-Ni-Mo			Stabilizer made of Ti-6Al-4V alloy		
	OZ	OY	OX	OZ	OY	OX
700	0,41	0,36	0,07	0,43	0,37	0,09
1000	0,58	0,51	0,12	0,61	0,53	0,12
1300	0,75	0,66	0,15	0,79	0,7	0,16
1600	0,93	0,83	0,18	0,97	0,86	0,19

Results of the analysis of stresses carried out for the lumbar spine - transpedicular stabilizer system made of Cr-Ni-Mo steel are presented below -Table 2.

Table 2 Maximum equivalent stress values evaluated for the lumbar spine - transpedicular stabilizer system

Load, N	Reduced stresses, MPa							
	Stabilizer made of stainless steel Cr-Ni-Mo				Stabilizer made of Ti-6Al-4V alloy			
	Connector	Screws	Vertebras	Intervertebral disc	Connector	Screws	Vertebras	Intervertebral disc
700	64	81	14	1,1	47	57	17	1,2
1000	92	116	21	1,6	67	81	24	1,8
1300	119	150	27	2,0	87	105	31	2,3
1600	147	185	33	2,5	107	129	38	2,8

Maximum equivalent stresses in the transpedicular screws loaded with the force 1600 N were equal to 185 MPa and were localized in the right upper screw in L3
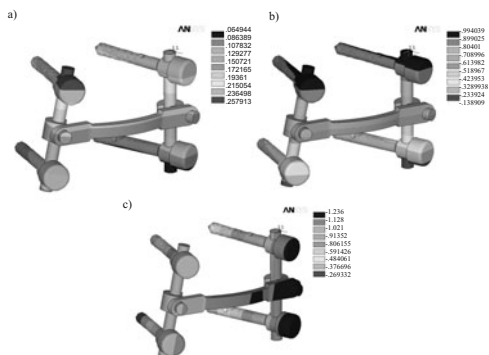
Fig. 5 Displacements in the spine of stabilizer loaded with the force 1600 N (Ti-6Al-4V): a) OX axis, b) OY axis, c) OZ axis

Fig. 6 Equivalent stresses in: a) the screws, b) contact arm, c) the vertebras L4-L5,d) the intervertebral disc loaded with the force 1600 N

vertebra. Maximum equivalent stresses for connector (contain by supporting rod and contact arm) loaded with the force 1600 N were equal 147 MPa. Area of maximum stresses was localized in contact place rod - connector on the edge of contact arm. Maximum equivalent stresses for vertebras loaded with the force 1600 N were equal 33 MPa and were localized in L4 vertebra the assembly hole of the stabilizer. Maximum equivalent stresses loaded with the force 1600 N in intervertebral disc L3-L4 were equal 2,5 MPa.

While results of the analysis of stresses carried out for the lumbar spine - transpedicular stabilizer system made of Ti-6Al-4V alloy are presented the following - Table 2., Fig. 6.

Maximum equivalent stresses in the transpedicular screws loaded with the force 1600 N were equal to 129 MPa and were localized in the right upper screw in L3 vertebra. Maximum equivalent stresses for connector (contain by supporting rod and contact arm) loaded with the force 1600 N were equal 107 MPa. Area of maximum stresses was localized in contact place rod - connector on the edge of contact arm. Maximum equivalent stresses for vertebras loaded with the force 1600 N were equal 38 MPa and were localized in L4 vertebra the assembly hole of the stabilizer. Maximum equivalent stresses loaded with the force 1600 N in intervertebral disc L3-L4 were equal 2,8 MPa - Fig. 6.

3.2 Results of Analysis of Lumbar Spine – Pate Stabilizer System

Results of the analysis carried out for the lumbar spine - plate stabilizer system are presented in Table 3 and 4 and Figs 7 and 8.

Table 3 Relative displacements of plate stabilizer for different loads and directions

Load, N	Displacements, mm					
	Stabilizer made of stainless steel Cr-Ni-Mo			Stabilizer made of Ti-6Al-4V alloy		
	OZ	OY	OX	OZ	OY	OX
700	0,21	0,22	0,04	0,27	0,28	0,05
1000	0,32	0,33	0,06	0,38	0,39	0,08
1300	0,45	0,46	0,1	0,50	0,51	0,10
1600	0,61	0,62	0,11	0,61	0,63	0,12

On the basis of the analysis it was affirmed that maximum displacements for stabilizer made of Cr-Ni-Mo steel for the maximum forces of 1600 N were determine in the OY axis - 0.62 mm. For other axis OZ and OX displacements were adequate 0.61 and 0.11 mm - Table 1.

While the maximum displacements for stabilizer made of Ti-6Al-4V alloy for the maximum forces of 1600 N were determine in the OY axis too - 0.63 mm. For the other axis OZ and OX displacements were adequate 0.61 and 0.12 mm - Fig. 7.

Results of the analysis of stresses carried out for the lumbar spine - plate stabilizer system are presented in Table 4 and Fig. 8.

Results of the analysis of stresses carried out for the lumbar spine - plate stabilizer system made of Cr-Ni-Mo steel are presented below.

Maximum equivalent stresses in the plate loaded with the force 1600 N were equal to 85 MPa. Area of maximum stresses was localized near the right hole. Maximum equivalent stresses for vertebras loaded with the force 1600 N were equal 32 MPa and were localized in L4 vertebra the assembly right hole of the stabilizer.
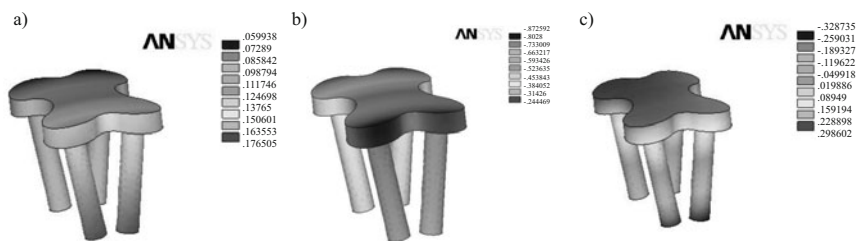
Fig. 7 Displacements in the spine of stabilizer loaded with the force 1600 N (Ti-6Al-4V): a) OX axis, b) OY axis, c) OZ axis

Table 4 Maximum equivalent stress values evaluated for the lumbar spine - plate stabilizer system

Load, N	Reduced stresses, MPa							
	Stabilizer made of stainless steel Cr-Ni-Mo				Stabilizer made of Ti-6Al-4V alloy			
	Plate	Screws	Vertebras	Intervertebral disc	Plate	Screws	Vertebras	Intervertebral disc
700	31	40	10	2,1	22	38	16	2,4
1000	51	63	17	3,2	32	54	23	3,5
1300	72	89	25	4,2	42	70	29	4,5
1600	85	115	32	5,4	52	86	36	5,6
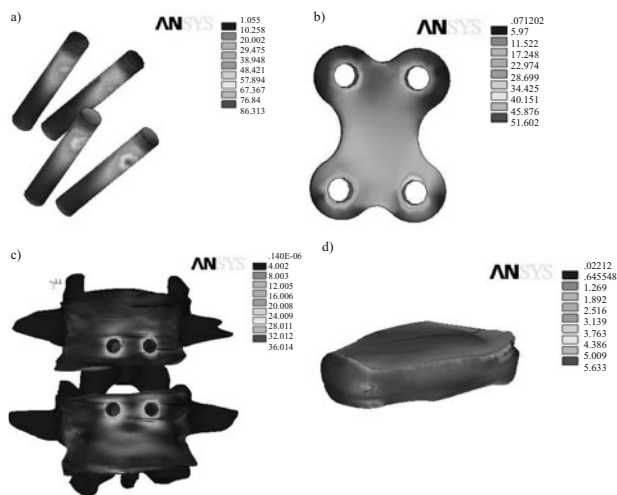
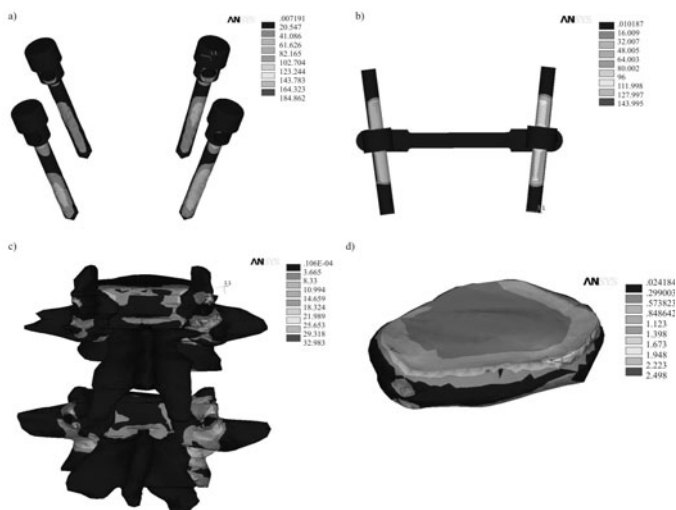**Fig. 8** Equivalent stresses in: a) the screws, b) plate, c) the vertebras L4-L5, d) the intervertebral disc loaded with the force 1600 N

Maximum equivalent stresses loaded with the force 1600 N in intervertebral disc L3-L4 were equal 5,4 MPa.

While results of the analysis of stresses carried out for the lumbar part of spine - plate stabilizer system made of Ti-6Al-4V alloy are presented the following - Table 4., Fig. 8.

Maximum equivalent stresses in the screws loaded with the force 1600 N were equal to 86 MPa and were localized in the right lower screw in L4 vertebra. Maximum equivalent stresses for vertebras loaded with the force 1600 N were equal 36 MPa and were localized in L4 vertebra the assembly right hole of the stabilizer. Maximum equivalent stresses loaded with the force 1600 N in intervertebral disc L3-L4 were equal 5,6 MPa - Fig. 8.

4 Conclusions

On the basis of the carried out biomechanical analysis for lumbar spine - transpedicular stabilizer system and lumbar spine - plate stabilizer system with assumed geometrical features, the values of displacements and reduced stresses were determine by the finite element method. Reduced stresses in the stabilizer system's elements were calculated. Spine' stabilizers made of the most often metallic biomaterials Cr-Ni-Mo steel and Ti-6Al-4V alloy were analyzed.

Effective stabilization of part of spine L3-L4 was the fundamental parameter for flexibility all system for strains applied loading. Therefore the displacements between L3-L4 vertebras, for the maximum loading of 1600 N, were calculated - Fig. 5 and 7. Small difference registered in displacements in the gap between vertebras calculated along the OZ axis were depended on the applied biomaterial - Table 1, 3. For transpedicular stabilizer and plate stabilizer the displacements didn't exceed value of 1 mm. That proves the stability and stiffness of the analyzed systems.

Maximum reduced stresses for lumbar spine - transpedicular stabilizer system were localized in transpedicular screws, in the right upper screw - Table 2, Fig. 6. Maximum reduced stresses for lumbar spine - plate stabilizer system were also localized in screws - Table 4, Fig. 8. Assembly of the stabilizers in L3-L4 segment and applying the maximum force of 1600 N does not cause the stress increase in the vertebral segments exceeding the value 160 MPa [5], what is very fundamental factor for correct treatment. Reduced stresses generated during the numerical analysis for stabilizers both made of Cr-Ni-Mo steel and Ti-6Al-4V alloy didn't exceeding yield point of metallic biomaterial (adequately $Rp_{0,2} = 690$ MPa, $Rp_{0,2} = 790$ MPa).

The lesser value of displacements and reduced stresses were observed for lumbar spine - plate stabilizer system, what proves the larger stability of analyzed system. The result of biomechanical analysis for transpedicular stabilizer and plate stabilizer obtained by FEM are very valuable for determination of construction features of the stabilizer, and for selecting mechanical properties of metallic biomaterial as well as degree of strain hardening of the metallic biomaterial. The obtained numerical results should be verified in "in vitro" tests.

References

1. Kiwerski, J.: Diseases and injuries of spine. PZWL, Warsaw (2004) (in Polish)
2. Bedziński, R.: Biomechanic and rehabilitations engineering. EXIT, Warsaw (2004) (in Polish)
3. Ciupik, L., Maciejczak, A., Pieniázek, J., Radek, A., Zarzycki, D.: Interappendix stabilization, lumbar: compromise between treatment functions, material and construction of implants. Zielona Gora: Spondyloimplantology of advanced spine treatment, 67–74 (2005) (in Polish)
4. Nabrani, F., Wake, M.: Computer modeling and stress analysis of the lumbar spine. Materials Processing Technology 127, 40–47 (2002)
5. Bedziński, R.: Engineering biomechanics, pp. 13–45. Printing House of the Wroclaw University of Technology, Wroclaw (1997) (in Polish)
6. White, A., Panjabi, M.: Clinical Biomechanics of the Spine, 2nd edn. J.B. Lippincott Company, Philadelphia (1990)
7. Clausen, J., Goel, V., Traynelis, V., Ryken, T., Zheng, Z., Roach, R.: Biomechanics of Caspar and Synthes plates in quasi-static and cyclic loading models. In: BED 24 Bioengineering Conf., pp. 618–620 (1993)
8. Abitbol, J., Zdeblick, T., Kunz, D., McCabe, R., Cooke, M.: Biomechanical Analysis of Modern Anterior and Posterior Cervical Stabilization Techniques. In: Proceedings of the American Academy of Orthopaedic Surgeons, pp. 10–11 (1994)
9. Gilli, S., Acar, B.: Comparison of distributed and collective loading on the stability of the spine. Studies and Monographies AWF Wroclaw 55, 1298–1340 (1998)
10. Marciniak, J., Szewczenko, J., Walke, W., Basiaga, M., Kiel, M., Mańka, I.: Biomechanical analysis of lumbar spine stabilization by means of transpedicular stabilizer. In: Information Technologies in Biomedicine. ASC, vol. 47, pp. 529–536. Springer, Heidelberg (2008)
11. Woźniak, W.: Human's anatomy. Elsevier Urban and Partner, Wroclaw (2003) (in Polish)
12. Bedziński, R., Filipiak, J., Pezowicz, C., Marciniak, J.: Transpedicular stabilization of spine to fractures and deformities treatment. Patent no 3356/29/03 (December 8, 2003) (in Polish)
13. Marciniak, J.: Biomaterials. Printing House of the Silesian University of Technology, Gliwice (2002) (in Polish)
14. Gzik-Zroska, B., Tejszerska, D., Wolański, W.: Stress analysis of funnel chest after stabilization with a plate. Modelling of Engineer, Gliwice 34, 37–42 (2007)

Numerical Analysis of Low Contact Plate Made of Alternative Metallic Biomaterials

Marcin Kaczmarek

Abstract. The aim of the work was biomechanical analysis of a low contact plate (patent no. P. 387934) applied in treatment of tibia. Shape of the plate was adapted to anatomical curvature of the bone. Biomechanical analyses were carried out for the implant made of two metallic biomaterials used in bone surgery - stainless steel and Ti–6Al–4V alloy. Finite element method was applied to calculate displacements and stresses. The obtained results allowed to work out biomechanical characteristics of the analyzed systems. These characteristics can be a basis for selection of strain hardening of the applied metallic biomaterials as well as the optimization of the plate's geometry.

1 Introduction

In the 60's of XX century a plate osteosynthesis according to the AO was introduced. Since the very beginning this method had many disadvantages, and the most important one was an osteolysis in a contact area (metallic biomaterial - bone). The another disadvantage was a bone atrophy in the fracture site. A large number of complications was reported (4 - 43%) [1, 2]. That's why the AO method should be recognized as the over-rigid method of stabilization, which lead to the demineralization of the bone tissue and the loss of the mechanical properties in consequence. The over-rigid stabilization also leads to the stress increase in the elements of the stabilizer which can cause the damage of the stabilizer. Furthermore, the initiation of cracks in the plate can occur, increasing the danger of the metalosis and bone union complications. Biophysical processes in bones and their properties as a mechanoreceptor are the justification for flexible methods of osteosynthesis. The methods guarantee the possibility of cyclic elastic strains of the bone while loading, so they activate

Marcin Kaczmarek

Silesian University of Technology, Institute of Engineering Materials and Biomaterials, Konarskiego 18a, 44-100 Gliwice, Poland

e-mail: marcin.kaczmarek@polsl.pl

the bone union. These methods of stabilization are recently appreciated in a clinical practice. However, flexibility of the fixation is not the only aspect that should be taken into consideration. Another very important factor, determining quality of fixation and positive clinical effect in consequence, is geometry of implant, in particular - the contact area of the applied bone plate. Large contact area causes necrosis of the bone as well as other biomechanical disadvantages (e.g. stress shielding). Thus, flexible low contact plates for osteosynthesis are the subject of research in many centers [1, 3, 4, 5, 6, 7, 8, 9, 10, 11, 12, 13, 14, 15, 16].

2 Materials and Methods

2.1 Geometrical Model

Geometrical model of tibia was worked out on the basis of data collected from computer tomography of a real bone. The following parameters of tibia were established: Young's modulus E = 18600 MPa and Poisson's ratio $v = 0.4$. The geometrical model of the low contact plate (LCP) was worked out in ANSYS v.11. The following material properties were established:

- stainless steel - $E = 2 \cdot 10^5$ MPa, Poisson's ratio $v = 0.33$
- Ti-6Al-4V alloy - $E = 1.06 \cdot 10^5$ MPa, Poisson's ratio $v = 0.33$.

Geometrical model of the tibia - LCP system with oblique fracture in distal part of the bone was presented in Fig. 1.
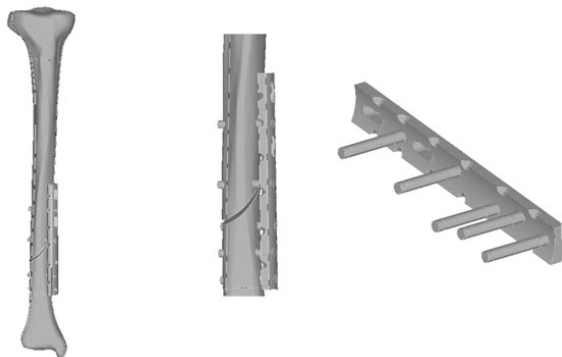
Fig. 1 Geometrical model of the analyzed tibia - LCP system

2.2 Numerical Model

The geometrical models were meshed with the use of SOLID95 finite elements - Fig. 2. This type of element is characterized by 20 nodes and 3 degrees of freedom in each node (displacements in x, y and z direction) - Fig. 3.
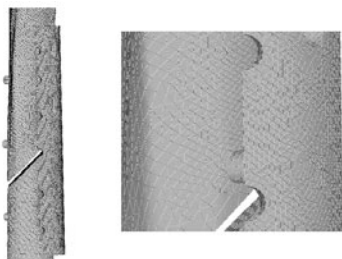
Fig. 2 Meshed model of the tibia - LCP system
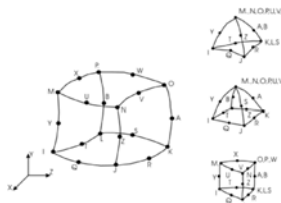
Fig. 3 The applied SOLID95 finite element

2.3 Boundary Conditions

The analysis was carried out in order to calculate displacements and stresses, depending on the applied mechanical properties of the plate. In order to carry out the calculations it was necessary to evaluate and establish initial and boundary conditions which imitate phenomena in real system with appropriate accuracy. The following assumptions were established:

- distal fragment of tibia was immobilized (all degrees of freedom of surface nodes were taken away). It enabled displacements of the proximal fragment, blocking possible rotation,
- upper epiphysis of the tibia was loaded with forces from 100 N up to 2000N with increment equal to 100 N.

Such high values of loading do not occur in reality during the fixation and rehabilitation. Such wide range of the loadings was established in order to present the biomechanical characteristics of the fixation in the widest possible range (from so called "biomechanical silence" - directly after the operation, till dynamic physiological loading). The results of the numerical analysis were presented for the loading F = 800 N that corresponds to statistical patient of weight equal to about 80 kg. Furthermore, this value of loading is reported in the literature as the limit value that provides safety of early rehabilitation. The analysis was carried out in order to calculate stresses and displacements in:

- elements of the tibia - stainless steel LCP system,
- elements of the tibia - Ti-6Al-4V LCP system.

Stresses and strains obtained in the analysis are equivalent values according to the Huber - Misses hypothesis.

3 Results

3.1 Tibia - Stainless Steel LCP System

The results of the stress and displacement analysis for the tibia - stainless steel LCP system were presented in Table 1 and Fig. 8. On the basis of the analysis, it was concluded that maximum equivalent stresses, caused by the loading F = 800 N, were observed in the bone screw implanted closest to the fracture gap (proximal tibia diaphysis). The stresses were not uniform on the bone screw surface. Maximum stresses were observed in the region of direct contact between the plate and the screw and were equal to σ_w = 415 MPa - Fig. 4, Table 1. The average equivalent stress in the plate did not exceed the value of σ_p = 297 MPa. However, maximum local stresses reached σ_{pmax} = 530 MPa and were placed in the proximal hole of the plate - Fig. 5. The applied loading (F = 800 N) does not cause the exceeding of the yield point of the material the plate and the bone screws are made of (stainless steel - 690 MPa).

Fig. 4 Equivalent stresses in the bone screws calculated for the applied loading F = 800 N

Fig. 5 Equivalent stresses in the plate calculated for the applied loading F = 800 N

Maximum displacements in the fracture gap, calculated for the loading F = 800 N did not exceed the value of u = 0.37 mm - Fig. 6 and 8. The obtained displacements were a basis to work out the biomechanical characteristics of the proposed implant. Furthermore, the displacement analyses showed that the displacement limit in the

fracture gap equal to 3 mm (determined on the basis of the clinical investigations) was not exceeded. It enables the use of the electromechanical effects which accelerate bone union. Maximum shear stresses in the bone were equal to $\tau = 145$ MPa and did not exceed the bone strength (~ 180 MPa) - Fig. 7. Maximum equivalent stresses in the bone were localized in the bone screws fixation regions. The biomechanical analysis of the proposed solution (LCP) indicates that for the applied boundary conditions, established on the basis of clinical recommendations (loading F = 800 N) and experimentally determined mechanical properties of the steel (TS = 950 MPa, YP = 680 MPa), this type of osteosynthesis can be applied in treatment of tibia fractures.

Fig. 6 Equivalent displacements in the OZ axis calculated for the applied loading F = 800 N
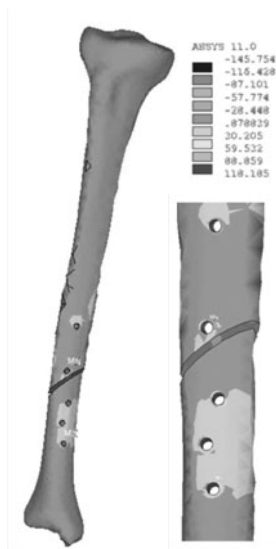
Fig. 7 Shear stresses in the bone calculated for the applied loading F = 800 N

3.2 Tibia - Ti-6Al-4V LCP System

The results of the stress and displacement analysis for the tibia - Ti-6Al-4V LCP system were presented in Table 1 and Fig. 8. On the basis of the analysis, it was concluded that maximum equivalent stresses, caused by the applied loading F = 800 N, were observed in the bone screw implanted closest to the fracture gap (proximal tibia shaft). Maximum stresses were located in the region of direct contact between the plate and the screw. Generally, the stress analysis of the tibia - Ti-6Al-4V LCP

Table 1 Results of the numerical analyses of the tibia - stainless steel and Ti-6Al-4V LCP system

Loading, N	Maximum equivalent stress in the bone screws, MPa	Equivalent stresses in the plate, MPa		Maximum shear stresses in the bone, MPa	Displacements in the fracture gap (OZ axis), mm	
		average	maximum		stainless steel	Ti-6Al-4V alloy
100	51.9	37.1	66.3	18.2	0.05	0.065
200	103.8	74.3	132.6	36.3	0.09	0.13
300	155.6	111.4	198.9	54.5	0.14	0.19
400	207.5	148.6	265.2	72.6	0.19	0.26
500	259.4	185.7	331.4	90.8	0.23	0.32
600	311.3	222.8	397.7	108.9	0.28	0.39
700	363.1	260.0	464.0	127.1	0.32	0.45
800	**415.0**	**297.1**	**530.3**	**145.2**	**0.37**	**0.54**
900	466.9	334.2	596.6	163.4	0.42	0.58
1000	518.8	371.4	662.9	181.5	0.46	0.65
1100	570.6	408.5	729.2	199.7	0.51	0.71
1200	622.5	445.7	795.5	217.8	0.56	0.78
1300	674.4	482.8	861.7	236.0	0.60	0.84
1400	726.3	519.9	928.0	254.1	0.65	0.91
1500	778.1	557.1	994.3	272.3	0.69	0.97
1600	830.0	594.2	1060.6	290.4	0.74	1.04
1700	881.9	631.3	1126.9	308.6	0.79	1.10
1800	933.8	668.5	1193.2	326.7	0.83	1.17
1900	985.7	705.6	1259.5	344.9	0.88	1.23
2000	1037.5	742.8	1325.8	363.0	0.93	1.3
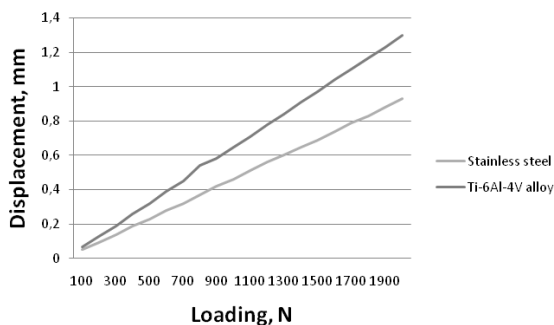
Fig. 8 Displacements in the fracture gap calculated in the OZ axis for the plates made of stainless steel and Ti-6Al-4V alloy

system indicated that the obtained equivalent stresses and their distribution are similar to the ones obtained for the plate made of the stainless steel. The results indicate that the applied loading (F = 800 N) does not cause the exceeding of the yield point of the material the plate and the bone screws are made of (Ti-6Al-4V alloy). However, the displacement analysis of the tibia - Ti-6Al-4V LCP system showed differences with respect to the plate made of stainless steel. Maximum displacements in the fracture gap, calculated for the applied loading F = 800N, were equal to u = 0.54 mm. The displacement analysis indicate that application of the Ti-6Al-4V alloy increases the flexibility of the fixation - Fig. 8. The biomechanical analysis of the proposed solution (LCP) indicates that also this type of osteosynthesis, realized with the use of the implant made of the Ti-6Al-4V alloy, can be applied in treatment of tibia fractures.

4 Conclusions

The aim of the work was the numerical analysis of the system for external stabilization of tibia. Biomechanical analysis of the tibia - LCP system was carried out for the implant made of two metallic biomaterials used in bone surgery - stainless steel and Ti-6Al-4V alloy. Finite element method was applied in order to calculate stresses and displacements in the system. The model of the tibia with oblique fracture in distal part of the bone was applied. The proposed fracture region was determined on the basis of the previously done analysis of unbroken bone. In the proposed region the maximum strain is observed. Furthermore, this type of fracture and its location is very common in clinical practice. In order to carry out the calculations it was necessary to evaluate and establish initial and boundary conditions which imitate phenomena in real system with appropriate accuracy. The analyzed systems were loaded with forces from 100 N up to 2000N with increment equal to 100 N. On the basis of the numerical analysis, it can be concluded that for the applied loading (F=100 ÷ 2000 N), diverse values of stresses and displacements were calculated. The maximum equivalent stresses, obtained for the axial loading with force of 800N, did not exceed the yield point for both stainless steel and titanium alloy. Implantation of the system and loading it with the force of 800N did not cause overstressing of the bone. But the maximum shear stress in the bone was close to the strength of the bone. Although, the allowable stresses in bone, equal to 180 MPa, were not exceeded. Displacement analyses for both stainless steel and titanium alloy showed that for the applied loading diverse values of displacements were observed. Maximum displacements in the fracture gap (for the applied loading F = 800 N), calculated for the stainless steel were equal to u=0.37 mm while for the titanium alloy reached 0.54 mm. Furthermore, the displacement analyses showed that the displacement limit in the fracture gap equal to 3 mm (determined on the basis of the clinical investigations) was not exceeded. Moreover, the displacement analyses showed that application of the plate made of Ti-6Al-4V alloy ensures more flexible osteosynthesis that could enable the use of the electromechanical effects which accelerate bone union. Generally, the obtained results allowed to work out the biomechanical

characteristics of the analyzed systems (u = f(F)). The biomechanical analyses of the both proposed solutions (LCP made of stainless steel and Ti-6Al-4V alloy) indicate that these types of osteosynthesis can be applied in treatment of tibia fractures. The obtained biomechanical characteristics can be a basis for selection of strain hardening of the applied metallic biomaterials as well as optimization of the plate's geometry.

References

1. Ramotowski, W., Granowski, R., Bielawski, J.: Osteosynthesis by ZESPOL method. Theory and clinical practice. PZWL, Warszawa (1988) (in Polish)
2. Granowski, R.: Zespol - a new method of stable osteosynthesis. Professor thesis. Medical University, Warszawa (1990) (in Polish)
3. Tanino, A.J., Davidson, C.L., Klopper, P.J.: Protection from stress in bone and its effects. Experiments with stainless and steel and plastic plates in dogs. J. Bone Joint Surg. 58-B, 107–113 (1978)
4. Marciniak, J.: Stresses in self-compression plates. Chir. Narz. Ruchu Ortop. Pol. LV 4-6, 273–277 (1990) (in Polish)
5. Marciniak, J.: Corrosion damage of bone plates and screws. Arch. Techn. Bud. Maszyn 8, 55–61 (1998) (in Polish)
6. Akenson, W.H., Woo, S.L.: The effects of rigidity of internal fixation plates on long bone remodeling. Acta Orthop. Scan 47, 241–245 (1976)
7. Steinemann, S.: The essential properties of bone plates for fracture fixation. Biomat. Biomech., 173–181 (1984)
8. Haas, N., Hauke, C., Schuetz, M., Kaeaeb, M., Perren, S.M.: Treatment of diaphyseal fractures of the forearm using the Point Contact Fixator (PC-Fix): results of 387 fractures of a prospective multicentric study (PC-Fix II). Injury 322, SB51–SB62 (2001)
9. Frigg, R.: Locking Compression Plate (LCP): an osteosynthesis plate based on the dynamic compression plate and the Point Contact Fixator PC-Fix. Injury 322, SB63–SB6 (2001)
10. Perren, S.M.: Evolution of internal fixation of long bone fractures. J. Bone Joint Surg. [Br] 84-B, 1093–1100 (2002)
11. Field, J., Hearn, T.C., Caldwell, C.B.: Bone plate fixation: an evaluation of interface contact area and force of the dynamic compression plate (DCP) and the limited contact-dynamic compression plate (LC-DCP) applied to cadaveric bone. J. Orthop. Trauma 11, 368–373 (1997)
12. Klaue, K., Fengels, I., Perren, S.M.: Long-term effects of plate osteosynthesis: comparison of four different plates. Injury 132, 51–62 (2000)
13. Arens, S., Schlegel, U., Printzen, G., et al.: Influence of materials for fixation of implants on local infection: an experimental study of steel versus titanium DCP in rabbits. J. Bone Joint Surg. [Br] 78-B, 647–651 (1996)
14. Uhthoff, H.K., Finnegan, M.: The effects of metal plates on post-traumatic bone remodelling and bone mass. J. Bone Joint Surg. [Br] 65-B, 66–71 (1983)
15. Chow, S.P.: Introduction to the point contact fixator (Part II). Injury 322, SB1–SB2 (2001)
16. Hofer, H.P., Wildburger, R., Szyszkowitz, R.: Observations concerning different patterns of bone healing using the Point Contact Fixator (PCFix) as a new technique for fracture fixation. Injury 322, SB15–SB25 (2001)

Metatarsal Osteotomy Using Double-Threaded Screws - Biomechanical Analysis

Anna Ziebowicz, Anita Kajzer, Wojciech Kajzer, and Jan Marciniak

Abstract. The fundamental purpose of this research was to determine the biomechanical characteristics of the first metatarsal bone - double-threaded screws system made of stainless steel (Cr-Ni-Mo) and an assessment of its stability. To define the biomechanical characteristics of the system, the finite element method and experimental method were applied. Geometric models of metatarsal bone and double-threaded screws, were discretized by means of SOLID 95 element. Appropriate boundary conditions imitating phenomena in the real system with appropriate accuracy were established. The aim of biomechanical analysis was calculation of displacements and stresses in the bone and the stabilizers in a function of the applied loading. The experimental method was carried out to calculate displacements of the analyzed system. The obtained results can be applied to determine the construction features of the stabilizer and to select mechanical properties of metallic biomaterial (selection of degree of strain hardening).

1 Introduction

The metatarsal bones are some of the most commonly fractured (broken) bones in the foot. There are two main types of metatarsal fractures:

- acute fractures - due to a sudden injury to the foot (commonly dropping a heavy object onto the foot, a fall or a sporting injury) [1]
- stress fractures - due to overuse, or repetitive, injury to a normal metatarsal bone [2].

The kind of fracture should be characterized and treatment initiated. Metatarsal fractures are divided into three sections - 1st, 5th and 2nd÷4th [3, 4]. Due to the head of

Anna Ziebowicz · Anita Kajzer · Wojciech Kajzer · Jan Marciniak
Silesian University of Technology, Institute of Engineering Materials and Biomaterials, Konarskiego 18a, 44-100 Gliwice, Poland
e-mail: anna.ziebowicz@polsl.pl

the first metatarsal being thought to bear one third of our body weight, any evidence of instability requires operative fixation [5].

The present-day alternative of small-bones reconstructions in orthopaedics is the double-threaded screws, that indicate many favorable features especially with reference to minimization of tissue traumas. The matter of these solutions is application of two threads of diverse diameter, that assure stabilization of bone fragments with the use of physiological effects [6]. From the biomechanical point of view, determination of hard tissue structures is crucial as well as stiffness of a bone-implant system.

2 Materials and Methods

The main aim of the work was the determination of the biomechanical characteristics of the first metatarsal bone - double-threaded screws fixation. On the basis of technical documentation, the geometrical model of screws was carried out in ANSYS v.10. In order to carry out the numerical analysis, the following material properties were as follows:

- bone: E=18600 MPa, v=0.3
- Cr-Ni-Mo steel: E=200000 MPa, v=0.33 [7, 8, 9].

The geometrical model of metatarsal bone - the double-threaded screws system takes into consideration the operation technique was presented in Fig. 1.
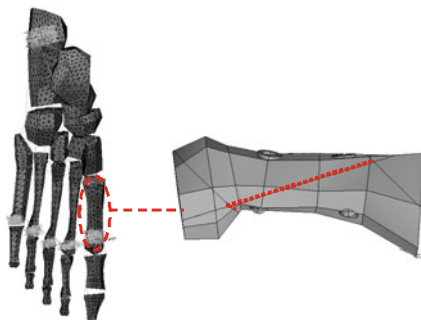
Fig. 1 Geometrical model of: a) human foot, b) metatarsal bone "I" - screw system

On the basis of the geometrical models a finite element mesh was generated with the use of SOLID95 finite elements. In order to carry out calculations, it was necessary to evaluate and establish initial and boundary conditions which imitate phenomena in the real system with appropriate accuracy [10, 11, 12]. The following assumptions were established:

- lower part of the metatarsal bone was immobilized (all degrees of freedom of nodes on external surfaces of condyles were taken away)

- there were three stages of solution performed: 1 - displacement 1 mm was established at the basis of metatarsal bone, 2 - force F=500 N was applied at the basis of metatarsal bone (Fig.2a), 3 = force F=3000 N was applied according to bending and compression tests (Fig. 2b).
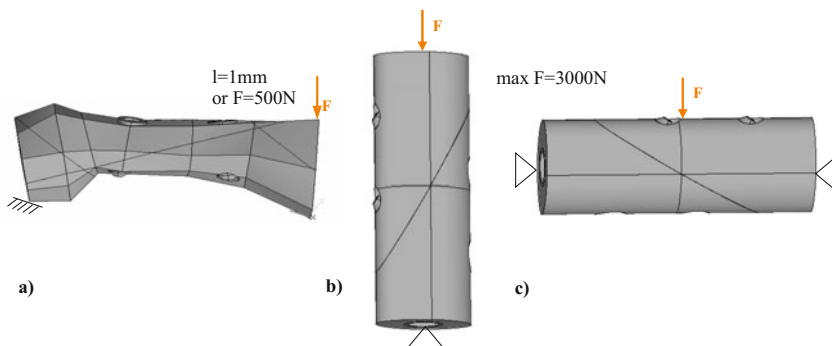
Fig. 2 Loading scheme of model

The scope of the analysis included the determination of displacements and stresses in elements of the metatarsal bone "I" - double-threaded screws made of stainless steel.

Stresses and strains obtained in the analysis are reduced values according to the Huber-Misses hypothesis.

In the experimental research of the metatarsal bone - double-threaded screws system (anatomical fracture simulated) the universal testing machine Zwick/Roell Z100/SN5A was applied. The experimental model was placed between cross-beams in order to do a compressing test. Measurement of the displacement values were done on the z axis direction - Fig. 4a. Measurement of the displacement values during the bending test were registered in the direction of the y axis - Fig. 4b.
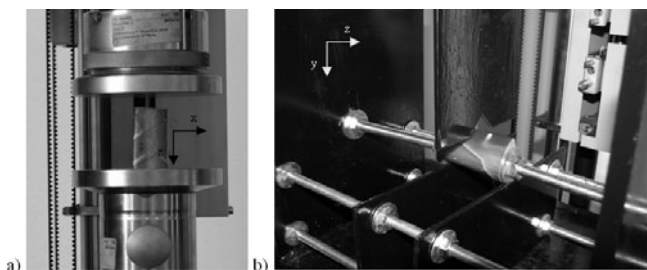
Fig. 3 Universal testing machine: a) compressing test, b) bending test

3 Results

The obtained results for the given boundary condition were presented in Table 1 as well as in graphic form - Fig. 4–7.

Table 1 Results of the numerical analysis of the metatarsal bone "I" - double-threaded screw system

Load steps		Displacement, mm				Strain, %	Stress, MPa
		x	y	z	Σ		
1 Displacement 1mm	System	0.300	0.030	0.160	1.069	0.32	4762
	Double-threaded screws						1389
2 Force F=500N	System	0.006	0.005	0.05	0.529	0.44	4525
	Double-threaded screws						541
3 Force F=3000N	Compression	0.009	0.019	0.004	0.329	0.034	1655
	Bending	0.001	0.011	0.031	0.148	0.031	818
	Double-threaded screws						690

Maximum stresses in the screws were localized in the transition zone between threads for the displacement equal to 1 mm. For the stainless steel screws and for the applied boundary conditions, maximum stresses were equal to 1389 MPa. However, the stresses on the whole surface for the applied force 500 N and the displacement equal to 1 mm, did not exceed 500 MPa.
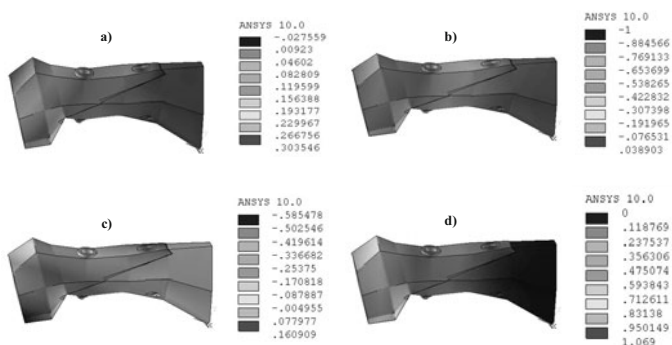
Fig. 4 Displacement distribution in bone - double-treaded screws system: a) axis OX, b) axis OY, c) axis OZ, d) displacement vector sum, load step 1
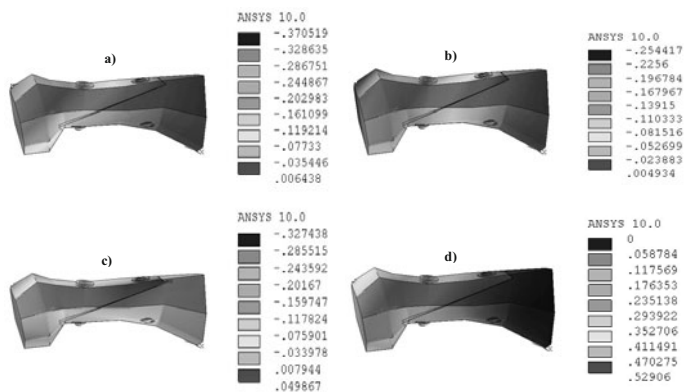
Fig. 5 Displacement distribution in bone - double-treaded screws system: a) axis OX, b) axis OY, c) axis OZ, d) displacement vector sum, load step 2
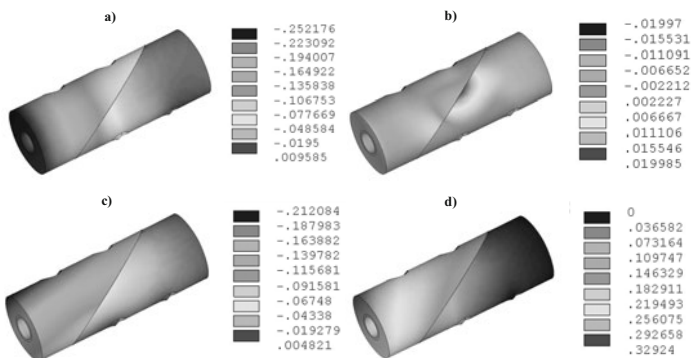
Fig. 6 Displacement distribution in bone - double-treaded screws system: a) axis OX, b) axis OY, c) axis OZ, d) displacement vector sum, load step 3 (compressing)

On the basis of the performed analyses, it can be stated that the displacement characteristics of the first metatarsal bone - double-threaded screws system in the experimental and numerical conditions were similar - Fig. 8.

Observations of the experimental model after the compression test revealed that one of the compression screws was broken.

Damage localization corresponded with the maximum values of stresses obtained from the numerical analysis - Fig. 9.

Analogous, stress analysis of the numerical model revealed that the maximum values of stresses obtained from the bending loads were localized in the place of screw narrowing - Fig. 10.

On the basis of the analysis, it was concluded that maximum equivalent stresses were localized the fixation site of the model and at the point of the applied loading.
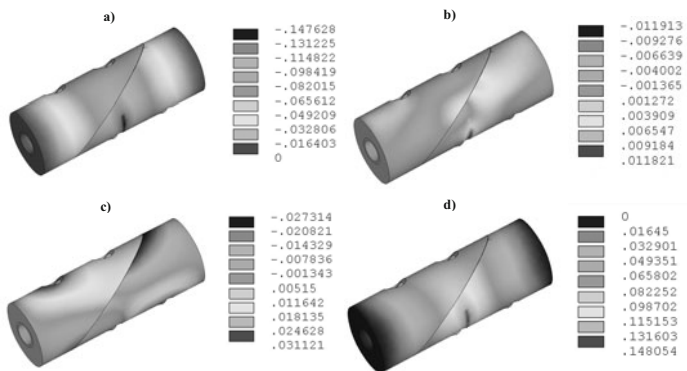
Fig. 7 Displacement distribution in bone - double-treaded screws system: a) axis OX, b) axis OY, c) axis OZ, d) displacement vector sum, load step 3 (bending)
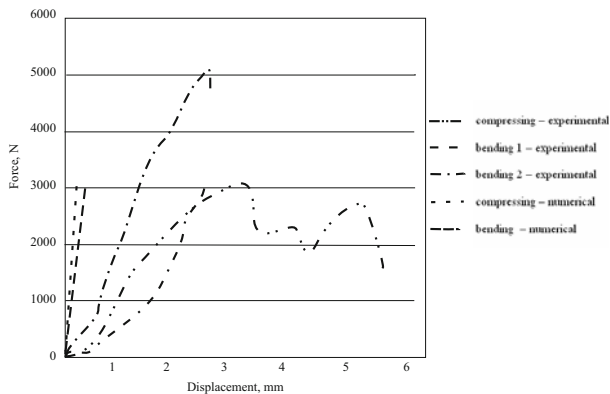
Fig. 8 Comparison of displacements for experimental and numerical analysis
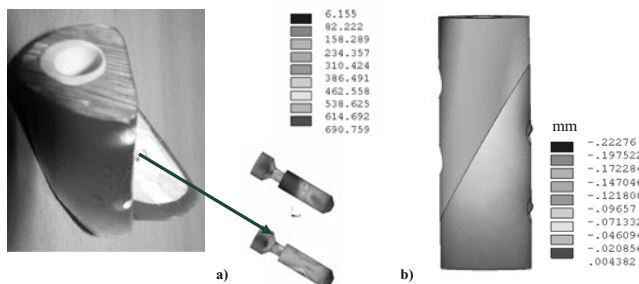
**Fig. 9** Compressing test: a) the place of screw damage, b) displacement distribution in bone
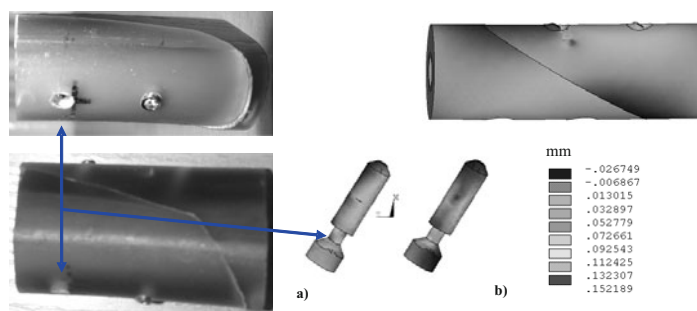
Fig. 10 Bending test: a) the place of the maximal screw effort, b) displacement distribution in bone

The obtained displacements for the metatarsal bone - compression screws system for both tests: compression and bending revealed, that maximum values did not exceed 0.22 mm and 0.15 mm respectively whereas displacements obtained from the experimental analysis were equal to 0.23 mm for the compression and 0.19 mm for the bending test.

4 Conclusions

The work presents results of biomechanical analysis of the first metatarsal bone - double- threaded screws system. The analyses were carried out with the use of finite element method and experimental method.

Proposed numerical solutions were followed by biomechanical analysis which allows the determination of characteristics connected with displacements in a function of applied loading. This fact is of great importance in risk assessment of the operation and the rehabilitation as well.

Knowledge of overloading causes dysfunctions as a consequence of instability determine further therapeutic management - both operative and rehabilitation. Of the back of the postoperative effects like decreased first metatarsophalangeal joint motion, shortening of the first metatarsal, dorsal displacement of the capital fragment deformation causes - generally functional disorders and dysfunctions of the foot - can be observed.

Displacements and stresses in the systems' elements were calculated. In the work presented, the most often using metallic biomaterial - Cr-Ni-Mo steel. Susceptibility of the system to displacement caused by the applied loading is the important parameter influencing the effectiveness of the proposed stabilization. Therefore, the numerical analysis of the metatarsal bone - double-threaded screws system for the applied metallic biomaterial indicated dangerous areas of the screws and is a starting point for the geometry optimization. The analysis of the obtained results showed that for the given way of loading, the damage of the screws is highly probable in the most vulnerable area i.e. the transition zone between threads. Experimental research

of double-threaded screws was focused on stability tests in order to verify the results of the numerical analysis.

On the basis of the obtained results, it can be stated that:

- the displacement characteristics of the first metatarsal bone - double-threaded screws system received with the use of the experimental method showed good correlation with the numerical results
- the maximum values of the screw stresses obtained from the numerical method confirm the damage localization of the canullated compression screw observed during the experimental analysis
- the obtained results are the basis for the selection of the structure and mechanical properties of the metallic biomaterial and geometrical features of the implant, it can also be applied in the selection of stabilization methods of metatarsal fractures.

References

1. Rosenberg, G.A., Sferra, J.J.: Treatment strategies for acute fractures and nonunions of the proximal fifth metatarsal. Journal of the American Academy of Orthopaedic Surgeons 8(5), 332–338 (2000)
2. Buckwalter, J.A., Brander, E.A.: Stress and insufficiency fractures. American Academy of Family Physician 56, 175–182 (1997)
3. Beck, M., Mittlmeier, T.: Metatarsal fractures. Der Unfallchirurg 111(10), 829–839 (2008) (in German)
4. Rammelt, S., Heineck, J., Zwipp, H.: Metatarsal fractures. Injury 35(suppl. 2), SB77–SB86 (2004)
5. Sorensen, M.D., Hyer, C.F.: Metatarsus primus varus correction: the osteotomies. Clinics in Podiatric Medicine and Surgery 26(3), 409–425 (2009)
6. Stryker Leibinger GmbH, Co. KG: TwinFix cannulated compression screw, Leibinger solutions for hand surgery. Procedural Guide (2004)
7. Marciniak, J.: Austenitic steel - the basic implantation material used in orthopaedic surgery. Orthopaedy, Traumatology, Rehabilitation 3, 52–58 (2000) (in Polish)
8. Marciniak, J.: Biomaterials, pp. 238–252. Silesian University of Technology, Gliwice (2002) (in Polish)
9. ISO 5832-1. Implants for surgery metallic materials – Part 1 – Wrought stainless steel (2007)
10. Walke, W., Marciniak, J., Paszenda, Z., Kaczmarek, M., Cieplak, J.: Biomechanical behaviour of double threaded screw in tibia fixation. In: Information Technologies in Biomedicine. Advances in Soft Computing, vol. 47, pp. 521–528. Springer, Heidelberg (2008)
11. Ziebowicz, A., Kajzer, A., Kajzer, W., Marciniak, J.: Biomechanical analysis of the 1st metatarsal - compression screws system. Engineering of Biomaterials (2009)
12. Kajzer, W., Kajzer, A., Marciniak, J.: FEM analysis of compression screws used for small bone treatment. Journal of Achievements in Materials and Manufacturing Engineering 33(2), 189–196 (2009)

Biomechanical Behaviour of Surgical Drills in Simulated Conditions of Drilling in a Bone

Marcin Basiaga, Zbigniew Paszenda, and Janusz Szewczenko

Abstract. The main aim of this work is a biomechanical analysis of a surgical drill-femur system under conditions simulating the bone drilling process, using a finite-element method. The geometrical model of the surgical drill was prepared for different point angle values of the drill tip ($2\kappa_1 = 90^o$ and $2\kappa_2 = 120^o$) and different diameters ($d_1 = 9.0$ mm, $d_2 = 4.5$ mm, $d_3 = 3.2$ mm and $d_4 = 1.0$ mm). The analysis included two variants of the drilling process: Variant I included drilling a single layer of the cortical tissue of a femur, while Variant II included the simulation of another step of the drilling process - drilling in the opposite area of cortical tissue. Calculations were made for two types of drill material. The biomechanical analysis may form the basis for improving the geometry of surgical tool tips and optimising a selection of the mechanical properties of the material used to manufacture them.

1 Introduction

In recent years there has been significant progress in medicine due to continuing efforts to improve the efficiency of treatment techniques. Modern medicine uses the achievements of many technical sciences, and this is particularly significant in methods used for the treatment of the human skeletal system. The continuing development of methods, as well as orthopaedic implant structural solutions, forces the need for constant modification and improvement of surgical instruments. Cutting tools are basic surgical instruments used in bone surgery, and comprises single, double and multiple tip cutting tools. The most frequently used multiple tip tools include drills and surgical taps, and they are most frequently used during osteosynthesis with the use of stabilizing-manipulating systems, such as Polfix [1].

Marcin Basiaga · Zbigniew Paszenda · Janusz Szewczenko
Silesian University of Technology, Institute of Engineering Materials and Biomaterials,
Konarskiego 18a, 44-100 Gliwice, Poland
e-mail: `marcin.basiaga@polsl.pl`

Drills used in bone surgery are instruments where use is forced by the development of osteosynthesis techniques. The variety of surgical techniques, the need to modify instruments to suit individual anatomical conditions and the tendencies towards the simplification of surgery has resulted in different drill types being manufactured. Apart from standard surgical drills, tools with special working elements and shank structures are being manufactured, such as drills with guided ends and cannulated drills. Drills used in machining are not the same as those used in surgery: they feature different end geometry due to the different mechanical properties of the material being machined: in this case, bone tissue [2, 3, 4, 5].

The huge demand made on surgical instruments means manufacturers try to improve the durability of their products. The literature on biomechanical aspects of these tools is, however, scant and mainly concerns analyses of dislocations, deformations and stresses and their functional purposes.

Such an analysis forms the basis for the optimisation of the geometric features of a tool and the selection of mechanical properties of the material used to make it. In most cases, issues concerning the thermal analysis of drills are described [6, 7]. This work concentrates on the analysis of the durability of surgical drills under conditions simulating the bone drilling process, with the use of a finite-element method.

2   Materials and Methods

2.1   Geometrical Model

Geometric models of drills were made on the basis of real tools selected according to their dimensions. Four tools with cylindrical shanks were selected; their diameters being: $d_1 = 9.0$ mm, $d_2 = 4.5$ mm, $d_3 = 3.2$ mm and $d_4 = 1.0$ mm. Additionally, the drill models analysed included two point angle values: $2\kappa_1 = 90^o$ and $2\kappa_2 = 120^o$. Total length and the length of the working section of each drill was constant at L = 150 mm and l = 60 mm respectively - Fig. 1a.

In order to perform the numerical analysis in conditions simulating the drilling process, a numerical model of a femur was prepared - Fig 1b. Due to the scope of the analysis, the femur model was simplified by removal of any condyles. This model also included an initial simulation of an opening having the same diameter as the drill and reflecting the geometry of the tool tip. Moreover, the model of a collet simulating the drill chuck was adapted - Fig. 1c. Geometrical models were made using Inventor Professional 2008 software.

Next, a geometrical model of a surgical drill-femur system for two drilling operation variants was prepared. The first variant reflects drilling in a single layer of the femur's cortical tissue. The second variant simulates another step of the drilling process - drilling in the opposite area of cortical tissue, and in this case the drill was inserted through a previously prepared opening - Fig. 2.
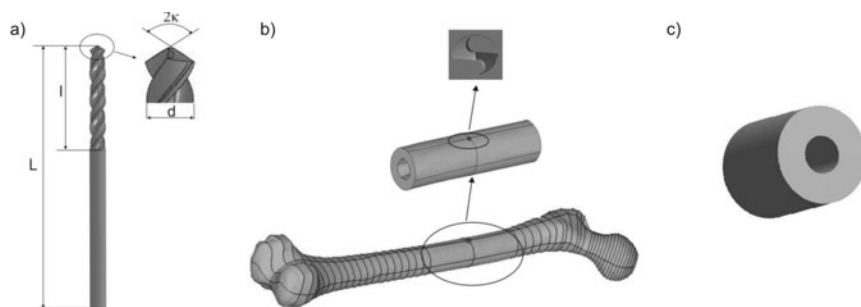
Fig. 1 Geometrical model: a) surgical drill, b) femur, c) collet simulating the drilling machine's chuck
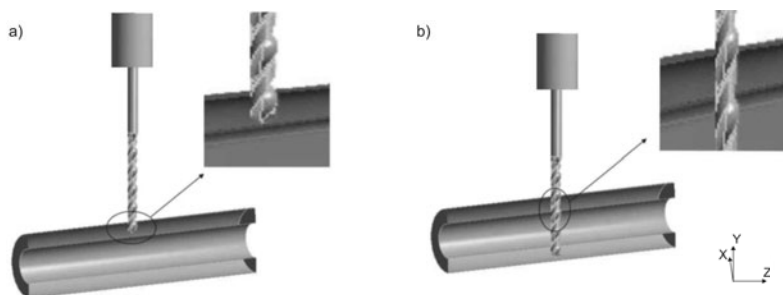
Fig. 2 Geometrical model of a surgical drill-femur system: a) variant I, b) variant II

2.2 Numerical Model

A grid for finite-element method calculations was generated for the geometrical models. The analysed elements of the system were digitalized by means of ANSYS Workbench v11 software. This software allows the automatic selection of an element type according to the geometry of the analysed object. In addition, the finite element network was made denser where it was suspected of having maximum shift, deformation and stress values - Fig. 3.

2.3 Boundary Conditions

In order to make the calculations, it was necessary to specify and set the initial and edge conditions to reflect appropriately the phenomena taking place in the real system. The following conditions were assumed [8]:
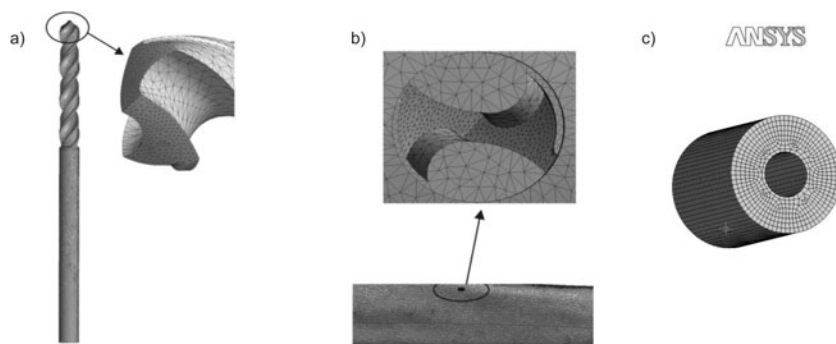
Fig. 3 Discrete models: a) surgical drill, b) femur, c) collet simulating the drilling machine's chuck

- drill loaded by an axial force, F = 60 N with a torque value, T = 0.04 Nm,
- supports were used to ensure the bone and chuck was unable to dislocate along the X, Y and Z axes,
- contact between the drill and bone along the cutting edges, the chisel edge of the drill and the drill margins near the opening made in the cortical tissue was simulated (variant II).

The analysis included designation of dislocations, deformations and stresses at separate points on the surgical drill in relation to each drilling process variant. The following material properties were assumed [9]:

- surgical drill,
  - X39Cr13 martensitic steel - E = 215,000 MPa, υ = 0.35,
  - Cr-Ni-Mo steel according to PN-ISO 5832-1 - E = 200,000 MPa, υ = 0.35,
- femur cortical tissue - E = 18,600 MPa, υ = 0.33.

3 Results

3.1 Strength Analysis Results - Variant I

The calculated results of the analysed diameters of a variable geometry drill are presented in Table 1. The analysis of these results shows that the distribution of deformations and reduced stresses across the tool working section vary. It was noticed that, independent of the diameter d, the maximum values of deformations and reduced stresses are present along the cutting edges in the external part of those drills with a point angle of $2\kappa_2 = 120^o$. Maximum perpendicular dislocations in respect to the axis of each drill (along the OZ axis) were observed for drills with a diameter of $d_4 = 1.0$ mm - Table 1, Figs. 4-6.

Table 1 Results of numerical analysis for X39Cr13 and D alloy drills - variant I

Tool diameter, d, mm	Point angle 2κ,°	Dislocations along OZ mm		Reduced deformations ε_{max}, %		Reduced stresses σ_{max}, MPa	
		Force F = 60, N					
		X39Cr13	D alloy	X39Cr13	D alloy	X39Cr13	D alloy
1.0	90°	0.25	0.24	0.60	0.59	1480	1415
	120°	0.31	0.30	0.93	0.89	2113	2100
3.2	90°	0.061	0.060	0.43	0.42	395	389
	120°	0.075	0.074	0.61	0.60	489	483
4.5	90°	0.013	0.012	0.17	0.17	226	224
	120°	0.015	0.014	0.28	0.27	313	308
9.0	90°	0.003	0.003	0.05	0.04	81	79
	120°	0.005	0.004	0.10	0.10	230	221
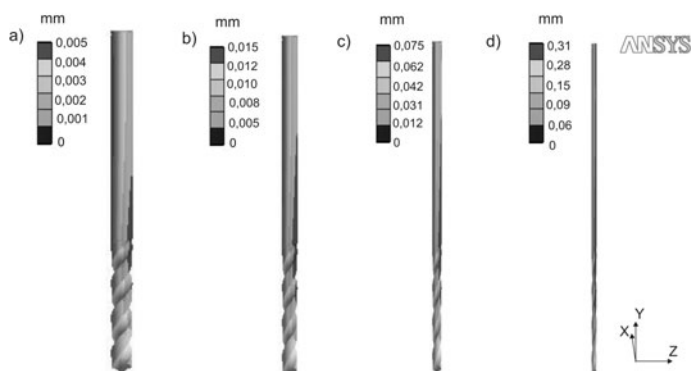
Fig. 4 Discrete models: Results of dislocation state analysis for X39Cr13 steel drill with the point angle of $2\kappa_2 = 120°$: a) $d_1 = 9.0$ mm, b) $d_2 = 4.5$ mm, c) $d_3 = 3.2$ mm, d) $d_4 = 1.0$ mm

3.2   Strength Analysis Results - Variant II

The calculated results of each analysed diameter of a variable geometry drill are presented in Table 2. This section mainly describes the strength analysis of the drills at the point of contact between the drill margin and model opening in the cortical tissue - Fig. 2b. The calculated results show that the distribution of dislocations, deformations and stresses in this section of the tool vary. Among all the analysed variants, the highest dislocation, deformation and reduced stresses were observed for drills with a diameter of $d_4 = 1.0$ mm - Table 2, Figs. 7-9.

Fig. 5 Discrete models: Results of reduced deformations state analysis for X39Cr13 steel drill with the point angle of $2\kappa_2 = 120^o$: a) $d_1 = 9.0$ mm, b) $d_2 = 4.5$ mm, c) $d_3 = 3.2$ mm, d) $d_4 = 1.0$ mm

Fig. 6 Discrete models: Results of reduced stress state analysis for X39Cr13 steel drill with the point angle of $2\kappa_2 = 120^o$: a) $d_1 = 9.0$ mm, b) $d_2 = 4.5$ mm, c) $d_3 = 3.2$ mm, d) $d_4 = 1.0$ mm

Fig. 7 Results of dislocation state analysis for X39Cr13 drill with the point angle of $2\kappa_2 = 120^o$: a) $d_1 = 9.0$ mm, b) $d_2 = 4.5$ mm, c) $d_3 = 3.2$ mm, d) $d_4 = 1.0$ mm

Table 2 Results of numerical analysis for X39Cr13 and D alloy drills - variant II

Tool diameter, d, mm	Point angle 2κ,°	Dislocations along OZ mm		Reduced deformations ε_{max}, %		Reduced stresses σ_{max}, MPa	
		Force F = 60, N					
		X39Cr13	D alloy	X39Cr13	D alloy	X39Cr13	D alloy
1.0	90°	0.12	0.12	0.41	0.40	562	555
	120°	0.15	0.14	0.61	0.61	608	600
3.2	90°	0.021	0.020	0.33	0.32	215	211
	120°	0.042	0.041	0.35	0.34	280	270
4.5	90°	0.007	0.007	0.15	0.14	152	147
	120°	0.008	0.008	0.16	0.15	180	169
9.0	90°	0.001	0.001	0.01	0.01	52	47
	120°	0.002	0.002	0.06	0.05	95	91
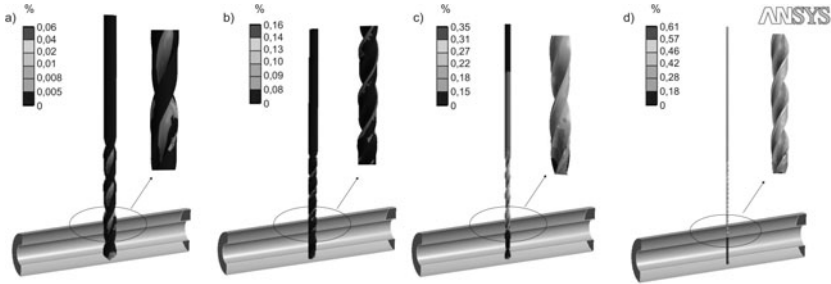
Fig. 8 Results of reduced deformations state analysis for X39Cr13 steel drill with the point angle of $2\kappa_2 = 120^o$: a) $d_1 = 9.0$ mm, b) $d_2 = 4.5$ mm, c) $d_3 = 3.2$ mm, d) $d_4 = 1.0$ mm

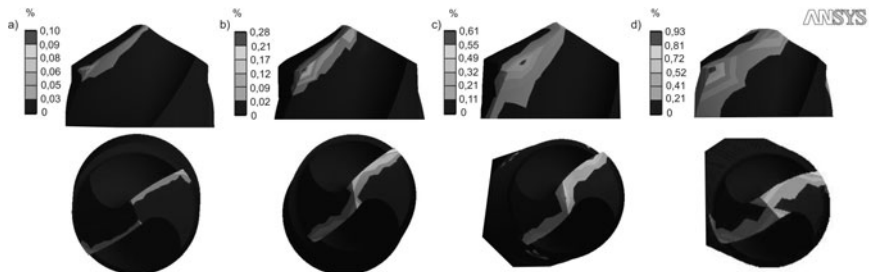**Fig. 9** Results of reduced stress state analysis for X39Cr13 steel drill with the point angle of $2\kappa_2 = 120^o$: a) $d_1 = 9.0$ mm, b) $d_2 = 4.5$ mm, c) $d_3 = 3.2$ mm, d) $d_4 = 1.0$ mm
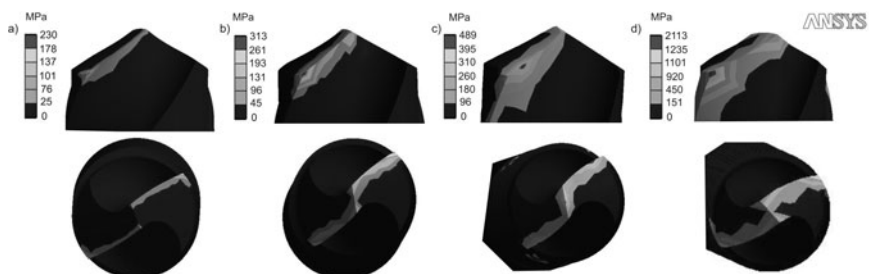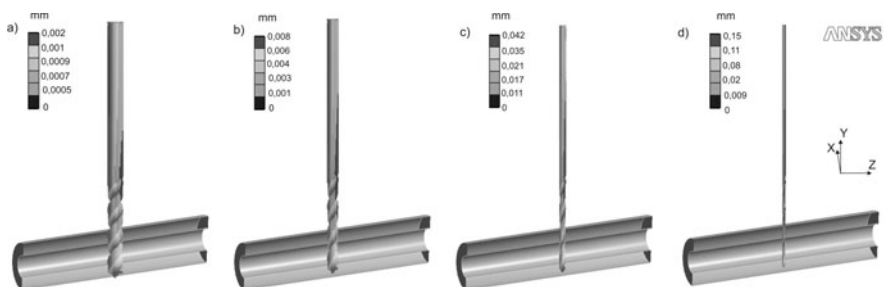
4 Conclusions

This work concentrates on the numerical analysis of selected surgical drills under conditions simulating the bone drilling process. The analysis included two variants of the drilling process. Variant I of the analysis reflects drilling in a single layer of the femur's cortical tissue and was intended to specify the correct value of point angle 2κ. The results show that, independent of the drill diameter value (d) and type of drill material, the highest deformation and reduced stress values can be seen at a point angle of $2\kappa_2 = 120^o$- Table 1, Figs. 4 to 6. Thus the most favourable solution was to use drills with a point angle of $2\kappa_1 = 90^o$. Moreover, it was found that in case of drills having a diameter of $d_4 = 1.0$ mm (independent of the value of 2κ angle) generated stresses exceeding the yield point, $Rp_{0.2}$, for both analysed materials. Thus as a consequence of the femur drilling process with load, F = 60 N, and torque, T = 0.04 Nm, excessive drill wear in the area of its cutting edges can occur.

Due to cases occurring where the drill breaks, the aim of variant II was to determine the distribution of dislocations, deformations and stresses at the point of contact between the tool and model opening in bone - Fig. 2b. The determined deformation and reduced stress values are lower than in case of area of cutting edges (determined in variant I). The perpendicular dislocations in respect to the drill axis (in both variants - I and II) were negligible - Table 1, 2.

This work is one excerpt from a research project by its authors looking into the functional properties of surgical tools used in osteosynthesis. A later stage of the research will include the analysis of the thermal phenomena accompanying the bone drilling process. Such a comprehensive study should be an important source of information for orthopaedic surgeons.

References

1. Paszenda, Z., Tyrlik-Held, J.: Surgical instruments. Printing House of the Silesian University of Technology, Gliwice (2003) (in Polish)
2. Price, M., Molloy, S., Solan, M., Sutton, A., Ricketts, D.: The rate of instrument breakage during orthopaedic procedures. International Orthopaedics 26, 185–187 (2002)
3. Guo, Y., Dornfeld, D.: Finite element modeling of burr formation process in drilling 304 stainless steel. ASME Journal of Manufacturing Science and Engineering 122, 612–619 (2000)
4. Karmani, S., Lam, F.: The design and function of surgical drills and K-wires. Current Orthopaedics 18(6), 484–490 (2004)
5. Allan, W., Williams, E.D., Kerawala, C.J.: Effects of repeated drill use on temperature of bone during preparation for osteosynthesis self-tapping screws. British Journal of Oral and Maxillofacial Surgery 43, 314–319 (2005)

6. Abouzgia, M.B., Symington, J.M.: Effect of drill speed on bone temperature. Journal of Oral and Maxillofacial 25, 394–399 (1996)
7. Davidson, S.R., James, D.F.: Drilling in bone: modeling heat generation and temperature distribution. ASME Journal of Biomechanical Engineering 125, 305–314 (2003)
8. Hillery, M., Shuaib, I.: Temperature effects in the drilling of human and bovine bone. Journal of Materials Processing Technology 92-93, 302–308 (1999)
9. Bedzinski, R.: Engineering biomechanics. Printing House of the Wroclaw University of Technology, Wrocław (1997) (in Polish)

FEM Analysis of Instruments Used in Root Canal Preparation

Witold Walke, Zbigniew Paszenda, and Piotr Winiarski

Abstract. This work describes the structural strength analysis of selected drills used for mechanical root canal preparation. The assumptions made in the biomechanical analyses included both the technique of performing the surgery and various shapes of root canal. The calculations were using two alternative types of metal materials used to manufacture surgical instruments - X39Cr13 martensitic steel and Ni-Ti alloy with super-elastic properties. The results of the analyses indicate that using Ni-Ti alloy in the production of endodontic drills assures safety during root canal treatment processes.

1 Introduction

Modern stomatology supports the trend towards minimising the need for causeless removal of problem teeth. Dental extraction causes the natural teeth arrangement to change, which can result in different complications or the need for an implant, in which case the patient's organism may react to the biomaterial. Taking into account possible problems connected with tooth extraction due to the irreversible pathological state of the pulp, dentists use a method of biomechanical root canal preparation which relies on removal of the inflamed pulp and tight filling of the canal with a filling material. This is known as endodontic treatment [1, 2, 3, 4].

The morphology of root canals depends mainly on such factors as: patient's age, presence of tooth decay or former injuries. Apart from the above factors, the process of endodontic treatment is difficult due to the large percentage number of canals having different curve profiles, and which are determined by radius and angle of curvature [1, 2].

Witold Walke · Zbigniew Paszenda · Piotr Winiarski
Silesian University of Technology, Institute of Engineering Materials and Biomaterials, Konarskiego 18a, 44-100 Gliwice, Poland
e-mail: witold.walke@polsl.pl

As endodontic treatment methods developed, many types of drills required in the process of mechanical preparation of tooth roots canals were manufactured. Using such tools, however, poses the risk of drill breaking while treating a root canal. If removal of a broken drill is impossible, it is necessary to perform a resection of the upper part of the tooth. The literature is scant on the influence of drill geometry and the mechanical properties of the material used to manufacture them concerning safety of operation during canal treatment - in particular literature concerning the assessment of the susceptibility of drills to deflection [5, 6]. This work is the initial stage of a comprehensive analysis of endodontic tools used for tooth canal treatment.

2 Materials and Methods

The main aim of this work was the strength analysis of an endodontic drill used in the root canal treatment process, with different anatomical structures taken into account. The analyses were made for the Dentsply Maillefer tool designed for mechanical root canal preparation; the tool's point angle $\varphi = 4^o$ and the working length l = 25 mm (ProFile 25.04.). The geometrical model of the tool's structure was made using SolidWorks 2009 software. During preparation of the tool model, geometric features and structural features typical for such drills were taken into account. Actual flute profiles and mutual position of flutes were utilised and a safe, non-sharpened tool tip was used - see Fig. 1.
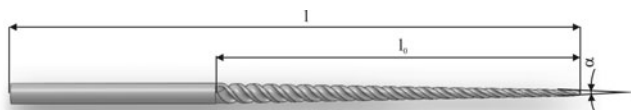
Fig. 1 Geometrical model of drill used in mechanical root canal preparation

For the need of analyses, the root canal model was simulated in the form of three rollers of diameter D = 2 mm [7]. This allowed three tool support points to be obtained - see Fig. 2,3. This system makes it possible to obtain variable angle values and radii of root canal curvature.

The geometrical models were used to generate a grid of finite elements, which were used for calculations using the finite-element method. The drill models and the three-roller system were digitalized using SOLID187 finite element. The scope of the analysis included determining of stresses generated by:

- distal fragment of tibia was immobilized (angular dislocation in the drill working section in the range $\varphi = 0 - 30^o$ (simulation of tool operation in a canal curved across its entire length) for two types of tool material - X39Cr13 martensitic steel and Ni-Ti alloy - see Fig. 4a),
- angular dislocation in the rage $\varphi = 0 - 30^o$ on the variable length of the drill working section (simulation of tool operation in a canal curved in its lower part) for Ni-Ti alloy drills - see Fig. 4b.
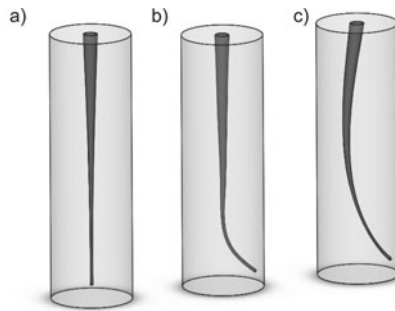
Fig. 2 Geometrical models of root canals: a) straight, b) curved in its lower part, c) curved on its entire length

Fig. 3 Three roller system model allowing for simulation of different tooth canals

The following material properties were assumed: X39Cr13 martensitic steel [8]:

- E = 215,000 MPa,
- Poisson's ratio $v = 0.3$,
- Rm = 760 MPa,
- $R_{p0.2}$ = 345 MPa,

Super-elastic Ni-Ti alloy with elastic memory [9]:

- E = 20,000 MPa,
- Poisson's ratio $v = 0.3$,
- Rm = 1068 MPa,
- $R_{p0.2} = 814 MPa$,

Dentine material [9]:

- E = 13,800 MPa,
- Poisson's ratio $v = 0.3$.

In order to make calculations, it was necessary to specify and set initial and boundary conditions which reflected appropriately the phenomena taking place in a real system. The following conditions were assumed for the needs of analyses:

- degrees of freedom of drill shank section end face and of the 1st roller were provided for all directions thus allowing for the rigid fixing of the drill's geometry,

a)

b)
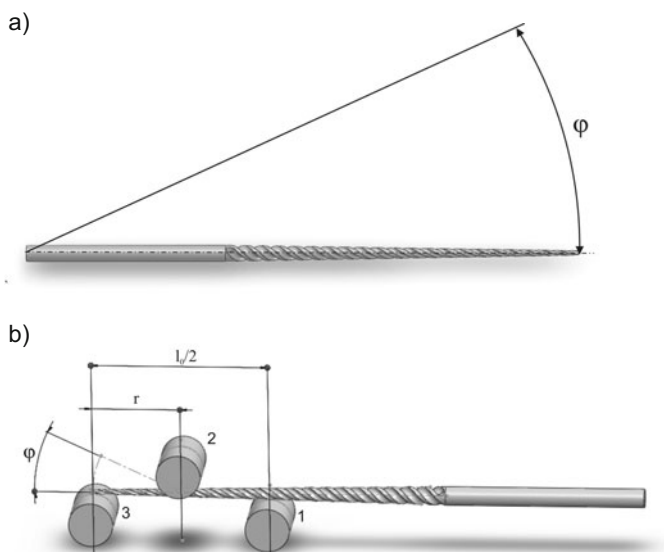
Fig. 4 Diagram of analysed calculation variants: a) simulation of drill's operation in a canal curved on its entire length, b) simulation of drill's operation in a canal curved in its lower part

- all nodes of the 2nd roller were dislocated along the drill axis by the following values: $r_1 = 3$, $r_2 = 4$, $r_3 = 5$, $r_4 = 6$ thus allowing the positioning of canal curvatures in relation to its top in the range, r = 3-6 mm,
- deflection of the drill tip in the angular range, $\varphi = 1 - 30°$ was obtained by dislocation of the 3rd roller perpendicularly in relation to the tool axis.
- a contact point was defined between the surfaces and edges of the system's elements to allow for their mutual dislocation.

The analyses did not include the rotational speed of the drills. According to the Huber-Mises theory, all deflections and stresses were reduced.

The results of the analyses show that higher reduced stress values for respective angular dislocations (φ) appeared in the working section of drill, the strength properties of which were the same as in case of X39Cr13 steel. The maximum stress values were generated in the area where tool's working section transits into the shank. Due to the values of generated stresses, higher strength properties than assumed for steel ($R_{p0.2}$, Rm) were present only for angular dislocations in the range, $\varphi = 1 - 5°$.

3 Results

The first stage of analyses included determining the influence of angular dislocation (φ) on the distribution of stresses generated in the working section of an endodontic drill for two alternate metal material types - X39Cr13 martensitic steel and superelastic Ni-Ti alloy. The calculated results are presented in Table 1, Figs. 5 and 6.

Table 1 Results of numerical analysis of endodontic drills

				Reduced stresses σ_{max}, MPa					
1°	2°	3°	4°	5°	10°	15°	20°	25°	30°
				Ni-Ti alloy					
29	59	89	119	149	298	447	596	746	895
				Martensitic steel – X39Cr13					
298	596	895	1193	1492	-	-	-	-	-

Fig. 5 Distribution of reduced stresses in X39Cr13 steel drill's working section: a) $\varphi = 1°$, b) $\varphi = 2°$, c) $\varphi = 1°$
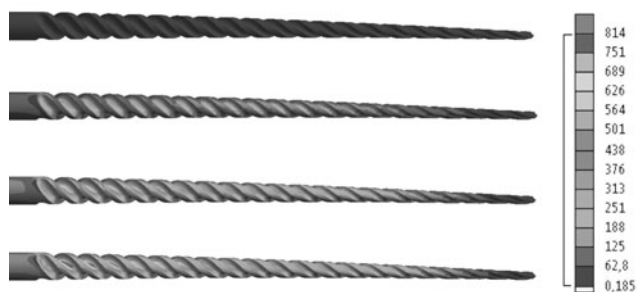
Fig. 6 Distribution of reduced stresses in Ni-Ti alloy drill: a) $\varphi = 1°$, b) $\varphi = 15°$, c) $\varphi = 25°$ d) $\varphi = 30°$

On the basis of the results obtained for both alternative materials, the biomechanical characteristics of the drill was also determined, showing the relationship between the maximum reduced stresses as being a function of angular dislocation φ - Fig. 7.

The aim of the second stage was to determine the influence of root canal geometry changes (in its lower part) on stresses generated in the Ni-Ti drill working section.
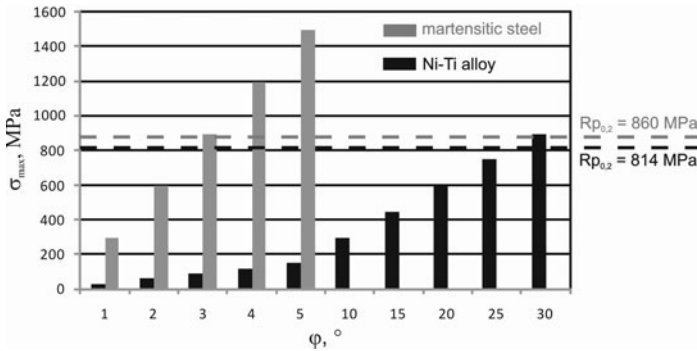
Fig. 7 Relationship between maximum reduced stresses as a function of angular dislocation φ for martensitic steel and Ni-Ti alloy drills

The results of the analyses are presented in Table 2. The results show that the stress values for respective angular dislocations (φ) are higher at lower radii of curvature

Table 2 Results of numerical analysis of Ni-Ti alloy drill for different angular dislocation values φ and radii of root canal curvature r

r, mm	Reduced stresses σ_{max}, MPa						
	5°	10°	15°	20°	25°	30°	35°
3	196	392	456	615	750	889	1020
4	136	262	395	527	664	770	890
5	113	226	338	447	552	653	701
6	99	210	313	413	511	605	693
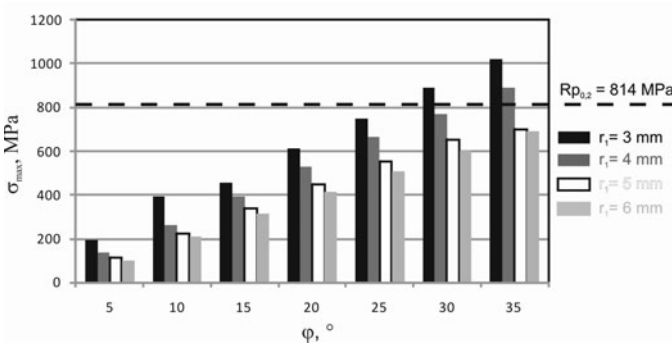
Fig. 8 Relationship between maximum reduced stresses as a function of angular dislocation φ and different radii r for Ni-Ti alloy drill

(r). Maximum values of reduced stresses were observed on the internal part of tool bending. The results were also used as the basis for specifying the biomechanical properties of the drill which determine the relationship between maximum reduced stresses generated in the tool's working section as a function of angular dislocation for different angle of curvature values (r) - Fig. 8.

4 Conclusions

This work describes the structural strength analysis of selected drills (Profile 25.04 manufactured by Dentsply Maillefer) used for mechanical root canal preparation. The assumptions made in the biomechanical analyses included both the technique of performing surgery and different shapes of root canal.

Using this type of tool poses the risk of them breaking inside a tooth root canal. Taking this into consideration, the first stage of the biomechanical analyses included an assessment of the drill's strength under conditions simulating its operation with a tooth root canal curved across its entire length. This calculation variant was made for two alternative types of metal materials used to manufacture surgical instruments - X39Cr13 martensitic steel and Ni-Ti alloy with super-elastic properties. The results show that in the case of martensitic steel drills a slight root canal curvature ($\varphi > 1°$) generates stresses higher than $R_{p0.2}$, and even the Rm value of the material - table 1, Figs. 5 and 7. Thus drills manufactured from martensitic steel can break inside a tooth root canal. It is advised to use a Ni-Ti alloy with super-elastic properties for drill production. The results of the analyses made for this variant show that only the bending of the drill's working section at an angle of $\varphi = 30°$ generates stresses exceeding the alloy's yield point, $R_{p0.2}$. One can thus assume that using Ni-Ti alloy (due to its resistance to elastic strain) in the manufacture of endodontic drills assures safety during root canal treatment processes.

The second stage of the calculations included the assessment of Ni-Ti drill strength under conditions simulating its operation with a tooth root canal curved across its entire length - see figs. 2b, 4b. This was possible thanks to a three-roller system and the ability for longitudinal and perpendicular movement in relation to 2nd and 3rd drill axis roller. These calculations confirmed the advantages of using such an alloy in the endodontic drill manufacturing process. Values of stresses exceeding the alloy's yield point $R_{p0.2}$ were observed only for angular dislocations of $\varphi = 30°$ and for tool radius of curvature $r \leq 4mm$.

These analyses are the initial stage of a research project, and the next phase should include tests on the influence of the tool's rotational speed on the biomechanical properties of drills and accompanying thermal phenomena. Such a comprehensive study should form an important source of information for dentists.

References

1. Arabska-Przedpełska, A., Pawlicka, H.: Endodontics - morphology, diagnostics, treatment. Wydawnictwo Medyczne, Warsaw (2004) (in Polish)
2. Hotz, P., Leisebach, T.M., Minder, K., Rocke, H., Sundqvist, G.: Endontology. PZWL, Warsaw (2001) (in Polish)
3. Cattaneo, P.M., Dalstra, M., Melsen, B.: The Finite Element Method: a Tool to Study Orthodontic Tooth Movement. Journal of Dental Reserch 84(5), 428–433 (2005)
4. Cheng, R., Zhou, X.D., Liu, Z., et al.: Finite element analysis of the effects of three preparation techniques on stresses within roots having curved canals. International Endodontic Journal 42, 220–226 (2009)
5. Stock, C.: Current status of the use of ultrasound in endodontics. International Dental Journal 41, 175–182 (1991)
6. Maceri, F., Martignoni, M., Vairo, G.: Mechanical behaviour of endodontic restorations with multiple prefabricated posts: A finite-element approach. Journal of Biomechanics 40, 2386–2398 (2007)
7. Cheung, G.S.P., Darvell, B.W.: Fatigue testing of a Ni-Ti rotary instrument. Part 1: strain-life relationship. International Endodontic Journal 40, 612–618 (2007)
8. Paszenda, Z., Tyrlik-Held, J.: Surgical Instruments. Printing House of the Silesian University of Technology, Gliwice (2003) (in Polish)
9. Marciniak, J., Kaczmarek, M., Ziębowicz: Biomaterials in stomatology. Printing House of the Silesian University of Technology, Gliwice (2008) (in Polish)

Specific Evaluation of Pelvic Radiograms and Hip BMD in Structural Scoliosis Reflectorica and Reactive Pain Conditions of the Backbone

Andrzej Dyszkiewicz, Paweł Połeć, Damian Chachulski,
Paweł Kępiński, and Jakub Zajdel

Abstract. An upright posture is a dynamic motion process, the stability of which depends on how the centre of gravity is projected onto the base of support. One of the basic external manifestations of this function is the dimensional symmetry of vectorial, angular and amplitudinal motion determinants. The nervous system, in its reaction to pain or to developed anatomical alterations (e.g. the shortening of a limb), strives to correct the body structure symmetry and its dynamic parameters, hence the asymmetry determiner of a feature related to a foci of pain or dysfunction may be used indirectly and directly to achieve a clinical quantitative evaluation. The aim of the study was to perform a comparative evaluation of the symmetry of standard densitometric parameters of the pelvic joints in relation to determinants of the pelvis x1-6 and lower body limbs, as well as to the difference in length of the lower limbs and symmetry of the shoulder girdle muscle structure determiners y1-3 in selected pain conditions. Following a radiogram analysis of selected patient groups, a high correlation of y1-3 asymmetry determiners in relation to the difference in length between the lower limbs and to the x1-6 asymmetry determiners was observed. The study showed only a slight correlation with the asymmetry of densitometric parameters of the hips evaluated using a DXA absorption meter.

1 Introduction

An externally perceivable symmetry of the human body is the result of symmetry within the sagittal plane, especially with regard to the structure of the skeletal, muscular, nervous, articular and ligament systems. Even dimensions of the subsequent bone pairs of the limbs and their correct ligamental stabilisation in the joints are a condition to achieve a balanced upright posture maintaining the pelvis and

Andrzej Dyszkiewicz · Paweł Połeć · Damian Chachulski · Paweł Kępiński · Jakub Zajdel
Laboratory of Biotechnology Cieszyn ul.Goździków 2 and Specialist Rehabilitation and
Rheumatology Outpatient Clinic "VIS" Cieszyn ul. Bielska 3a
e-mail: a.dyszkiewicz@po.opole.pl

shoulder girdle plane parallel to the ground. A similar situation occurs with regard to twin skeletal muscle pairs of the trunk and limbs, which causes muscles capable of generating the same concentric and eccentric power, to affect joints manifesting a comparable level of ease of motion and movement range [15, 16].

However, for structural symmetry to demonstrate a symmetry of motion, on top of a mirrored bone, joint and muscle pair structure, it is necessary to have a similarly symmetrical structure of peripheral nerves linked to efferent pathways of the spinal cord, which are connected to the proper areas of the motor cortex. The presented structural features demonstrate only a few ways in how functional symmetry assumes and maintains a balanced upright posture or how well it performs cyclic motions. An upright posture is a dynamic motion process which results in the projection of the centre of gravity on the base of support. One of the external manifestations of the correct delivery of this function is a symmetric alternation of statokinetic reactions made by twin skeletal muscle systems. That is why both the determiners of statokinetic micromotions in an upright posture and walking phases demonstrate symmetry and alternation, indicating the proper operation of the articular, joint, muscular and most importantly nervous systems [17, 18].

During infancy, subsequent phases in the motor learning process, depend not only on the symmetry of the anatomic structure, but most importantly on the performance of the muscles, nerves and nerve-muscle connections. Key to this are the processes of myelinization and development of those parts of the brain, which in the process of flexor and extensor use, perform experimental motions and encode multi-muscular coordination engrams of the most successful movements.

The creation and consolidation of optimal coordination engrams is the result of an averaging of all the gathered experiences resulting from millions of motion experiments. Motion skills, which are gradually developed and become increasingly simplified, are the basis for the development of further motions, and subsequently become incorporated into more complex motion patterns.

Control of the skeletal muscle system, which is performed by the brain and has been accepted based on previous experiences, is not a static condition, but oscillates around the centre of balance and demonstrates a tendency for optimisation. If then osteosynthesis disorders occur in a developing body, which in turn lead to an uneven length of one of the lower limbs causing asynchrony of the pelvis motion determiners, the system works to compensate the dysfunction in the backbone side bend mechanism and to limit the extension of the other leg in the knee joint.

If the problem involves a shortening of a limb in the early stages of development, even an experienced therapist will find it difficult to notice qualitative, not to mention quantitative changes in the symmetry of a patient's motions. The situation appears to be completely different when the dysfunction concerns a sudden anatomic change in a person with a previously developed pattern of coordination. This may happen for instance if a limb has been shortened as a result of fracture. A engram then created, which compensates the anatomic change, is less effective and significantly distorts the symmetric alternation of motion [19].

Pain to a large extent modifies the motions of a body as well. It serves as an emergency reaction location indicator and alters the motion coordination engram which

has so far remained symmetrical, and decreases the amplitude of motion vectors which lead to the stimulation of a foci of pain. An invariable decision imperative, which focuses on performing a motion task despite the existing pain, tolerates the necessity for a one-sided decrease in the amplitude of motion, and in turn causes a compensating increase of motion in another, generally symmetrical area of the body and includes additional balancing reactions from the head and trunk, which distorts a fluid and alternating sequence of walk determiners.

The basic biomechanical criterion for the existence of a symmetrical limb system is the automatic effort a body makes to equally balance the load on both the limbs, which ensures their balanced wear and tear and guarantees their proportional usability. Practically speaking, every clinical problem linked directly or indirectly to the locomotor system has a modifying effect on the walk mechanism, affecting the size and range of lower limb bone and joint load asymmetry, which after a a longer period of time leads to the alteration in the particular components of the anatomic structure.

The question thus is what kind of an effect does short-term or long-term asynchronous compensation of motion determiners have in the biomechanical and molecular context of bone tissue?

The bone is a tissue which is subject to constant reconstruction during its lifetime, thus its present state is a consequence of 2 undergoing processes i.e. osteolysis and rebuilding, which serve to adapt the skeleton to changing mechanical loads. The direction vector for the modification of local bone tissue strength is the spatial distribution of force affecting bone trabeculae trajectory nodes, or concentrations of bone cortex (Fig. 1a,b). Mechanical forces alter the dimensions of bone trabeculae below their normative values and produce a microscopic piezoelectric effect in the protein crystal tissue, which leads to an inhibition in the activity of hematopoietic cells, osteoblasts and initiates and intensifies the activity of osteoclasts. A reverse reaction occurs when strong mechanical forces lead to overnormative deformations leading to increased piezoelectric potential in a bone which is unprepared for such circumstances, and leads to the inhibition in the osteolytic activity of osteoclasts and intensifies osteosynthesis by osteoblasts. In this situation the piezoelectric potential gradient is one of the key factors determining the spatial location and scale in the balance between osteosynthesis and osteolysis, leading to alterations in the trajectory of maximum mechanical load on the bone[1, 3, 4].

Putting aside for a moment the consequences of anatomical skeletal asymmetry, in good health, the processes of resorption and bone formation remain balanced until the fourth and fifth decade of a human's life. In the initial period of menopause and in various metabolic disorders that come with age, and as a result of treatment using some types of medicine or due to immobilisation, the balance becomes distorted and resorption (Fig. 2b) takes lead over bone formation (Fig 2a). This eventually results in progressive loss of osseous tissue and dissipation of bone trabeculae as well as bone cortex osteones, which in turn leads to a decrease in the mechanical strength of the skeleton and higher potential for fracture[5, 6, 7, 8].

For many years now medicine has sought to counteract osteoporosis by using antiresorption treatment in cases justified by age or symptomatology, all the more
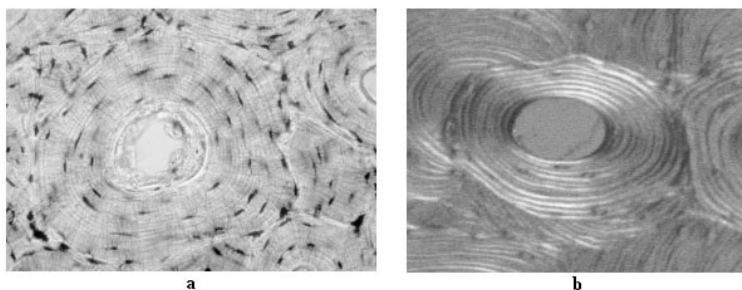
Fig. 1 Image of Havers' osteome of the bone cortex in: (a) an optical microscope; (b) a polarising microscope
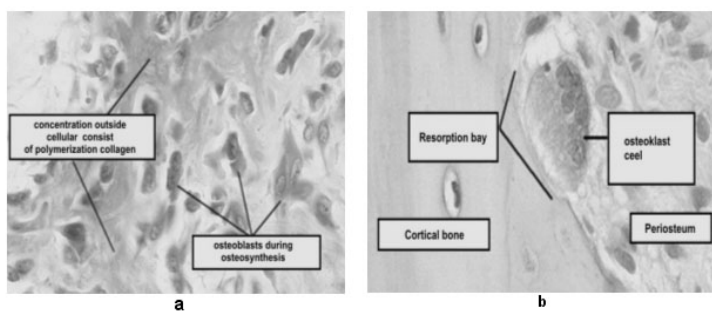
Fig. 2 Synthesizing cells, which modify the structure of osseous tissue: (a) osteoblasts during osteosynthesis; (b) osteoklasts in a resorption bay during osseous erosion

that the course of osteoporosis is often asymptomatic. Radiological diagnostics for a long time failed to fulfil the criteria required in assessing bone density due to a lack of sufficient standards regarding the photochemical processing of film. Many interesting bone tissue studies failed due to a high fluctuation of densitometric image parameters[11, 12, 13, 14, 20, 22]. In addition, limitations in the successful ability to perform a visual assessment of bone density alterations by a radiologist were of great significance. A significant improvement occurred once photonic matrix converters were introduced, which allowed for a direct breakdown of X-rays to electronic and digital formats.

The bone densitometers used these days make use of the same method used in absorption meters i.e. measure the dispersion and reflection of an X-ray, gamma ray or mechanical vibration wave. The device incorporates assemblies which emit ionizing radiation or ultrasounds. They are also equipped with sensitive detectors connected to analogue and digital converters, which are linked up to a computer. X-ray radiation or ultrasound emission through tissue leads to a weakening of the beam in relation to the standard encoded in the computer. Apart from the unquestionable advantages such a solution brings, the main shortcoming is the difficulty in finding

representative skeletal bone density areas, which in standard cases can improve the screening process but where there are complications, it may lead to omission of a pathological foci in an apparently well formed skeleton. Unfortunately, in rheumatology, such cases occur very often [10]. The reason why this problem occurs is the common and heedless use of algorithms which calculate average values in selected measurement areas without the possibility to highlight anatomical structures constituting markers of particular skeletal disorders [27, 26, 25, 24, 23, 21]. As a result, screening methods which are built thus are reliable only in simple clinical conditions [4, 9].

The axial load of the backbone is transferred to the sacroiliac joints, hip joints and then through the thigh bones to the knees and along the shin bones through to the ankles and feet. The symmetry of force distribution has a visible impact on the development of an internal symmetrical structure of twin bone components. The concentration of trabeculae and osteones of the bone cortex, which occurs in reaction to external forces, is visible on X-ray images as bold white lines, which represent trabeculae groups. Single trabeculae can be assessed by means of microtomography.

Leonardo da Vinci once said that "Mechanics is the paradise of the mathematical sciences, because by means of it one comes to the fruits of mathematics." The author of one of the first studies ever, which covered stress within a bone structure was Galileo. In the 19th century, Meyer's studies pointed to the relationship between the architecture of bone fracture and its statics and mechanics, while in 1866 Culmann linked the structure of the spongy bone to the trajectory of main stress and introduced the model of the so-called Culmann's rod. In 1869, Julius Wolf announced a thesis that biosynthesis and resorption of the bone is a biological and controlled process and depends on the value of local stress loads. This thesis, following some corrections made by Roux in 1881, became the official theory behind the "functional adaptation of the bone", which single-handedly shows the abilities of osseous tissue to adapt to particular functions in the body and treats the state of main stress trajectories as a balance between two-way modelling processes, allowing supportive tissues to transfer external forces while maintaining optimal material wear.

Strengthening of the structure of the bone results from the thickening of the cortex layer and an increase in the saturation of the existing trabeculae. This process is visible in radiograms and is generally noticed by experienced radiologists. Thus, when asymmetric load distribution, resulting from a shorter limb occurs, the load bearing elements of the shorter limb become stronger and thicken in size. Experiments have shown that reflectoric assymetry in the distribution of osseous density is not an ultimately defined matter. Radiological image analysis performed after a 10 month period since a limb was levelled by use of a levelling insert, has proven the existence of two parallel processes: (1) lowering of the osseous density in the bones of the limb bearing a greater weight (the shorter one), the length of which was increased by use of a levelling insert /thus decreasing the load/; (2) increasing of the osseous density in the bones of the longer limb, the load on which increased after application of an insert under the initially shorter limb [18, 19, 20].

Methods for local and sectorial estimation of the symmetry of density features within visually perceivable groups of trabeculae, allow for the evaluation of the

results of a previous history of unbalanced static and dynamic exposure on the skeletal system. These estimates are based on the assumption that the distribution of force trajectories, which had remained balanced for a long time, leads, within the load-bearing elements, to a modelling of the structural density, the features of which work to achieve symmetry. Dynamic motion pattern changes, which persist for a period of weeks or months and which are defined by pain or by the shortening of a limb, lead to the consolidation of an altered, asymmetric trajectory of forces in the skeleton's nodes and consolidation of bone remodelling compensation effects.

1.1   Study Objective

The objective of the study was to perform a comparative analysis involving the symmetry of standard densitometric parameters of the hip joints and the symmetry of the optical density in reference points of pelvic radiograms (X1-6) and comparing the two to back muscle symmetry determiners (Y1-3) and the lower limb length difference (Z) in patients with: (1) LS pain without scoliosis reflectorica or neuro-vertebral conflict, (2) LS pain lasting for 1-3 months, with neuro-vertebral conflict and scoliosis reflectorica and without a shorter limb, (3) LS pain without neuro-vertebral conflict, with scoliosis reflectorica caused by a shorter lower limb present for at least 2 years. The following research questions were posed:

(1) Is there a difference between the asymmetry coefficient BMD (Bone Mineral Density) in the hip joints and the averaged values of x1-x6 pelvic radiogram image optical density asymmetry determiners in patients in groups A, B, C?
(2) Is there any difference between the averaged back muscle tension asymmetry determiners (y1-3) in patients in groups A, B, C?
(3) Is there any correlation between the BMD asymmetry determiner of the hips and the pelvic radiogram asymmetry determiner(x1-x6); and between the back muscle tension asymmetry determiner(y) and the lower limb length asymmetry determiner(z)?

1.2   Patients Studied

89 patients who qualified for the study were subdivided into the following groups (Fig. 3):

1. Group A consisting of 28 patients including 16 women and 12 men 46.8 ± 7.5 years of age. All the patients reported pain in the LS region of the backbone and had no history of scoliosis reflectorica or any radiological alterations in the L1-L5 areas.
2. Group B consisting of 32 patients, including 18 women and 14 men 45.2 ± 5.8 years of age experiencing pain and with scoliosis reflectorica caused by a neuro-vertebral conflict in the L3/4, L4/5 lub L5S1 areas. The pain occurred suddenly following an instance of physical motion or as exacerbation following a period of remission lasting at least 6 months.

3. Group C consisting of 31 patients including 15 women and 16 men 48.6 ± 8.3 years of age with no history of radiculitis, experiencing pain in the LS region of the backbone lasting for at least 2 years, caused by scoliosis resulting from a shorter limb.
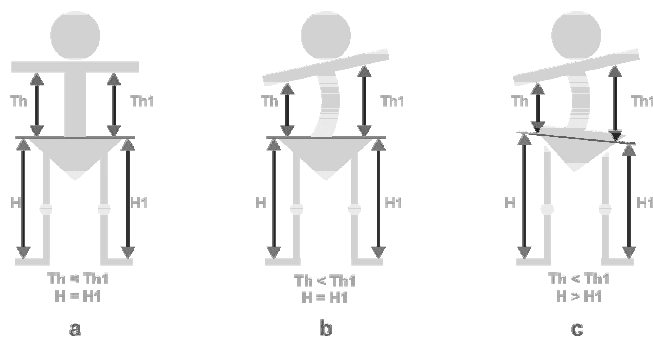
Fig. 3 Posture patterns in groups: (a) symmetrical (horizontal pelvis); (b) reflectoric, caused by pain and muscle tension (horizontal pelvis); (c) reflectoric caused by a shorter limb (tilt-edpelvis)

1.3 Exclusion Criteria

Group A:

(1) LS pain syndrome lasting for 1-3 months without radiculitis features nor scoliosis reflectorica. (2) positive bowstring sign, (3) negative Lasegue sign, (4) negative downward head compression test, (5) X-ray image showing level pelvis and no changes in the L3/4, L4/5, l5/S1 regions.

Group B:

(1) symptoms of radiculitis lasting for 1-3 months with LS-type scoliosis reflectorica, (2) positive Lasegue sign, (3) positive bowstring sign, (4) positive downward compression test, (5) radiological narrowing of one of the following regions L3/4, L4/5, L5S1.

Group C:

(1) one lower limb shorter by at least 6mm, (2) LS-type pain with no signs of radiculitis and with structural scoliosis reflectorica, (3) X-ray image showing a tilted pelvis with LS-type scoliosis, no changes in the L3/4, L4/5, l5/S1 regions.

Exclusion criteria:

(1) LS region or lower limb injury, (2) cancer, (3) collagenogenosis, (4) systemic muscle and nerve disease, viral hepatitis, pancreas diseases, atherosclerotically induced pain radiating to the LS region, (5) a history of operations of the backbone, bones or lower limb joints, (6) condition following endoprosthetics of the joints or backbone.

2 Methods

2.1 Scoliosis Angle Assessment

During the patient pre-selection stage, LS X-ray images were performed at a front and back projection in a 60 x 40 cm format. The images were scanned to bmp format and then assessed by means of a three-layer (with one layer hidden), one-way neuron network implemented into a Qnet 2000 Trial environment (Fig. 4), which automatically assessed radiograms allowing the studied patients to be divided into two groups: (1) Group A (Cobb's angle) $< 10°$; (2) Group B, C (Cobb's angle) $> 10°$.
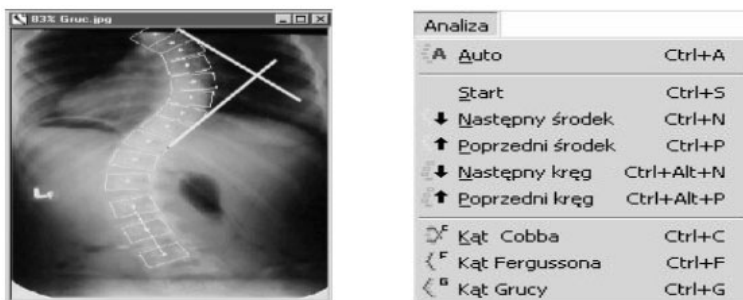
Fig. 4 Software dialog box used to measure the scoliosis angle by means of Cobb's, Grucy's and Fergusson's methods

2.2 Assessment of the Hip Column by Means of the DXA Method

Testing of the density of the hip column was performed by using a standard DXA bone densitometer in the left and right hip joints and assessed by means of a standard diagnostics screening program (Fig. 5). The BMD parameters obtained, expressed in [g/cm3] were used to calculate the BMD asymmetry coefficient of the hip joints (D).

Region	Area (cm²)	BMC (g)	BMD (g/cm²)	T-Score	Z-Score
Neck	4.99	1.84	0.370	-4.3	-2.4
Troch	10.72	4.40	0.470	-2.9	-1.5
Inter	20.50	11.76	0.574	-3.4	-2.0
Total	**36.20**	**18.00**	**0.497**	**-3.6**	**-2.0**
Ward's	1.09	0.17	0.154	-5.0	-2.3

Total BMD CV 1.0 %, ACF = 1.025, BCF = 1.001, TH=5.161
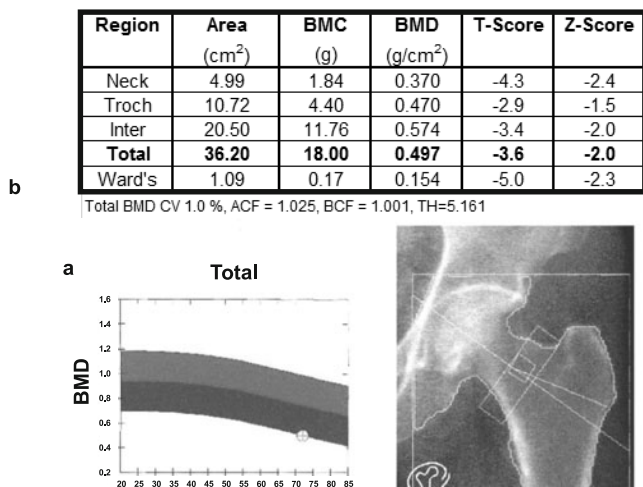
Fig. 5 Hip column test report performed using the DXA method, containing a sample image with a measurement field

2.3 Assessment of the Reference Points in the Pelvis

Another planimetric module allows for the subtraction of the image, containing the load-bearing elements of a selected part of the skeleton (Fig. 8), with the use of erosion at a defined binarisation threshold, followed by colour indexation, as per the optical density scale, and application of active edge contour to expose the views of the load-bearing elements on a 2-dimensional image matrix. In and around the pelvis of patients diagnosed with scoliosis, 6 sectors were selected X1, X2, X3, X4, X5, X6, thus creating a type of measurement mask for the evaluation of further images (Fig. 7). The mask reflects the course of the main trajectories of forces transferred from the backbone through the sacro-iliac joints to the socket of the hip joint, next to the head of the thigh bone and the cortex layer of the thigh bone shaft. The process of matching the measurement mask to the individual changes in the size of radiograms was performed manually. In the future, an active-contour model based program will be used. Measurements performed in each sector's left and right-handed areas were averaged and then the optical density asymmetry determiner of that sector was estimated (Fig. 6).

Optical density tests of radiograms in a measurement window net was performed using the author's "Densytometria 1.0" software (Fig. 9,10), the algorithm of which is based on the Finite Element Theory. The program performs an erosion of the matrix of the image for the binerisation threshold processed earlier, and then adds up and averages the greyness of pixels in the subsequent symmetrical measurement fields and calculates the quotient of the left and right field as coefficients X1-6.

$$X(1) = \frac{A(l)}{A(p)}; X(2) = \frac{B(l)}{B(p)}; X(3) = \frac{C(l)}{C(p)}; \tag{1}$$

$$X(4) = \frac{D(l)}{D(p)}; X(5) = \frac{E(l)}{E(p)}; X(6) = \frac{F(l)}{F(p)}; \tag{2}$$

Fig. 6 Method of asymmetry coefficients (X1-6) estimation
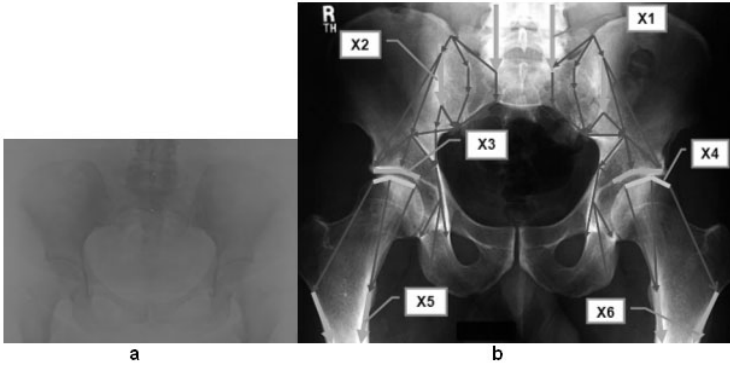
Fig. 7 Pelvic image processing stages: (a) image following binary erosion; (b) overlaying the measurement mask onto the image
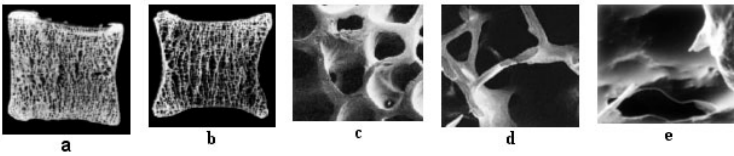
Fig. 8 Tests of the system on various osseous tissue elements: (a-b) Longisections of vertebral bodies; (c) trabeculae; (d) erosion trabecula at the verge of breaking; (d) broken trabecula
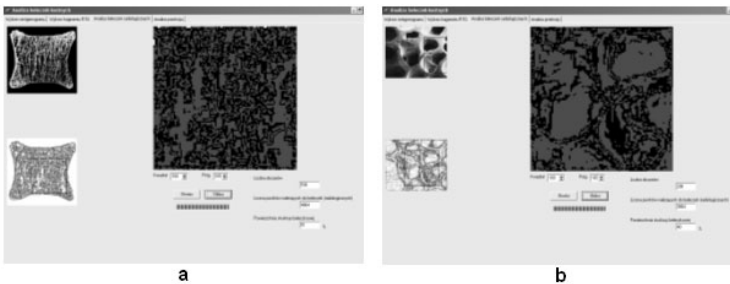
Fig. 9 Program dialog box used for performing a binary erosion of an image, classifying its structure by means of the Finite Element Method and finally determining the quantitative proportion between the number of pixels corresponding to continuous and closed structures in contrast to the entire image matrix: (a) 51%; (b) 40%
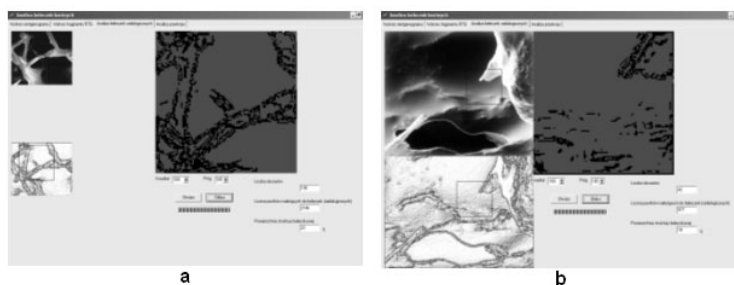
Fig. 10 Program dialog box: (a) erosion trabecula at the verge of breaking 22%; (b) stub of a broken trabecula 10%

2.4 Photoplanimetric Assessment of the Muscular Structure of the Back

Static contourography is a valuable method which makes it possible to assess the indicator of silhouette contour asymmetry of the body or feet, which is the result of injury or pain stimulus. It enables for the precise determination of the initial condition, which can then be compared with measurements performed during the observation of a patient (Fig. 11). Pain leads to a muscle-activated defensive response from the backbone, which involves the back muscles flexing asymmetrically and serves to limit the mobility range of structures exposed to the pain-inducing nerve. Muscle asymmetry can be easily recognized by the naked eye. In the course of treatment, the back gradually returns to its initial shape. By using a digital camera generated photograph, thanks to image processing, a level oriented structure of the muscle build of the back can be obtained. Additionally, the left and right side of the back muscle structure can be compared to each level. This is how the back structure asymmetry indicator (y1-3) is determined in practice (Fig. 12, 13).
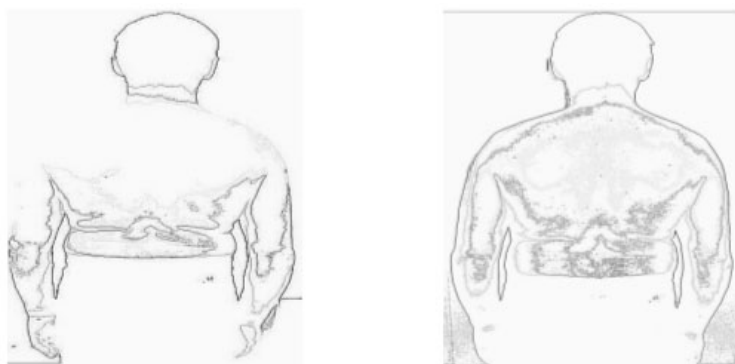
Fig. 11 Back muscle build structure (1-yellow, y2-violet, y3-blue); (a) before, (b) after pain treatment

Fig. 12 Image of a patient's back, muscle build contourography and a patient's radiogram with slight silicosis reflectorica of the backbone in a condition of radiculitis
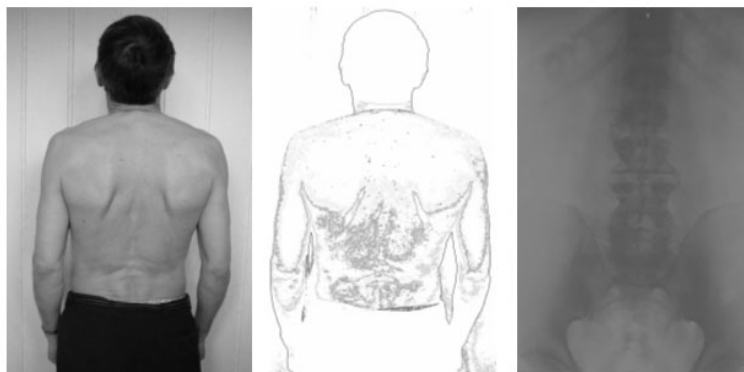
Fig. 13 Image of a patient's back, muscle structure contourography and a patient's radiogram with visible scoliosis reflectorica of the backbone as a result of a shorter right lower limb

3 Results

Average values and standard deviations of the coefficients W(BMD), X(1-6), Y(1-3) and Z in groups A,B,C have been presented in Table 1.

Table 2 shows the significance level of the difference between the values of the coefficients (BMD), X(1-6), Y(1-3), Z in groups A, B, C

Table 1 Average values and standard deviations of the coefficients W(BMD), X(1-6), Y(1-3), Z in groups A,B,C

indicator	group A (n = 28)	group B (n = 32)	group C (n = 31)
w(BMD)	0.94±0.16	0.92±0.18	0.88±0.21
x1	0.93±0.11	0.91±0.17	0.84±0.17
x2	0.95±0.12	0.91±0.14	0.7±0.16
x3	0.94±0.17	0.93±0.15	0.75±0.14
x4	0.96±0.15	0.935±0.14	0.8±0.12
x5	0.93±0.15	0.91±0.17	0.72±0.13
x6	0.95±0.12	0.92±0.13	0.77±0.14
y1	0.92±0.085	0.69±0.12	0.7±0.12
y3	0.9±0.11	0.72±0.13	0.67±0.14
y3	0.88±0.12	0.71±0.11	0.73±0.12
z	0	0	0.82±0.13

Table 2 the significance level of the difference between the values of the coefficients (BMD), X(1-6), Y(1-3), Z in groups A, B, C

indicator	Group A	group B	group C	
w(BMD)	W(BMD)A W(BMD)B $P < 0.5$	- W(BMD)B W(BMD)C $P < 0.1$	- W(BMD)A W(BMD)C $P < 0.1$	-
x1	X(1)A - X(1)B $P < 0.1$	X(1)A - X(1)C $P < 0.05$	X(1)B - X(1)C $P < 0.05$	
x2	X(2)A - X(2)B $P < 0.05$	X(2)A - X(2)C $P < 0.01$	X(2)B - X(2)C $P < 0.01$	
x3	X(3)A - X(3)B $P < 0.5$	X(3)A - X(3)C $P < 0.01$	X(3)B - X(3)C $P < 0.01$	
x4	X(4)A - X(4)B $P < 0.5$	X(4)A - X(4)C $P < 0.01$	X(4)B - X(4)C $P < 0.01$	
x5	X(5)A - X(5)B $P < 0.5$	X(5)A - X(5)C $P < 0.01$	X(5)B - X(5)C $P < 0.01$	
x6	X(6)A - X(6)B $P < 0.5$	X(6)A - X(6)C $P < 0.05$	X(6)B - X(6)C $P < 0.05$	
y1	Y(1)A - Y(1)B $P < 0.01$	Y(1)A - Y(1)C $P < 0.01$	Y(1)B - Y(1)C $P < 0.1$	
y3	Y(2)A - Y(2)B $P < 0.01$	Y(2)A - Y(2)C $P < 0.01$	Y(2)B - Y(2)C $P < 0.1$	
y3	Y(3)A - Y(3)B $P < 0.01$	Y(3)A - Y(3)C $P < 0.01$	Y(3)B - Y(3)C $P < 0.1$	
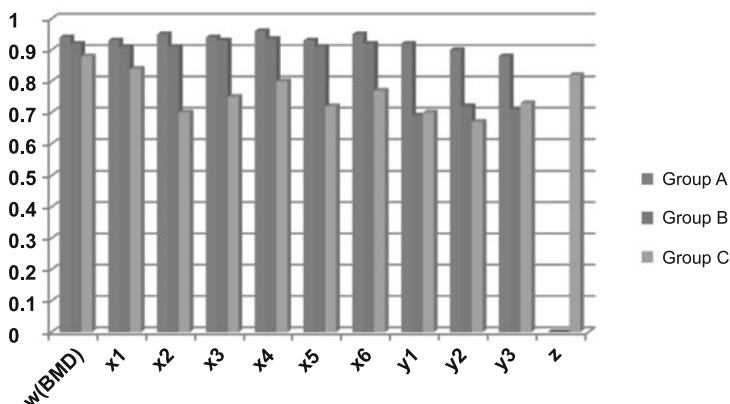
Fig. 14 Average values of the coefficients W(BMD), X(1-6), Y(1-3), Z in groups A,B,C

4 Conclusions

1. The non-specific asymmetry coefficient BMD in the hip joints produced a slightly higher value among patients in group C than in groups A and B, however, it failed to reach a statistical significance value in test t, nor any relevant correlation with the specific optical density asymmetry determiners of the pelvic diagrams (x1-x6) and back muscle structure symmetry determiners (y1-y3).
2. The back muscle tension asymmetry expressed by the determiners (y1-3) is statistically significant among patients in groups B and C, it does not however appear so in group A.
3. Statistically significant asymmetry of specific optical density determiners of pelvic diagrams, shown in the following order: X2 >X5 >X3 >X6 >X4 >X1 was observed, statistically insignificant slight asymmetry in group B, and no relevant asymmetry was seen in group A (Fig. 14).
4. In contrast to groups A and B, group C showed a significant correlation of specific asymmetry determiners in the pelvic diagrams (x1 âĂŞ x6) compared to back muscle tension asymmetry determiners (y1-3) and lower limb length difference (z), without correlation to the non-specific BMD asymmetry determiner.

4.1 Discussion

Osseous tissue, despite its high mechanical resistance, is subject to constant redevelopment due to the forces affecting the skeleton, that is why the assumption was made in the study that the symmetry of the mineral composition of mirror parts of the skeleton should constitute a derivative of the symmetry of their mechanical load.

X-ray image analyses in groups of people experiencing back pain but not suffering from scoliosis (group A), persons with back pain and scoliosis but without

a tilted pelvis (group B) and people with back pain, scoliosis reflectorica with a shorter limb showed significant variation in the correlation range between the types of biomechanical disorders in particular groups and the type of assessment method used.

Evaluation of the hip joints using the preferred DXA method showed that the non-specific asymmetry coefficient BMD, the measurement of which is based on the density asymmetry of the hip column, demonstrates only a slightly greater value among group C patients than patients in group A and B, and does not reach any statistical significance in the t test, nor any significant correlation with specific optical density asymmetry determiners of pelvic radiograms (x1-x6) and back muscle asymmetry determiners (y1-y3). Such a result may come as a big surprise and may be a signal that the DXA image analysis methodology requires thorough redevelopment focusing on the need to analyse discrete elements, which are more important from the point of view of bone reaction to load.

The analysis of pelvic structure discrete elements analysis, defined as specific determiners X(1-6), produced much more interesting results. Group C recorded a statistically significant asymmetry of specific optical density determiners of pelvic radiograms, projected in the following order: X2 >X5 >X3 >X6 >X4 >X1, group B produced slight asymmetry with no signs of statistical significance and no relevant asymmetry was noted in group A. The sequence of the significance of changes among the determiners used, which have been demonstrated by the above relation and referenced by the image, reflects well the asymmetry of the main stress prevalent in the pelvic structure which has been tilted as a result of lower limb shortening.

An analysis of the tension of the back muscles expressed with the determiners (y1-3), based on photographic images, has been just as interesting. It showed very clear asymmetry in patients suffering from pain and shorter limb-induced scoliosis (group B). Back muscle structure parameter symmetry fluctuations not exceeding 10.

By studying the correlation between the particular parameter groups, only in group C, in contrast to groups A and B, was there a significant correlation observed between the specific pelvic radiogram asymmetry determiners (x1 - x6) compared to the back muscle tension asymmetry determiners (y1-3) and the lower limb length difference (z), and no correlation was seen to exist with the non-specific BMD asymmetry coefficient.

As a final remark it has to be mentioned that the study, however interesting it may seem, was performed on a small group of patients and the results must be approached carefully. Despite achieving very clear differences in the optical density symmetry of mirror discrete skeletal components in reaction to pelvic biomechanical asymmetry, this method, in its current form, which is based on the interval scale, is not suitable for determining osseous tissue estimates expressed in g/cm3. However, the results achieved give us hope that supplementing the software with a relational osseous density base of patients sequenced in ascending age groups will eliminate this shortcoming.

References

1. Badurski, J., Sawicki, A., Boczoń, S.: Osteoporosis, Osteoprint, Białystok, pp. 15–48. Springer, Berlin (1994) (in Polish)
2. Bąk, R., Burczyński, T.: Strength of materials with elements of computer recognition. WNT, Warszawa (2001) (in Polish)
3. Będziński, R.: Biomechanical Engineering - zagadnienia wybrane, Oficyna Wydawnicza Politechniki Wrocławskiej, Wrocław (1997) (in Polish)
4. Binkowski, M., Wróbel, Z., Dyszkiewicz, A.: Application of modal analysis in diagnosis of mechanical properties of bone tissue. Acta of Bioengineering and Biomechanics 4(suppl. 1) (2002); 13th Conference of European Society of Biomechanics, Wrocław, December 1-4 (2002)
5. Boyle, I.T.: Secondary osteoporosis. Baillleres Clin. Rheumatol. 7, 515–534 (1993)
6. Burger, H., de Laet, C.E.: i wsp: Risk factors for increased bone loss in an elderly population: the Rotterdam Study. Am. J. Epidemiol. 147, 871–879 (1998)
7. Cowin, S.C.: Bone poroelasticity. J. Biomechanics 32, 217–238 (1999)
8. Cowin, S.C.: Bone Biomechanics Handbook. CRC Press, Boca Raton (2001)
9. Czerwiński, E., Działak, P.: Diagnosis of osteoporosis and fracture risk assessment. Ortopedia Traumatologia Rehabilitacja 4(2), 127–134 (2002) (in polish)
10. Dyszkiewicz, A., Kucharz, E.J.: Comparative analysis of the forearm bone density and femoral neck in the form of ischemic and postinflammatory degenerative disease of the hip joint. Annal Acad. Medic. Siles 47, 24–31 (2002) (in Polish)
11. Dyszkiewicz, A., Sapota, G., Wróbel, Z.: Photometry of radiological images in bone structure in creating computer densitometric algorithms. In: Konf. TIM 1999, Jaszowiec, November 18-20 (1999) (in Polish)
12. Dyszkiewicz, A., Sławiec, M., Wróbel, Z., Binkowski, M.: Perspective for the application of microwaves to assessment of changes in bone structure. In: V Symp. Chor. Tkł, Ustroń (2003) (in Polish)
13. Dyszkiewicz, A., Wróbel, Z., Binkowski, M., Gaździk, T.: Resonance stimulation of bone growth in the fracture gap. MPM Krynica, May 13-17 (2002) (in Polish)
14. Dyszkiewicz, A., Opara, J.: Computerised system for evaluation of X-ray postural parameters in scolioses. V Miedzynarodowa Konferencja, Ruch i Zdrowie, Głuchołazy, November 17-18 (2006)
15. Dyszkiewicz, A., Gaździk, T.: Immunomodulatory medicine use in the bi-symptomatic neuro-vertebral conflict. Ortop Traum Reh 2, 190–197 (2004)
16. Dyszkiewicz, A., Opara, J., Gaździk, T.: Monitoring the treatment of low back pain Rusing non-steroid anti-inflammatory drugs and aromatic oil components. Ortop Traum Reh 2(6), 210–218 (2006)
17. Opara, J., Dyszkiewicz, A.: Meaning of Stabilometrii and stabilografii in the prevention of falls in Parkinson's disease. Jurata (September 2006) (in Polish)
18. Opara, J., Mehlich, K., Bielecki, A., Dyszkiewicz, A., Szczegielniak, J., Spetruk, P.: Walking index for spinal cord injury-wisci. Journal of Rehabilitation Medicine, abstracts of 16th European Congress of Physical and Rehabilitation Medicine, Brugge, July 3-6 (2008)
19. Dyszkiewicz, A., Wróbel, Z., Opara, J.: Computerised system for evaluation of asymmetry of postural parameter coefficients in scolioses. In: Biosignal 2008, Funchail, Madeira, January 28-31, pp. 277–280 (2008)
20. Dyszkiewicz, A., Wróbel, Z., Binkowski, M.: New prospect of acquiring and saving tomographic images using format bmp in the time. In: V Symp. Chor. Tk łącznej, Ustroń (2003) (in Polish)

21. Ruimerman, R., Hilbers, P., van Rietbergen, B., Huiskes, R.: Mechanical regulation of bone cell metabolism and structural adaptation in trabecular architecture. Acta of Bioengineering and Biomechanics 4(suppl. 1) (2002), 13th Conference of European Society of Biomechanics, Wrocław, September 1-4 (2002)
22. Dyszkiewicz, A., Wróbel, Z., Lamza, A.: Densitometric's algorithms in analysis of radiological images of the skeletal system. Annal. Acad. Medic. Siles 47, 37–41 (2002) (in Polish)
23. Nigel, K., Arden i Timothy D.: Osteoporosis current state of knowledge Spector, Red. polskiego wydania Badurski Janusz E., Wyd. Med. Borgis, Warszawa (2000) (in Polish)
24. Nowak.A., Badurski., J.E. i wsp.: Białystok Osteoporosis Study (BOS): Epidemiology of low trauma fractures in the female population. Osteoporosis Int. 12, 1 (2001)
25. NIH Consensus Development Panel on Osteoporosis Prevention, Diagnosis, and Therapy.: Osteoporosis prevention. Diagnosis and Ther., JAMA 2001, 285, 785-795 (2001)
26. Kanis, J.A., Gluer, C.C.I.: wsp.: An update on the diagnosis and assessment of osteoporosis with densitometry. Osteoporosis Int. 11, 192–202 (2000)
27. Gmiński, J.: Raloksyfen - new perspectives of treatment in postmenopausal osteoporosis Annales Academiae Medicae Silesiensis, Monografia Tematyczna IV Śląskie Sympozjum Chorób Tkanki Kostnej, Ustroń, suppl. 47, 83–93 (2002) (in Polish)

The BRONCHOVID – Computer System Supporting Bronchoscopy Laboratory

Mariusz Duplaga, Jarosław Bułat, Mikołaj Leszczuk, Mirosław Socha,
Piotr Romaniak, and Paweł Turcza

Abstract. The bronchoscopy diagnostics consists of numerous tasks including but
not limited to the treatment planning on the basis of computed tomography, reg-
istration and analysis of endoscopic images during the inspection of the tracheo-
bronchial tree and procedure management. There is no comprehensive solution for
a computer system supporting bronchoscopy laboratory. Since the limited time of
medical personnel, high volume and multimodal data created during bronchoscopy
procedure and complex workflow we decide to build a dedicated system addressing
these issues. The paper presets an overview of the bronchoscope diagnostics, user
needs and requirements related to the procedure and the proposed solution. Finely,
the deployment results as well as future plan is presented.

1 The Rationale for Development of Next Generation Computer System for Bronchoscopy Support

The main element of the bronchoscopy is an inspection of the tracheo-bronchial
tree carried out by a physician performing bronchoscopy. His or her knowledge and
experience determines the ability to detect abnormal images and structures. With

Mariusz Duplaga
Jagiellonian University Medical College, Grzegórzecka Str. 20, 31-531 Kraków, Poland
e-mail: `mmduplag@cyf-kr.edu.pl`

Jarosław Bułat · Mikołaj Leszczuk · Piotr Romaniak
Department of Telecommunications, AGH University of Science and Technology,
al. Mickiewicza 30, 30-059 Kraków, Poland
e-mail: `kwant@agh.edu.pl, leszczuk@agh.edu.pl,`
`romaniak@agh.edu.pl`

Mirosław Socha · Paweł Turcza
Department of Measurement and Instrumentation, AGH University of Science and
Technology, al. Mickiewicza 30, 30-059 Kraków, Poland
e-mail: `socha@agh.edu.pl, turcza@agh.edu.pl`

technological progress, the quality of the images obtained during the procedures improved considerably. The process of digital registration of endoscopic images results in a whole range of new options related to the image processing as well as archiving and managing the stored contents. The areas of interest for bronchoscopy.

1.1 The Role of Bronchoscopy in Respiratory Medicine

The diagnosis in respiratory medicine is based on the employment of the whole scope of different techniques and procedures. The main diagnostic domains relevant for this speciality include imaging, pulmonary function tests and endoscopy. The endoscopy of respiratory system may be performed with a rigid or flexible bronchoscope. Development of bronchofiberoscope was possible due to the application of optical fibers. In most cases, pulmonary diagnostics is based on the bronchofiberoscopy as it is related with better acceptance by patients, ease of examination and the scope of the bronchial tree available for inspection in comparison to rigid bronchoscopy. The strategy of bronchoscopic examination relies on the inspection of tracheo-bronchial tree in the range available for assessment and, subsequently, on performance of the sampling procedures for specific tests performed in different laboratories according to indications of a referring physician or those araising from the findings during the examination. The bronchoscopist is obliged to check if the structure of tracheobronchial tree is normal and if it corresponds to anatomical variants. The assessment of potency and mobility of all parts of the airways available for evaluation is one of key elements of the evaluation. The appearance of mucosa and contents in trachea and bronchi is also checked. During the whole procedure, bronchoscopist is able to evacuate liquid contents from the lumen of the airways, e.g. secretion or blood. Furthermore, he can also rinse the endobronchial space with saline or solutions of therapeutic agents if needed. The working channel of the bronchoscope serves also for introduction of different types of tools, e.g. scissors or needle on guide wire.

The bronchoscopy is a procedure which strongly relies on the subjective assessment of images. Thus, the experience of the endoscopist is a key factor influencing the reliability of the bronchoscopic assessment. His or her agility and ability to detect characteristic features of the endobronchial image remains of key importance in search of early malignant lesion in tracheobronchial tree. It is also a precondition for the appropriate selection of the sampling site for further pathological workup and final diagnosis.

The progress in endoscopy results in equipment enabling delivery of procedures reserved so far to rigid bronchoscopy with bronchofiberoscopy. Currently, traditional optical bronchofiberscopes are substituted with videobronchoscopes. The tip of the videobronchoscopes is equipped with CCD (charge couple device). Endobronchial images are registerd digitally and transmitted to a video processor displaying them on the screen. Such an approach results in a considerable improvement of the image quality and possibility of procedure performance with several people

simultaneously. The use of videobronchoscopes affects positively dissemination of the digital registration and archiving bronchoscopic examinations.

1.2 The Evolution of User Needs in Relation to Computer Support for Bronchoscopy Procedures and Data Management

The areas of interest for bronchoscopy environments in terms of potential application of computer systems include:

- archiving and indexation of video records registered during bronchoscopy procedures,
- (semi)automatic detection of pathological lesions on bronchoscopy images performed in real time or retrospectively on the recorded content archived in digital video library,
- bronchometric measurements performed on acquired images,
- automatic classification of lesions detected with different imaging techniques (white light imaging, narrow band imaging, autofluorescence, and tomographic method - endobronchial ultrasonography and optical coherence tomography),
- the support for invasive sampling procedures, particularly transbronchial needle and lung biopsies, with three-dimensional presentation of the tracheobronchial tree and surrounding structures from data obtained with computed tomography or other imaging modalities,
- the use of navigational tools based on the electromagnetic tracing of the sensor integrated with tools used for tissue sampling and registering of the imaging space to three-dimensional space of data obtained with imaging modalities.

Most of the computer systems offered currently to bronchoscopists is driven mainly by the aim of improved patient data management and simple registration of still images or video recording during the procedure. Advanced options for real-time support or image processing are limited to few products available on the market, e.g. SuperDimension [3] or Arthemesis [2] (dedicated to the colonoscopy procedure). Surpaisingly, the adoption of the software based on the use of DICOM standard in relation to CT or MRI data by bronchoscopy suits is limited. Software packages for DICOM data display provided on free basis with imaging data of individual patients usually offer only limited options for standard two-dimentional data presentation.

The function of video registration is a routine option included in software packages offered by the providers of endoscopy equipment. It relies on the storage of the data of patients undergoing endoscopic procedures accompanied by still images or video recordings taken during the procedure. More advanced options of classification of the video recordings or separate frames, selection of sequences or generation of summaries is not covered and requires off-the-shelf products for video processing. Advanced options for processing the images from endoscopy video recordings are rarely available in commercial products. The use of several software packages for efficient management of video resources generated in bronchoscopy suit is unrealistic due to time pressure experienced by most physicians.

The concept of the BRONCHOVID system is a response to potential needs of the pulmonologist involved in bronchoscopy procedures. Apart from the standard functions including management of patients' data, registration of the video recordings of the procedures and archiving the recorded videos within digital video library, the system brings additional functionalities useful either for management of the archived resources in routine work of the bronchoscopy suit or for advanced image processing and classification. The system integrates also the function of the presentation of individual patient's CT data for support and guidance during bronchoscopic biopsy procedures. CT data can be displayed as multiplanar reconstructions (MPR) or as three dimensional models of the thoracic structure including virtual bronchoscopy option.

2 Requirements

The analysis of the user requirements for the BRONCHOVID system was performed by the interdisciplinary team of computer specialists and users involved in bronchoscopy diagnostics. The general assessment of the user needs and specific requirements for the system functionality was based on the initial broad approach. In the next phase, the cluster of priority requirements was determined in order to accommodate for the limited resources available for the system development.

The concept of the BRONCHOVID system relies on the integration of all those functionalities which are relevant for the support of bronchoscopy procedures and workflow in the bronchoscopy suit. The range of perceived needs of the physician and researchers involved in the bronchoscopy was treated as a starting point to define specific functions supporting administrative, clinical and research tasks.

The process of the user requirement analysis was performed within several iterations to improve the understanding between developers and users. The main requirements resulting from these iteration are summarized in the Table 1.

3 System Architecture

The concept of the system is a response to expectations and requirements of the bronchoscopists in the areas summarized in the Table 1.

On the basis of the requirements the system consists of the following components which have been built (see Fig. 1): *data base* - comprehensive repository of information gathered and created during medical procedure, *video recorder and real-time analyser* - gathering video stream from bronchoscope, analysing (on-line/offline) and recording to the file repository, *virtual bronchoscopy* - visualization of CT data in 3D environment and treatment planning, *Editor* - tool for creating referential image library and ontology, *user interface* - on site and remote (WWW based) interface for data management, searching and the starting point of each action performed on the BRONCHOVID system.

During the procedure, bronchoscopists as well as medical personnel are engaged in the procedure. That is why, the system should be easy to use (eg. support touch

Table 1 The inventory of the functional requirements for the BRONCHOVID system from the users' community

Requirement	Additional features comments
Video recording of bronchoscopy	– the registration of the whole procedure – easy initiation and termination of the recording procedure – data entry before and after completion of the bronchoscopy – direct transmission of the video signal from the endoscopy equipment – the view of the video from the graphical workstation
Automatic detection of meaningful images	– automatic detection of non-informative frames – real-time detection of the significant images during the bronchoscopy – retrospective detection of preselected lesion within the resources stored in the digital video library
Annotation of resources (frames, sequences) with meaningful content	– manual annotation of selected frames – management of the library of exemplary images – automated annotation of video resources stored in a video library – user-driven modification of the classification system for contents annotation
Management of the resources stored in the digital video library	– access to the resources – advanced search options based on the query-by-example approach – definition of the parameters of the summaries generation – definition of the parameters for long-term archive – automatic exclusion of non-informative frames based on predefined detection algorithms – generation of the custom-made summaries and short video previews – anonymisation of the resources for the authorized external users of the digital video library
Management of the patient record	– entry of patient-specific information before and after the procedure – generation of the bronchoscopy report for medical history – access to imaging data (CT) and video recordings of the patients – search function within the patient data categories – access to data base for stratified reports generation
Advanced interface for exploration and presentation of the data from other imaging modality	– upload of CT data – MPR and three-dimensional CT data presentation before and during the bronchoscopy – planning of the biopsy sites – navigation support during bronchoscopy
Support during the bronchoscopy	– automatic detection of the priority pathological lesions – software-based image enhancement – accompanying CT data presentation – biopsy site tracing for repetitive sampling procedures
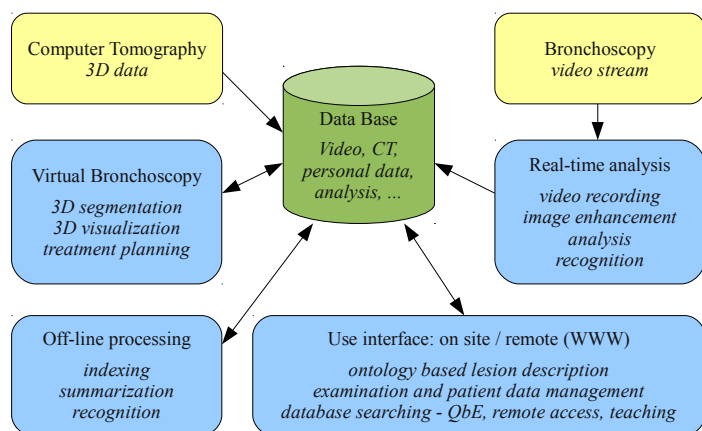
Fig. 1 Architecture of the BRONCHOVID system: main system components and the information flow

screen) and prompt useful information such as automatically detected features in real-time.

Furthermore, the ontology should be built during the creation of referential image library. With the help of QbE (Query by Example) algorithm and the knowledge from ontology the automatic classification of new video fragments or individual frames could be performed.

In the following subsections detailed information about all of the BRONCHOVID components is presented in details.

3.1 Hardware and Software Solution

Because of large number of archived video recordings, real-time analysis and limited time of medical personel the bronchoscopy laboratory need a dedicated solution. We decided to build it around a standard server/workstation, high grade software libraries and stable, high performance operation system.

The system uses a 4-way UniWide workstation (`www.uniwide.com`) equipped with two core Opteron processor, 16 GB RAM, 5TB RAID-5 disk array, NVidia GeForce 9800 GX2 graphics card and two 24" LCD displays. Large redundant array disk is necessary to store video stream without additional compression. Video recording is gathered from bronchoscope by FireWire interface and requires 2GB disk storage on average. It is stored in DVSD format (MJPEG codec) with resolution 720x576 and 28800.0 kbps data stream. Unfortunately, there is no way to acquire raw video stream by means of digital interface from the bronchoscope we use in system implementation. Eight core server with 16 GB RAM help us process large amount of data and real-time video analysis. Additionally, graphics card

accelerates OpenGL library as well as general purpose computing with the help of CUDA interface [4].

The system was built around high grade Open Source library and Linux operating system. The reason for using Linux was its proved stability, performance and flexibility. For the user interface we use cross-platform Qt4 library [1] which help us with rapid application development. Remote access to the system has been built as a dynamic WWW page with the help of Apache web server and PHP scripting language. All the information acquired and generated by the system is stored in a MySQL relational database except the video streams. For data processing the following libraries are used: VTK, ITK, GDCM, OpenCV and various other Open Source libraries with C/C++ bindings as well as algorithms written in C/C++ language. Another issue is an algorithm parallelization. We chose an MPI [12] framework in order to create a message-driven system which is able to take advantage of all available processors simultaneously. In that way, real-time analysis and off-line analysis, which are the most time-consuming parts of the BRONCHOVID system, were divided into several processes performed simultaneously.

All the libraries and frameworks used in the system are cross-platform (at least Linux and Windows) and distributed under LGPL or more liberal license. It allow us to produce a commercial system without incurring the cost of external libraries and avoiding vendor lock-in (eg. Linux only or Windows only system).

3.2   Data Repository

Central point of the BRONCHOVID system is a data repository. It consists of a file system and SQL database.

Patient's personal data and bronchoscopy examination results are stored in the highest level of the proposed database structure. Another level refers to the metadata of visual recordings from the examinations stored in the file system using DV (Digital Video) video format. Each examination may be assigned with one or more recordings. Additional information stored on this level allows us to identify video frames containing artifacts and other content to be neglected in further procedures. All annotated frames (frames that were assigned with pathological changes during the manual procedure) are stored in the file system as lossless PNG (Portable Network Graphics) files. The set of pathological changes which constitute the ontology was defined by bronchoscopy experts and is stored in the same database as the predefined list. Also, one or more regions of interest may be selected on each frame with possibility to assign any (distinctive) pathological changes to each. Such regions (called masks) are stored in binary PNG form in the file system. Each manually generated annotation (referred to as the truth) stores also information about its creator. The other type of supported annotations stored in the databases refers to the results obtained from recognition algorithms operating in automatic, and preferably, real time mode.

Another stored data type, supported by the proposed database structure, is related to virtual bronchoscopy. Similarly to the real visual recording, metadata is related to

a certain bronchoscopy examination and stored in analogical video and frame levels. The binary data from CT scans is stored in the file system in the DICOM (Digital Imaging and Communications in Medicine) format.

As a database engine we used MySQL server. For the purpose of data storage, ext3 (third extended filesystem) journaled file system has been used.

3.3   Real Time Analysis

One of the most important features of BRONCHOVID system is recording and analysing video stream. It is designed to capture video stream from videobronchoscobe by means of FireWire interface, recording video into the repository as well as patient's personal data, procedure parameters and partial treatment results. Additionally it performs real-time video adjustment such as: brightness, contrast and gamma, video enhancement as a deinterlace, histogram equalization and selective sharpening for better feature detection. What is more, each frame is analysed for automatic detection of the following features: artifacts, overexposure, carinas and bleeding. On the basis of SIFT (Scale-invariant feature transform) algorithm the navigation aid has been implemented.

All the above presented algorithm (sharpening and bleeding detection are still under development) could be switched on/off from the graphics user interface. Results of the operating algorithms are presented in real-time on the screen. This system is able to operate off-line, without user interface. In this operation mode it automatically analyses all recently recorded videos and saves results of all algorithms for each frame into the repository. Stored data can then be used for other purposes (eg. video summarization of bronchoscopy procedures).

This part of the system is created as stand-alone application written in C/C++ language. Since the system needs to perform multiple tasks simultaneously, we decide to apply a message driven approach with several asynchronous processes. The component architecture and data-flow are presented in the Fig. 2. Arrows and rectangles represent messages and processes respectively. Messages are implemented as structures in C/C++ language which are queued in a non-blocking way and transmitted by means of MPI [12] framework operating in the point-to-point mode.

In that way, the pipeline of data processing is created. First step consist of video stream acquisition and decompression (streamer), then image frame is deinterlaced and spread over several processing engines (*RT0*). Each engine (*RT1 – RT7*) process video frame, calculate results and send it to the *Master* or *GUI*. Process called *Master* is responsible for system logics and high level data processing, in turn *GUI* is a user interface presenting original and enhancement video stream, results of analysis. What is more, it is responsible for any interaction with user such as: system configuration or patient data recording.

The system is flexible and highly configurable. For example, we can easily add a new data processing algorithm by increasing the number of RT processes and adjusting a message flow. Moreover, for an algorithm which is too slow to operate in the real time we can perform an analysis by means of two processes separately
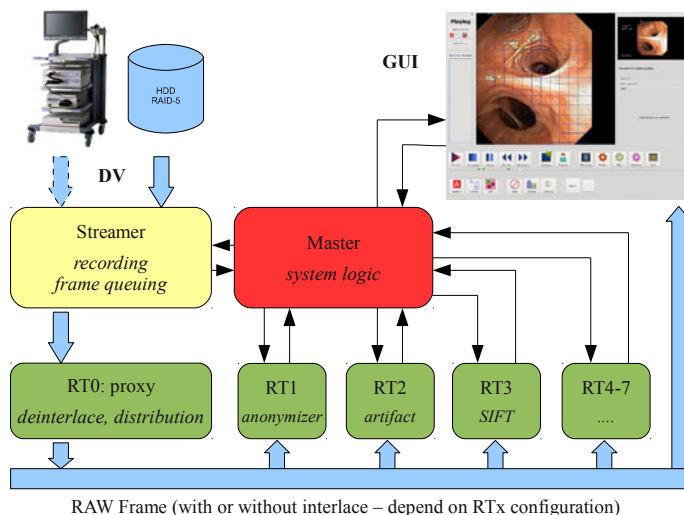
Fig. 2 Diagram of data-flow in the system for video stream recording and analysis

for even and odd frames. In that way, the algorithm will be accelerated by factor 2 at an expense of a larger delay.

3.4 Editor

The editor was designed for video manipulation after recording. It is an easy-to-use tool for video analysis, performing frame annotation - assigning it with pathological changes, building and manipulating the ontology. Among others it allows for basic video manipulation such as: play with different speed, stop, fast-forward, adding a mask with pathological changes to a chosen frame, review and manipulate previous recordings.

The technology behind the Editor is exactly the same as the implementation of the component for real time recordings and analysis described in Sec. 3.3. It is created in C/C++ with the help of MPI and Qt4 framework. All the data generated during video editing is stored in the repository.

With the help of the editor, the ontology has been created as well as a description of pathological changes for thousands of frames. This data is essential for further analysis and other components of the BRONCHOVID system. It is used for example in QbE (Query by Example) engine.

3.5 Virtual Bronchoscopy

The visualization component use Visualization ToolKit (VTK) [6] for visualization, Insight Segmentation and Registration Toolkit (ITK) [9] for data processing and

Qt4 library [1] in order to build a user interface. It can read and write CT data from DICOM files, using GDCM library [11]. With the help of the OpenGL the VTK is capable of efficient, hardware accelerated presentation and manipulation of 3D data. The visualization is fully interactive. It can be controlled in various ways by the user. An exemplary screenshot of a working application is presented in the Fig. 3.
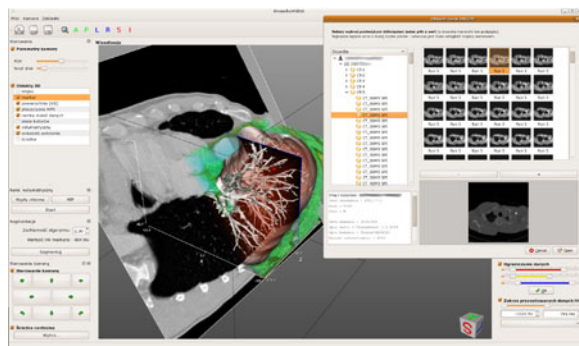

Fig. 3 User interface of visualization software with DICOM input dialog and sample visualization

This component offers a number of data visualization techniques widely used for computer aided software for diagnosis and therapy planning [8]. Four planes are used for a slice-by-slice data examination. It is a sample of a two-dimensional Multiplane Reformatting (MPR) visualization. There are four planes for visualization of volume data intersection (slice). Three of them are fixed and orthogonal to each other, the fourth is free and can be moved, rotated and scaled around the data. Widely known from the medical workstation Surface Shaded Display (SSD) is the use of interactive virtual bronchoscopy visualization. In this case, the computed isosurface is represented by polygons, which are efficiently handled and accelerated by the graphic card. Surface rendering is used for virtual bronchoscopy (VB) visualization as well as the presentation of the results from the segmentation algorithm.

Additionally, volume rendering is implemented in two different modes. First can generate 2D projection of volumetric data with the help of Maximum Intensity Projection (MIP). It is mainly useful in diagnosing of vascular structures. Second mode, uses two transfer functions: one for colour determination and the second for pixels transparency. This kind of visualization allow us to "see through" the medical data. The VB component uses fast, but low quality (draft) volume rendering during interactive manipulation of virtual camera position. When the camera stops, the high quality visualization is applied.

All the above presented techniques could be applied at the same time for visualization. Additionally, the real endoscopy light has been simulated for the virtual bronchoscopy which makes use of SSD technique for visualization of the trachea surface.

3.6 *Data Browser*

The system contains a Web-based GUI (Graphical User Interface) that allows for resource searching and browsing. The search functionality is based on simple meta-data search and more advanced, QbE (Query by Example) mechanism.

The first method is based on regular SQL queries. Found frames are clickable, allowing the doctor to be automatically transferred to the video editor, tuned to the desired patient, video and frame.

The QbE method allows for a content based search on a library of patterns of endoscopic images. The result is a way to search for lesions in database created by a QbE mechanism [10]. The mechanism of this interest (in this case, your doctor or student) gives as an example query an interesting lesion in the form of the recorded image change. Changes similar to those indicated in the example are searched in a database and cataloged. The tool can be an invaluable assistance both in diagnosis and education. On the basis of login/password it supports to the level of data access, with or without data anonymization.

This component uses MPEG-7 descriptors [5] to extract features of an example and compare them with the characteristics of the data contained in the database [7]. Since the descriptors for MPEG-7 are vectors, the comparison is quick and can get an almost immediate response.

4 Deployment, Results and Future Development

The BRONCHOVID system has been implemented in the Bronchoscopy Laboratory of Department of Pulmonology, Jagiellonian University Medical College in Kraków. The system successfully replaced the existing solution built around the Endobase (The Endoscopy Management and Image Filing System).

A year and a half (since September 2008) of continuous operation has resulted in a vast amount of bronchoscopy data including video recordings, metadata and annotations which were gathered. Around 2.1 TB of data was stored in the repository of the BRONCHOVID, but the number is still growing. Currently, the BRONCHOVID contains data (personal as well as examination) of 803 distinctive patients and 1011 related video recordings (163 hours of bronchoscopy examinations). A number of over 14 million of video frames with related metadata is stored in the system repository. The set of pathological changes proposed by the bronchoscopists contains 82 distinctive classes. Currently 204 out of 1011 videos were manual annotation resulting in identification of 5264 pathological changes.

Recently implemented module for real-time recording, image enhancement and analysis is the last stage of the BRONCHOVID system deployment. During the test run in the off-line mode, the system performs analysis of all the video frames stored in the repository within last 30 hours.

Despite the implementation of core BRONCHOVID functionality a number of features are still under development and testing. In the future we would like to add new algorithms for real-time analysis to the system as well as improve Virtual

Bronchoscopy component by means of implementing real-time synchronization with a video stream gathered from bronchoscope.

References

1. Blanchette, J., Summerfield, M.: C++ GUI Programming with Qt 4. Prentice Hall PTR, Englewood Cliffs (2006)
2. Liu, D., Cao, Y., Kim, K.-H., Stanek, S., Doungratanaex-Chai, B., Lin, K., Tavanapong, W., Wong, J., JungHwan, O., de Groen, P.C.: Arthemis: Annotation software in an integrated capturing and analysis system for colonoscopy. Computer Methods and Programs in Biomedicine 88(2), 152–163 (2007)
3. Gildea, T.R., Mazzone, P.J., Karnak, D., Meziane, M., Mehta, A.C.: Electromagnetic Navigation Diagnostic Bronchoscopy. A Prospective Study. Am. J. Respir. Crit. Care Med. 174, 982–989 (2006)
4. Owens, J.D., Houston, M., Luebke, D., Green, S., Stone, J.E., Phillips, J.C.: GPU Computing. Proceedings of the IEEE 96(5), 879–899 (2008)
5. Manjunath, B.S., Salembier, P., Sikora, T. (eds.): Introduction to MPEG-7: Multimedia Content Description Interface. Wiley, Chichester (2002)
6. Schroeder, W., Martin, K., Lorensen, B.: The visualization toolkit: an object-oriented approach to 3D graphics, 3rd edn. Kitware Inc. (2004)
7. Mezaris, V., et al.: A Test-Bed for Region-Based Image Retrieval Using Multiple Segmentation Algorithms and the MPEG-7 eXperimentation Model: The Schema Reference System. In: Enser, P.G.B., Kompatsiaris, Y., O'Connor, N.E., Smeaton, A., Smeulders, A.W.M. (eds.) CIVR 2004. LNCS, vol. 3115, pp. 592–600. Springer, Heidelberg (2004)
8. Preim, B., Bartz, D.: Visualization in Medicine: Theory, Algorithms, and Applications. The Morgan Kaufmann Series in Computer Graphics. Morgan Kaufmann Publishers Inc., San Francisco (2007)
9. Schroeder, W., Ibanez, L.: The ITK Software Guide 2.4. Kitware Inc. (2005)
10. Zloof, M.M.: Query-by-Example: a data base language. IBM Systems Journal 16(4) (1977)
11. Cross-platform library Grassroots DICOM or GDCM for DICOM medical files, http://sourceforge.net/projects/gdcm/
12. High performance and widely portable implementation of the Message Passing Interface (MPI), http://www.mcs.anl.gov/research/projects/mpich2/index.php

3D Segmentation and Visualisation of Mediastinal Structures Adjacent to Tracheobronchial Tree from CT Data

Andrzej Skalski, Mirosław Socha, Mariusz Duplaga,
Krzysztof Duda, and Tomasz Zieliński

Abstract. In the paper, an advanced visualisation module of recently developed BRONCHOVID system designed for efficient data exploration and bronchoscopy guidance is presented. It brings an intuitive and user-friendly interface developed with several open source subroutines as well as diversified modes and algorithms of thoracic CT of data segmentation and visualisation including a surface shaded display (SSD), volume rendering and multiplanar reformatting. For enhanced concurrent visualisation of thoracic structures located in the vicinity of or adjacent to trachea and bronchial tree (lymph nodes, blood vessels, pathological masses) a new dedicated segmentation algorithm has been developed. It is based on a region growing method followed by the use of deformable models. The module integrates also the options of central path calculation by means of distant transform in lower airways and interactive virtual bronchoscopy. Its functionality covers also an option for measurements of dimensions in volume of CT data.

1 Introduction

The use of computer technologies for the support of medical interventions is a promising domain. Great progress in computational power resulted in many

Andrzej Skalski · Mirosław Socha · Krzysztof Duda
Department of Measurement and Instrumentation, AGH University of Science and Technology, Al. Mickiewicza 30, 30-059 Kraków, Poland
e-mail: `skalski@agh.edu.pl, socha@agh.edu.pl, duda@agh.edu.pl`

Mariusz Duplaga
Jagiellonian University Medical College, Grzegorzecka Str. 20, 31-531 Kraków, Poland
e-mail: `mmduplag@cyf-kr.edu.pl`

Tomasz Zieliński
Department of Telecommunications, AGH University of Science and Technology,
Al. Mickiewicza 30, 30-059 Kraków, Poland
e-mail: `tzielin@agh.edu.pl`

applications enabling for three-dimensional (3D) presentation of data obtained with various medical modalities during or before medical procedures. This field is usually referred to as computer-assissted surgery (CAS) [1], but the scope of possible solutions spans from relatively simple interventions or therapy planning to real-time guidance for complex surgical operations. This trend comes in parallel with the requirements for broader introduction of medical procedures of limited invasiveness but preserved or greater effectiveness and increased patient safety. Nowadays, we observe a radical transformation of diagnostic and therapeutic procedures due to extensive use of endoscopic and videoscopic approach. New innovative strategies are developed e.g. natural orifice transluminal endoscopic surgery (NOTES) [17].

The use of surgical robots and broad use of videoscopic techniques excited interest in advanced simulation environments enabling data exploration before planned interventions, support during interventions and initial training of medical professionals before their involvement in real operations. The most advanced solutions are based on the use of virtual reality solutions to set up training conditions with the data set of individual patients selected for a real operation. This approach is called by some authors a virtual reality assisted surgery programme (VRASP) [12]. The simulation of the operation in the space of imaging data obtained from the patient before the surgery prepares the surgeon or other specialist to specific, highly variable, anatomical and pathological conditions which can occur in an individual. It has a positive positive effect on risk contingency and effectiveness of real intervention. Opportunities related to advanced techniques of presentation of imaging data were widened significantly with increased computational power of computer stations which can be introduced to the operating theatre. The resolution of data generated with modern equipment used for medical imaging was also considerably improved. All these favourable circumstances lead to an extensive use of advanced display modalities in clinical practice. The modelling of imaging data with associated molecular, histological or physiological information has become an important research and development direction emphasised also in current Framework Programme of European Commission as Virtual Physiological Human priority [7].

This paper is focused on the task of computed tomography (CT) data segmentation and visualisation for support and guidance during bronchoscopy. The overall progress in medical technologies results also in the increasing use of endoscopic approach for diagnostic and therapeutic purposes. The effectiveness of these procedures depends frequently on the perfect spatial orientation of the performing physician in anatomical structures located near tubular organs examined with an endoscope. The surroundings of the tubular structures (trachea, bronchial tree, gastrointestinal tract) may be visualised during endoscopy with endobronchial ultrasonography. Another option, explored in the paper, is based on the provision of two- and three-dimensional (2D, 3D) visualisation of the CT data in endoscopy suit. In case of bronchoscopy, the presentation of CT data in virtual bronchoscopy (VB) mode is also of value [8, 20]. This mode may be used for earlier selection and marking of potential sites of tissue biopsies.

The authors describe dedicated segmentation and visualisation module included in the BRONCHOVID system which was developed within the project funded from a national research and development programme.

The module allows for the visualisation of thoracic CT data in different modes with the use of both 2D and 3D data presentation with the options of a standard sequence of slices, multiplanar reformatting, maximum intensity projection. 3D images are generated with a surface shaded display (SSD) and volume rendering (VR) algorithms. For enhanced support of sampling procedures the interactive virtual bronchoscopy (VB) is available. The support of bioptic techniques with thoracic CT data required development of several advanced algorithms for segmentation for thoracic structure (tracheobronchial tree, lymph nodes, blood vessels), a navigation path generation and a semitransparent effect.

The paper is structured as follows. Section 2 presents the segmentation algorithm implemented in BRONCHOVID system. Section 3 describes the method of automatic generation of the navigation path used in VB mode of data presentation. Visualisation methods and GUI are described in Section 4. Section 5 includes the discussion of the results for BRONCHOVID advantaged and conclusions.

2 Segmentation of Mediastinal Structures Located in the Vicinity of the Tracheobronchial Tree

The segmentation module included in the BRONCHOVID system was developed with the aim of the efficient CT data presentation and support for invasive sampling procedures performed within a bronchoscopic examination. The authors implemented a two step procedure based on a region growing algorithm in conjunction with deformable models technique. Main target structures for this approach included lymph nodes blood vessels and possible pathological lesions adjacent to or surrounding the tracheobronchial tree.

Efficient segmentation of thoracic structures which is supposed to yield high quality 3D data presentation is a challenging task. Pixels corresponding to the aorta, lymph nodes and pulmonary arteries usually reveal the values of the coefficient of absorption in the range from -80 to 100 HU.

Irregularity of intensity decomposition is another difficulty in the process of thoracic CT data segmentation. This results in a situation when pixels belonging to the same anatomical structures have different density values depending on their location. Pathological lesions affecting these structure, e.g. the presence of calcifications or infiltrates increases their heterogeneity.

3D reconstruction of mediastinal lymph nodes seems to be the most difficult tasks in the automatic segmentation of thoracic CT data. They may differ significantly in size (from a few millimetres to even several centimetres in some diseases) and their usual kidney-like shape also may be distorted by a pathological process. Depending to their location, lymph nodes are classified in tophograhic groups highly important for the assessment of the tumour stage.

A simple approach to segmentation tasks relies on the intervention of a medical professional with relevant background in medical imaging and manual segmentation of mediastinal structures (contours outlined on the consecutive CT scans). The process is time consuming and not feasible in clinical practice. Another approach based on the active contour segmentation technique applied separately to every CT scan [9]. This method requires definition of an initial contour. It should be located near the boundary of the object planned for segmentation.

Next approach was presented in [18]. It is based on a fast marching algorithm which is a special version of a level set technique proposed by other authors [13, 14]. Additionally, the authors applied information about intensity values and gradient information on the evolution equation. Stop condition proposed in [18] remains in contrast with the classical condition based on gradient absolute value. It introduces a "hard" criterion based on the circle equation. A user is supposed to mark two points: one in the centre of a segmented lymph node and another one near its border. Using this information the circle equation is calculated. When the contour evolution reaches the circle, the algorithm is stopped.

Sun et al. [15] use a mean shift slice by slice algorithm. The algorithm is initialised in 32 x 32 regions, suggested with a region growing technique.

Dornheim et al. [6] were using 3D spring-mass models described earlier [5]. On the basis of 25 CT data sets and the results of manual segmentation they created a model of lymph nodes used for a segmentation process consisting of three steps. First, an initial placement of the model within the data set is indicated by a user. Then, a value range corresponding to lymph nodes is calculated. It is based on the point indicated by the user and on two values deduced from the application of the experimental model. Finally, model adaptation is performed with respect to a set of parameters. The parameters were initially adjusted and then applied to all data sets during the evaluation phase.

2.1 Segmentation Method Based on Region Growing and Deformable Models

In this section a novel algorithm for segmentation of anatomical structures located close to or adjacent to the trachea and bronchial tree is presented. Its originality lies on sequential usage of two methods: region growing and deformable models.

Fast and simple initial segmentation is a first step of the proposed algorithm. It gives preliminary knowledge about locations, geometry and number of structures that should be segmented from the CT data.

As an initial segmentation procedure the *confidence connected* region growing [19] has been selected. It is based on voxels classification with a pre-defined condition. The algorithm is started from a seed point indicated by a user. Then, the region growing procedure is executed. If a voxel located near the voxels belonging to the region satisfies the condition e.g. its value belongs to the pre-defined range, it is added to the growing region. Then, the process is repeated until all the possible voxels are tested and added to the region. In the confidence connected version, the

algorithm calculates the mean value μ and the standard deviation σ of voxels that have already been added to the regions. If the value of the neighbouring voxel is in the range:

$$I(x,y,z) \in [\mu - f \cdot \sigma, \mu + f \cdot \sigma], \tag{1}$$

where f is a constant coefficient, then this voxel is attached to the region. If no, the voxel cannot satisfy this above condition, μ and σ values are calculated for a new voxel set. The process is repeated a defined number of times [19].

The binary masks received from the region growing algorithm are filtered with morphological operations in order to remove topology errors and small holes. The obtained results are treated as an initial surface in deformable models (DM) algorithm proposed in [3] used in our research. For a 3D binary mask, deformable mesh are calculated with marching cubes algorithm [11].

3D deformable models are defined as deformable surfaces which are influenced by two forces: external and internal. The external force usually uses information present in the image or it is defined as a physical process e.g. balloon force [4]. Image force is usually related to gradient information. Internal forces help keep continuity of the surface and incorporate the a priori knowledge. Model dynamics can be presented as Lagrange equation [3, 19]:

$$\dot{\mathbf{d}} + \mathbf{K}\mathbf{d} = \mathbf{F_{ext}}, \tag{2}$$

where $\mathbf{d}$ represents local deformations, and $\mathbf{K}$ is a matrix representing model stiffness. Details concerning $\mathbf{d}$ and $\mathbf{K}$ matrix $\mathbf{K}$ can be found in [3, 16, 19].

For the noise reduction, the Gauss filtration in the external field has been used [3]:

$$\mathbf{F_{ext}} = -\nabla(\alpha|\nabla conv[\mathbf{G}(x,y,z), I(x,y,z)]|)^2, \tag{3}$$

were α is a positive weighing factor, $\mathbf{G}$ - 3D Gauss function, ∇ - gradient and *conv* - convolution operator. Deformation updating for each mesh knots in eq. 2 is made consecutively according to the following equation [3]:

$$\mathbf{d_{new}} = \dot{\mathbf{d}} \cdot \Delta t + \mathbf{d_{old}}. \tag{4}$$

2.2 Analysis of Segmentation Effectiveness

The algorithm described above has been tested on 8 CT data sets. Exemplary results of lymphatic nodes segmentation, presented in Fig. 1 confirm the effectiveness of the proposed method. Since visual examination is usually insufficient the results of automatic segmentation are compared to those obtained with manual segmentation. In our work such verification has been applied to large medical structures like the bronchial tree or blood vessels because small error in manual segmentation does not propagate to calculation of segmentation effectiveness as opposed to smaller structures (e.g. lymphatic nodes).

In our work a 3D computer model (Fig. 3) of lymphatic nodes has been developed. The model takes into account probability distribution of voxel values

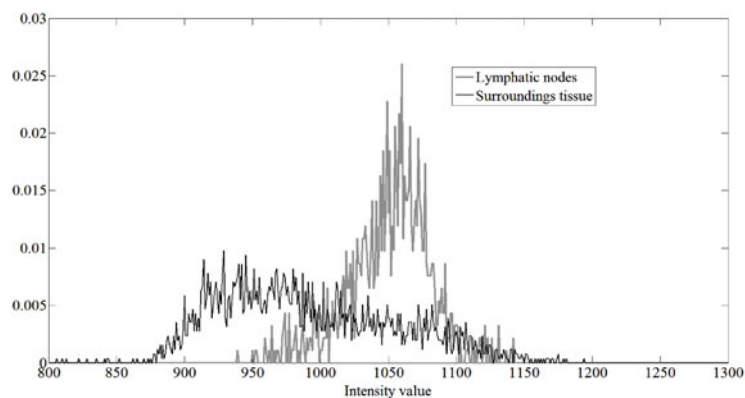**Fig. 1** Exemplary results of lymphatic nodes segmentation

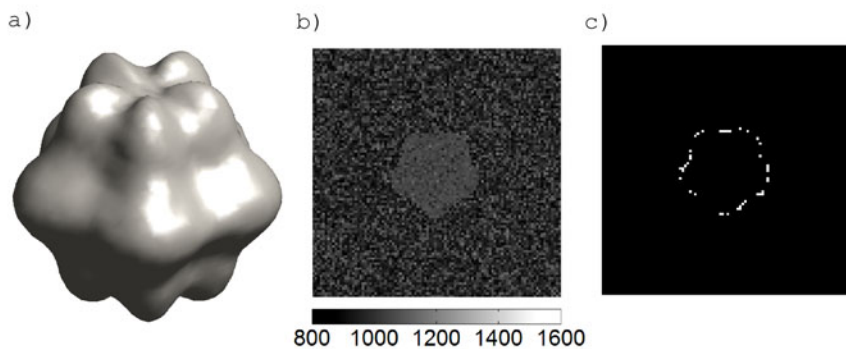**Fig. 2** Probability density function used to model generation

Fig. 3 a) 3D model of lymphatic nodes; b) 2D profile of model; c) segmentation error (white pixels)

belonging to object and background the same as in real CT data (Fig. 2). Probability density functions have been calculated based on the manual segmentation done by an expert.

In all tests the segmentation effectiveness has been estimated with the following equation:

$$\mathbf{FF_{3D}} = \left(1 - \frac{\sum_{x=1}^{N} \sum_{y=1}^{M} \sum_{z=1}^{L} |\mathbf{I_{GT}}(x,y,z) - \mathbf{I_S}(x,y,z)|}{\sum_{x=1}^{N} \sum_{y=1}^{M} \sum_{y=z}^{L} \mathbf{I_{GT}}(x,y,z)} \right) \cdot 100\%, \qquad (5)$$

In which a relative number of wrong classification is calculated ($\mathbf{I_{GT}}$ is binary mask received from manual segmentation, $\mathbf{I_S}$ - mask received from algorithm).

Segmentation effectiveness is presented in tab. 1.

Table 1 Segmentation effectiveness of the proposed method calculated from eq. 5

Anatomical structures	Effectiveness [%]
Bronchial tree	88.63%
Blood vessels	82.07%
Lymphatic nodes[a]	91.33%

[a] Results for 3D model described in text.

3 Automatic Generation of the Navigation Path

The navigation path enables an efficient inspection of the 3D visualization of tracheobronchial tree. It should be noticed that, contrary to the real bronchoscopy, in virtual bronchoscopy the camera is not limited by physical objects (i.e. bronchial wall) and may easily go through the virtual walls. The navigation path should keep the virtual camera in the centre of the bronchial lumen which is inspected. For practical reasons, a fully automatic computation of the path is strongly desired and our algorithm fulfills this requirement.

The computation of the navigation path is based on the following stages:

1. Pre-processing of the CT data.
2. Bronchial tree segmentation.
3. Evaluation of the distance transform (DT).
4. Selection of the local maxima of the DT.
5. Selection of the navigation nodes.

Pre-processing of the CT data includes data cropping, intensity reversing and optional data smoothing. The original size of a single CT scan is 512x512 pixels as shown in figure 4a, but the volume of the data set containing bronchial tree, depicted in figure 4b, is significantly smaller. For a number of different CT data the

cropping illustrated in Fig. 4 resulted in a significant reduction of the memory required to handle the data. The data was reduced an average 15 times (e. g. original CT data file size of 104 005 062 bytes reduced to size of 6 540 436 bytes cropped CT data file). Intensity reversing represents the bronchial tree with high levels (ones), and not zeros, which is a standard approach in Matlab toolbox [10]. Optional smoothing is performed to aid the segmentation, which is the next step. We use a 3D Gauss filter. Bronchial tree segmentation is performed with a global threshold and 26-connectivity model of the voxels representing the same object. Before DT, the segmented bronchial tree is morphologically dilated. This operation removes any artifacts that may be still present after segmentation. In that way, our algorithm is, to a certain degree, resistant to segmentation errors.

It is visible in figure 5a that some artifacts remained after segmentation inside the bronchial tree between nodes no 2 and 3; nevertheless, the computation of the navigation path is correct. After DT computation we determine the local maxima as follows. For the current DT voxel the values of its neighbors are checked, if the value of the neighboring DT voxel is higher then this voxel, it becames a new current voxel. This algorithm rejects the DT voxels with small values, thus the remaining
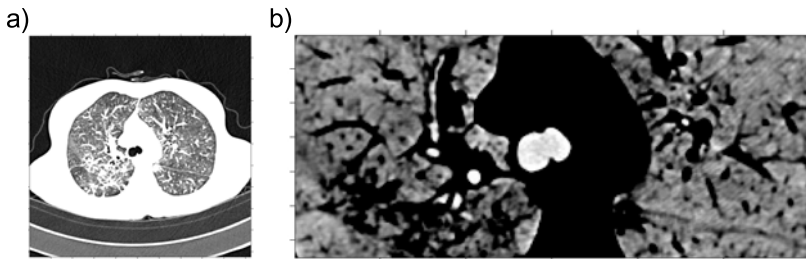

Fig. 4 Cropping CT data: a) original data, b) region of the bronchial tree with reversed intensity
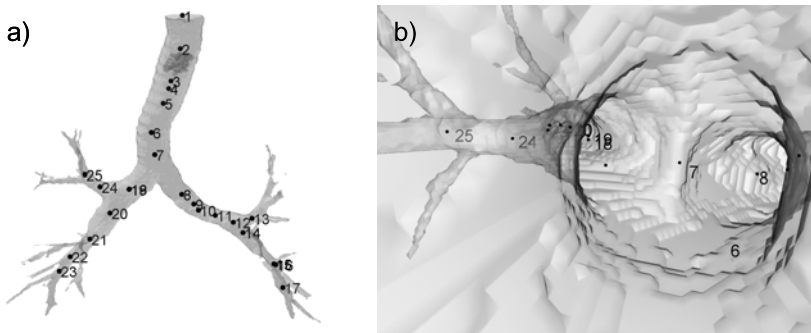

Fig. 5 a) Navigation nodes in the bronchial tree; b) The view from the node no 6 in the direction of the node no 7

voxels are placed in the centre of the bronchial lumen. Stages 1-3 are implemented with the standard image processing algorithms available in the Matlab toolbox [10], whereas algorithms behind stages 4-5 were implemented as a result of the analysis of different CT data sets.

The final result is a data structure containing navigation nodes as those presented in Fig. 5a. With each node some additional nodes visible from this node are associated in the structure. As an example, consider node 1 in figure 5b for which, the associated nodes may be those in position 2, 3, 4, 5, 6, 7 but definitely not 25 because this node cannot be seen from node 1 "through the tree". Thus it is possible to go from the current node to any associated node following the straight line and remain in the lumen of the tracheobronchial tree. Then the navigation nodes are used for moving the virtual camera by the user. Figure 5b shows the view from node no 6 in the direction of node no 7. From node 6 the user may travel to any associated node for example: 5 (backwards), 7 (forwards), 8 (forwards-right), or 18 (forwards-left).

4 Visualisation

An advanced visualisation based on the individual patient's data is widely used for diagnostic, therapeutic and training purposes [2]. Visualisation techniques generate images with 2D projection (e.g. image on monitor) of volumetric (tree-dimensional) medical data. The presentation of the three-dimensional views from CT data is available in the BRONCHOVID system with following options:

- Maximum Intensity Projection (MIP) - the images are generated with a tracing ray from camera through volumetric data. The maximum intensity value found in the ray path determines pixel colour of the view-plane. The MIP display mode does not require a user interaction and is mainly used mainly in imaging of vascular structures.
- Surface Shaded Dispay (SSD) - the generated image is a 3D surface created with polygonal meshes connecting adjacent voxels with the given threshold value. Surface details are produced with virtual light source and photo-realistic or non-photo-realistic surface illumination models. This technique receives a strong hardware acceleration in modern graphics card.
- Volume Rendering - presented image corresponds to a whole data set visualised with semitransparent renditions based on two transfer functions. One is used for mapping intensity values to color coding, and another for generating transparency values.
- Multiplanar Reformatting (MPR) - contrary to slice-by-slice 2D mode of data presentation, the MPR slice can be rotated and moved within the volume of the data set. It allows for a demonstration of 2D cross-sections in any direction.
- Virtual Bronchoscopy - data presentation mode simulating view from a real bronchoscope.
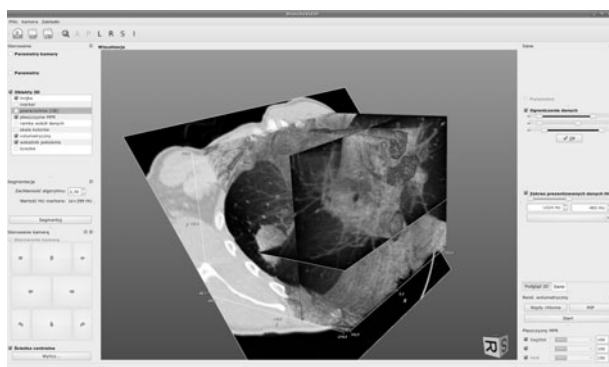
Fig. 6 User interface of visualisation software with surface and volume rendering of CT data

The visualisation module of the BRONCHOVID system was developed with a cross-platform Open Source library Visualization ToolKit (VTK)[1], Qt4[2] and Insight Segmentation and Registration Toolkit (ITK)[3]. The Visualization ToolKit uses OpenGL API for 3D graphic card which supports hardware acceleration of image generation. Qt4 library has been used for user interface and the ITK was employed for data processing. The what was shown in 6. The central part of the screen demonstrates an exemplary image of 3D data presentation. The floating widget with a control interface for data processing and visualisation can be docked in the interface.

The visualisation model implemented in the BRONCHOVID system enables fully interactive virtual bronchoscopy on the basis of the series of CT data in DICOM format. Additionally, in the virtual bronchoscopy mode of data presentation, the light source from the endoscope tip is simulated (Fig. 8b). In order to increase the depth perception the optical depth-of-field is simulated as well. An exemplary visualisation in different modes is shown in figures 7 and 8.

5 Summary

The pilot implementation of the BRONCHOVID system was carried out in the Bronchoscopy Laboratory of Department of Pulmonology, Jagiellonian University Medical College. The segmentation and visualisation module is currently tested in conditions of a routine bronchoscopic examination performed in the Laboratory. First feedback from the users is promising. The use of general purpose multicore and multiprocessor hardware platform, standard CUDA nVidia graphics cards (accelerators), open source Linux operating system and VTK Visualization Toolkit adds to a good profile of cost-effectiveness of the BRONCHOVID system as well as its con-

---

[1] http://www.vtk.org
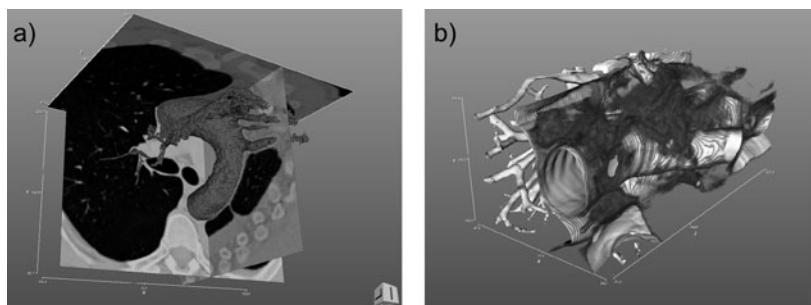[2] http://qt.nokia.com
[3] http://www.itk.org

Fig. 7 Sample view of visualization: a) orthogonal slice (MPR) with result of segmentation and b) surface rendering of trachea and volume rendering of lymph nodes tissue
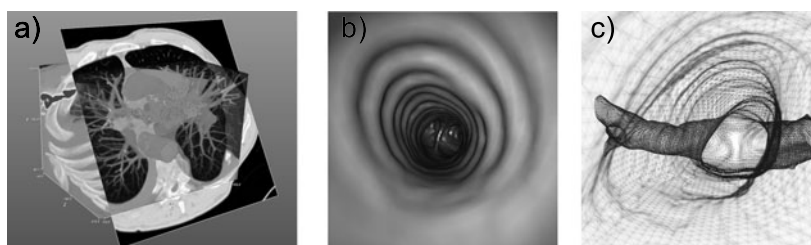
Fig. 8 Sample view of visualisation: a) MIP projection with MPR slices and segmented iso-surface (SSD) b) Virtual bronchoscopy with bronchoscopy lighting simulation c) depth of field simulation presented on wireframe trachea surface

siderable efficiency in graphic data processing. After the completion of pilot phase, a broader implementation of the system is planned. The authors anticipate further research and development activities related to real-time synchronization of 3D CT-based views with real endobronchial images coming from a bronchoscope in order to determine its position in tracheobronchial tree and to guide bioptic procedures.

References

1. Adams, L., Krybus, W., Meyer-Ebrecht, D., Rueger, R., Gilsbach, J.M., Moesges, R., Schloendorff, G.: Medical Imaging: Computer-Assisted Surgery. IEEE Comp. Graphics 10, 43–51 (1990)

2. Preim, B., Bartz, D.: Visualization in Medicine: Theory, Algorithms, and Applications. The Morgan Kaufmann Series in Computer Graphics. Morgan Kaufmann Publishers Inc., San Francisco (2007)
3. Chen, T., Metaxas, D.: A hybrid framework for 3D medical image segmentation. Medical Image Analysis 9, 547–565 (2005)
4. Cohen, L.D.: On active contour model and balloons. CVGIP: Image Understanding 53(2), 211–218 (1991)
5. Dornheim, L., Tnnies, K.D., Dornheim, J.: Stable dynamic 3D shape models. In: Int. Conf. Image Proc. ICIP (2005)
6. Dornheim, J., Seim, H., Preim, B., Hertel, I., Strauss, G.: Segmentation of Neck Lymph Nodes in CT Datasets with Stable 3D Mass-Spring Models: Segmentation of Neck Lymph Nodes. Acad. Radiol. 14, 1389–1399 (2007)
7. DG INFSO & DG JRC, Virtual Physiological Human. Towards Virtual Physiological Human: Multilevel Modelling and Simulation of the Human Anatomy and Physiology. White Paper (2005)
8. Fetita, C.I., Prâteux, F., Beigelman-Aubry, C., Grenier, P.: Pulmonary Airways: 3-D Reconstruction From Multislice CT and Clinical Investigation. IEEE Transactions on Medical Imaging 23(11), 1353–1364 (2004)
9. Honea, D.M., Ge, Y., Snyder, W.E., Hemler, P.F., Vining, D.J.: Lymph node segmentation using active contours. In: Proceedings of SPIE, Medical Imaging, vol. 3034, pp. 265–273 (1997)
10. Image Processing Toolbox User's Guide Version 5
11. Lorenson, W.E., Cline, H.E.: Marching cubes: a high-resolution 3D surface construction algorithm. In: Proceedings of the 14th Annual Conference on Computer Graphics and Interactive Techniques, pp. 163–169 (1987)
12. Robb, R.A., Cameron, B.: Virtual Reality Assisted Surgery Program. In: Satava, R.M. (ed.) Interactive technology and the new paradigm for healthcare, pp. 309–321
13. Sethian, J.A.: A fast marching level set method for monotonically advancing fronts. Proceedings of the National Academy of Sciences of the United States of America 93(4), 1591–1595 (1996)
14. Sethian, J.A.: Level set methods and fast marching methods. Cambridge University Press, Cambridge (1999)
15. Sun, S.S., Li, H., Hou, X.R., Kang, Y., Zhao, H.: Automatic Segmentation of Pulmonary Nodules in CT Images. In: The 1st International Conference on Bioinformatics and Biomedical Engineering, ICBBE 2007, pp. 790–793 (2007)
16. Terzopoulos, D.: Dynamic 3D Models with Local and Global Deformations: Deformable Superquadrics. IEEE Transactions on Pattern Analysis and Machine Intelligence 13(7), 703–714 (1991)
17. Vosburgh, K.G., Estepar, S.J.R.: Natural Orifice Transluminal Endoscopic Surgery (NOTES): an opportunity for augmented reality guidance. Stud. Health Technol. Inform. 125, 485–490 (2007)
18. Yan, J., Zhuang, T., Zhao, B., Schwartz, L.H.: Lymph node segmentation from CT images using fast marching method. Computerized Medical Imaging and Graphics 28, 33–38 (2004)
19. Yoo, T.S. (ed.): Insight into Images. Principles and Practice for Segmentation, Registration, and Image Analysis. A K Peters, Wellesley (2004)
20. Yu, K.C., Gibbs, J.D., Graham, M.W., Higgins, W.E.: Image-Based Reporting for Bronchoscopy. Journal of Digital Imaging 23(1), 39–50 (2010)

Algorithms for Automatic Recognition of Non-informative Frames in Video Recordings of Bronchoscopic Procedures

Michał Grega, Mikołaj Leszczuk, Mariusz Duplaga, and Rafał Fraczek

Abstract. The video recordings of endoscopic procedures performed within respiratory tract include both frames of adequate and inadequate quality for the assessment by the endoscopist. The frames of inadequate quality were called by some authors blurred or "non-informative". The fraction of blurred frames within video recording of bronchofiberoscopy may be considerable and it varies from case to case. Therefore, the function of automatic exclusion of "non-informative" frames would bring substantial benefits in terms of the volume of the archived video recordings of bronchofiberoscopic procedures. Furthermore, it could also save the time of users accessing medical video library established with archived resources. In this paper, the authors have proposed, tested and compared several algorithms for detecting blurred video frames. The main focus of this paper is to compare various, independent algorithms for automatic recognition of "non-informative" frames in video recordings of bronchoscopic procedures. The results demonstrated in the paper show that the proposed methods achieve F-measure, sensitivity, specificity and accuracy of at least 87% or higher.

1 Introduction

Although medical image processing is one of the most rapidly growing fields of research, relatively low interest was assigned to endoscopic procedures. Research focused on the processing of images obtained during bronchofiberoscopy has been

Michał Grega · Mikołaj Leszczuk · Rafał Fraczek
Department of Telecommunications, AGH University of Science and Technology, al. Mickiewicza 30, 30-059 Krakow, Poland
e-mail: grega@kt.agh.edu.pl,
leszczuk@kt.agh.edu.pl, rafalfr@agh.edu.pl

Mariusz Duplaga
Jagiellonian University, Medical College, ul. Grzegorzecka 20, 31-531 Krakow, Poland
e-mail: mmduplag@cyf-kr.edu.pl

particularly neglected. Furthermore, most of the systems enabling recording of bron-
chofiberoscopic procedures do not offer more advanced functions of automatic im-
age indexing or recognition.

The authors are involved in the project whose aim is to develop a computer
system supporting management of video recordings created during routine bron-
chofiberoscpic procedures performed on an every day basis in a bronchoscopy lab-
oratory. The system is supposed to improve the work-flow within the laboratory
by means of video recording, archiving, indexing of recorded videos as well as the
automatic image recognition both with archived resources and in real-time during
bronchofiberoscopic procedures.

The video recordings of endoscopic procedures performed within respiratory
tract include both frames of adequate and inadequate quality for the assessment
by the endoscopist. The frames of inadequate quality were called by some authors
blurred or "non-informative" (see Fig. 1). The fraction of blurred frames within
standard video recording of bronchofiberoscopy may be considerable and may vary
from case to case. It is known that even 30% of frames within video recordings
of colonoscopy (being a procedure visually similar to bronchofiberoscopy) may
be blurred. This fraction may be even higher in video recording of bronchofibero-
scopies as the occurrence of the factors which can impair endoscopic image quality
is higher (relatively small diameter of the lumen of bronchi, frequent accumulation
of mucous or pus in pathological cases, coughing and respiration movement over-
lapping with manipulations with bronchofiberoscope) [1].

The "out-of-focus" frames make a considerable part of "non-informative" frames
in video recording of bronchofiberoscopy. It depends partially on the fact that the
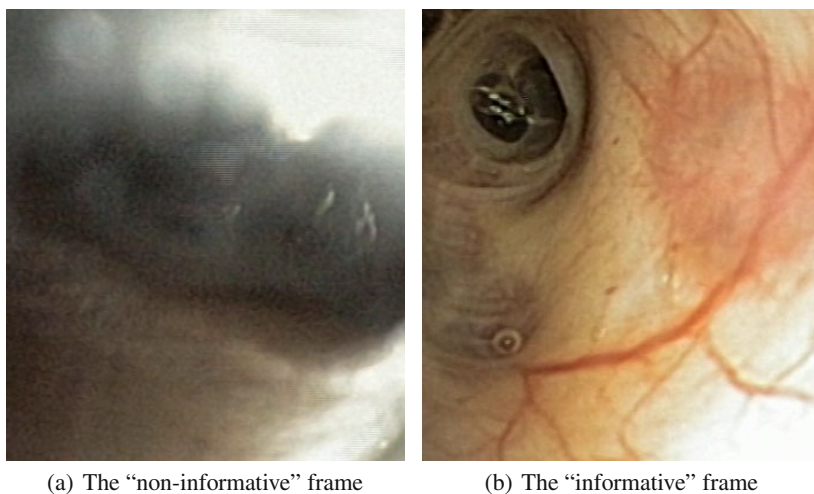vision system of the endoscope usually includes only single wide-angle lens located

(a) The "non-informative" frame   (b) The "informative" frame

Fig. 1 Examples of the "non-informative" and "informative" frames

at the tip. In the situation when the bronchofiberoscope or surrounding bronchus is moving rapidly, "out-of-focus" frames may easily be captured. The lens of the bronchofiberoscope may also be covered with the fluids or substances occurring in physiological or pathological conditions in the lumen of trachea and bronchi (sputum, pus, blood).

Furthermore, it may also occur that all the light coming from the source within the endoscope will be totally reflected and white/mirror spot will be seen in some area of the endoscopic image. It happens that during bronchofiberoscopy this phenomenon is augmented by the presence of blood filling the lumen or covering the wall of bronchi.

The function of automatic exclusion of "non-informative" frames could bring substantial benefits in terms of the volume of archived video recordings of bronchofiberoscopic procedures. Furthermore, it would also save the time of users accessing medical video library established from archived resources.

For this reason an appropriate algorithm of automatic recognition of blurry or "non-informative" frames should be proposed. One of the works that tackles the problem of blurring detection ("non-informative" frames) is [2]. The authors proposed a method based on texture features extraction by means of DFT (Discrete Fourier Transform). Extracted features are classified with a clustering algorithm. The method attains 97% classification accuracy. The main downside of the proposed method is the fact that the difference between Fourier spectrum distribution of informative and non-informative frames is not significant. This fact makes the DFT unsuitable for some video frames. In order to overcome this drawback, another approach has been proposed. Other authors [3] proposed a method which makes use of the Discrete Wavelet Transform (DWT) and automatic classification using Support Vector Machine (SVM) algorithm. The source image is decomposed into a set of sub-bands using Daubechies orthogonal wavelet family with four vanishing moments. Given image decomposition, twenty features are extracted (e.g. entropy, homogeneity, correlation, energy and histogram). In order to classify a given frame, a 20 element feature vector is classified using the SVM method with a linear kernel function and Least-Squares distance measure. The method was tested on two sets of video frames and achieved 95% accuracy. The method also scored 97% sensitivity which is important in the context of diagnostic content selection where no frame with symptoms of pathology can be omitted.

Liquid and bubble-like shapes are the other type of blurring that may be seen in the bronchoscopy videos. The possible approach, mentioned in the literature [4], to detect this type of blurring is to use a bank of Gabor [5] filters. The method has been proved to perform best in the detection of bubble-shaped blurring. The idea is to filter each frame with a set of 16 filters with 4 different orientations and 4 different scales. As a result, 16 filtered images are obtained. The filters provide a high response in all regions where bubble-like blurrings are present. The next step is thresholding which is applied in order to separate two regions of a video frame: the region with liquid and the one with no liquid evidence. Finally, frames with the detected region of bubbles grater than 50% of the visualisation area are considered as not valid for further analysis. The method has been proved to perform well in

the detection of bubble-shaped blurring. Another solution [6] makes use of second order statistics of the wavelet domain. The statistical information is obtained using co-occurrence matrices forming textural signatures of the corresponding regions. Neural networks are used for classification purposes of the the frames examined. Other approaches make use of mpeg-7 descriptors [7], features from the texture spectra in the chromatic and achromatic domains [8], color pattern changes [9], edges extraction and anlysis [10].

In this paper, the authors have proposed, tested and compared several algorithms to detect video frames impacted by blurring. The general methodology was based on the assumption that a frame can be classified as either useful (not blurring) or useless (blurring). Methods based on edge detection, HSV (Hue, Saturation, Value) histogram with neural networks, MPEG-7 descriptors as well as DCT (Discrete Cosine Transform) have been developed and tested. All the four approaches have been fine-tuned to achieve the best possible accuracy (expressed in terms of the commonly used benchmarks, including sensitivity and specificity). Then, the approaches have been faced with each-other, in order to draw conclusions on their applicability.

The main novelty of the presented research is related to comparison of various, independent algorithms for automatic recognition of "non-informative" frames in video recordings of bronchoscopic procedures. Most of the proposed algorithms are tunable in terms of maximising their F-measure, sensitivity, specificity or accuracy.

The remaining part of the paper is structured as follows. Section 2 presents the algorithms developed for the purpose of the detection of non-informative frames. Section 3 presents the results of the evaluation of the performance of the algorithms. Section 4 concludes the paper. Section 5 gives an insight into the further development of the presented research project.

2 Approaches to Detection of "Non-informative" Frames

This section presents four approaches for detecting "non-informative" frames. Methods based on edge detection, HSV histogram, MPEG-7 descriptors as well as DCT are presented.

2.1 Edge Detection

The method of detection of "non-informative" frames in the bronchoscopy video recording with use of edge detection algorithms is based, similarly to other presented methods, on the fact, that the "non-informative" frames of the recording usually do not contain many edges. Fig. 2 depicts two examples of edges of "non-informative" and "informative" frames. It can be observed that the edges almost do not occur in the "non-informative" frames whereas they are commonly seen in the "informative" frames.

In the edge detection-based approach, edges were detected using the zero-cross method. The classification was based on the value of the sum of the pixels representing the detected edges. The algorithm is depicted in Fig. 3.
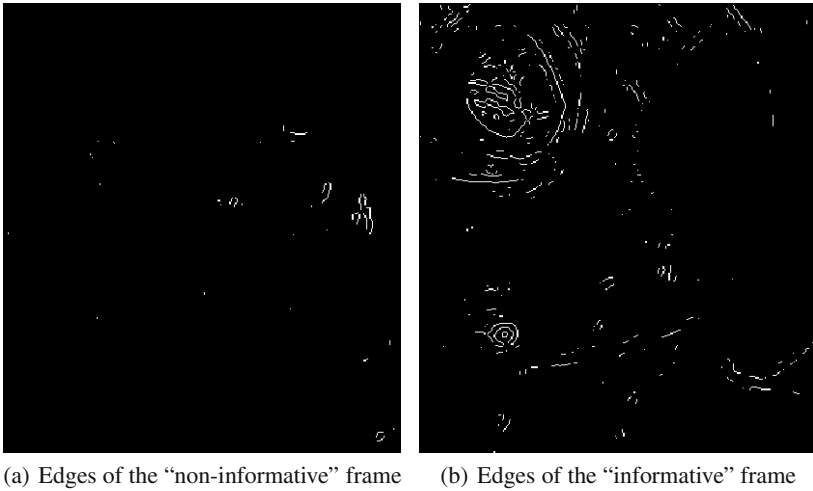
(a) Edges of the "non-informative" frame   (b) Edges of the "informative" frame

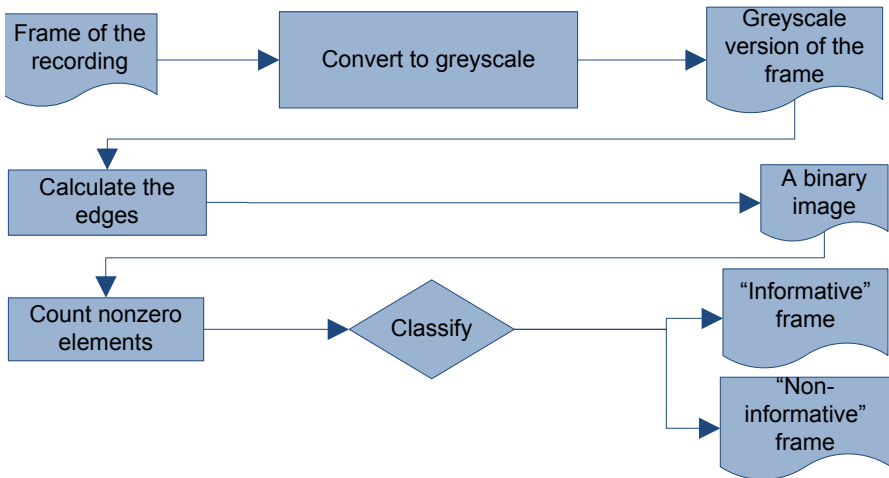**Fig. 2** Comparison of occurrence of edges in the "non-informative" and "informative" frame

Fig. 3 The blurring classification algorithm based on the zero-cross edge detection method

2.2 MPEG-7 Descriptors

The method of "non-informative" frames detection in the bronchoscopic examination recording with use of the MPEG-7 [11] descriptors is based, like other presented methods, on the fact that the "non-informative" frames of the recording usually do not contain many edges.

In this method, an image containing the detected edges is generated by means of the MPEG-7 descriptor extraction tool "EdgeHistogram". This descriptor creates a

histogram of edges contained in the picture. It takes into account the vertical, horizontal, 45-degree, 135-degree, 225-degree and non-directional edges. It is expected, that for the "non-informative" frames the total number of edges in the image will be low, when compared with the informative frames. The classification is based on the sum of values of the EdgeHistogram descriptor. The algorithm is depicted in Fig. 4.
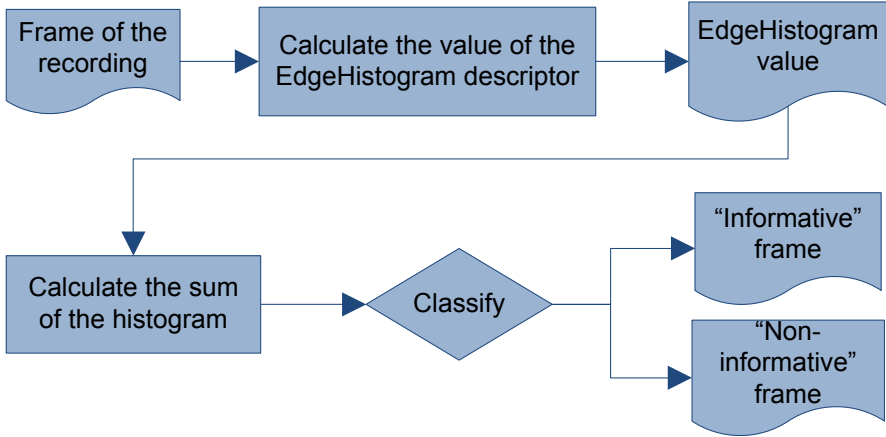

Fig. 4 The blurring classification algorithm based on the EdgeHistogram descriptor of the MPEG-7 standard

2.3 HSV Histogram and Neural Networks

This method makes use of a colour histogram in order to classify frames as informative and non-informative. Each frame is processed in the following way. First, the given image is converted from RGB to HSV colour space. Then, three histograms (for H, S and V channels) are calculated. H and S histograms consist of 40 bins and V histogram has 20 bins. The reason is that H and S components are more important in context of blurring detection, so it is reasonable to have a better resolution in case of these components. Finally, we obtain a vector containing 100 coefficients. Now, all 100 values are normalised so that the maximum value is 1. The next step is the classification with a neural network. We use a 3-layer non-linear feed forward network. The input layer consists of 100 non-linear neurons, the second layer contains 10 non-linear neurons. Both non-linear layers are composed of neurons with the hyperbolic tangent transfer function. The output layer consists of 1 linear neuron. The network is trained on the test set using the standard back-propagation training algorithm. After training, the network recognises both types of frames.

2.4   Discrete Cosine Transform Method

This method of detection of the "non-informative" frames is based on the fact, that images which do not contain numerous edges are easier to compress using algorithms based on Discrete Cosine Transform (DCT) such as the JPEG algorithm. Such images have much narrower spectra in the frequency domain than the images which contain numerous edges. This feature of the DCT allows one to use it as a simple yet effective edge detection algorithm. Unlike more sophisticated edge detection algorithms when using DCT we can only have information whether there are any edges in the image, but we are unable to locate them. This is however enough for the task of the blurred frame detection.

The algorithm of the DCT-based blurring detection is presented in Fig. 5. In the first step a frame of the bronchoscopic recording is converted into the greyscale by discarding the hue and saturation while retaining the luminance. In the second step the DCT coefficients of the image are computed. In the third step the values of the magnitude which are lower than 20 are set to 0. The value of 20 was selected experimentally as giving the best results in terms of precision and recall (see section 3). In the final step non-zero elements of the DCT matrix are counted and used for discrimination.
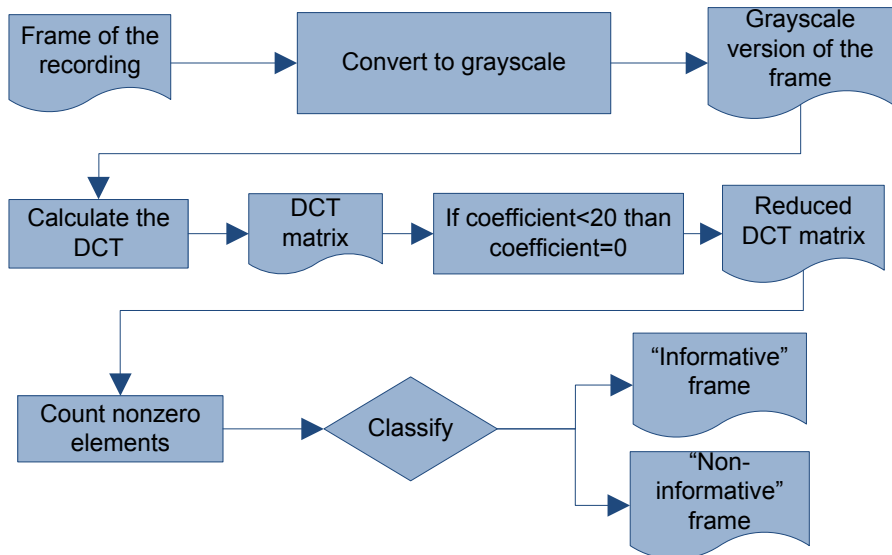

Fig. 5 The classification algorithm based on the Discrete Cosine Transform for "informative" and "non-informative" frames

3 Evaluation and Results

This section discusses evaluation of the above-mentioned algorithms. The evaluations environment, the results as well as their analysis are presented.

3.1 Evaluation Environment

The evaluation has been performed on a set of 1538 frames, manually annotated as "non-informative" (669 images) and "informative" (869 images) by the experienced bronchoscopist. The set acted as a ground-truth. Then, the images have been evenly (but randomly) split to: the training set and the testing set (see Fig. 6). The algorithms have been trained over the training set solely, whilst the results presented in the subsection 3.2 were obtained with the testing set only.

	True positivies	True negatives
■ Training set	334	434
■ Testing set	335	435
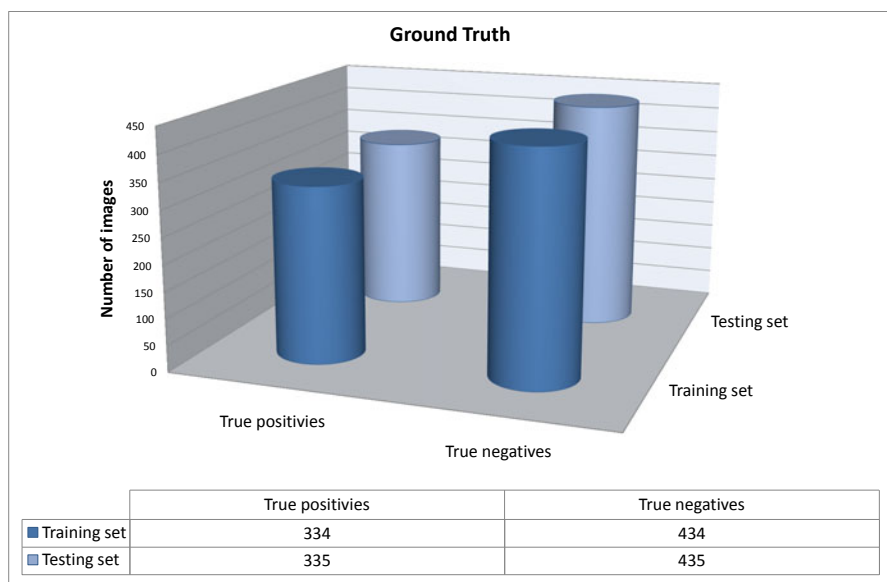
Fig. 6 The ground truth

3.2 Analysis of Results

Four metrics have been used in order to analyse the performance of the algorithm: F-measure, sensitivity, specificity and accuracy. This set of metrics allows for a detailed assessment of the performance. It is a standard set of metrics used for the assessment of the performance of the binary classification.

In order to formally define those four metrics four terms have to be introduced.

- *True Positives* (T_p) — are the correctly recognised non-informative frames. #T_p is the number of true positives in a test set.

- *True Negatives* (T_n) — are the correctly recognised informative frames. $\#T_n$ is the number of true negatives in a test set.
- *False Positives* (F_p) — are the incorrectly recognised non-informative frames. In other words – non-informative frames recognised as informative frames $\#F_p$ is the number of false positives in a test set.
- *False Negatives* (F_n) — are the incorrectly recognised informative frames. In other words – informative frames recognised as non-informative frames $\#F_n$ is the number of false negatives in a test set.

Sensitivity (1), also referred to as recall, is a measure of correctly identified positives in a test set. Specificity (2) is a measure of correctly identified negatives in a test set. Accuracy(3) is a proportion of true positives in relation to the whole population of the results. Precision(4) is a fraction of true positives calculated against the sum of true and false positives. F-measure (5) is a harmonic mean of precision and sensitivity. F-measure allows us to express the overall quality of the classification method with a single value (the higher the better, ideal at value of 1).

$$S_e = \frac{\#T_p}{\#T_p + \#F_n} \tag{1}$$

$$S_p = \frac{\#T_n}{\#T_n + \#F_p} \tag{2}$$

$$A_c = \frac{\#T_p + \#T_n}{\#T_p + \#T_n + \#F_p + \#F_n} \tag{3}$$

$$P_r = \frac{\#T_p}{\#T_p + \#F_p} \tag{4}$$

$$P_r = \frac{P_r \cdot S_e}{P_r + S_e} \tag{5}$$

The results of the performance assessment are presented in Table 1. The last column, "Tunability" informs whether the algorithm can be tuned in terms of tradeoff between sensitivity and specificity without the learning process. The only algorithm, that cannot be tuned is the NN based algorithm, as it would require re-training of the whole neural network. In case of other algorithms – tuning requires adjustment of a threshold value.

The authors were unable to compare the accuracy of classification of the presented methods to the methods described e.g. in [2] or [3]. In order to make such comparison the algorithms would have to be tested on a common image test set. Unfortunately, the research community does not have a common and standardised test set for such purposes.

One of the algorithms, the DCT-based one, has been chosen for implementation in the system used to summarise of the bronchoscopic examination recordings [12]. This algorithm has been chosen as it offers good classification results, is relatively easy to implement and offers highest performance in terms of classification time.

Table 1 The evaluation of the performance of the blurring detection algorithms

Metric	F-measure	Sensitivity	Specificity	Accuracy	Tunability
Edge	0.92	0.91	0.94	0.93	✓
EH	0.87	0.90	0.89	0.89	✓
DCT	0.92	0.93	0.93	0.93	✓
NN	0.89	0.89	0.90	0.90	✗

In the final implementation in the C++ programming language the classification decision was made in approximately 10ms, excluding the time needed to load the frame into the memory. It is short enough to allow the algorithm to analyse the recording of the bronchoscopic procedure in real time on a 25 FPS video stream.

4 Conclusions

The paper has presented four methods to detect blurring in video frames recorded during bronchoscopic procedures. Three of the methods are based on the analysis of the edges present in the frame. These algorithms utilise the MPEG-7 Edge Histogram descriptor, the zero-cross edge detection method and the analysis of the Discrete Cosine Transform spectrum of the frame. One method is based on the artificial neural network.

The training and verification of the algorithm was performed with the use of a large database consisting of approximately 1500 images extracted from bronchoscopic examination recordings.

The results demonstrated in the paper show that all of the presented methods achieve F-measure, sensitivity, specificity and accuracy of at least 87% or higher. Three of the proposed algorithms are tunable in terms of maximising their accuracy-related measures. This allows for tuning the algorithms to be under- or over-sensitive.

5 Further Work

The next research step anticipates preparation of the super-classifier, considering the above-presented algorithms as tributary classifiers. The plans also include inclusion of algorithms not described in the paper, as for example the algorithm presented in [3]. Efforts on automatically recognising other features of the bronchofiberoscopic images are currently being investigated as well.

References

1. Hwang, S., Oh, J., Lee, J., Cao, Y., Tavanapong, W., Liu, D., Wong, J., de Groen, P.C.: Automatic measurement of quality metrics for colonoscopy videos. In: MULTIMEDIA 2005: Proceedings of the 13th annual ACM International Conference on Multimedia, pp. 912–921. ACM, New York (2005)
2. Hwang, S., Oh, J., Lee, J.: Informative frames classificatin for endoscopy video. Medical Image Analysis 11(2), 100–127 (2007)
3. Jozwiak, R., Przelaskowski, A., Duplaga, M.: Diagnostically useful video content extraction for integrated computer-aided bronchoscopy examination system. In: CORES 2009 (2009)
4. Vilarino, F., Spyridonos, P.: Automatic detection of intestinal juices in wireless capsule video endoscopy. In: 18th International Conference on Pattern Recognition (2006)
5. Jain, A., Ratha, N., Lakshmanan, S.: Object detection using gabor filters. Pattern Recognition 30, 295–309 (1997)
6. Karkanis, S., Iakovidis, D., Karras, D., Maroulis, D.: Detection of lesions in endoscopic video using textural descriptors on wavelet domain supported by artificial neural network architectures. In: IEEE ICIP, pp. 833–836 (2001)
7. Coimbra, M., Cunha, J.: Mpeg-7 visual descriptors - contribution for automated feature extraction in capsule endoscopy. IEEE Transactions on Circuits and Systems for Video Technology 16, 628–637 (2006)
8. Kodogiannis, V., Lygouras, J.: A computerised diagnostic decision support system in wireless-capsule endoscopy. In: 3rd International IEEE Conference Intelligent Systems, pp. 638–644 (2006)
9. Lee, J., Oh, J., Shah, S., Yuan, X., Tang, S.: Automatic classification of digestive organs in wireless capsule endoscopy videos. In: Proceedings of the 2007 ACM Symposium on Applied Computing, pp. 1041–1045 (2007)
10. Cao, Y., Liu, D., Tavanapong, W.: Automatic classification of images with appendiceal orifice in colonoscopy videos. In: 28th IEEE EMBS Annual International Conference, pp. 2349–2352 (2006)
11. ISO/IEC: Information technology – multimedia content description interface. ISO/IEC 15938 (2002)
12. Grega, M., Leszczuk, M.: The prototype software for video summarization of bronchoscopy procedures with the use of mechanisms designed to identify, index and search. Paper submitted for 2nd International Conference on Information Technologies in Biomedicine (2010)

Using MPEG-7 Descriptors and Scoring Model to Automatically Recognize Medical Events in the Record of Bronchoscopy Video

Lucjan Janowski, Mariusz Duplaga, and Krzysztof Suwada

Abstract. A medical digital video library can contain numerous bronchoscopy video sequences. Searching such database is very difficult and can take lots of time of a medical specialist. Therefore, automatic searching algorithms should support such a task. In this paper we presented two models supporting automatic detection of bleeding and mucosal pallor. Both models are based on MPEG-7 descriptors and both were built with a scoring model. The presented ROC plots show that the obtained results can be very helpful in a real system.

1 Introduction

The frames with significant contents within bronchoscopy video make of a relatively small fraction of a total number of frames. On the other hand, the volume of the video recordings stored in the medical digital video library of the bronchoscopy laboratory is continuously growing and the use of efficient algorithms of meaningful frames retrieval is of key importance for the usability of the archived resources. An optimized approach to storage and retrieval of video resources collected in the medical video library is based on two strategies. First of them is focused on the removal of non-informative frames. This strategy reduces the quantity of stored video resources and spares time of a medical professional searching for meaningful frames.

Lucjan Janowski
AGH University of Science and Technology, al. Mickiewicza 30, 30-059 Krakow, Poland
e-mail: janowski@kt.agh.edu.pl

Mariusz Duplaga
Jagiellonian University Medical College, ul. Grzegorzecka 20, 31-531 Krakow, Poland
e-mail: mmduplag@cyf-kr.edu.pl

Krzysztof Suwada
StatSoft Polska, ul.Kraszewskiego 36, 30-110 Krakow; AGH University of Science and Technology, al. Mickiewicza 30, 30-059 Krakow, Poland
e-mail: suwada@agh.edu.pl

Another strategy is based on detecting images of significant informative value through the application of the appropriate algorithm to automatically classify the video contents. According to the predefined criteria, this strategy should lead to the extraction of those parts of the video recordings which fulfill expectation of the medical professional.

Automatic detection of predefined objects or images remains a challenge not only in the domain of medical video recordings. Numerous papers related to this topic are published every year. This paper is focused on the domain of predefined image detection in digital video library developed for the bronchoscopy laboratory. Medical domain offers a large number of areas for automatic image recognition and retrieval. Development of new diagnostic tools brings about new challenges related to the image processing. This applies to the use of capsule endoscopy to diagnose gastrointestinal diseases [1, 2]. The application of capsule endoscopy presents us with two types of research challenges: development of efficient positioning system and automatic recognition of pathological lesions in gastrointestinal tract. Efficient screening of the video recordings of capsule endoscopy could be supported with the function of automatic exclusion of non-informative frames [3]. Automatic detection of specific types of lesions creates the potential for further improvement of the screening process [4, 5]. An ideal system for automatic detection of medical images should have effectiveness comparable with a medical specialist.

Automatic recognition of objects or events in images and video sequences is an important issue addressed also by the MPEG (Moving Pictures Expert Group) community which proposed the MPEG-7 standard describing different image, video and sound features. MPEG-7 specifies descriptors' definitions i.e. for algorithms used to extract specific features. These features combined with a statistical tool help to build an index useful in detecting events.Such methodology was used by some authors [4] to detect frames with images of bleeding and ulcers.

To the authors' best knowledge the MPEG-7 descriptors were not applied to bronchoscopy videos. One of the main obstacles in the development of the systems for automatic contents detection in video recordings is making it easier to access medical digital video libraries with annotated different examples of pathological lesions. This obstacle was overcome with the development of the BRONCHOVID system enabling the annotation of representative examples of key pathologies on frames contained in bronchoscopy video recordings and close collaboration with bronchoscopy community. The project supported with the grant from Polish Ministry of Science resulted in the development of a large data base of bronchoscopy videos with annotations prepared by experienced pulmonologists. From this database the authors selected ten typical features of bronchoscopy images represented on a sufficient level in the data base to build a model. For each image type a scoring analysis was performed. In two cases , the results were sufficiently convincing to consider their application to resources stored in the bronchoscopy digital video library.

This papers contains the description of MPEG-7 descriptors and BRONCHOVID data base (Sect. 2), scoring methodology implemented in STATISTICA [6] and a review of results (Sect. 3). The obtained results are presented in Sect. 4. The last section includes a short summary and a description of future research plans.

2 MPEG-7 and Collected Data

The BRONCHOVID system enables the collection, storage and annotations of bronchoscopy video recordings resulting from the activities performed in the Bronchoscopy Laboratory of the University Hospital in Krakow. MPEG-7 descriptors were applied to index the frames with XM (eXperimentation Model) driven software. This section includes descriptions of the MPEG-7 descriptors and a structure of the BRONCHOVID database.

2.1 MPEG-7 Description

MPEG-7 is a standard proposed by the MPEG group and defined by ISO/IEC 15938 documents. Contrary to the previous MPEG-1, MPEG-2 and MPEG-4 standards, it does not describe a compression algorithm but provides a formal way to describe an image, video and sound. This information can be stored in an XML format which supports its availability to different systems. The concept was explored by some authors [7] who used XML format to store additional medical information.

MPEG-7 defines not only a storage format. It also defines descriptors for images, videos and sounds . A descriptor is an algorithm extracting some specific features of images, videos or sounds. In this paper, we are focusing on the frames and the image analysis; therefore, in the remaining part of the paper we shall refer to the image descriptor as descriptor.

The image descriptors are grouped in different categories related to such features as colour, texture and shape. We have implemented seven different descriptors. The short explanation of the features of these descriptors and the notation used throughout the paper is given below.

We used four colour descriptors [8]

- Colour Layout Descriptor (CLD). It is prepared to represent correctly spatial distribution of colours. It is represented by 192 values grouped in three groups (denoted by Y_i, Cb_i, and Cr_i) each representing a different colour dimension.
- Colour Structure Descriptor (CSD). It jointly represents colour distribution and the local spatial structure. It can be represented by various different values, on our research we used 32 values (denoted by $\bar{h}_s(i)$).
- Dominant Colour Descriptor (DCD). It describes the most common colours in the frame. The number of colours being described ranges from one to seven, depending on the overall colour variance in the frame. For each colour (described by c_{ij} where i denotes the colour value (Y, V, and U) and j the extracted colour index) additional information i.e. colour variance v_{ij}, percentage p_j and special coherency s_j is also extracted.
- Scalable Colour Descriptor (SCD). It is a Haar transform run on a specially prepared colour histogram. It is represented by 256 values (denoted by SC_i).

We also implemented two texture descriptors [8]

- Edge Histogram Descriptor (EHD). It counts edges in different picture regions and directions. EHD is represented by 80 values (denoted by $h(i)$).

- Texture Browsing Descriptor (TBD). It represents perceptual characteristics of the texture and it is represented by 5 values v_1 to v_5.

The last used descriptor is Region Shape Descriptor (RSD). It represents a shape as a combination of orthogonal shapes. RSD is represented by 62 values (denoted by M_i).

Since we used such a set of descriptors, each frame block was represented by 683 values. For some medical events some descriptor values have not changed, therefore, in the final analysis, a subset of descriptor values has been analyzed.

2.2   *Describing Bronchoscopy Videos Examinations*

The mian aim of the BRONCHOVID project was to develop the the environment supporting registration and analysis of the resources collected in the bronchoscopy digital video library. Diversified modules were developed and implemented in the BRONCHOVID system. One is a recording software installed on a dedicated hardware enabling storage of many video recordings. Next module is used for the annotation of the recorded frames by the experienced pulmonologists. Other modules bring about extended search functions, including a query-by-examples interface.

Within a frame a medical specialist can draw a shape bordering a frame region and link it with a name of a medical event that he/she recognizes in it. On a single frame numerous regions can be drawn, therefore, a single frame may contain different medical event descriptions. Note that different medical events shapes (bordered by a medical specialist) can overlap with each other.

A medical specialist can add a new name if a new medical event is detected. Note that some medical events are rare thus adding a new one is always possible.

Thanks to a medical specialist and the created tools it was possible to create a large database of the described frames. In total more than 1.000 videos have been recorded or linked in the database (some old records can also be added). 3.078 different regions were described. 92 medical events and bronchial tree regions have been represented. Of course, for some of them just a few examples are recorded since they are rare. In such a case we were not able to build an automatic detection model.

3   Scoring Methodology

Thanks to MPEG-7 descriptors each frame is represented by a large number of values. Some of the values are not correlated with the considered medical event. Therefore, we need a statistical tool which would make it possible to select the most important descriptor features and then build a model predicting a specific medical event.

Numerous statistical tools can be used to choose the correct explanatory variables which can help to predict a medical event. One of the interesting options are clustering algorithms which can support the division of a highly dimensional space

into some groups, where each group could represent a different medical event or a group of medical events [9].

The clustering algorithms are effective tools. However, the data which we are analyzing is strongly unbalanced, i.e. a number of frames within a particular medical event is much smaller than the total amount of frames. Note that one could think about solving this problem by sub-sampling the data set in such a way that a more balanced sample is obtained. Nevertheless, such a methodology may result in a model which is very sensitive (it detects an event with high probability) but with high false positives (i.e. a large number of frames would be described as containing a particular event even if they are not). The problem of unbalanced sample occurs in many different situations for example churn analysis, modeling probability of default or fraud detection. There are some modeling techniques like boosted trees that can be used in such case but we decided to use simpler linear model.

The goal of building a scoring model is to predict, if a credit will be paid on time by a person or a company [10]. Our prediction (score) has to be based on the history of mature credits - clients who already know if they have paid the credit ("good" ones) or not ("bad" ones). Since most of the clients paid their credits on time and just a small percentage did not, the historical sample is strongly unbalanced.

The scoring methodology is complicated and it will not be described here in detail. Just the most important parts, used in our analysis, are shown. The main idea of scoring methodology can be divided into steps (see Fig 1). Each step is computed separately with a different part of the scoring module (called *STATISTICA* Scorecard) of *STATISTICA* software [11].

It is worth mentioning that a score is not simply a number - it has an interpretation. Every N point, the odds of falling to the "good" class, doubles. That parameter is called PDO - points to double the odds.

In the first step we have to find out which explanatory variables (descriptor values) best predict the response variable (a variable being 1 if a medical event appears in the frame, such a frame is called negative - "bad" or 0, in case of a positive frame - "good"). In order to initially rank variables the IV (Information Value) is computed [10].
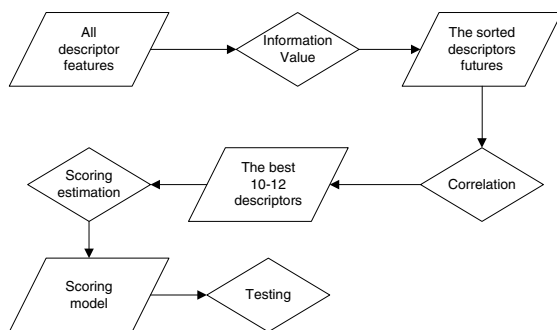

Fig. 1 The brief explanation of scoring methodology. Only steps used in our research are presented.

The IV is an indicator of the overall predictive power of characteristic. We can compute this measure as

$$IV = \sum_{i=1}^{n} (Good_i - Bad_i) \cdot \ln\left(\frac{Good_i}{Bad_i}\right),$$ (1)

where n is the number of attributes (levels, intervals, bins) of variables, $Good_i$ and Bad_i refer to the column-wise percentage distribution of the total "good" and "bad" cases.

The obtained results can be interpreted as the strength of the relation between particular descriptor value and the response variable. Note that the considered relation is one to one, only.

The second step is to remove some variables. We could simply remove all variables with low IV. However, using the first n predictors (in sense of IV) does not necessarily lead to the best model estimation. Some explanatory variables could correlate strongly. One of the consequence of strong correlation is that actual additional information brought by the two correlated variables is very close to the information which we already have by using just one of them. Therefore, the second step is to remove variables which are strongly correlated. This step is not fully deterministic since we cannot define clearly what "strong correlation" means. Moreover, if two variables are strongly correlated but their origin is different (for example, these are different descriptor values) it can be a good idea to preserve both of them - it will also result in a more stable scorecard. The final criteria used in this research was to limit explanatory variables number to about 12 (a dozen variables is usually recommended when building a credit scoring model).

The third step is to build attributes because a scorecard model is always built using discrete data. Each attribute (bin) is an interval (if the variable is continuous) or a set of values (if variable is discrete).

We are trying to divide the explanatory variable into classes where each class can be clearly interpreted. It means that for two different classes we should observe a different relationship between positive and negative frame number (frames with and without a medical event).

This step can be seen as information lost, since we change a continuous variable into a few discrete values. For example, the response difference between value 10 and 11 can be very high if the interval boundary is 10.5. This is a drawback of digitalization nevertheless if we use an explanatory variable x as a linear continuous predictor then the difference between 10 and 20 is large even if in fact a value larger than 10 indicates that a frame does not contain a particular medical event at 80%.

The digitalization step is also complicated. Best results can be obtained by proposing the intervals by a specialist. In our case, where MPEG-7 descriptors are used, it is difficult for a medical specialist to specify particular boarding values. Therefore, in the research we used a standard methodology which makes it possible to estimate automatically the interval borders. The *STATISTICA* Scorecard builds bins using CHAID analysis described (for example in [12]) and Weight of Evidence (WoE).

Weight of Evidence is a statistical measure that is very helpful in assessing goodness of attributes. It is based on the log of odds formula and is calculated as follows.

$$WoE = \ln\left(\frac{Good}{Bad}\right) \cdot 100 \qquad (2)$$

Notice that if there is a strong lack of balance in a particular bin - for example there is 90% "good" and 10% "bad," WoE will be high ($>> 0$). On the other hand, if there is 15% "good" and 85% "bad," WoE will be low ($<< 0$). Big absolute values of WoE indicate strong relation with the dichotomous dependent variable, where for the balanced bins with more or less 50% the observations in each class, WoE is very close to 0.

In most cases CHAID analysis generates three different intervals where one of them indicates high probability of the negative answer ($WoE << 0$) the second one suggests that the answer should be positive ($WoE >> 0$) and one can be described as abstaining from the answer ($WoE \approx 0$).

Changing all the variables, to discrete values which additionally can be easily interpreted as pro or against a particular answer, helps to understand and use the scoring model. Note that a specialist can change a particular suggestion since he/she understands each answer.

Using "variables voting" is correct from the democratic point of view but it is not optimal. Note that for one variable can predict the negative answer can be predicted with 80% of accuracy, on the other hand, a different variable can give only 60% of accuracy. Therefore, each class of value is described by a number indicating the strength of the particular conclusion.

Combining all the considered variables results in the final scoring model. From medical point of view it is important that the final model can be understand. It is understandable as long as each explanatory variable is. Additionally, the model answer is a score, the interpretation is done by a specialist. Therefore, we can easily exchange the specificity and the sensitivity of the obtained results.

4   The Model Estimation

The medical records collected in BRONCHOVID project and described by a medical specialist contained numerous medical events. Some medical events overlap with each other (see description given in Sec 2.2). For example, in case of specific veins' structure commonly seen in cancer a specialist will mark both the cancer and the veins' structure as two separate medical events. They are in fact separate events since each of them can occur separately.

Such a database structure is more difficult to analyze since if a region is marked as a medical event a we cannot say for sure that each region with description b is not a since in some cases it is. Therefore, the first step of our analysis was to choose a subset of medical events in such a way that the considered medical events do not overlay with each other.

It is quite obvious that same events are more frequent than others. On the other hand, we need to have at least 3-4 examinations with a particular medical event to try to build a model. This constraint was another limitation.

Contrary to the previous restriction we suffered from too many similar frames. Note that the created database is not only dedicated to support automatic recognition. Therefore, an interesting case of a specific medical event could be represented with up to 20 frames and a less interesting case of the same medical event could be represented with just a few frames. Note, that using all the cases of a specific medical event could result in creating a tool which would recognize a specific case of the medical event but would not be able to generalize the obtained results just because one of the events is over-represented. Therefore, we had to limit the maximum number of frames with a specific medical event and coming from a single medical examination (a single record). To obtain the optimal balance we decided to use 3 frames.

The last considered problem was the medical event size. Note that most of the events cover less than half of the frame. Therefore, using descriptors computed for the whole frame has to result in a poor model. The best possible solution would be to compute the descriptor value from the region bounded by a medical specialist. Nevertheless, the final algorithm cannot properly chose the region in which descriptor should be counted. Therefore, we decided to divide each frame into blocks of 64x64 pixels.

Each block can share a different percentage of bounded region i.e. a different percentage of the medical event is "seen" in a particular block. We decide that a block contains a medical event if the event covers at least 80% of the block. Note that if 30% of the frame pixels were bounded by a medical specialist and named bleeding then more than 60% of blocks are counted as positive. Moreover, in case of the bleeding model, all other medical events are counted as positive, since they are positive in the sense they are not bleedings. Such data construction is one of the reason why the rations between positive and negative values is so huge.

The final database used in the learning and testing process consists of ten different medical events and the total number of 42.729 blocks. The chosen events are widening/blunting of carina, narrowing/constriction of bronchial lumen, mucosal pallor, endobronchial tumour mass, bleeding, mucosal infiltration, vascular engorgement/widening, purulent secretion,extravasations, and mucosal atrophy. All considered blocks were divided into a training set (75% of the cases) and a test set (25%) of the cases. All the models were built on the same training. For each medical event different records were marked as negative and positive values.

For each considered event a model was built. Nevertheless, for eight of them the obtained results were not good enough to be implemented in real environment. Two best models, however, are good enough and they are presented in this paper.

4.1 Bleeding

Based on the scoring methodology presented in Sec. 3 12 best explanatory variables were chosen. The explanatory variables were taken from all the considered colour descriptors: CLD, DCD, CSD and, SCD (see Sec. 2.1). From CLD and CSD only one value is used. From DCD and SCD five values are used. The correlation between the variables are not higher than 0.75 and most of them is lower than 0.2 (see Table 1).

Table 1 The correlation matrix for explanatory variables used in the bleeding model. The variables names are explained in Sec 2.1.

	Cb_0	$h_s(1)$	c_{U0}	c_{U1}	c_{U2}	v_{U0}	v_{U1}	SC_{12}	SC_{48}	SC_{56}	SC_{88}	SC_{96}
Cb_0	1.00	-0.73	-0.74	-0.42	-0.27	-0.38	-0.23	-0.56	-0.27	-0.21	-0.19	0.01
$h_s(1)$	-0.73	1.00	0.71	0.50	0.37	0.40	0.29	0.59	0.46	0.51	0.42	-0.36
c_{U0}	-0.74	0.71	1.00	0.47	0.28	0.43	0.23	0.67	0.13	0.25	0.25	-0.16
c_{U1}	-0.42	0.50	0.47	1.00	0.55	0.27	0.53	0.33	0.27	0.27	0.13	-0.12
c_{U2}	-0.27	0.37	0.28	0.55	1.00	0.18	0.25	0.14	0.29	0.27	0.13	-0.10
v_{U0}	-0.38	0.40	0.43	0.27	0.18	1.00	0.24	0.24	0.22	0.16	0.13	-0.08
v_{U1}	-0.23	0.29	0.23	0.53	0.25	0.24	1.00	0.05	0.27	0.20	0.12	-0.05
SC_{12}	-0.56	0.59	0.67	0.33	0.14	0.24	0.05	1.00	-0.06	-0.06	-0.04	-0.16
SC_{48}	-0.27	0.46	0.13	0.27	0.29	0.22	0.27	-0.06	1.00	0.52	0.39	-0.41
SC_{56}	-0.21	0.51	0.25	0.27	0.27	0.16	0.20	-0.06	0.52	1.00	0.44	-0.42
SC_{88}	-0.19	0.42	0.25	0.13	0.13	0.13	0.12	-0.04	0.39	0.44	1.00	-0.30
SC_{96}	0.01	-0.36	-0.16	-0.12	-0.10	-0.08	-0.05	-0.16	-0.41	-0.42	-0.30	1.00

The final model is the final score being a sum of 12 different individual scores obtained for each descriptor value. Note that, the final score is obtained for each frame block. Each block can be positive (non bleeding) or negative (bleeding), therefore, scoring can be understood as mapping all blocks to a single number. The obtained mapping does not divide the set of blocks into positive and negative values. A specialist has to choose the Cut-off level (the border between negative and positive answer). The big advantage of scoring methodology is that such a decision can be easily changed. In order to help choose the correct threshold we can use ROC plot (Receiver Operating Characteristic) where sensitivity versus 1-specificity is drawn. The ROC plot obtained for the test set of bleeding scoring model is presented in Fig 2.

The presented ROC plot shows that with specificity 0.9 we can obtain sensitivity close to 0.7. Such a result helps in reduct searching time significantly.

4.2 Mucosal Pallor

Based on the scoring methodology presented in Sec. 3 11 best explanatory variables were chosen. The explanatory variables are taken from three different colour
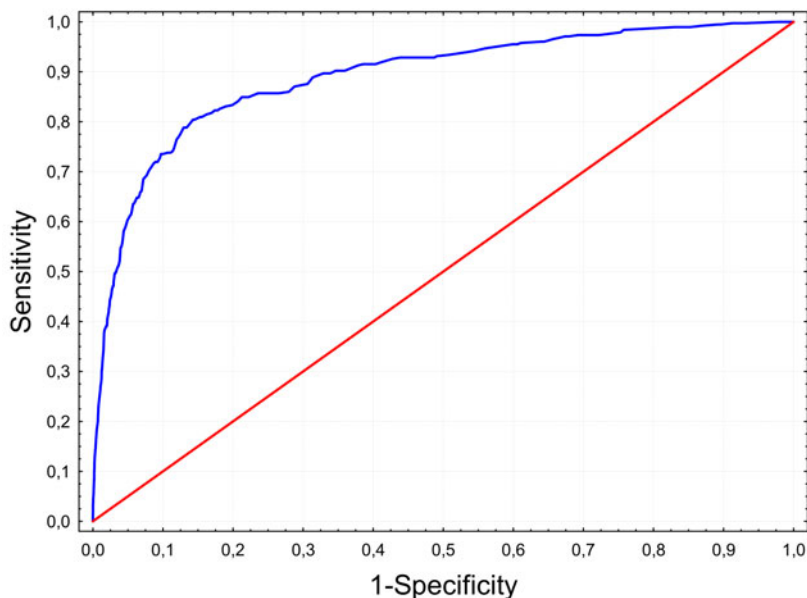
Fig. 2 ROC plot obtained for bleeding model using test set

descriptors, CLD, DCD, and, SCD (see Sec. 2.1). The correlation between the variables is not higher than 0.7 and for most of them it is lower than 0.2, similarly to bleeding model (see Table 2).

Table 2 The correlation matrix for explanatory variables used in the mucosal pallor model. The variables names are explained in Sec 2.1

	Cr_0	c_{U1}	c_{U2}	v_{U0}	SC_{12}	SC_{24}	SC_{27}	SC_{56}	SC_{200}	SC_{208}	SC_{216}
Cr_0	1.00	0.44	0.25	0.45	0.66	0.06	-0.09	0.16	-0.09	-0.35	-0.37
c_{U1}	0.44	1.00	0.55	0.27	0.33	0.01	-0.12	0.27	0.02	-0.17	-0.34
c_{U2}	0.25	0.55	1.00	0.18	0.14	-0.07	-0.09	0.27	0.04	-0.09	-0.24
v_{U0}	0.45	0.27	0.18	1.00	0.24	-0.03	-0.05	0.16	-0.06	-0.22	-0.26
SC_{12}	0.66	0.33	0.14	0.24	1.00	0.51	-0.22	-0.06	-0.01	-0.39	-0.45
SC_{24}	0.06	0.01	-0.07	-0.03	0.51	1.00	-0.11	-0.07	-0.04	-0.28	-0.28
SC_{27}	-0.09	-0.12	-0.09	-0.05	-0.22	-0.11	1.00	0.03	-0.28	0.05	0.10
SC_{56}	0.16	0.27	0.27	0.16	-0.06	-0.07	0.03	1.00	0.02	0.11	0.09
SC_{200}	-0.09	0.02	0.04	-0.06	-0.01	-0.04	-0.28	0.02	1.00	0.49	0.05
SC_{208}	-0.35	-0.17	-0.09	-0.22	-0.39	-0.28	0.05	0.11	0.49	1.00	0.41
SC_{216}	-0.37	-0.34	-0.24	-0.26	-0.45	-0.28	0.10	0.09	0.05	0.41	1.00

The mucosal pallor model is based mostly on SCD and U colour part of DCD. Similarly to the bleeding problem, we can easily change the threshold separating negative and positive answers. The threshold change can be used to specify the correct specificity or sensitivity depending on the particular case. The overall ROC curve obtained for the test set is presented in Fig 3.
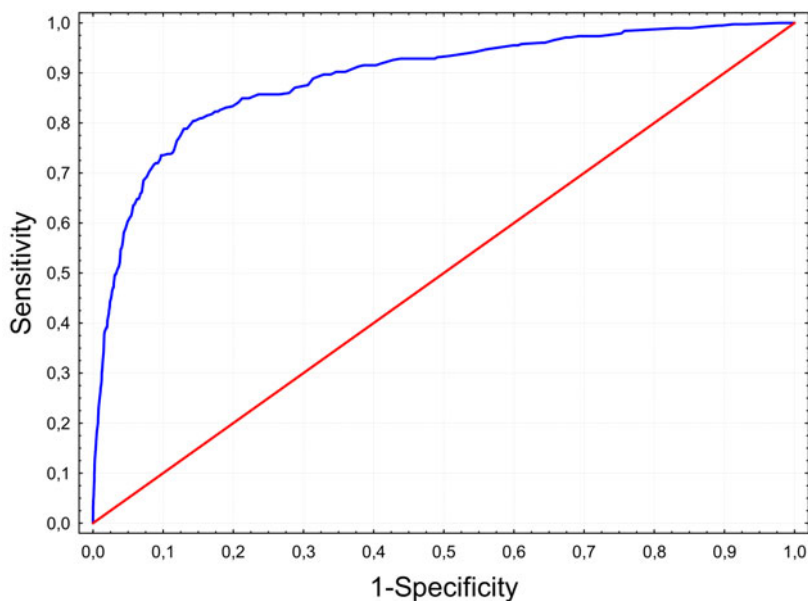
Fig. 3 ROC plot obtained for mucosal pallor model using test set

The presented ROC plot shows that similarly to the bleeding recognition with the specificity 0.9 we can obtain sensitivity close to 0.7. Moreover, in this case if sensitivity is decreased to 0.5 we will detect all mucosal pallor cases.

5 Conclusions

The presented work shows that using MPEG-7 descriptors and score models may result in obtaining an effective and useful recognition model. The two obtained models have ROC plots showing high sensitivity and specificity which additionally can be easily exchanged. Such an easy exchange, which results from the use the scoring methodology, can be specially important from the medical point of view.

Scoring methodology has an additional advantage. In case where the descriptors values are known or can be computed very fast (using CUDA, for example) the score it self is easily obtained since a few variables discretization and a sum are needed. Scoring models can also be adjusted since the obtained ROC plot shows different threshold levels which could be chosen.

In our research not only Bleeding and Mucosal Pallor were analyzed. For eight other medical events the obtained results are not good enough to be implemented in practice. It does not mean that a better model cannot be built. Nevertheless, to do so a different set of descriptors could be considered. Additionally more examples of medical events could help to build a precise model. These tasks are left for future research.

References

1. Cunha, J., Coimbra, M., Campos, P., Soares, J.: Automated topographic segmentation and transit time estimation in endoscopic capsule exams, vol. 27, pp. 19–27 (2008)
2. Lee, J., Oh, J., Shah, S.K., Yuan, X., Tang, S.J.: Automatic classification of digestive organs in wireless capsule endoscopy videos. In: SAC 2007: Proceedings of the 2007 ACM symposium on Applied computing, pp. 1041–1045. ACM, New York (2007)
3. Vilarino, F., Spyridonos, P., Pujol, O., Vitria, J., Radeva, P.: Automatic detection of intestinal juices in wireless capsule video endoscopy. In: ICPR 2006: Proceedings of the 18th International Conference on Pattern Recognition, Washington, DC, USA, pp. 719–722. IEEE Computer Society, Los Alamitos (2006)
4. Coimbra, M.T., da Silva Cunha, J.P.: Mpeg-7 visual descriptors - contributions for automated feature extraction in capsule endoscopy. IEEE Trans. Circuits Syst. Video Techn. 16, 628–637 (2006)
5. Iakovidis, D.K., Maroulis, D.E., Karkanis, S.: A An intelligent system for automatic detection of gastrointestinal adenomas in video endoscopy. Computers in Biology and Medicine 36, 1084–1103 (2006); Intelligent Technologies in Medicine and Bioinformatics
6. Statsoft, Inc., STATISTICA (data analysis software system), version 8.0 (2010), `http://www.statsoft.com`
7. Rege, M., Dong, M., Fotouhi, F., Siadat, M.R., Zamorano, L.: Using MPEG-7 to build a human brain image database for image-guided neurosurgery. In: SPIE, vol. 5744, pp. 512–519 (2005)
8. Choi, Y., Won, C.S., Ro, Y.M., Manjunath, B.S.: Texture Descriptors. In: Manjunath, B.S., Salembier, P., Sikora, T. (eds.) Introduction to MPEG-7, Multimedia Content Description Interface (2002)
9. Gan, G., Ma, C., Wu, J.: Data Clustering: Theory, Algorithms, and Applications. ASA-SIAM Series on Statistics and Applied Probability. Illustrated edition. SIAM, Philadelphia (2007)
10. Siddiqi, N.: Credit Risk Scorecards: Developing and Implementing Intelligent Credit Scoring. SAS Publishing (2005)
11. StatSoft: STATISTICA Scorecard (2010), `http://www.statsoft.com/products/statistica-scorecard/`
12. Shea, P., Bidjerano, T.: Community of inquiry as a theoretical framework to foster epistemic engagement and cognitive presence in online education. Comput. Educ. 52, 543–553 (2009)

Three Stage Method Assisting Endobronchial Tumor Mass Recognition in Bronchoscopy Images

Artur Przelaskowski and Rafal Jozwiak

Abstract. Current problem of computer assistance of bronchoscopy neoplasmatic lesion interpretation is still open and exceptionally challenging question. Strongly diversified pathology appearance, lack of reference patterns, subjective criteria of lesion assessment and often unsatisfactory quality of registered video limit diagnostic effectiveness of bronchoscopic studies. Fundamental part of presented research is an analysis of various endobronchial tumor manifestations in a context of acquired image sequences, bronchoscope navigation, artifacts, lightening and reflections, changing color dominants, unstable focus conditions, etc. Representative patterns of pathologies in bronchoscopy images and standardized features of malignancy were sought. Proposed method of neoplasmatic areas indication was based on three fundamental steps of preprocessed video analysis: 1) informative frame selection, 2) block-based unsupervised determining of enlarged textural activity, 3) indication of the regions with potentially tumor signatures, based on feature selection in different domains of transformed image followed by SVM classification. Efficiency of pathology recognition was verified with a reference image dataset of 14 examinations containing diversified neoplasmatic endobronchial tumor patterns. Experimental results reveal promising accuracy of recognition for differential forms of endobronchial tumor manifestations. Test set of selected informative blocks was classified as pathological or normal with accuracy of 85%.

1 Introduction

Growing amount of diagnostic images and videos in medicine are captured, interpreted and stored in digital forms during everyday clinical practice. Easy and unrestricted access to 3D medical data sets (CT, MRI, etc.) and medical videos together

Artur Przelaskowski · Rafal Jozwiak
Institute of Radioelectronics, Warsaw University of Technology, Nowowiejska 15/19, 00-665 Warszawa, Poland
e-mail: `arturp@ire.pw.edu.pl, rjozwiak@ire.pw.edu.pl`

with full availability of advanced visualization techniques have shown a marked improvement in diagnosis and treatment efficiency. However, the growth of imaging capability requires advanced computer assistance in analysis and interpretation of huge amount of additional data with highly detailed content. Generally, objectified criteria guide to standardized reasons of diagnostic decisions and increased clinical usefulness of image information.

Recent advances in video technology used for endoscopic imaging allow enhanced quality of visual inspection for diagnosis or treatment of the inside of the human body without or with a very small scars. This trend is highly correlated with modern medicine requirement for lowering the invasiveness of the medical procedures with simultaneous preserved effectiveness and safety. The introduction of the more sophisticated diagnostic and therapeutic endoscopy methods is closely related to this trend [1]. Even though endoscopic examination procedures still impose direct contact with patient and results interpretation process is highly subjective and strongly depends on individual physician skills and knowledge.

Stored in digital video databases, different forms of medical endoscopy procedures are characterized by high amount of diversified and often ambiguous medical information. For example, medical video endoscopy examinations (e.g. gastroscopy, colonoscopy, bronchoscopy, etc.) contain different diagnostic and therapeutic events related to presence of versatile pathological changes and realized therapeutic procedures (e.g. biopsy). This diagnostically useful video content usually compose only a small fraction of whole video data, while the greater part of the record usually is poor quality or it contains completely non-informative frames (e.g. blurred, out-of-focus, damaged, etc.).

1.1 Informative Frames in Videobronchoscopy

A basic diagnostic procedure used in pulmonology that involve visualization of the inside of a patient's lung is bronchofiberoscopy. It becomes nearly obligatory when lung neoplasm is suspected in the patient. The procedure is usually accompanied by other diagnostic modalities enabling sampling of suspicious tissues for pathology evaluation. The modern video technology exerted an influence also on bronchoscopy examination procedures and equipments - the new video fiberbronchoscopes have an integral video camera system at the distal end, which is illuminated by optical fibers, and finally the real-time video image is observed on the screen by the physician. Unusually important factor is wide skill level variation between different physicians in performance and interpretation. The assessment of bronchoscopic video has not been standardized and currently relies solely on procedure logbooks and subjective letters of competency [2].

Bronchoscopic images demonstrate many common features with natural video sequences, e.g. general image features and natural content perception, color space, textural features, data dynamics, dominant objects properties. Different parts of bronchoscopic examinations are distinguished by diversified movement characteristics - from slow motion to dynamic video with fast camera movement across variable

diagnostic content. Reviewing bronchoscopy videos for the presence of pathology signs, where we may see one pathology instance only after having seen thousands of different video frames, is really difficult and diagnostically challenging task.

In bronchoscopy video there are typically a significant number of illegible, redundant video fragments or manifesting itself in a form of unreadable or insignificant frames. While the content of the frames cannot be recognized and interpreted by any means because of limited acquisition conditioning or case-dependent specific image appearance, it is impossible to extract any diagnostic information. Such frames with unrecognized content was described as non-informative frames [3]. The appearance of this frames is strongly diversified due to different origin and unlike arising mechanism. Essentially, we can distinguish: out-of-focus frames (occurred due to wrong camera position - too far/too close focus into/from mucosa of bronchi), blurred (motion blur due to rapid camera movement through the bronchial space), bloody (due to pathology presence or as a result of sampling of suspected tissues for pathology evaluation) and bubbled (as a result of camera lens cleaning). Informative frames carry potentially important amount of diagnostic information.

However informative frames are not equal in the sense of visual quality, which change rapidly depending on current camera situation, position and movement. For example, any camera movement introduce versatile amount of motion blur (rapid or very fast camera movement can even lead to total loss of frame readability), while camera lance being temporally covered by body fluids or secretions cause loss of global focus condition. Despite of the diversified visual quality, most of informative frames represent normal tissue manifestation and different anatomical parts of bronchi tree. The most important video content compose relatively short and diagnostically important frame groups, which reveal the presence of different pathology forms. Various pathology manifestations are strongly diversified both inter-class (between different types of lesions) as well as intra-class (between different manifestations of the same pathology). Additionally every informative frame can be potentially affected by additional artifacts or distortions (e.g. specular reflections, lightening, etc.) which additionally hamper process of analysis. Examples of bronchoscopy video content, including non-informative and informative frames, different lesions manifestations and diversification as well as possible distortions are presented in Fig. 1.

1.2 Computer Assistance of Bronchoscopy Diagnosis

Different forms of computer assistance for bronchoscopy are mainly concentrated on advanced visualization aspects like virtual bronchoscopy [4, 5] or video (camera motion) tracking [6, 7]. Our research was focused on computer assisted automatic detection of suspicious lesions in bronchoscopy video. To the best of our knowledge, similar researches have been reported so far only for other endoscopic modalities like colonoscopy [8], but not for bronchoscopy.

Among different pathology manifestations, first of all explicit signs of tumor are the object of interests. Endobronchial tumor mass constitutes one of the most

Fig. 1 Bronchoscopy video content. First row shows examples of non-informative frames. Second row illustrates informative frames, readable with good visual quality. Example of onerous visual quality diversification is presented in third row (adjacent frames from the same part of video examination). Finally various bronchi lesions are presented in fourth row.

common form of neoplasmatic bronchial lesion manifestation - Fig. 2. Most of tumors develop within a bronchus of subsegmental size or greater. Usually appear as a soft masses covered with intact bronchial epithelium, mostly very vascular and pink to purplish in color.

The general purpose of reported research was computer aided detection of suspicious neoplasmatic lesions, especially extraction, indication and visualization of highly probable tumor mass manifestations in bronchoscopic images. Presented method was based on texture analysis of preprocessed images with different forms of useful information selection. Firstly, enhanced textures were classified as informative or non-informative indicating diagnostically useful frames. Next, regions of increased texture activity of informative frames were selected to be finally verified
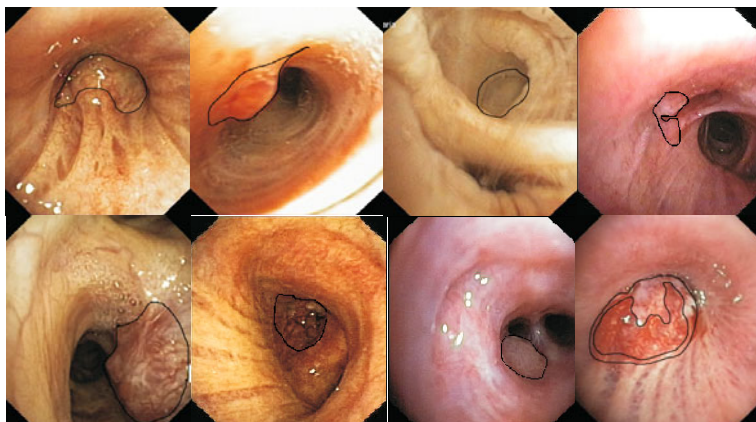
Fig. 2 Examples of different endobronchial tumor mass manifestations. Pathology were outlined manually by experienced physician.

as probably containing tumor symptoms. Implemented algorithms were optimized and verified experimentally.

2 Material and Methods

General task of effective recognition of diagnostically significant features in bronchoscopic images is really tough, challenging and case dependent because of *unstable*, seriously limited quality of image information. To succeed, endobronchial tumor mass recognition was based on an analysis of bronchoscopic video frames according to precise successive selection of specified regions of interests (ROIs): informative frames, blocks of important content and blocks of potentially mass appearance.

Because dominant image feature used for recognition was texture, ROIs selection was based generally on textural data characteristics complimented with the factors of energy distribution in different data domains, entropy-based characteristics of stochastic information and other statistical measures of dominant signal trends.

2.1 Three Stage Method Description

Proposed method of neoplasmatic areas indication was based on three fundamental steps of video analysis:

- IFS procedure, i.e. Informative Frame Selection, based on a whole frame characteristics of possible artifacts, unusual data and dominant texture recognition; texture features extraction and selection with supervised classification were used;
- BUD method, i.e. Block-based Unsupervised Determining of blocks of interests, i.e. enlarged textural activity areas in IFS frames, based on energy distribution

analysis and directional image characteristics in polar 2D Fourier space; unsupervised classification of several local block features was applied;

- BRT method, i.e. Block-based Recognition of Tumor tissue, based on texture feature extraction and selection in image, frequency, wavelet, and contourlet domains of BUD blocks, followed by supervised classification.

Prior all of those successive procedures, wavelet-based image preprocessing was applied to extract texture image for further analysis.

2.1.1 Initial Texture Extraction

A sequence of the following procedures was used:

- broncho frame normalization by successive conversions: a crop of source broncho image area with mirror fulfilling of irregular corners, and conversion to grayscale image (G_I) - see Fig. 3;
- contrast-limited adaptive histogram equalization (CLAHE) of G_I with 4×4 pixel blocks and contrast function adjusted to 0.02: $CL_{4 \times 4, 0.02}(G\_I) = I_{AC}$;
- distorted wavelet synthesis of smoothed source image $I_S = \mathscr{W}^{-1}(\mathscr{W}(I_{AC}))$ and differential, texture image estimation as: $I_T = |I_{AC} - I_S|$, where $\mathscr{W}$ is 2-scale dyadic wavelet transformation based on non-perfect reconstruction filter bank;
- adaptive histogram equalization of texture image as follows: $I_{AT} = CL_{4 \times 4, 0.02}(I_T)$.

Selected results of texture extraction were presented in Fig. 3.
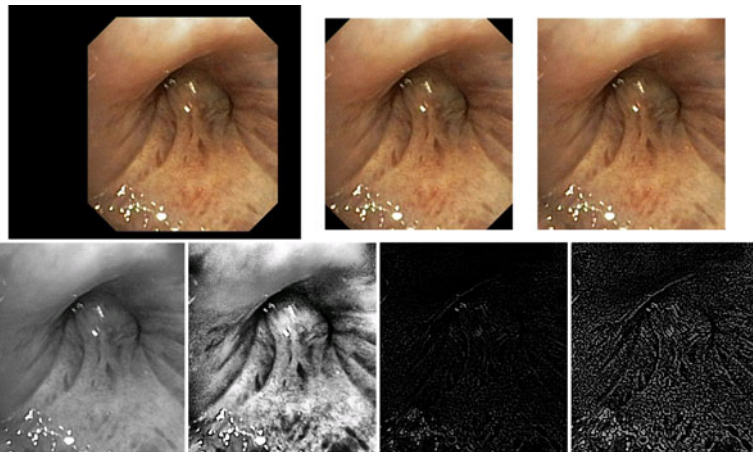
Fig. 3 The effects of successive image preprocessing procedures: (left-right, top-down) source broncho frame, cropped image window, image with fulfilled corners, greyscale normalized version (G_I), adaptively enhanced G_I, textures extracted by wavelet-based procedure, texture enhanced by CLAHE.

CLAHE enhances local contrast of images by transforming the values in the intensity image. It operates on small data blocks so that the histogram of the output region approximately matches the uniform histogram. The neighboring blocks are bilineary interpolated to eliminate induced discontinuities on the block boundaries. The contrast, especially in homogeneous areas, is limited by contrast enhancement limit parameter to avoid amplifying the actual image noise or insignificant textures.

Multiresolution signal analysis according to wavelet-based concept is typically implemented with specific types of digital filter banks (FBs) known as two- channel perfect reconstruction (PR) filter banks. Those filters are associated with scaling functions (low pass one h) and the wavelets (high pass one g) of the transform kernel according to the following two equations (scaling and wavelet, respectively): $\phi(t) = \sqrt{2}\sum_n h_n \phi(2t-n)$ and $\psi(t) = \sqrt{2}\sum_n g_n \phi(2t-n)$. Conditions of the perfect reconstructions (Y is almost, i.e. according to the assumed precision, equal to X) with l delays for two-channel FB are as follows:

$$h(z)\tilde{h}(-z) + g(z)\tilde{g}(-z) = 0 \tag{1a}$$

$$h(z)\tilde{h}(z) + g(z)\tilde{g}(z) = 2z^{-l} \tag{1b}$$

Generally, wavelet decomposition requires the filters to be FIR (finite impulse response) and linearly phased to form orthogonal FBs. However, only Haar filter fulfill such requirements. Often used solution is biorthogonal FBs with insignificant redundancy of wavelet representation. For texture-oriented image processing we decided to design orthogonal FB by softening PR condition. The first term (eq. 1a) traditionally called the alias (cancellation) term is often fulfilled by using quadrature mirror filters (QMFs) with conditions: $h(z) = \tilde{g}(-z)$ and $g(z) = -\tilde{h}(-z)$, as we did. However, the second term (eq. 1b) called the distortion elimination term was used to control the distortion introduced in data processing to extract basic (lower frequency) signal content. Resulting spline non–PR FB with $h = [1/4, 1/2, 1/4]$ and miror $g = [-1/4, 1/2, -1/4]$, its magnitude responses in frequency domain and associated basis functions were given in Fig. 4.
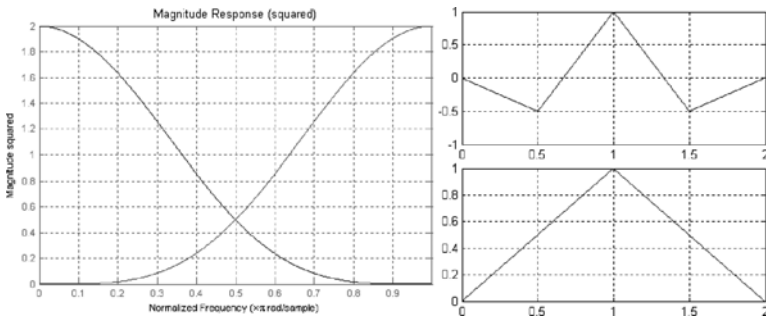
Fig. 4 Characteristics of the filter bank used for multiscale image processing: magnitude responses, associated wavelets and scaling functions, respectively

2.1.2 Texture Characteristics and Recognition

We considered energy distribution characteristics across scales and subbands of wavelet domain diversified significantly classified tissue. Different classes of wavelet energy based features and histogram-based features from normalized wavelet coefficients were used. Moreover, entropy features (memoryless and joint, for subbands compositions) and homogeneity, correlation, energy and contrast of successive scale co-occurrence matrix of quantized coefficients were applied. SVM with optimized kernels and quality criteria was applied for classification and feature reduction procedures.

Informative frame selection (IFS) was based on a whole image I_{AT} characteristics for possible artifacts, regions of unusual data (non–informative), informative regions with dominant texture recognition. A set of 48 selected textural feature was used for informative frame recognition as follows:

- 15 features in image domain, i.e.

    – statistical variance, kurtosis, skewness, entropy and energy
    – joint entropy, contrast, correlation, energy and homogeneity based on co-occurrence matrix
    – according to Tamura texture characteristics: coarseness, directionality, and contrast

- 16 features in wavelet domain with symlet2 kernel of nearly symmetrical wavelets (2 scales of block decomposition were used), i.e.

    – energy of approximation related to the energy of details
    – distribution of detail energy and entropy across scales
    – joint entropy of distribution if max magnitude details for successive scales
    – joint entropy, contrast, correlation, energy, homogeneity for co-occurrence matrix of quantized maximum magnitude details
    – maximum detail value of different subbands related to mean approximation energy

- 16 features of directional spectrum in polar 2D Fourier domain, i.e.

    – statistical moments of angle histogram of coefficient magnitudes
    – energy of angle histogram
    – parameters of polynomial approximation of angle histogram

- one feature of directional spectrum in contourlet domain – entropy of two scale coefficients

Informative frames were extracted according to supervised classifier of over 800 training frames. Cross-validated SVM classifier with radial basis was optimized for universal broncho applications.

Block-based unsupervised (BUD) determining of enlarged textural activity areas was used for fast defining of blocks of interests. Idea of second step of tumor extraction was high risk area segmentation through block-oriented cover of the image. Blocks of 50×50 pixels were verified basing on energy distribution analysis

and directional image characteristics in polar 2D Fourier space. Two phase threshold selection: for energy distribution factors and directional factors was optimized for over 1000 test cases. Such simple selection of blocks of interests can be used as on-line approximation of the regions susceptible to tumor masses. However, BUD blocks were essentially used for complexity reduction of time consuming BRT procedure.

Block-based recognition of tumor tissue (BRT) was designed for final recognition of selected, active image blocks as potentially covered by tumor mass tissue. Recognition scheme was optimized for large test set of several thousand of test BUD blocks basing on textural feature extraction and selection for effective case classification. Cross-validated SVM procedure with radial basis was used to classify each BUD block as diagnostically suspected of having pathology symptoms or normal.

Graphical form of selection and recognition results was used for indication of frame status as non–informative (purple mark in top left corner) or informative (lack of purple mark), while informative frame regions could be covered by red (i.e. BUD) or yellow (i.e. BRT) blocks.

Proposed three stage method assisting endobronchial tumor mass recognition was implemented in MATLAB environment. For classification purpose we used SVM classifiers from Matlab Toolbox for Pattern Recognition PRTools4 [9]. Additionally we used some extra procedures form Contourlet Toolbox [10], Beamlab [11] and Wavelab [12].

3   Experiments and Results

The examples of the results achieved for the implementation of described algorithm were presented and explained in Fig. 5. Illustration of the method adjusting to concrete examination and user requirements were outlined in Fig. 6.

Proposed method was verified with a reference image data set containing different bronchoscopy video content exemplification (e.g. varied pathologies, diversified anatomical bronchi structures, therapeutic and diagnostic interventions, possible artifacts, etc.) clinically selected by experienced physicians from near 300 recorded and stored real bronchoscopy examinations. A reference set of close to 1300 images containing informative/non-informative frames was used to asses IFS efficiency. For the purpose of BUD and BRT assessment 14 diversified cases of endobronchial tumor manifestations were considered, each containing several especially selected frames with additional manual pathology outline. Every frame was divided into blocks of size 50x50, where each block was categorized to norm or pathology according to available physician outline. Near 900 selected blocks were finally used as a test set.

Experimental results reveal considerably high accuracy of IFS-BUD-BRT method for independent classification of individual differential forms of endobronchial tumor patterns – the overall accuracy for whole dataset reached over 83% (73% of sensitivity and 90% of specificity). Moreover, over 95% of accuracy was achieved for selected as representative, distinct bases of masses. More precisely, IFS tested
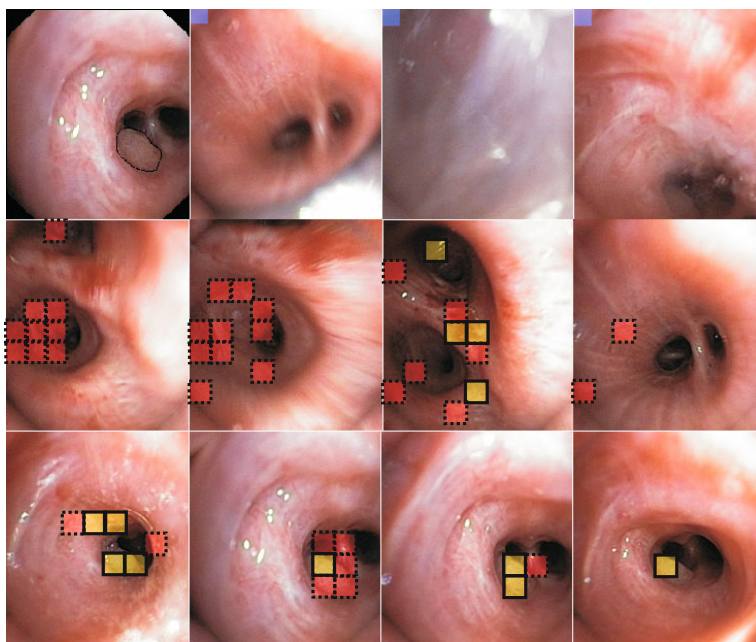
Fig. 5 Example results of proposed three stage method applied to selected video examination with endobronchial tumor mass (reference frame with outlined pathology is presented in top left corner). Other frames of first row, marked with purple block (no outline), were classified as non-informative (first stage of algorithm). Red blocks (dotted outline) represent areas with high texture information activity (related directly to second stage of proposed method) while yellow blocks (solid outline) marked out presence of pathology area (related directly to third stage of proposed method). Second row illustrates informative frames without clearly visible pathology (frames preceding appearance of pathology). Yellow blocks noticeable on third frame in this row (from left) represent false positive (FP) indications. Frames with visible pathology are present in third row. As we can see, pathology existence are indicated more or less precisely, but mainly correctly (yellow block are present in places corresponding to area outlined originally on reference frame). Some miss-classification examples can be seen on first frame (form left) - two yellow blocks located above pathology area.

against close to 1228 test frame gave 89% accuracy of informative/non-informative selection. Sensitivity of BUD method was adjusted to 92% of 888 test control or pathology blocks with accuracy close to 70% (significant amount of false positives verified in the next stage by BRT procedure). BRT effectiveness was 86%. Preliminary selection of texture activity blocks by BUD allows reduction of computational complexity of the whole method up to 5 times.
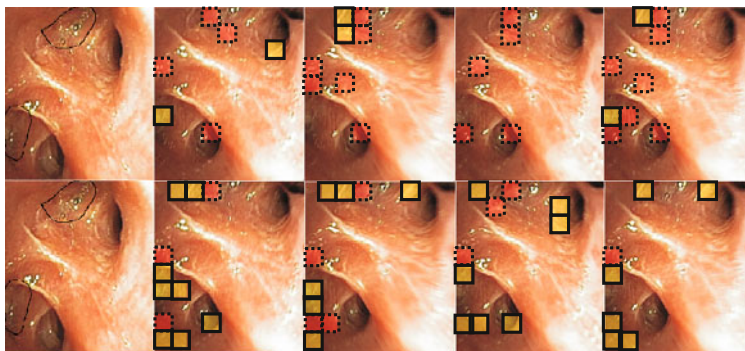
Fig. 6 Impact of method parametrization for overall detection efficiency. Each row illustrates results for different set of method parameters. Depending on the selected set of initial presets proposed method is more or less sensitive. Selection of this parameters should set a compromise between method sensitivity and specificity.

4 Conclusions

It is very difficult task to verify clinical usefulness of proposed method. Not only participation of several experienced bronchoscopists is required. Reliable experimental procedure strongly depends on significantly diversified technical conditions of bronchofiberoscopes and test cases. Moreover, examination protocol is not standardized and criteria of evaluation and interpretation are significantly subjective. However, automatic indications in almost on-line mode (second stage of the method) or more reliable in off-line mode (full method application) occurred really helpful as assistant tool for more careful broncho video analysis. Objectified indicators of special regions of interests are useful for standardized protocol design, comparative analysis and education of inexperienced doctors. As far as we know it is the first attempt of such supporting tool for bronchoscopic diagnosis.

References

1. Duplaga, M., Leszczuk, M., Przelaskowski, A., Janowski, L., Zieliński, T.: BRON-CHOVID - integrated system supporting bronchoscopic diagnostics. Przegląd Lekarski 64, 42–48 (2007) (in Polish with English summary)
2. Bowling, M., Downie, G., Wahidi, M., Conforti, J.: Self-Assessment Of Bronchoscopic Skills In First Year Pulmonary Fellows. Chest 132(4) (2007)
3. Hwang, S., Oh, J., Lee, J., Tavanapong, W., de Groen, P.C., Wong, J.: Informative Frame Classification for Endoscopy Video. Medical Image Analysis 11(2), 100–127 (2007)

4. Chung, A.J., Deligianni, F., Shah, P., Wells, A., Yang, G.Z.: Patient Specific Bronchoscopy Visualisation through BRDF Estimation and Disocclusion Correction. IEEE Transactions of Medical Imaging 25(4), 503–513 (2006)
5. Duplaga, M., Socha, M.: VTK-based application supporting bronchofiberoscopic procedures. Bio-Algorithms and Med. Systems l(l/2), 191–196 (2005) (in Polish with English summary)
6. Rai, L., Merritt, S.A., Higgins, W.E.: Real-time image-based guidance method for lung-cancer assessment. In: IEEE Conf. Computer Vision and Pattern Recognition, vol. 2, pp. 2437–2444 (2006)
7. Mori, K., Deguchi, D., Sugiyama, J., Suenaga, Y., Toriwaki, J., Maurer Jr., C.R., Takabatake, H., Natori, H.: Tracking of a bronchoscope using epipolar geometry analysis and intensity-based image registration of real and virtual endoscopic images. Med. Image Anal. 6, 321–365 (2002)
8. Iakovidis, D.K., Maroulis, D.E., Karkanis, S.A.: An Intelligent System for Automatic Detection of Gastrointestinal Adenomas in Video Endoscopy. Computers in Biology and Medicine 36(10), 1084–1103 (2006)
9. Duin, R.P.W., Juszczak, P., Paclik, P., Pekalska, E., de Ridder, D., Tax, D.M.J.: A matlab toolbox for pattern recognition. PRTools4, Delft University of Technology (2004), http://prtools.org/
10. Do, M.N., Vetterli, M.: The contourlet transform: an efficient directional multiresolution image representation. IEEE Transactions Image on Processing 14(12), 2091–2106 (2005), http://www.ifp.illinois.edu/ minhdo/software/ contourlet_toolbox.tar
11. Donoho, D.L., Huo, X.: Beamlets and Multiscale Image Analysis, Computational Science and Engineering. In: Multiscale and Multiresolution Methods. Springer, Heidelberg (2001), http://www-stat.stanford.edu/ beamlab/ BeamLab200PR2.zip
12. Buckheit, J.B., Donoho, D.L.: WaveLab and Reproducible Research, Dept. of Statistics Stanford University, Tech. Rep. 474 (1995), http://www-stat.stanford.edu/~wavelab/Wavelab_850/ WAVELAB850.ZIP

Application of SIFT Image Analysis Method to Support Transbronchial Needle-Aspiration Biopsy

Piotr Pawlik and Mariusz Duplaga

Abstract. The paper presents results of SIFT (Scale-Invariant Feature Transform) method application to support transbronchial needle-aspiration biopsy. An image generated during a bronchoscopic examination is often disturbed by vomiting reflex of the patient, or by sudden influxes of saliva or mucus. The presented system supporting the doctor is capable of monitoring the examined spot and signalling return to this spot after the disturbance ends or after the repeated examination of the same fragment of bronchial tree. A modified SIFT method is used, with a particular focus on real-time SIFT calculation.

1 Introduction

The main reason for bronchoscopic examination is the assessment of the trachea and the bronchial tree as well as obtaining of samples for further laboratory tests. The sensitivity of the assessment depends on the experience of a physician performing the examination. Detecting of the areas in the trachea and bronchi which suggest the presence of pathological lesions necessitate forceps biopsy. Sampling of the tissue follows the inspection of the whole bronchial tree available for assessment. Due to a relatively high mobility of the tracheobronchial tree, the position of the bronchoscope tip is not stable in the bronchial lumen. This results in a need for repositioning of the bronchoscope tip during sequential tissue sampling. Furthermore, endobronchial view may deteriorate due to secretion or other contents, e.g. blood accumulating in the airways. The evacuation of fluid contents with the suction

Piotr Pawlik

Department of Automatics, AGH University of Science and Technology, Al. Mickiewicza 30, 30-059, Cracow, Poland
e-mail: `piotrus@agh.edu.pl`

Mariusz Duplaga

Jagiellonian University Department of Medicine, Ul. Skawinska 8, 31-066, Cracow, Poland
e-mail: `mmduplag@cyf-kr.edu.pl`

applied to the working channel of the bronchoscope enables for the preservation of appropriate endobronchial visibility. However, during this operation the location of the tip of the bronchoscope may change and the endoscopist must reposition it to the position assuring optimum conditions for next attempt of tissue sampling. The use of the positioning system with a memory of selected location within the lumen of the trachea or bronchi may be useful for two biopsy techniques: transbronchial needle aspiration (TBNA) and forceps biopsy of bronchial mucosa.

Conditions for the support of the TBNA

TBNA is a method of sampling of the structures located outside the lumen of the trachea and bronchi (usually lymph nodes or tumour masses) for cytological or histological assessment. It may be also used to obtain aspirates from submucosal bronchial lesions or masses located in peripheral areas of the lung. TBNA is particularly important for the diagnostics and staging of lung cancer.

TBNA is performed with a special needle which can be passed through the working channel of the bronchoscope. Then, in the lumen of trachea or bronchi, depending on the preferred site of biopsy, special mechanism controlled externally allows for pulling out the needle from the cover and piercing of the wall of airways (see Fig. 1). Currently, the needles used for TBNA differ in the diameter and collected material may be feasible either for cytological or histological examination. TBNA is a relatively safe procedure offering important input to pulmonary diagnostics.

TBNA became popular method in diagnostic of mediastinal lesions due to activities of Ko Wang who published first convincing results of its application during bronchoscopy [14, 15].

If performed without additional imaging guidance, this procedure is characterized by limited sensitivity, especially in inexperienced hands [4]. To increase diagnostic yield of TBNA, different support techniques were proposed including computer tomography (CT) fluoroscopy and endobronchial ultrasonography (EBUS) [16]. Currently, EBUS is probably the most popular option of the support for TBNA, however, the cost of the equipment and the need for additional training limit its use for routine bronchoscopic examination in most laboratories. Furthermore, the most
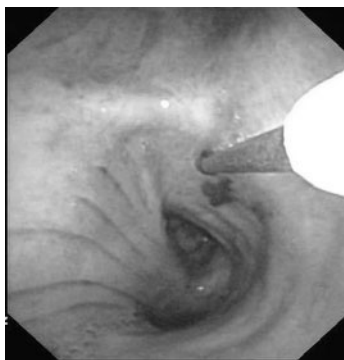
Fig. 1 TBNA procedure: the biopsy of the lymph node located below the main carina

effective version of EBUS support, offering real time guidance during TBNA, requires the use of a dedicated bronchoscope and processor for the ultrasound image presentation. A cost-effective version of the support based on the use of CT data sets and dedicated software for generation of virtual bronchoscopy (VB) visualization could be used in most bronchoscopy laboratories. The use of an interactive VB application enabling the presentation of the biopsy sites selected during earlier CT data exploration and implemented on personal computer installed in the bronchoscopy suit may yield encouraging effects [2].

The use of supportive methods for TBNA, which do not assure real time guidance, could be further enhanced with the method for fixing and retrieval of the optimum locations for the biopsy. The solution which offers a memory of preselected locations and an option for a quick return to the optimum position is described in detail in this paper.

The forceps biopsy of bronchial mucosa at location determined with emerging imaging options

A growing number of imaging modalities which can be used during bronchoscopy results also in the need for the additional support for triggering and the position fixing method in relation to the performance of the forceps biopsy. These modalities include both established methods e.g. narrow band imaging (NBI) [13] or autofluorescence bronchoscopy [11] and new emerging techniques. The application of reflectance and light scattering spectroscopy [1], near-infrared Raman spectroscopy [5] or optical coherence tomography [12] for bronchoscopic examination is still a subject of intensive research. Main rationale for the use of these techniques is search for the areas of precancerous lesions or early cancer. The positive identification of a suspicious area should be followed with biopsy of the bronchial mucosa for further histological evaluation.

As only part of these imaging modalities enables for real time guidance of the biopsy procedure, the method for registering of the optimum location for the tip of the bronchoscope is of relevance here. Such approach would allow for repeated precise forceps sampling of the bronchial mucosa from the site which is suspicious.

Both potential areas of application for the method of bronchoscope location registration assume the use of the computer support during bronchoscopy and the visualization of the processed endoscopic video image on additional display.

Navigating robots with the use of visual information [10, 6, 3], where the SIFT method [7] was successfully applied, is very similar to the problem of returning to the same examined spot in the procedure of transbronchial needle-aspiration biopsy. This examination involves moving a bronchoscope tip over the bronchial tree, which is parallel to movement of a robot using a visual system. Similarity of this problem to navigation of robots suggested that the SIFT method can also be applied to support transbronchial biopsy. An additional reason to use this method was provided by the results of studies demonstrating the advantage of SIFT descriptor over other descriptors of characteristic points [8].

Putting this idea into practice required modification of the SIFT algorithm for its Real-time calculation [9].

2 Outline of the SIFT Method

The SIFT method, presented by David Lowe, finds stable local features (characteristic points) on the basis of a pyramid of images with decreasing resolution. These images are gradient images, resulting from a subtraction of two images generated after filtering the initial image with Gauss filters of different σ parameters. The pyramid is divided into so-called octaves. Images in one octave are of the same resolution but differ in terms of the Gauss filter size (see Fig. 2). Images in the next octave are filtered with the same filters but their resolution is two-fold decreased.

The local features that are sought after are the surroundings of local minima and maxima in the DoG pyramid.

For the detected points a vector of features is calculated. This vector is a kind of a histogram of gradients calculated in the vicinity of the points. These features are to a large extent, insensitive to the intensity of light (because of gradients), rotation (the direction of gradients is recorded in relation to the main direction of the characteristic point) and scale (thanks to the application of the pyramid of images).

For such appointed feature vectors the pattern characteristic points are searched.
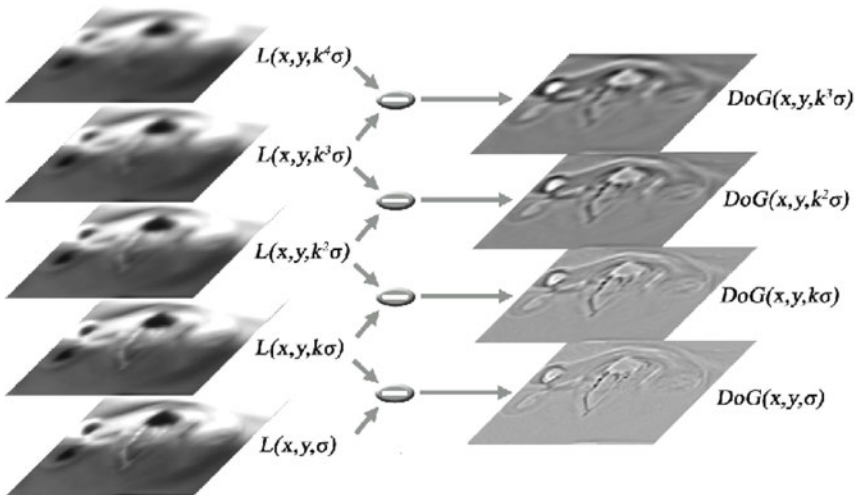
Fig. 2 Procedure of obtaining a single octave DoG (Difference of Gaussian)

3 Modification and Implementation of the SIFT Method

The complexity of the SIFT method hampers its application for purposes requiring real-time calculations [9]. However, assuming that the area of doctor's interest is the surroundings of a single characteristic point (the fragment of the image used for SIFT descriptor for a given point), the time used for calculations can be significantly reduced. This reduction includes two components:

- thanks the extent of the suitable area of interest, there is no need to search for characteristic points in the whole DoG pyramid; this can be reduced to images of the lowest resolution,
- focusing on one characteristic point significantly shortens the phase of searching for similar points.

Given that transbronchial biopsy images do not include important unique details which are only found in images of higher resolutions (in lower octaves), restricting the analysis only to higher octaves of the pyramid is fully justified.

However, reducing the analysis to just one point has also some limitations:

- the choice of area of interest cannot be unlimited - it has to be determined as the surroundings of one of the recorded characteristic points,
- despite the fact that characteristic points in the SIFT method are highly stable, they can disappear without significant deterioration of the image quality.

To minimize the risk that a characteristic point disappears, its detection threshold was decreased (down to 0.0001). Addition ally, in determination of extremes, values of first DoG images in each octave were excluded. This allowed to increase the number of characteristic points detected in the transition between octaves. The increased number of these points consequently increased the number of options in choosing the area to be examined.

Reducing the analysis time was possible thanks to:

- modification of the SIFT algorithm,
- paralleling the calculations.

The most important factor of algorithm modification was to exclude the analysis of the lower levels of the pyramid. It was restricted to Gaussian blur of the first (initial) image of the octave and deleting every second row and column of the blurred image. After these transformations the image was used as the initial image for the higher octave. The value of the σ parameter of the Gauss filter was selected to allow for obtaining for the same effect with a single blurring as with multiple Gauss filtrations within the octave with the classic algorithm.

To parallel the calculations, Streaming SIMD Extensions (SSE) was used. Two available libraries were tested:

- Fast SIFT Image Features Library (libsiftfast) [17], with classic implementation of the SIFT method (published by D. Lowe) enhanced with SSE paralleling mechanisms.

- Open Computer Vision Library (OpenCV) [18] initiated by Intel. This library was used only to calculate the Gaussian blur, because the analysis of the time required calculation of separate stages of the SIFT algorithm showed that the highest share was held by the calculation of the Gauss filtration.

4 Verification of the Quality of the Method on Sequences of Pictures Generated during Bronchoscopic Examination

To verify the described method, 2-minute sequences of bronchoscopic examination images were used. The middle frame of each sequence was selected by a doctor as the image illustrating a pathological change and the extent of this change was marked. This was the basis for selection of a characteristic point near the marked change. It was tested if the same area of interest will be selected by the SIFT method in the preceding and the following frame.

Tests were positive in most cases of disappearance of the area of interest resulting from artefacts.
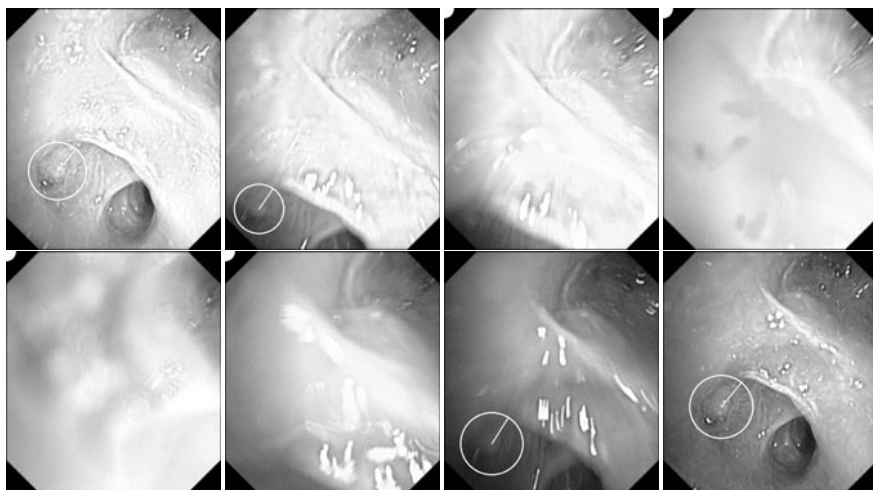
Fig. 3 Fragment of image sequence. Upper row - frames 11, 18, 19, 20, lower row - frames 27, 36, 37, 41. The area of interest is marked with a circle with a radius (in frames where it was detected).

Fragments of the sequence in Fig. 3 show disappearance of the clear view between frames 18 and 37. Although the image remained unclear fairly long, the SIFT method was able to detect and mark the area of interest that had initially been selected. It is remarkable that the method is capable of detecting and marking the area of interest despite considerable image deformation by artefacts (frames 18 and 37).

The characteristic points in the presented pictures are marked with circles representing the area used to determine the vector of features (descriptor) for a given point (radius of these circles represents the main orientation of descriptors).

The well-known advantage of the SIFT method is its significant insensitivity towards rotation and translations. The sequence in Fig. 4. shows the ability of the method to track the area of interest despite movements of the bronchoscope tip (frames with artefacts in this sequence, between 38 and 48, were correctly excluded while tracking).
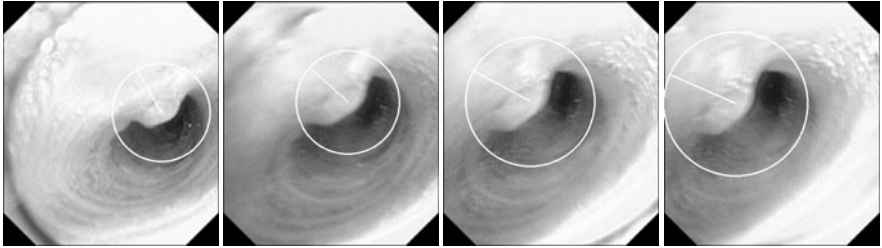
Fig. 4 Fragment of image sequence; frames 36, 50, 53, 54

The SIFT method remains also insensitive towards changes in the size of the area of interest. An example sequence in Fig. 5 shows almost 2-fold increase in the area after draw forward of the bronchoscope tip. Despite this change, the area of interest is tracked correctly.
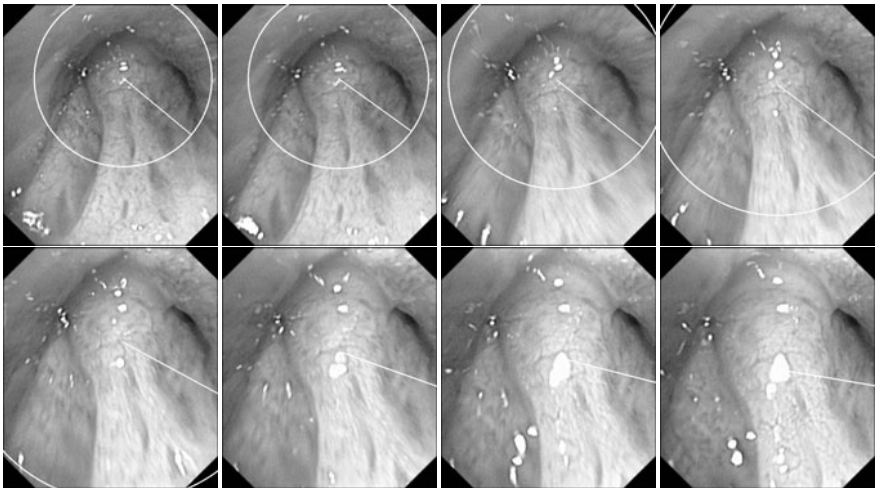
Fig. 5 Image sequence with over twofold magnification of the area of interest

Tests of the method were carried out for 31 sequences (99 frames each) of a bronchial tumour. There were some difficulties in assessing the effectiveness of the method, resulting from the lack of objective criteria. In principle, there are two scenarios in an image sequence: the following frame is either correct and the area of interest is well visible, or it is incorrect (has significant artefacts, or the area of interest is missing). These two possibilities incur potential errors: inability to track and mark the area of interest that was initially selected, or selecting and marking an incorrect area. There are no criteria allowing unequivocal classification of the frames into correct and incorrect. For instance, artefacts in frames may be only minor, or the area of interest may be only partially invisible, which causes that the assessment of the frame quality is bound to be based on a subjective impression of the observer. Taking these into account, 1439 frames among the analysed sequences (out of 3069) were classified as frames that had the area of interest initially selected. In the remaining frames the area was either completely missing, significantly distorted by artefacts, or large parts of it were invisible.

Although in the presented method there were some difficulties in sequences where artefacts (disturbance) occurred, the effectiveness was 70%. The method can therefore be regarded as helpful to support re-location of the area of doctor's interest. Application of the method to sequences in which images were undistorted increases its effectiveness to 80%.

5   Verification of Real-Time Calculation Capability of the Method in Longer Image Sequences (Films)

To test the effectiveness of the method in longer image sequences, 4 films generated during transbronchial biopsy were selected. The films differed in terms of length and average resolution of frames (Table 1).

Table 1   Parameters of films used for testing the method

	Film "122"	Film "137"	Film "329"	Film "455"
Average resolution	470x531	402x457	470x531	363x381
Number of frames	8470	30872	26537	4608

The term average resolution of frames is used here because the analysis was done not for the whole frame (with the standard 720x576 resolution) but its fragment where the image contains a useful information. Depending on the equipment used for examination and the level of disturbance affecting the image generated with the bronchoscope, the suitable fragment may cover a different area of the frame. The average resolution of frames is the resolution of suitable fragments of the majority of frames within the film. Although films "122" and "329" have the same average resolution, there are fewer disturbed frames with lower resolution in the first one.

As a result, this film requires longer average time to calculate one frame.
Tests were carried out using a computer with 2.13 GHz Intel Core 2 Duo processor
and 64-bit Linux system. 4 implementations were tested:

- "classic" - without acceleration
- „siftfast" - with SSE instructions set
- "opencv" - with the Gaussian blur in OpenCV library
- "siftfast + opencv" - with both SSE instructions set and OpenCV library

During the tests algorithm calculation times were measured after excluding differ-
ent numbers of octaves (levels of the DoG pyramid). Times calculated for classic
implementation with no acceleration were significantly different from the assumed
0.04 s, which is a standard for 25/s images (Table 2). In practice, it was expected
that the required time would not be longer than 0.03 s because of 0.01 s overheads of
the system using the presented algorithm (e.g. additional pre- and post-processing
operations for each frame).

Table 2 Calculation times for the SIFT algorithm where the first three octaves were excluded

	Film "122"	Film "137"	Film "329"	Film "455"
"classic"	0.0524	0.0364	0.0512	0.0275
"siftfast"	0.0279	0.0204	0.0266	0.0155
"opencv"	0.0213	0.0145	0.0206	0.0110
"siftfast+opencv"	0.0207	0.0140	0.0198	0.0108

Times gained thanks to the application of mechanism of acceleration calculations
are presented in Table 2 for the algorithm operating on the octaves 4 and higher. The
first three octaves (counting from the base of the pyramid) were excluded according
to the procedure described in Sect. 3.

Table 3 Calculation times for the SIFT algorithm where the first two octaves were excluded

	Film "122"	Film "137"	Film "329"	Film "455"
"classic"	0.0678	0.0468	0.0647	0.0354
"siftfast"	0.0392	0.0267	0.0360	0.0218
"opencv"	0.0346	0.0226	0.0311	0.0177
"siftfast+opencv"	0.0312	0.0202	0.0278	0.0159

As the time for accelerated implementations with three octaves excluded was
significantly shorter than the required 0.03 s, the tests were repeated with only two
first octaves excluded (Table 3) and finally, only one initial octave (Table 4).

Table 4 Calculation times for the SIFT algorithm where the first octave was excluded

	Film "122"	Film "137"	Film "329"	Film "455"
"classic"	0.1176	0.0813	0.1081	0.0585
"siftfast"	0.0707	0.0481	0.0623	0.0347
"opencv"	0.0727	0.0481	0.0633	0.0341
"siftfast+opencv"	0.0591	0.0383	0.0507	0.0268

For comparison, Table 5 presents calculation times for the complete SIFT algorithm. Results of all tests show that none of the methods is capable of real-time calculations of the complete algorithm.

Table 5 Calculation times for the complete SIFT algorithm

	Film "122"	Film "137"	Film "329"	Film "455"
"classic"	0.3055	0.0813	0.2784	0.1442
"siftfast"	0.1788	0.1292	0.1523	0.0803
"opencv"	0.2074	0.1514	0.1825	0.0941
"siftfast+opencv"	0.1517	0.1092	0.1290	0.0641

The tests proved that acceleration of calculations is, to a large extent, dependent on the speed of the Gaussian blur calculation. Application of the optimized function for this calculation ("opencv") in almost all cases yielded better results than application of the SSE extension. The only exception was when calculations were done with only the first octave excluded but in this case calculations for larger images are not performed in real-time.

Combining the two methods ("siftfast+opencv") for calculations on higher levels of the pyramid does not result in significantly stronger accelerations than using "opencv" itself. The differences become obvious only in the lower levels, when the number of the analysed characteristic points increases and the influence of the Gauss filter on calculation time decreases.

To sum up, the presented algorithm (operating on the octave four and higher) in the classic implementation can be applied only for films with the average resolution of 360x380. For higher resolutions some acceleration mechanism is required. Such mechanisms allow not only to calculate the algorithm for larger images but also to generate results for the lower level of the pyramid (the third octave). In this case it is recommended to SSE extensions with the effective implementation of the Gauss filter. With this combination ("siftfast+opencv"), also the second octave can be calculated, although only for lower resolutions (approximately 360x380).

6 Conclusions

Results of the experiments allow for the following conclusions:

- the SIFT method enables tracking of the initially chosen and marked areas and is insensitive to significant changes in their size, brightness, location or orientation
- the SIFT method allow us to exclude the frames with artefacts and tracking of the area can be automatically continued after the disturbance ends.

The results demonstrate that it is possible to use the modified SIFT algorithm in real-time analysis of bronchoscopic images. However, it requires limiting the calculations to higher/upper levels of the SIFT pyramid.

Problems that require further development of the method include:

- lack of characteristic point whose surrounding covers the entire area of interest
- occurrence of frame sequences with artefacts that cause disturbances in the continuity of tracking the chosen area.

Both problems could be solved by the application of a few (instead of one) points covering the entire area of interest. Since such a change would increase calculation time, it is necessary to focus on further development of the SIFT algorithm. Achieving higher accelerations seems to be possible only by introducing a multiprocessor (multicore) calculations, or hardware implementation, which should become the subject for further studies.

References

1. Bard, et al.: Optical spectroscopy for the classification of malignant lesions of the bronchial tree. Chest 129, 995–1001 (2006)
2. Duplaga, M., et al.: The comparison of effectiveness of virtual bronchoscopy and non-real time endobronchial ultrasonography for the support of transbronchial needle aspiration in patients with suspicion of the lung cancer. Przegl Lek. Wyd. Spec.: Inż. Med. 64, 36–41 (2007)
3. Gordon, I., Lowe, D.G.: Scene modelling, recognition and tracking with invariant image features. In: International Symposium on Mixed and Augmented Reality (ISMAR), Arlington, VA, pp. 110–119 (2004)
4. Haponik, E.F., Shure, D.: Underutilization of Transbronchial Needle Aspiration. Chest 112, 251–253 (1997)
5. Huang, Z., et al.: Near-infrared Raman spectroscopy for optical diagnosis of lung cancer. Intl. J. Cancer 107, 1047–1052 (2003)
6. Ledwich, L., Williams, S.: Reduced SIFT features for image retrieval and indoor localisation. In: Proceedings of Australasian Conference on Robotics and Automation, ACRA (2004)
7. Lowe, D.G.: Distinctive image features from scale-invariant keypoints. International Journal of Computer Vision 60(2), 91–110 (2004)

8. Mikolajczyk, K., Schmid, C.: A performance evaluation of local descriptors. IEEE Transactions on Pattern Analysis and Machine Intelligence 10(27), 1615–1630 (2005)

9. Shi, F., Gale, A.G., Purdy, K.: Sift Approach Matching Constraints for Real-Time Attention Responsive System. In: Proceedings of the 5th Asia Pacific International Symposium on Information Technology, Hangzhou, China, pp. 31–34 (2006)

10. Se, S., Lowe, D.G., Little, J.: Vision-based mobile robot localization and mapping using scale-invariant features. In: Proceedings of the IEEE International Conference on Robotics and Automation (ICRA), vol. 2, pp. 2051–2058 (2001)

11. Shibuya, K., et al.: Fluorescence bronchoscopy in the detection of preinvasive bronchial lesions in patients with sputum cytology suspicious or positive for malignancy. Lung Cancer 32, 19–25 (2001)

12. Tsuboi, M., et al.: Optical coherence tomography in the diagnosis of bronchial lesions. Lung Cancer 49, 387–394 (2005)

13. Vincent, B.D., Fraig, M., Silvestri, G.A.: A pilot study of narrow-band imaging compared to white light bronchoscopy for evaluation of normal airways and premalignant and malignant airways diseases. Chest 131, 1794–1799 (2007)

14. Wang, K.P., Terry, P.B., Marsh, B.R.: Bronchoscopic needle aspiration biopsy of paratracheal tumors. Am. Rev. Respir. Dis. 118, 17–21 (1978)

15. Wang, K.P., et al.: Transbronchial needle aspiration for diagnosis of lung cancer. Chest 80, 48–50 (1981)

16. Wang, K.P.: Continued Efforts to Improve the Sensitivity of Transbronchial Needle Aspiration. Chest 114, 4–5 (1998)

17. Fast SIFT Image Features Library (libsiftfast-1.2) (2009),
    `http://sourceforge.net/projects/libsift`

18. Open Computer Vision Library (OpenCV-2.0.0) (2009),
    `http://sourceforge.net/projects/opencvlibrary`

Analysis of Images of Bronchial Tree Ramifications for Summarization of Bronchoscopic Videos

Zbigniew Mikrut and Mariusz Duplaga

1 Introduction

Intensive endoscopic examinations result in an increasing number of records in video format. Storing whole videos is ineffective when considering mass storage devices usage. Additionally, reviewing these videos is a very time-consuming task.

In the BRONCHOVID [1] project some methods of elimination of less informative video parts were proposed. The final effect was a very shortened registration which was called a *summarization*. A summarized video could be supplemented with additional information (data), important from the diagnostic or anatomic point of view. The first group consists of markings of biopsy sites and frames on the basis of which lesions were diagnosed. In the BRONCHOVID project, similarly as in other congruent projects, the aim is to detect pathologies automatically. Information obtained in this way should be verified by a doctor.

Primarily the anatomic information is the actual location of the bronchoscope tip in the bronchial tree. At present, the localization corresponds to marking frames, on which characteristic points (ramifications of the bronchial tree) are visible.

Automatic detection of bronchial tree ramifications in digital images is the main aim of the presented work. This is accomplished by multi-thresholding of a gray-scale image. Additionally, an evaluation of the particular orifice's shape is conducted in two aspects:

1. range of thresholds, in which the object's shape remains constant, is determined,
2. in this range shape descriptors are computed. In the future this set of descriptors will be used to detect selected pathologies - e.g. bronchial stenosis.

Zbigniew Mikrut
AGH University of Science and Technology, Mickiewicza Ave 30, 30-059 Krakow, Poland
e-mail: zibi@agh.edu.pl

Mariusz Duplaga
Jagiellonian University, Medical College, Grzegorzecka Str. 20, 31-531 Krakow, Poland
e-mail: mmduplag@cyfronet.pl

2 Algorithm

The input to an algorithm is a gray-scale image, obtained from one RGB frame of a bronchoscopic video. After applying a binary mask (to eliminate black corners - see examples in 4) and a Gaussian filter an image is processed in the following way:

1. several initial parameters are defined, e.g. the threshold range, threshold step, the stability conditions for the shape descriptors,
2. the image is binarized using succeeding thresholds, which are taken step-by-step from the defined range,
3. the binary image is labelled,
4. small objects and those touching a frame border are removed,
5. holes in the detected objects are filled,
6. shape descriptors are computed and stored.

During the next stage shape descriptors, which have been computed for all the detected objects in every multi-thresholding step, are analyzed. The intervals of semi-constant descriptor values are computed for each object (see 4). Then the threshold corresponding to the middle point of the computed interval is taken into account. This threshold determines the final shape of the particular object. Such objects are recognized as bronchial orifices - the characteristic points of tracheobronchial tree, which had to be detected.

3 Shape Descriptors

Basing on almost 20 years of our experiences in Biocybernetic Laboratory [3, 5] the Haralick [2], $W8$ and Blair-Bliss [5] shape descriptors have been chosen:

$$Har = \frac{\mu_R}{\sigma_R}, \quad W8 = \frac{2\sqrt{\pi S}}{L}, \quad BB = \frac{S}{\sqrt{2\pi \sum_S (r)^2}}, \tag{1}$$

where μ_R and σ_R are the mean and the standard deviation of distances R from the center of the object to any part of its perimeter, S and L are the object area and the perimeter respectively and r is the distance between the center of the object and any object's pixel. Furthermore $m7$ - a geometric moment [5] (in [4] is referred to as I_8) was computed:

$$m7 = \frac{\left(m_{20} - \frac{m_{10}^2}{m_{00}}\right)\left(m_{02} - \frac{m_{01}^2}{m_{00}}\right) - \left(m_{11} - \frac{m_{10}m_{01}}{m_{00}}\right)^2}{m_{00}^4}, \quad m_{pq} = \sum i^p j^q, \tag{2}$$

where i, j are the coordinates of binary object pixels.

4 Examples

In this section two exemplary results of the above mentioned image processing algorithm are presented. In Fig.1 the multi-level thresholding process can be observed. Numbers below each binary object are the consecutive threshold levels. They should be compared with numbers describing the x axis in Fig. 2.

Shape descriptors computed while multi-level thresholding are presented in Fig. 2. Double arrow denotes the interval in which all the descriptor values are approximately constant. The vertical dashed line corresponds to the threshold which defines the final shape of the detected object (see also object 69.png in Fig.1).

The second example concerns an image containing three objects. In Fig.3 (on the left) the selected labeled images correspond with the thresholding levels indicated by arrows in plot (on the right). These levels are different for the three detected objects. In this case the $m7$ geometric moment is a base for final threshold computation.
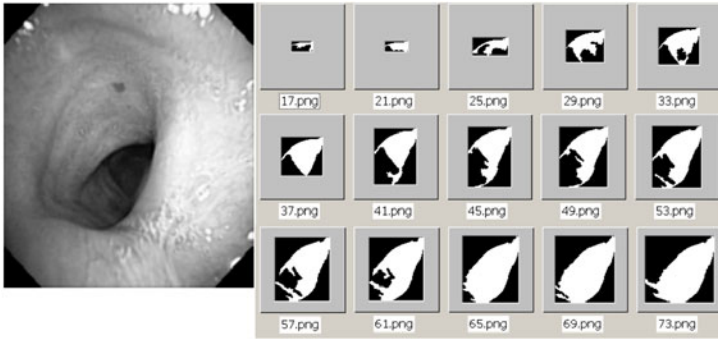
Fig. 1 Multi-thresholding binarization of bronchoscopic video frame
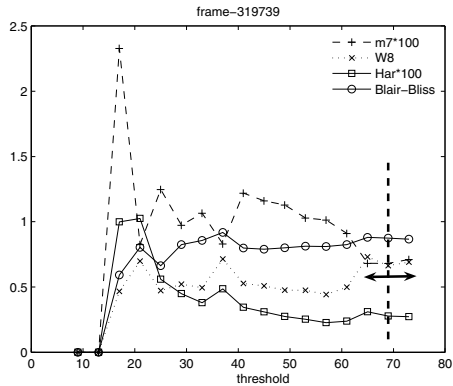
Fig. 2 Shape descriptors corresponding to object silhouettes presented in Fig.1
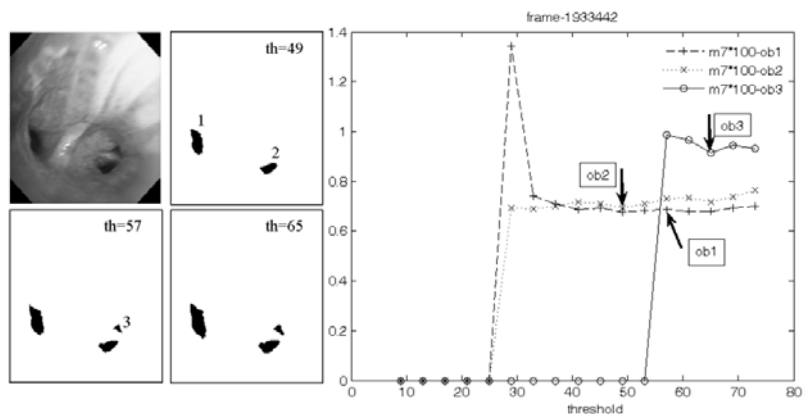
Fig. 3 Left: three stages of frame thresholding, *th* denotes threshold level. Right: geometric moment *m*7 computed for three objects - bronchial orifices.

5 Concluding Remarks

The image processing algorithm described in Sec. 2 meets the authors' expectations. Multilevel thresholding in conjunction with computing shape descriptors' values is an effective way to obtain the object's silhouettes. This makes it possible to detect the "stable" shapes of the objects representing bronchial orifices.

From the diagnostic point of view the set of shape descriptors can be used for detecting abnormal forms of bronchial orifices, e.g. bronchial stenosis (narrowing). This will be done in the nearest future. Another goal to be reached is the acquisition and analysis of image sections between every two orifices. The authors believe that widening and distortion of the carina could be detected in this way.

References

1. Duplaga, M., Bułat, J., Leszczuk, M., Romaniak, P., Socha, M., Turcza, P.: The BRON-CHOVID - computer system supporting bronchoscopy laboratory. In: Demazeau, Y., et al. (eds.) Trends in PAAMS. AISC, vol. 69. Springer, Heidelberg (2010)
2. Haralick, R.M.: A measure of circularity of digital figures. IEEE Trans. Systems, Man and Cybernetics 4, 394–396 (1974)
3. Pilch, J.: Analysis of the selected shape descriptors. PhD Thesis, AGH University of Science and Technology, Krakow (1991) (in Polish)
4. Sluzek, A.: Identification and inspection of 2-D objects using new moment-based shape descriptors. Pattern Recognition Letters 16, 687–697 (1995)
5. Tadeusiewicz, R.: Vision systems for industrial robots. WNT, Warsaw (1992) (in Polish)

Prototype Software for Video Summary of Bronchoscopy Procedures with the Use of Mechanisms Designed to Identify, Index and Search

Mikołaj Leszczuk and Michał Grega

Abstract. Individual bronchoscopy test event takes about 20 minutes. Most of this time is the video recording process, placing and removing bronchoscope endings in the patient's airways. A sizable part of the record is unreadable because of obstruction by secretion of physiological image. The analysis of such recordings for teaching purposes or diagnostic tests is time-consuming — the doctor or student is forced to view a large number recordings of little value to find the fragments of interest — those showing lesions. In research, we develop a prototype system to create shortcuts (called summaries or abstracts) of bronchoscopy research recordings. Such a system, based on the model described in the preceding paper paragraphs uses image analysis methods to delete the recording fragments of the bronchoscopy test which have no diagnostic value for teaching and create a few minute-long, valuable video sequences.

1 Introduction

Individual bronchoscopy test event takes about 20 minutes. Most of this time is the video recording process, placing and removing bronchoscope endings in the patient's airways. A sizable part of the record is unreadable because of obstruction by secretion of physiological image. The analysis of such recordings for teaching purposes or diagnostic tests is time-consuming — the doctor or student is forced to view a large number of recordings of little value to find the fragments of interest — those showing lesions.

Viewing the summary video sequences is an integral part of the process of reviewing medical digital video library. It should pass the case because of the fact that manual review of the video sequences such as half an hour long (in search for

Mikołaj Leszczuk · Michał Grega
Department of Telecommunications, AGH University of Science and Technology,
al. Mickiewicza 30, 30-059 Krakow, Poland
e-mail: `leszczuk@agh.edu.pl, grega@kt.agh.edu.pl`

interesting fragments) takes a long time. Only by viewing the summary, one can read the contents of the video sequence without having to send it across the network and watch all of it. Summaries should present an easy and convenient overview of medical digital video library. The merit of the problem is to be able to select key shots to represent the whole video sequence. The mechanism to facilitate this process enables the algorithm in an automatic way to analyse the sequence of shots that occur in the video and choose the most important ones.

As mentioned above, the process consists of summarizing a number of aspects related to the analysis of the content of the video sequence, allowing to allocate it to the shots and scenes [1] and other parts of a coherent theme [2], or to present it in a hierarchical form [3, 4, 5, 6]. It happens that there are hierarchical relationships between both parts of one sequence of the video, as well as between different video sequences [7].

Unfortunately, medical digital video libraries are still seldom technically advanced enough to include summary subsystems. The authors found in the literature a small number of studies of summarizing video sequences which contain medical content [8, 9]. An interesting, related approach has been presented in [10]; however, the application area of the paper is not bronchoscopy but wireless capsule video endoscopy. In [11], the authors present a method of clustering large image databases. The paper considers general multimedia content thus it has no strict relation to the specific, bronchoscopy images. Similarly, presented in [12], the approach of involving end-users into content-based image retrieval, useful in summarizing generic digital video libraries, does not consider modalities of medical images. Consequently, a method tailored strictly to bronchoscopic video content, had to be created, based only partly on related approaches, including the above-mentioned ones.

The authors assumed that the summary must be considerably shorter than the whole video sequence. In the first estimation, based on the experience of editors, it could be assumed that the volume of the summary should be reduced about 60 times when compared to the original video, which is: one second of the summary should illustrate one minute of the original video sequence. At the same time, it has not been adopted to create summaries of volume shorter than 30 seconds.

In research, we develop a prototype system for creating shortcuts (called summary or abstracts) of bronchoscopy research recordings. Such a system, based on the model described in the preceding paper paragraphs uses image analysis methods to delete the recording fragments of the bronchoscopy test which have no diagnostic value for teaching and create a few minute-long, valuable video sequences [13, 14, 15]. The prototype summary system is a part of the BRONCHOVID project [16].

The remaining part of the paper is structured as follows: Section 2 presents the algorithm developed to summarize the bronchoscopic videos. Section 3 presents the implementation of the algorithms. Section 4 concludes the paper and gives an insight into further development of the presented research project.

2   Algorithm

The algorithm for the selection of key shots of bronchoscopic video sequences, has been based on several factors. These factors could be divided into inclusive and exclusive factors. Shots consisting of frames tagged around inclusive factors tend to be included into the summarised video while the algorithm tries to exclude shots consisting of frames tagged around exclusive factors.

The basic exclusive factor are "non-informative" (artifact) frames. The following factors are considered as the inclusive ones:

- markers from medical treatment,
- frames annotated by medical doctors as references to pathologies,
- trachea-bronchial tree branching (ramifications), and
- automatically discovered pathologies (e.g. mass of the tumour, bleeding, etc.).

The following subsections present methods in which the above-mentioned inclusive/exclusive factors can be acquired.

2.1   "Non-informative" Frames

This section presents an approach for detecting "non-informative" frames. The presented method has been based on DCT (Discrete Cosine Transform).

The video recordings of endoscopic procedures performed within respiratory tract include both frames of adequate and inadequate quality for the assessment by an endoscopist. The frames of inadequate quality were called by some authors blurred or "non-informative" (see Figure 1). The fraction of blurred frames within video recording of bronchofiberoscopy may be considerable and it varies from case to case.

The method of detection of the "non-informative" frames is based on the fact, that images which do not contain numerous edges are easier to compress using algorithms based on Discrete Cosine Transform (DCT) such as the JPEG algorithm. Such images have much narrower spectra in the frequency domain than images which contain numerous edges. This feature of the DCT allows to use it as a simple yet effective edge detection algorithm. Unlike more sophisticated edge detection algorithms using DCT we can only obtain information whether there are any edges in the image, but we are unable to locate those edges. This however is enough for the task of the blurred frame detection. Figure 2(a) depicts two examples of spectra of "non-informative" and "informative" frames. It can be observed that in the "non-informative" frame, the energy is condensed around the harmonics of the lower order whereas in the "informative" frame the energy is more evenly distributed in the spectrum.

The algorithm of the DCT-based blurring detection is presented in Figure 3. In the first step a frame of the bronchoscopic recording is converted into the grey-scale by discarding the hue and saturation while retaining the luminance. In the second step the DCT coefficients of the image are computed. In the third step the values of the magnitude which are lower than 20 are set to 0. Value of 20 was selected

(a) The "non-informative" frame (b) The "informative" frame

Fig. 1 Examples of the "non-informative" and "informative" frames

(a) Frequency spectrum of the "non- (b) Frequency spectrum of the "infor-
informative" frame mative" frame
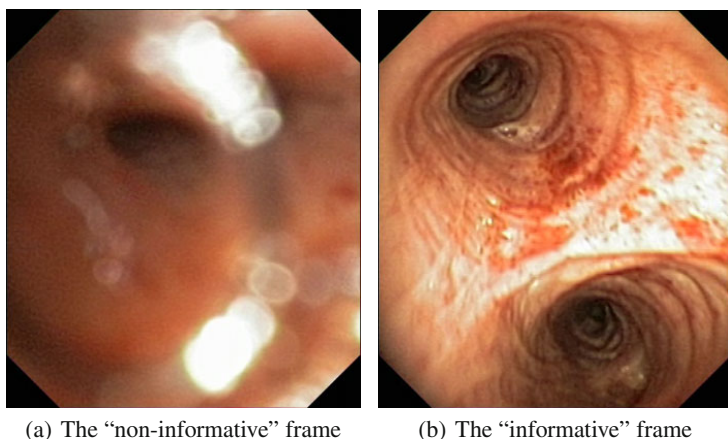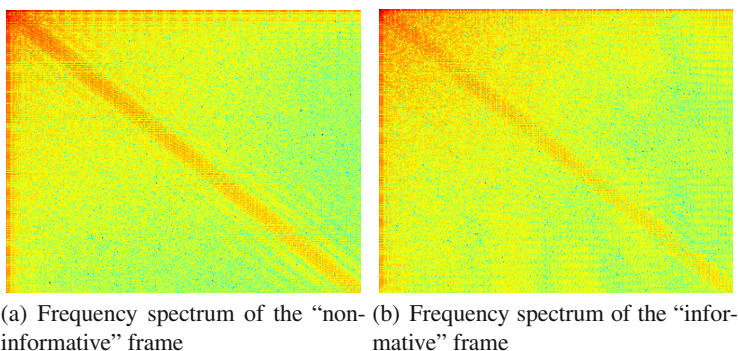
Fig. 2 Comparison of the frequency spectra of the "non-informative" and "informative"
frames

experimentally as giving the best results in terms of precision and recall (however,
the algorithm can be easily tuned in terms of sensibility). In the final step non-zero
elements of the DCT matrix are calculated and used for discrimination.

The evaluation has been performed on a set of 1538 frames, manually annotated
as "non-informative" (669 images) and "informative" (869 images) by the expe-
rienced bronchoscopist. The set acted as a ground-truth. Then, the images were
evenly (but randomly) split to: the training set and the testing set. The algorithms
were trained over the training set solely, whilst the presented results were obtained
with the testing set only.

Four metrics have been used in order to analyse the performance of the algo-
rithm: F-measure, sensitivity, specificity and accuracy. This set of metrics allows for

Fig. 3 The classification algorithm based on the Discrete Cosine Transform for "informative" and "non-informative" frames
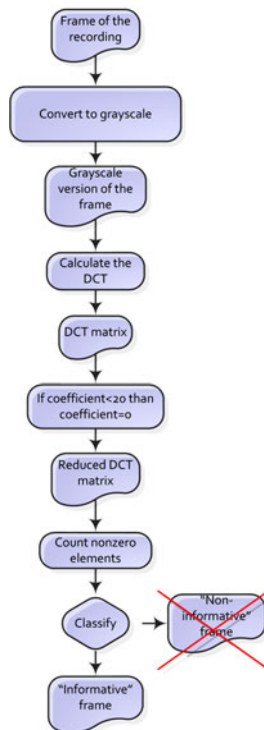
comprehensive assessment of the performance. It is a standard set of metrics used to assess the performance of the binary classification. The results of the performance assessment are presented in Table 1.

Table 1 The evaluation of the performance of the DCT blurring detection algorithm

Metric	Definition	Value
F-measure	$F\text{-}measure = \dfrac{\frac{tp}{tp+fp} \cdot \frac{tp}{tp+fn}}{\frac{tp}{tp+fp} + \frac{tp}{tp+fn}}$	0.92
Sensitivity	$Sensitivity = \dfrac{tp}{tp+fn}$	0.93
Specificity	$Specificity = \dfrac{tn}{tn+fp}$	0.93
Accuracy	$Accuracy = \dfrac{tp+tn}{tp+fp+fn+fp}$	0.93

Where: tp — true positives, tn — true negatives, fp — false positives and fn — false negatives.

The algorithm has been described in detail in [17]. A related approach has been presented in [18].

2.2   Markers from Medical Treatment

Computer algorithms will probably reach an accuracy of human perception without haste. Therefore, it has been assumed that the algorithm will consider some manually marked shots as well. Consequently, the summary system considers them as well, treating human contribution as the most important inclusive factor.

It was assumed that (most likely) manual markings will be created during the medical procedure by means of some easy and intuitive mechanism (e.g. hitting a space-bar). The manual markings are accepted without changes and further discussion about the way they appear as well as about their accuracy, is out of scope of this paper.

2.3   Frames Annotated by Medical Doctors as References of Pathologies

Another human-based inclusive factor is related to the frames previously described by an experienced bronchoscopist. While the markers from medical treatment are generated online (during the medical procedure), the frame description process is an optional, offline post-processing operation. The quality of such descriptions is considered to be very high. Furthermore, it is possible to distinguish between several descriptions (and, e.g., attach different inclusion weights to them).

The possible range of pathologies is a wide set, consisting of a total number of more than 100 pathologies. Examples include, e.g. mass of the tumour, bleeding, etc.

2.4   Trachea-Bronchial Tree Branching (Ramifications)

The trachea-bronchial tree (see Figure 4) is the structure from the trachea, bronchi, and bronchioles which forms the airway which supplies the air to the lungs. The structure looks like a tree because the trachea splits into the right and left main-stem bronchi, which branch into progressively smaller structures [19].

Based on consultations with experienced bronchoscopist, it was assumed that video frames presenting traverses of trachea-bronchial tree branching (ramifications) are of special interest. Consequently, the summary algorithm includes automatically detected branching (ramifications) traversals as inclusive factors.

The automatic algorithm is based on an assumption that relatively large, dark (non-illuminated) trachea endings could be easily detected and counted. More than one visible trachea ending indicate a traverse through branching (ramifications). The algorithm first finds all the dark objects, then filters the results to pick out the objects of certain size. The basic concepts of image opening/closing (with various sizes of morphological structuring elements), thresholding (by means of image complementing), labelling, and measuring properties of image regions demonstrated were successfully utilised. The algorithm has been described in detail in [20].

Fig. 4 The trachea-bronchial tree (source: public domain image, copyright expired)
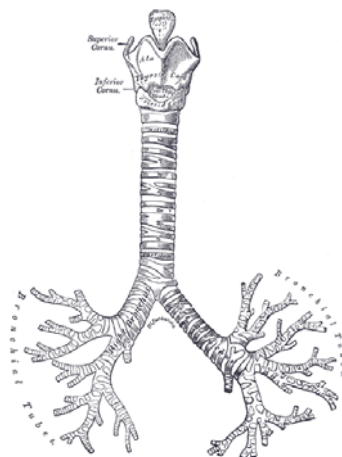
2.5 Automatically Discovered Pathologies

Not only manually entered but also automatically discovered pathologies can be included as inclusive factors for summarization. The summarization system utilises several techniques, including DWT (Discrete Wavelet Transform), MPEG-7 standard [21] as well as colour analysis. Obviously, both the number of automatically discovered pathologies and the discovery accuracy are limited. The markings based on automatically discovered pathologies are accepted "as is" and further discussion about the way they appear as well as about their accuracy, is out-of-scope of this paper, as the algorithms have been described in detail in [22, 23, 24].

3 Implementation

At the moment of the paper submission, the summary system has been partially implemented. The system consist of two main parts: implementation of methods for acquiring inclusive/exclusive factors and implementation of a Web-based GUI (Graphical User Interface). Both parts have been described in the following subsections.

3.1 Implementation of Methods for Acquiring Inclusive/Exclusive Factors

The basic exclusive factor is detection of the "non-informative" frames. As the speed of the algorithm is of critical importance the algorithm for detection of the "non-informative" frames was implemented in the C++ programming language. The implementation requirement was that the algorithm is supposed to be calculated in less than 40 ms, so that it would be possible to analyse the frames on-the-fly of a 25 FPS video.

The image is loaded into the memory and stored within *IplImg* structure. Both the loading function and the structure used in the implementation are a part of the Open-CV library [25], which is well-known among the image processing community.

The Discrete Cosine Transform (DCT) is computed with use of the FFTW3 library [26]. This library allows for computation of the Fast Fourier Transform (FFT) and related transforms in one or multiple dimensions. The library is highly optimized and, according to the authors its transform implementation is faster than other competitive implementations. In the implementation process it occurred, that even this implementation is too slow, as the average computation time for the algorithm was approx. 50 ms, which is longer than the requirement. Our solution was to crop the frame to the shape of the square and a pixel size of the edge of power of 2. The experiments have shown, that this modification does not have influence on the specific character and sensitivity of the algorithm. This modification allowed us to significantly reduce the computation time of the DCT.

After the FFT is computed the number of the above-threshold coefficients is computed and the classification decision is made. The average decision time for a bronchoscopic frame in our implementation is approx. 10 ms, excluding the time needed to load the frame into the memory. This has satisfied our design requirement.

The summary system acquires markers from medical treatment and frames annotated by medical doctors as references to pathologies, manually entered into the central BRONCHOVID database [16]. Similarly, the summary system acquires information about trachea-bronchial tree branching (ramifications) and automatically discovered pathologies from the database as well. This time, however, the information is based on computer-vision algorithms.

3.2 Implementation of Graphical User Interface

The algorithm of the summary GUI has been depicted in Figure 5. First, the user can choose the desired video sequence. Then, partial decompression and analysis takes place. Next, crucial to the whole summary process, is to choose and set the parameters of summary. The process considers various options in (above-mentioned) inclusive/exclusive factors in the summary. After that, it is possible to review the planned summary statistics, as well as to manually fine-tune the automatically generated shots (Figure 6(a)). Unsatisfactory results allow the user to come back to setting the parameters of summary, while satisfactory ones bring him or her to the decision on choosing how to write/present the result. The straight way is to decide to download the summary immediately and to proceed to the download dialogue. However, the user might want to first preview the summarization. It is possible with use of the Flash Player (Figure 6(b)). On completing watching the preview, the user can decide whether to accept it and proceed to the download dialogue, or, alternatively, to still come back to setting the parameters of summary.
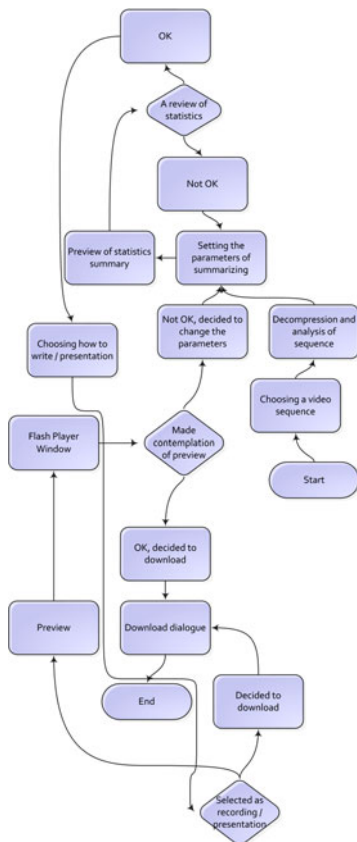
Fig. 5 The algorithm of the summary GUI
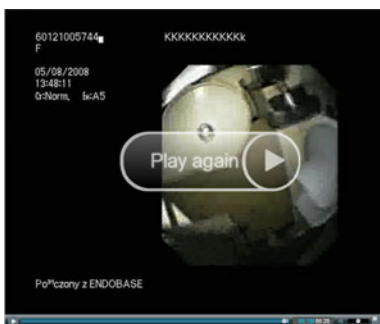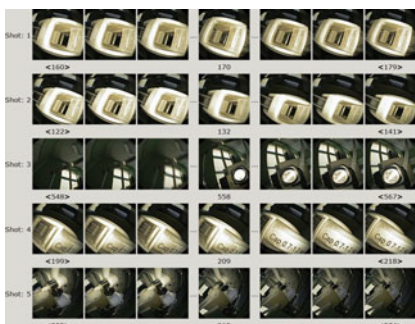
(a) Manual fine-tuning of automatically generated shots

(b) Web-based play-out of a generated summarized video

Fig. 6 Screen-shots from the GUI (Graphical User Interface) of summary (for presentation in the paper, actual frames from bronchoscopy procedures have been substituted by frames recorded outside patient's body)

4 Conclusions and Further Work

In the study, the scientific basis was developed for the construction of prototype software to synthesise the records of bronchoscopy procedure (leaving the most representative fragments) with the use of mechanisms designed to identify, index and search. Currently, the advanced implementation process takes place.

The final result of the proposed project will be a prototype device developed in the form of software. The exact specification of hardware requirements will be given, compliance with which is a prerequisite for its proper operation. In particular, the planned final result will be developed of a prototype software designed to synthesise records of bronchoscopy procedure. Parallel to the analysis of video sequences indexing and shortening will be made. All this information will be stored in a database along with the video recording. This means that during each survey database disease cases will be enriched with more data.

References

1. Kender, J.R., Lock Yeo, B.: Video scene segmentation via continuous video coherence. In: Proc. IEEE Int. Conf. on Computer Vision and Pattern Recognition, pp. 367–373 (1998)
2. Adjeroh, D.A., Lee, M.C.: Scene-adaptive transform domain video partitioning. IEEE Transactions on Multimedia 6, 58–69 (2004)
3. Aghbari, Z.A., Kaneko, K., Makinouchi, A.: A Content-trajectory approach for searching video databases. IEEE Transactions on Multimedia 5, 516–531 (2003)
4. Fan, J., Elmagarmid, A.K., Member, S., Zhu, X., Aref, W.G., Wu, L.: Classview: Hierarchical video shot classification, indexing, and accessing. IEEE Trans. on Multimedia 6, 70–86 (2004)
5. Skarbek, W., Galiński, G., Wnukowicz, K.: Tree Based Multimedia Indexing — a Survey. In: Proc. Krajowa Konferencja Radiokomunikacji, Radiofonii i Telewizji KKRRiT 2004. Konferencja Radiokomunikacji, Radiofonii i Telewizji, Warszawa, Krajowa, pp. 77–85 (2004)
6. Yuen Chen, J., Taskiran, C., Taskran, C., Albiol, A., Delp, E., Bouman, C.: Vibe: A compressed video database structured for active browsing and search (2001)
7. Lombardo, A., Morabito, G., Schembra, G.: Modeling intramedia and intermedia relationships in multimedia network analysis through multiple timescale statistics. IEEE Transactions on Multimedia 6, 142–157 (2004)
8. Walid, X.Z., Walid, G., et al.: Medical video mining for efficient database indexing, management and access (2003)
9. Zhu, X., Fan, J., Aref, W.G., Elmagarmid, A.K.: Classminer: Mining medical video content structure and events towards efficient access and scalable skimming. In: DMKD (2002)

10. Vilarino, F., Spyridonos, P., Pujol, O., Vitria, J., Radeva, P.: Automatic detection of intestinal juices in wireless capsule video endoscopy. In: ICPR 2006: Proceedings of the 18th International Conference on Pattern Recognition, Washington, DC, USA, pp. 719–722. IEEE Computer Society, Los Alamitos (2006)
11. Choupo, A.K., Berti-Équille, L., Morin, A.: Optimizing progressive query-by-example over pre-clustered large image databases. In: CVDB 2005: Proceedings of the 2nd international workshop on Computer vision meets databases, pp. 13–20. ACM, New York (2005)
12. Arevalillo-Herráez, M., Ferri, F.J., Domingo, J.: A naive relevance feedback model for content-based image retrieval using multiple similarity measures. Pattern Recogn. 43, 619–629 (2010)
13. Duplaga, M., Juszkiewicz, K., Leszczuk, M., Marek, M., Papir, Z.: Design of Medical Digital Video Library. In: Proc. Fourth International Workshop on Content-Based Multimedia Indexing, CBMI 2005, Latvia, Riga, Content Based Multimedia Indexing (2005)
14. Lee, H.Y., Lee, H.K., Ha, Y.H.: Spatial color descriptor for image retrieval and video segmentation. IEEE Transactions on Multimedia 5, 358–367 (2003)
15. Leszczuk, M.: Analiza możliwości budowy internetowych aplikacji dostępu do cyfrowych bibliotek wideo. PhD Thesis, AGH University of Science and Technology, Faculty of Electrical Engineering, Automatics, Computer Science and Electronics, al. Mickiewicza 30, PL-30059 Kraków, Poland (2005)
16. Duplaga, M., Bułat, J., Leszczuk, M., Socha, M., Turcza, P., Romaniak, P.: Overview of the BRONCHOVID computer system supporting bronchoscopy laboratory — medical and technical perspective. In: BRONCHOVID: The Computer System for Bronchoscopy Laboratory Integrating the CT-Based Bronchoscopy and Transbronchial Needle-Aspiration Biopsy Planning, Virtual Bronchoscopy, Management of the Bronchoscopic Procedures Recordings, Automatic Image-Based Data Retrieval, Artifact and Pathology Detection and Interactive 2D & 3D Visualization. Springer, Heidelberg (2010)
17. Grega, M., Leszczuk, M., Frączek, R., Duplaga, M.: Algorithms for automatic recognition of non-informative frames in video recordings of bronchoscopic procedures. In: BRONCHOVID: The Computer System for Bronchoscopy Laboratory Integrating the CT-Based Bronchoscopy and Transbronchial Needle-Aspiration Biopsy Planning, Virtual Bronchoscopy, Management of the Bronchoscopic Procedures Recordings, Automatic Image-Based Data Retrieval, Artifact and Pathology Detection and Interactive 2D & 3D Visualization. Springer, Heidelberg (2010)
18. Jóźwiak, R., Przelaskowski, A., Duplaga, M.: Diagnostically Useful Video Content Extraction for Integrated Computer-Aided Bronchoscopy Examination System. In: Computer Recognition Systems 3. Advances in Soft Computing, vol. 57. Springer, Heidelberg (2009)
19. Johnson, S.B.: Tracheobronchial injury Seminars in Thoracic and Cardiovascular Surgery, vol. 20, pp. 52–57 (2008)
20. Mikrut, Z., Duplaga, M.: Analysis of images of bronchial tree ramifications for summarization of brochoscopic videos. In: BRONCHOVID: The Computer System for Bronchoscopy Laboratory Integrating the CT-Based Bronchoscopy and Transbronchial Needle-Aspiration Biopsy Planning, Virtual Bronchoscopy, Management of the Bronchoscopic Procedures Recordings, Automatic Image-Based Data Retrieval, Artifact and Pathology Detection and Interactive 2D & 3D Visualization. Springer, Heidelberg (2010)
21. ISO/IEC: Information technology – multimedia content description interface. ISO/IEC 15938 (2002)

22. Janowski, L., Suwada, K.: Fast MPEG-7 image features-based automatic recognition of the lesion in the bronchoscopic recordings. In: BRONCHOVID: The Computer System for Bronchoscopy Laboratory Integrating the CT-Based Bronchoscopy and Transbronchial Needle-Aspiration Biopsy Planning, Virtual Bronchoscopy, Management of the Bronchoscopic Procedures Recordings, Automatic Image-Based Data Retrieval, Artifact and Pathology Detection and Interactive 2D & 3D Visualization. Springer, Heidelberg (2010)
23. Pawlik, P.: Application of SIFT image analysis method to support of transbronchial needle-aspiration biopsy. In: BRONCHOVID: The Computer System for Bronchoscopy Laboratory Integrating the CT-Based Bronchoscopy and Transbronchial Needle-Aspiration Biopsy Planning, Virtual Bronchoscopy, Management of the Bronchoscopic Procedures Recordings, Automatic Image-Based Data Retrieval, Artifact and Pathology Detection and Interactive 2D & 3D Visualization. Springer, Heidelberg (2010)
24. Przelaskowski, A., Jóźwiak, R.: Three stage method assisting intrabronchial tumor mass recognition in real bronchoscopy. In: BRONCHOVID: The Computer System for Bronchoscopy Laboratory Integrating the CT-Based Bronchoscopy and Transbronchial Needle-Aspiration Biopsy Planning, Virtual Bronchoscopy, Management of the Bronchoscopic Procedures Recordings, Automatic Image-Based Data Retrieval, Artifact and Pathology Detection and Interactive 2D & 3D Visualization. Springer, Heidelberg (2010)
25. Bradski, G., Kaehler, A.: Learning OpenCV. O'Reilly Media Inc., Sebastopol (2008)
26. Frigo, M., Johnson, S.G.: The design and implementation of FFTW3. Proceedings of the IEEE 93, 216–231 (2005); Special issue on Program Generation, Optimization, and Platform Adaptation

Perception Enhancement of Bronchoscopic Video

Grzegorz Ostrek, Artur Przelaskowski,
Mariusz Duplaga, and Aleksandra Rutczyńska

Abstract. The perception enhancement of bronchovideoscopy examination was the subject of reported study. Proposed methods enrich diagnosis and treatment giving real-time additional view based on following adjusted concepts: contrast enhancement, histogram equalization, sharpening, color correction. Additionally wavelets, edge preserving and morphological filters were involved in the image processing. Wavelet texture extraction and sharpening were considered as the most useful and included into complex system of bronchoscopy storage, review and analysis called "Bronchovid". Extended capabilities of classical white light bronchoscopy which has higher resolution than other autofluorescence and spectroscopy based diagnostic methods can be complementary for them in case of any endobronchial biopsy suspicious findings.

1 Background

Lung cancer is one of most important civilisation and environmental diseases.

It is the most common diagnosed malignant cancer and leading mortality reason across cancerous diseases. Lung cancer account for approximately 30% male and 26% female cancer deaths [1]. Rate of the cancer vary between male and female, across countries worldwide depending on cultural and economic conditions including industrial development. Lack of screening programs and limited social awareness of the problem are some of complex reasons of late lung cancer recognition and high mortality. Knowledge of risk factors such as tobacco use, overweight, low

Grzegorz Ostrek · Artur Przelaskowski · Aleksandra Rutczyńska
Institute of Radioelectronics, Warsaw University of Technology, Nowowiejska 15/19, 00-665 Warszawa, Poland
e-mail: `gostrek,arturp, arachock @ire.pw.edu.pl`

Mariusz Duplaga
Medical College, Jagiellonian University, Grzegorzecka Str. 20, 31-531 Kraków, Poland
e-mail: `mmduplag@cyf-kr.edu.pl`

fruit and vegetable diet, physical inactivity, alcohol use, urban air pollution, radon exposure and passive smoking (involuntary inhalation of tobacco smoke) [2, 3] is essential in prevention and managing disease extension. About 30% of cancers can be prevented by avoiding the mentioned risk factors, additionally early recognition is chance for successful treatment.

Distinction between major carcinomas: *small cell lung carcinoma* (SCLC) and *non-small cell lung carcinoma* (NSCLC) (16% and 80% cancers respectively [4]) is important indication for treatment. Less common SCLC are stronger associated with smoking, gives worse prognosis and often are metastatic while NSCLC (also found in non-smoker patients) usually grow slower .

Last decade came with tremendous development of ideas and systems improving bronchoscopist work and diagnosis conditions. Many ideas are based on pushing to the limits bronchofiberoscopy tools, focused on optical phenomenas, which led to establishing a variety of diagnosis facilities. Introduced storage systems of bronchoscopy examination in medical practice gave opportunity for collaboration between pulmonologists and image processing engineers. Our work was aimed to:

- Extend diagnosis capabilities of classical white light bronchoscopy.
- Conduct test of proposed methods.

Some of techniques which were developed and implemented for bronchoscopy are described below. Bronchoscopic video assessment is demanding task therefore spectrum of diagnostic facilities emerge.

2 Assessment of the Bronchoscopy Image

Bronchoscopy is based on the visual assessment of the tracheobronchial tree made by the physician performing the procedure, usually pulmonologist or thoracic surgeon. The ability of the detection of pathological images and structures is based on his knowledge and experience. The assessment of airways carried out during bronchoscopy includes the appearance of the endoluminal side of the walls of trachea and bronchi, their patency and mobility in the range which depends on the reach of the edoscope. Apart from the classical endoscopy based on viewing the structures available for inspection inside the lumen of tubular organs, in case of bronchoscopy of trachea and bronchi. Techniques focused on improvement of the imaging capacity during endoscopy and increased diagnostic yield in comparison to classical assessment in white light, with most of them used also during bronchoscopy [5], include endoscopy with image enhancement based on optical, digital, optico-digital methods (autofluorescence, narrow band imaging (NBI)), magnified endoscopy based on optical and digital methods and endoscopic microscopy.

2.1 Bronchoscopy with Image Magnification

One of the strategies aiming for better visualisation of mucosa in airways is based on the use of bronchovideoscope yielding image magnification. In such

bronchovideoscope, the image acquired by the charge coupled device (CCD) located in the tip is first magnified by the lens. Images may be magnified 100-110 times in relation to standard images obtained with bronchovideoscopes. This imaging option was used for the search for characteristic pattern of blood vessels occurring in bronchial dysplasia [6]. The option of image magnification was also tested in conjunction with NBI to obtain better visualisation of vessels in the areas of squamos dysplasia in heavy smokers with a high risk of lung cancer [7]. Some authors used magnification bronchoscopy for the assessment of the degree of the increased vasculature in new cases of bronchial asthma [8].

2.2 Narrow Band Imaging

Narrow band imaging (NBI) was introduced with the aim of the improved visualisation of the vasculature and texture of superficial layer of mucosa during endoscopic examination. It is based on the application of narrow band filters and enlightening of the endobronchial tissues with the light representing only narrow band of wavelength. NBI enables the best contrast between vascular structure and surround mucosa. The systems used nowadays use blue light (415 nm) for improved visualisation of vessels situated in superficial layers of the mucosa and green light (540 nm) to emphasize the pattern of vessels in deeper layers of mucosa and in submucosa [9, 10]. Narrow band imaging becomes a routine option in new generation bronchovidescopes which can enhance diagnostic efficiency in detection of precancerous lesions and early cancer in tracheobronchial tree [11]. Another application field is precise assessment of the extent of the neoplastic tissue in the tracheobronchial tree which cannot be fully assessed with white light bronchoscopyi [12].

2.3 Autofluorescence Bronchoscopy

Autofluorescence bronchoscopy uses the source which generates the light of appropriate wavelength to differentiate between precancerous and neoplastic lesions from normal tissue. Dysplasia, carcinoma in situ and cancer of limited invasiveness cannot be usually detected in white light bronchoscopy [13, 14]. Autofluorescence does not require provision of agents increasing tissue fluorescence. Autofluorescence bronchoscopy is applied in screening examination addressed to patients with high risk of lung cancer development. It can be also used in these patients in which cytological examination of sputum yields abnormal results and no evident tumour mass is found in standard white light bronchoscopy. The control of the patients after thoracic surgery for lung cancer may be another indication for autofluorescence bronchoscopy.

2.4 Endobronchial Thermic Measurement

Neoplastic tissue is usually rich in vessels and its temperature may to some extent higher than the temperature of neighbouring normal bronchial mucosa. Such

assumption formed the rationale for attempts of the application of endobronchial temperature measurements for detection of cancerous tissue. Stefanidis et al. used thermographic probe introduced to the working channel of the bronchoscope for the measurements of the temperature of malignant and benign lesion in tracheo-bronchial tree. They published results indicating that threshold temperature difference of $1.05°$ enables differentiation between benign and malignant lesions with sensitivity of 64% and specificity of 91% [15]. The results obtained by another team which used contact thermometer for endobronchial temperature assessment tend to confirm this observation. The difference in temperature between tumor and normal mucosa was on average $1.4°$. [16].

2.5 Spectroscopic Techniques

Current research directions in endoscopic diagnostic are focused on the use of reflectance and diffuse light spectroscopy. The results of first studies indicate that reflectance spectroscopy may increase specificity of autofluorescence bronchoscopy [17, 18]. Furthermore, light scattering spectroscopy is tested for assessment of precancerous lesions [19, 20]. The differentiation between tumor and normal tissue in tracheobrochial tree may be also improved with near-infrared Raman (NIR) spectroscopy. The first ex vivo and in vivo tests seem to yield promising results [21]. Specific value of the NIR spectroscopy may rely on the ability of lowering false positive results of autofluorescence bronchoscopy [22]. The tests of probes enabling NIR spectroscopy during endoscopic examination are continued [23].

2.6 Endoscopic Microscopy

Microscopic assessment during endoscopy is possible with techniques registering reflected photons or photons released in the fluorescence process [24, 25]. Confocal reflection microscopy enables imaging of the tissue with appropriate quality to depth of $30 \mu m$. The use of coherence microscopy may yield images even to depth of $500 \mu m$ but effective resolution in biological environments is lower. The images obtained with fluorescence microscopy depend strongly on the chemical characteristics and structure of tissues [26].

3 Methods of Perception Enhancement

Proposed methods are aimed to give additional display by applying adjusted image analysis and processing methods. Presented procedures could be applied *on-line* (real-time) during examination or *off-line* in case of recording and video data storage. We consider it useful as noticeable perception and image quality enhancement result was obtained. Inability to determine between carcinoma in situ and dysplasia, even equipped with mentioned autofluorescence and spectroscopy methods, still demand searching for suitable methods extending available visualisations for

physician performing procedure. Furthermore desired limiting unnecessary endo-bronchial biopsy is under concern our methods. Combining existing methods is a practised solution [18] commonly accepted by physicians.

3.1 Material

From database containing over 500 bronchoscopic video examinations selected key frame examples of endobronchical tumor (104 lesions) , mucosal infiltration (113 lesion) and carcinoma (7 lesions) were chosen. Medical records with histopatho-logic confirmation suspicious findings were available. Preliminary image prepara-tion and preprocessing steps were found necessary due to acquisition conditions and brnchofiberoscope limitations. Our interest focused on the image analysis and pro-cessing tools and concepts well established and found useful in common video pro-cessing applications. Available sequences obtained from bronchovideoscopy were in digital video DV lossy compression interlacing format.

3.2 Methods

Undesirable loss of image content while bronchoscope tip rapid movement, typi-cal during examination set searching useful deinterlacing methods as first step. In standard view interlacing is not much concern but any artifact or failures produced by deinterlacing were amplified and extracted at following processing steps. Testing flexibility and parameters setting optimization was achieved thanks to VirtualDub (VD) application, which comes with number of community proposed plugins im-plementation and tested solutions. OpenCV [27] advanced image processing library used to tackle images in real-time (RT). VD uses internal system video for Windows (VfW) codecs, reading DV was available through ffdshow[1] VfW encoder interface. Implementation of following deinterlacing methods was examined:

- *mencoder* implementations of Yadiff and ELA algorithms[2];
- *mjpeg tools* aimed low level video acquisition[3];
- *smart deinterlace* VD proposed method[4];
- *area based* another VD plugin[5].

Solutions delivered by mencoder were found useful and real-time optimized Yadiff like implementation was applied to "Bronchovid" system.

Conducted by physicians and engineers preliminary test selected following ready for use plugins giving noticeable improvement of perception conditions:

---

[1] http://ffdshow-tryout.sourceforge.net/

[2] http://www.mplayerhq.hu/

[3] http://mjpeg.sourceforge.net/

[4] http://neuron2.net/smart/smart.html

[5] http://www.guthspot.se/video/index.htm

- *MSU Smart Sharpen 1.4* MSU Graphics & Media Lab idea based on unsharp mask[6];
- *MSU Smart Brightness and Contrast* another idea from the same group[7];
- *sharpen* internal VD plugin;
- *Color Mill (2.1)* of many useful color transformations[8];
- *Color Equalizer v.1.1* channel amplification and offset due to $C = A * C + O$ formula [9];
- *window histogram equalizer* plugin implementation[10];
- *brightness-contrast-gamma* sample implementation[11];
- *morphological* OpenCV based erode filter[12].

Processing steps

Proposed processing methods were involved in following scheme:

1. colorspace conversion from RGB to YUV or YCbCr,
2. processing luminance composite,

   - contrast limited adaptive histogram equalization;
   - wavelets analysis denoising and contrast enhancement;
   - morphological and edge preserving filters;

3. back to RGB colorspace

Adjusted methods

Promising results were achieved with contrast limited adaptive histogram equalization (CLAHE) [28, 29]. Implementation suitable for real-time sequences in VLSI technique was also proposed in [30]. Egde preserving denoising filters like adaptive partial averaging filter (APAF) [31] were tested. Computational complexity and slight effects didn't proved usability found in other medical applications. Erode filter from OpenCV implementation was also considered in preliminary test, but rejected due to enhancing artifacts caused by fiberoscope construction structure.

Wavelets denoising and contrast enhancement was introduced giving promising results. From set of orthogonal, biorthogonal and non-perfect orthogonal wavelet

---

[6] http://graphics.cs.msu.ru/en/science/research/videoqualityincreasing/smartsharpen

[7] http://www-koi.compression.ru/video/smart_contrast/index_en.html

[8] http://fdump.narod.ru/rgb.htm

[9] http://home.mit.bme.hu/ bako/filter/filter.html

[10] http://neuron2.net/winhistogram.html

[11] http://emiliano.deepabyss.org/

[12] http://www.crim.ca/en/r-d/vision_imagerie/telecharger.html

basis biorthogonal Antonin filter[13] followed by MiddleEnhance wavelets coeffi-
cients modification rule yield most interesting results.

MiddleEnhance methods parameters are $range1, range2$ (determining lower and
upper modification levels) and p (powerlaw parameter), modification rule follows

1. Find difference d between minimal (min) and maximal coefficient in subband,
   and calculate c and m with respect to minimal coefficient as: $c = min + range1 \cdot d, m = min + range2 \cdot d$.
2. Calculate multiplier $mul = (c/m)^p$.
3. If subband coefficient x satisfy $|x| < c$ then $x = x \cdot mul$
   else if $|x| < m$ then $x = x \cdot (m/|x|)^p$.

Some problems remain not solved because of computational and time complexity
or were not marked as urgent problems by physicians. One of them is removing
specular reflections, some interesting approach to the problem can be find in [32,
33]. Additionally motion blur compensation techniques are recently proposed and
we predict their usefulness in improvement of traditional bronchoscopy value [34,
35, 36].

4 Experimental Study

Preliminary subjective tests were performed to verify the usability of proposed
methods. Under concern of reviewers were color modifications clarity, pattern
extraction or preserving (overall additional value feel and look). 8 observers par-
ticipated in the experiment: 2 endoscopists, medical imaging professionals and bio-
engineering students assessed prepared images of 8 various bronchial pathologies.
Each example was processed by 8 chosen methods with experimentally set parame-
ter values: windowed histogram equalization, MSU Smart Sharpen, CLAHE with 3
values of normalized cliplimit (C1=3,C2=5,C3=8) parameter and Antonini wavelet
analysed followed by MiddleEnhance with 3 powerlaw values (w1=0.42,w2=0.53,
w3=0.63) while other parameters were fixed ($range1 = 0.1$ and $range2 = 0.9$). One
of test's set examples reviewed in experiment is presented in Fig. 1. Assessment
scale took scores form -3 to 3 where:

-3 not acceptable worsen perception;
-2 worsen perception;
-1 noticeable worsen perception;
  0 no enhancement or worsening of perception;
  1 noticeable enhanced perception;

---

[13] Kernel defined by
$$\tilde{h} = \begin{bmatrix} 0.03782845550699535 & -0.02384946501937986 & -0.1106244044184226 \ldots \\ 0.3774028556126536 & 0.8526986790094022 & 0.3774028556126537 \ldots \\ -0.1106244044184226 & -0.02384946501937986 & 0.03.782845550699535 \end{bmatrix}$$
$$\tilde{g} = \begin{bmatrix} -0.06453888262893856 & -0.04068941760955867 & 0.4180922732222124 \ldots \\ 0.7884856164056651 & 0.4180922732222124 & -0.04068941760955867 \ldots \\ -0.06453888262893856 \end{bmatrix}$$

Fig. 1 Example test set presented in the experiment. Left corner original image followed by windowed histogram equalization, MSU Smart Sharpen, CLAHE enhanced (middle row) and wavelets enhanced (bottom row).

2 enhanced perception;
3 superb perception enhancement.

Table 1 Perception enhancement methods assessment results. Methods names where C1,C2,C3 are CLAHE derived and w1, w2, w3 are wavelet based methods with respect to parameters order mentioned in the text.

Observers	Method	MSU S.S.	w.h.e	C1	C2	C3	w1	w2	w3
Endoscopists	Mean score	1.94	-1.81	0.16	-1.04	-1.59	0.66	1.44	1.41
	Std. dev.	0.08	0.44	0.66	0.05	0.47	0.04	0.08	0.22
Engineers	Mean score	-0.10	-0.44	1.58	-0.42	-1.33	1.40	1.52	1.47
	Std. dev.	1.96	1.42	0.54	1.81	1.76	0.55	0.99	1.46

Some other examples of enhancement were presented in Fig. 2 and Fig. 3.

According to obtained results in both observers groups presented methods yield above noticeable perception enhancement. Endoscopists group found MSU Smart
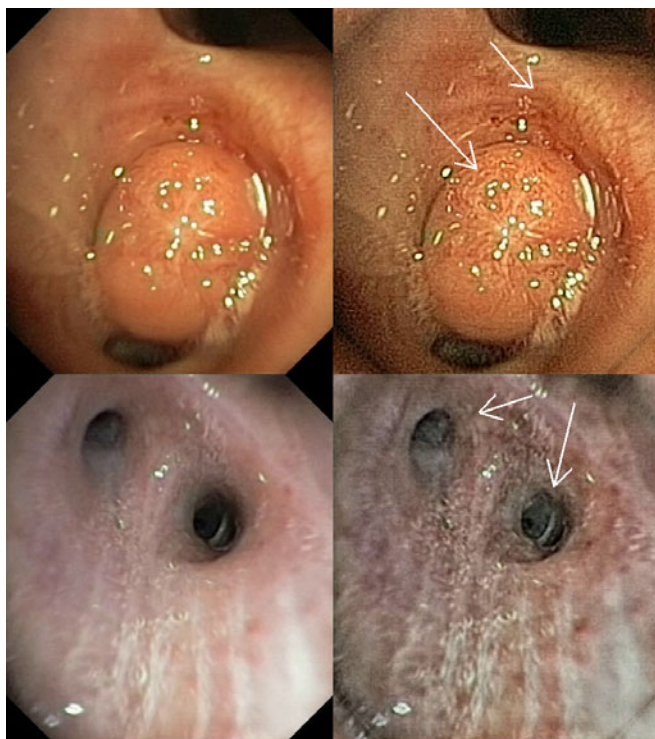
Fig. 2 Selected frames processing examples. Left hand side are original, right hand side processed with windowed MSU Smart Sharpen (top) and wavelet based w3 (bottom). Noticed perception enhancement marked by arrows.

Sharpen processing results the most helpful. Level of details and information extracted by the method was not understood and appreciated by engineers. All reviewers found wavelet based methods useful where highest ratings got w2 method while windowed histogram equalization achieved poor scores. CLAHE based method C2 was found useful by engineers getting highest overall score in this group. The method was not so much appreciated by endoscopists. Frame based examples of processing results yield view with some additional information based on digital video content.

Edge and texture extraction were achieved by CLAHE and wavelets based methods. Carcinoma changes occur with mucosa affections so indirect signs may be hidden in some pattern therefore extracting is expected by physicians. Wavelets enhancement gave *shadow* areas better visible in endoscopists opinions. Physicians marked MSU proposed Smart Sharpen and color correction facilities as most promising.
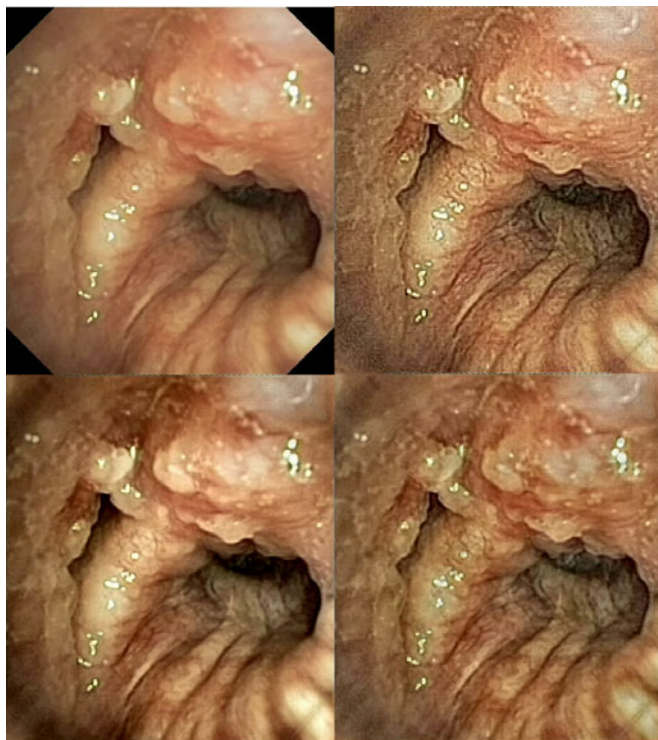
Fig. 3 Selected from experiment frame processing examples. Original frame in upper left corner, followed by MSU Smart Sharpen, C2 and w3 (bottom row).

5 Conclusions

Archiving procedures in bronchovideoscopy gives wider field for collaboration between pulmonologists and image processing engineers. Reported results yield second look at traditional bronchoscopy procedure enhancing it capabilities with low cost computing machines need and enrich diagnostic procedures. Our result can be easily reproduced and improved due to open development ideas. Video can be processed *on-line* while frame capture is available or *off-line* on archived sequences. Problem of human color perception and adjusting bronchoscope display capabilities should be considered in connection with existing laboratory equipment. As number of methods can be combined in different ways, exhausting subjective test should be conducted covering various bronchoscopy stations vendors in multicenter clinical trial to approve usability of proposed methods.

References

1. Jemal, A., Siegel, R., Ward, E., et al.: Cancer Statistics. CA Cancer J. Clin. (2009), doi: 10.3322/caac.20006
2. Danaei, G., Van der Hoorn, S., Lopez, A.D., et al.: Causes of cancer in the world: comparative risk assessment of nine behavioural and environmental risk factors. Lancet 366(9499), 1784–1793 (2005)
3. Alberg, A.J., Samet, J.M.: Epidemiology of Lung Cancer 123(S1), 21S–49S (2003)
4. Travis, W.D., Travis, L.B., Devesa, S.S.: Lung Cancer 75(S1), 191S–202S (1995)
5. Tajiri, H.: Advances in Endoscopic Imaging and Diagnosis: Toward Molecular Imaging in New Challenges in Gastrointestinal Endoscopy, pp. 29–39. Springer, Heidelberg (2008)
6. Shibuya, K., Hoshimo, H., Chiyo, M., et al.: Subepithelial vascular patterns in bronchial dysplasias using a high magnification bronchovideoscope. Thorax 57, 902–907 (2002)
7. Shibuya, K., Hoshino, H., Chiyo, M., et al.: High magnification bronchovideoscopy combined wiht narrow band imaging could detect capillary loops of angiogenic squamous dysplasia in heavy smokers at high risk for lung cancer. Thorax 58, 989–995 (2003)
8. Tanaka, H., Yamada, G., Saikai, T., et al.: Increased airway vascularity in newly diagnosed asthma using a high-magnification bronchovideoscope. Am. J. Respir. Crit. Care. Med. 168, 1495–1499 (2003)
9. Gono, K., Obi, T., Yamaguchi, M., et al.: Appearance of enhanced tissue features in narrow-band endoscopic imaging. J. Biomed. Opt. 9, 568–577 (2004)
10. Kuznetsov, K., Lambert, R., Rey, J.F.: Narrow-band imaging: potential nad limitations. Endoscopy 38, 76–81 (2006)
11. Vincent, B.D., Fraig, M., Silvestri, G.A.: A pilot study of narrow-band imaging compared to white light bronchoscopy for evaluation of normal airways and premalignant and malignant airways diseases. Chest 131, 1794–1799 (2007)
12. Zaric, B., Becker, H.D., Perin, B., et al.: Narrow band imaging videobronchoscopy improves assessment of lung cancer extension and influence therapeutic strategy. Jap. J. Clin. Oncol., Advance Access (2009)
13. Lam, S., MacAulay, C., Palcic, B.: Detection and localization of early lung cancer by imaging techniques. Chest 103(suppl.),12S–13S (1993)
14. Shibuya, K., Fujisawa, T., Hoshino, H., et al.: Fluorescence bronchoscopy in the detection of preinvasive bronchial lesions in patients with sputum cytology suspicious or positive for malignancy. Lung Cancer 32, 19–25 (2001)
15. Stefanadis, C., Chrysohou, C., Panagiotakos, D.B., et al.: Temperature differences are associated with malignancy on lung lesions: a clinical study. BMC Cancer 3, 1–5 (2003)
16. Votruba, J., Bruha, T.: Measurement of Endobronchial Temperature in the Diagnosis of Lung Cancer. J. Bronchol. 12, 6–8 (2005)
17. Bard, M.P.L., Amelink, A., Skurichina, M., et al.: Improving the specificity of fluorescence bronchoscopy for the analysis of neoplastic lesions of the bronchial tree by combination with optical spectroscopy: preliminary communication. Lung Cancer 47, 41–47 (2005)
18. Bard, P.L.M., Amelink, A., Skurichina, M., et al.: Optical spectroscopy for the classification of malignant lesions of the bornchial tree. Chest 129, 995–1001 (2006)
19. Biglio, I.J., Bown, S.G.: Spectroscopic sensing of cancer and cancer therapy. Cancer Biol. Ther. 3, 259–267 (2004)
20. Backman, V., Wallace, M.B., Perelman, L.T., et al.: Detection of preinvasive cancer cells. Nature 406, 35–36 (2000)

21. Huang, Z., McWilliams, A., Lui, H., et al.: Near-infrared Rama spectroscopy for optical diagnosis of lung cancer. Intl. J. Cancer 107, 1047–1052 (2003)
22. Zeng, H., McWilliams, A., Lam, S.: Optical spectroscopy and imaging for early lung cancer detection: a review. Photodiagn. Photodynamic. Ther. 1, 111–122 (2004)
23. Short, M.A., Lam, S., McWilliams, A., et al.: Development and preliminary results of an endoscopic Raman probe for potential in vivo diagnosis of lung cancers. Optics Letters 33, 711–713 (2008)
24. George, M.: Optical methods and sensors for in situ histology surgery and endoscopy. Min. Invas. Ther. & Allied Technol. 13, 95–104 (2004)
25. Koenig, F., Knittel, J., Stepp, H.: TechSight: diagnosing cancer in vivo. Science 291 (2001)
26. Thiverville, L., Moreno-Swirc, S., Vercauteren, T., et al.: In vivo Imaging of the bronchial wall microstructure using fibered confocal fluorescence Microscopy. Am. J. Respir. Crit. Care. Med. 175, 22–31 (2007)
27. Bradski, G., Kaehler, A.: Learning OpenCV: Computer Vision with the OpenCV Library. O'Reilly, Cambridge (2008)
28. Pizer, S.M., Amburn, E.P., Austin, J.D., et al.: Adaptive Histogram Equalization and its Variations. Computer Vision, Graphics and Image Processing 39, 355–368 (1987)
29. Zuiderveld, K.: Contrast limited adaptive histogram equalization, Graphics gems IV, pp. 474–485. Academic Press Professional, Inc., San Diego (1994)
30. Reza, A.M.: Realization of the Contrast Limited Adaptive Histogram Equalization (CLAHE) for Real-Time Image Enhancement. Journal of VLSI Signal Processing 38, 35–44 (2004)
31. Takahashi, N., Lee, Y., Tsai, D.-Y., Ishii, K.: Novel noise reduction filter for improving visibility of early computed tomography signs of hyperacute stroke: evaluation of the filter's performance preliminary clinical experience. Radiation Medicine (2007), doi: 10.1007/s11604-007-0129-3
32. Stehle, T.: Removal of Specular Reflections in Endoscopic Images. Acta Polytechnica 46(4), 32–36 (2006)
33. Ortiz, F.: Real-Time Elimination of Brightness in Color Images by MS Diagram and Mathematical Morphology. In: Kropatsch, W.G., Kampel, M., Hanbury, A. (eds.) CAIP 2007. LNCS, vol. 4673, pp. 458–465. Springer, Heidelberg (2007)
34. Caiy, J.-F., Jiz, H., Liuy, C., Shen, Z.: Blind motion deblurring from a single image using sparse approximation. In: CVPR: IEEE Computer Society Conference on Computer Vision and Pattern Recognition (2009), http://www.math.nus.edu.sg/~matzuows/blind_deblurring3.pdf (Cited March 8, 2010)
35. Cai, J.-F., Ji, H., Liu, C., Shen, Z.: Building text features for object image classification. Journal of Computational Physics 228, 5057–5071 (2009)
36. Fergus, R., Singh, B., Hertzmann, A., Roweis, S., Freeman, W.: Removing camera shake from a single photograph. ACM Transactions on Graphics 25(3), 787–794 (2006), http://cs.nyu.edu/~fergus/papers/deblur_fergus.pdf (Cited March 8, 2010)

Analysis of Magnetic Field Distribution and Mechanical Vibration of Magnetic Field Exciter under Different Voltage Supply

Tomasz Trawiński, Marcin Szczygieł,
Joanna Wyszkowska, and Krzysztof Kluszczyński

Abstract. The aim of the study performed in the Department of Biophysics of Nicolaus Copernicus University is to investigate the effect of extremely low frequency electromagnetic field (ELF-EMF) exposure on animal nervous system function. American cockroach (Periplaneta americana) serves as a model in experiments. Insects are placed into the chamber inside the coil (electromagnetic field exciter) designed and manufactured by „Elektronika i Elektromedycyna Sp. J.". Before starting the exposure it is necessary to determine: (1) what kind of field is applied, (2) the parameters of exposure and (3) the area of homogenous field. Only well established set-up characteristics can provide correct and comparable conditions of exposure to EMF. As well as, before starting the observation of the EMF influence on insects it is necessary to exclude factors which are associated with EMF exposure (such as temperature changes and vibrations) and could affect the organism function (behavior of animal). Especially cockroaches are very sensitive to vibrations and mechanical disturbances. Thermal conditions during the whole period of EMF exposure have been established earlier 1. The research that has been conducted by the authors so far included methodology of measurements of mechanical vibration spectrum and magnetic field distribution in interior part of electromagnetic field exciter on insects putted into research chamber. The vibration of electromagnetic field exciter occurs due to current flow by the exciter windings 2,3, and they acts on it in radial and longitudinal direction. In this paper the vibration and field distribution of field exciter measurements results are presented.

Tomasz Trawiński · Marcin Szczygieł · Krzysztof Kluszczyński
Silesian University of Technology, Electrical Faculty, Department of Mechatronics,
Krzywoustego 2 st., 44-100 Gliwice, Poland
e-mail: tomasz.trawinski@polsl.pl, marcin.szczygiel@polsl.pl,
krzysztof.kluszczynski@polsl.pl

Joanna Wyszkowska
Nicolaus Copernicus University, Department of Biophysics, Gagarina 9 Street, 87-100 Toruń,
Poland
e-mail: jwyszk@umk.pl

1   Introduction

Effect of electromagnetic field (EMF) on organisms, first of all on human being, is a trendy subject mainly because of wide cell phone utilization. In highly developed countries the intense increase of production of extremely low frequency electromagnetic field (ELF - EMF) is observed; all home appliances are the source of such EM radiation however this problem seems to be less popular. Hundreds of papers, less or more scientific, appeared describing effect of ELF electromagnetic energy on different physiological functions however there is no unambiguous conclusions. And finally we don't know is it irrational to sleep near electric socket or ganglion of electric cables or not. Biological effects of EMF exposure can be observed on molecular, cellular and organ level as well as animal and human behavior can be studied. Nervous system "is driving" the whole organism function and each variation in its activity can influence different life's processes [1].

Certainly nervous system can serve as a highly sensitive *receptor* of EMF influence. Changes in different parameters characterizing nervous system activity have been observed under ELF- EMF exposure however their mechanisms are still unknown [4]. The aim of our study is to better determine the effect of ELF EMF on nervous system function. We decided to perform complex study on insect nervous system. American cockroach (Periplaneta americana) has been selected due to several reasons: (1) conclusions are easier when experiments are performed on more simple models; (2) american cockroach is known as a good model in neurobiological studies; (3) cockroach nervous system is relatively large and well accessible and several electrophysiological techniques can be applied to observe its function; (4) physiology of cockroach is rather well known and we can suspect that this knowledge can help us to explain our observations. One of the factor which can influence the success of the studies is to obtain stable, well defined conditions of exposure to EMF. Special coil (electromagnetic field exciter) designed and manufactured by Elektronika i Elektromedycyna Sp. J and we intend to use this coil in all our experiments. It's size has been adjusted to experiments with 2 or 3 insects. EMF strength can be regulated. Insects are placed in the coil in glass chamber with aeration and with insect movement sensors. Proper experiments must be preceded by studies in which it is necessary to determine: (1) what kind of field is applied, (2) the parameters of exposure and (3) the area of homogenous field. Only well established set-up characteristics can provide correct and comparable conditions of exposure to EMF. Addtionally, before starting the observation of the EMF influence on insects it is necessary to exclude factors which are associated with EMF exposure (such as temperature changes and vibrations) and could also affect the organism function. Especially cockroaches are very sensitive to vibrations and mechanical disturbances. Thermal conditions during the whole period of EMF exposure have been already established [1, 5]. In the paper the methodology and results of measurements of mechanical vibration spectrum and magnetic field distribution in interior part of electromagnetic field exciter are presented. The vibrations of electromagnetic field exciter occurs due to current flow by the exciter windings, and they acts in radial and longitudinal direction.

2 Scope of the Work and Laboratory Equipment

The investigations of electromagnetic field exciter were performed into two main steps connected with its mathematical model formulation and comparison of simulated and measured results. Furthermore it was important to measure on real object the relation between value of voltage supply and generated magnetic flux density into its interior part, as well determination of the space magnetic flux density distribution. And finally the vibration spectrum on real exciter was measured.

The experimental stage for vibration and for field distribution measurements consists of two measuring Keyence LC-2420 [2, 3] laser displacement heads, magnetic field sensor, heavy inertial masses, stiff supporting frame and elastic suspension of magnetic field exciter. The laboratory stage is in Fig. 1 presented. The displacement measuring resolution of laser heads was 10 nm (nanometers) and the magnetic field sensor resolution was 0.1 mT (militesla).
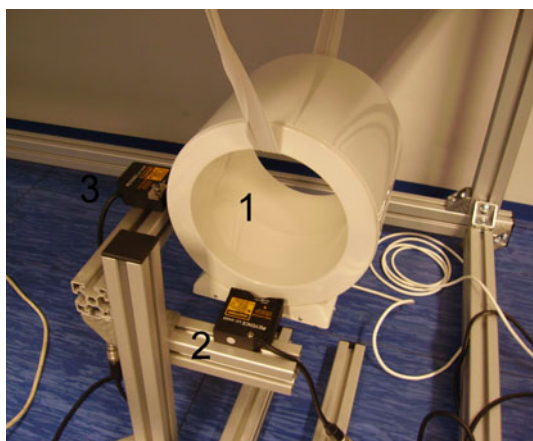
Fig. 1 Most important part of laboratory stage: (1) - field exciter, (2) - laser head for longitudinal displacement measurements, (3) - laser head for radial displacement measurement

3 Mathematical Model Formulation of Field Exciter and Results of Simulation

The mathematical model of electromagnetic field exciter was implemented in Comsol Multiphisics program, which allows for electromagnetic field analysis using finite element methods (FEM). The discredited geometry of exciter model consisted with 56000 degrees of freedom in axial symmetry mode and is presented in Fig. 2.

The main aims of finite element analysis was determination of space distribution of magnetic flux density and determination the homogenous space with magnetic field flux density equaling or grater than values of B1= 0.7 mT, B2= 1 mT and B3= 7 mT. The calculated homogenous spaces are in Fig. 3 presented.

Fig. 2 Generated FEM
mesh of electromagnetic
field exciter in axial symme-
try mode
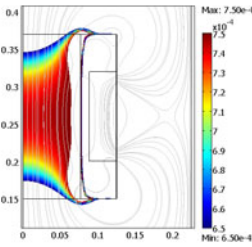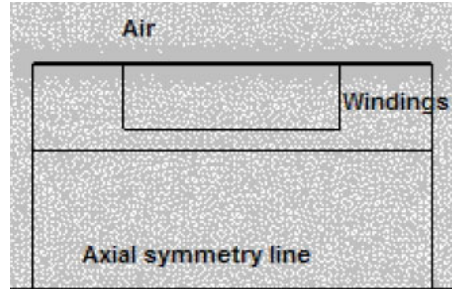
(a)
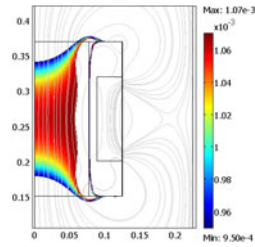
(b)
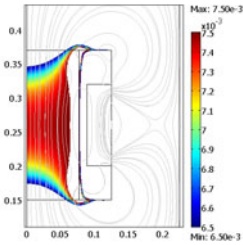
(c)

Fig. 3 Electromagnetic field calculated homogenous spaces: a) 0,7 mT, b)1 mT, c) 7mT

   Basing on simulation results of space field distribution two homogenous spaces
was determined, and they may be approximated by cylinder spaces. First cylinder
space with magnetic flux densities lower than 2 mT and second cylinder space with
values grater than 2 mT, both spaces are presented in Fig. 4. Fig. 4 presents isomet-
ric, transparent view of exciter and position of homogenous cylinder spaces. The
geometrical dimensions of cylinder spaces are as follows: first cylinder space - 80
mm high and 130 mm in diameter, second cylinder space - 70 mm high and 130 mm
in diameter.

Fig. 4 Electromagnetic field exciter with homogenous spacer approximated by cylinders. (1) - exciter frame, (2) - cylinder space with B < 2 mT, (3) - cylinder space with B > 2 mT

Calculated value of magnetic flux density norm distribution (under 20V, 30 V and 210 supply) along longitudinal symmetry axis of exciter cylinder is presented in Fig. 5(a)-5(c).
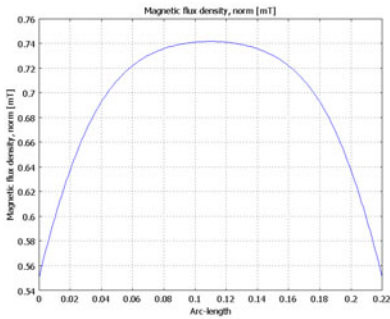
(a) 20V, 50 Hz supply
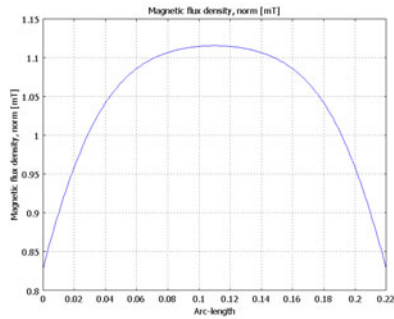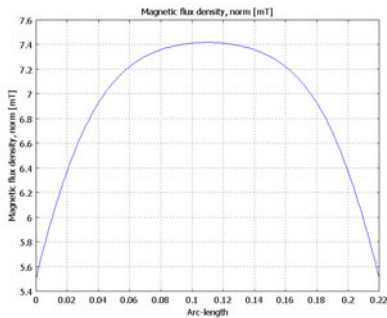
(b) 30V, 50 Hz supply

(c) 210V, 50 Hz supply

Fig. 5 Calculated magnetic flux density norm on longitudinal symmetry axis

Calculated value of magnetic flux density norm distribution (under 20V, 30 V and 210 supply) in radial direction (at half high of exciter frame)) is presented in Fig. 6(a)-6(c).

(a) 20 V, 50 Hz supply

(b) 30 V, 50 Hz supply

(c) 210 V, 50 Hz supply
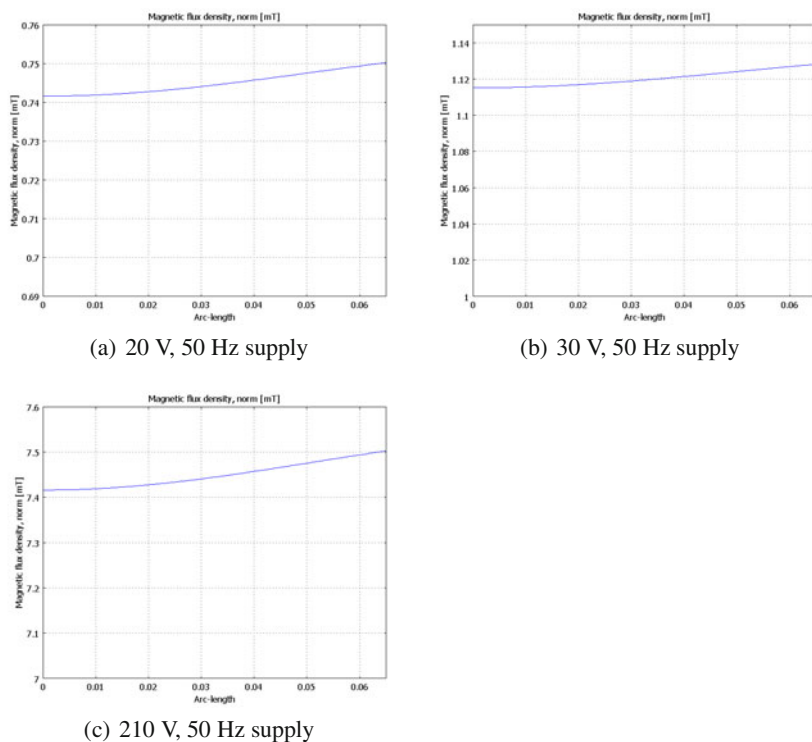
Fig. 6 Calculated magnetic flux density norm in radial direction

4   Measurement Results of Real Exciter

In Fig. 7(a)–7(c) the measured value of magnetic flux density Bz components along the longitudinal axis and under different voltage supply (20,30 and 210 V) are presented.

In Fig. 8(a)–8(c) the measured value of magnetic flux density Bz components in radial direction (at half high of exciter frame) and under different voltage supply (20,30 and 210 V) are presented.

In Fig. 9 is presented relation described the value of generated magnetic flux density in central part of exciter versus supply voltage. This characteristic is very convenient because shows what the value of voltage should be applied to exciter terminals to get desired value of magnetic field.

5   Results of Vibration Measurement

The final step was related with vibration measurements of magnetic field exciter frame in longitudinal and radial direction. The measurements were made using two laser displacement head - one for radial displacement measurement and the
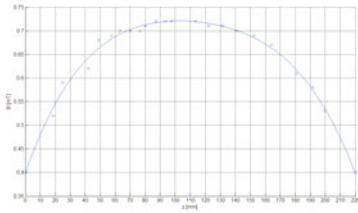
(a) 20 V, 50 Hz supply
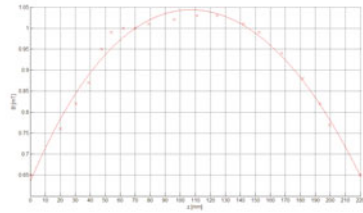
(b) 30 V, 50 Hz supply
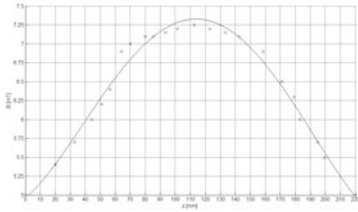
(c) 210 V, 50 Hz supply

Fig. 7 Measured magnetic flux density Bz component on longitudinal symmetry axis
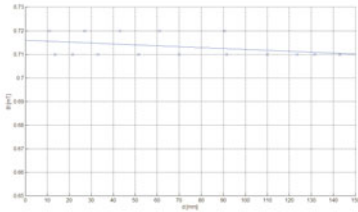
(a) 20 V, 50 Hz supply
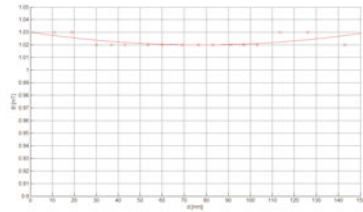
(b) 30 V, 50 Hz supply
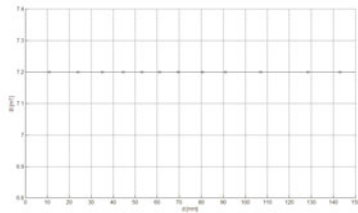
(c) 210 V, 50 Hz supply

Fig. 8 easured magnetic flux density Bz component in radial direction
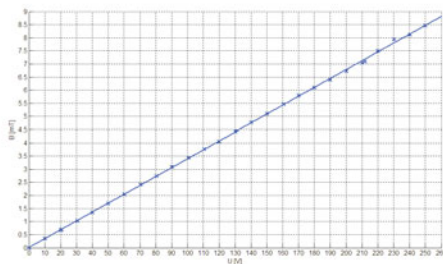
Fig. 9 Magnetic flux density Bz component versus supply voltage

second for longitudinal displacement. The results of experiment are in Fig. 10(a)-10(f) presented.

6 Summary

Taking into consideration results of vibration presented in Fig. 10(a)–10(f), it is easy to observe that under voltage supply with frequency equaling 50 Hz in vibration spectrum appears the vibration harmonics equaling double value of supply frequency - 100 Hz. Also the exciter frame shakes with frequency of supply voltage. The summarized vibrations amplitudes are presented in Table 1. The results related with B equals zero shows the bias vibration spectrum, it is mean that magnetic field exciter shakes upon external disturbances related for example with building motion, and us a results in the vibration spectrum are present harmonics with frequencies equals: 50, 100 and 150 Hz. The vibration spectrum do not change in significant way, when exciter excite the magnetic field on level 1 mT (in its interior part), in both directions - radial and longitudinal. Some changes are observed when magnetic flux density equal 7 mT is excited, and then it results in increase the vibration in radial direction. But only vibration harmonics at frequency 50 Hz increase with significant way. Such behavior of magnetic field exciter is related with the way of his suspension on laboratory stage by the means of elastic belt, which gives different stiffness and vibration dumping for both directions - highest in longitudinal direction. The magnetic fields exciter may be used in researches process of different organisms (like cockroaches), because it have relatively high homogenous space of magnetic flux densities higher than 2 mT. The magnetic field exciter may excite the vibration of laboratory stages at frequencies 50 and 100 Hz. Described above electromagnetic fields exciter may be used in investigating the influence of electromagnetic field on the animals. It allows to obtain good uniformity of the electromagnetic field inside in its internal part and the comparable EMF exposure conditions for the different experimental series. The dimension of the homogenous EMF area permits to perform the experiments also on animals larger than insects such as for example mice. The estimated own vibrations of magnetic field exciter may induce the vibration of laboratory stages at frequencies 50 and 100 Hz. In the further study it is planed to assess in details the vibrations in experimental setup during EMF
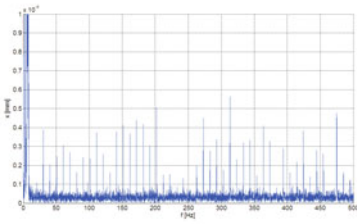
(a) Without supply (longitudinal direction)
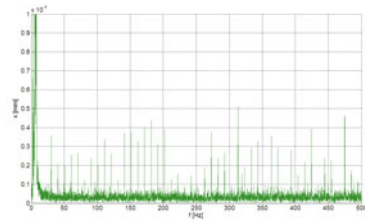
(b) With 30 V (50 Hz) supply (longitudinal direction)
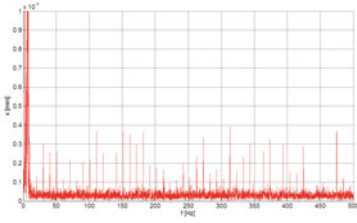
(c) With 210 V (50 Hz) supply (longitudinal direction)
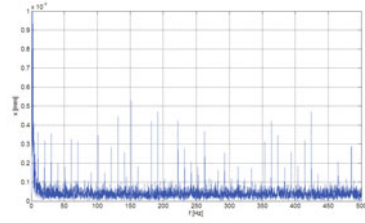
(d) Without supply (radial direction)
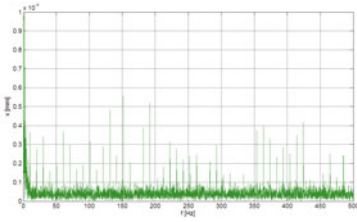
(e) With 30V (50 Hz) supply (radial direction)
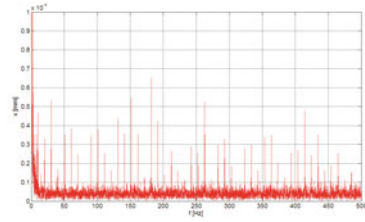
(f) With 210V (50 Hz) supply (radial direction)

Fig. 10 Amplitude vibration frequency spectrum of magnetic field exciter

exposure. It is necessary for future studies to precise in what extent the vibrations will transfer from the coil to the chamber with insects or another animal. In such case we will be able to determine the participation of different factors on animal behavior.

Table 1 The summarized vibrations amplitudes (frequency of voltage supply: 50 Hz)

Flux density	B = 0mT		
Vibration frequency of exciter	**50 Hz**	**100 Hz**	**150 Hz**
Amplitude of longitudinal vibration	245 nm	235 nm	412 nm
Amplitude of radial vibration	179 nm	340 nm	530 nm
Flux density	**B = 1mT**		
Vibration frequency of exciter	**50 Hz**	**100 Hz**	**150 Hz**
Amplitude of longitudinal vibration	195 nm	202 nm	376 nm
Amplitude of radial vibration	186 nm	318 nm	558 nm
Flux density	**B = 7mT**		
Vibration frequency of exciter	**50 Hz**	**100 Hz**	**150 Hz**
Amplitude of longitudinal vibration	260 nm	217 nm	368 nm
Amplitude of radial vibration	352 nm	380 nm	545 nm

References

1. Wyszkowska, J., Stankiewicz, M., Krawczyk, A.: Examination of nervous system exposed to electromagnetic field on the example of cockroach (Periplaneta americana). Electrical Review, R 82, 66–67 (2006/5)
2. Trawinski, T., Wyszkowska, J., Szczygieł, M.: Vibration measurement of chamber under influence of alternating magnetic field with the help of laser displacement meters. Elektromagnetyczne Techniki w Ochronie Zdrowia, ch. 8, 83–95 (2007) (in Polish), ISDN 978-83-7373-013-7
3. Trawinski, T., Szczygieł, M., Wyszkowska, J.: Vibration measurement of chamber under influence of alternating magnetic field, vol. 3, pp. 137–146. Scientific Papers of Silesian University of Technology, Elektryka (2007) (in Polish)
4. Wyszkowska, J., Stankiewicz, M.: Extremely low frequecy electromagnetic field and nervous system - review of recent results. Electrical Review 12, 170–173 (2009/12) (in Polish), ISSN 0033-2097
5. Wyszkowska, J., Stankiewicz, M., Krawczyk, A., Zyss, T.: Thermal aspects in the studies on the electromagnetic field influence on insect nervous system function, Bioelektromagnetyzm - teoria i praktyka, Centralny Instytut Ochrony Pracy - Panstwowy Instytut Badawczy, Warszawa, pp.11–22 (2006) (in Polish), ISBN 83-7373-112-1

Author Index